

AN EXPERIMENTAL CHARACTERIZATION OF DAMPING PROPERTIES OF THERMAL BARRIER COATINGS AT ELEVATED TEMPERATURES

DISSERTATION

Oliver T. Easterday, Capt, USAF
AFIT/DS/ENY/11-17

DEPARTMENT OF THE AIR FORCE
AIR UNIVERSITY

AIR FORCE INSTITUTE OF TECHNOLOGY

Wright-Patterson Air Force Base, Ohio

APPROVED FOR PUBLIC RELEASE; DISTRIBUTION UNLIMITED

The views expressed in this dissertation are those of the author and do not reflect the official policy or position of the United States Air Force, Department of Defense, or the United States Government. This material is declared a work of the U.S. Government and is not subject to copyright protection in the United States.

AFIT/DS/ENY/11-17

AN EXPERIMENTAL CHARACTERIZATION OF DAMPING PROPERTIES OF THERMAL BARRIER COATINGS AT ELEVATED TEMPERATURES

DISSERTATION

Presented to the Faculty

Graduate School of Engineering and Management

Air Force Institute of Technology

Air University

Air Education and Training Command

In Partial Fulfillment of the Requirements for the

Degree of Doctor of Philosophy

Oliver T. Easterday, B.S.M.E., M.S.M.E.

Capt, USAF

March 2011

APPROVED FOR PUBLIC RELEASE; DISTRIBUTION UNLIMITED.

AFIT/DS/ENY/11-17

AN EXPERIMENTAL CHARACTERIZATION OF THE MECHANICAL PROPERTIES OF THERMAL BARRIER COATINGS AT ELEVATED TEMPERATURES

Oliver T. Easterday, B.S.M.E., M.S.M.E.
Capt, USAF

Approved:

/SIGNED/	16 Dec 2010
Dr. Anthony N. Palazotto Dissertation Advisor	date
/SIGNED/	16 Dec 2010
Dr. William P. Baker Committee Member	date
/SIGNED/	16 Dec 2010
Lt. Col. Richard Branam Committee Member	date
/SIGNED/	16 Dec 2010
Dr. Tommy George Committee Member	date

Accepted:

/SIGNED/	27 Jan 2011
M. U. Thomas, PhD Dean, Graduate School of Engineering and Management	date

Abstract

Modern gas turbine engines have routinely utilized thermal barrier coatings for the past three decades to coax greater thermodynamic efficiency out of jet engines. In service, it has been noted that these ceramic materials are also effective at suppressing high cycle fatigue in the engine components, increasing their respective fatigue life. Recent efforts have been made to mechanically characterize these materials; this has been a challenge as they are thin coatings, prone to history effects, and are materially nonlinear. Refinement of the apparatus have occurred and it is now desired to characterize them across a range of likely service temperatures.

A free-free beam apparatus has been adapted to accomplish this. Important to achieving viable results is the design, analysis, and experimental validation of the chamber in regards to the free-free specimen being heat-able, modally detuned and free-hanging, and the preservation of a non-contacting excitation method. Critical to success is ensuring a near-isothermal heated beam specimen. After successful validation and calibration of the chamber, a common thermal barrier coating, 8-YSZ, was tested, primarily using the free-decay, logarithmic decrement method, using the chamber from 70-900degF. Materially non-linear behavior was observed and findings of material storage modulus and loss coefficient that are consistent with previous studies were obtained. The chamber was also used to characterize the bare metal beam blanks and bond-coat only specimens. The apparatus was found to be sensitive when determining the storage modulus and damping, more so than the baseline configuration. This was due to changes in design to proof it against high temperature. Resulting, it clearly characterized the anisotropic modulus of titanium and determined that bond coating had a negligible contribution to the beam system. Design life criteria with the properties of the coating could now be adopted across a range of temperatures.

Table of Contents Page

1. Introduction....1
1.1. Background....7
1.2. Overview....7
1.3. Thermal Barrier Coating....9
1.3.1. Anatomy of a TBC....9
1.3.2. Material Systems/Composition....12
1.3.3. Application Processes....14
1.3.4. Strain History Accumulation....17
1.3.5. Bond Coating....18
1.4. Previous Work - Chronological Summary....20
1.4.1. Experimental Highlights....54
1.4.2. Numerical Highlights (Structural Dynamics/FEA)....54
1.4.3. Analytical Highlights....58
1.4.3.1. Beam Isothermality....60
1.5. Eclectic Vacuum Chamber Techniques....61
1.6. High Stark Number in Vacuum....63
1.7. Error Analysis Conventions....64
1.8. Objectives....67
2. Design of the Test Chamber and Surrounding Apparatus - Theory....77
2.1. Heat Transfer Theory of Chamber (Method of Heating)....78
2.1.1. Motivation and Isothermal Beam as a Requirement....80
2.1.2. Decoupled Analysis....82
2.2. The Current System and the Conceptual Design....83
2.2.1. Heat Transfer Problem....85
2.3. Dimensional Analysis and the Stark Number....90

2.4. Modeling of the Heat Transfer.....94
2.4.1. Analytical Model of the Beam System.....95
2.4.2. Derivation.....99
2.4.3. Finite Difference Modeling of the Beam System.....100
2.4.4. Features and Implementation of the Finite Difference.....108
2.4.5. Finite Element Modeling of the Chamber.....113
2.4.6. FEA Model Details and Solution Methodology.....123
2.4.6.1. Parametric Studies.....124
2.4.7. Comparison of Model Predictions.....126
2.5. Isothermality of the Beam and Coating System.....127
2.5.1. Power Needed and Temperature Ranges Achieved.....127
2.5.2. Calculation of Flux At Beam From Lamps.....127
2.6. Global Heat Transfer Analytical Revisited.....134
2.7. Free-Free Suspension (Method of Suspension).....136
2.7.1. On Vacuum.....137
2.7.2. Passive Node.....139
2.7.3. Suspending the Beam.....140
2.8. Excitation (Method of Loading).....144
2.8.1. Electromagnetic Coil.....145
2.8.2. Permanent Magnets at the Active Node 155
2.8.3. Magnet Sensitivity.....158
2.8.4. Magnet Fastening.....162
2.8.5. Calibration Techniques of Method of Loading.....163
2.9. Thermal Stresses in the Beam-TBC System 163
2.9.1. Analytical Model, 1-D.....167
2.10. Finite-element Thermal Stresses Model.....170
2.11. Design Summary.....175

3. Description, Fabrication, Calibration/Validation of the Test Apparatus.....177
3.1. Main Chamber Pressure Housing (Vacuum).....181
3.1.1. Main Housing and Optical Ports.....182
3.1.2. Base Slab.....184
3.1.3. Lamps, Insulation, and Cooling (Method of Heating).....187
3.1.4. Electromagnet and Cooling System (Method of Loading).....195
3.1.5. Active Node of Specimen (Method of Loading).....196
3.1.5.1. Electromagnet 199
3.1.6. Passive Node of Specimen (Method of Suspension).....203
3.1.7. On Filtering.....207
3.1.7.1. Characterization of Rigid Body Modes and Noise Floor.....208
3.1.7.2. Reflectors Dots – 3M and Mica Tape 208
3.2. Multi-point Temperature Results.....208
3.3. Thermal IR Imaging.....213
3.3.1. Thermal IR Imaging Technique.....213
3.3.2. Thermal IR Imaging Results.....218
3.4. Isothermality Findings.....227
3.5. Dummy Titanium Specimen Calibration/Bias.....231
3.6. Chamber Power Curve Calibration.....231
3.7. Magnet Coil Calibration.....238
3.7.1. Dynamic Calibration 241
3.8. Components Adaptability to High Temperature.....246
3.9. Low Damping Chamber.....256
3.10. Closure on the Chamber.....260
4. Determining Coating Complex Modulus – Theory and Concepts.....261
4.1. Damping Models.....262
4.1.1. On Damping and Complex Modulus.....262

4.1.2. Constitutive Models and Damping Review.....263
4.2. Analytical Modeling.....277
4.2.1. Analytical Solution of Classic Free-Free Beam System 280
4.2.2. Non-Uniform Dynamic Beam System.....285
4.3. Numerical Simulation Using Finite Element Analysis.....294
4.3.1. Bare Beam FEA Models in 1-D, 2-D and 3-D.....297
4.3.2. Coated Beam FEA Models in 1-D, 2-D and 3-D.....299
4.3.2.1. Results of Dimensionality, Mesh and Element Selection.....301
4.3.3. Building the Predictive Polynomials.....308
4.4. Sensitivity Studies to Magnet Mass in 1-D and 3-D.....314
4.4.1. Use of Harmonic Integration to Determine Scaling Factor.....314
4.4.2. On the Mechanics of the Suspension Wires.....315
4.5. Combining the FEA Analysis with the Experimental Results to Extract Coating-Specific Properties.....318
4.5.1. Extraction of System Damping and Resonance Frequency from Testing. 318
4.5.2. Combining the FEA Analysis with the Experimental Results to Extract Coating-Specific Properties.....324
4.5.3. On Use of Filtering.....328
4.5.4. FRF Forced Response Measurements for the System 331
4.5.5. On Use of Functional Fits Instead of Smoothing Splines.....332
4.5.6. Closing the Loop for Fully Transient Modeling.....336
5. Determining Coating Complex Modulus – Experimental Study.....338
5.1. The Specimens.....338
5.1.1. Fabrication of Specimens.....341
5.1.1.1. Partially Coated Specimen.....346
5.1.2. Testing the TI Blanks for Modulus-Orientation Findings.....347
5.1.2.1. Micro-scale Investigation.....352

5.1.3. Aging-In Protocol....358
5.2. Testing Procedure....363
5.2.1. Specimen Prep and Loading Into Chamber....365
5.2.2. Reaching Set-point Temperature....366
5.2.3. Core Testing....366
5.2.4. Extract Coating Bulk Modulus....372
5.3. Bare Beam Specimen Findings....372
5.3.1. Chamber Characterization of Boundary Conditions....378
5.4. Bond Coat Only Specimen....379
5.5. Coated Beam Specimens....381
5.6. System Level Damping and Resonance Frequencies....382
5.6.1. Coating Specific Loss-Factor and Storage Moduli....386
5.7. Scanning DVL Study....392
5.8. FRF Studies....395
5.8.1. FRF Sensitivity Studies....397
6. Conclusions and Recommendations....403
6.1. Chamber Findings....403
6.2. Coating Study....405
6.2.1. Bare Beam....406
6.2.2. Bond Coat Only Test....407
6.2.3. TBC Coated Beam Study....408
6.3. Recommendations....410
6.3.1. Chamber....411
6.3.2. Coated Beam Study....413
6.4. Impact....422
APPENDICIES....425
1. Analytical Model - Heat Transfer in a Thin Beam....426

2. Uniqueness Proof of Thermal Distribution in Solution.....451
3. Source Code for Finite Difference Heat Transfer Model.....454
4. Chamber Detail Drawings.....458
5. Coated Oberst Beam Theory.....461
6. Derivation of Experimental Free-Free EC and ηc.....465
7. Dynamic FEA Details, Information, and Results.....470
8. Exponential Decay Harmonic Function Integration.....477
9. Time Domain Data Reduction 480
10. FRF to Measure Damping and Natural Frequencies.....483
11. Orientation Imaging Microscopy Background and Details.....491
12. Matlab Data Reduction Routine.....495
13. SDOF Analogy Method 498
14. A Note on Damping Ratio, Quality Factor, and Loss Coefficient.....501

List of Tables Page

Table 1: Parameters in the Finite Difference Code Runs.....90
Table 2: Various Runs of the ¼ Domain FEA model (Radiation-Conduction).....96
Table 3: Permanent Magnetic Materials (adapted from Stanford Magnetics Catalog).....129
Table 4: Natural Frequencies of Bare Ti-6Al-4V Beam as a function of Magnet Mass 132
Table 5: Magnet Mass Sensitivity Parameters.....133
Table 6: 1-D Thermal Stress Analysis 138
Table 7: Thermal Stress Analysis Results Comparison.....143
Table 8: Parametric Study of the Free-Free System Boundary Conditions for ANOVA.....212
Table 9: Loss Coefficients of some Bulk Materials (Beards, 2006).....225
Table 10: Damping Model Comparison (Braun, 2002).....226
Table 11: Classical and Rayleigh Beam Results.....241
Table 12: Mesh Refinement and Element Selection Study on 2-D and 3-D Model 251
Table 13: Rigid Body Motions (Modes).....270
Table 14: The Material Properties Used in the Simulations.....390
Table 15: FEA Model Mesh Summary.....391
Table 16: 2-D FEA Polynomials, Bare Beam.....392
Table 17: 2-D FEA Polynomials, 8.3 mil TBC coating (normal).....392
Table 18: 2-D FEA Polynomials, 12.5 mil TBC coating (thick).....393
Table 19: 2-D FEA Polynomials, 5.7 mil TBC coating (thin).....394
Table 20: Error Between Free-Decay and Forced Response Forms.....396

List of Figures Page

Figure 1: Turbine Inlet Entry Temperature (Cumpsty, 2003).....2
Figure 2: Modern Aircraft Engine, Image of the Trent 800 (Cervenka, 2000, courtesy Rolls-Royce) 3
Figure 3: APS and EB-PVD Applied Thermal Barrier Coatings (Sevostianov, 2001).....9
Figure 4: Air Plasma Spray Process. (Ivancic, 2003).....12
Figure 5: Intra- and Inter-Splat Formation from APS Process (Wachtman, 1993) 13
Figure 6: FRF Curves History at Various Cycles of Loading (Pearson, 2008).....14
Figure 7: Cantilever Clamp with Guideposts (Blackwell, 2004).....19
Figure 8: Modulus of Ti-6Al-4V Across Temperatures (Mil-Handbook-5H, 1998) 22
Figure 9: Ishikawa Error Analysis Diagram of the Allen Setup (Lee, 2006).....25
Figure 10: Cantilever Beam Specimen, Partially Coated (Patsias, 2006) 25
Figure 11: FEA Model of Partially Coated Cantilever Specimen (Tassini, 2006). 26
Figure 12: Results of Patsias and Tassini for 8-YSZ (Tassini, 2006).....28
Figure 13: Dynamic Eigen-system FEA model, 3-D.....28
Figure 14: Dynamic Eigen-system FEA model, 1-D.....31
Figure 15: Findings of Loss and Storage Moduli Across Strain Amplitudes (Reed, 2007).....33
Figure 16: 8-YSZ and Mag Spinel Loss Coefficient and Storage Moduli (Pearson 2008).....39
Figure 17: SEM of Untested (left), and Tested (right) 8-YSZ, 1600X Mag (Pearson, 2008).....40
Figure 18: Reconstruction of FRF from Up- and Down-Swept Data (Deleon, 2009) 41
Figure 19: Apparatus and Specimens used in Elevated Temperature Testing

(Gregori, 2007).....44
Figure 20: Loss Factor, 7-YSZ (left) and 8-YSZ (right) Specimens vs Temperature (Limarga, 2007; Gregori, 2007).....45
Figure 21: Laminated Beam Types (Nashif, 1985).....51
Figure 22: Free-Free Setups of Reed (left) and Pearson (right) (Reed, 2007; Pearson, 2008).....70
Figure 23: Concept Design of Elevated Temperature Free-free Apparatus.....71
Figure 24: Thermal Circuit for Beam, Specimen, Chamber, and Surroundings….72
Figure 25: Side View of Beam in Thermal Chamber 73
Figure 26: Top View of Beam in Thermal Chamber.....74
Figure 27: Cooling Curves using Spherical Solution at Various Emissivities.....79
Figure 28: Beam Coordinate System, Dimensions.....80
Figure 29: First- and Second-Order Effects on Temperature, Variation with Parabolic Irradiation Profile.....82
Figure 30: Computational Domain and Finite Difference Grid.....84
Figure 31: Surface Node in Radiation-Conduction Model.....88
Figure 32: FD Isotherms in Kelvin (TBC coating is bottom center "notch" region) 93
Figure 33: Surface Plot of the Temperature in Kelvin (TBC coating is bottom center "notch" region).....93
Figure 34: Ti-6Al-4V Surface Temperature vs Illumination Intensity.....94
Figure 35: FEA Full Domain Model, Cutaway Half View of Beam and Lamps…96
Figure 36: FEA Quarter Domain Model, Two-Cavity Model.....97
Figure 37: FEA Quarter Domain Model with Temperature Variation.....102
Figure 38: 3-Segment Flat Lamp Reflectors.....104
Figure 39: Lamps Out Scenarios; None Out (left), One Out (center) and Four Out (right).....105

Figure 40: Quartz Halogen Lamp Assemblies.....107
Figure 41: Thermal Circuit with Radiation Shielding Added to Circuit.....112
Figure 42: Air Damping Effects on the Bare Beam Loss Factor (Reed, 2007)....115
Figure 43: Biot-Savart Law (Hoover, 2004).....121
Figure 44: Finite Length Air Core Solenoid (Dennison, 2009).....123
Figure 45: Off-axis Field Strength of Finite Air-core Solenoid (Dennison, 2009) 124
Figure 46: Transfer Function of Coil Current as a Function of Log(Freq.).....128
Figure 47: Mode I Sensitivity to Magnet Mass 0X (upper left), 1X (upper right), and 10X (lower right) Mass; 1-D.....132
Figure 48: Mode I Sensitivity to Magnet Mass 0X (top), 1X (middle), and 4.5X Mass (bottom); 3-D.....133
Figure 49: 1-D Model for Thermal Stress.....139
Figure 50: Thermal Stress FEA solution Results, 3-D.....142
Figure 51: Thermal Stress FEA solutions, 2-D.....143
Figure 52: Peel Stress Plots from 3-D FEA.....144
Figure 53: Chamber Setup, On Table.....149
Figure 54: Chamber Setup, Below Table.....150
Figure 55: Base Slab Dimensions.....155
Figure 56: Base Slab with Support Rods Mounted.....156
Figure 57: Chamber with Heating Lamps, Free-Free Beam, and Dummy Specimen, view from top.....158
Figure 58: Active Node of Beam (left), Magnets and Sets of Hardware (right). .165
Figure 59: Passive Node of Beam.....170
Figure 60: Thermocouple Channel Assignments.....175
Figure 61: First Heated Run-up of Chamber, TC Temperatures vs Time.....177
Figure 62: Second Heated Run-up of Chamber, TC Temperatures vs Time.....178

Figure 63: Thermal Camera Characterization (FLIR SC600 User Manual, 2010) 179
Figure 64: FLIR-SC660C Thermal Validation Setup..... 182
Figure 65: Thermal IR Image at 300degF Set-point (Temperatures are degF)… 183
Figure 66: Thermal IR Image at 600degF Set-point (Temperatures are degF)… 184
Figure 67: Thermal IR Image at 900degF Set-point (Temperatures are degF)…. 185
Figure 68: Optical Image of Beam in Chamber from IR Camera View..... 186
Figure 69: FEA; (left), Highly Polished (εTI = 0.10), (right), Near Blackbody (εTI = 0.95) 187
Figure 70: IR Imaging of outer chamber. 188
Figure 71: Comparison of Temperature Findings Down the Length of the Beam 191
Figure 72: Temperature on Channel #3 versus Time Elapsed..... 194
Figure 73: Power Curves Calibrated for 100W and 200W Set of Eight Lamps... 195
Figure 74: Beam Pseudo-Time Constants, Temp on Chan. #3..... 197
Figure 75: Static Magnet Moment Couple Calibration Setup..... 198
Figure 76: DC Coil Magnet Calibration Curves, Moment of a Function of DC Current..... 199
Figure 77: Phasing Between Beam and Magnetic Field..... 204
Figure 78: Undamped System and Response, SDOF (Beards, 1996)..... 221
Figure 79: Viscously Damped System and Response, SDOF (Beards, 1996)….. 222
Figure 80: Coulomb (Dry) Damping System and Response, SDOF (Beards, 1996) 224
Figure 81: Hysteresis Damping System and Response (Beards, 1996)..... 225
Figure 82: Damping Models for SDOF, Capacities and Quality Factors (Braun, 2002)..... 228
Figure 83: Diagram of the Beam (Reed, 2007)..... 230

Figure 84: Free-Free Beam Roots and Shapes (Braun, 2002).....233
Figure 85: Whole and Denominator of Curvature Function.....235
Figure 86: Three-Region Beam of Uniform Cross Section.....237
Figure 87: Fitted Cubic Functions on to Coated DVL Data.....239
Figure 88: Real, Stiffness- and Mass-Equivalent Beams.....241
Figure 89: Cubic Fitted to Classical Solution with Bare Beam DVL Data.....242
Figure 90: Coating Modulus as a Function of Frequency.....249
Figure 91: Transverse Displacement as a Function of Candidate Coating Modulus 250
Figure 92: Bending Strain as a Function of Candidate Coating Modulus.....251
Figure 93: Strain Energy Ratio as a Function of Candidate Coating Modulus….252
Figure 94: Coating Modulus as a Function of Frequency.....254
Figure 95: Transverse Displacement as a Function of Candidate Coating Modulus 255
Figure 96: Bending Strain as a Function of Candidate Coating Modulus.....256
Figure 97: Strain Energy Ratio as a Function of Candidate Coating Modulus….257
Figure 98: Beam Curvature Changes with Coating Moduli; whole (left), close up (right); 70degF.....259
Figure 99: Fan Impingement FFT (left), Typical Free Decay Test with Rigid Modes (right).....261
Figure 100: Typical Coated Beam Datasets, Clean (left) and with Rigid Body Motion (right).....264
Figure 101: Off-Line Process Reduce System Properties to Bulk Coating Complex Moduli.....270
Figure 102: 5th-Order Butterworth High Pass Filter Bode Plot.....272
Figure 103: Original, Noisy, and Filtered Ring-down Signals.....273
Figure 105: Process to Obtaining System Level Damping and Resonance

frequency.....275
Figure 104: Time Indexing of Decay Signals.....275
Figure 106: Interim Off-Line Processing Plots.....277
Figure 107: Bare (upper), Bond Coated (middle), and 8-YSZ Coated (lower) Beam Specimens 281
Figure 108: Bending Strain at Coating-Beam Interface Mid-plane along Length (Deleon, 2009).....287
Figure 109: Characterizing the Bare Beams for Modulus.....288
Figure 110: Bare Beam Resonance Frequencies.....289
Figure 111: Titanium Cooling and Micro Structure Forms (Pilchack, 2009).....292
Figure 112: Titanium Cooling and Micro Structure Forms (Wang, 2003).....292
Figure 113: α- and β-phase Phase Fraction Map.....294
Figure 114: Large-scale OIM Scans; Top, 0001 parallel to ND (RD X TD), Bottom, 0001 Parallel to RD.....295
Figure 115: Macroscopic α-Phase Texture, Probabilistic Density.....295
Figure 116: Ti-6Al-4V Modulus by Axial Pull (left), α-crystal Orientation Summary (right) (Wang, 2003).....296
Figure 117: Coating Beam Aging, Resonance Frequency as a Function of Cycles 298
Figure 118: Coating Beam Aging, Damping Ratio as a Function of Cycles.....299
Figure 119: Aging; Resonance Frequency as a Function of Cycles at Various Temperatures.....300
Figure 120: Aging; Damping Ratio as a Function of Cycles at Various Temperatures.....300
Figure 121: Typical Bare Beam Dataset.....306
Figure 122: Chattering Magnets with Linear Decay Envelope.....308
Figure 123: Ti-6Al-4V Loss Factors Versus Temperature.....309

Figure 124: Titanium Ti-6Al-4V Modulus Versus Temperature.....312
Figure 125: Ti-6Al-4V Loss Factor versus Temperature (Lee, 1966). 314
Figure 126: Bond Coat Specimen System Loss Coefficient 315
Figure 127: Bond Coat Specimen System Resonance Frequencies across Temperature.....316
Figure 128: Resonance Frequency Peaks at Various Amplitudes.....317
Figure 129: System Loss Factor (ηsys) and Resonance Frequency (fr) – Specimen 01.....318
Figure 130: System Loss Factor (ηsys) and Resonance Frequency (fr) – Specimen 05.....318
Figure 131: System Loss Factor (ηsys) and Resonance Frequency (fr) – Specimen 07.....319
Figure 132: System Loss Factor (ηsys) and Resonance Frequency (fr) – Specimen 09 (thin).....319
Figure 133: System Loss Factor (ηsys) and Resonance Frequency (fr) – Specimen 12 (thick).....320
Figure 134: Complex Modulus; Loss Coefficient ηc and Storage Modulus Ec – Specimen 01.....321
Figure 135: Complex Modulus; Loss Coefficient ηc and Storage Modulus Ec– Specimen 05.....322
Figure 136: Complex Modulus; Loss Coefficient ηc and Storage Modulus Ec– Specimen 07.....323
Figure 137: Complex Modulus; Loss Coefficient ηc and Storage Modulus Ec– Specimen 09 (thin).....324
Figure 138: Complex Modulus; Loss Coefficient ηc and Storage Modulus Ec– Specimen 12 (thick).....324
Figure 139: DVL Scan of Bare Beam, Specimen #23, 70degF.....326

Figure 140: DVL Scan of Coated Beam, Specimen #7, 70degF.....327
Figure 141: DVL Data Plotted Over Assumed Mode Curves for ½ Beam; (left) Bare, (right), Coated.....328
Figure 142: Beam Specimen #1 (left), 5 (ctr), and 7 (right) FRF Sweeps.....329
Figure 143: FRF Sweeps 2000mA with Varying Shielding Thicknesses.....330
Figure 144: Low-Hanging Beam in Foil Cup.....331
Figure 145: FRF Sweeps at Various Beam to Electromagnet Distances.....332
Figure 146: FRF Sweeps at Various Temperatures, 2000mV Stimulation.....333
Figure 147: Free-decay versus FRF based System Loss Factors.....334
Figure 148: Coating Bulk Loss Factors for Various Temperatures (500mVp-p excitation).....335
Figure 149: Beam coordinate system, dimensions.....354
Figure 150: Chamber Assembly – View 1.....381
Figure 151: Chamber Assembly – View 2.....382
Figure 152: Chamber Assembly – View 3.....383
Figure 153: 1-D, 2-D and 3-D FEA modal models for the Polynomial extraction. 392
Figure 154: Forced Response FRF Frequency Domain Signal.....402
Figure 155: Section of non-linear FRF (Braun, 2002).....405
Figure 156: The "Jump" Phenomenon (Braun, 2002).....407
Figure 157: Orientation Imaging Microscopy (OIM) Schematic (Schwartz, 2000) 408
Figure 158: OIM Colormap Interpretation (Pilchak, 2009).....409
Figure 159: Typically Axial Load and Unload Curve.....417

Acknowledgements:

The research endeavor, while it often seems very lonely, in hindsight, is highly dependent on teamwork I have come to find. So here I'll acknowledge the critical help with which this work would never have come to fruition;

Mr. Brian Crabtree and Mr. Daniel Ryan - machining expertise and a lot of trying eclectic stuff like burning holes through magnets and making two tiny-tiny tunnels meet end-to-end

For practical experimental advice, insight, and fabrication support: Mr. John Justice (Labview Programing), Mrs. Angie Still, Mr. Phillip Johnson, and the rest of the TEFF group.

For FEA help and expertise: Dr. Rebecca Hoffman, Maj. Aaron Norris, Maj. Armando Deleon, Lt. Col. Chad Hale, and Solidworks help: Mr. David Huber

For metallurgical expertise and assistance: Dr. Al-Arubib, Dr. Pilchak, Dr. Rosenberger

On detailed thermal imaging expertise: Mr. Chris Zickafoose

For free-free experimental system help: Lt. Col. Reed, Lt. Pearson, Lt. Schwartz (scanning DVL)

Lt. Col. Branam for one-on-one numerical technique direction and proofing of Matlab code that violates the rules of good structure, and Dr. George and Mr. Brian Runyon for a wealth of expertise on experimental techniques and the art of vibrational studies. Dr. Baker for expert direction on analytical mathematical techniques, just plain enthusiasm, and posing very introspective “what-if's” and Dr. Palazotto, my advisor, patiently advocating on a certain approach for many an issue and being right on the vast majority, despite my often rushed ideas and impulsive thinking, and for assistance on the fine art of FEA, both ABAQUS and scratch-coded. Finally for my Wife and family for patience and a listening ear and asking “How is it going?”and the Lord Above for giving me the patience and wherewithal to plug on.

AN EXPERIMENTAL CHARACTERIZATION OF DAMPING PROPERTIES OF THERMAL BARRIER COATINGS AT ELEVATED TEMPERATURES

1. Introduction

This study will seek to adapt a current free-free beam apparatus that is used for mechanical characterization of thin thermal barrier coatings to high temperatures while retaining its non-contacting boundary conditions and forcing with the advantages these confer. The apparatus after validation and calibration will be used to determine the complex modulus of air plasma sprayed 8% yttrium stabilized zirconium.

For the standard, Brayton open-cycle, gas turbine, typical of modern aircraft power plants, the thermodynamic efficiency is heavily driven by the engine-inlet-to-turbine-first-stage-inlet temperature ratio, commonly known as the "T_4/T_2 ratio." The turbine stages, often known as the "hot section," of gas turbine engines have been recognized for years to impose a severe mechanical loading environment complicated by high temperature and chemically reactive species. Modern turbine inlet temperatures (T_4) can run around 1700-1800K (2600-2780F), well above the melting point of the blade alloys (Cumpsty, 2003:55). The evolutionary progression of various coping technologies including; nickel based super-alloys, blade-core cooling using compressor bleed air, blade film-boundary layer thermal isolation (again using bleed air), and ceramic thermal barrier coatings to achieve further isolation have been developed to cope with this severe operational environment (Younossi, 2002). As can be seen from Figure 1, these

techniques have allowed operating the engine components at progressively higher temperatures with the attendant gains realized in greater thermodynamic efficiency.

Blade creep, fatigue from low- and high-cycle fatigue (LCF/HCF), and thermal cycling, are all compounded in effect by high temperature and shorten the blade design life. Modern blades are mostly design-limited by, as well as experience sudden failure from, HCF loading. (Garrison, 2001; Brun, 2009) "Fatigue is typically termed either High Cycle Fatigue or Low Cycle Fatigue (LCF). While LCF was at onetime a concern, it has been largely negated due to design requirements which emphasize damage tolerance and a retirement-for-cause philosophy (2). This leaves HCF as the dominant cause of fatigue failure, and a primary source of concern" (Lee, 2006).

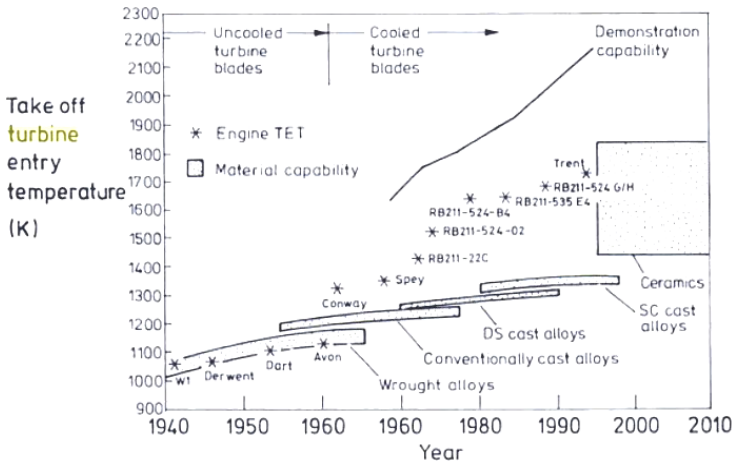


Figure 1: Turbine Inlet Entry Temperature (Cumpsty, 2003)

Typical HCF loading on compressor and turbine blades is driven by many factors including: aerodynamic excitation (caused by engine flow path pressure perturbations that primarily affect blades and vanes), mechanical vibration (caused by rotor imbalance

which affects external components, engine plumbing, and static structures), rubbing interaction (which affects blade tips and gas path seals), airfoil flutter (caused by aero-mechanical instability, affecting blades, and acoustic fatigue and affecting mostly sheet metal components in the combustor, nozzle, and augmenter or afterburner) (Cowles, 1996).

Figure 2 (Cervenka, 2000) depicts a modern gas turbine engine, as can be seen from the pressure and temperature profiles plotted on it. The continuous evolution of aircraft engines, for purposes of increasing both thermodynamic efficiency (η_t) and power-to-weight ratio, has driven an increase in compression ratios in modern civil aircraft engines to around 40:1. The labels stand for: HPC and LPC for the high- and low-pressure compressor, LPT, IPT, and HPT for the low-, intermediate-, and high-pressure turbine. This is a direct consequence of seeking a higher T_4/T_2 ratio, yielding higher thermodynamic efficiency (η_t) values. The associated temperatures have risen in concert with the compression ratios. Titanium, specifically the alloy Ti-6Al-4V, which exhibits good ductility, toughness, and density relative to other alloys, is commonly used in the inner stage compressor blades in the "cold section." It is noted that the term "cold" section is definitely in a relative sense to the combustor and turbine; modern compressor inner stage exit temperatures can now operate at temperatures of up to 870K (~1100F) (Cumpsty, 2003:58).

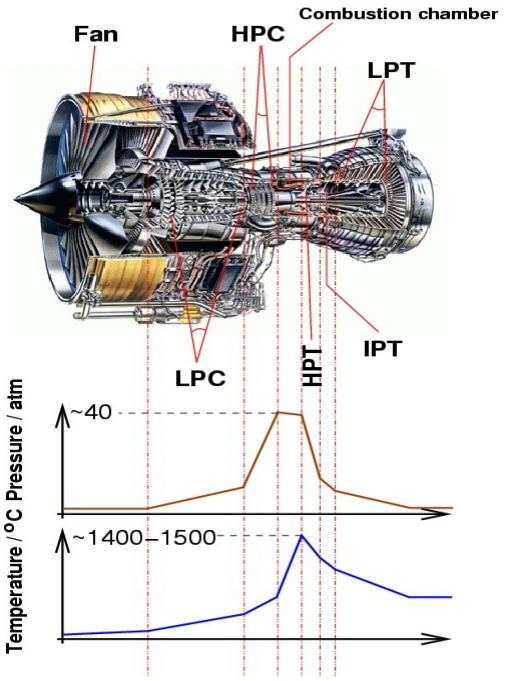


Figure 2: Modern Aircraft Engine, Image of the Trent 800 (Cervenka, 2000, courtesy Rolls-Royce)

Meanwhile, the state of the art in gas-turbine engines for aircraft has for almost three decades routinely utilized thermal barrier coatings (TBC) in the turbine stages, as Figure 1 depicts. The motivation to employ these has been for thermal isolation by providing a low conductivity barrier between hot gas flow and the blade metallic core with its active cooling. While these coatings, typically sputtered ceramics or ceramic metal mixtures ("cermats"), were implemented for thermal control, they have been found to also possess beneficial mechanical side effects, specifically, a high internal damping relative to the super alloy blades to which they are customarily applied (Cumpsty, 2003; Tamarin 2002; Bose, 2007). The most common TBC utilized in industry is yttrium-stabilized zirconium (YSZ), with an 8% mass of yttrium, due to a favorable combination of properties. These include: low thermal conductivity, ease of application, high temperature oxidation/corrosion resistance, thermal expansion compatibility with nickel

based super alloy substrate metals. This reduces spallation and coating failures from thermal cycling, a form of low cycle fatigue (LCF) caused by differential thermal expansion (Tamarin, 2002). The 8% by weight YSZ, designated commonly as 8-YSZ ($ZrO_2 \cdot 8\% Y_2O_3$), is used most often in the industry today due an the optimal trade-off of these properties. Many other TBC materials exist and have come under study, including magnesium aluminate spinels ("mag spinel"), and chromium stabilized aluminum oxide ($Al_2O_3 \cdot Cr_2O_3$) (Tamarin, 2002).

High cycle fatigue (HCF) is characterized by loading that is: in the elastic region of the structure being loaded, relatively high in number of load cycles, modest in amplitude, and stochastic in nature. HCF is a major driver in limiting blade life in compressor stages so recent work has focused on the quantifying and characterization of the mechanical damping properties of TBC's to facilitate their employment in cold sections specifically to reduce HCF (Brun, 2009; Movchan, 2005). Successful mechanical characterization, to include a workable constitutive model, is a necessary precursor to the incorporation of TBC's into blade, stator, and vane models for HCF reduction by design. Traditional avoidance of catastrophic failures due to HCF has been through life- and time-change intervals based on test data. The bulk of this work to date has been at room temperature and has wrestled with many challenges inherent to these materials including: material break-in, non-linear material properties to include both damping and effective modulus, anisotropic properties of the coatings, the need for high strain-rate and strain levels to characterize, and from the macroscopic structure of the coatings not being bulk monolithic materials (Reed. 2007; Scott-Emuakpor, 2008; Shen,

2008). It is also suspected that the means of application of the coatings and the parameters of the application can vary the properties of the coating as well. Also procedural/experimental challenges have been overcome in measuring the true damping of the coatings by systematically controlling system damping sources of error in not only the coating but also the suspending apparatus and surroundings. Achieving high strain (and strain rates) in a non-contact manner to allow non-linear properties to be fully characterized has been a challenge for past efforts. Interest in adapting TBC materials into the compressor rotor and stator blades in modern engines motivates the study of the mechanical properties of these materials at elevated temperatures (Younossi, 2002).

The free-free beam apparatus will be employed for mechanical characterization of thin thermal barrier coatings to high temperatures. The apparatus after validation and calibration will be used to determine the complex modulus of air plasma sprayed 8% yttrium stabilized zirconium. A necessary activity though will be the designing, validation and calibration of the free-free apparatus to allow testing across the temperature range desired. Accomplishing the above will be done by adapting the past methods of Pastsias, Tassini, Runyon, Reed, Palazotto, and Pearson to obtain mechanical behavior of the TBCs using an adaptation of the apparatus and techniques developed by them. This will be attempted across a high range of strain (and strain rate). This wide range is necessitated by the non-linear nature of the material. However, adaptation of the apparatus and procedures to allow for high temperature characterization does require some foresight as many challenges are imposed by a high temperature environment, even on design temperatures set to the upper working limits of a modern axial compressor,

which are a relatively mild 900degF (488degC). This objective is a major portion of the current effort and is critical to achieving any characterization study at elevated temperature.

1.1. Background

Most of the background material will be addressed in this Chapter, although some of the specific material for accomplish some tasks will be covered elsewhere where more pertinent. This includes information on electro-magnetics, radiation heat transfer (Chapter 2), and damping (Chapter 4).

1.2. Overview

Chapter 1 will be an overview of the nature of the coatings, the application processes, and the thermal and mechanical characterization findings to date from previous work. A historical overview of past work to arrive at these results will be covered. Most of the chronology will be loosely highlighted by the investigative approach, i.e., experimental, numerical (including finite element analysis (FEA)), and analytical. The chapter is closed with the co-objectives of the current study; one being to successfully design, validate and characterize the apparatus and associated processes for high temperature mechanical characterization of TBC's using free-free methods, and the second is to conduct an initial study to characterize one TBC using the product of the first objective. To accomplish a characterization of these coatings there are two major efforts; first is to analyze, design, calibrate, and validate the apparatus and techniques to test the specimens in a minimally damped environment, and the second is to perform the

dynamic mechanical analysis and experimental work to determine the coatings mechanical properties. Covering a topical breakdown, Chapter 2 will cover the theory, both numerical and analytical, that is required to guide the design of the apparatus. Particular emphasis will be on heat transfer as it is critical to the accuracy of the technique employed in the study, especially the highly non-linear radiation dominated problem. Investigation into mechanical boundary conditions, and thermally induced stresses will also be covered. Chapter 3 will detail the implementation of the apparatus, based on insight gained from the studies in Chapter 2, then will cover calibration and validation efforts to establish that the environment desired for testing is actually obtained. The theory required and the modeling studies needed for the second half of the study, that is the characterization of the TBC coating on the beam specimens, is the focus of Chapter 4. Both analytical and numerical (finite-element) techniques using non-dimensional (modal coordinate) linear solutions will be covered. The technique of determining system-level properties in the experiment will be covered, and then how to reduce system-level quantities to coating specific qualities. In the current study particular emphasis on free-decay techniques using logarithmic decrement is used. Chapter 5 will detail the experimental effort to determine the system-level properties, and present the system-level findings. Details of the specimens and the procedure to reduce the system level data will be covered and the coating bulk mechanical properties are presented. Also, in this Chapter additional validation efforts performed are covered, among these are boundary conditions sensitivity studies, displacement envelope shape verification, the de-coupling of aging effects of the coatings from temperature, and error determinations in

the apparatus and procedure. Chapter 6 covers the conclusions on the two major efforts; the chamber as a design effort and the coating property study. Chapter 6 also details recommendations and suggestions for future efforts.

1.3. Thermal Barrier Coating

It is important to review some background about thermal barrier coatings (TBC's) as they are currently utilized in the industry. Typically the following factors have a great influence on the thermal and mechanical properties of the TBC layer: application method, chemical composition, and service history. These are covered below.

Traditionally TBC's were employed primarily for the high thermal resistivity that they imposed on the coated system, and secondarily for the corrosion resistance conferred to the metallic substrate shielded from the hot combustion gases and byproducts. Thermal barrier coatings, in routine use in the hot sections of turbine engines by the 1970's, were recognized early on to also have the beneficial side effect of high damping in service (Bose, 2007; Tamarin, 2002). This section will discuss the coatings in terms of their basic structure, material systems, and means of application. Then a review of past work in characterizing TBC coatings will be covered. Highlights of parallel development in numerical and analytical techniques will also be covered.

1.3.1. Anatomy of a TBC

There are four main regions to a TBC system and they are: 1) the metal substrate, 2) a metallic bond coat, 3) a thermally grown oxide layer, and 4) the ceramic topcoat.

(Padture, 2002; wikipedia, 2009). The metallic substrate is the bulk structural material, typically a nickel-based super alloy blade or stator. This is the structural blade or stator material. Alumina is the main component of the oxide layer and it protects the substrate from thermal oxidation and corrosion by acting as a barrier to diffusion of oxygen radicals. The metallic bond coat is typically a mixed powder comprised of varying amounts of nickel, cobalt, chromium, aluminum, and yttrium (NiCoCrAlY) sprayed onto the metal in molten form. The bond coat provides enhanced adhesion by providing a rougher surface with mechanical asperities for the ceramic topcoat to bind to and providing a buffer layer of intermediate properties. Typically, comparatively thin compared to the ceramic topcoat, this layer can be tailored to provide an intermediate thermal expansion and other properties between those of the substrate and topcoat thereby reducing the severity of property mismatch(es). The last layer is the ceramic top coat which can be applied by direct mechanical spraying or a diffusion processes. Typically, composed of YSZ, this is the thickest layer (except for the substrate) and has a high thermal resistivity and low chemical reactivity in the typical operating environments for the engine components it is applied to.

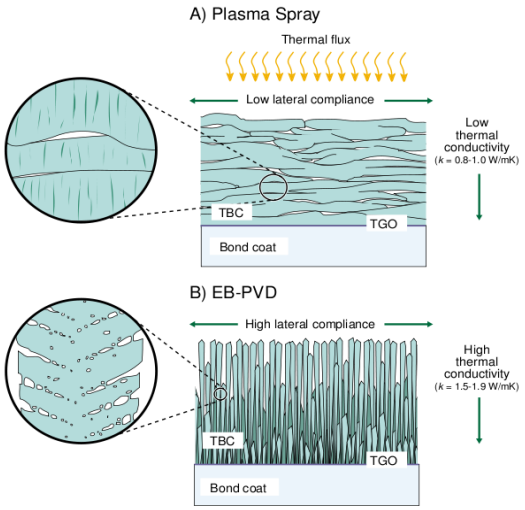


Figure 3: APS and EB-PVD Applied Thermal Barrier Coatings (Sevostianov, 2001)

Figure 3 (Hass, 2000) displays this anatomy for the two most common processes by which TBC coatings are applied. The first is from the air plasma spray (APS) process and the second results from electron-beam physical vapor deposition (EB-PVD). In both structures, the substrate below the bond coat is not depicted. It is observed that the thickness of the plasma spray coating must be maintained in a relatively thin state (< 0.5 mm) or de-lamination of the coating is likely. (Wachtman, 1993) This is suspected due to the failure to relieve stresses by the limited crack motion allowed (Younossi, 2002).

As can be seen from the Figure, the thermal and mechanical properties of the coatings are anisotropic (Sevostianov, 2001) and orientation of the highest magnitude is determined by the process in which they are applied. Mensah summarizes the differences well:

> The advantage of the air plasma spray process over EB-PVD is that the thermal conductivity of TBCs produced by the air plasma spray process is lower than EB-PVD. But the main draw back is that it has less strain tolerance to the thermal stresses at high temperatures [due to the crack orientation not allowing strain relief from thermal expansion

> of the substrate]....because of which spallation failure takes place in TBCs. By introducing vertical segmented cracks into the coating structure which is also called macro-cracked TBCs this can increase the strain tolerance in the air plasma coatings (Mensah, 2006).

This suggests the APS process, while not as optimal in the very high and heavily fluctuating thermal environment of the hot sections, may be a better suited process for the more thermally steady conditions in the compressor stages where the mechanical suppression of HCF is the primary motivation for the use of TBC materials.

1.3.2. Material Systems/Composition

Tailoring of the thermal and mechanical properties can be achieved by the selection of the chemical composition of the TBC. Some broad classes of TBC materials include: oxide ceramics (including YSZ and mag spinel), alumina compounds, and refractory metals. Selection among the materials for use is subject to many factors. In gas turbines the oxide ceramics, specifically yttrium stabilized zirconium (YSZ), are the predominating TBC materials. Other oxide ceramic TBC materials include magnesium aluminate spinel ("mag spinel") commonly used in refractory liners in smelting, and chromium stabilized aluminum oxide.

Yttrium-stabilized zirconium (YSZ) ($ZrO_2 \cdot 8\% Y_2O_3$) is the most common in the commercial and military engines due a to good balance between cost, ease of application, thermal expansion comparability with common super alloy materials, and chemical stability at elevated temperatures. The 8% by mass dopant of yttrium allows the lattice to readily conduct free oxygen radicals which helps to chemically stabilize the TBC from

erosion from combustion radicals.

Magnesium aluminate spinel ($Al_2O_3 \cdot MgO$) is another common TBC material more commonly used in refractory brick and ladle lining applications (Racher, unknown). The magnesium aluminate spinels are used as a thermal barrier coating for molten steel crucibles and molding equipment to extend service life. Magnesium aluminate spinel ($MgAl_2O_4$) or $MgO \cdot Al_2O_3$ is a powder coating commonly applied by plasma spray. Its properties make it useful for erosion resistance against gas streams at elevated temperature, an important characteristic for application in gas turbine engines (APS Materials, 2001). Shen (Shen, 2007) observed that energy dissipated by a magnesium aluminate spinel coating did not behave in a manner consistent with hysteresis, suggesting that the energy dissipation may be from friction between the powder particles; this may be evidence for a dry-friction damage based model. Torvik, et al. have reported mag spinel provides sufficient damping to be of interest to the propulsion community (Torvik, 1992). Pearson determined that mag spinel was roughly 2.5X more stiff (typical values of the elastic modulus for mag spinel range from 65 to 50Gpa) than 8-YSZ (typical values from 17 to 27Gpa) in the storage modulus over a wide range of strain values, yet not as an effective a damping material. In comparison to 8-YSZ, the values of the loss coefficient (to be discussed in subsequent chapters, but it is a way to express material damping) ranged from some 50% to 75% below that of 8-YSZ, typically across the same range of strain inputs (Pearson, 2008).

Chromium stabilized aluminum oxide ($Al_2O_3 \cdot Cr_2O_3$) and Gadolinium ziroconate

($Gd_2Zr_2O_7$) are another couple of TBC ceramics that have been studied for damping at various temperatures while again offering good thermal barrier properties (Limarga, 2007).

1.3.3. Application Processes

TBC coatings can be applied by a number of processes, among these are: electron beam physical vapor deposition (EB-PVD), air plasma spray (APS), high velocity oxygen fuel spray (HVOF), electrostatic spray assisted vapor deposition (ESAVD), direct vapor deposition (DVD), detonation gun (D-Gun), and low pressure plasma spray (LPPS), various sputtering methods (including EB-PVD and DVD) and electric arc spray, among others. Bose has an excellent overview of the processes (Bose, 2007).

Figure 3, shown above, shows the strong dependence of the coating structure based upon the application process, despite the identical chemistry. While the APS structure has that of "splats" and cracks resembling a bin full of pancakes heaped in it with a horizontal grain to the structure, the EB-PVD has a vertically grained structure that resembles intestinal villi. Splats are the term applied to the droplets after they have impacted, congealed, and cooled. As a result the effective storage and damping moduli are dependent on the orientation of the structures and therefore the application process (Tassini, 2005; Patsias, 2006). Additionally, the thermal conductivity of both of these structures is orthotropic in nature (Hass, 2000).

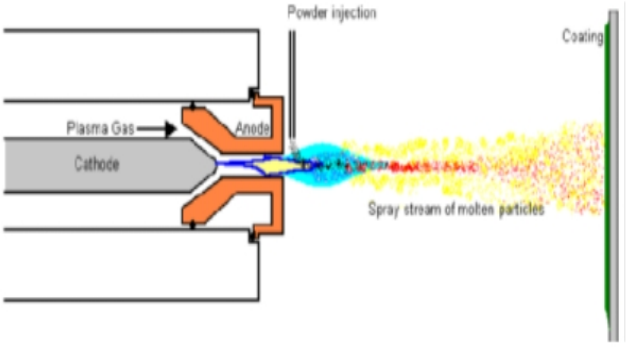


Figure 4: Air Plasma Spray Process. (Ivancic, 2003)

The air plasma spray process, shown in Figure 4 (Ivancic, 2003) in schematic form, feeds the TBC ceramic in a powder form into a high pressure carrier gas that is subsequently fed into a high temperature arc. The power is melted and entrained into the spray which obtains a very high velocity and is ejected out of the gun (Bose, 2007). This is a line of sight processing technique aimed at the substrate where the high-velocity, and now molten, droplets of TBC material impact, adhere, and rapidly cool against the substrate, in the process forming the now elongated drops and grains known by the term "splats".

Figure 5 (Wachtman, 1993) displays the formation of splats and cracks (both intra- and inter-droplet). The air plasma spray process is well understood in industry and avoids excessive heating of the substrate during processing, often heating it to less than 100-300degC. This is an advantage as it avoids adversely affecting the substrate metal by softening or heat annealing. The process is also quite rapid in the deposition rate.

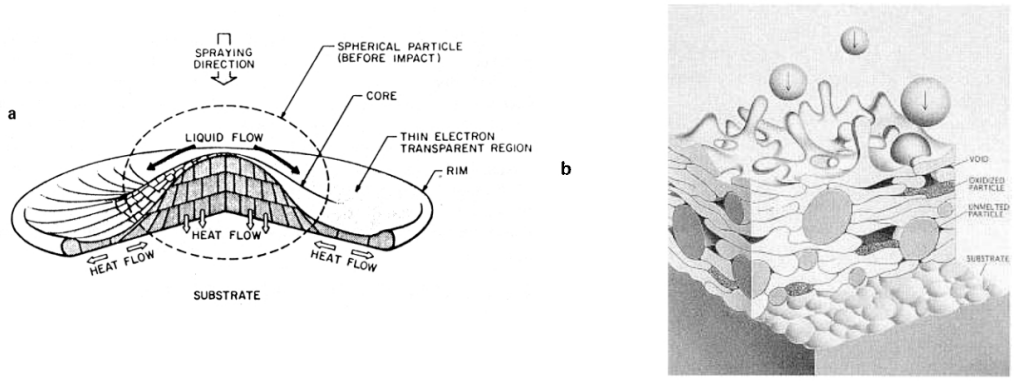


Figure 5: Intra- and Inter-Splat Formation from APS Process (Wachtman, 1993)

Electron Beam Physical Vapor Deposition (EB-PVD) is the other process in common use and is widely used in TBC layers for current engine turbine components. An energetic electron beam is used to vaporize the coating material in a high vacuum environment wherein it deposits itself in the confines of the chamber to any surface, including the intended target material. The target for the coating has a DC bias voltage applied to it of a couple hundred volts and is preheated with another beam so as to facilitate proper condensation conditions for the vaporized material. The structure of the growth is crystalline and orderly in a vertically-oriented fashion. These coatings, relative to APS applied coatings, have a better thermal cycling fatigue resistance, hence the predominating use of this process in modern turbine blades and stators, where thermal mismatch fatigue is a major driver of service life limits. But there are drawbacks as well, these include less thermal resistance than across APS-applied layers, and the substrate metal reaches up to 1000degC while processing, limiting its use to super alloy substrates. Also, the chemical composition of the TBC is much harder to tailer to service requirements when using vapor deposition processes. (Bose, 2007)

The air plasma spray process will be used in the current study due to it being the process with the most favorable micro-structure for cold section blade and stator application, a higher damping ratio in bending modes due to the horizontal grain of the APS splats, and a higher economy of application relative to vapor deposition techniques. These properties, combined with more mild spallation from thermal fatigue in the cold sections, makes the APS process the one most of interest (Tzimas, 2000). Additionally, APS features a tolerable processing temperature for Ti-6Al-4V, a very common alloy used in modern engine cold sections, blade and stator alike.

1.3.4. Strain History Accumulation

TBC coating layers exhibit not only non-linear frequency response function (FRF) curves that are strain-softening in nature (Reed, 2007; Patsias, 2006), but also display a distinct history dependence; Figure 6 shows the history dependence of various FRF sweeps sampled at various times of a coated beam under continuous loading in some data obtained by Pearson (Pearson, 2008). With increasing cycle accumulation on the specimen, the FRF curve can be seen to exhibit both an increase in the frequency of the resonance peak along with a reduction in its associated amplitude. The latter indicates an enhancement in damping effectiveness with a lower peak velocity. The system also appears to increase in the stiffness (or storage) modulus with increasing cycle accumulation, but this is an artifact of the non-linear, strain-softening coating, wherein reduction in amplitude of the FRF response results in a shift in resonance frequency due to a curved backbone curve.

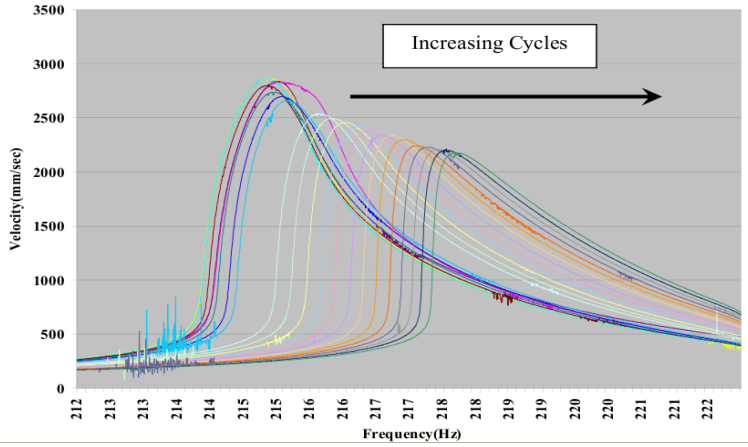


Figure 6: FRF Curves History at Various Cycles of Loading (Pearson, 2008)

This is phenomenological evidence that a damage accumulation model involving frictional crack motion losses may be appropriate for modeling the evolution of TBC properties as hypothesized by some (Abu Al-Rub, 2010; Shen, 2007). How the strain history parameter will be controlled in the current study is dealt with in Chapter 6. The effort will focus on characterizing fully mature specimens. It is felt this will be a valid approach; the typical engine HCF rates will age-in blade coatings to a fully mature state within a short fraction of the total design time lifespan (or time change interval) of the blade and coating systems.

1.3.5. Bond Coating

Ivancic reported two important observations when performing a fatigue-to-failure study on both coated and uncoated specimens. First, the specimen lifespan grew from about 800,000 cycles to about 5,000,000 cycles, and second, that the coatings chipped off in localized regions (Ivancic, 2003). Examination of the author's images shows a shiny metallic substrate indicating that it was probably not roughened by adhesion enhancing

treatments. Bond coating, as a process, helps to mitigate this problem and extend fatigue life (Tzimas, 2000). It also helps with halting crack growth into the substrate from the coating. Pearson used a NiCrAlY-based bond coating applied 3 mils (0.0762mm) in depth by APS Materials, Inc. of Dayton (Pearson, 2008). This configuration will be adopted for the current study as well. Pearson neglected modeling of the bond coat in his associated 3-D ANSYS FEA model. He reasoned that the bond coat layer was very thin relative to both the beam and TBC layers of the system so that he could neglect its impact without detriment (Pearson, 2008). It is common industry practice to treat the surfaces ready to receive a TBC. The bond coating provides the following benefits: physical erosion protection and isolation from chemically reactive combustion products and contaminants, crack arresting between the TBC and metallic substrate, and the reduction of thermal expansion mismatch gradient (Bose, 2007; Tamarin, 2002). Since the current study will age-in the specimens to a fully mature state, they will feature a bond coat layer, as Pearson's specimens did, to minimize the risk of mechanical de-lamination during the age-in process.

In closing on TBC coatings discussion, it is worth noting that 8-YSZ is the predominate coating in use in the industry despite the existence of other coating materials. This is due to the thermal expansion compatibility of 8-YSZ to the nickel-based super alloy substrate typically utilized in jet engine turbine stages (Bose, 2007). Additionally the adoption of EB-PVD, a diffusion based method, as the dominant process has occurred due to its micro structure offering the best resistance to LCF from thermal spalling; this, despite a lower thermal resistance across the layer relative to APS

processing layers (Tamarin, 2002).

1.4. Previous Work - Chronological Summary

Qualitatively, the ceramic coatings were noted to have high damping for a relatively rigid material back in the early 1970's (Sridharan, 1974). Attempts to qualitatively assess by experimental means the damping and other mechanical qualities of hard coatings on plates were undertaken by Torvik and Patsias around 2000. Most research into the the non-thermal aspects of the coatings did not occur until after 2000.

Vaidya performed some early static testing using 3-point bend specimens coated with ceramics, in contrast to latter dynamic studies, he reported that the presence of the coating reduced the effective strength of the system. This was due to cracks in the coating serving as stress concentration sites before growing into the metallic substrate (Vaidya, 1995).

From a methodology standpoint, Bartlett (1994), in a unrelated study, used a bar specimen with a coil that was polymeric, free-free, and cylindrical suspended between a large U-shaped permanent magnet. He used this to determine complex moduli for polymeric materials using transverse and longitudinal bending modes as well as torsional. The setup he employed is very similar to the setup employed be Reed in 2007. Bartlett tested his polymeric specimens using non-contact excitation, non-contact measurement using forced response techniques for complex shear and Young's moduli, as well as damping. The specimens being polymeric materials with glassy and rubbery regions, this setup featured the ability to enforce controlled temperature variations (Bartlett , 1994).

Hoover, in 2004, working with the same group that Reed later joined, studied a technique to magnetically excite free-free thin beams, a non-contact method. The beam specimens had a set of rare earth, neodymium iron boron (NdFeB), magnets mounted at the lowest end of the beam, and suspending mono-filament lines to the zero-displacement regions of the beam. These beam specimens were suspended over a permanent magnet that was AC stimulated. Hoover has a thorough review of electromagnetic theory and interaction and presents useful methodology for generating current-to-force calibration curves between the coil and the magnet sets (Hoover, 2004).

Ivancic was one of the first researchers to systematically study the impact of hard coatings on specimens that were shaped to approximate the aspect ratio of fan- and low pressure compressor blades. Using two specimen sizes; a 5-1/4” x 4-1/4” x 0.050” (thin plate) and a 6-1/2” x 4-1/2” x 0.125” (thick plate) each geometry featured a bare and APS- coated plate. Two coating thickness of mag spinel were applied to both sides of the plates, 0.005in and 0.010in. Ivancic's comprehensive study focused on the 2nd bending (Plate Mode 3) and "2-stripe" (Plate Mode 4) modes of the plates. For experimental data capture both a Stress Pattern Analysis by Thermal Emissions (SPATE) system and a 2-D scanning DVL were used for stress field and multi-point displacement collection, respectively. The plates were excited as a clamped cantilever system (known as a “clamped-free-free-free” or “clamped-free x3”). Using a sine sweep or “chirp” excitation, which is a harmonic stimulation signal where the frequency is slowly varied in a linear fashion over time, the half-power bandwidth response was used to determine damping ratios at the various excitation frequencies and amplitudes based on the

frequency response function (FRF) curves obtained. Natural frequencies were obtained by dynamic ping testing using an impulse hammer and piezoelectric based accelerometer.

Ivancic also modeled the bare plates both numerically, using NASTRAN finite element analysis (FEA) (with "QUAD4" plate elements), as well as analytically using the Kirchhoff thin plate theory. Agreement between his experimental results, the FEA, and the analytically determined natural frequencies were high for the thin plates, within 1-2% of each other. For the thick plates, agreement between the models and and the experiment varied by up to 10%. Ivancic did not pose a reason for this finding, but this may have been due to a breakdown in thin plate theory as well as the lack of repeatability in the clamping condition with the thicker plate experiment. Ivancic also achieved good agreement between the iso-stress lines as determined by SPATE and those predicted in FEA analysis.

Ivancic, using only a bare plate (titanium) specimen tested a hanging free-free-free-free (free x4) plate and produced modal shapes using magnetic excitation. This was performed both at room temperature and within an oven heated to 275degF. He observed that the damping ratio for the bare plate varied by up to 30% when temperature varied from room temperature (about 60-70degF) up to 275F. Unfortunately, Ivancic did not perform free x4 tests on coated plates, and with the cantilever setup Ivancic had repeatability issues in the results obtained. The author concluded these were driven by variability in the clamping condition due to different torques, slight alignment differences, and other issues that varied upon each specimen being mounted, nonetheless,

strong qualitative trends emerged. The clamp was suspected also to the major source of system damping as well (Ivancic, 2003, 2005).

Ivancic also performed fatigue-to-failure tests by loading plates at a constant forcing amplitude, a dwell test. Loading both a coated and bare plate in the clamped-free x3 cantilever configuration, he found the the thin mag spinel coating extended the fatigue-to-failure life of the bare plate from about 800,000 cycles to over 5,000,000 cycles. This was a powerful qualitative demonstration of the mechanical potential of these coatings to extend fatigue life (Ivancic, 2003).

Blackwell tested plates with a cantilever area of 4-1/2in by 4-1/2in by 0.125in thick in the free, that is, non-clamped area, and his investigation focused on plate bending modes 3 and 4, (again, the 2nd cantilever bending mode and the “two-stripe” mode). Guide-shafts to the clamping blocks Ivancic had developed were added, along with matching socket holes in the specimens' grip area to help keep the geometry of the clamp-up consistent when changing the specimens (see Figure 7). This was to help control the variability of damping that the clamp introduced between each test.

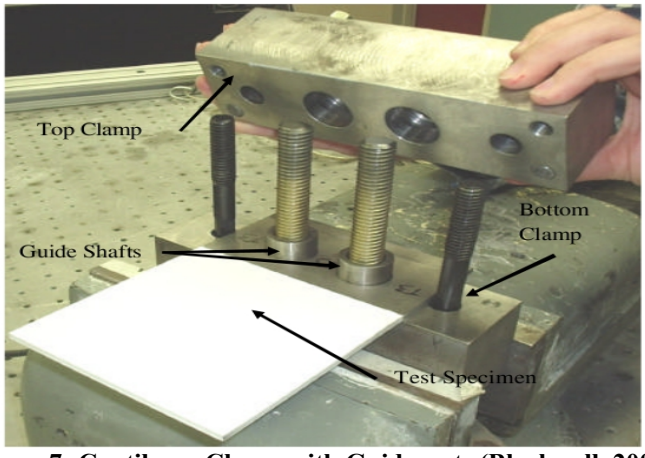


Figure 7: Cantilever Clamp with Guideposts (Blackwell, 2004)

Blackwell modeled the specimens using both Kirchhoff thin plate theory and FEA using NASTRAN (again using "QUAD4" plate-type) with 2-D elements. The samples were excited by a 6,000lb capable shaker table for large amplitude excitations, while for small amplitude strains, an air horn was employed. Both excitation methods used sine swept chirps in a forced response. The ½ power bandwidth technique to extract system damping and the natural frequency peaks was incorporated. Conducted in air, he obtained improved repeatability over Ivancic's results for his intra-sample testing while determining system damping and resonance points. This validated use of the more controlled clamping condition that the locating pins provided.

Blackwell obtained close agreement between the FEA eigen-system decomposed model for modes 2 and 3, and the experimental natural frequencies. Obtaining FRF sweeps of the coated plates around the mode 3 and 4 resonance peaks, Blackwell noticed distinct non-linearities in the FRF curves with variations in forcing amplitude. These plots exhibited classic strain softening, relative to the corresponding (vertical) FRFs of the bare plates. Some salient trends emerged from Blackwell's results in regard to damping of hard coatings: the damping of any coated plate is significantly higher than that of the bare plate at the same excitation frequency and amplitude, the loss quality reported for both bare and coated plates decreases as the strain amplitude increases, and while the damping curve as a function of strain amplitude did not change significantly across the two modes for the bare plate it did increase significantly for the coated plate when going to mode 4 from 3 (Blackwell, 2004). In closing, Blackwell recommended that further work be done to refine the clamping system to help reduce the uncertainty in

damping determination, that higher strain variations be investigated given the non-linearities encountered in the FRF's, and this key recommendation: "This research should also be repeated at temperatures characteristic of fan, compressor, and turbine blades, since that is the ultimate purpose of this research and the Air Force's interest in damping treatments in general." (Blackwell, 2004).

The next set of tests on plates was performed by Allen, in 2006, who tried to combine the lessons learned from the works of Ivancic and Blackwell. This investigation involved designing a vacuum chamber to place over 18,000 lb and 6,000 lb shaker unit heads, thus eliminating air damping on the plate, which the previous authors suspected could be significant. Further controlling the variation in the (significant) clamp-induced damping was also attempted, among other things a torque sequence was introduced into the methodology. Allen also performed characterization studies to ensure the optical pressure port window, made out of polycarbonate and riding on the shaker head, and therefore moving between the specimen and laser velocimeter, would not bias the laser measurement accuracy. The chamber featured this clear window on the top of the chamber to allow single axis DVL non-contact measurement of the specimen.

While performing the study on a clamped configuration plate, Allen also performed studies on a free x4 hanging plate of a "dual" size that exploited symmetry in a clever fashion. This sample was twice as long as the cantilever plate specimens; modes were stimulated that were mirrored across the line of symmetry. ANSYS FEA models using the "Solid 45" elements were built for the clamped and free x4 plates and an

undamped eigen-system response was determined. It is important to note that this element implies that this FEA model is a fully 3-D model as opposed to a 2-D plate/shell element one. This may help to explain the closer agreement Allen obtained obtained between his FEA model predictions and the experimentally determined natural frequencies and modal displacements than in previous work. This was the case despite the studies of both Blackwell and Allen using the equivalent of Ivancic's thick plates.

Though the experimental setup was promising in design, the base plate and handles of the vacuum chamber had undesirable vibrational modal coupling interference with that desired from the specimen clamped within the chamber. To correct the handle coupling Allen tried a clever arrangement of bungee cords to detune their respective resonance point away from that of the specimen. For the base plate coupling, no workable solution was found during the course of his studies. Nonetheless, some valuable findings emerged out of the results. While the shift in natural frequency of the specimen was small relative to its magnitude, this variation was close to linear in nature. It also distinctly had a relationship that depended on the air pressure around the cantilever system. The quality factor, Q, had a significant variation when air pressure was controlled in the chamber, though the variation was not very linear. Allen suspected this may have been due to complex coupling between the mode shape displacements and the baseplate under the test specimens las inked by a compressive standing wave interference in the air gap. Various mode shapes may have varying degrees of aero-elastic coupling that are peculiar to a given mode shape; an extreme example would be a compressive mode of longitudinal waves wherein the modes have very little apparent rigid body motion out of plane, and

therefore, minimal aero-elastic coupling. Changing the tuning of this resonance chamber was attempted by Allen using a piece of foam in order to to break up the standing sonic waves.

Among some of Allen's significant findings were: the natural frequencies of the bare plate had a dependence on the ambient temperature of the specimen under test, verification of this numerically in the FEA model was performed using modulus data from MIL-HNDBK-5J (See Figure 8), the antisymmetric modes of the free x4 plate of double size had the same mode shapes over the half-plate domain as the cantilever clamped plate, modal detuning of the apparatus could allow for extraction of useful data, and the Doppler velocity laser (DVL) and accelerometer techniques had good match in data up to where the contact sensor, which was a piezoelectric accelerometer mounted with to the plate wax, stated to saturate.

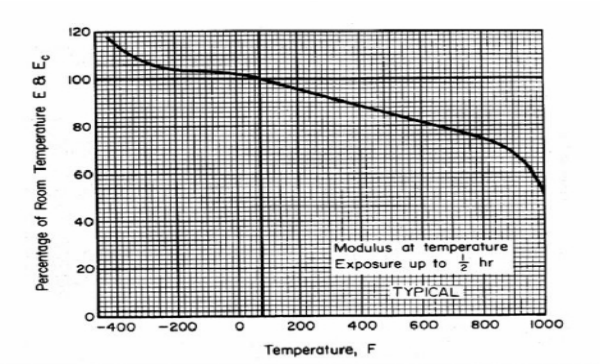


Figure 8: Modulus of Ti-6Al-4V Across Temperatures (Mil-Handbook-5H, 1998)

Large strain amplitudes could not be produced in the free x4 bare specimen due to the plate being a relatively rigid body compared to the weak coupling of the forcing magnet and coil exciter. Allen did report a 20% increase in system damping on the total

system as this plate was brought from a vacuum condition up to standard atmospheric pressure.

Allen closed with this recommendation;

> Finally, this investigator feels that there are great difficulties in quantifying air damping when there is significant damping caused by other sources. This is especially true with the influence of the clamped constraints. Exciting titanium specimen in a free- free-free-free condition would alleviate the specimen from this damping source. Testing at higher strain levels in the free-free-free-free condition may provide insight into the damping properties of mag spinel hard coating. Additionally, shaker testing at high strain levels (> 1,000 in/in) in partial pressures may yield greater difference between near vacuum and the full atmosphere condition (Allen, 2004).

Lee's investigation refined the technique developed by Allen, enabling extraction of useful data out of the system. Lee continued investigation of the mag spinel coating effects upon the 2nd bending and two-stripe modes of cantilever plates while trying to control for clamp- and air-damping. Lee performed extensive design modeling in ANSYS FEA not only of the specimen in modal vibration, but also of the base plate of the chamber clamped on the shaker heads. This was in attempt to detune it from the anticipated specimen resonances. His model was fully 3-D using the ANSYS-FEA "Solid 45" 8-noded brick element. Lee attempted modal decoupling by using two sizes of mounting heads and redesigned Allen's original base plate to shift the apparatus resonance away from those of the specimen (Lee, 2006). This was accomplished by stiffening it. To control for clamp damping variances, Lee added a set of torque values and sequences for the clamp system employed by Blackwell in an attempt to minimize

variation in the damping due to clamping interface changes. Clamp damping represents a significant fraction of the system damping. Lee performed extensive analysis of variations (ANOVA) testing in an attempt to determine the factors that were significant damping determinative factors in Allen's apparatus.

The free x4 suspended plate (bare only) with air horn excitation was investigated by Lee, the antisymmetric modes he obtained matched those of his cantilever (bare) sample, but only low strain amplitudes could be achieved and the sonic excitation ruled out testing in a vacuum. A clever arrangement of four DVL sample collection dots and employment of an averaging technique allowed for removal of rigid body motion from the specimen data set as opposed to signal processing in a hardware or software filter. Lee performed a comprehensive analysis of variations ANOVA study upon the apparatus to determine that there is a positive significance from applied forcing amplitude, mode shape, and air pressure upon the specimens' response.

Lee noted that the air horn excitation could only produce small displacements, and therefore strains, in the free x4 plate. The quality factors reported in this linear system (bare plate) were on the order of 10X that of those he obtained of the equivalent size clamped bare plate, an important finding that suggests clamp energy dissipation dominated over those of the surrounding air or even internal specimen hysteric losses (Lee, 2006).

To back up the results of the FEA design analysis, a battery of ping impulse hammer tests were performed on the modified and assembled pressure vessel, plate,

sample, and shaker rig. Lee determined that DVL data obtained through the polycarbonate pressure vessel window correlated well with data obtained from a contact piezoelectric accelerometer, and found no evidence of significant modal interference at either mode 3 or 4.

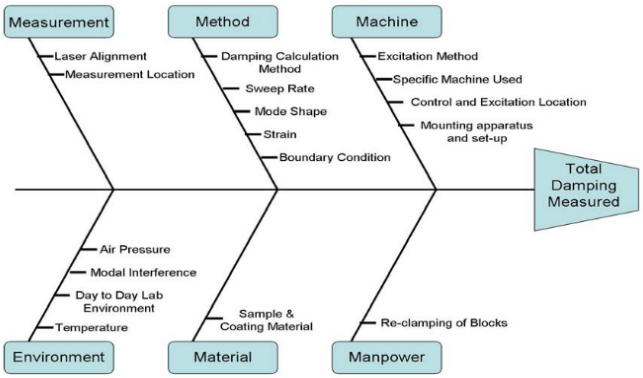


Figure 9: Ishikawa Error Analysis Diagram of the Allen Setup (Lee, 2006).

Lee makes some insightful observations, "The plots in this section for the uncoated sample are fully consistent with the results found by Allen in his experimentation. The data from his study also indicated the presence of air damping in mode 4, while data for air damping in mode 3 was more difficult to interpret. The constraint blocks show varying movement across the upper surface. The clamped condition is non-uniform, and this condition changes each time sample is reattached to the blocks via torqued bolts. Repeatability worsens when the sample is reattached between runs." Lee continues with a key recommendation,..."The lack of repeatability in the blocks makes them undesirable, even if the damping they introduced was known. Repeatability could be improved, of course, if beams were tested instead. A clamp for a beam would have less opportunity for a non-uniform clamping surface, due to its smaller width. This, however, would defeat

the purpose of determining damping properties for plates" (Lee, 2006). Figure 9, an Ishikawa root cause or “fishbone” diagram, is indicative of Lee's determined attempts to identify and control for system damping quantities for the cantilever plate.

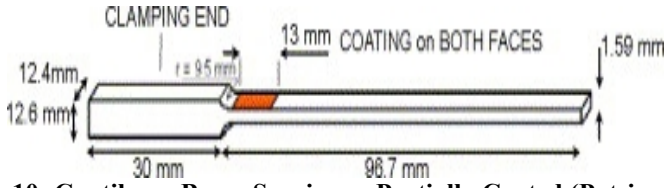


Figure 10: Cantilever Beam Specimen, Partially Coated (Patsias, 2006)

Patsias, Tassini, et al. performed testing on cantilever beam specimens (see Figure 10) partially coated with 8-YSZ in an approach very similar to Reed in methodology but using a forward, iterative method of FEA property determination of the coatings (the forward sense will become clear shortly) and a cantilever beam specimen with the TBC coating on the root region of the beam. Meanwhile, the specimens were modeled with an associated FEA model built in ABAQUS using 3-D solid elements as per Figure 11.

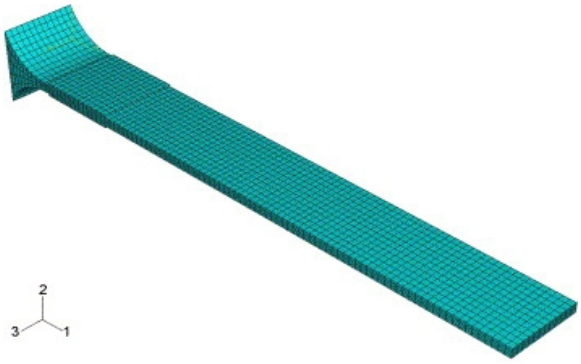


Figure 11: FEA Model of Partially Coated Cantilever Specimen (Tassini, 2006)

Patsias et al outline their approach, "the resonance frequency of the first flexural mode of the uncoated specimen was calculated to be 154.68 Hz by the software, which differs from the experimental value by 0.01%. A package ‘Fella’ is used to add the coating

layer(s) using 20-node quadratic brick elements. A routine written in a programming language Matlab modified the assumed value of Young's modulus of the coating, saved the new model and instructed the FE software to run an eigenvalue analysis for the first flexural mode. This process is repeated for each strain level tested (Patsias, et al., 2006)." The authors determined curves of system loss factor (η) and resonance frequency versus peak strain, and FRF magnitude versus excitation frequency. Using this iterative method, it was cumbersome to recover the material properties compared with the "inverse" method Reed later employed but was a breakthrough in determining the bulk material properties of the TBC material in an extrapolated sense. By adopting the cantilever beam with associated FEA model, Patsias and Tassini were able to determine the bulk mechanical properties (complex moduli) of the coatings from the specimen responses, Figure 12 is typical of their results for the coatings where the loss factor, η, of the coating and the storage modulus, E are plotted against the initial ("starting") free-decay strain imposed.

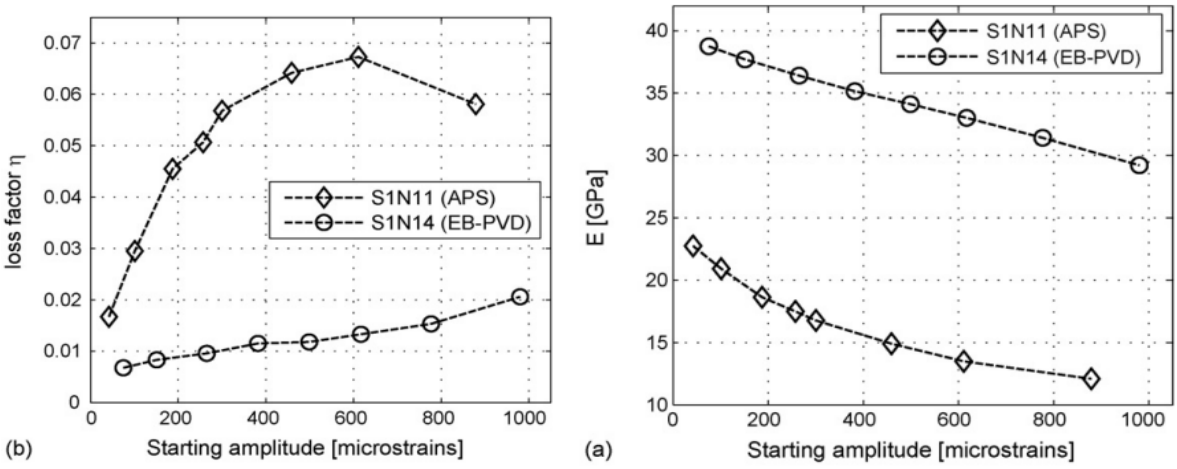


Figure 12: Results of Patsias and Tassini for 8-YSZ (Tassini, 2006)

As can been seen from the Figure, Tassini and Patsias also compared coatings applied by APS and EB-PVD, on otherwise identical specimens, against each other. APS was reported to have a lower effective modulus while having a significantly higher loss factor than EB-PVD, up to 3-4X (Patsias, 2006; Tassini, et al., 2006). Both of application processes demonstrated material nonlinearities. How the clamp damping was approached and handled as a significant source of variation and error was not elaborated on. Again, recommendations for elevated temperature testing were made. This work was a major leap forward as bulk properties inherent in the material were determined, orthotropic qualities in the materials were suspected, and a non-contact method of determination of strain using scaled modal FEA analysis was presented.

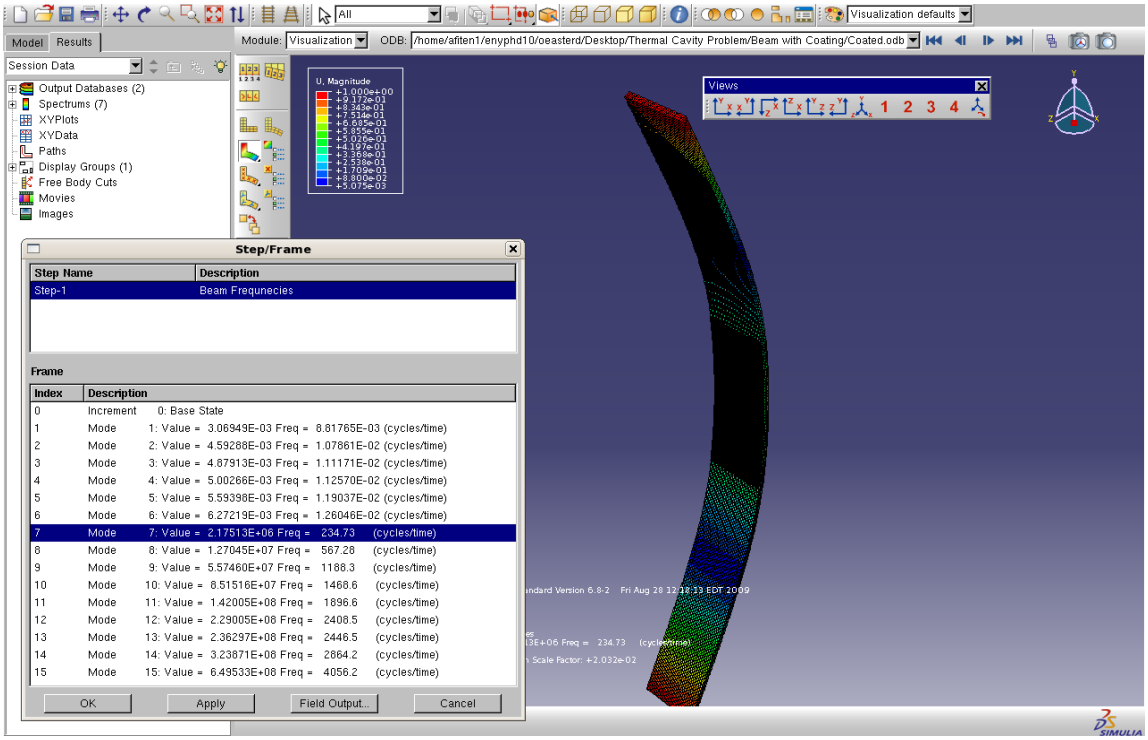


Figure 13: Dynamic Eigen-system FEA model, 3-D

The investigation of Reed employing the recommendations of Allen to employ free conditions in vacuum, Blackwell to focus on beams, Ivancic and Hoover (Hoover, 2004) to utilize non-contact magnetic excitation, and Lee to abandon clamping, brought altogether, was a great leap forward in the methodology by refining Tassini, Patsias, et\ al.'s approach (Reed, 2008). Reed also choose to use a thin beam geometry, which featured the following benefits: adoption allowed employment of classical (dynamic) Euler-Bernoulli thin beam theory easily explore what modal shapes and frequencies the specimens would produce, allowing the relatively weak electro-magnetic system to produce large strain amounts on a relatively flexible specimen within a vacuum (large amplitude strains would be difficult to achieve with thick beams and/or plates), and simplifying employment of totally free boundary conditions to eliminate clamp damping. Reed was, after Patsias, et al., the first to be able to successfully reduce the system damping and natural frequencies into geometry-independent, bulk values of effective modulus and loss factor for the coating material. In his studies the TBC studied was mag spinel applied by APS. The author focused on exciting the bending mode-I resonance in pairs of thin beam specimens, one coated in a dual layer of mag spinel running for the middle 25% of the length of the beam specimen across the entire width, and one of the bare Ti-6Al-4V titanium of the same dimensions. These beams were hung vertically in a vacuum chamber suspended from nylon mono filament lines running along the two zero displacement nodes in the fundamental bending mode (mode-I) in what is referred to as a free-free condition, where both ends of the beam are inertially unconstrained in space. A set of magnets were bonded at the lower node point and an AC current air-core coil was

placed below the beam to setup a fluctuating couple on that beam node. Reed's literature review had a comprehensive review of past researcher's attempts to achieve a free-free state in beams within the laboratory. The apparatus of Reed had some advantages over previous TBC coated specimens. It allowed a relatively simple FEA model using 1-D beam elements as was later demonstrated by Deleon (Deleon, 2009) and very high strain levels can be excited by even the relatively weak electromagnet coupling system which will continue to work in a vacuum, unlike an air horn. Additionally, a wide variety of literature on various beam geometries, including laminated beams, is available as developed by Oberst, Torvik, and others.

While the author chose thin beams as his specimen geometry, he performed extensive FEA modeling (See Figure 11, 13 and 14) using ANSYS based models of the beam system using a full 3-D model comprised of eight-noded elements of the ANSYS "Solid45" type. Reed's modeling consisted of eigenvalue and -vector decomposition of the primary modes, focusing especially bending mode-I. These analyses were critical in transforming the experimentally determined coated beam (and associated bare beam) system damping values and natural frequencies into effective modulus and loss factor as would be encountered in a Rayleigh (also known as proportional) damping model.

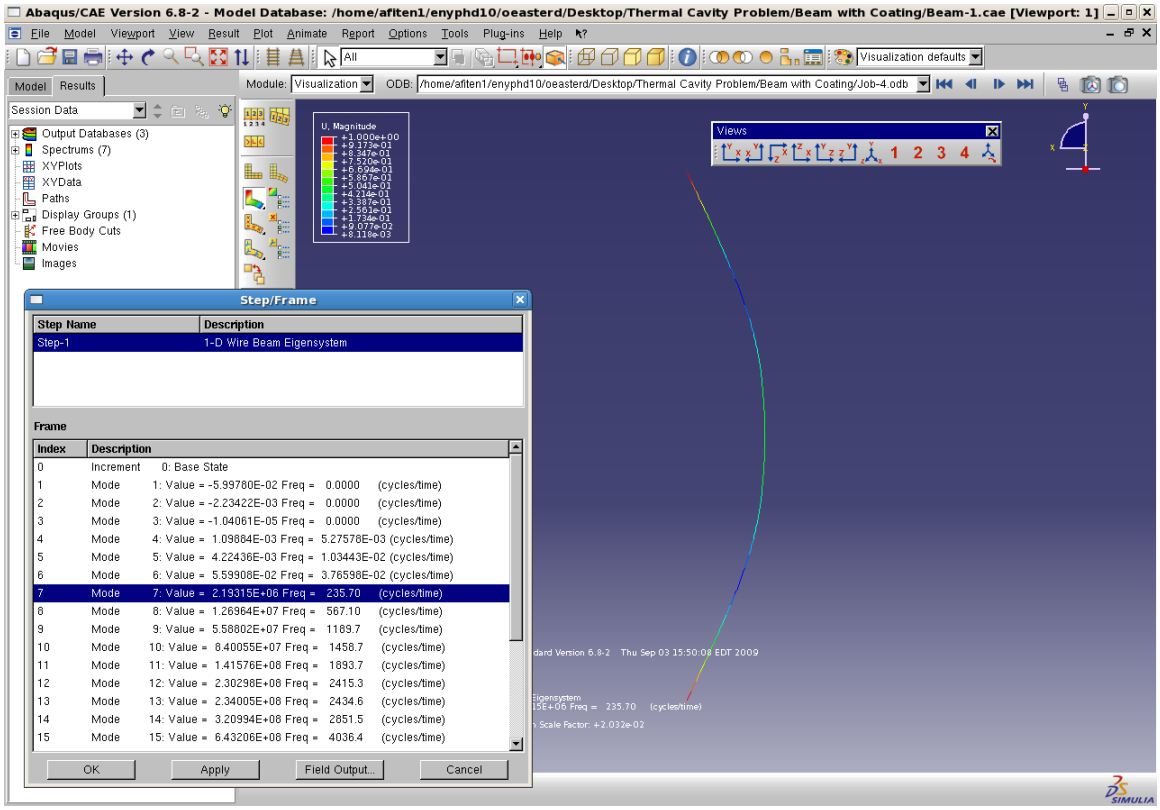


Figure 14: Dynamic Eigen-system FEA model, 1-D

The author modeled the coating within the FEA model using a Hookian (linear elastic) solid with an assigned effective modulus. While Patsias, et al., iteratively refined the assumed coating effective modulus to match the model output frequency of the simulation to that of their experiments, Reed in contrast, cleverly determined the coating effective modulus using the inverse procedure. The author systematically varied the coating modulus across N+1 simulations and built an Nth order polynomial of coating modulus as a function of mode-I natural frequencies obtained from the eigen-system model results. He then built N-th order polynomials of normalized center beam displacement as a function of coating modulus, normalized bending strains, and elastic strain energy ratio between coating and the beam metal. The (modal) center

displacements are dimensioned and scaled by applying the associated experimental data at a given natural frequency, from which the coating modulus is obtained from the initial function, and then the normalized displacement of the center point from the second polynomial is extracted. The the real bending strains are obtained from the third polynomial relation, then scaled against the actual center point displacement from the DVL data. This inverse procedure saved having to iterate and refine the assumed coating modulus towards the experimental value with intensive amounts of simulation modeling using the forward "guess and check" method. It is noteworthy that Reed collected both his coated and bare beam data using both a frequency-domain (forced response with ½ power bandwidth) and time domain technique (free decay using log-decrement), see Figure 15. Reed did not extend the numerical studies into a fully transient modeling using his material properties determined for the TBC. It is noted that the shape of the forced response based curves are similar to those of Tassini shown in Figure 12, both the loss coefficient and the storage modulus curves share similar topologies.

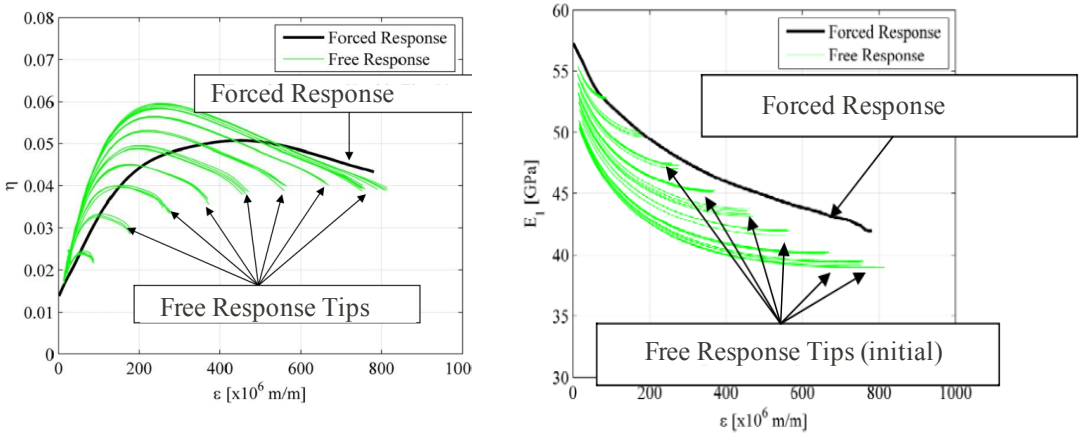


Figure 15: Findings of Loss and Storage Moduli Across Strain Amplitudes (Reed, 2007)

The free- and forced-response curves are shown, it is noted that the free-response data has a different trajectory against the strain level based on the initial amplitude of the forcing function before its removal. Reed posits that three possible mechanisms could account for the differing trajectories: thermal effects, strain-rate dependence, and strain history. He suggests (Reed, 2007; 219) that the third is the major driver of the differing trajectories. This may not be the case either (assuming the coatings are fully mature, see Section 5.1.3) and it is argued by the current author that this may be driven by the nature of the loss mechanism instead. A good qualitative agreement with his modified Iwan model was achieved that generated separate curves of similar form for both the bare beam with pure viscous damping and the non-linear beam with only a range of dry friction damping applied (Reed, 2007). This suggests that the nature of the coating loss mechanism is responsible for generation of these curves. One can view the beam, both bare (linear) and coated (non-linear), as a tuned resonator trading potential energy

$PE = \frac{1}{2} m_{eff} x^2$ (at the extremes of bending displacement) for kinetic energy

$KE = \frac{1}{2} k_{eff} \dot{x}^2$ (at the neutral, unbent displacement). This occurs at 2X the rate of the resonance frequency, once for the beam stroke to each extreme of the bending shape, (ignoring higher modes for the moment). The viscous loss mechanism, being linear, should scale with the current output amplitude, of the system, once the forcing function power is switched off. One could by analogy argue over one cycle that:

$$E_f = E_i - \Delta E \quad ; \quad \Delta E = \begin{cases} c\,\dot{x} & \text{for linear system} \\ c & \text{for dry loss} \end{cases} \tag{1}$$

where E_f is the energy at the end of a cycle, E_i is the energy at the beginning and ΔE is the energy lost over the course of a single cycle, which is of the form $c\dot{x}$ for the linear system and c (a constant) for the dry system. So while E scales as the square of the forcing amplitude the sink term scales linearly with amplitude as well for viscous losses. This is not the case for dry friction. With a dry friction sink term, start from a smaller amplitude (energy level) and the damping effect will be smaller relative to that particular initial energy level amplitude. With each cycle, the total energy of the viscous system changes from cycle to cycle, e.g., the linear system energy loss scales with the change in displacement amplitude associated with the energy change, the dry Iwan model does not feature this, the total energy loss remains the same cycle to cycle, regardless of the current amplitude.

Meanwhile, for a forced response, the coupling driver keeps the beam at the same total energy state in a harmonic fashion, swapping forth between extremes of potential energy and kinetic energy (assuming the chirp sweep rate change is slow enough relative to the mode-I resonance frequency to be essentially steady harmonic) and therefore the system damping losses are replenished over the course of any given cycle by the forcing function couple moment as per

$$E_f = E_i - \Delta E + \Delta E_{electromag} \tag{2}$$

For the linear (viscous) beam the coupling moment ($\Delta E_{electromag}$) changes from cycle to

cycle (e.g. $E_f \approx E_i$ and $\frac{\Delta E}{\dot{x}} = c$ for a viscous system while $\Delta E = c$ for a dry one) whereas for the dry, coated beam it does not. In the viscous system this is to compensate for the variation in damping as output magnitude changes upon approaching, passing through, and leaving the resonance point. As a result the magnitude of the damping loss in the dry system does not vary based on the initial energy state and trace separate trajectories for free decay. In summary:

· pure (viscous) linear damping → log decrement magnitude scales with amplitude (instantaneous) → pure exponential decay envelope function → loss coefficient (η) is constant across the strain levels

· pure (coulombic) dry damping → log decrement magnitude constant with amplitude (instantaneous) → linear decay envelope function → loss coefficient (η) is not constant across the strain levels, maximal at low amplitude.

This maximal peak suggests that Reed's results may have a combination of the two at work. Explaining this is not an objective of the current study, but valuable insights into this may crop up in the current study. An excellent overview of mixed damping models as well as experimental damping determination is given in an on-line paper by Peters (Peters, 2002).

This suggests several things: one, is that forced response is a good technique for the linear system as well as the non-linear system loss mechanism quantization. Examining Reed's plots of η and E_c versus the strain closely(see Figure 15), one can see

that as the conditions of the two tests converge in a cycle-to-cycle sense (e.g. as one starts with a very small amplitude in a free decay and forcing with a small amplitude in a forced response testing) the peak loss coefficient determined from the free decay envelope coincides nicely with the response amplitude in the forced system. In this region, $E_f \approx E_i$ and the variation of damping with energy change becomes almost equivalent whether by viscous or coulombic mechanism. Saturation can be seen in both free- and forced- responses as the trend of the initial tips of the (green) free response curves trace a logarithmic type function at successively higher initial amplitudes and trace of the forced response curve (black) levels out then descends slightly.

Reed's data also suggest that viscous loss mechanisms exist along with the dry friction loss mechanism with the variance of the loss factor across the strain amplitudes, when measured by either free decay or forced response methods. While the non-linear, coated, systems ring-down during a free decay their resonance frequencies are constantly shifting during the ring down as the resonance frequencies are displacement amplitude dependent due to the non-linearity of the coating. This is deducible from the strain softening backbone curves where the FRF peaks are functions of both the forcing frequency and current amplitude. Also, it was reported by Reed that to set up a free decay ring-down test, after selection of a new initial forcing amplitude, determination of the resonance frequency peak by sweeping the forcing frequency had to be performed to find the new resonance peak, before proceeding with the free decay envelope collection (Reed, 2007).

Reed smoothed his data in processing using the Matlab **csaps** function, this may not have been so critical due to the signal to noise (noise being jitter and high mode signals on the bending mode-I harmonic) ratio being around 0.025 m/sec over a range of 4.0 m/sec, yielding around 160:1, which is very favorable. A critical data processing step Reed performed was to smooth his data with a running average of the last 100 data points to eliminate the ringing artifacts imposed on the signal by application of the Hilbert transform to an asymmetric dataset. He used a cubic smoothing spline to reduce the (small) effects of the around 10 Hz rigid body motion effects that show up as oscillations on the decay envelope (Reed, 2007).

Reed, and later Pearson, tried to perform sweep rate studies using the 1/2 power bandwidth technique to determine whether the discrepancy between the complex moduli derived by 1/2 power bandwidth versus those from free decay was influenced by lack of a quasi-static change to the harmonic condition. Deleon found that while the bare beam was sensitive to sweep rate changes, the coated beams were fairly tolerant of a faster change in sweep rate (Deleon, 2009). This was due to the much higher damping in the coated beam systems (Reed, 2007; Pearson, 2008). Deleon and Palazotto hypothesize that the up-swept data (for strain softening materials like 8-YSZ or Mag Spinel) used in conjunction with the 1/2 power bandwidth technique may resolve much of the discrepancy (Deleon, 2009).

Obtaining frequency domain data involved sweeping the resonant system at various levels of coupling moment, achieved by setting the amplitude of the AC current

feeding the coil, and capturing the frequency response functions around the bending mode-I point. Time domain technique involved tuning the excitation frequency to the maximum amplitude of harmonic response at a pre-selected amplitude of AC coil current, and once the beam was in a steady, harmonic condition, the excitation was then shut off and the decay response recorded. This was repeated at various initial amplitudes and each decay envelope was obtained; this was performed to deal with non-linearity in the response across various strain levels. Each of these runs traces one of the arcs on the loss factor and effective stiffness modulus curves. Many techniques were refined by the experimenter in the course of this study including: the use of software filtering for eliminating rigid body motion from the time series data, vacuum sensitivity studies for assessing air damping significance, and a methodology to reduce the material effective properties from the experimentally measured system. Reed summarizes:

> Torvik presented damping data from a cantilevered, uncoated Hastelloy-X beam. His data also indicates that system damping increases as the strain amplitude increases. The magnitude of the damping in his data is significantly larger than that seen in the present experiment. For example, for a beam vibrating in its second mode at a strain level of 500 με (V~1 m/sec), the author reports a $\eta = 0.0010$. By performing the experiment in a low pressure environment and using a simulated free-free boundary condition, a constant loss factor of $\eta=0.0004$ is achieved up to a strain level of nearly 1600 με as shown in Figure 88 [see (Reed, 2007)]. This nearly 2.5x reduction in loss factor suggests that the complexity involved with this experimental setup may be justified. (Reed, 2007).

While the primary motivation for performing the experiment with a free-free boundary condition in a vacuum chamber was to reduce the system damping to as low a level as possible, the other benefit is that the beam, coupled with free-free boundary conditions,

behaves linearly, predictably and repeatably (Reed, 2007). It became clear why the freely suspended system is so advantageous over clamped systems when studying very slight variations in systemic damping.

Pearson studied beams coated with either mag spinel or 8-YSZ applied by APS in a refinement of Reed's work. He employed only frequency domain measurement in conjunction with half-power bandwidth to characterize them. He was able to corroborate and replicate many of Reed's results for mag spinel and added the much more commercially utilized 8-YSZ to the study, but his mag spinel results feature some 10-15% higher damping for it than were reported in Reed's results for the coating loss coefficient values. This was later thought reduced to a much smaller discrepancy when Deleon reviewed the methodology and corrected for an error in determining the strain energy ratio (SER) using the method derived by Torvik (Reed, 2007; Deleon, 2009). Unfortunately, the current author noted that while Pearson reported an incorrect equation term in his methodology, his data processing instead using the correct form of the equation. An important finding by these two for the strain softening coatings is that the up-swept FRF curve extracted from the frequency domain method, when processed by the linear 1/2 power bandwidth method, agrees much more closely with the time-domain based data. Deleon hypothesizes that this is due to the jump phenomenon taking one through the region of non-linear material (strain softening) behavior more rapidly, and he suspects sweep rate may play a role if not close enough to a quasi-static change in the harmonic state. The up-swept FRF data features a more sharp maximum resonance peak, in contrast to down-swept data. It is suspected by the current author that up sweeping

through the peak places more energy into the system (assuming that amplitude is roughly the same at frequencies just below and just above the resonance peak) and such is taken in and absorbed readily, as opposed to when sweeping down in frequency, dissipative energy has be shed from the system while the beam seeks a lower energy harmonic state. Some of this may be dissipated in the coating, but some energy may also be lost in the magnet coil interaction ("back emf"), the suspension wires, and the bulk substrate motion. Phenomenologically speaking, the down swept FRF curve is less well defined and is less topologically like the symmetric, even peak that typifies the FRF of a linear system but the down swept curve accurately captures the resonance frequency peak of the FRF curve that the up-swept curve cannot do for strain softening materials. This is because the jump phenomenon takes place before the resonance peak is reached on the FRF curve. Pearson's data for YSZ and mag spinel are presented in Figures 16 and 18, respectively.

It is noted that both materials exhibited similar qualitative trends with strain softening FRF "backbone" curves, loss moduli that logarithmically increase, and storage moduli that decrease in similar fashion. Compared to the mag spinel material Reed had characterized, 8-YSZ was a less stiff and a more effective damping material (Pearson, 2009).

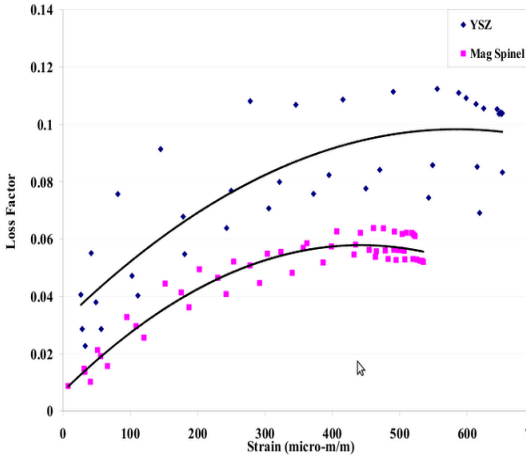


Figure 69: Material Comparison of Loss Factor

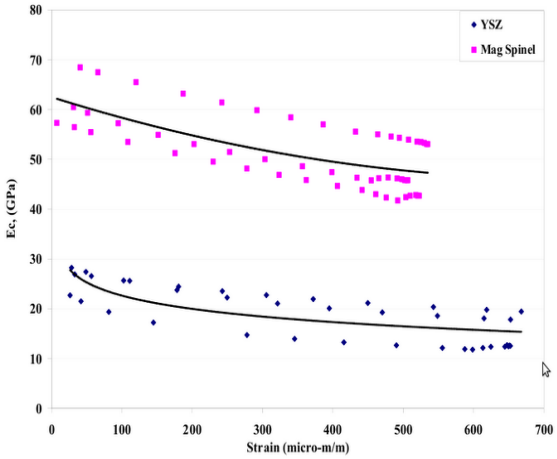


Figure 68: Material Comparison of Coating Modulus

Figure 16: 8-YSZ and Mag Spinel Loss Coefficient and Storage Moduli (Pearson 2008)

In addition having noted Reed's observation of a history effect, Pearson performed a qualitative comparison study involving scanning electron micrography (SEM) of both virgin and cyclically loaded beams, both 8-YSZ and mag spinel coated. These before and after shots of the coating micro-structure were valuable to hypothesizing that a damage model of crack growth with strain cycle accumulation could account for the change in the system damping (as well as coating effective modulus) over the loading history (Pearson, 2008; Abu Al-Rub, 2010). A typical micro graphic evolution of cracks and splats that he found is shown in Figure 17. Even though these before and after photos are of not the same exact sample compared across time alone, it shows that loading history influences the crack density in the TBC, and therefore energy dissipation. Patsias and Tassini, et al. also presented similar findings (Patsias, Tassini, et al., 2004).

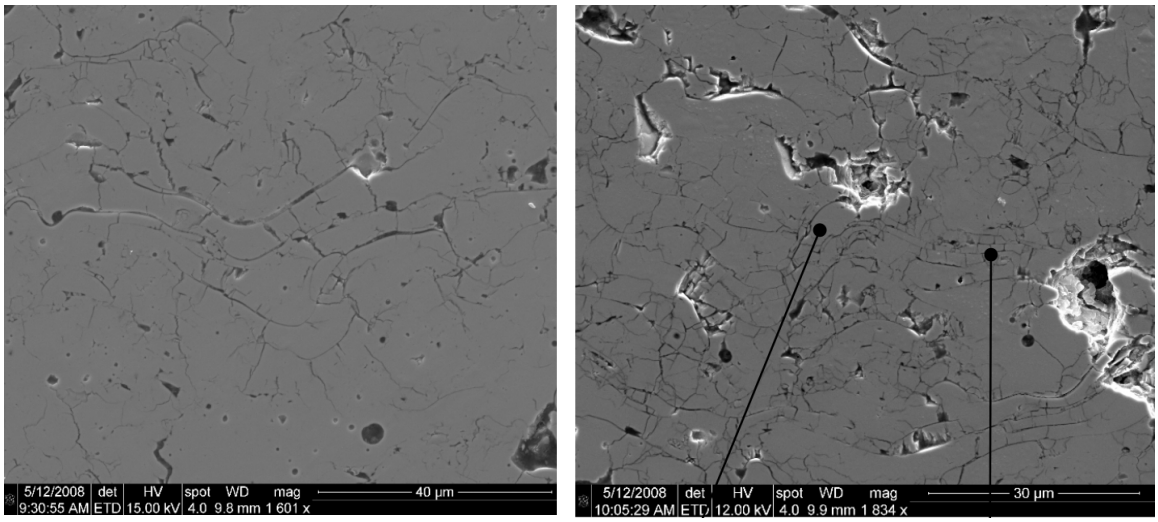


Figure 17: SEM of Untested (left), and Tested (right) 8-YSZ, 1600X Mag (Pearson, 2008)

In the course of analyzing his data, while Pearson made many bold assumptions, one such was assuming non-linear artifacts in the bare beam FRF sweeps; such were later determined by Deleon to be second order overshoot ringing. Nonetheless, the author achieved by physical intuition some major improvements in the testing apparatus and methodology. Among these were: reducing rigid body motion of the beam to negligible levels by shortening and tightening the suspending mono-filament lines while adding a tension bar in the back, raising the active node and magnets above the coil end plane and finding an optimal distance for stability in the resonance pattern while preserving a high driving coupling force, how to model and include bond coat into the specimen system, and how to control for strain history effects in the TBC materials (e.g. establishing an aging protocol) (Pearson, 2008). Some of these were later quantitatively confirmed by Deleon (Deleon, 2009). The first improvement was particularly useful as it eliminated the need for cumbersome software and/or hardware processing and filtering of the time series

data that Reed had used to separate the desired transverse vibrational motion out from the undesired rigid body motions of the beam. Pearson's second improvement prevented the electromagnet from imposing rigid body motions and rotations on the beam system from over-coupling with the magnet (Pearson, 2008).

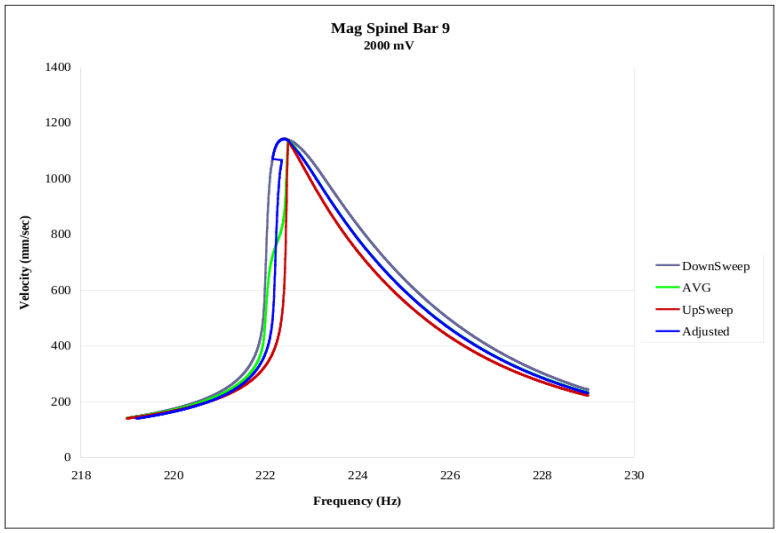


Figure 18: Reconstruction of FRF from Up- and Down-Swept Data (Deleon, 2009)

Deleon reconstructed the data of Pearson and re-analyzed some of it, and made strides forward in reconciling non-linearities in the forced response data. He attempted to reconstruct the true curves including within the non-linear "jump" region using Pearson's up-swept as well as down-swept data like in Figure 18. The jump region is where the beam will suddenly undergo sudden magnitude changes when proceeding from one stable state to another through the region of instability. However, without the benefit of data with a set of large linear-region in the tails to match, the experimental peaks are well separated in their respective amplitudes due to the jump occurring on the up-sweep for strain softening materials like YSZ. Despite this he proceeded to match the peaks within

the jump region together and then attempt to synthesize the real FRF curve. It is to be noted that for the current study, the matching of the up and down sweep data will be in the "linear" behavior regions well removed from the jump phenomenon near the resonance peak. Deleon tried several techniques to extract the system's damping and resonance frequency from Pearson's data as shown in Figure 18.

These attempts included: a straightforward application of ½ power bandwidth theory after averaging the two curves together across their respective magnitude values, using a polynomial extrapolation technique to determine true resonance frequency across amplitudes developed, and applying a energy based method developed by Torvik to correct for the non-linearities. (Deleon, 2009). It is to be noted that the method by Torvik asserts that, for non-linear materials, a reduction in the error due to measurement uncertainty with non-linear systems may be reduced by taking an energy fraction much lower than the customary half-power level, as long as other resonance peaks are not close enough to interfere with that given FRF peak and mode, like a "¼ power bandwidth" (Torvik, 2003). This assumes that modal resonance points are well-separated.

Deleon working with Palazotto on the bare beam system, hypothesized that it may be able to be accurately modeled by the employment of an analogous single degree of freedom (SDOF) system. The mass of the beam system was used as the effective mass, an effective (tuned) spring stiffness, and experimentally determined damping from the physical system that are effective equivalent values placed into the SDOF analogy model and tuned to the experimental output response. This was an attempt to determine the

force needed to excite the beam in a fully transient FEA model that was developed by Deleon to obtain a given output amplitude at a prescribed frequency and magnitude of harmonic excitation force. This also has been attempted by others with success, Youssef and Lagache presented notes where a flexural beam with a thin piezoelectric patch on the root with tunable stiffness was modeled with a 3-dof. (degree-of-freedom) model in lieu of FEA simulations (Youssef, unknown).

Deleon made some compelling recommendations to be employed in the current study. Among these are: to load the suspension mono-filaments to a high- and controlled tension to make their vibration dynamics specified and known, to characterize experimental mode shapes by using either a scanning DVL or a single axis DVL on a adjustable height stand, to age in specimens to a mature state (in terms of strain history), and to perform a thermal stress analysis on the coated beam system to determine the residual stress state in the beam system when static (Deleon, 2009).

Only three study groups have performed mechanical characterization of the hard coatings at elevated (above room ambient) temperatures to date. Gregori tested dual layer 7-YSZ coated cantilever beams placed within an air-filled furnace; this apparatus is depicted in Figure 19 (Gregori, 2007). Of course clamp- and air-damping were present in the findings based on the design of the apparatus; the author tested the samples up to 1000degC. The author reported that there was a large maximal spike in the loss coefficient at around 200degC where it was around 0.01 (Note the loss factor is the reciprocal of the quality factor, e.g. $\eta = 1/Q$). A large level region of the loss coefficient

curve was at around 0.002 for 8-YSZ from about 400degC on up. This can be seen on the right side of Figure 20. For most of the temperature range, this damping value was about double that of the bare super-alloy beam, whereas Reed had around 10X damping difference between bare- and coated-beam during his studies. Meanwhile, the storage modulus of the coating reported by Gregori seemed to roughly linear and decreased with increase of temperature. Limarga characterized 7-YSZ and $Gd_2Sr_2O_7$ as shown in the left of Figure 20 (Limarga, 2007).

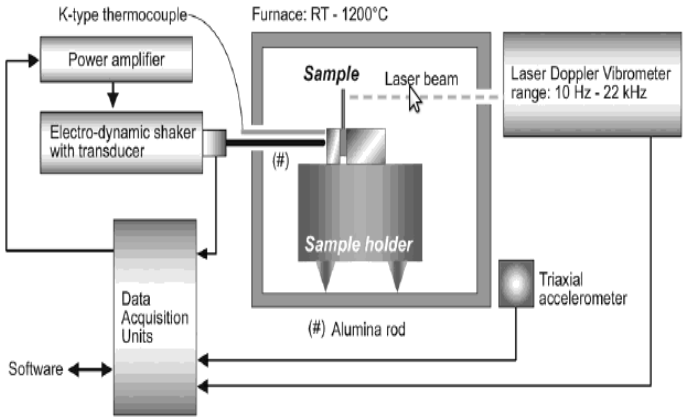


Figure 19: Apparatus and Specimens used in Elevated Temperature Testing (Gregori, 2007)

Again, it is noted that the same high sources of damping from the air and clamp still exist with the setup of Gregori and Limarga, nonetheless, valuable qualitative data on how the coatings behaved with temperature changes was obtained (Limarga, 2007) and (Gregori, 2007).

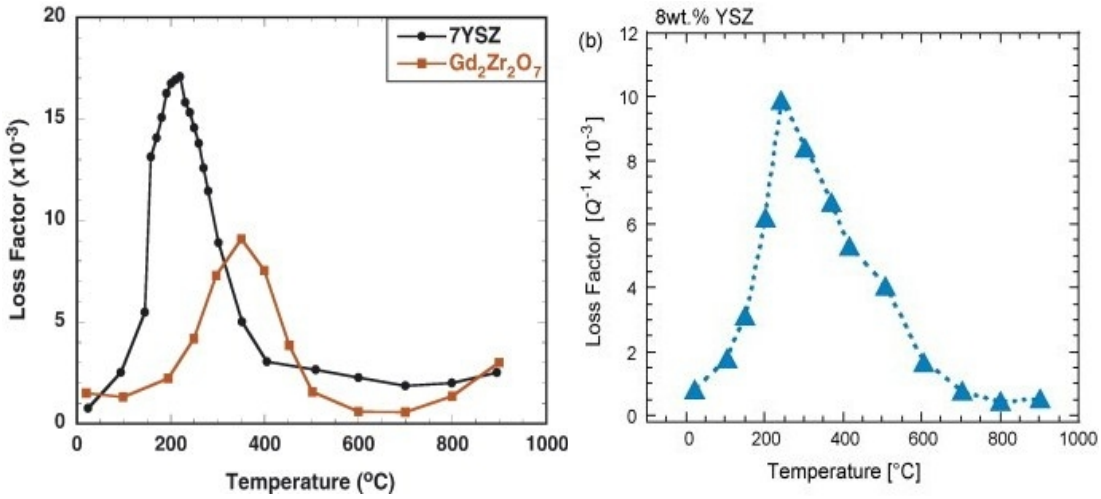


Figure 20: Loss Factor, 7-YSZ (left) and 8-YSZ (right) Specimens vs Temperature (Limarga, 2007; Gregori, 2007)

For the second high-temperature study, Reijda fabricated monolithic axial test specimens from APS-applied 8-YSZ and $CaTiO_3$ coatings, by machining and chemically etching away the low carbon steel substrate to which they were applied on some dog-bone shaped specimens. Axial testing on MTS machines was accomplished with zonal induction heating up to 800degC to test the fatigue life and the hysteresis of the load and unload curves. This can yield the loss factor in the slowly loaded state. This appears to invalidate the need for the current study, but it is noted that the in-service usage of TBC are generally in a composite structure and that the substrate coating interaction is not replicated here. These specimens may fail to capture the substrate-coating interactions that are important to lifespan and maturity of the coated systems. It is noted that most HCF modes of the turbine blades are those of bending. Aging-in of the coatings to a mature state was not performed, and the strain loading rates were very low, essentially quasi-static from the standpoint of HCF type loadings. Nonetheless, this study is a useful

benchmark of what is ahead and the results may provide data to get a baseline of the static properties of the 8-YSZ coating in terms of loss coefficient and storage modulus (Reijda, 1996).

For the third study, Guidoni performed elevated temperature testing of 4-point bend specimens with 8-YSZ coatings. While overcoming the limitations of monolithic specimens, this was essentially static testing (Guidoni, 2005). These tests given insight to the static properties of the TBC coating, but as HCF is very much a dynamical loading situation, the free-free resonator setup still is going to be very attractive to employ at elevated temperatures.

It is worthy to close with a note on the damping of classical engineering materials, such as metallic alloys, plastics, and wood, in that both the amount of any material data on damping for materials is sparse in the literature but that the determination of these are quite sensitive to procedural approach, specimen preparation, and test apparatus. One the few works to catalog the damping of a wide range of materials was performed by Lee back in 1966 for the USAF Materials Laboratory (Lee, 1966). Lazan, in his seminal book on damping in 1968 before presenting data of various materials cautions the reader...

> Damping is one of the most structure sensitive properties. Thus, it is often found that slight differences in composition, thermal treatment, and mechanical processing can lead to significantly different results for the "same" material. Publications often do not include detailed information on important chemical, thermal, and mechanical features, and as a result it is often very difficult to associate differences in the measured values of damping with these features. Small differences in temperature and humidity may also have significant effects on damping, particularly in elastomers, polymers, and other non-metallic materials. (Lazan, 1968)

This is indicative that the seeking of low-bounded conservative design values is perhaps the realist objective for the current study.

1.4.1. Experimental Highlights

The techniques of the proposed study are the direct beneficiary of the lessons learned and recommendations of the previous work. So a discussion and coverage of the highlights of the past work will yield insight into how to conduct the current study. A breakdown of the chronology reveals that the free-free beam geometry within a vacuum is an optimal configuration. This is due to the following factors: it minimizes damping errors from clamping and air, it allows for high strain rates to be achieved hence capturing a good range of the non-linear effects, it is non-contacting in nature for both measurement and excitation hence reduces errors, induced damping, and increases repeatability, it has a simple analytical theory supporting it, and it is relatively easy to numerically model by FEA. For these reasons it has emerged as a good geometry and methodology to characterize the coating bulk properties.

1.4.2. Numerical Highlights (Structural Dynamics/FEA)

Paired with many of the experimental studies have been numerical studies and these have been introduced already. The major evolution and refinements of the models is worth covering. The main steps in the evolution of numerical modeling has followed: matrix methods/structural dynamics (lumped), finite element analysis (FEA) modeling using time-independent modal decomposition, and FEA using fully transient and dimensional models.

Matrix methods using state space and modal decomposition of plates and beams has largely been superseded because of the geometric limitations of these approaches. For a beam system discretization of the beam into infinitely rigid segments of appropriate mass separated by torsional springs (the same could be done for plates only now across two dimensions) can be performed. While a classical numerical technique, has been superseded for a long time by FEA methods (Meirovitch, 2001; Cook, 2001).

FEA-based modal decomposition has been used in the vast majority of the studies introduced in Section 1.4 for both plates and beams. All of these simulations were time-independent modal reductions, performed in various commercial FEA software packages, that were non-dimensional in nature and derived solely from the stiffness- and mass-matrices built for the system (no damping). FEA packages used include ANSYS, (FEMAP) NE-NASTRAN, and ABAQUS (Pearson, 2008; Reed, 2007, Ivancic, 2003; Allen, 2005). It is noted that virtually all commercial FEA packages handle linear elastic modal decomposition well and can be used with success.

Patel and Palazotto studied a fully transient model of a steel plate with an applied harmonic forcing load function derived from piston theory in order to model the HCF that might occur in turbine blades. The authors discovered during this study that modeling non-linear geometric displacement was important to accurately match an associated experimental plate under the same loading. (Patel, 2004).

Deleon applied a fully implicit transient modeling approach to the hard TBC coated beam system of Pearson and Reed in the ABAQUS FEA code. Some important

findings he reported included: having to carefully select the time step for time integration to ensure stability of the solution, the necessity to utilize a one-dimensional (1-D) element to achieve convergence within reasonable time- and CPU-resource limits, and the importance of tuning the damping factors to achieve both similarity to experiments as well as a bounding on numerical solution. The coating material was modeled as a linearly elastic (Hookian) solid and the damping applied to the beam system using the proportional model (Deleon, 2009). The solution was obtained by performing a direct-integration dynamic analysis (Newmark method) using ABAQUS/Standard (See Section 6.3.2 of the ABAQUS Analysis User's Manual). The inclusion of damping into the closure of Deleon's model involves a form of viscous damping; in his case Rayleigh damping. Recent work into integrating other damping models into MDOF modeling beyond the viscous model can be found in the works of Poudou (Poudou, 2007) and Adhikari (Adhikari, 2000).

For the current study, characterization of the coatings by a complex modulus is attempted. This should allow selection of the damping models that can be utilized (Hibbitt (ABAQUS), 2002). Since the specimens are tested and simulated at a single resonant frequency and the associated simulations are run, the hysteresis damping (after transformation to equivalent viscoelastic damping) should yield an accurate model prediction; e.g. the frequency dependent nature of the viscoelastic damping should not enter into the model. As per the ABAQUS Manual (in of itself an excellent reference)...

> Structural damping is a commonly used damping model that represents damping as complex stiffness. This representation causes no difficulty for

> frequency domain analysis such as steady-state dynamics for which the solution is already complex. However, in the time domain, the solution must remain real-valued. To allow users to apply their structural damping model in the time domain, a method has been developed to convert structural damping to an equivalent viscous damping. This technique was designed so that, in the frequency domain, the viscous damping applied is identical to structural damping if the projected damping matrix is diagonal. (ABAQUS, 2008).

Adding dry (Coulomb) damping into the FEA model to achieve closure on a transient FEA model in order to simulate the ring down experimental results, will have to be by one of two routes: 1) directly programming a material model incorporating Coulomb damping into a UMAT file for ABAQUS, or 2) transforming the dry friction at each resonant frequency (and amplitude) into an equivalent viscous damping model. De Silva's text on Section 2.5 presents a energy based technique to approximate it for a SDOF system. Fertis's text in Section 3.4 outlines this energy approach where for each cycle the damping energy loss due to dry friction is equated to that lost by viscous effects (De Silva, 2007; Fertis, 1995). Also, the unpublished paper of Peters is a good guide (Peters, 2002).Without elaboration, this yields the equivalent viscous damping coefficient (c_e) (or matrix($[C]_e$)):

$$c_e = \frac{4F_f}{\pi \omega_f X} \tag{3}$$

where F_f is the friction force, ω_f is the resonant radial frequency and X is the displacement amplitude at a steady harmonic condition (Fertis, 1995). It is noted that while simple in theory, in practice this may be difficult to implement on ABAQUS as the matrix of damping coefficients is dependent on the whole maximum displacement field

of the structure, which varies down the axial length of the coated beam (spatially dependent).

Oldfield used the Jenkins elements with Coulomb slider elements in his modeling of bolted joint slippage in ABAQUS models he simulated in both Standard and Explicit. It is noted that the elements employed by Oldfield to capture the dry friction losses are surface contact phenomena as opposed to bulk, volumetrically generated, losses as in the Torvik beam, so the Jenkins element technique may not be directly applicable to capturing dry damping (Oldfield, 2005).

A cursory survey of the major FEA packages of ABAQUS, ANSYS, and Femap/NE-NASTRAN indicate that the main types of volumetric damping that are presented to the analyst are viscous, hysteresis, and derivatives of these two. The physical transformation of a SDOF dry model to a 3-D model element requires a thought. If, as Palazotto and Abu Al-Rub suspect, dry damping is involved in the system, incorporation of friction damping into the numerical model is a major challenge (Abu Al-Rub, 2010). This model could be seeded with the initial position of the analytical solution at its extreme of displacement, scaled to various initial amplitudes, and then allowed to decay from this initial position of maximum potential energy.

1.4.3. Analytical Highlights

Section 4.2.1 covers the details of the analytical models. Much like with numerical highlights, the analytical modeling of the beam has been covered in the review of the experimental efforts, but the major advancements are detailed here.

The plate specimen configurations were generally compared against thin plate theory as formulated by Kirchhoff. The solution to the dynamic case of clamped-free x3 by Liessa (Liessa, 1969) were generally employed (Ivancic, 2003). Generally, these were limited to comparison of the characteristic equation roots against the measured resonance frequencies; although mode shape extraction and comparison would be possible but tedious due to the product of series approximated solutions. It is noted that these characteristic equations are not exact solutions but are based on the Rayleigh-Ritz method of assumed displacement functions for the plate. In most studies, FEA simulations were used for the mode shape determinations (Lee, 2006; Allen, 2005).

The adoption of a beam geometry allowed simplification of the classical thin-plate theory to the Euler-Bernoulli (E-B) thin-beam theory with the three moments (and strains) of the classical plate theory, two bending and one in-plane shear, collapsing into only one significant strain, that of bending strain induced by transverse vibrations. This is the bending along the longitudinal axis. This simpler treatment of the dynamic problem and an exact dynamic solution, first worked out by the 1920's, is useful for comparison to the experimental results. Extensions to the dynamic free-free beam, among other configurations, have been determined, but have not been applied to previous work in TBC coating characterization (Nafeyah and Pai, 2004; Farchaly, 1995; Han, 1999).

For the coated beam problem the chief issue faced is the non-uniform stepped nature of the beam. Two papers have very general solutions presented by El-Din, Mahmoud and Nassar as well as Lee, Ke and Kuo. Both papers present a methodology to

build up the characteristic equation in determinant form for a stepped beam from a n-segmented beam, where each segment can have varying stiffness and even a linear taper. The solution methodology is general enough to account for varying supports at each interface and generalized boundary conditions. Needless to say the generation of the characteristic equation by this method leads to a very large determinant (rank is 12 x 12) for the case for the 3-segment beam of interest in the current study. (El-Dinin, et al., 2002; Lee, et al., 1990).

1.4.3.1. Beam Isothermality

There is surprisingly little literature regarding radiation-conduction problems. A notable exception was one recent paper by Lim and Kar that did investigate the coupled series radiation-conduction problem with a TBC coating using a 1-D model, though their abstract claims that reflectivities, absorptivities and conductivities of the coating and metals affect the thermal gradients, examination of their presented results shows that these were actually very weak in nature as Branam, Baker, and Palazotto have determined in their own respective analyses to be detailed in later sections (Lim, 2009).

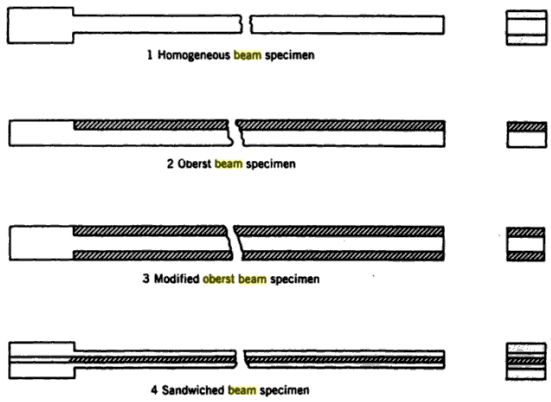


Figure 21: Laminated Beam Types (Nashif, 1985)

Isothermal conditions in the Ti-6Al-4V beam are critical to maintain as the free-free system is evaluated in a beam bending mode-I (see Figure 13 on page 35) for which both the frequency and mode shape are predicted based on a modified Oberst thin E-B Beam. This assumes that stiffness is constant down the length of the beam, and that the modulus is a component of stiffness. It is important to note that the "Oberst beam" is a cantilever beam with a second layer of different, typically more pliant, but homogeneous, material applied on top of the beam, the "modified Oberst beam" has two equally thick layers above and below the metallic layer. The "sandwich beam" interchanges the location of these materials from the modified Oberst beam and is useful for determination of the shear behavior of the encapsulated layer. Figure 21 illustrates these beam geometries. Nashif has a good overview of the beams, historical development, and usage (Nashif, 1985).

1.5. Eclectic Vacuum Chamber Techniques

It is recognized that a major portion of the current study is the apparatus itself, a review of the literature on vacuum chambers does not reveal much for the combining of

mechanical damping minimization, thermal isolation and insulation, and non-contact excitation and sensing, all within the same experimental setup. Indeed, literature seems to indicate vacuum chamber design and use is more of a learned art than precise science, few texts exist that cover vacuum chambers as a research issue per se, they focus instead on the art of maintaining a "good" vacuum. Nonetheless, chamber use at varying grades of vacuum is very widespread in commercial and research applications. Some examples of vacuum chambers in use, ranging from commonplace to exotic are:

Mechanical effects - vacuum bagging, degassing, bubble and volatiles removal, low temperature boiler/distillers (low vacuum from 0.5 to 0.05atm)

Acoustic/vibrational isolation (0.1-0.01atm)

Thermal isolation - Dewar flasks, thermos bottles, radiation-only heating (0.1-0.001atm)

Removal of interfering/contaminating media - scanning electron microscopy (SEM), vapor deposition, mass spectrometry, air-damping elimination ($<10^{-4}$ torr).

Simulation of deep space - hall effect thrusters, oxygen radical erosion, etc. ($< 1x10^{-5}$ torr)

While chambers are in wide use from everything ranging from fine quality contamination control, to providing a low vapor pressure environment, to ensuring thermal isolation, to allow acoustic/vibrational isolation, it seems combining all of these effects together into the current apparatus makes it quite novel in development. It is noted

that the major objective relies on fairly elementary theory combined in a novel fashion. Many of these design issues and theory that is relevant to getting the apparatus to a working state will be touched on in the first half of Chapter 2. The practical implementation of the experimental apparatus and procedures for conducting the experimental portion of the study will be covered in Chapter 3. Due to lack of much literature to provide guidance, these chapters will read more akin to a basic design review, implementation, and proof of concept rather than a detailed theoretical development that the mechanical characterization studies entail.

1.6. High Stark Number in Vacuum

Radiant heating and vacuum processing are commonly utilized in many industrial processes, a quick survey of any industrial equipment catalogs makes that clear. Such processes as freeze drying, thin film deposition, vacuum heat treatment, and vacuum brazing exploit one or both. Little is reported in the literature of the details of design or analysis of such equipment.

The combination of vacuum and heating an isolated solid by radiant means, along with minimal contact with the surroundings creates a serial radiation-conduction thermal circuit. Well known in heat transfer is the isolated solid immersed in a surrounding fluid (the quenching problem) involving a serial convection-conduction thermal circuit. The strength of spatial to time dependence of temperature is conveyed in the well-known Biot number which is a ratio of the thermal resistance inside the body to that at the convective surface (Incropera, 1996). Little known is the equivalent which is a serial radiation-

conduction equivalent known as the “Stark” number or “radiation Stefan” number, it appears in the literature on occasion. The one close situation may be in satellite thermal design.

Analytical analysis of this problem, despite its widespread relevance, are not common. Campo and Villasenor worked the problem to model transient cooling of a spherical particle (Campo, 1996) and Stickler determined a solution using a non-linear Volterra integral equation for a planar metal slab with an insulated backside (Stickler, 1961). Campo reported on using a dimensionless number of the form:

$$N_{RC} = \frac{\epsilon \sigma R T_i^3}{k} \tag{4}$$

where ε is the surface emissivity of the solid, σ is the Stefan-Boltzmann constant (5.67 x 10^{-8} W/m·K^4), R is the characteristic length of the solid, T_i is the absolute temperature at the surface interface, and k is the thermal conductivity of the solid. Mention was made that the reciprocal of the number N_{RC} is the “Stark” number, Sk, used mainly in Russian literature. More recently, Tan, Su and Su considered conduction through a wall using a lumped model. For this multi-mode heat transfer problem they obtained two-point Hermite approximations for integrals (Tan, et al., 2009). Thus the lumped capacitance is in effect, where the body is near-isothermal can be classified as a low Biot number or high Stark number situation.

1.7. Error Analysis Conventions

For the processing of uncertainties in the experimental results in this study the Root Sum

Square (RSS) method presented by Kline and McClintock is utilized unless otherwise specified. This method assumes that for any value derived from others measured in a experiment, here designated, r and, X_i, respectively as per:

$$r = r(X_{1,} X_{2,} .., X_n) \tag{5}$$

For this relationship, measurement error consisting of one or more random (or sample or precision, denoted as P) errors, and one or more systematic (or bias, denoted as B) errors can be propagated through Eq. (5) as per:

$$U_r^2 = \left(\frac{\partial r}{\partial X_1}\right)^2 UNC_{X_1}^2 + \left(\frac{\partial r}{\partial X_2}\right)^2 UNC_{X_2}^2 + ... + \left(\frac{\partial r}{\partial X_n}\right)^2 UNC_{X_n}^2 \tag{6}$$

Random errors are generally reduced by repeated measurement sampling and bias errors are controlled by careful calibration and validation testing of the experimental setup in question. If Eq. (5) is of monomial form as per:

$$r = kX_1^a X_2^b X_3^c \tag{7}$$

Then Eq. (6) reduces in form to:

$$\left(\frac{UNC_r}{r}\right)^2 = a^2\left(\frac{UNC_{X_1}}{X_1}\right)^2 UNC_{X_1}{}^2 + b^2\left(\frac{UNC_{X_2}}{X_2}\right)^2 UNC_{X_2}{}^2 + c^2\left(\frac{UNC_{X_3}}{X_3}\right)^2 UNC_{X_3}{}^2 \tag{8}$$

Precision error is typically quantified by scatter in the data, here defined for two standard deviations for the 95% confidence interval (CI):

$$P_{X_i} = 2S_{X_i} = 2\left[\frac{1}{N_i - 1}\sum_{k=1}^{N_i}[(X_i)_k - \overline{X_i}]^2\right]^{1/2} \tag{9}$$

Bias error is trickier to quantify, typically by careful validation and calibration it can be reduced to a negligible amount or quantified to allow carrying through the analysis.

This is done by determination of the 0^{th} order estimates of B_i and P_i for the experimental setup. Use Eq. (6) to propagate each set of errors through any relations used in the experiment to obtain reportable parameters. This is typically performed separately as bias data can self cancel through cross-correlation. The combination of the two is as per a sum of squares:

$$UNC_r = (B_r^2 + P_r^2)^{1/2} \tag{10}$$

to characterize the single-sample total error of the experimental rig from precision and bias errors. This is referred to sometimes as the "0^{th} order replication analysis". "1^{st} order replication analysis" follows when multiple samples are statistically characterized for mean and scatter. Then, from this, the true random variations can be determined as per:

$$(P_H)_{1st}^2 = (P_H)_{0th}^2 + (P_H)_{Mat}^2 \tag{11}$$

Then combine them to get the true inter-sample variation corrected for that of the measuring apparatus.

For a thorough coverage of this topic the text by Coleman and Steele is recommended. The convention in this study when errors and uncertainties are reported is to use the 95% confidence interval (CI) at two standard deviations ($\pm 2\sigma$) out for random error and the best-determined bias errors. These are used for 0^{th}, 1^{st} , and Nth order replication analysis for propagation of the error. Regression functional fit bounds are reported that are 95% likely to contain functional fits using the data set. Whether this is (Coleman, 1999)

1.8. Objectives

The objectives of the current research are detailed here and will build upon the results of Runyon, Reed, Pearson, and Deleon, among others. The chief objective of the current research is to successfully adapt the current free-free experimental apparatus and associated procedure to allow high temperature mechanical characterization of the TBC coatings. It is recognized that this is very much a design-oriented problem; the emphasis here is designing a chamber that combines vacuum, radiation heating, non-contact harmonic motion excitation and measurement, free suspension, with these all together. There are many issues to be dealt with and these problems will be attacked with a combination of analytical work, experimental characterization (validation and calibration), and numerical simulation. The many anticipated issues that have been worked, or will be, are covered in Chapter 3. Unfortunately, as with any design problem, not every challenge to implementation will be foreseen so guided trial-and-error and mechanical/procedural refinement no doubt will be important in the study. It has been established that the free-free beam geometry enclosed in a vacuum is a very good system to establish the high-strain (and strain-rate) environment needed to not only characterize the full range of non-linear dependent mechanical characteristics of the TBC, but also allow for aging-in of the coating's histories in a reasonable time. Also, the vacuum and boundary conditions minimize the many problems in achieving a system with minimal variation in damping from air and clamping. That being stated, there are many design challenges to successfully adapting the current apparatus to high temperatures and there are implementation risks.

These objectives to get a working high temperature experiment include (where noted relevant procedural and theoretical underpinnings are cross referenced) and are prefixed with an “I”:

Ia) Magnet to coil interaction study - find, validate, and calibrate a high temperature magnetic forcing method. Analyze by analytical techniques, magneto-static numerical, and, experimental coupling. Build a couple moment versus coil current calibration curve using the methods developed by Hoover (Hoover 2004). Provide the data for later studies to model the coupling function on a bare beam FEA model by simulation techniques developed by Deleon (Deleon, 2009).

Ib) Isothermal condition of samples - determine the temperature distribution of the coated beam specimens for the past and present studies in a uniform thermal radiation field by mathematical analysis, numerical finite difference modeling, dimensional analysis, and experimental characterization by means of multi point thermocouple measurements and thermal camera imaging. The thermal imaging tests will be performed when building a temperature as a function of radiation source power calibration curve.

Ic) Chamber heat transfer - the transfer of heat from the chamber to the external environment is critical to sizing of the power sources, radiation shielding placement and quantity. To assess the design, a 3-way approach was to used: paper and pencil analysis, an FEA radiation model using ABAQUS and Matlab finite difference (FD) code, and thermal measurement of the exterior when accomplishing the chamber calibration curve.

Id) Boundary condition control - based on the insights of Reed, Pearson and

Deleon, rigid body motion is a problem of the free-free beam and has to be eliminated and/or controlled. Pearson's approach of shortening and tensioning the suspension mono-filament line lengths, combined with Deleon's recommendation to prescribe the dimensional lengths, mass, and tension, were to be adopted in the design of the current study, so the dynamics will be known from straight-forward application of the transverse wave equation. Modal tuning studies to ensure that the filaments are well-removed from bending modes 1 (and perhaps 2) of the specimen were performed. This will be analogous to the work Lee performed on Allen's apparatus in regards to de-tuning the baseplate from the specimen. The design was to propose using a set of 0.005 in diameter steel wires with a system of sash weights and/or pre-tensioned coil springs to maintain the uniformity of the suspension from test to test.

Ie) Solve temperature-induced failure issues of the sealing glands, electromagnet coil, permanent magnets, magnet bonding, wires, suspension tube, chamber walls, etc.. This was predicated on the results of the heat transfer analysis, and involved a combination of spot cooling with water coils, radiation shielding by means of foil, and selection of heat resistant components. A lot of this work was accomplished by empirical testing.

If) Solve magnet mounting issues. The differential thermal expansion of the heated beam/magnet/fastener system will impose a need for pre-load and built in compliance issues. The main approach here will be experimental in nature. Some anticipated solutions that were investigated were machine screws with bellvue washers,

high temperature glues, and rivet systems.

Ig) Assess the impact of magnet mass changes upon the system. The changing from rare earth to ALNICO magnets for temperature resistance resulted in a weaker coupling. Making up lost coupling moment required either more magnet volume (and mass) on the beam, a more powerful electromagnetic coil or a combination of the two. This was explored by FEA modeling and experimental comparison.

Ih) Provision for either whole-field imaging of the beam via a 2-D scanning laser vibrometer or via controlled location multi-point sampling with the current single-axis unit to allow reconstruction of the mode shape from experimental measured data. This supplemented and validated FEA or analytical assumptions in the past work. This helped to remove such uncertainties in the past work and is expected to help further their validity.

Ii) Gather knowledge of the electromagnet system with magneto-static modeling and/or experimental characterization so that the true coupling force of the electromagnet system is known. Included in this was investigating the mechanical fastening of the ALNICO magnets via drilled holes to ensure repeatability in positioning as well as a method of hanging the beam to ensure repeatability in terms of its location with respect to the coil and its associated AC-field. This was to allow for a check on any transient FEA models, e.g in order to setup a proper magnitude of the forcing couple or force pair at the active node.

Ij) Maintain prescribed control of the boundary condition in the suspension wires.

Changing the current mono filament nylon lines to fine drawn carbon steel wires was performed. Based on qualitative evolutionary refinement in controlling beam ridged body motion in the past works, the current apparatus controlled for the tension, span, and positioning of the wires to ensure that rigid body motions were kept to a minimum and that energy dissipation from the intended resonance modes of the beam into the wires were minimized by deliberate detuning. The adaption of the current polymeric guide tube to a temperature resistant mount was addressed as well.

Ik) Validate the chamber experimentally in regards to the following:

· Ensure that the beam and TBC system achieved a near-isothermal state; this was confirmed by multi-point thermocouple measurements and by means of thermal camera imaging of the system.

· Confirming that modal decoupling occurs between the suspension lines and the free-free specimen; this was a repeat of the comparative measurement of the wire suspension velocities in comparison to the measurement point at the center and the passive beam nodes.

· That the coil magnet system provides the prescribed couple forcing moments; this calibration curve was built by adaption of methods developed by Hoover (Hoover, 2004).

Ij) Build calibration curves for the chamber, these are closely related to the objectives above, except here, the building of calibration curves will be important for testing utilizing the chamber in the second half of the studies. The following will be determined:

· AC couple/force pair as a function of coil current (or voltage). This was conduct statically but one must be aware of, and spot check for, the coil's self-inductive loss effects. An bode magnitude and phase plot of the coil built in a strict experimental sense with harmonic AC input will be accomplished to allow this corrective factor, or the 1st order electrical model will be used.

· Beam temperature as a function of the lamp power settings (current/volt-amp or voltage) - this was critical to prescribing a known temperature. A dummy piece of Ti-6Al-4V was used to build the a second curve as well to allow closed-loop monitoring in the second half studies. Also attention to characterizing the thermal time constant of this first order system was performed as well ensured that the settling time to a prescribed set-point is known.

It is recognized that not all design challenges were going to be foreseen and/or admissible to analysis by means of numerics or analytics. Trial and error was a critical part of meeting this first half of the major objectives. Assuming a successful adaptation of the test chamber and procedures, the second major portion of the proposed study featured preliminary characterization studies for TBC materials.

In the second half, the mechanical characterization was performed at various prescribed temperatures, using the chamber as the product of the first half of the study. Coverage of issues and underlying theory pertinent to this half of the study will largely be in Chapter 4. The initial characterization study was to span the full thermal range to be anticipated in a modern gas turbine "cold section"; that is at controlled temperatures up to

about 510degC (950degF) from that of room temperature ambient (70degF). In summary the second major objective was to utilize the characterized and calibrated free-free chamber apparatus to perform some initial high temperature characterization studies of a typical TBC material; 8-YSZ . The methods and lessons learned developed in the course of studies by Torvik, Patsias, Tassini, Runyon, Reed, Pearson, Deleon, among others, were applied. Refinements to the procedures were applied in the course of this study.

Broken down and prefixed with a “II”, these objectives include:

IIa) Establish the degree of temperature dependence (or independence) of the effective modulus and loss coefficient of the 8-YSZ to the variation of temperature. This was a key discriminator as to the nature of the primary damping mechanism that is operating in the TBC materials, Abu Al-rub and Palazotto suspected a damage based mechanism (which is dry friction) which should be fairly invariant with temperature. If instead it was more a structural damping, internal plasticity, or viscous-based damping mechanism at work, then a much stronger variation with temperature was to be anticipated in the bulk material properties. Attempts to perform large strain (and strain rate) measurements to fully capture non-linear behavior was a key aspect of the Reed beam apparatus.

IIb) Perform age-in studies on the TBC coated specimens. This is an attempt to control and minimize the effects of history of YSZ (and mag spinel) observed by Shen, Reed, and Torvik. A secondary objective of this effort, NOT to be a part of the proposed study, will be to provide samples for a follow-on scanning electron microscopy (SEM)

analysis to allow examining micro-structural evolution as a function of loading history. This may help in forming a damage-based constitutive model for this TBC. Pearson's age in protocol was adapted for this study.

IIc) Fabrication of the specimens - a controlled and quantifiable process to fabricate the specimens in accordance with industry best-practices, standardization of the process, and quantification of the fabrication was developed for this testing. Weighing on a precision balance (along with cleaning and specimen de-greasing) at each stage and precision rotary micrometer measurement at initial cut stage, bond coat application, and final application of the YSZ coatings was performed. Masking to prevent coating buildup on the sides of the specimens was done to eliminate geometric uncertainties/inhomogeneities encountered in previous studies. Comparative bare and YSZ-coated beams were made. This careful attention to fabrication of the samples was performed to minimize inter-sample differences due to mass uncertainties, batch uncertainties, grain orientations, and similar such details.

IId) Repeat the methodology of Reed to reduce the observed system-level damping and natural frequency of the coated specimens to the bulk properties of storage modulus and loss modulus (or, alternatively, effective modulus and loss factor) of the coating materials across both amplitude and temperature variations. This testing was performed by time domain techniques (free response decay ring-down). Reed's FEA polynomial data cannot be utilized to accomplish this as they are ranged for mag spinel values, and Pearson's, while derived for 8-YSZ, has some systemic inaccuracies and are

calibrated for difference coating thicknesses, so FEA simulations using a refined version of Deleon's model (using Reed's method) was used to build a new set.

IIe) Attempt to obtain the coating effective modulus and loss coefficient relations using an all-experimental approach. The current study attempts to use the elastic strain energy density function for elastic solid media, partitioned appropriately into the metallic and TBC regions using a classic elasticity model coupled with a empirically fit curvature function from the beam from a 1-D array of beam displacement data obtained by a scanning Doppler velocity laser (DVL). Reliance on the geometric kinematic displacements inherent in Euler-Bernoulli (E-B) thin beam theory were utilized to determine a SER to compare against SER values obtained by using 3-D FEA models.

IIf) Perform a finite element analysis study of the beam and coating system in the static state to determine the residual thermal stress distributions in the beam resulting from differential thermal expansion between the beam substrate material and the ceramic 8-YSZ coatings. This model will use both a 2-D and 3-D model with a steady-state, uncoupled, loading, thermal stress methodology, uncoupled from any thermal effects imposed by vibrational stimulation. This is because the beam heating effects are anticipated to be very small relative to direct thermal radiation heating. A simplified 1-D lack of fit-type analysis will also be performed.

IIh) Perform a refinement of the analytical solution of the beam into a three region solution using $E_1I_1/E_2I_2/E_1I_1$ regions of the beam for the bare tips and coating region. The E_2I_2 region will be worked using the method of adjusted areas to correct for the differing

moduli between the titanium and TBC, in conjunction with the parallel axis theorem from classic strength of materials methods. Compare this refined analytical model for determining the beam modal shape and characteristic frequency against the 3-D FEA models and experiments. If these compare well, see if a simple program/script can recover a strain energy of the coating, strain energy of the beam, an therefore SER as the values obtained by a full 3-D FEA model simulation. Agreement within 10-15% by using the theory alone may prove valuable and simplify use of the technique from that of special purpose computing tools to a more general semi-numerical analysis.

2. Design of the Test Chamber and Surrounding Apparatus - Theory

This Chapter will deal with the theory underpinning one of the two major objectives of the current proposed study, that of the theory involving the chamber design, with particular emphasis on heat transfer. This concerns the chamber setup in terms of analysis and theory; the experimental implementation, fabrication, calibration and validation of the chamber will be covered in the next Chapter. The second objective is the high temperature characterization studies for theoretical and experimental analysis of the TBC coating and is covered in Chapters 5 and 6, respectively.

It is noted that the first objective is more design-oriented in nature, while the second will be more specific in nature, evolving directly on the work of past authors. The apparatus in the current study involved much anticipatory analysis and design prior to its fabrication to ensure that the objectives of the study could be meet. Some such issues were: Can the beam remain isothermal? Can it reach the temperatures required?, and will support components survive and be adaptable to the high heat environment?

An important point to challenge in the current study is why use a free-free system despite the potential theoretical, implementation/processing, and procedural complexities involved. There are a couple of key reasons: first, the free-free system promises to be the most accurate means to characterize low damping materials accurately, almost all the extraneous and significant damping sources like clamps and other moving

elements/fixture are eliminated from the specimen system, second, for the non-linear materials that are the objective of this study, achieving larger strains is of interest to capture more of their non-linear behavior, and three, bending (and torsional), rather than axial loading are the modes that TBC and blade systems will mainly undergo within turbo machinery so exciting these modes is of the most interest. The free-free setup is well suited to achieving this.

Before proceeding in this Chapter it worthy to point out to the reader that the objective of the next two Chapters was to realize a workable test facility to characterize the TBC coatings using the free-free technique. Therefore, Chapters 2 and 3 will read more like a design treatise than formal proofs of theory. An example is the radiation FEA modeling, once the model was reasonably accurate in predicting the experimental conditions, excessive effort was not devoted to accurately characterizing every single component, or adopting temperature dependent surface and material models, even those readily available in the literature. Most of the efforts here were geared towards feasibility and sensitivity studies.

2.1. Heat Transfer Theory of Chamber (Method of Heating)

The current study relied on some preemptive analysis (preemptive to avoid problems), consisting of numerical simulation and modeling to avoid many complications. Realistically all contingencies and complications were not foreseen and the iterative process of experimental refinement was also critical to successful implementation, some of these issues are covered in the next Chapter. The goal is

characterization of nonlinear TBC-coated (in this case using 8-YSZ) beams using extension and refinement of current techniques. The chamber utilizes a novel combination of techniques that will be used to study the coating properties using the free-free methodology. Systematic handling, characterization, and/or control of the system were required.

These issues will be covered in detail later in this Chapter but an overview is presented now. The new apparatus is an evolutionary refinement beyond the apparatus used by Reed and Pearson in their respective studies (Reed, 2007; Pearson, 2008). It continues to use vacuum for elimination of air damping from the beam system, however, the vacuum now also plays a second critical role in helping to allow the beam to reach high temperature with a uniform thermal distribution and only require moderate power to do so. Thermal radiation heat transfer into the coated specimen combined with an enclosing vacuum will be used to minimize free convective effects within the chamber. Due to the high temperatures encountered, the pressure chamber utilized in previous studies which provided a room temperature vacuum atop a dynamic shaker head, was modified and had components added to maintain both a vacuum and impose a high temperature environment. Provisions for radiation shielding and spot cooling were also to be added as needed.

As an elevated temperature environment where control of the temperature of the specimen is an important prescribed parameter, the heat transfer environment deserves detailed analysis and design consideration. The motivation for this is discussed along

with the problem setup; several methods of analysis of the problem are then presented. A quick analysis of the beam to exterior heat transfer has been performed by classical methods, these include a radiant heat power requirements estimate. Most analysis then focused on a specimen-centric heat transfer between the beam and the enclosing cavity which must impose a near isothermal field within the beam itself. A review of the specimen-to-chamber and chamber-to-ambient room heat transfer mechanisms/effects are covered as well. These include: a dimensional analysis, a finite difference model, and an analytical model. All of these involve a Kirchhoff gray environment and are serially coupled conduction-radiation problems. Finally, there is a cavity-radiation FEA model and analysis presented.

There is not much literature in this area regarding radiation-conduction problems. A notable exception was one recent paper by Lim and Kar that did investigate the coupled series radiation-conduction problem with a TBC coating using a 1-D model, though their abstract claims that reflectivities, absorptivities, and conductivities of the coating and metals affect the thermal gradients, examination of their presented results showing these were actually very weak in nature as Branam, Baker, and Palazotto have determined in their own respective analyses to be detailed in later sections (Lim, 2009).

2.1.1. Motivation and Isothermal Beam as a Requirement

The testing of the 8-YSZ coatings using the free-free system required a set of preliminary studies to assure that the thermal aspects of testing at elevated temperature could be successfully accomplished. Among the complications of elevating the

temperature concerning the beam specimen were: 1) maintaining an isothermal (or nearly-) state in the beam to avoid modulus variations in the parent substrate that would impact the bending mode-I resonance shapes, 2) staying below magnet working/Curie temperature limits, 3) replacing and/or hardening temperature sensitive components including the electromagnetic coil and mono-filament suspension lines with substitutes that resist high temperatures, and 4) keeping the power required for heating to the design temperatures to a reasonable level.

It is important to note that ensuring that the beam specimen could be set to prescribed temperatures and maintaining an isothermal state is very critical to the current study. As the beam is a tuned resonator system in the free-free state, it is important that the flexural stiffness of the system remain constant down its length except for intentional variation imposed solely from the thin TBC coating. The design range of the test chamber is to be planned to range from room temperature (about 70degF) up to about 780degK (950degF). As seen in Figure 8, the modulus of the titanium beam will soften from about 110 down to 80Gpa, as the temperature is increased from about 25degC (70degF) up to about 510degC (950degF). Though the modulus variation is close to linear with respect to the temperature, it does vary by up to about 27% as the temperature ranges from the room temperature value up to around 950degF. The beam's effective modulus could vary only about 3% with an imposed 50degC temperature difference maximum. Significant variation in localized temperature will, for many metals, drive significant variations in the modulus, and therefore flexural stiffness. This requirement was deemed critical enough that much of the analytical and numerical heat transfer analysis was focused on ensuring

this was the case. Experimental validation, by both multi-point thermocouple readings, as well as infrared (IR) imaging, of the analytical studies is covered in the next Chapter.

2.1.2. Decoupled Analysis

All of the heat transfer models (analytical, finite difference and finite element) are assumed to be decoupled from the mechanics of the system and hence analyzed separately. This assumption was deemed to be appropriate based on the following features of the system:

· The time scale of the mechanical oscillations of the beam in the chamber is very small, roughly on the order of 0.005 seconds per cycle, relative that of the heat transfer which has a pseudo-time constant on the order of 3600sec to reach the fourth time constant. "Pseudo time constant" is the term as the system is known to not be linear in rate law and therefore not a true exponential variation of temperature with time. Hence the beam's geometry in the interior of the chamber for receiving incoming thermal flux from the lamp sources can essentially be spatially averaged. Thus the beam would appear to the incoming radiation as a statically hanging unexcited beam when seen over a sufficiently long time scale.

· The beam system is intended to undergo small, and therefore elastic, deformations in bending, as a result, the heat generated from internal friction losses is negligible relative to incoming heat flow from the lamps as well as that emitted (outgoing) to the surroundings.

With the problem decoupled, the heat transfer models can be analyzed separately

from the mechanical system (and vice versa).

2.2. The Current System and the Conceptual Design

The current free-free system consists of a free-hanging beam suspended from the upper node of the bending mode-I shape with a set of magnets at the lower node, which are restrained between a pair of fine test nylon mono-filaments. Figure 23 displays the setup as employed by Reed in his work on the left (note the electromagnet is not shown) and the modified setup used by Pearson on the right. These are placed within a vacuum chamber when testing that is maintained at about 0.05atm. The main modifications made by Pearson was to shorten and increase the tension on the upper and lower lines. Though this increased the resonant frequency of the rigid body motions of the beam towards that of the bending mode-I of the beam, these frequencies were still well-separated and the magnitudes of the rigid body motions were dramatically reduced.

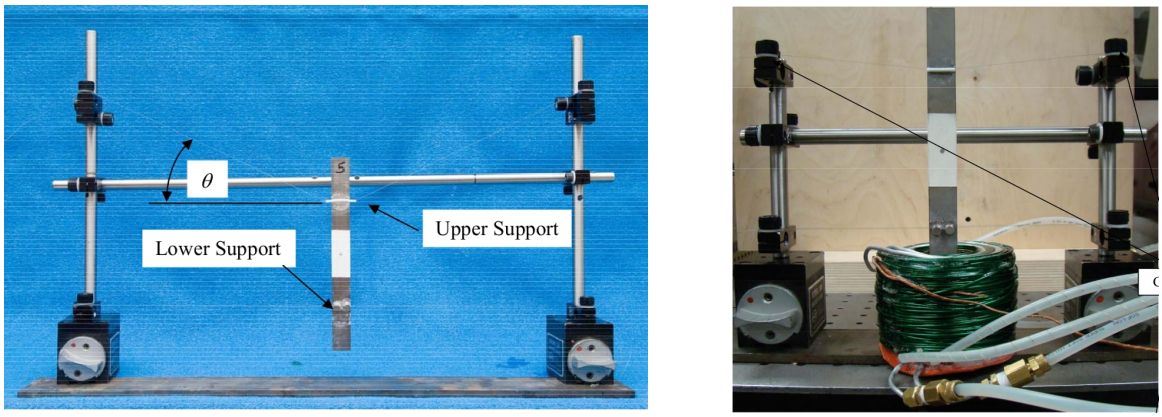


Figure 22: Free-Free Setups of Reed (left) and Pearson (right) (Reed, 2007; Pearson, 2008)

This setup proved to be quite sensitive to extracting coating properties by either the free-decay or forced response techniques. It represented a good concept to adopt in

the current study. The adaption of this setup to high temperature was deemed a valid approach to characterizing the coatings at elevated temperatures, but as it was to feature an eclectic use of basic principles: high Stark number heat transfer system, very low damping boundary conditions, use of numerical simulation to extrapolate field variables in the specimen (strain, displacement, etc.), among others, that a characterization and study of the system before fabrication was deemed critical to realizing valid results. Figure 23 displays a solid model designed in Solidworks v2007 of the conceptual design that was used to establish fit tolerances, extract dimensional details for modeling, and generate shop-ready drawings from which analytical studies indicate a high probability of success.

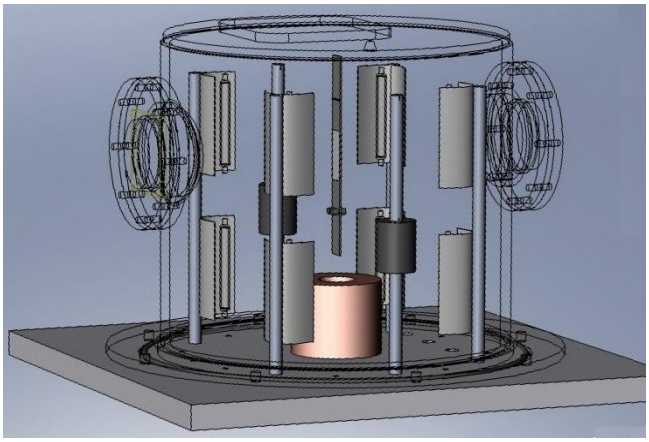


Figure 23: Concept Design of Elevated Temperature Free-free Apparatus

The beam is shown directly above the electro magnet, which is the copper-colored cylindrical object at the bottom. The whole free-free assembly is enclosed in a pressure jar, which is shown in a wire frame here to show the interior detail, to maintain vacuum to eliminate both the air damping effect and the free convection heat transfer within. The free-free setup is centered between four lighting assemblies to provide near-uniform

illumination of the beam. Two rods with weighted collars, shown as black cylinders were to provide the support of the beam suspension lines. This was later changed to a hanging weight on a sub-span of the wire due to clearance issues. Much of the detail of the adaption and hardening of components is not clearly shown in this diagram, but it allowed the analyses to proceed.

2.2.1. Heat Transfer Problem

Globally, the chamber can be thought of as a multi-mode heat transfer problem that can be modeled using a thermal circuit like the one shown in Figure 24, the chamber features a heat flow crossing the thermal potential from the lamp sources out to the laboratory ambient surroundings. The beam specimen, radiation shielding, chamber wall, surface air can all be represented as thermal nodes with resistances to the heat fluxes between them. Likewise, it was planned by maintaining and testing in a low vacuum environment that the three legs of convection transfer within the chamber were made negligible. Of particular concern are several issues to assess that will have bearing on whether the chamber is a realistic design. Is the beam isothermal (or nearly so)?, what is the amount of power is needed from the lamps, is such a power level sufficient to maintain a 900degF beam, and will the chambers outer walls get excessively hot? Varying levels of analysis were to address these concerns.

First, a pair of diagrams depicting the environment around the beam is worth discussion based on the anticipated design of the enclosing chamber. Figure 25 is a side view schematic of the coated beam suspended between the linear radiant sources that

will heat it. The relevant dimensions of the titanium as well as the thin coatings in the middle region are called out. It it noted that the dimensions of the beam sample are identical to those used in the studies of Pearson and Reed.

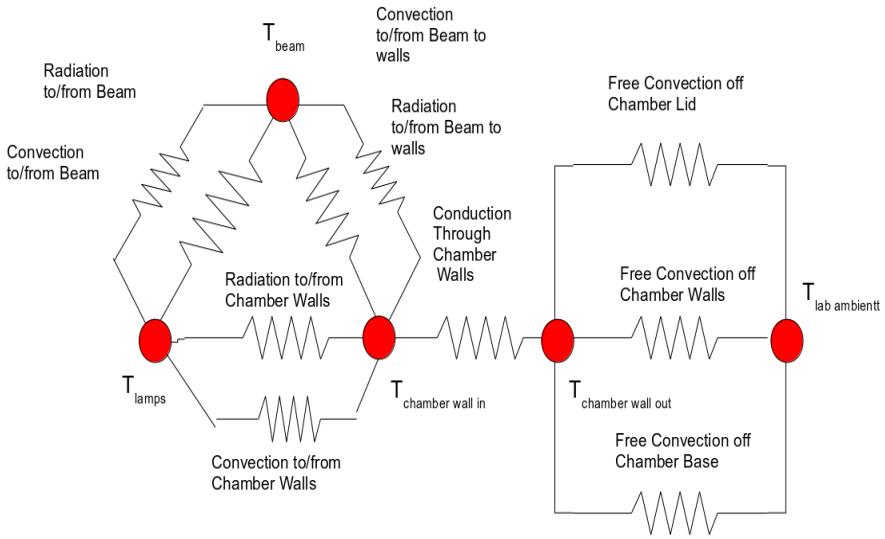


Figure 24: Thermal Circuit for Beam, Specimen, Chamber, and Surroundings

The linear thermal radiation sources consist of four sets of two lamps; aligned end-to-end these pairs are suspended in a radial array around the beam system as shown here in a top-view schematic, as per Figure 26. The four thermal source pairs were required to help ensure a near-uniform incidence intensity of thermal radiation striking the beam. For the analytical analysis and finite difference code these were collapsed to two virtual sources that were treated a uniform, planar emission source to reduce the dimensionality of the problem. The two thin black rectangles in Figure 25 depict these virtual sources. This was predicated on the array being centered on, and

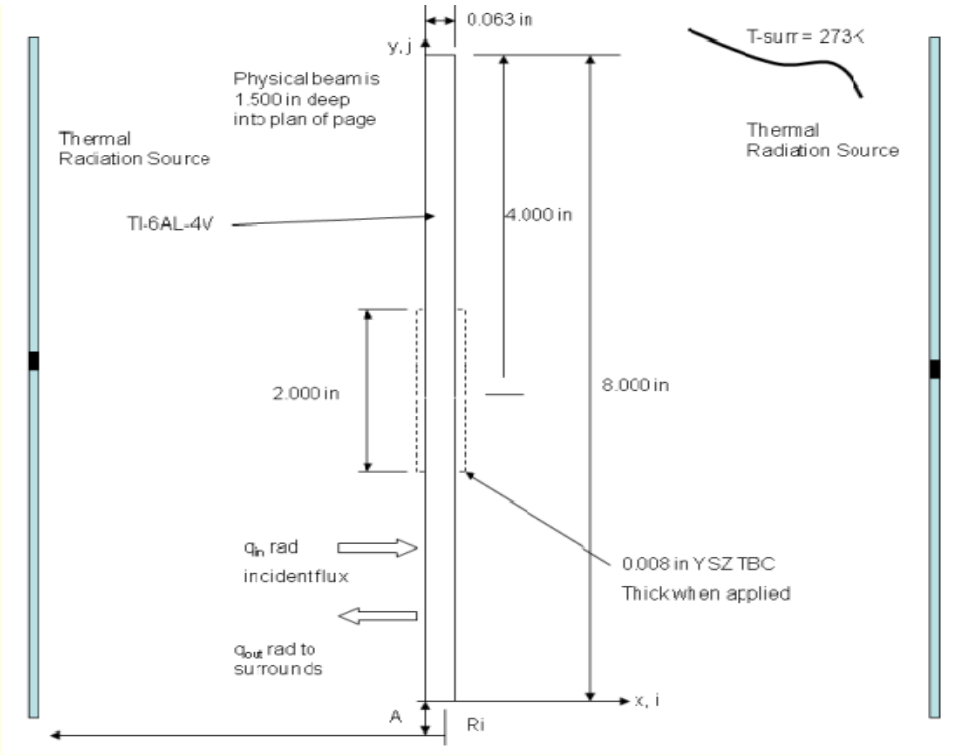


Figure 25: Side View of Beam in Thermal Chamber

radially symmetric about the beam center, with the array's circular radius large enough to ensure sufficient standoff distance from the beam. This distance allows the circular radiant intensity profile chord from the direct emission side of each lamp to appear nearly-uniform across the span of the beam by the time the wavefront reaches the beam face. Equipped with linear parabolic ("trough") reflectors and sufficient standoff distance from the beam, and spreading of the sources along the entire length of the beam, there is confidence that the radiation field arriving is near uniform to use such in the analyses. It is still noted, that thermal characterization of the field in an indirect fashion, by means of multi-point thermocouple data collection and thermal camera imaging was a critical validation of the test chamber as is covered in Chapter 3.

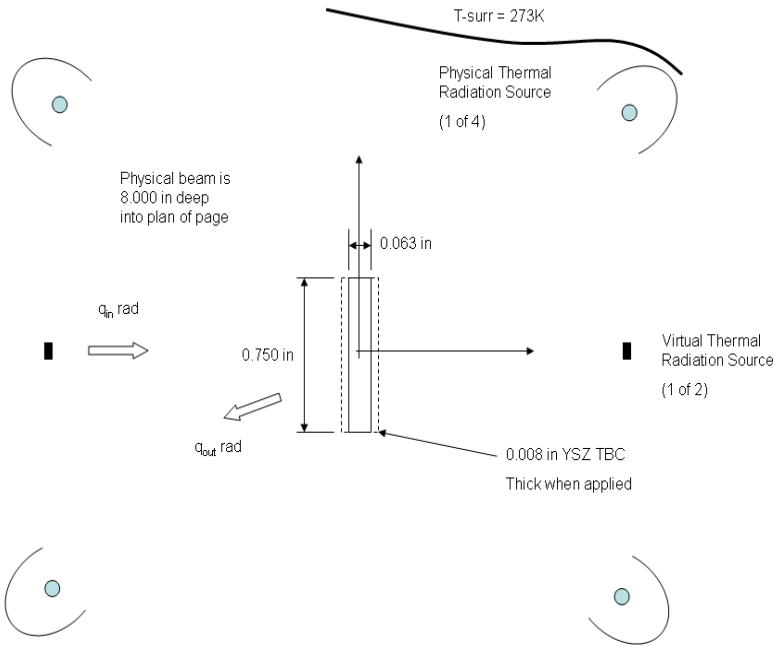


Figure 26: Top View of Beam in Thermal Chamber

From Figure 26 one can also note that based on radial symmetry, the 3-D problem was collapsed into a 2-D for the numerical finite difference and analytical study. The virtual sources where used for these analyses except for the 3-D FEA cavity problem which used the real source geometry with the lamps and reflectors. The finite difference model was formulated as a 2-D domain from the outset and, for the analytical study, the incident radiation was treated as a uniform flux intensity.

It is illustrative to show the overall thermal circuit of the specimen, surrounding apparatus and lab environment overall; this is shown in Figure 24. The delta network is the chamber interior modes of heat exchange between the chamber walls, the lamps, and the specimen itself. There are other components in there: the mirrors, electromagnetic coil, and so forth, but these can be grouped into the sources and surroundings,

respectively as they are passive or small influence on the flux exchange within. By supplying a vacuum of around 0.01-0.03atm, the outer legs of the delta representing modes of free convection can be eliminated, quick calculation on free convection flux of a thin vertical plate (like the beam) established it was less than 2% of the radiation flux in estimated conditions of the chamber. This yields a 3-surface cavity radiation problem, albeit one with non-trivial view factors. This problem has been analyzed in multiple fashions, the most geometrically accurate being a simulation in ABAQUS Standard v6.8-2 using the radiation interaction module. The verification of the reasonable power requirements, isothermality of the specimen, and low enough chamber outer wall temperatures for safety are the critical objective take-aways of the whole system thermal circuit analysis.

Heat flow proceeding outward from the chamber interior conducts through the walls of the chamber. Hand analysis of the problem was performed with reasonable approximations. These include treating a the chamber wall conduction as a 1-D conduction problem with the average thermal resistivity weighted based on the thicknesses across various areas of aluminum in the different portions of the chamber enclosure. Another was to assume the outer wall of the chamber is a vertical smooth wall unwrapped to a flat plate with free convection while the top and bottom slabs are horizontal plates with free convective plumes. The convection (and some radiation) to the ambient laboratory occurs from the air-cooled chamber. Meanwhile, the thermal emissivities inside the chamber can be estimated including the view factor geometry. The main objectives of this analyses, conducted by classic techniques, is to determine the

reasonableness of the more precise simulated solutions. The secondary objectives were to determine if pumped coolant will be needed to enhance heat rejection, safety aspects concerning the temperatures on the outer portions of the vessel, and the places to focus localized cooling, if needed, to protect heat sensitive items (o-rings, wire potting plugs, etc.).

2.3. Dimensional Analysis and the Stark Number

To gain an initial insight into whether a near isothermal state will exist in the titanium beam, a initial estimate of the system thermal behavior was obtained by employing the traditional lumped capacitance analogy modified to a radiation-conduction problem. It is typically applied to a serial, two-part convection-conduction thermal circuit to establish whether there is spatial invariance in a problem and, if so, enable the method of "lumped capacitance" to be used (Incropera, 1996). This was adapted to the serial radiation-conduction problem for our beam. For a traditional surface convection boundary condition into a conductive body, the dimensionless Biot (Bi) number, is typically defined as per Eq. (12):

$$Bi = \frac{hL_C}{k} \tag{12}$$

where k is the thermal conductivity in W/m·K, h is the surface convective coefficient in W/m^2·K, L_C is a characteristic length, typically defined $L_C \equiv \frac{V_{body}}{A_{surface}}$ where V_{body} and $A_{surface}$ are the volume and surface of the solid conduction mass (Incropera, 1996). If the

Biot number is well below unity (e.g. Bi << 1) then the spatial variations in the temperature field can be neglected and the problem is merely dependent in time (e.g. $T(x,y,x,t) \rightarrow T(t)$). This is because the conduction thermal resistance is very small relative to the convective one, requiring far smaller temperature gradients to drive the same heat flux within the solid as opposed to across the vacuum. Biot number for convection is defined as (Incropera and DeWitt, 1996):

$$Bi = \frac{R_{cond}}{R_{conv}} = \frac{\frac{\Delta x}{kA}}{\frac{1}{hA}} = \frac{h \Delta x}{k} \tag{13}$$

where Bi is the Biot number, R_{cond} and R_{conv} are the thermal resistances to conduction and convection, h is the surface convection coefficient, and Δx is the characteristic length of the solid (often a ratio between the surface area and volume). Since radiation is a surface phenomenon, much like convection, a similar ratio of thermal resistance in series circuit can be worked out to arrive at a "radiation" Biot number as per Eq. (13):

$$Bi = \frac{1}{Sk} = \frac{R_{cond}}{R_{rad}} = \frac{\frac{\Delta x}{kA}}{\frac{1}{h_r A}} = \frac{\frac{\Delta x}{kA}}{\underbrace{1/\epsilon \sigma (T_{surf}^2 + T_{surr}^2)(T_{surf} + T_{surr})}_{h_r} A} \tag{14}$$

where Sk is the Stark number, R_{rad} is the thermal resistance to radiation, h_r is the surface radiation heat transfer coefficient, ε is the surface emissivity, σ is the Stephan-Boltzmann constant (5.67×10^{-8} W/m^2·K^4)), T_{surr} and T_{surf} are the absolute temperatures of the surroundings and solid surface, and A is the surface area of the solid. Simplifying Eq. (14) yields:

$$Bi = \frac{1}{Sk} = \frac{\Delta x \sigma \epsilon A (T_{surf}^2 + T_{surr}^2)(T_{surf} + T_{surr})}{k} \quad (15)$$

where the radiative coefficient is defined as (Incropera, 1996):

$$h_r \equiv \epsilon \sigma (T_{surf}^2 + T_{surr}^2)(T_{surf} + T_{surr}) \quad (16)$$

It is noted that for the Ti-6Al-4V beam heated to a maximum of 755K (900degF), with the conductivity for titanium (K = 29.0 W/m·K), the "radiation Biot" number is 0.00062 << 1. The reciprocal of this dimensionless group, the "Stark" number is Sk ≈ 1612 >> 1; what is deemed a high Stark number system. Therefore, it can be anticipated that the isotherms in the beam will be very gradual gradients, and the conductive transport is very strong relative to that of the radiative. This reinforces the importance of maintaining a good vacuum around the free-free beam system in order to prevent R_{rad} from being lowered by any significant free convection. That would couple it to a (low) parallel convective resistance (R_{conv}) in the thermal circuit.

Campo presents a lumped temporal response solution for a spherical mass to the radiation-conduction problem. Lumped, transient solutions for radiation conduction from a wall have been presented by Tan et al. These two papers should be useful for establishing thermal settling times in the proposed chamber system (Tan, 2007). Note that these will not be true time-constants as usually denoted by τ as the rate equation is 4th order in temperature and not linear.

The solution from Campo for a spherical mass is presented as:

$$\bar{\Phi} = (1 + 3N_c' \tau')^{-1/3} \quad (17)$$

where:

$$\Phi = \frac{T}{T_i}$$
$$\tau' = \frac{\alpha t}{(V/A)^2} \qquad (18)$$
$$N_{rc}' = \frac{\epsilon \sigma (V/A) T_i^{\,3}}{k}$$
$$\Phi_s = 0 \qquad surroundings\,temperature$$

where α is the thermal diffusivity, Φ is the non-dimensional temperature, Φ_s is the non-dimensional surroundings temperature, t is the time elapsed, V/A is the volume-to-surface area ratio, k is the thermal conductivity of the solid, σ is the Stephan-Boltzmann constant, and ε is the surface emissivity of the solid body (Campo, 1996). τ' and N_{rc}' are the non-dimensional time and the strength factor of surface radiation to internal conduction; the prime denotes non-dimensionality. The bar notation in Eq. (17) indicates a spatially averaged value. From this a good estimate of the thermal settling time can be obtained. Figure 27 displays the curves generated at various surface emissivities for the titanium beam. For the effective radius to use in the solution the ratio of the beam volume-to-surface area ratio was used to define the quantity "V/A" in Eq. (18), this accounts for the dispersed area of the beam and its greater emission surface to volume ration than a sphere of equivalent mass. These curves are cooling curves, but if the beam is in a highly reflective cavity the same rate law should apply to heating as long as the driving temperature potentials are of the same magnitude but just reversed. It does give an estimate of the time required for the beam to approach the surroundings temperature at 70degF.

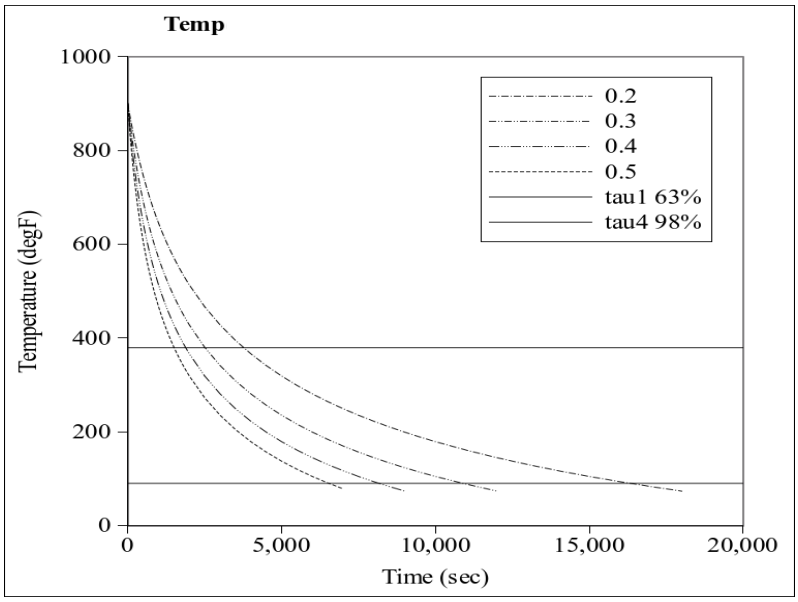


Figure 27: Cooling Curves using Spherical Solution at Various Emissivities

It is noted that at a higher emissivity, the beam will more rapidly heat and cool, and that this may allow gross estimation of beam emissivity based on the experimental timing. Care should be taken in employing time constants, these curves are not exponential decay curves as the system is not linear in rate w.r.t. to temperature. Also, the beam is not of spherical geometry so geometric inaccuracies exist. As a result these will be referred to as ”pseudo time constants”. Though the curves settle somewhat faster than linear rate curves, it is clear set-point overshoot is a good idea to quicker heat to the test/steady-state temperature. To accomplish this provision for closed loop temperature monitoring for the system is called for.

2.4. Modeling of the Heat Transfer

The Stark number result in the dimensional analysis above gave confidence that the proposed design will feature an isothermal beam system when heated within a

vacuum. The system also appears to have a slow pseudo-time constant as well, indicating a high thermal resistance to discharge the temperature potential through exists. To gain greater insight into the distribution of temperature within the the beam-coating system and address “is it isothermal?”, more detailed modeling studies were performed. During this design details that influenced heat transfer could be specified for when the apparatus entered fabrication.

2.4.1. Analytical Model of the Beam System

An analytical study of the coated beam system was conducted in parallel to the numerical study. This study employed the following assumptions: the radiation field around the beam was uniform, local illumination is temporally invariant due to the symmetric nature of the oscillating displacement of the beam, the system is at a steady state, and a similar geometric shape was employed with a thin aspect ratio (Baker, 2008).

The problem was worked using the Fourier conduction law in the interior of the beam solid while the surface boundary conditions where radiation exchanges occurred was defined according to the Stephan-Boltzmann law. In contrast to the finite difference and finite-element models presented in the next sections, the TBC patch was treated as vanishingly thin, e.g. it is was treated as surface property variation only with the variation in emissivity and absorptivity.

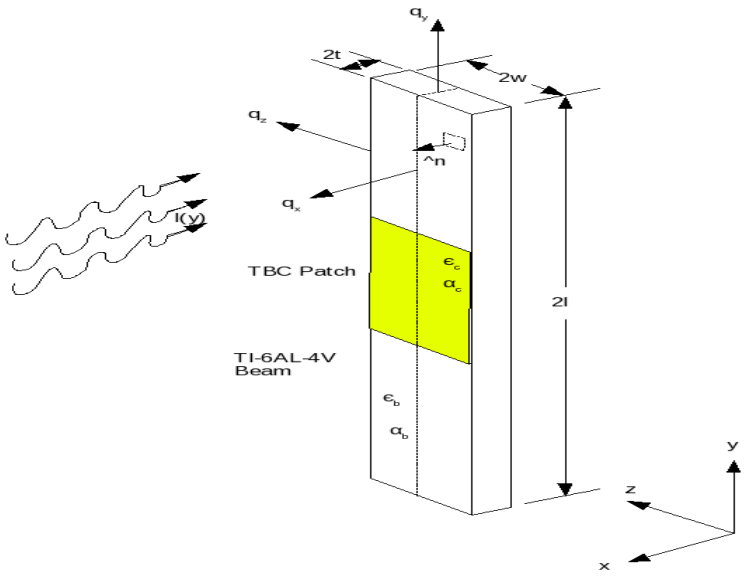


Figure 28: Beam Coordinate System, Dimensions

Figure 28 depicts the beam and relevant dimensions used in the analytical model of the beam heat transfer, while Figures 25 and 26 detail its location among the heat sources. The results for the analysis are stated here without elaboration; the fine details of the analysis are covered in Appendix 1. The shaded region on the beam, shown in Figure 28, is the patch of TBC material. It is is characterized with a length, L_C. The beam has a thin aspect ratio. Restated, $2t << 2w << 2L$, and the thickness of the TBC coating patches, which are on both sides of the beam, are much less than that of the titanium beam, e.g., $t_c << 2t$, and so the TBC can be treated as negligible for conductive transport.

The end results achieved by the analysis is presented here:

$$v(y:d)=u^{1/4}(y)+\frac{1}{\sqrt{\alpha}}\left[B\exp[-Q\sqrt{\alpha}(y+1)]+D\exp[-R\sqrt{\alpha}(1-y)]\right]+O\left(\frac{1}{\alpha}\right)$$
$$B=\frac{\sqrt{\epsilon\lambda}}{2}[u(-1)]^{-3/8}[\hat{G}_y^{\,-}-\hat{G}_s(-1)]+\frac{u'(-1)}{8\sqrt{\epsilon\lambda}[u(-1)]^{9/8}} \qquad (19)$$
$$D=\frac{\sqrt{\epsilon\lambda}}{2}[u(+1)]^{-3/8}[\hat{G}_y^{\,+}-\hat{G}_s(+1)]+\frac{u'(+1)}{8\sqrt{\epsilon\lambda}[u(+1)]^{9/8}}$$

where the variables, many of non-dimensional form, are defined as per:

$$u(y)=\{\delta^4+\hat{G}_s(y)\}$$

$Q=R=2\sqrt{\epsilon\lambda}[u(\pm1)]^{3/8}$	*beam tip irradiances* (*lower* and *upper*)
$\lambda=\frac{l\sigma}{K}T_r^{\,3}\quad;\quad(\lambda\approx1)$	*radiation − conduction strength factor*
$\delta=\frac{T_a}{T_{ref}}\quad;\quad(\delta\approx1)$	*non − dimensional scaled temperature*
$\alpha=\frac{(t+w)l}{tw}\quad;\quad(\alpha\approx140\gg1)$	*volume − surface area aspect ratio*
$v\equiv\frac{T}{T_{ref}}\quad;\quad(v\approx1)$	*non − dimensional temperature*
$\hat{G}_s(y)=\frac{G_s(y)}{\sigma T_r^{\,4}}$	*non − dimensional irradiance*

(20)

ν is the non-dimensional temperature, scaled to an arbitrary reference temperature, λ is the amplification factor (akin to the Biot, or 1/Sk, number) that relates the radiative flux to conductive flux strength, δ is the non-dimensional ambient temperature, α is the surface-to-volume aspect ratio taken as the ratio of surface to the cross-sectional area of the smallest section, and Ĝ is the irradiation imposed onto the beam in a non-dimensional form scaled to the reference temperature ,T_r. It is noted that y is the dimensional coordinate down the beam in normalized coordinates running from the lower tip (where y = -1) to the upper tip (y=1). G(y) is the incident irradiation flux as function of location down the length, u is the non-dimensional net irradiation.

It is noted that the effects of the solution breakdown by order from the boundary layer analysis as per Eq. (19). It is noted that the influence of surroundings temperature and direct irradiation of the beam are of a lot stronger order of influence on any final temperature distribution down the beam than either the tip irradiation or surface emissivity variations on the beam.

$$v(y:d)=\underbrace{\{\delta^4+\hat{G}_s(y)\}^{1/4}}_{\text{heat source}(=u^{1/4}(y))}+\frac{1}{\sqrt{\alpha}}(\textit{Tips Boundary Irrad.})+\frac{1}{\alpha}(\textit{Surface Prop. Varic} \qquad (21)$$

This insight was most useful for the experimental design, suggesting that excessive effort to account for emissivity variations between the bare titanium regions

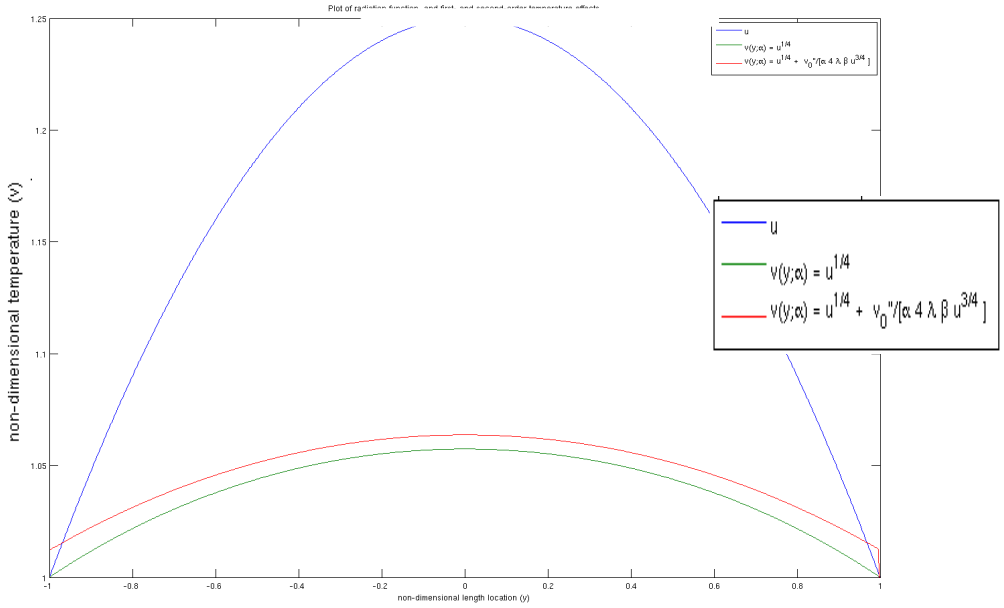


Figure 29: First- and Second-Order Effects on Temperature, Variation with Parabolic Irradiation Profile

and TBC-coated region of the beam are unnecessary. On the other hand , preserving a near uniform illumination field as well as far-surroundings temperature field should receive some due attention in the design. An example of the sensitivity of the beam

temperature to the variations in illumination is shown here in Figure 29. The irradiation profile is a weakly parabolic function with 25% greater flux intensity in the center of the beam than at the tips. The resulting temperature distribution is shown with just the first order effects (green curve) and then second order effects (red curve). It is seen that the severe variation in irradiative flux is damped out by just inclusion of the first order effects. These are the absorption of imposed radiation as well as re-radiation of heat to the surroundings. Second-order effects from the diffusion of heat within beam further dampen out any variation. The plotted functions from the solution are:

$$\begin{aligned} &\textit{Source Variation}: u \textit{ parabolic function} \\ &\textit{first-order effects} \quad : v(y;\alpha) = u^{1/4} \\ &\textit{second-order effects} \quad : v(y;\alpha) = u^{1/4} + \frac{v_0''}{\alpha 4 \lambda \beta u^{1/4}} \end{aligned} \tag{22}$$

It is noted that even when a relatively strong non-uniformity in the irradiation intensity strikes the beam it provokes a much weaker thermal non-uniformity within it. This is further evidence that the diffusive conduction transport of heat within the beam faces much less resistance than that of radiative exchange across the vacuum. This also hints that the requirement of very uniform radiant illumination of the beam might not be as critical as thought, e.g. slight hot spots and weakly shaded areas might not drive large thermal gradients after all.

2.4.2. Derivation

The detailed derivation of the analytical solution is contained in Appendix 1. It is a reduction of the Fourier Heat Transfer law of conduction within the solid that is

bounded on all the surfaces by the radiation exchange governed by the Stephan-Boltzmann law. The incident heating radiation flux is specified, along with the temperature of the surroundings to ground the problem. The thin beam's aspect ratio is considered wherein the conductive resistance along the length is much higher than through the thickness or across the width. This allows reduction of the 3-D partial differential equation (PDE) to a 1-D ordinary differential equation (ODE) using an analogous method inspired by boundary layer theory. The conduction into and out of the thickness of the beam is predominant due to the much larger cross-sectional area in this direction, parallel to the x-axis in Figure 28. Applying a simple expansion upon the cross-sectional area aspect ratio yields a non-dimensional temperature distribution that is valid removed from the edges (Baker, 2008).

Another valuable finding from the analytical study was a proof of uniqueness and existence. Detailed in Appendix 2, this gave confidence that even though the beam solid had all flux boundary conditions on the surfaces (an all “Neumann” boundary condition situation), that given a environmental sink temperature in the surroundings, that the solution function will converge to a unique distribution of values within the beam. This insight gave confidence that the numerical thermal fields that were obtained at steady-state equilibrium were driven by the boundary conditions and not by artifacts of the numerical method chosen.

2.4.3. Finite Difference Modeling of the Beam System

A numerical simulation of the coated beam specimen using a 2-D finite difference model was undertaken to gain further design insight into the system. The variation of

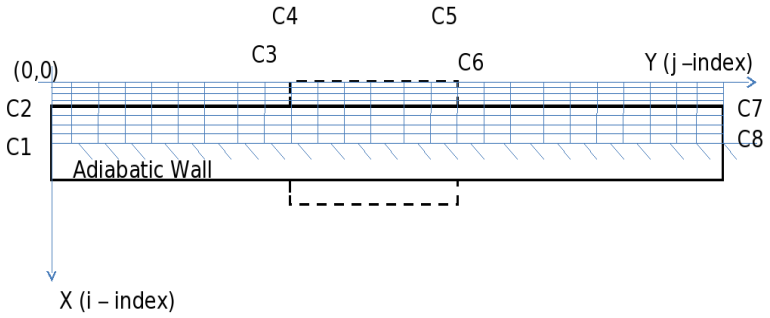


Figure 30: Computational Domain and Finite Difference Grid

properties across the TBC to that of the titanium beam in regards to thermal conductivity as well as surface emissivity, absorptivity, and reflectivity was hypothesized to be a potential source of steep thermal gradients within the system. Conductivity problems are routine, but surprisingly, literature that addresses the highly non-linear radiation surface boundary condition is quite sparse. One source material was the work of Bohnert who modeled a Hall effect thruster by means of a finite difference code featuring radiation surface boundary conditions. His solution techniques were adapted into the current model, and were employed in handling of the highly non-linear surface boundary condition during the solution process. (Bohnert, 2008).

The problem domain was a planar slice down the longitudinal axis at the mid-width of the beam, as shown in Figure 30. It is noted that the grid is non-uniform in the X-direction (through the thickness of the coating) due to the very thin nature of the coating, as well as the anticipation of needing to capture very high thermal gradients through this (relatively) poor conductor. The overall grid was nine nodes deep in the x-

direction; one at the adiabatic (by-symmetry) back wall, four in the titanium beam, one at the surface of the titanium, and four either in space or within the ceramic layer depending on the location down the y-direction. The y-direction was 26 nodes long. After successful convergence of the code, grid refinement studies with a 2X as dense grid did not appreciably change the final solution field that was arrived at (<1% relative difference). It was also noted that convergence to the same steady-state solution was achieved (given the same boundary conditions), regardless of the initial temperature field supplied for the ceramic-beam system.

The source code of the finite difference model is provided in Appendix 3 with the various physical constants, solution methodology, and grid parameters detailed. The code was developed in Matlab to be extensible and allow for easy parametric variation and sensitivity analysis. Some assumptions employed are: 1) the beam is vibrating at or around the Mode-I shape in the vacuum but the characteristic time scale of the mechanical oscillations is slow compared to the thermal irradiation so the time-averaged (static) beam will be utilized for the geometric boundaries, 2) the solution sought was a 2-D steady state heat conduction within the beam problem with radiation on the boundaries, and 3) the four physical sources are mapped to two virtual sources (see Figure 26) to collapse from a 3-D to 2-D geometry. The irradiation sources were mapped from a physical pair on each side of the beam facing a major face to a virtual source in the mid-plane of the beams transverse cross-section. This was approximated as a uniform specified irradiation value.

The governing equation in the interior of the beam solid and TBC solids, which were isotropic in nature with respect to thermal conductivity, was the well-known two-dimensional finite difference form of the conductivity equation, derived as, for a non-uniform grid (Branam, 2008; Incropera, 1996):

$$T_{i,j}=\frac{1}{2\left(\frac{\Delta x}{\Delta y}+\frac{\Delta y}{\Delta x}\right)}\left(\frac{\Delta y}{\Delta x}(T_{i,j+1}+T_{i,j-1}) \; + \; \frac{\Delta x}{\Delta y}(T_{i+1,j}+T_{i-1,j})\right) \tag{23}$$

where Δx and Δy are the length and depth of the finite difference volume containing the node in question, T is the temperature, and subscripts i and j are the x- and indices of the node of interest. Note due to radiation transport in some parts in the grid, absolute temperatures are used. Where a nodal volume contains the interface between the beam and TBC ceramic solid, a cross-sectional area-weighted thermal conduction path resistance approach was used to enforce flux and temperature compatibility across the interface. Using a local conservation of energy approach to conduction across the node a finite difference volume formulation leads to:

$$T_{i,j}=\frac{A}{\left(\frac{k_c\Delta y}{\Delta x_c}+\frac{k_c\Delta x_c}{\Delta y}+\frac{k_b\Delta y}{\Delta x_b}+\frac{k_b\Delta x_b}{\Delta y}\right)} \tag{24}$$

where the term A is defined as per:

$$A=\left[\frac{\Delta y}{\Delta x_c}T_{i-1,j}+\frac{\Delta y}{\Delta x_b}T_{i+1,j}+\frac{k_c\Delta x_c}{2\Delta y}(T_{i,j+1}+T_{i,j-1})+\frac{k_b\Delta x_b}{2\Delta y}(T_{i,j+1}+T_{i,j-1})\right] \tag{25}$$

The "c" and "b" subscripts to variables denote to which region they apply; TBC ceramic and titanium beam, respectively; k is the thermal conductivity of the solids. Δx and Δy are the cell size for the finite difference grid in the x- and y-directions. For a typical edge-

facing node such as that depicted in Figure 31, in this case that of the bare-titanium surface facing out towards the lamps, was derived as (Branam, 2008):

$$q_{in} = 0 = \frac{(k)(1)\left(\frac{\Delta x}{2}\right)}{\Delta y}\left(T_{i,j+1}+T_{i,j-1}\right)+\frac{(k)(1)(\Delta y)}{\Delta x}\left(T_{i-1,j}\right) \\ -T_{i,j}\left[\frac{2k\frac{\Delta x}{2}}{\Delta y}+\frac{k\Delta y}{\Delta x}\right]+I\,\alpha(\Delta y)(1)-\epsilon\sigma(\Delta y)(1)\left(T_{i,j}^4-T_{surr}^4\right) \quad (26)$$

where k is the conductivity of the titanium (or ceramic TBC, depending on location), Δx and Δy are the distance between nodes in the x- and y-directions, $T_{i,j}$ is the temperature at the node of interest, q_{in} is the heat flux in/out of the grid cell volume (which is set to zero in the steady state condition), I is the surface irradiation power in power per unit area (W/m^2), ε is the thermal emissivity of the titanium surface (or TBC) α is the absorptivity of the titanium surface (or TBC), σ is th Stephan-Boltzmann constant, and T_{surr} is the temperature of the enclosing surroundings here set to 273K. The fourth term on the r.h.s. of Eq. (26) is the absorbed incident radiation, while the fifth, highly non-linear term (and transcendental in terms of $T_{i,j}$), is the re-radiated energy from the beam system. Implicit in the derivation of this surface equation is the opaque surface assumption (where transmissivity is zero, $\tau = 0$). The Kirchhoff Law of radiation is in effect which implies that at thermal equilibrium, a body's absorptivity is equal to its emissivity ($\alpha = \varepsilon$). An assumption was made, based on analysis of the size of the heat fluxes in the first through fourth terms, versus those of the fifth and sixth, that conduction was the dominating flux. All surfaces are idealized diffusive emitters that are constant across solid angles and

temperatures. Since $T_{i,j}$ is a highly non-linear term, a convergence loop was needed to be run on each boundary condition when marching the finite difference stencil around on the i- and j- indices's (the grid).

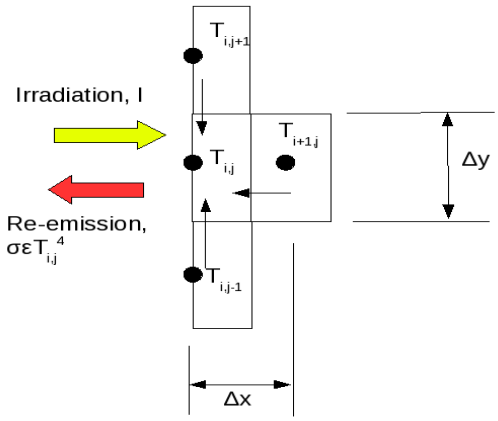


Figure 31: Surface Node in Radiation-Conduction Model

Two ways to deal with surface non-linearity were proposed: 1) assume $T_{i,j}$, equals the value from the previous iteration step (designated as $T_{i,j}^{0}$), and solving for the nodal temperature using the previous value of $T_{i,j}^{0}$, until a tolerance of difference between $T_{i,j}$ and $T_{i,j}^{0}$ is achieved by iteration within each node as the stencil moves through the grid, and 2) linearize the radiation emission term around $T_{i,j}^{0}$ from a previous the previous step, Taylor expand, and rearrange Eq. (23) in terms of $T_{i,j}$ to apply as the stencil moves through the grid (Bohnert, 2008; Branam, 2008) .

Employment of the second method upon Eq. (26) yields:

$$q_{in\,rad} = \epsilon\sigma(1)(\Delta y)\left(T_{i,j}^4 - T_{surr}^4\right) \approx q_0 + \frac{\partial q}{\partial T_{i,j}}\left(T_{i,j0}^4 - T_{surr}^4\right) + H.O.T. \tag{27}$$

with the locally linear form:

$$q_{in\,rad} \approx \epsilon\sigma(1)(\Delta y)(T_{i,j0}^4 - T_{surr}^4) + 4\epsilon\sigma(1)(\Delta y)(T_{i,j0}^3)(T_{i,j0} - T_{i,j}) \tag{28}$$

Placing (28) into the last term on the r.h.s. of (26), and rearranging yields the following:

$$q_{in}=0=\frac{(k)(1)\left(\Delta\frac{y}{2}\right)}{\Delta x}(T_{i+1,j}-T_{i-1,j})+\frac{(k)(1)(\Delta x)}{\Delta y}(T_{i,j-1})-T_{i,j}\left[\frac{2k\frac{\Delta y}{2}}{\Delta x}+\frac{k\Delta x}{\Delta y}\right] \\ -I\alpha(\Delta x)(1)-\epsilon\sigma(1)(\Delta y)(T_{i,j0}^3)(T_{i,j0}-T_{i,j}) \tag{29}$$

which can be solved for $T_{i,j}$ in a closed form and applied in the code without requiring intra-node iteration and convergence checks at each individual i,j address. Using the second method (which was the one implemented within the finite difference code (See Appendix 3 for the Matlab source code)), the 4th-order radiation emission term was calculated with the previous iteration's values of $T_{i,j}$, and since the impressed radiation (I) is the source term driving the solution (as opposed to emission), the system will converge, albeit slightly slower than more refined numerical techniques. Radiation net heat flux (q_{in} rad) in the current step was calculated from $T_{i,j\,0}$. The rest of the terms, being linear, were solved in a closed-form fashion.

Iteration occurring at each node could be performed to handle convergence of the non-linear radiation flux (the first method), though this was not necessary here, due to the relatively modest temperature range encountered. As a result mild non-linearity from the nodal radiation boundary conditions entered the approximation in Eq. (28). This forward difference in "pseudo"-time (a steady-state solution was sought, and so iterations did not correlate to time steps; the thermal storage term, the product of mass and heat capacity (or ρC_p) being set to zero in each node), was less refined than the second method of locally linearizing around $T_{i,j}$ or a pseudo-backward time difference method (which is

inherently stable; a 1-D code was used to evaluate this).

The symmetry line down the mid-plane of the beam was treated as a adiabatic wall as per:

$$T_{i,j}=\frac{1}{\frac{\Delta y}{\Delta x_b}+\frac{\Delta x_b}{\Delta y}}\left(\frac{\Delta y}{\Delta x_b}(T_{i,j-1}+T_{i,j+1})+\frac{\Delta x_b}{\Delta y}2\mathrm{T}_{i-1,j}\right) \tag{30}$$

The other notable locations within the domain were the interface nodes that spanned the titanium beam and the ceramic TBC materials. A rule of mixtures approach based on a volumetric average of conductivities into and across the node-volume enforced flux and temperature compatibility requirements (Branam, 2008):

$$T_{i,j}=\frac{1}{2\left(\frac{\Delta x_c}{\Delta y}+\frac{\Delta y}{\Delta x_c}\right)}\left(\frac{\Delta y}{\Delta x_c}(T_{i,j+1}+T_{i,j-1})+\frac{\Delta x_c}{\Delta y}\left(T_{i+1,j}+T_{i-1,j}\right)\right) \tag{31}$$

Tracking of the locations of the nodes was performed within the code and the stencil locations selected in a cascaded set of if-then statements. If optimization of the code was required, a set of state index vectors of Δx_b, Δx_c, k_b, k_c, α_b, α_c, ε_b, and ε_c would be stored and called when the i- and j- indices are at the appropriate locations in the solid, this being far more computationally efficient than nested conditional loops. As the solution convergence with the code was acceptably fast (e.g. 30,000 iterations on a 1.5GHz PC within a couple of hours), in practice this optimization was not performed.

The code was deemed converged in a global sense after about 30,000 iterations (though some checks were run to 2M iterations). The area weighted average of all

temperatures in the TBC and titanium solids was calculated in each iteration; when the ratio of the differences in the average temperatures between successive runs over that of the first weighted temperature average was less than 0.0001 (often denoted as ε or iteration error) it was considered converged. This condition was meet after 30,000 counts.

The finite difference code was considered to have converged by about 30,000 iterations; a calculation of the difference of the average temperature field in the metallic and coating domains between successive iterations as defined as $\varepsilon = (T_{ave\ i} - T_{ave(i-1)})/T_{ave(i-1)}$, was about 1.0×10^{-8} which. Taking the simulation out to 2 million iterations. The final runs where performed with a 700degF blackbody surroundings and and imposed radiation of $I = 4500 \times (6.0/8.0)$ W/m^2, this was derived from 6.0in long lamps over the 8.0in long beam back calculated from 4X the solar constant (1370W/m^2 x 4.0). This resulted in a near isothermal beam at around 890degF.

2.4.4. Features and Implementation of the Finite Difference

Simulations with the code resulted in a largely isothermal temperature field and the results at 30,000 iterations is depicted here in Figure 32. It is to be noted that the scale between the x- and y-directions is not uniform, the steepest isotherm gradients having been anticipated to be into the depth of the beam thickness around the edges of the ceramic coating. The typical parameters the code was run with are outlined in Table 1.

The customary tests to check the physical realism of the code were performed. A

grid that was twice as dense was run with no appreciable change in the steady state temperature field achieved. The convergence from above and below was checked with the uniform initial temperature field above and below the final converged solution, the convergence to the same final steady temperature field was achieved (For proof on existence and uniqueness by Baker, see Appendix 2). The code was established to have converged after about 30,000 iterations by the author and 2 million iterations by Branam (Branam, 2008). Parametric variation by varying the emissivity (and absorptivity) of the titanium and TBC regions had little impact on the temperature variation, although the whole field average temperature value did raise and lower appropriately.

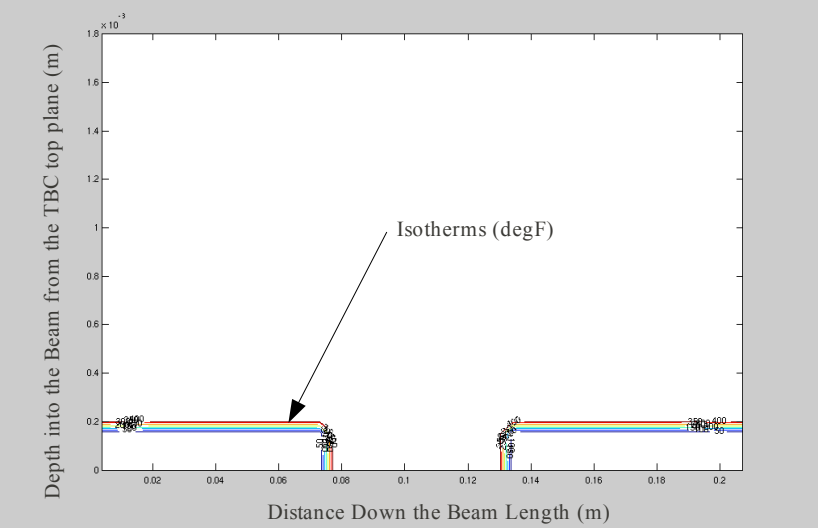


Figure 32: FD Isotherms in Kelvin (TBC coating is bottom center "notch" region)

The thin ceramic coating, modeled as 0.008in thick and 2.0in long, centered on the beam is the lower, centered, 2.0in long, notch region of TBC on the 8.0in long beam length. The most obvious feature of the solution is how all of the isotherms pile up up right at the surface of the beam and the coating. No significant isotherms exist within the

region of either solid. This is again indicative of a lumped capacitance situation that a high Stark number would characterize.

Table 1: Parameters in the Finite Difference Code Runs

Variable	Symbol	Units	typical values
Irradiative power	I	W/m^2	17,280 (10X solar constant)
thermal emissivity, averaged across freq, solid ang.	ε_c	dimensionless	0.3
thermal emissivity, averaged across freq, solid ang.	ε_b	dimensionless	0.3
Stephan-Boltzmann constant	σ	W/m^2K^4	$5.67x10^{-8}$
thermal absorptivity, TBC	α_c	dimensionless	0.3 (Kirchhoff)
thermal absorptivity, bare, Ti-6Al-4V	α_b	dimensionless	0.3 (Kirchhoff)
thermal conductivity, TBC	k_c	W/m·K	2.0
thermal conductivity, Ti-6Al-4V	k_b	W/m·K	29.0
Parameters			
length of beam, the y-coordinate, j-index	L	m	0.2032
width of the beam	W	m	0.01905
thickness of YSZ coating, the x-coordinate, i_c-index	t_c	mm	0.203
thickness of titanium beam, the x-coordinate, i-index	t_b	mm	1.588

Thermal resistivity of the radiation from the source illumination into the surface regions of the beam metal and ceramic solids is much higher then the conduction resistance to thermal flow within either solid region. At the selected irradiation level of 10 times the solar constant (which is about 1370 W/m^2), the solution will converge to about 703K (812deg F), which seems like a physically realistic solution with the beam suspended in far-field blackbody surroundings at 273K. A surface plot of the same solution field illustrates the lack of any significant isotherms in either the titanium metal or the ceramic TBC. Again the scale of the x- and y-axis are not consistent, the x- is exaggerated to display any isotherms into the depth of the ceramic and/or beam solids. Figure 32 is a plot of the isotherms a converged solution of the beam, note that the top

edge of the plot is the centerline of the beam and the notch region in the lower, center of the plot is the TBC layer. Figure 33 shows the same in a surface plot, the TBC region is the notch facing the lower-right of the plot.

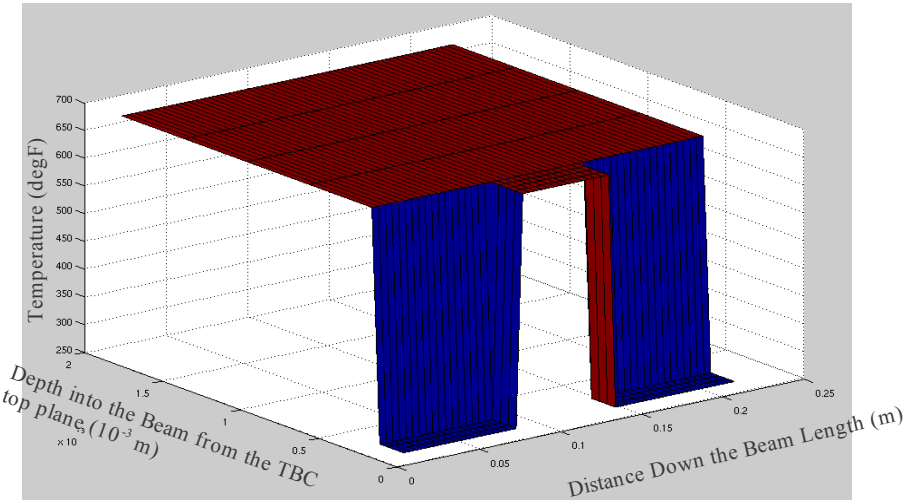


Figure 33: Surface Plot of the Temperature in Kelvin (TBC coating is bottom center "notch" region)

It was later found that the surroundings temperature, Tsurr, being a cold blackbody was a strong cold sink and the radiation imposed was very much higher than needed in the experiment, where the beam was "seeing" hot and low-emissivity foil in the surroundings.

A useful takeaway from these numerical studies is a preliminary calibration curve that the current study can anticipate in terms of uniform lamp illumination intensity flux, e.g. I in W/m^2, versus the beam surface temperature. Experimentally building a thermal calibration curve (See Chapter 3.6) was done but this study gives a good estimate of the needed power requirements and chamber heat loss loads to be encountered. Figure 34 shows the variation of surface irradiation needed to produce variations in the beam

surface temperature.

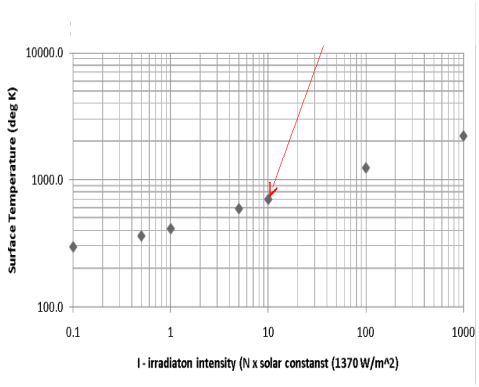


Figure 34: Ti-6Al-4V Surface Temperature vs Illumination Intensity

A follow on study and refinement to the numerical and analytical models was to be done to impact the assessment of shadowing effects from the electro magnetic coil (or coil pair) shading the lower tip of the beam. Subsequent findings in the lab while performing a 2-D Doppler velocity laser (DVL) dataset capture of the beam (using a Polytec PSV-400), along with recommendations by Pearson resulted in the dropping of this work. Subsequent experimental confirmation that adequate coupling by ALNICO magnets using the existing TEFF electromagnetic coil negated the need to perform these refinements to these studies.

The source code for the finite difference model which was developed in Matlab v2007 is listed in Appendix 3. Accurate tuning of the code to the chamber was not performed as the finite element model was developed and tuned performance of that to both models would be a redundant effort. It is noted that the code has some inaccuracies that were not corrected, first it assumed the beam was hanging a a relatively cold blackbody surroundings at 32degF, when it was, in the final realization of the chamber design suspended in a highly reflective cavity at around 730-750degF with far less

irradiative intensity directed at it. Capturing this 3-D geometry was largely done in the last analysis method (attempted in the next section). That said, the code is included in the Appendix 3 as not much is available in the literature for handling non-linear boundary conditions.

2.4.5. Finite Element Modeling of the Chamber

The last radiation heat transfer analysis attempted of the chamber interior utilized a finite-element model built using the ABAQUS Standard v6.8-2 commercial code, specifically employing the radiation heat transfer capabilities of the software. ABAQUS Standard is limited in the allowable degrees of freedom (element surface facing nodes) to 16,000 degrees-of-freedom (e.g. nodal temperatures participating in the radiation exchange network on any free surface of an element) due to the highly non-linear nature of radiation exchange networks and the need to iteratively solve for a converged solution. The fully implicit closed-cavity radiation method was used, which assumes that the surfaces are gray in nature, that the diffusive emissions are of intensity that is independent of wavelength and orientation, that the thermal exchange is in equilibrium (steady state), and that thermal exchange is contained within the enclosure of the surfaces (ABAQUS v6.8-2 Analysis Users Manual, 2007).

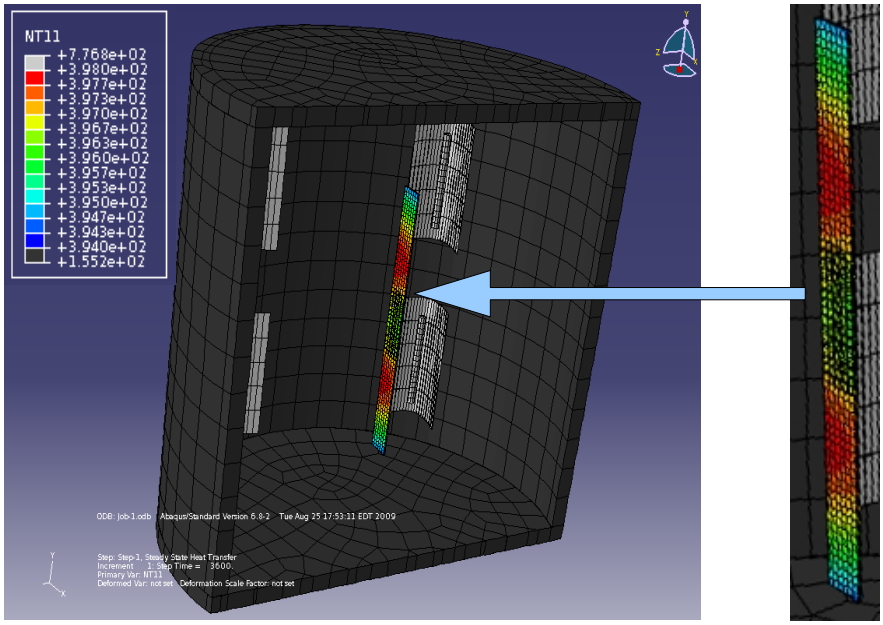


Figure 35: FEA Full Domain Model, Cutaway Half View of Beam and Lamps

Two models were developed, the first one was a full model that included the eight lamps with their parabolic reflectors, the coated beam, and the chamber walls and lids as shown in the sliced view in Figure 35. The items that were not felt to be significant impacts on the heat transfer exchange like the support rods, the electromagnet, and the suspension wires, were not included in the model to keep geometric simplicity and avoid exceeding the nodal limit. With the outer walls now being modeled explicitly, the outer walls of the chamber were fixed to the environmental ambient temperature in the room (T_∞ = 70.0degF) by Newton's law of Cooling, where (Incropera, 1996):

$$q'' = h_{conv}(T_{surf} - T_\infty) \tag{32}$$

The convection coefficients, h_{conv}, specified for the top/bottom lids and the side walls were 10.0 W/m^2 and 1.0 W/m^2, respectively, which are commonly cited values for free-convection in quiescent air (Incropera, 1996). The beam is shown with the isotherms compressed on it, hence the colored appearance of just the beam in Figure 35. The range

of temperature across the whole beam-TBC system displayed from this particular run is from 394degC to 398degC (741.2-748.4degF). There is very little variation in temperature across the beam-TBC system supporting the previous findings supporting isothermality. As can be seen from the lack of color band change when traversing across the width of the beam, the assumptions of areal flux density in the analytical solution are supported by this model. In light gray, indicative of temperatures above the range of the beam, are the lamps and reflectors, and in darker gray, indicating cooler temperatures, are the chamber walls. This model of the full chamber was dimensionally accurate to the chamber as later fabricated and it was used for preliminary thermal sensitivity analysis of it. Scenarios with flat mirrors in lieu of parabolic ones were run, single lamp and four lamp failures, were also run. The last condition represented a whole branch of lamps going out. It is noted that this model was very close to the degree of freedom limit in the radiation exchange network. The need for radiation shielding was indicated based on beam temperatures that were too low, associated high outer wall temperatures that were of a safety concern, and an excessive amount of power needed to reach the design temperature of 900degF (482.2degC) for the beam. To accommodate a reasonable mesh density a second model was developed.

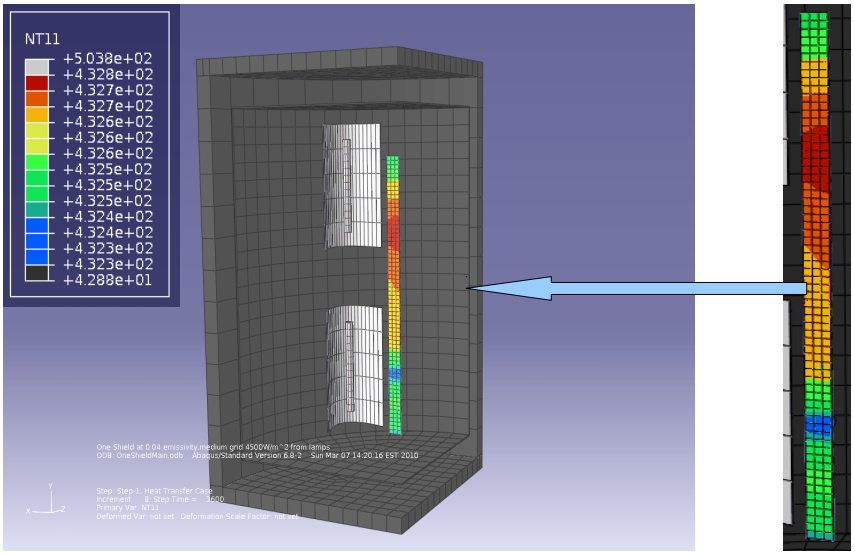


Figure 36: FEA Quarter Domain Model, Two-Cavity Model

This second model, depicted in Figure 36, is a quarter domain model that exploits two of the radial planes of symmetry that the beam-lamp-chamber system as viewed from above exhibits.

Again, the lamps, parabolic reflectors, beam-TBC system, chamber walls and lids are in the model. Newly added is a thin foil layer than encloses the heat sources, reflectors, and beam (the "hot core"). This is the radiation shield that was determined to be needed to add additional thermal resistance between the heat sources and the room temperature sink of the lab thus cutting the power needed to achieve a 900degF (482.2degC) beam and keep the outer chamber walls from getting dangerously hot.

Multiple runs were needed to tune the model into realistic values. Table 2 details some of the runs performed in order to achieve this. As the Table shows, a lot of tuning of the model was required to obtain results that were close to those of the experiment, which was entering validation efforts at the end of the FEA modeling effort.

The elements chosen for the modeling were the ABAQUS 8-noded continuum element, "C3D8", which has a single nodal degree of freedom for the temperature; temperature being a scalar field. Diffusive temperature transport is indicated in the solver module for the conduction. Where the elements have a surface that opens upon a cavity space with radiation transport indicated, as per the ABAQUS "interaction" module, they have associated surface emissivity assigned and participate in a multi-surface radiation exchange network, where each element face is a surface.

Table 2: Various Runs of the ¼ Domain FEA model (Radiation-Conduction)

Model Situation of ¼ domain model	Lamps Temp.		Beam Temp.		Chamber Walls		Reflector		Radiation Shielding		Notes
	Max.	Min.	Max.	Min.	Max.	Min.	Max.	Min.	Max.	Min.	DegC / DegF
Upper temperatures are in degC and lower is in degF											
No shields	776.9	-	421.0	418	164.1	153.9	458.4	455.9	none	none	No Shields, ε_{wall} = 0.30, Lamps at prescribed temp (100W equiv.)
	1430.3	-	789.8	784.4	327.4	309.1	857.1	852.6	none	none	
Polished AL Shielding of ε = 0.01	776.8	-	742.6	742.4	45.4	43.8	745.2	744.8	622.5	609.7	Lamps at prescribed temp (100W equiv.)
	1430.2	-	1368.7	1368.3	113.7	110.84	1373.4	1372.6	1152.5	1129.5	
Oxidized AL Shielding of ε = 0.10	776.8	-	599	597.9	102.7	95.7	612.7	611.2	519.9	499.5	Lamps at prescribed temp (100W equiv.)
	1430.2	-	110.2	1108.22	216.8	204.3	1134.8	1132.2	967.8	931.1	
Oxide AL Shielding of ε = 0.10	575.3	574.8	438	437.2	63	59.8	448.2	447.6	380	367.4	Flux Intensity = 11,000 W/m^2 at lamp glass
	1067.5	1066.68	820.4	818.9	145.4	139.6	838.7	837.7	716	693.2	
Beam titanium regions coated with developer	501.4	501.2	431.4	430.9	42.8	44.4	435.9	436.2	367.8	356.3	ε_{TI} = 0.95, ε_{TBC} = 0.95, $\varepsilon_{shielding}$ = 0.04
	934.5	934.2	808.5	807.6	109.0	111.8	816.6	817.2	694.0	673.3	
Beam titanium regions w/o developer; polished shielding	503.5	503.7	432.7	432.2	443.5	428.8	437.7	437.4	367.8	356.2	ε_{TI} = 0.10, ε_{TBC} = 0.95, $\varepsilon_{shielding}$ = 0.04
	938.3	938.6	810.8	809.9	830.3	803.8	819.8	819.3	694.0	673.2	
Fine Mesh	552.5	551.8	406.5	405.6	59.3	56.4	416.6	415.6	340.3	330.9	Flux Intensity = 11,000 W/m^2 at lamp glass
	1026.5	1025.2	763.7	762.1	138.7	133.5	781.2	780.1	644.5	627.6	
Normal Mesh	503.8	503.6	432.3	432.7	42.8	44.3	437.5	437.8	356.3	367.8	Flux Intensity = 4,500 W/m^2 at lamp glass
	938.8	938.5	810.1	810.8	109.4	111.7	819.5	820.0	673.3	694.0	
Coarse Mesh	560.3	562.9	439.7	425.5	57.6	55.3	439.6	438.4	382.6	358.4	Flux Intensity = 11,000 W/m^2 at lamp glass
	1040.5	1045.2	823.4	797.9	135.7	131.5	823.3	821.1	720.7	677.1	
Default emissivity values: ε_{Lamps} = 1.00, $\varepsilon_{shielding}$ = 0.10, $\varepsilon_{AL\ walls}$ = 0.12, $\varepsilon_{reflectors}$ = 0.05, ε_{TBC} = 0.45, $\varepsilon_{TI\ bare}$ = 0.23, , $\varepsilon_{ALNICO\ magnets}$ = 0.80											

The modeling of the FEA was attempted with the lamp sources as a both a

specified flux and a specified temperature boundary condition(s). The temperature of the lamps for the specified temperature boundary conditions was found by using the radiative power law at the outer envelopes of the quartz bulbs, as per,

$$P = A \epsilon \sigma T^4_{bulb} \tag{33}$$

where P is the power of the lamp (in Watts), A is the outer surface area of the bulb's quartz envelope (in m^2), ε is the emissivity of the glass (assumed to be blackbody, ε = 1.0), sigma is the Stephan-Boltzmann constant ($\sigma = 5.67 \times 10^{-8}$ W/m·K), and T is the outer, radiative (absolute) temperature of the bulb's envelope. In the experiment the bulbs were at about 185W each to yield a 900degF beam, so solving Eq. (33) yielded for T_{bulb} about 987degK (1317degF). Modeling of the outer quartz bulbs as opposed to the tungsten filaments was performed for two reasons. One, it was much easier to mesh the bulb envelopes with a set of elements that were well-formed and reasonable in number, they being closer in their characteristic scale to that of the rest of the objects, and two, it was much easier to measure and estimate the area of the envelope as opposed to the filament from the as-built chamber.

After some initial runs with specified temperature at the lamps, a specified flux boundary condition approach was attempted. These specified flux surfaces were the outer surface of the bulbs. This approach worked reasonably well except that the magnitude of the flux had to be set much lower than expected from calculations. Despite this, the bulb outer temperatures, beam, shielding foil layer, and outer chamber temperatures were all reasonably close to what was measured after the chamber's thermal validation test. When later working with the infrared IR imaging system (See Section 3.3.2) the reasonableness

of this approach became clear. Before spraying the beams with dye penetrant developer in order to eliminate the specular thermal reflections of the lamps off of the bare titanium regions, the specular reflections were on the order of about 950-970degF (1223-1243K), which is likely that of the bulb envelopes of 200W lamps radiating at 66% of their full rated power. This is very close to what the chambers supplied power-versus-beam-temperature calibration curve was determined to be for a beam at 900degF. This also indicated that the quartz bulbs are IR opaque and that they absorb the emissions from the filaments and re-radiate them, even though they are themselves transparent to the wavelengths of visible light. Otherwise, the infrared camera would be indicating the reflective temperatures of the filaments in excess of 1500degC (2700degF) in these reflected hot spots.

Ultimately, a close match between the experimental chamber and the FEA model could be obtained but this would require characterizing the emissivities of many of the chamber components and the outer free film convection layers accurately, by direct experiment. This was not done as the main purpose of the modeling, once it was reasonably close to the physical chamber, was to examine sensitivity of the chamber to variations, ensure an (near-) isothermal beam would result, and design for safe working temperatures for the components and outer vessel exterior.

The full domain model, the first one to be developed, yielded low beam temperatures and a (relatively) hot outer wall of the chamber (around 130-150degC) and required excessive lamp power. Just adding more power was not a viable option, as the variable AC transformers had already been sized along with lamps, drastically increasing

the power would exceed their rated power. The option taken was to increase the thermal resistance in the circuit from the lamps to the room (See Figures 41 with a new resistance added) by adding a triple layer foil radiation shield within the vacuum enclosure but outside the lamps, beam, and dummy specimen. Tantalum foil was suggested but aluminum was deemed of sufficiently high performance if used in a triple layer. This was in effect creating a highly reflective/low emissivity enclosure around the hot section of the chamber.

Addition of the foil shielding and keeping a reasonable mesh density required making the FEA model a ¼ of the full chamber by exploiting two lines of radial symmetry. This still captured the essential features. Even so, only one layer of heat shield was modeled in the FEA with appropriate adjustments made to the emissivities of the inner- and outer- facing surfaces to build an equivalent thermal resistance to simulate the physical 3-layer foil shielding. Note this adjustment of resistances method in a thermal circuit involving radiation can result in results that are globally correct but have large localized errors, this is due to the non-linearity of the radiative heat transfer. Initial attempts to adjust the emissivity of the inner wall of the pressure chamber to a "high polish" condition ($\epsilon \sim 0.01$ to 0.03) to simulate the equivalent resistance of both it and the shielding together was performed. While allowing the beam temperature to elevate (but still fall well below target temperature) at reasonable power levels, the chamber also had very hot outer walls. By tying the shielding to the outer wall it become very cold and so the beam is in effect surrounded by (and subsequently radiates to) a cooler radiative environment. Modeling the shielding in a geometrically accurate fashion maintains the

resistance to heat flow from it to the outer wall, but also allows the shielding to get hot, and therefore the beam to experience a hot surrounding temperature. If radiant cooling was a linear potential process, this simplification would have been acceptable.

One of the latest runs is shown in Figure 37 which is ¼ of the beam, the center line of symmetry is towards the bottom of the Figure. The dark blue canister is the ALNICO magnet which had a conservatively high emissivity value of 0.8, which represented the heavily oxidized state they took on after their first cycle of high heat exposure; most likely the value is quite a bit less. Bulk temperature is around 432degC (810degF), this was with 100W equivalent lamps. The isotherms are indicating that the main gradients run the length of the beam. The pin fin-like extension of the solid that the magnet forms cools the lower end of the beam very slightly from that of the upper half. High confidence existed from these modeling efforts that an isothermal beam would be realized. The traversing of isotherm colors, thereby indicating temperature gradient changes only occurs to a significant degree when running parallel to the long axis of the beam. This occurs to only a very slight degree running parallel to the width and negligibly running parallel to the thickness. This is good evidence that the boundary layer inspired simplification in the analytical thermal solution in Appendix 1 is a valid assumption for the thin beam.

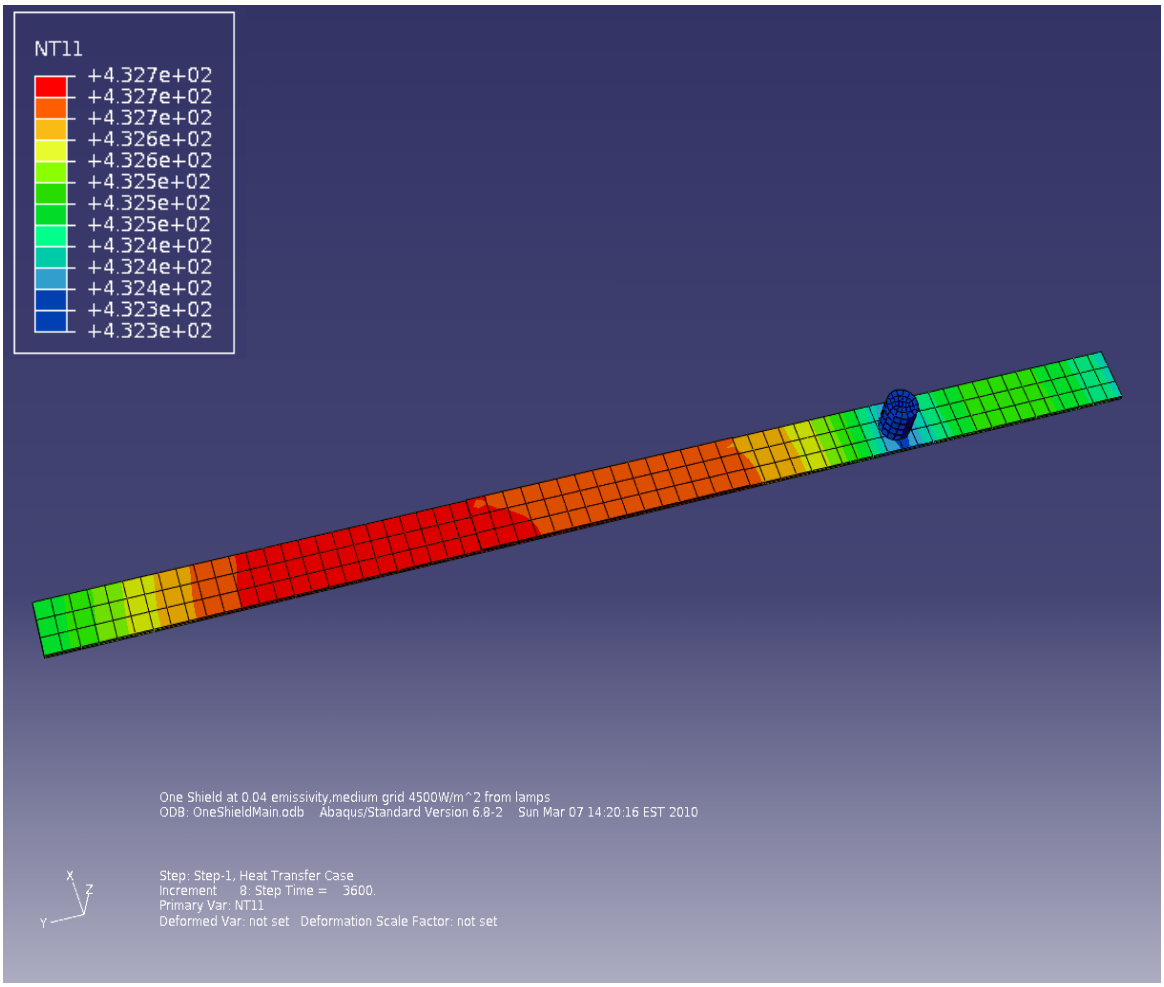


Figure 37: FEA Quarter Domain Model with Temperature Variation

It is worth closing with a note as to the convergence conditions applied to the non-linear radiation portion of the code. The conduction within the solid bodies, as well as the outer surface free convections, are governed by Newton's Law of cooling and as a result are all linear in nature. However, the radiation exchange within the cavity is non-linear and for this the ABAQUS defaults were accepted. These are that the zero heat flux upon convergence relative to the time-averaged heat flux be less than 1.0×10^{-5} in relative error, similarly, the convergence criteria for the residual heat flux when there is zero flux is less

than $1.0x10^{-5}$ as well. The surface flux at the beam, as back calculated from the lamps, to arrive at a near 900degF beam is about 4,500W/m^2 at the surface of the beam.

2.4.6. FEA Model Details and Solution Methodology

The FEA model was constructed in Abaqus v6.8-2 and was a heat transfer focused model that was solved independent of any mechanical loading (de-coupled analysis). The ABAQUS 3-D continuum elements are used, in this case, linear single degree of freedom w.r.t. temperature, 8-noded bricks in structured grids for the prismatic solids (the beam, coatings, lamp reflectors, chamber walls) and semi-structured grids for the cylindrical lids, lamps envelopes, and magnets. A finer mesh density was placed in the beam and TBC regions, which are modeled as separate solids, to capture any temperature gradients should they occur. The "interaction" module of contact conduction was used between the coating and the TBC layers, as well as the lids and chamber walls to establish that these solids were tightly joined at the interface with no effective thermal contact resistance (e.g. temperature continuity was maintained across the gaps with no thermal contact resistance). The exchange of the heat between the various surfaces in the cavity, of which there was one in the full domain model and two in the ¼ domain model with the shield layer present, was established in the ABAQUS "interaction" module for thermal radiation exchange. As mentioned before the chamber walls had prescribed free convection on their exterior; radiation to the lab surroundings temperature was neglected due to the small expected thermal gradient. All the solutions run were steady-state where

convergence in the solution was sought indicting thermal equilibrium.

2.4.6.1. Parametric Studies

The FEA model was very useful for performing sensitivity studies for the configuration of the chamber to assess the impact of parameter variations on the heat transfer of the chamber-beam system. Some of the solutions ran were performed on the full model.

Figure 38 was a simulation using flat reflectors to assess the effect of using flat 3-segment reflectors upon the thermal distribution within the beam. These had the same opening aperture area that the default parabolic trough reflectors had. The higher temperatures were due to a higher power

being used to overcome the lack of thermal shielding. The significant finding was that the beams average temperature was very close (with 5degC) to that of the base case run with the parabolic ones; the near-isothermal state is preserved. There is only about 2.4degC of variation in temperature throughout the beam, indicating that the much simpler to fabricate flat reflectors would work.

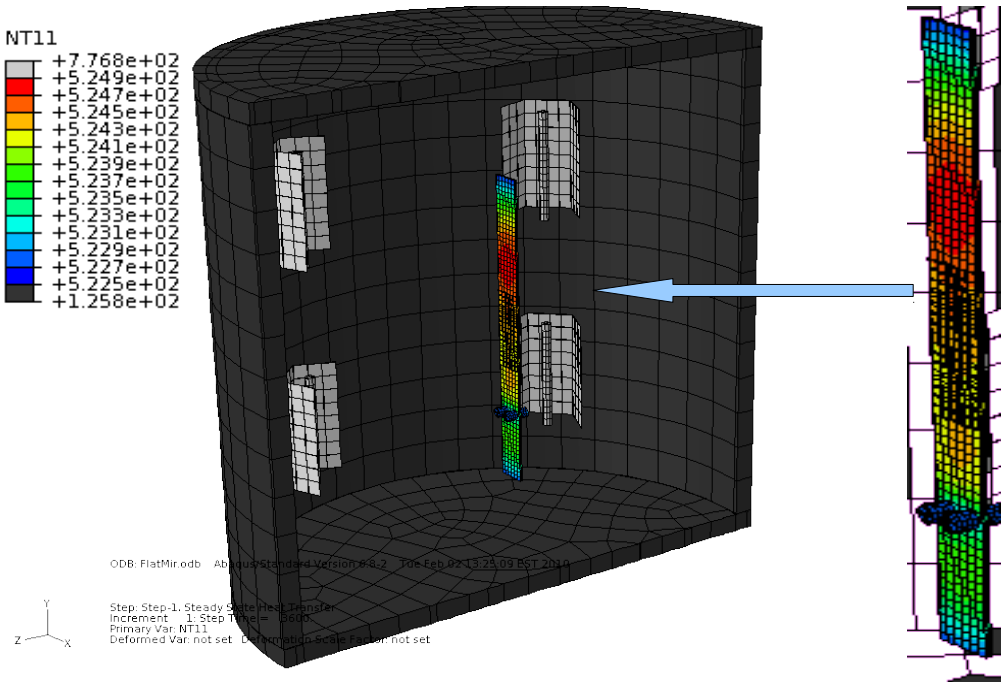


Figure 38: 3-Segment Flat Lamp Reflectors

Lamp failure was thought to be likely at the time the chamber was designed, due to the harsh environment the halogen lamps would be working in with no cooling, power settings that would be below where the halogen refresh cycle could occur, etc. Since it would be cumbersome to halt a test in the midst of conducting one, sensitivity studies were run with lamp failures. Figure 39 shows the result of the comparative studies, the default condition on the left side of the Figure is around 529degC (984degF) in bulk average beam temperature with a 3.0degC (5.4degF) maximum variation, loosing one light in the lower lamp set cools the tip of the beam in a localized fashion. Beam average temperature is still 510degC (950.0degF) and the spread is increased to 6.0degC (11degF), still quite acceptable. The case where one whole branch of four lamps fails, due to a short or overload as shown in the right diagram of Figure 39, shows the average temperature to be

around 432.5degC (810.5degF), quite a downward depression of temperature, but with the near-isothermality still preserved with only a 2.1degC (3.8degF) spread. This is due to the fact that the lamps were wired to maintain symmetry across each level, and be antisymmetric between the lower and upper set of four.

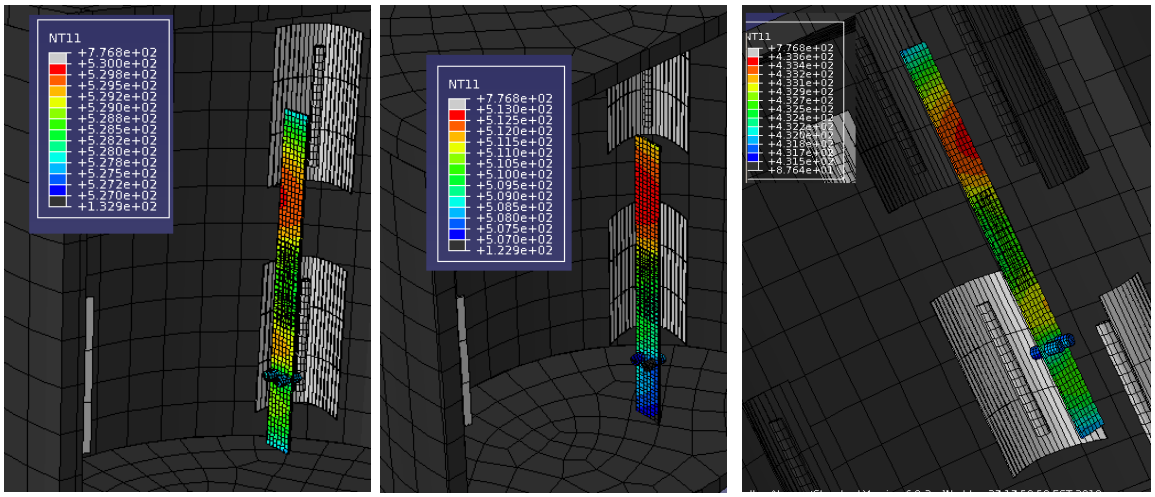


Figure 39: Lamps Out Scenarios; None Out (left), One Out (center) and Four Out (right)

Later studies, to be covered in Chapter 3, utilized the ¼ domain model with a bounded study to determine the beams isothermality and bulk temperature changes with the beam metallic regions in a state of polish and coated with a high emissivity power. This was used to determine if the IR imaging data of the beam was valid, even with the high emissivity powder added to it. Mesh refinement studies were carried out on the ¼ domain model with roughly one half of the node density per unit length, equivalent values in the bulk temperature were found, although finer temperature gradients in the beam and TBC layers were not apparent at this coarser mesh.

2.4.7. Comparison of Model Predictions

Comparison of the models is illuminating especially when shown with the

experimental results characterizing the chamber as it was physically constructed. These results are deferred to Chapter 3 (Section 3.4).

2.5. Isothermality of the Beam and Coating System

Fortunately, the chamber is predicted to feature a beam that will approximate an isothermal state based on all the analysis conducted. The high Stark number situation ensures a lumped capacitance environment. The maintenance of the vacuum is critical to maintaining the isothermal beam. Figure 37 shows a typical temperature distribution, with only about 0.5degC variation predicted through the beam-TBC-ALNICO magnet system.

2.5.1. Power Needed and Temperature Ranges Achieved

It was determined from the FEA model that flux from the lamps at around 1056 Watts (at 66% power setting x 200W per lamp x 8lamps), would produce enough power to heat the beam to close to 900degF. When actually calibrating the chamber for beam and dummy specimen temperature as a function of power, the value required was very close to that predicted by the FEA model.

2.5.2. Calculation of Flux At Beam From Lamps

A key question in the analysis for the analytical and finite difference models is how to determine the effective irradiative flux that strikes the beam from each of the eight lamp sources. While the FEA model is fully 3-D and employ this, the 2-D models need a means to approximate the incident flux.

The design is to incorporate the eight lamps using quartz halogen linear bulbs in an radial array with four stations positioned around the beam. Figure 40 depicts such lamp assemblies with parabolic trough reflectors. Mounted onto chemistry stand rods these will be aimed onto the free-free beam suspended centered between them. As can be seen from Figure 40, maintaining a polar array that is radially symmetric w.r.t. the beam and sufficiently far removed from the beam will help ensure a near-uniform irradiation intensity at the beam's location.

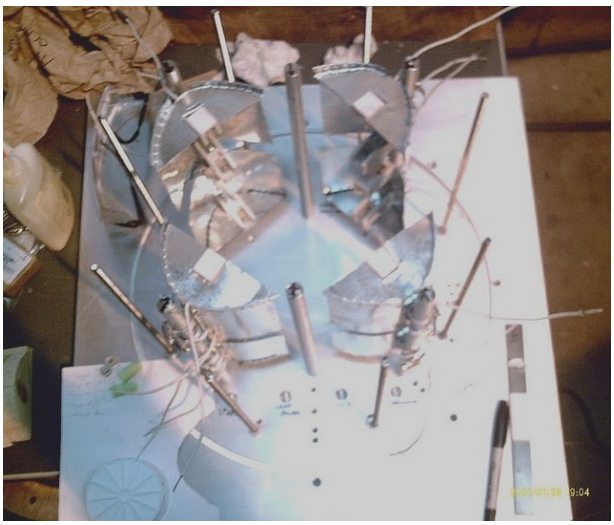


Figure 40: Quartz Halogen Lamp Assemblies

These bulbs filaments are close to ideal blackbody emitters of about 2800-3000degC in real life. Again though the bulbs are IR opaque and that is what the beam sees. The emission spectra closely follow the Planke's Law curves of an ideal black body, and the Stephan-Boltzmann Law can be used to estimate the emission intensity, E, in W/m^2 to a good degree of accuracy as per:

$$E = \epsilon \sigma T^4 \tag{34}$$

where the constant (σ) is 5.670×10^{-8} W/m^2·K^4, and the emissivity, ε, is the ratio of energy flux emission from the actual surface compare to that of a blackbody (perfect) emitter. This generates a curve of emission intensity as a function of frequency. This leads to a distribution of flux intensities across the emission frequencies. For the analysis in the current study the varying emission intensities across the spectra is reduced to an average intensity (ε_{ave}) across the spectra wavelengths (λ_1,λ_2) in the emission spread as per (Incropera, 1996):

$$\epsilon_{ave}(T) = \frac{\int_0^{\infty} \epsilon_{\lambda}(\lambda, T) E_{\lambda, b}(\lambda, T) d\lambda}{E_b(T)} \tag{35}$$

Where $\varepsilon_\lambda(\lambda,T)$ is the directionally and temperature dependent emissivity, $E_{\lambda,b}(\lambda,T)$ is the emissive power flux that is also directionally and temperature dependent, and $E_b(T)$ is the blackbody emission power flux.

This is a reasonable assumption to make as the beam specimen has a fairly weak variation of optical absorptivity as function of wavelength, at least for the oxidized titanium surfaces. An additional assumption is that the radiation transfer is non-specular, where the absorptivity, emissivity, and reflectivity as a function of incidence is neglected. Lastly, the implications of the Kirchhoff Law, where a surface's emissivity is the same as its absorptivity across all wavelengths and directions, is invoked as the surfaces are: within an enclosure (one that re-reflects at that), are assumed to be at thermal steady-state, and are close to diffuse in nature. This is the "gray surface" assumption (Incropera, et al., 1996).

These assumptions underlie the beam isothermality and temperature analyses, both analytical and numerical, as well as anticipated power calibration curve needed. Another assumption made is that the beam's flexing surface in space, when temporally averaged out across time, is that of the static (unstrained) state. This is deemed reasonable as the characteristic speed of the thermal radiation process is very much faster than the motion of the beam through space; it is essentially an instantaneous process. An analogous decoupling of problems would be solving for mechanical and thermal fields when the thermal field evolves very slowly in time relative to the displacement fields.

The lamp array will exploit radial symmetry to maintain a near-uniform radiation flux environment on the surface of the beam. The lamp arrays will need to be kept a minimum distance from the beam to ensure the illumination intensity profiles are nearly uniform when they arrive at the beam. To achieve a design temperature of 755.37K (or 482.2degC / 900degF), the illumination flux intensity of the lamps at the beam's location at the center of the array will need to be about 18,036 W/m^2, as can be estimated from a simple 1-D radiation flux in and re-emission out steady-state balance as per:

$$T_{surface} = \sqrt[4]{\frac{I}{\sigma} + T_{surr}^{\ 4}} \tag{36}$$

Where $T_{surface}$ is the absolute temperature of the beam, I is the intensity of the radiation striking the beam (in W/m^2), and σ is Stephan-Boltzmann constant (5.67×10^{-8} $W/m^{4,\cdot}K$). This assumes that the beam and lamps are in room-temperature (T_{surr} = 70degF/21.1degC/294K) surroundings and that the view-factor of the beam to the lamps is small compared to the view factor of the beam to the surroundings. This is about 13X

the solar constant (solar constant = 1350 W/m^2) that is striking the beam's surface and seems realistic. It is noted that assuming the blackbody surroundings of the beam are at room temperature of 21.1degC (or 70degF, 294.3K) is quite severe and results in an overestimate of power needed from the lamps. An incident during the initial heating trials of the chamber resulted in adjusting the T_{surr} drastically upward to 750degF (398.9degC/672K). This adjustment was based on a multi-point thermocouple test where one thermocouple detached from the beam due to a bonding failure and came to rest on the lower radiation shielding and recorded its temperature for the duration of the test. This was around 750degF when the beam was at 900degF (See Section 2.6). Using this as the surroundings temperature in Eq. (36) yields I = 6890 W/m^{2,}, a much more reasonable power level.

With consideration for the geometry and style of the lamps an idea of the power needed can now be obtained. Using Figure 26 as the top vantage point for the system, and neglecting end dispersion effects, for the long, cylindrical lamps the direct illumination flux density I_L (in W/m^2) at a distance, L (in m), from the lamps at a given power setting to the lamps, P (in Watts for each lamp array), yields for unshielded lamps:

$$I_L = n\frac{P}{2\pi L \cdot 1}\cos(\theta) \tag{37}$$

where n is the number of lamp arrays, and θ is the angle between the beam surface normal and the beam surface to point source vector (the 1 is a placeholder dimension, in m, to indicate unit length of the 2-D system). Eq. (37) discards any light rays that are not directly incident to the beam. For 6.0in long lamps (two 3.0in lamps positioned end-to-

end) in a 4 position array, around 1371 Watts of power would be needed to heat and maintain the beam at 900degF (482.2degC). This assumes a standoff distance, L, that is about 20cm, roughly the length of the beam itself. It is noted that L cannot be made too small (less than about 3/4 to 1/2 the beam length) as otherwise the uniformity of the flux breaks down from the circular intensity profile curvature of the emitted radiation from each source becoming more pronounced, and the additivity of these wavefronts from the different lamps becoming highly varied across the beam width. Adding more lamp positions in the radial array can allow for squeezing them in closer, but this would curtail easy access of the DVL laser to the beam, as well as that of any optical/infrared imaging cameras. The power needed without reflectors is quite high with resultant cooling issues, high power draw, and hot chamber surfaces.

By adding a trough reflector that is parabolic with an opening (w_l) about 4cm across and placing these so the focii are coincident with the lamp bulb filaments and aiming them towards the beam centerline, one can obtain the following relationship:

$$I_L = \frac{1}{2} n \frac{P}{2\pi L \cdot 1} \cos(\theta) + \frac{1}{2} n \frac{P}{w_l \cdot 1} \tag{38}$$

This assumes that the naked bulb half (that which emits light directly at the beam) of the irradiation profile is circular, while the reflected half from the parabolic mirror, is uniform (rectangular shaped intensity profile) in cross section, which is a fairly reasonable simplification for this geometry. Working with the incident radiant power striking the beam (I_L = 6890 W/m^2) the power needed for each of the eights lamp is 64.8 Watts. The actual calibrated power curve that was generated required about 130W per

lamp to hold the beam at 900degF (See Section 3.6). Equation (38) underestimates the actual power that was required due to dispersion of the radiation that occurs, as the illumination intensity profile from the reflector proceeds towards the beam it disperses out and weakens in intensity. One could refine Eq. (38) with a dispersion term using the equation of the Gaussian to model dispersion, and integrated to maintain conservation of energy across the aperture, but this refined model would increase complexity and more direct measurement may work better.

When the power of the lamps which is 1056W (= 8 lamps x 96% full power x 200W/lamp) is divided by the area of the glass bulb, which is 0.0190m^2, this yields a flux at the lamps of 55,574 W/m^2. The light leaving from the beam-facing half was assumed to undergo intensity reduction in direct proportion to the flux area (note: diffraction and dispersive effects were neglected), which is about 0.011m^2 for the each of the eight lamps out at a 3.5in radius, the average bulb-to-beam separation distance. This leads to a ratio of bulb glass surface to beam distance surface flux of about 9.3. Meanwhile, for the half of the radiation that was reflected for the backside of the lamps, all of which was assumed to be a parallel off of the reflectors, the flux area is the aperture area of the opening of the reflectors, about 0.0081m^2 per reflector. This yields a ratio of bulb glass surface to beam distance flux surface of 6.7, which averages to 8.06 for the bulb overall. Dividing the glass flux of 55,574W/m^2 by the the areal ratio yields 6893 W/m^2 which is pretty close to the value used in the corrected 2-D analyses where the surroundings were set to around 750degF.

It is to noted that power may be somewhat less than this as much of the chamber walls, top, as well as heat sensitive static components like the electromagnet coil will be under or wrapped in multiple layers of foil shielding. As a result, the enclosure will not be as severe a thermal sink as a room temperature blackbody enclosure as these surfaces' emissivity (and there absorptivity due to Kirchhoff's Law) is very low relative to a blackbody. From physical intuition, the thought experiment of placing two 100 Watt light bulbs in the chamber, realizing that they must sink to the room around the chamber, it can be anticipated that the chamber will get hot, perhaps uncomfortably so, but it will not be in danger of melting seals and parts breaking down from conductive heating. The thermal circuit analysis as well as the ¼ domain FEA model, both with the foil shielding in place predicted that the outer walls of the chamber remained at around 60degC maximum (140degF).

LeskerTech has whimsical, but content laden bulletin on the basics of heating within a vacuum environment (LeskerTech, 2008). Since the lamps will be needed to be ramped up and down in power to set the temperature level, some type of power supply setup was needed. Classical thermal load calculations estimate that the power needed to obtain 900-950degF on the beam specimen with the shielding in place would be about 140-160Watts of power per lamp (70-80% of full power).

2.6. Global Heat Transfer Analytical Revisited

Once a fairly accurate estimate of the inner chamber thermal environment was determined, a global analysis of heat transfer was performed using classical heat transfer

techniques to check the modeling. Figure 30 displays the original overall thermal circuit for the system. This analysis was a check for the reasonableness of the thermal models and get a global sense of the system behavior. Figure 41 shows the revised thermal circuit with the addition of the radiation shielding as added based on insight gained from refinement of the FEA model and confirmed by classic techniques.

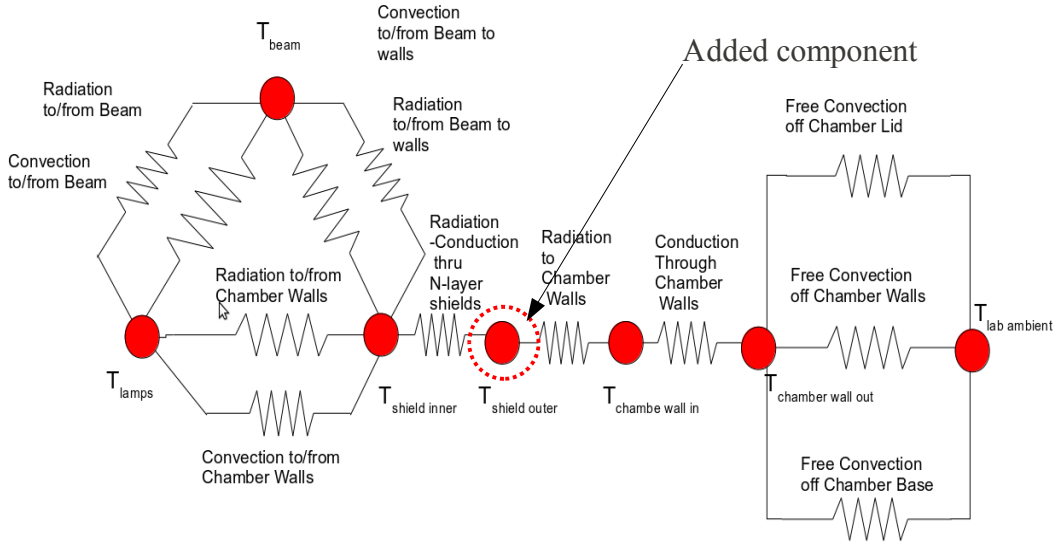


Figure 41: Thermal Circuit with Radiation Shielding Added to Circuit

The foil shielding, can be added to the thermal circuit of the chamber in the classical analysis as per the infinite parallel plate transfer rate equation for radiation:

$$q_{shields} = \frac{A_1 \sigma (T_1^4 - T_2^4)}{1/\epsilon_1 + 1/\epsilon_2 - 1} \tag{39}$$

where A_1 is the area of the emitting plate, sigma is the Stephan-Boltzmann constant, T_1 and T_2 are the temperatures of the two surfaces exchanging heat, and ε_1 and ε_2 are emissivities of the two surfaces (Incropera, 1996). Of course this will need to be recast

into resistance form and being 4th order w.r.t. temperature this will make the paper and pencil heat loss analysis iterative in nature (as $R_{shields} = f(T)$). It is noted that Eq. 39 applies whether the exchange radiation is specular or diffuse (Siegel, 2002). Adding more shielding layers (N layers) and assuming their all of the same material ($\varepsilon_1=\varepsilon_2=\varepsilon_S$) cuts the heat transfer rate (q) even further, so that:

$$q=\frac{\sigma\left(T_1^4-T_2^4\right)}{(N+1)(2/\epsilon_S-1)} \tag{40}$$

where N is the number of foil layers, ε_s is the emissivity of the layers (Incropera, 1996).

This was what was added into the classical analysis between T shield inner and T shield outer in the hand analysis and was added as a single solid in the ¼ domain model. Only a single layer was added in the FEA analysis to avoid exceeding the degree of freedom limit that four thermal cavities would require (one between the beam and lamps and the inner shield, one from the outer shield layer to the pressure case, and two between the triple layers). To achieve the same thermal resistance and keep the global heat flux correct, the inner emissivity of the shield was set to a realistic value for pure aluminum foil and the outer foil emissivity was set to a value that yielded the equivalent resistance to three real layers using Eq. (40).

2.7. Free-Free Suspension (Method of Suspension)

The free-free method has been adopted due to a practical realization that a large source of both absolute error and variation of that contribution in system damping occurs from clamping of a beam. Despite careful refinements in test protocol including precision

locating guide shafts, torque sequences and values, and careful attention paid to the root design of cantilever specimens, the clamp damping remains a disproportionately large contribution towards the system damping and remains highly sensitive to large variances with slight changes in procedural techniques. For this reason, the free-free system was adopted for the current study to harden to high temperatures. The free-free technique though still requires care and an understanding of the influence of the boundary conditions on the experiment if steady, repeatable results are to be extracted for the coating materials.

2.7.1. On Vacuum

The chamber will have vacuum for a two-fold reason: 1) minimize air damping especially at larger bending amplitudes, and 2) elimination of free convective cooling of the beam (which is critical to maintenance of isothermal condition). A low quality vacuum is sufficient to meet both needs, between 0.05-0.01 atmospheres of pressure will suffice. Figure 42 below, obtained by Reed, clearly show this for loss coefficient, which is twice the damping ratio. This level of vacuum can be maintained via a dual stage vane (roughing) vacuum pump. Reed determined that for the bare beam at various pressures the following relation holds:

$$\eta = \eta_0 + kV^2 \tag{41}$$

where η_0 is the loss factor at zero velocity, k is an experimentally determined constant, and V is the peak velocity per cycle of the beam (Reed, 2007). The value of k varies with the pressure surrounding the beam system. Reed emphasized that by keeping the pressure

below 0.05atm, the air damping was of negligible influence on the system.

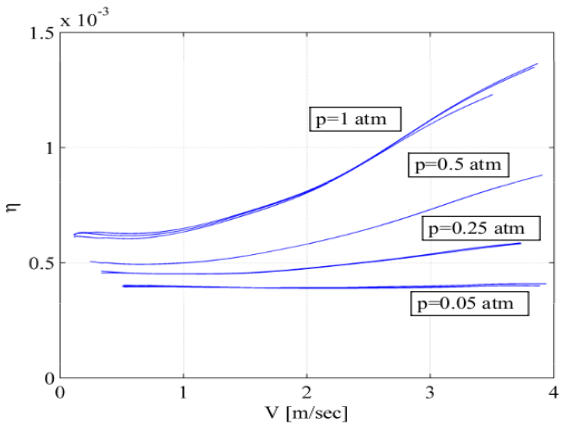


Figure 42: Air Damping Effects on the Bare Beam Loss Factor (Reed, 2007)

The second reason to have a low vacuum is to reduce to a negligible amount the contributions of free convection upon the beam for heating and cooling. A 600degF static hanging beam within ambient 70degF air will loose about 130 Watts of heat, so that amount of incident thermal radiation would be needed to maintain its temperature in equilibrium. In practice, it may resemble a forced convection situation as the vibrations of the beam would fan it through the air, although this would be mitigated somewhat by the air entrained in the chamber heating up along with sample. A strong free convection cell may well form inside the chamber (with an annular hot air updraft around the lamps, and descending cooling core along the beam). To remove this uncertain effect to the isothermal state of the beam and reduce the heater power required, a vacuum will be supplied. With the same beam suspended in a 0.03atm environment, the loss to free convection drops to 11Watts, and that is assuming relatively cold air/surroundings to the beam at 70degF (the low emissivity chamber walls and/or shielding actually get to be

quite hot, over 700degF and so the rarefied air in the chamber will as well). Since the free-convection is roughly linear in nature it is about 1/6th of this value, or 2.0Watts. The vacuum will reduce convective heat transfer to a negligible amount within the chamber thus setting up essentially a radiation-conduction series thermal circuit in as far a heat flowing from the lamps to the beam specimen.

2.7.2. Passive Node

There was some theoretical concerns surrounding the passive node. The nylon mono-filament was replaced with nichrome wire; this material was chosen for its creep resistance at higher temperatures. The old suspension technique of using plastic tubes to guide the line would not survive the maximum design temperature, so a couple of ideas were identified as possible solutions: welding small beads to the beam to drill guide holes through, drilling two small holes through the thickness of the beam to allow threading of the nichrome wire in one across the span to the other and passing it on, and to bore a very small hole through the width of the beam on the neutral axis. Concerns of heat affected zone softening of the beam from welding and eccentric loading conditions resulting from the cross drilled holes lead to selection of the bored hole.

This was not without issues though. Fine wire-plunge electrostatic discharge milling (EDM) was chosen for boring and it was able to bore a 0.008in diameter hole through the beam. Flaring of the holes out to 0.012in diameter was a problem but deemed acceptable. Far more critical was keeping the center of the hole to within 0.002in of the beam' centerline plane, which contains the neutral axis of bending. This was to keep the

stiffness of the beam to either side of the hole symmetrical and reduce eccentric loading. Material removed from the bending cross section near to the neutral axis has far less influence on the stiffness of the system than material further out (as per $I_{bend} = \int_A r^2 dA$ where r is the distance of the removed material from the neutral axis) as well (Higdon, 1967).

As a confirmatory check the 3-D FEA model of bare beam was run with EDM hole and the two cross holes for mounting magnets at active node and assessed for impact on the mode shape and frequency. There was very little discernible impact to the model by adding these features.

2.7.3. Suspending the Beam

Proper control of the boundary conditions is critical. Reed and Pearson had to deal with rigid body motion and control for it. Several things are to be achieved in a good suspended condition. The first to minimize the rigid body motion of the beam, or if not possible to suppress it, correct for it. Reed suspended his beam in a fashion where the statics of the system were easily known and solved for. He did obtain rigid body motion in his free decay data sets of around 3 and 7 Hz for the swinging and rotational modes, respectively, but eliminated these by employing cubic smoothing splines on the ring-down envelope dataset to eliminate the rigid body motion. For his forced response testing the Vibration View software used can filter the results. Also, when in a steady harmonic state under a slow chirp sweep, the rigid body modes decay away. Pearson was able to

eliminate rigid body motion to any detectable degree by shortening the nylon mono-filament spans and adding more tension to them. This could have potentially caused trouble by as can be seen by Eq. (42), which is the characteristic equation for transverse vibration in a string:

$$\omega_s = \frac{n\pi\sqrt{\frac{T_s}{\rho}}}{L} \tag{42}$$

where ω_s is the resonance radial frequency of the line, n is the mode of interest, T_s is the line tension, ρ is the density of the wire/line, and L is the free span length (Deleon, 2009). It is important to note that the beam's mass should be accounted within the density of the string as well, or a refined solution with a concentrated mass should be used. As seen below, the former technique was demonstrated valid on a replicated setup of Pearson.

Pearson's increasing of the tension, T_s, and shortening the span, L, may have increased the resonance frequency to where the natural frequency of the lines could potentially modally couple with the bending mode-I of the beam. This would result in excessive energy loss into the lines as they were excited by the beam. This is similar to the problem that the baseplate and handles of Allen's chamber had. Fortunately, Deleon modeled the system boundary conditions in his FEA model and reported a rigid body mode of only 22.5Hz frequency, higher than Reed, but still well separated from the frequency of bending mode I (Deleon, 2009). A static pluck test performed on Pearson's replicated setup as well as using Eq. (42) with the beam mass “smeared” into the density of the suspension line yielded similar values ranging from 20-23Hz, depending on the

mono-filament tension; this was a good indicator of lack of modal coupling.

Debate did occur as to what the effective mass of the string resonances were during a replication study of Pearson's setup. It was determined by testing the beam system for rigid body rotation and translation, that when suspended on the nylon mono-filaments, the mass of the beam should be distributed into the strings (as a corrected ρ in Eq. 42). The length, L, used, was the entire span of the string segments to each side and the width of the beam summed together. The calculated value of 20.2 Hz was confirmed by using a static pluck test to excite the various modes, where 22.5Hz was measured for the transverse mode across the direction of gravity. The main goal here is to minimize the amplitude of rigid body translation and rotation by keeping the spans short and tight (Deleon, 2009; Pearson, 2008). A secondary objective is to ensure that the modal coupling of the rigid body modes between the beam and the bending mode-I is weak by keeping the resonance frequencies well separated. This confirmed the validity of Pearson's corrections to the apparatus despite the rise of the frequency of the fundamental mode of the lines towards that of the rigid body mode in bending mode-I. This frequency rise was caused by his shortening and tensing of the suspension lines. The slight closing of the frequency gap between the bending mode-I resonance and that of the beam was more than offset by the stiffer support.

Meanwhile, the mono filament lines, as an unloaded span, have inherit resonances that must located be well away from that of the beam. Eq. (42) can be used for predictive design, this time the length of each individual span along with mass of the string in that

span is used. The upper string has the first three modes at 1469, 2937 and 4404 Hz, all well above the bending mode-I of the beam located at around 200-215 Hz. Low amplitude tests in air were performed with the Doppler velocity laser (DVL) aimed at a piece of 3M retro-reflective tape applied to the mid-span of one of the upper strings. This was while using a replicated setup of Pearson's; the DVL response was feed into a spectrum analyzer to confirm that coupling into the suspension strings was minimal. Relative to the displacement of the beam center being excited at its Mode-I bending resonance, the relative amplitude here was -32.2 dB (about 1/100th of the amplitude) confirming that the conditions in the experiment were close to a free-free. Rigid body motion displayed a peak at around 15 Hz. This was off from 22.5 Hz due to the limitations of the spectrum analyzer's digital to analogue conversion (DAC) resolution, and the frequency range of interest; the bins width was about 8Hz and was -70.0dB off of the magnitude at the center of the beam, indicating that rigid body translational motion across the vertical plane (the DVL was a single axis unit) induced into the string was very small relative to the beam's customary test point motion as the reference magnitude. The other peaks in the string were the various harmonics of the beam's bending fundamental frequency. This experimental work confirmed Pearson's qualitative improvements to the suspension of the system and Deleon's finding that the boundary condition tuning, in terms of stiffness, was fairly minimal on the system (Deleon, 2009).

The design of the current chamber attempted to follow that of Pearson, but achieving the same very limited rigid body motion was not possible for three reasons: 1) the supporting apparatus had to be keep from shadowing both the beam and temperature

dummy from the lamps, so the wire spans were necessarily longer, 2) the tension could not be as high due to less tensile and fatigue strength in the wire, and 3) the material used in the filaments, a 0.005in diameter nichrome wire, has less inherent damping than the 6lb test nylon mono-filament used in the past. The third point is not all negative though, it actually reduced the energy loss out of the beam. This is achieved by using a low damping wire material, which was the case in this study (admittedly the change of material was driven by temperature survival considerations and the low damping was discovered after the fact, see Section 5.3.1), and by ensuring that there was modal decoupling between the beam's bending mode of interest and any harmonics in the wires to avoid sympathetic stimulation of them.

The third issue concerns consistency in positioning the specimen between tests to ensure uniform magnetic coupling. This is addressed in Chapter 3. To correct for rigid body motion in the current study, due to the longer and less damping prone spans of the suspension wire, a software filter was used in the data acquisition code written to capture the free-decay datasets. The details of this are covered in Chapter 6.

2.8. Excitation (Method of Loading)

The non-contact loading of the beam was a great leap forward in eliminating a significant system damping source that was hard to control in a repeatable fashion; that of the clamp and the clamp interface. For this reason, the non-contact excitation method was retained. Hoover extensively covered the relevant design theory and equations in the setup used by Runyon, Reed, and Pearson. Additionally, he built a calibration curve of

force versus coil current, and moment versus coil current for magnets placed in a controlled location within the coil field (Hoover, 2004). There were some issues in adapting the setup to the current study, the need to suspend the beam higher to accommodate thermal shielding and adapt the sub-assemblies and components, chiefly the electromagnetic coil and permanent magnets, to withstand the higher amount of heat.

2.8.1. Electromagnetic Coil

The coil design did not require much adaptation for the new study, a new coil was fabricated in the same basic fashion. The major difference was the employment of coolant tubing with a much larger bore and more windings to enhance the heat removal rate. Runyon, Goerge, Cross, Drew, and Jones, seeking to minimize damping from clamping specimens, proposed the method of non-contact excitation (Runyon, et al., 2004) along with Bartlett (Bartlett, 1994). This did require study and Hoover quantified the method proposed by Runyon et al. After an extensive review of electromagnetic theory and coil design, Hoover experimentally characterized a coil and magnetic system used to excite thin beams similar to those of Pearson and Reed. Hoover used a pair of end mounted magnets on a beam to determine if various bending modes could be excited. He also performed some mapping of the coils field in a DC excitation by use of a gauss meter. Calibration of the coil-field-to-permanent-magnet coupling moment was also performed by Hoover using a clever setup of a coil, a stack of magnets, a lever system, and a precision balance. These methods were used in the current study to determine the true beam stimulation couple moment (or force pair) at the active node, this would be

useful if seeking to perform a transient FEA modeling of the beam using the Deleon FEA model, and is a more direct way to report the stimulation signal magnitude. (Hoover, 2004).

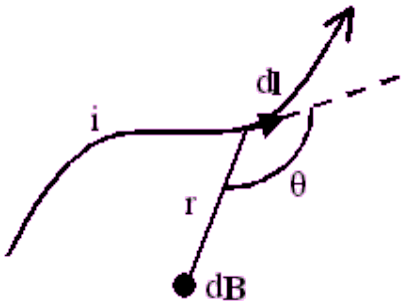


Figure 43: Biot-Savart Law (Hoover, 2004)

For design of the coil, analytical study of the coupling between the electromagnet and permanent magnet fields is complicated as it is a field theory problem that is governed by Maxwell's Equations. The need to solve the fully coupled equations (typically by FEA/FD methods) is not necessary as the lineal dimensions of the coil are much lower than the wavelength of the stimulating AC current, e.g. the AC frequency is very low (Telfeld, 1990). In the case of the coil under study, at 200Hz these are 8 orders of magnitude separated. As a result the four PDE equations collapse to one ODE that can be treated as a line integral down the conductive path, the Biot-Savart Law (See Figure 43), as a magneto-statics problem. Some analytical and series-approximated solutions for the Biot-Savart Law for coil and solenoid geometries exist, when the magnets are removed.

Hoover states that characterization of the coil is possible by analytical and numerical techniques. The main relation is the Biot-Savart Law which relates the

magnetic field at any given point in space for a nearby conductor with current flowing through it:

$$d\vec{B} = \frac{\mu_0 i}{4\pi} \frac{d\vec{l} \sin\theta}{r^2} \tag{43}$$

based in the following conventions and the geometry of Figure 43, where μ_0 is the magnetic permeability (of free space which is $4\pi \times 10^{-7}$ H·m^{-1}or N·A^{-2}) , i is the current flowing in the conductor (in Amps), $d\bar{l}$ is the differential length and orientation of conductor contributing to the field, r is the magnitude of the vector between the point and the conductor segment, θ is the angle between the differential segment and $\bar{r}$, and $d\bar{B}$ are the vectorial components of the magnetic field at the point from that conductor segment.

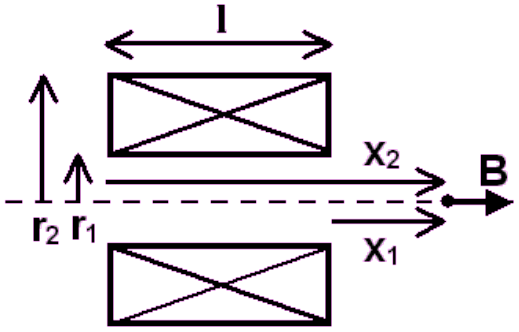


Figure 44: Finite Length Air Core Solenoid (Dennison, 2009)

Applied to an air-core, finite-length solenoid shown in Figure 44, the Biot-Savart Law when integrated for the on-axis field yields:

$$\vec{B} = \frac{\mu_0 i n}{2(r_2 - r_1)} \left[x_2 \ln \frac{\sqrt{r_2^2 + x_2^2} + r_2}{\sqrt{r_1^2 + x_2^2} + r_1} - x_1 \ln \frac{\sqrt{r_2^2 + x_1^2} + r_2}{\sqrt{r_1^2 + x_1^2} + r_1} \right] \tag{44}$$

where $\bar{B}$ is the magnetic field, in Teslas (or N·sec/C·m), at any point on the axis of the solenoid. The direction of the field is parallel to the solenoid axis, n is the number of turns of wire per unit length in the solenoid, I is the electrical current in the solenoid, r_1 is

the inside radius of the solenoid, r_2 is the outside radius of the solenoid, and x_1 and x_2 are the distances, on axis, from the ends of the solenoid to the magnetic field measurement point (Dennison, 2009). Applied to an air-core, finite-length solenoid, the Biot-Savart Law when integrated and approximated through Legendre polynomials, yields for off-axis magnetic field flux values:

$$B_x = B_0\left(1+\epsilon_2\left(\frac{r}{r_1}\right)^2\rho_2(u)+\epsilon_4\left(\frac{d}{r_1}\right)^4\rho_4(u)+\ldots\right) \tag{45}$$

where B_0 is the central field strength of the solenoid and

$$\epsilon_2 = \frac{1}{2\beta^2 c_5}\left(c_1^{3/2}-c_3^{3/2}\right) \tag{46}$$

$$\epsilon_4 = \frac{1}{12\beta^4 c_5}\left(c_1^{3/2}\left(1+\frac{3}{2}c_2+\frac{15}{2}c_2^2\right)-c_3^{3/2}\left(1+\frac{3}{2}c_4+\frac{15}{2}c_4^2\right)\right) \tag{47}$$

$$\epsilon_6 = \frac{1}{30\beta^4 c_5}\left(c_1^{3/2}\left(1+\frac{3}{2}c_2+\frac{15}{2}c_2^2\right)-c_3^{3/2}\left(1+\frac{3}{2}c_4+\frac{15}{2}c_4^2\right)\right) \tag{48}$$

$$\epsilon_8 = \frac{c_1^{3/2}}{56\beta^8 c_5}\left(1+\frac{3}{2}c_2+\frac{15}{8}c_2^2+\frac{35}{16}c_2^3+\frac{315}{16}c_2^4-\frac{2079}{16}c_2^5+\frac{3003}{16}c_2^6\right)-\frac{c_3^{3/2}}{56\beta^8 c_5}\left(1+\frac{3}{2}c_2+\frac{15}{8}c_2^2+\frac{35}{16}c_2^3+\frac{315}{16}c_2^4-\frac{2079}{16}c_2^5+\frac{3003}{16}c_2^6\right) \tag{49}$$

Where (Dennison, 2005):

$$c_1=\frac{1}{1+\beta^2}\ ;\ c_2=\frac{\beta^2}{1+\beta^2}\ ;\ c_3=\frac{\alpha^2}{\alpha^2+\beta^2}\ ;\ c_4=\frac{\beta^2}{\alpha^2+\beta^2}\ ;\ c_5=\ln\left(\frac{\alpha+(\alpha^2+\beta^2)^{1/2}}{1+(1+\beta^2)^{1/2}}\right) \tag{50}$$

and

$$\alpha=\frac{r_2}{r_1}\ ;\ \beta=\frac{l}{2r_1} \tag{51}$$

r_1, r_2, and l are inner, and outer coil radii, and coil length, respectively. d is the distance from the coil center to the field measurement point, q is the angle between the

measurement point position vector and the coil axis, and the corresponding Legendre polynomials, r_n, are:

$$\begin{gathered}\rho_2(u)=\frac{1}{2}(3u^2-1)\\ \rho_4(u)=\frac{1}{8}(35u^4-30u^2+3)\\ \rho_6(u)=\frac{1}{16}(231u^6-315u^4+105u^2-5)\\ \rho_8(u)=\frac{1}{128}(6435u^8-12012u^6+6930u^4-1260u^2+35)\\ u=\cos\theta\end{gathered} \tag{52}$$

for the radial components of the magnetic field flux:

$$B_R=B_0\left(0+\epsilon_2\left(\frac{d}{r_1}\right)^2\rho_2'(u)+\epsilon_4\left(\frac{d}{r_1}\right)^4\rho_4'(u)+\ldots\right) \tag{53}$$

where r^{l}_{n} are derivatives of the even Legendre polynomials, such as:

$$\rho_2'(u)=\frac{1}{2}(6u)u' \quad ; \quad u'=\sin\theta \tag{54}$$

The geometry of this system is as per Figure 45 (Dennison, 2005).

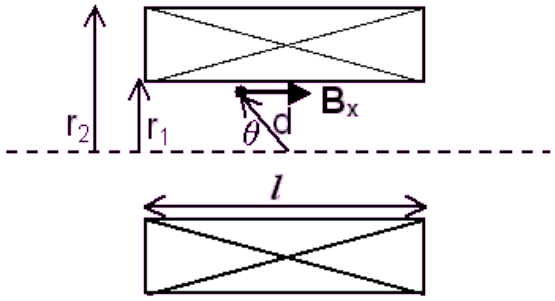


Figure 45: Off-axis Field Strength of Finite Air-core Solenoid (Dennison, 2009)

A quick Matlab script based on these solutions just presented was coded to assess the field strength and uniformity at various locations around the coil. It is noted that the

field strength as demonstrated by the density of the flux lines is changing and not constant across the bulk volume of the permanent magnets on the beam, especially above the end-plane of the coil where the flux lines diverge out from the centerline axis. This lends importance of controlled, consistent beam positioning in the chamber w.r.t. the coil. It was also noted that while the coil was being fabricated that much departure from ideal geometry occurred, this was due to winding around and filling the gaps between the two interlocking copper cooling coils.

The problem could also be tackled numerically, by FEA methods using the Maxwell's equations to determine the B- and E-fields or modeling the magneto-static problem using Biot-Savart Law. Finite Element Method Magnetics is a good example of a 2-D Maxwell Equation modeling FEA code with good reference and documentation that could model the coil field effectively (Meeker, 2009). In a magneto-statics situation, the four Maxwell equations, reduce to two. Gauss's Law and Ampere's Law further reduce to the Biot-Savart Law. A less involved approach is to invoke the assumption that current is constant DC at any given point in time (the most logical choice being the root-mean-square or peak-to-peak value of the AC current) and coding a magneto-static integration solution. Now integration of the individual wire segments with their individual current contributions for any given point in space can be performed. It is noted that such effects as self-induction, electrical field changes, and electrostatic charge effects are ignored in this solution. Again, a magneto-static approach is reasonable when any characteristic length of the coil is far smaller that the AC electrical wavelength, this is indeed the case with the TEFF coil (Telford, 1990).

The method chosen to quantify our design was to experimentally calibrate the permanent magnet set and electromagnetic coil setup using a method similar that presented by Hoover. This was performed for four different sets of magnets using the geometry of the current setup. Coupled with a good, consistent placement of the beam specimen, the coupling moment as a function of coil current was determined. (Section 3.7 details on the calibration and results).

One important detail to note on the electromagnetic coil is that it can act as a low pass filter to the excitation stimulus. It can be characterized electrically as a transient series inductance-resistance ("LR") circuit. The reluctance of the coil to current, which is directly coupled to the magnetic field strength, varies with the excitation frequency from the amplifier source powering the coil. Approximating the coil as an LR, circuit excited by a sinusoidal current or voltage source (depending on what mode the MB Dynamics amplifier, introduced in Chapter 3, is set to), it is a low pass filter as per:

$$I(t)_{out} = \frac{V(t)_{in}}{2\pi L j f + R} \tag{55}$$

where I(t) is the current in the series circuit, L is the coil inductance in Henry's, R is the DC resistance of the coil in Ohms, and f is the excitation voltage frequency in Hz (Nilsson, 2007). For a multilayer air core coil, which is a close approximation to that of the study, one can use the empirically derived approximation from Wheeler (Wheeler, 1928):

$$L = \frac{0.8\mathrm{r}^2 N^2}{6\mathrm{r} + 9\mathrm{l} + 10\mathrm{d}} \tag{56}$$

where L is the inductance in μHenrys, r is the mean radius of the coil in inches, l is the physical length of the coil winding in inches, N is the number of turns, and d is the depth of the coil in inches. Depth, d, is defined as the outer radius minus the inner radius. For the designed coil this yields an inductance of around 0.0002 to 0.0006 Henry's (depending on the final wind count, effects of coolant tubing, etc.), enough that when driving the coil at around 200 Hz, the current drops by 20% if the driving voltage remains constant, due to the self-inductance. Another formula gives inductance for a finite coil as:

$$L = \frac{\mu_0 K N^2 A}{l} \tag{57}$$

where L is the inductance in Henry's (H), μ_0 is the permeability of free space = $4\pi x10^{-7}$ H/m, is the K is the Nagaoka coefficient, N is the number of turns, A is the area of cross-section of the coil in square meters (m^2), and l is the length of coil in meters (m) (Nagaoka, 1909).

It is immediately clear from Eq. (55) that the specified current output is the desired excitation mode to avoid attenuation effects; this was not made clear in the past work. When reporting the excitation strength by means of coil voltage, it is important to either report in terms of coil current (and set the driving amplifier in a constant current mode to overcome the varying impedance), or correct the coil voltage to an effective voltage value by de-rating it as a function of coil current at that given frequency over the zero Hz current. Figure 46 depicts the roll-off of current as the excitation source frequency is increased, whether the TEFF coil is at the higher- or lower-bound of the

inductance, one can see that this is around the log of 2.3-2.4 (~230 Hz)), close to where the past beams resonated and the range of frequencies where swept for FRFs. For the current study, whether a new coil is constructed or not, it is probably wise to calibrate this curve in order to know the true current, and therefore couple moment on the magnet stacks, through the coil at any given prescribed voltage and frequency. Fortunately a couple of things in the current study avoid this problem: 1) the power amplifier feeding the coil, the MB-Dynamics, has a current feedback mode which sources out enough current in proportion to the input command signal voltage thus compensating for the change in reluctance of the coil as the stimulation frequency is changed, 2) for free-decay capture one crisp frequency is imposed and the change in forcing function amplitude is non-existent, and 3) for any forced response sweeps the range of the sweeps around the bending mode-I resonance point is small, typically under 5Hz span, and so the variation of the effective stimulation amplitude as shown in Figure 46 is very small.

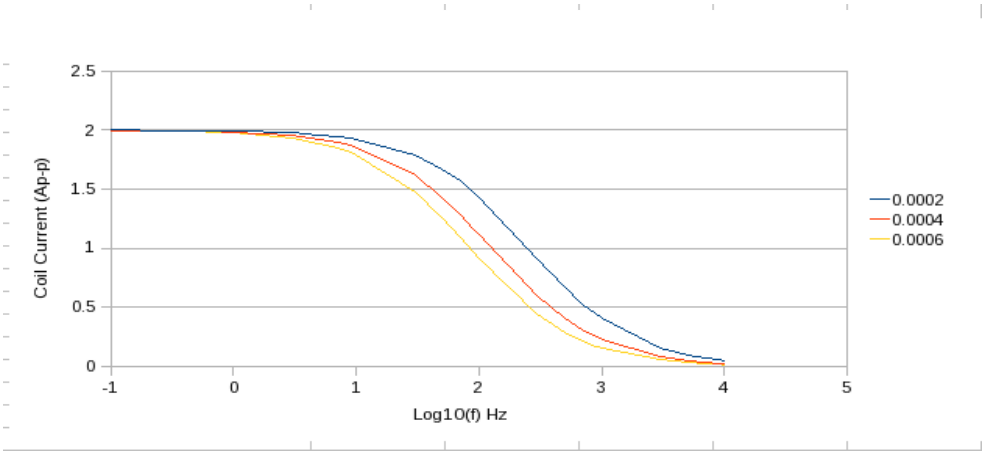


Figure 46: Transfer Function of Coil Current as a Function of Log(Freq.)

This can be accomplished by using a shunt resistance in series to the coil with an

oscilloscope channel to capture current and another shunt and channel in parallel with it to capture excitation voltage. Electrical phase lag can also be captured this way; though the mechanical beam system will lock to this, it is important to be aware that the whole systems phase lag from AC supply as input to DVL velocity as output will have phase lag, but the majority share will be from the electromagnetic coil. In short, it is important to report the coil strength in terms of current or corrected voltage to ensure the excitation amplitude has the same peak-to-peak strength at different frequencies.

As the construction of the TEFF coil is not documented (Reed, 2007; Pearson, 2008; Hoover, 2004), a bounded estimate was made of its construction based on several observations, among these: measurements of the physical size, wire, and insulation of the coil, weight, resistance measurements, and estimates of the wire packing efficiencies. Based on the measurement uncertainties and being comprised of 12 gage AWG wire, it most likely contains between around 600 turns, close to Reed's reported value of 650 turns. This yields an inductance between 0.0002 to 0.0006 Henry's, with 0.0004 Henry's as the center estimate. The cutoff frequency is around 9.8 Hz; this is well below the excitation frequency of Mode-I around 300Hz. Knowing the topology of the magnetic field will help establish the importance of precise beam positioning with respect to the coil, Pearson procedurally fixed the volumetric centroid of the 8 magnets 1.0in above the end-plane of the coil and on the centerline axis of the coil (Pearson, 2008). In the current study this was replicated, but the coil wind dairy was in doubt due to many partial winds that were performed to fill in gaps caused by the coolant tubing as well as cross between the wind voids. Pearson's careful attention to positioning was made a feature of the

chamber design to reduce uncertainties in the location of the beam's permanent magnets in relation to the electromagnetic coil.

2.8.2. Permanent Magnets at the Active Node

The beam carries a set of permanent magnets to generate the alternating couple moment to excite the beam. Given a uniform, externally imposed magnetic field of strength B, the interaction with a permanent magnet in the field produces:

$$\vec{\tau} = \vec{\mu} \times \vec{B} \tag{58}$$

where $\vec{\tau}$ is the torque, measured in Newton-meters, $\vec{\mu}$ is the magnetic moment, measured in ampere meters-squared, and $\overline{\mathbf{B}}$ is the magnetic field, measured in Tesla, or equivalently, in Newtons per Ampere-meter (Hoover, 2004). The magnetic moment is inherent to the nature of the material comprising the permanent magnets, the volume of the material, and the state of alignments of the domains (the "magnetic charge"). If the material volume of the magnets is the same, it is the value of the magnetic moment that varies up and down as a function of the volume of the ferromagnetic material.

The dipole moment to field coupling equation is:

$$\vec{\tau} = \vec{m} \, x \, \vec{B} \tag{59}$$

where τ is the torque vector (typically in N·m), $\overline{m}$ is the dipole moment equivalent of the magnet (typically in Amp/m^2), and $\overline{B}$ is the uniform magnetic field imposed setup by the electromagnet around the magnet (in Tesla's). The vector, $\overline{m}$, is normally defined for a loop of wire carrying current within the B-field, where the vector of the area of loop, denoted as $\overline{A}$, is referenced to the loop surface normal. A permanent magnet, like the those used Pearson and Reed, can be defined in equivalence to the current loop as per:

$$\vec{m} = I \cdot \vec{A} = \frac{\vec{B}_i \cdot V}{\mu_0} \tag{60}$$

I is the loop current (Amps), $\overline{A}$ in the vector with magnitude based on size (m^2) and direction based on the surface normal of the loop, $\overline{B}_i$ is the intrinsic induction of magnet (Tesla's); measured at one of the poles (either end), V is the volume of magnetic material (m^3), and μ_0 is the permeability of free space (1.256×10^{-6} $m \cdot kg/s^2 \cdot Amp^2$) (Hoover, 2004). $\overline{A}$ and therefore $\overline{m}$, is determined by the class of magnetic material and the volume.

Table 4, a summery of all the classes of permanent magnetic material, explains why neodymium iron boron rare earth (NdFeB) magnets were selected for use in the free-free setups of Hoover, Reed, Pearson, and Runyon. They have the highest flux density and energy product to react with the external field generated by the electromagnetic coil. Unfortunately, this class of magnets also has the lowest working and Curie temperatures where the initial degradation and total loss of the magnetic charge occur, respectively. Per unit volume (and mass when density is accounted for) the NdFeB magnets have the ability to produce the strongest mechanical moment within a given magnetic field imposed by the coil. Further inspection of the Table reveals the NdFeB magnets suffer from limited high temperature capability and are unable to function in the design temperatures n 510degC (950degF) as was planned for the free-free rig design. The total loss of field for NdFeB occurs at the Curie temperature (at 310degC/590degF) and degradation in the working load starts near 150degC (302degF), which is well short of the design goal.

Due to high temperatures planned for the free-free setup and a situation with no

easy way to cool the permanent magnets mounted to the beam, the neodymium iron boron magnets (NdFeB) were replaced with aluminum nickel cobalt alloy (ALINCO) ones. This does raise some complications. The ALNICO magnets have a much weaker dipole moment coupling per a given volume of magnetic material in comparison to NdFeB. The change from NdFeB to ALNICO magnets results in a loss of the force couple strength driving the specimen as a reduction in magnetic moment occurs. This loss can be compensated for in two ways: 1) increase the amount of magnet material mounted to the beam, or 2) increase the field coil strength by increasing the number of winds and/or coil current capacity. If the field coil strength is kept unchanged from the previous studies, than the magnet mass will have to up to 10X the baseline amount to achieve the same driving couple moment amplitude. It is noted a combination of the two methods can also be used.

Table 3: Permanent Magnetic Materials (adapted from Stanford Magnetics Catalog)

Material	**Magnetic Flux Density (Residual Induction)**		**Magnetic Field Intensity (Intrinsic Coercive Force)**		**Magnetic Maximum Energy Product**	**Temp. de-rating**	**Working Temp**	**Curie Temp**
	B_r	B_r	H_c	H_c	BH_{max}	T_{coef} of B_r	T_{max}	T_{curie}
	Gauss	Tesla	Oersted	kA/m		%/deg C	deg C	deg C
NdFeB – Neodymium Iron Boron	12800	1.28	12300	980	40	-0.12	150	310
SmCo – Samarium Cobalt	10500	1.05	9200	733	26	-0.04	300	750
Alnico – Aluminum Nickel Alloy	12500	1.25	640	51	5.5	-0.02	540	860
Ceramic or Ferrite – Iron Ferrite	3900	0.39	3200	255	3.5	-0.2	300	460

The first method is limited by its impact on the dynamics of the beam system; adding mass and rotational inertia at the active node may begin the excessively impact the

dynamics of the tuned resonant system. So a simple dynamic sensitivity study was performed using the ABAQUS FEA code. Since the thermal environment has selected the class of material, in compensating for reduced dipole moment strength of the ALNICO magnets more magnet mass will be added to the active node to yield the same level of coupling input into the beam system. The impact of this is considered in the next section.

2.8.3. Magnet Sensitivity

A simple 42-element FEA model was made of the bare Ti-6Al-4V beam using the same dimensions as those used by Pearson and Reed. The elements were 2-noded, 1-D Euler-Bernoulli bending beam elements, a "B31" in the ABAQUS element catalog (ABAQUS Analysis User's Manual, version 6.8). An modal eigenmode analysis was performed on this model and since this model recovered natural frequencies to within 2% of those measured from the experiment for bending mode-I, as well as that of the classical analytical solution, no element selection or mesh refinement study was performed. Also, the eigenvector shape of each model in bending was recovered.

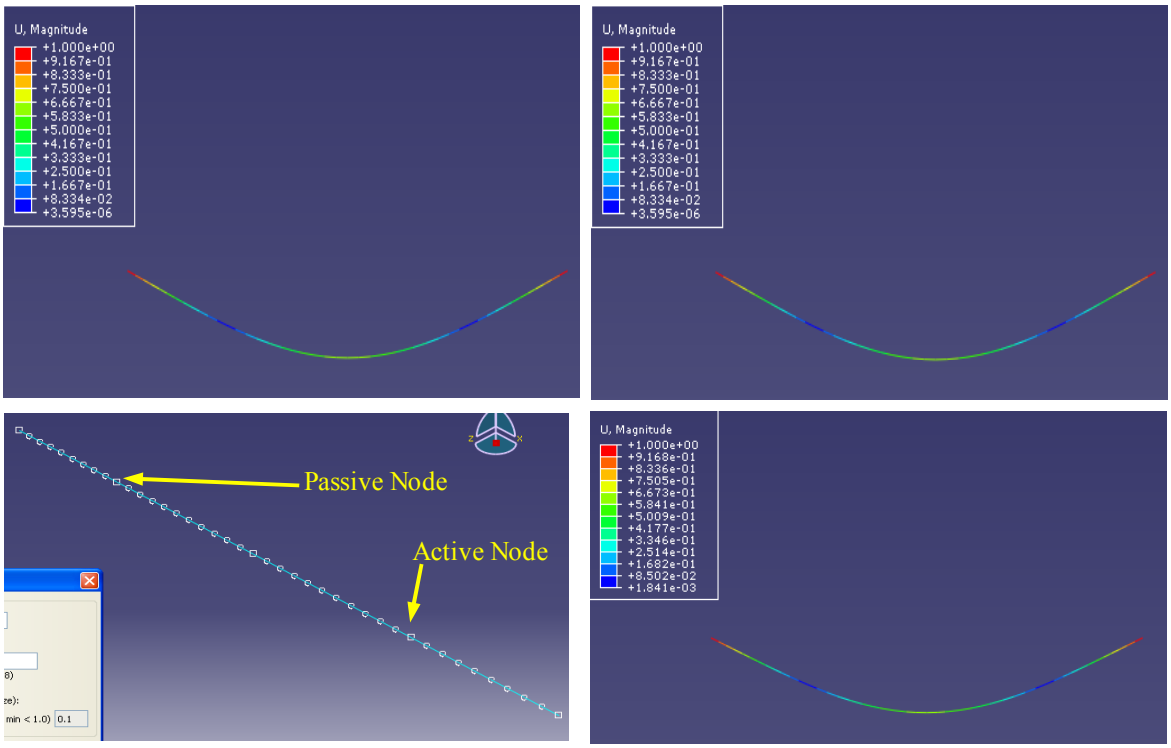


Figure 47: Mode I Sensitivity to Magnet Mass 0X (upper left), 1X (upper right), and 10X (lower right) Mass; 1-D

The model has the active and passive nodes located at 0.224L and 0.776L down the beam, as per Figure 48 on the lower left and indicated by a square node. The active node is where either 0X, 1X, or 10X of both the mass and rotary inertia of the set of eight disk magnets (NdFeB) were added to the beam system as a point mass and point rotary inertia. The lower left of Figure 47 also displays the mesh of 42 linear beam (ABAQUS refers to these as "B31") elements. The bending mode-I results are shown in Figure 47 a with the respective eigenvalues of ω_r = 202.75Hz for no magnets in the upper left, ω_r = 202.48Hz for a set of NdFeB magnets in the upper right, and ω_r = 200.08 Hz for a set of ALNICO magnets of equivalent strength (10X mass) in the lower left. The impact on the bending mode-I shape is quite minimal. As can be seen from Table 4, which summarizes

the results, fit is noted that for bending mode-II, the impact of the magnet mass upon the frequency is quite large as the mass is no longer located at a nodal point. This is anticipated as the magnets now sit at a portion of the beam that undergoes near maximal displacement in this mode. The impacts are on the mode-I bending are relatively small as the mass is increased from a pure bare beam to 10X that of the mass (and rotary inertia is scaled up) used in the past experiments.

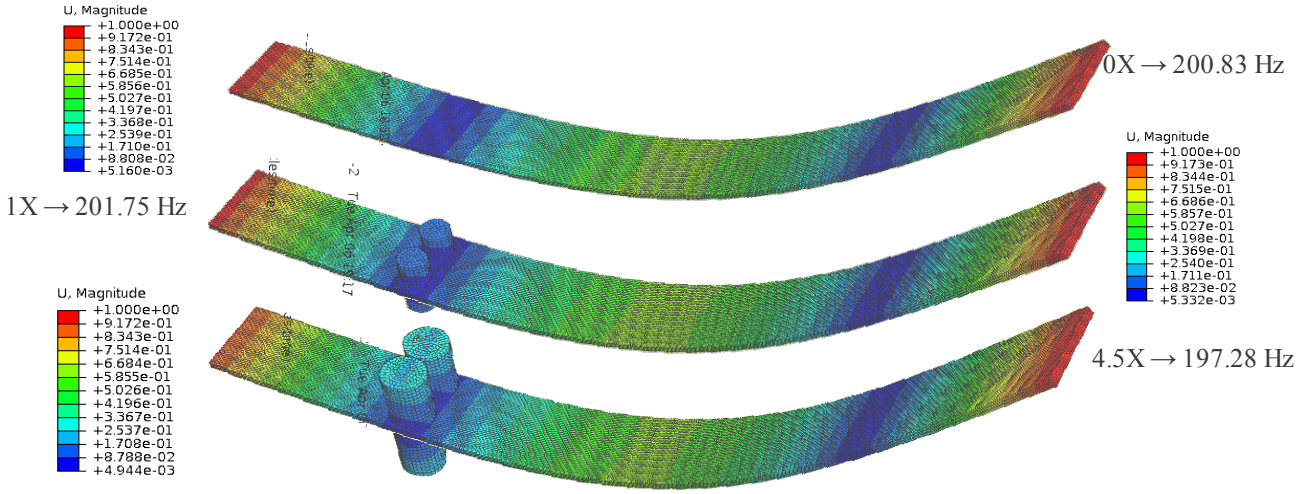


Figure 48: Mode I Sensitivity to Magnet Mass 0X (top), 1X (middle), and 4.5X Mass (bottom); 3-D

As can be seen from Figure 48 the sensitivity runs were later performed with the 3-D model developed for the building of the polynomials. The magnets in the 3-D model could only be scaled up to about 4.5X the baseline mass without volumetric clearance issues as can been seen from the lower beam of Figure 48. Whereas the 1-D model reduces monotonically in frequency with the addition of mass to the mass matrix, the 3-D model accounts for the localized stiffening (the K matrix effect) upon the beam system that occurs with the (localized) addition to the cross-sectional area from the magnets.

This initially increases the resonant frequency, and then depresses it. The added mass scales by the lineal dimension cubed while the competing effect of the localized stiffening effect down the length of the beam scales directly with the lineal dimension. The apparent system stiffness dominates initially (thus an increase in resonance frequency) it then drops off as the mass influence asserts itself. From Table 4, in the current study one could add almost 5X more mass (and attendant rotary inertia) and only shift the resonance frequency of the system a little over 2% as seen in the worst case. This may be a way to recover some lost coupling moment in future efforts with ALNICO magnets that are sized wider and/or longer. Table 5 details the parameters of the beam system used in the model.

Table 4: Natural Frequencies of Bare Ti-6Al-4V Beam as a function of Magnet Mass

Natural Frequencies as a function of Magnet Mass - 1-D FEA model						
	1-D no magnets (0X Mass)	1-D 8 NdFeB rare earth magnets (1X) mass	1-D 8 ALNICO rare earth magnets (10X mass)	3-D no magnets (0X Mass)	3-D no magnets (1X Mass)	3-D no magnets (4.5X Mass)
Mode-I Bending	202.75 Hz	202.48 Hz	200.08 Hz	200.83 Hz	201.75 Hz	197.28 Hz
% of no magnet	-	-0.13%	-1.31%	-	+0.45%	-1.76%
Mode-II Bending	558.05 Hz	521.28 Hz	451.64 Hz			
% of no magnet	-	-6.58%	-19.06%			

From these modeling efforts it was concluded, while the apparatus was being designed, that both the 1-D and 3-D models were disturbed from a truly bare free-free beam ideal condition by less than 0.50% with the same mass of magnets as in the past studies.

Furthermore, for a 4.5X mass, only a 1.5-2.0% variation was predicted by the FEA model. So this addition of mass in varying amounts was not thought to be a problem and therefore neglect-able. In practice, the chamber was found to be very precise (and accurate) for determining resonance peak frequencies, to within 0.0100 to 0.0010 of a Hertz on the bare (and coated) beam. Since this precise determination of resonance frequency for a given specimen was repeatable across multiple trials, it is recommended that for future studies the additional fidelity of 3-D FEA analysis be employed, although 2-D models were used in the current study (this level of precision not known until after the bulk of testing was completed).

Table 5: Magnet Mass Sensitivity Parameters

Parameter	
Beam Length	0.2032m (8.00 in)
Width	0.0191m (0.75 in)
Thickness	0.0016m (0.0625in)
Material	Ti-6Al-4V and ALNICO
Beam Mass	0.0274 kg
1X Magnets Thickness	0.0032m (0.125in)
1X Magnets Diameter	0.0064m (0.250in)
Mass of eight magnets	0.0048 kg

2.8.4. Magnet Fastening

Additional issues affecting the magnet stack is the thermal stresses caused by differential thermal expansion between the magnets and beam which could trigger failure

of the adhesive bonding, or loosening of the magnets, specifically of the glue or mechanical fastening of the magnets to the beam, respectively. This issue was handled by experimental trial and error in the lab.

2.8.5. Calibration Techniques of Method of Loading

The previous body of work was useful for design but there were too many departures from the geometric idealism; e.g. coil windings around tubing coils, precision co-linearity of beam to coil, filtering effects, etc., so rather than attempt indirect estimation of the couple moment by means of simulation and/or analysis of the the electromagnetic interaction between the electromagnet coil and the ALNICO magnets on the beam, it was felt more directly useful to control the position of the beam to fairly tight tolerances w.r.t the electromagnetic coil location, and then using that geometry to directly calibrate the beam using methods adapted from Hoover (Hoover, 2004). This is a static DC relationship between the coil and the effective magnetic moment achieved on the beam. The details of this procedure are in Section 3.7.

2.9. Thermal Stresses in the Beam-TBC System

The beam-TBC system is subjected to a wide range of temperatures in the current study and is a tightly conjoined system of two different materials and this inhomogeneous system may see significant thermal stresses as a result. The questions that come to mind include: 1) Will these thermal stresses result in total strains, that when combined with mechanical loading, exceed the creep- or plastic limits of either material?, 2) Will the thermal stresses trigger coating disbondment?, and 3) Will these stresses have a major

impact on the global mode-shape? To gain insight some thermal stress analysis were run. It is noted that these are upper bound, worst-case studies where the TBC layers are modeled as homogeneous in nature, whereas in the samples it is known there is an extensive network of cracks and voids that help alleviate thermal stresses (Pearson, 2008; Tassini, 2006). The micro-structure of even a freshly applied cermat TBC layer exhibits the "splat" structure with dense network of cracks and voids formed from the initial molten droplets. The main objectives for the thermal stress analysis are to:

· Ensure that the thermal stresses, coupled with those of the mechanical bending loading, do not result in total stress field that exceeds the yield limit of the titanium beam.

· Verify that the coating will not adhesively fail and dis-bond from the beam, especially in the edge stress regions. For this situation, the stresses orthogonal to the bond interface plane, dubbed "peel" stresses, are examined.

· Ensure that the thermal stress field will not significantly impact the global bending mode-I shape.

Existence of the cracks and splats that form upon fabrication to relieve the initial stresses as well as the existence of low cycle fatigue (LCF) thermally induced spallation of TBC, tends to suggest that differential thermal expansion is important in the coating-substrate interaction. Better resistance to the thermally induced dis-bonding of the coating, often known as spallation, is provided by the bond coat layer due to the asperities in it that allows the TBC to infiltrate into and mechanically hold to. Spallation, driven by the thermal expansion mismatch, is a major reason that industry has adopted

EB-PVD over APS in general practice despite the higher thermal conductivity of APS applied TBC coatings across the barrier layer (Tamarin, 2002). Mechanical fatigue can trigger disbondment as well, particularly when there is no bond coat layer (Ivancic, 2003). The coatings damage evolution as it it successively loaded, forming additional cracks with additional thermal and mechanical load cycles accumulating, may be a possible explanation to the history effect Reed and Pearson observed and controlled for, respectively.

There are several key assumptions made in the thermal stress study. It was already noted that the first is that the coating is a solid, homogeneous, and isotropic layer of elastic material. This will be a conservative assumption that will over-predict thermal stresses in both the actual beam and TBC layer. The actual thermal stresses should be less severe due to the presence of the cracks, splats and voids in the TBC allowing for localized relief of thermal stresses and lowering of the global thermal stress field. The actual material is suspected to have a different modulus across the thickness than co-planer to the bond line, e.g. it has an orthotropic Young's modulus. Since the system is a beam and the TBC layer is thin relative to the beam, an isotropic modulus model should be an acceptable assumption as the predominate stresses will be parallel to the bond plane. The bond coat layer is neglected and is folded into the TBC layer, in reality its localized irregularity will probably influence the localized (mainly axial) stress field as a function of how much irregularity there is in the layer in a localized fashion.

A classical analysis of the possible stress state using techniques covered in the

text by Boley and Weiner will give some insight into the worst-case thermal stresses that might arise in the system. This analysis would be best approached as a one-dimensional solution of a half domain slab of the TBC material on a substrate of the beam (Boley and Weiner, 1960). This would yield a useful upper bound estimate of the axial thermal stresses that may be seen in the test specimen at the various design temperatures. This would be similar to a classic lack of fit analysis in most undergraduate textbooks to determine the general stress levels. Extending this to a 2-D solution to gain insight into the regions of maximal stress gradients could be performed analytically (Boley and Weiner, 1960), but this can also be accomplished by FEA modeling of the differential thermal expansion using ABAQUS as it allows for entry of thermal expansion data into the material models. The current study will proceed in this manner. It is noted that this model is still limited by the coating being modeled as an homogeneous solid, when in reality there is stress relief occurring in the real specimens with the formation of cracks and splats.

An attempt to model crack formation and the resultant effect on effective thermal residual stresses is covered in Tamarin and Abu Al-Rub (Tamarin, 2003:203-204; Abu Al-Rub, 2010). The author shows a relation from this FEA analysis that relates the theoretical maximum relative stress to the reduced amount as a function of the vertical crack density in this 2-D model. Tamarin also hypotheses that formation of the cracks in the initial life of the coating helps to measurably extend service life by reducing TCF thermal spallation. It is important to note that this model was influenced by the TBC structure derived from the EB-PVD process.

2.9.1. Analytical Model, 1-D

Thermal stress modeling was performed on an analytical model. The 1-D model is a classical lack-of-fit analysis covered in many introductory texts as well as Boley and

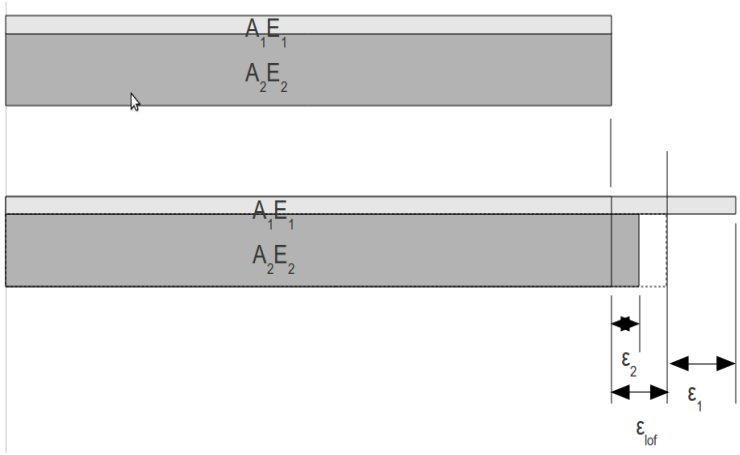


Figure 49: 1-D Model for Thermal Stress

Wiener. To scale the potential functions to the stress levels anticipated, the one dimensional lack of fit problem is useful to estimate these. Ignoring any 2nd and 3rd dimensional effects the interface can be modeled as a 2-region bar; refer to Figure 49.

The top Figure depicts the two materials at the reference temperature before heating and the lower shows the two materials, unrestrained from one another, after heating to the extreme limit of 900degF (482.2degC). Enforcing the strain compatibility condition along the interface brings them into a state of thermal stress and this is the strain lack of fit. Performing a sum of forces in each bar to equal zero, one obtains:

$$F_1 = F_2 \quad \rightarrow \quad \sigma_1 A_1 = \sigma_2 A_2 \quad \rightarrow \quad (\epsilon_{lof} - \epsilon_1) A_1 E_1 = (\epsilon_2 - \epsilon_{lof}) A_2 E_2 \tag{61}$$

where the product of the axial area (A_i) and modulus (E_i), determine the resistance in each material. Rearranging (61) one obtains for the strain lack of fit:

$$\epsilon_{lof} = \frac{(A_1 E_1 \epsilon_1 + A_2 E_2 \epsilon_2)}{A_1 E_1 + A_2 E_2} = \frac{(A_1 E_1 \alpha_1 + A_2 E_2 \alpha_2) \Delta T}{A_1 E_1 + A_2 E_2} \tag{62}$$

from this the stress levels of tension and compression can be determined in each region as per:

$$\begin{matrix}\sigma_{TBC} \\ \sigma_{TI}\end{matrix} = \begin{cases}(\epsilon_{lof} - \Delta T\,\alpha_1)\,E_1 \\ (\epsilon_{lof} - \Delta T\,\alpha_2)\,E_2\end{cases} \tag{63}$$

This yields a conservative upper bound (a more severe state predicted than is likely to be encountered with inhomogeneous, cracked coatings with a multidimensional structure) estimate of axial stress.

For all of the analysis work on thermal stresses Table 6 lists the properties. The results of the 1-D analysis can be considered an approximated upper bound, the stresses from the thermal mismatch are fairly low, 1380psi compressive in the coating and about 400psi tension in the titanium beam.

Table 6: 1-D Thermal Stress Analysis

Temperature Range			
Initial Temperature	T_0	21.1 / 70	(degC / degF)
Final Temperature	T_1	482.2 / 900	(degC / degF)
Properties of Titanium Ti-6Al-4V			
Thickness	w_2	0.019050	(m)
Width	w_1	0.019050	(m)
Young's Modulus	E_2	115.5×10^9	(N/m^2)
Coeff. of Thermal Expansion	α_2	9.76×10^{-6}	(m/m▪degC)
Properties of Air Plasma-sprayed 8-YSZ			
Thickness	t_1	0.000457	(m)
Width	w_1	0.019050	(m)
Young's Modulus	E_1	30.0×10^9	(N/m^2)
Coeff. of Thermal Expansion	α_1	10.50×10^{-6}	(m/m▪degC)
Results			
Stress in the Coating-bulk	$\sigma_{xx,1}$	-9.52×10^6 / -1381.36	(Pas / psi)
Stress in the Titanium-bulk	$\sigma_{xx,2}$	2.74×10^6 / 397.83	(Pas / psi)
Force Pair	F_1=-F_2	82.95	(N)

2.10. Finite-element Thermal Stresses Model

To gain insight into the thermal stresses acting within the beam system a 2- and 3-D finite-element (FEA) model in ABAQUS v6.8-2 were built. The FEA models had the same material properties as detailed in Table 6. The boundaries, that is all of the outer surfaces of the beam and TBC system are all stress-free. Strain compatibility was enforced across the beam-coating interface. The geometry and dimensions were the same as for the coated specimens tested (See Section 4.2). The 2-D model utilized the plane-stress assumption. Neither model was set up to take advantage of the symmetries in the

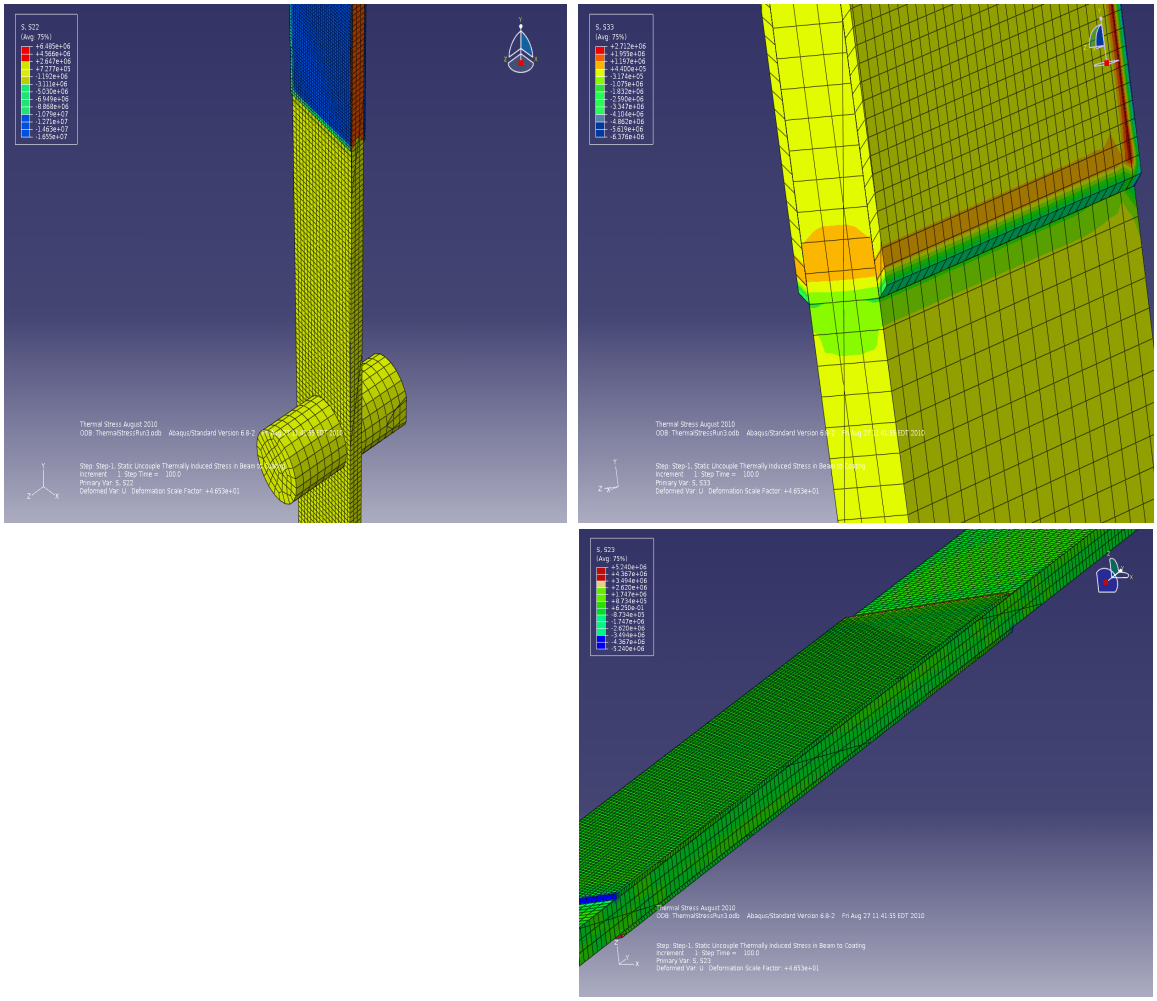


Figure 50: Thermal Stress FEA solution Results, 3-D

beam although both had 2- and 3- planes of symmetry for 2-D and 3-D models, respectively. Solution of the full model was performed due to the reasonable time to reach solution with a mesh that was sufficiently dense. The elements chosen were the same as in the modal dynamic models, the linearly elastic 4-noded plane-stress element and the 8-noded linear brick element; both of incompatible strain mode ("CPS4I" and "C3D8I").

Both models assumed that the two TBC regions and beam were rigidly adhered to one another; "constraint tie" is the nomenclature that the ABAQUS software uses to indicate this condition. The reference field of zero-stress and zero-strain was deemed to be 70degF (21.1degC), then the whole structure was allowed to uniformly assume a temperature of 900degF (482.2degC). The three regions of material undergo a thermal expansion constrained to one another, and the direct stress field was solved for based in the imposed strain mismatch. Figure 50 displays the 3-D model results and Figure 51 for those of the 2-D model.

The 3-D model is displayed with half of the model suppressed from view to allow the mid-lateral plane stresses to be shown and to allow comparison to the 2-D model results. It is noted the axial stresses from the two models are reasonably close to the 1- and 2-D analytical models about as shown in Table 7, which will be discussed below.

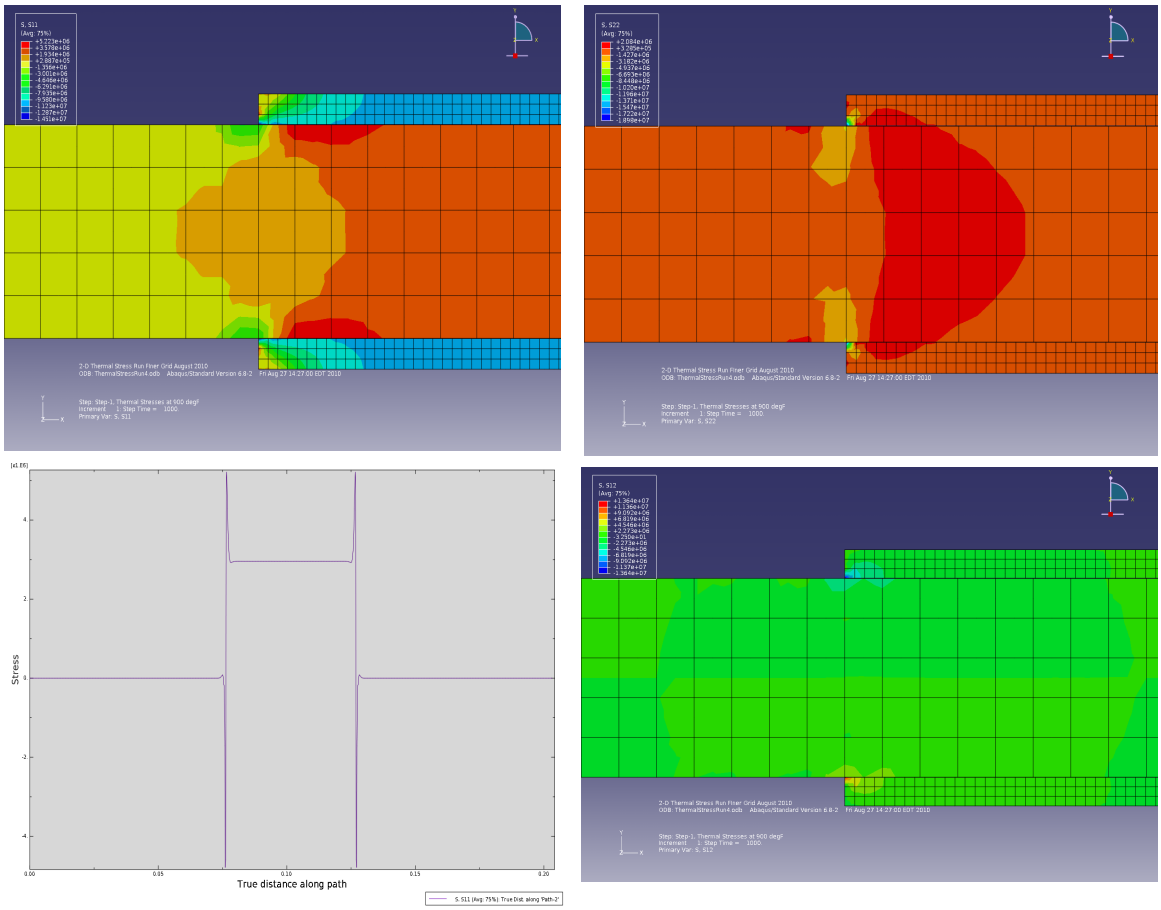


Figure 51: Thermal Stress FEA solutions, 2-D

The bulk axial (compressive) stress distribution in the coating and titanium (tensile) regions is near uniform across the majority of the two material regions; significant gradients are only experienced near the edges of the TBC patch. Figures 50 and 51 show the axial stresses in the upper-left, for the 3-D and 2-D, respectively. The 2-D plot also has a plot of the axial stress in the titanium beam's outer surface down the

mid-line from tip-to-tip. This line runs across the interface plane between the TBC and beam in the middle 2.0in of the span. The stress in the beam is very close to 2.96MPa within the coated regions except near the edges of the coating where the stress peaks at around 5.25MPa. Just in from the edge, is a compressive stress in the titanium of -4.75MPa. Both of these extremes exist in a localized region near the edge, about 20% of the length of the patch (counting each end of the path region). These edge discontinuities, whether caused by thermal or bending stresses, suggest that some minimal patch length needs to be employed to reduce the undue influence of these regions from invalidating the uniform stress field that the FEA extrapolation infers. The dynamically bent beam has a non-uniform radius of curvature so the patch length should not be made too long or this non-uniform stress field effect will become significant.

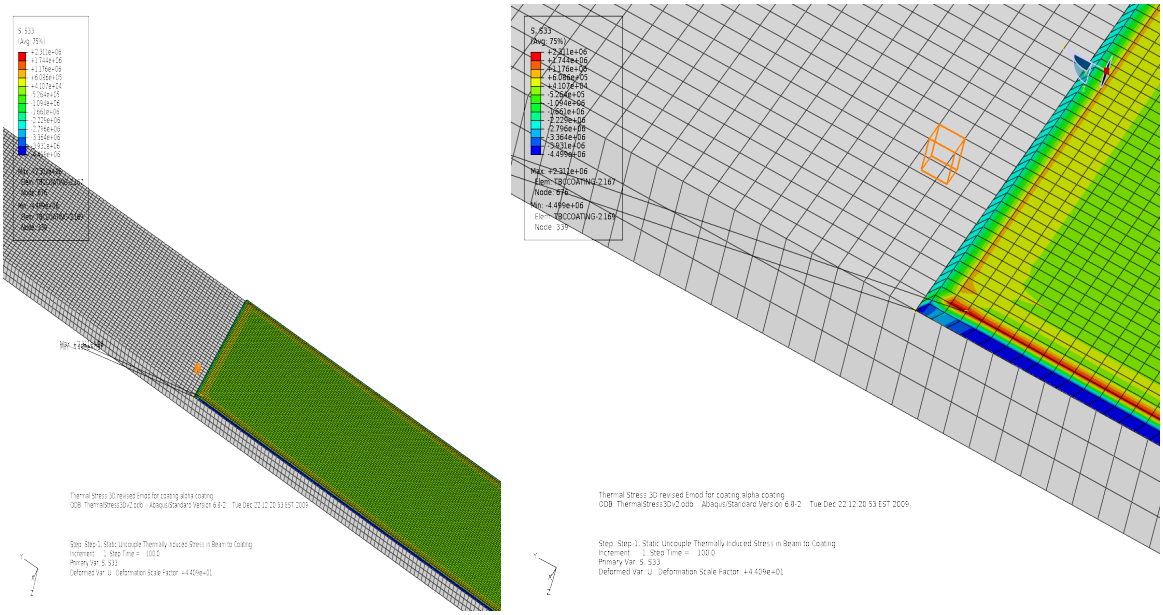


Figure 52: Peel Stress Plots from 3-D FEA

The 3-D solution also shows (Figure 52) that the highest peel stresses, those that are orthogonal the to TBC-beam interface plane, are along the free edges on the beam.

The edges that are coating-to-beam (where the $y = L \pm (L_c/2)$) have a lesser peel stress maximum. The maximum peel stresses are about 2.3MPa (about 334psi), which are well below the adhesive strengths reported for 8-YSZ, where the lowest measurements of adhesive strength of 8-YSZ to a NiCrAlY bond coat are around 20MPa as assessed by static pull tests (Zhou, 2007).

Table 7 summarizes the bulk axial stresses found by each method to allow comparison. The general magnitude of the thermal stresses in the axial direction of the beam within the beam is small, -2.96MPa (-0.43 kpsi). Even combined with the bending stress field that comes with maximal beam displacement (at 1.3m/sec, the highest reported displacements in the previous studies for the coated beam, the bending stress, σ_{xx}, is ±67.73MPa or ±9.82 kpsi) the total stress from thermal and mechanical loading stays under 71MPa. This is well below the yield limit for the Ti-6Al-4V alloy, even at 900degF where the yield value is around 248.0MPa / 36.0kpsi (Mil-HandBook-5H, 1998). Since the system for the beam remains within the elastic range (assuming superposition of the two loading sources) gaging their effect on the beam system using linear material models should remain valid. The true state of thermal stress in the actual beam and the 3-D FEA model is a bi-axial stress state, where the principle stresses that is normal to the beam-TBC bond plane are zero, as there is no acting constraint from differential expansion in this direction. The methods are all reasonably close for the far-removed maximum axial stresses in the titanium. For the TBC, the 3-D FEA model does capture a higher maximum axial stress, but it is the only model that can capture the bi-axial state.

Table 7: Thermal Stress Analysis Results Comparison

	Titanium, Far-Removed Axial Coating Stress	TBC, Far- Removed Axial Coating Stress	Tensile Peel Stress of Coating from Titanium	Shear at Edges
Model	(MPa/psi)	(MPa/psi)	(MPa/psi)	(MPa/psi)
1-D Analytical	2.74 / 397.40	-9.52 / -1380.75	NA	NA
2-D Analytical	2.44 / 354.23	-9.54 / -1383.7	approx 0.006 / 1.0	0.137 / 20
3-D FEA Model	2.88 / 417.70	-11.93 / -1730.30	0.997 / 144.60	0.284 / 17.259

2.11. Design Summary

Based on the analytical and numerical modeling work in this Chapter it seemed clear that making a chamber to accommodate Reed and Pearson's free-free setup was very likely to work. Heating the beam in a near-isothermal state using moderate power would be possible using a vacuum environment, a highly multilayer reflective enclosure, and enclosing radiant sources as indicated by analytical and numerical modeling. All the models made the important prediction that the chamber would achieve a high Stark number situation with a resultant isothermal beam; this with relatively modest power requirements to heat to the design temperature maximum. Indeed, with further careful characterization effort (to measure the free convection off the chamber, directly determine the component emissivities, etc.) the FEA model could be made quite accurate to the experiment. This was not pursed as the goal was to realize the actual apparatus and procedural technique. The heating of support equipment outside the radiant shielding was predicted to be modest.

The magnets and coil would have to be adapted to higher temperature environments. Enhancement of the coil cooling capacity and appropriately shielding it

would be required. Due consideration will have to be given for a loss of magnetic coupling strength in using the only class of magnets that will work in the temperature range of the chamber, ALNICO. Accurate and consistent suspension of the test specimens over the coil was deemed important. FEA based sensitivity studies indicated that Mode-I bending would not be adversely impacted by additional magnetic mass, but dimensionally accurate modeling of the magnets would help minimize uncertainties.

There are additional design concerns and associated theory, like those of a free-free beam, the dynamics of the suspending filaments, and the extraction of strain using analytical and numerical modeling, specific to the beam system, these topics are covered in Chapter 4.

3. Description, Fabrication, Calibration/Validation of the Test Apparatus

This Chapter details the chamber and support apparatus used for the high temperature characterization studies as finally realized in physical construction based on the fundamental analysis and theory covered in the previous Chapter. This overview will focus on the apparatus, operation, and experimental validation of the chamber and apparatus needed to obtain isothermal high temperature ring-down (free-decay) responses from the TBC coated specimens. The specifics of how the test specimens were measured and the data processed are deferred until Chapters 4 and 5.

The high Stark number chamber has three main cavities, the uppermost, inner cavity contains the specimen under test along with the lamps, dummy specimen, and suspension wires. This is the "hot core" section of which the outer boundary is delineated by the triple-layer aluminum foil thermal shields that enclose and form a highly re-reflecting enclosure. The annular space between the outer layer of the shielding and the main pressure vessel, which is the second cavity, is where sensor and power wiring are routed and suspension wires to the specimen are tied off. While the inner target beam is at 900degF and the inner surface of the radiation shields are at around 720-750degF, the outer layer of the triple shield is around 215-220degF; this space is cool enough to allow use of non-rubber and non-plastic electrical splicing material. The final open space, located below the bottom layer of triple layer shield, remains relatively cool at about 150degF, in here the water-cooled electromagnet sits directly below the suspended beam.

Also, routing of the vacuum, cooling and other services are routed in and through this space.

The chamber was designed to allow it to reach 900-950degF (482-510degF); this limit was chosen as a design goal for two reasons, 1) it is safely within the the upper end of the working temperature of ALNICO magnets, the class of permanent magnet featuring the highest working temperatures, and 2) the innermost stages of modern 30-40:1 turbo-machinery compressors experience working temperatures in this range (as determined by adiabatic compression of air). These "cold sections" are where the TBC materials would be used principally for their mechanical qualities, assuming they can be mechanically characterized and modeled. In actual testing the chamber was used on bare beams up to 1050degF.

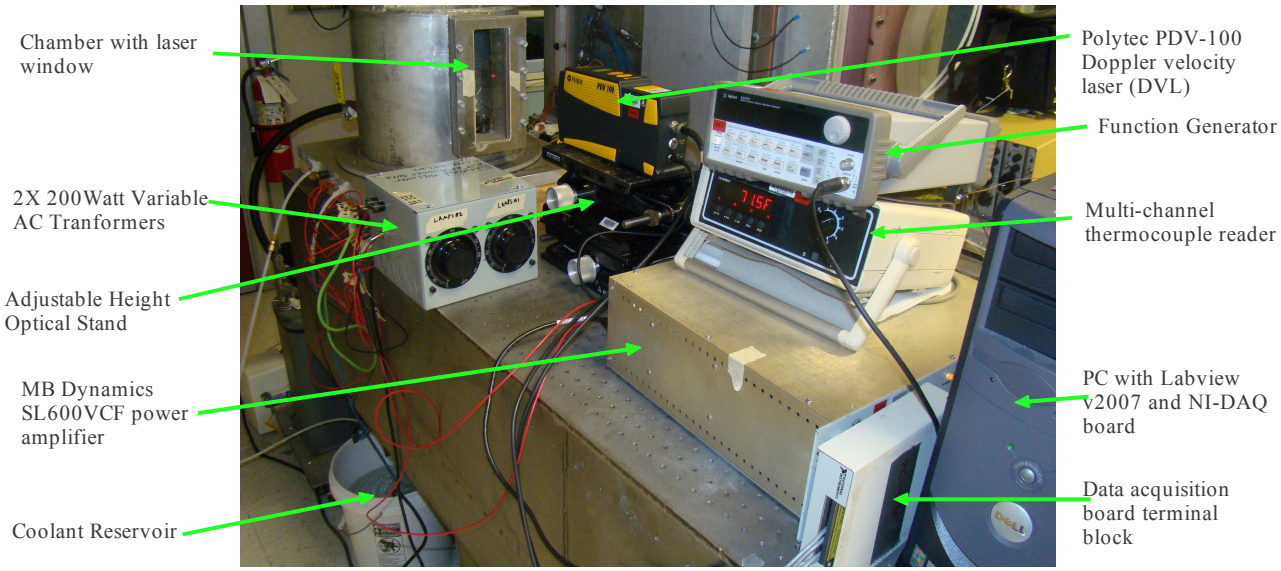


Figure 53: Chamber Setup, On Table

Besides the chamber itself, as shown in Figures 53 and 54, there is much ancillary support equipment to excite, heat, cool, and measure the specimen within. From back to

front in Figure 53, are the pressure chamber with the specimen within (silver cannister), the dual variable-AC transformer power supplies for the lamps (the gray box), the DVL laser on a precision z-axis table, the power amplifier for driving the coil electromagnet, a thermocouple reader, a function generator, and a data acquisition computer equipped with Labview 2007. Figure 54 displays support equipment down on the floor including: a cooling reservoir with submersible coolant pump, the main pressure gages, and a vacuum pump. The large cylindrical object to the right is the leg of the optical table upon which the setup rests for acoustic isolation. These major pieces of support apparatus include:

· Dual variable ac-transformer system (2X Superior Electric Type 21) - to power the two lamp circuits each featuring four 200W halogen lamps each rated at 0.80kVA each.

· Function generator - an Agilent 33120A, to excite the beam via the power amplifier. This was used to tune in the find resonance peaks at a given temperature and amplitude setting.

· Vacuum Pump (Varion DS301) – a dual stage vane pump reduced the chamber pressure to about 0.010-0.015atm to provide for elimination of air damping and convective heat transfer.

· Pressure Gauges – These were a low- and higher-precision gauges that allowed monitoring of the low vacuum levels within the chamber.

· A voltage controlled AC amplifier (MB Dynamics SL600VCF) – this allowed for high current AC stimulation of the electromagnetic coil. Receiving a voltage waveform signal from either the National Instruments board equipped PC and/or the function generator the current output sourced is a function of the voltage control signal. The unit was run in

current feedback mode to eliminate any attenuation effects from the coil acting as a low-pass filter, even though the frequencies ranges traversed were quite small.

· Doppler Velocity Laser (DVL) - (Polytech PDV-100) on a precision z-axis stand; this was the main sensor for reading the beam's instantaneous velocity as a function of time. It was aimed at a small piece of mica tape glued to the beam at the center of one of the two large faces.

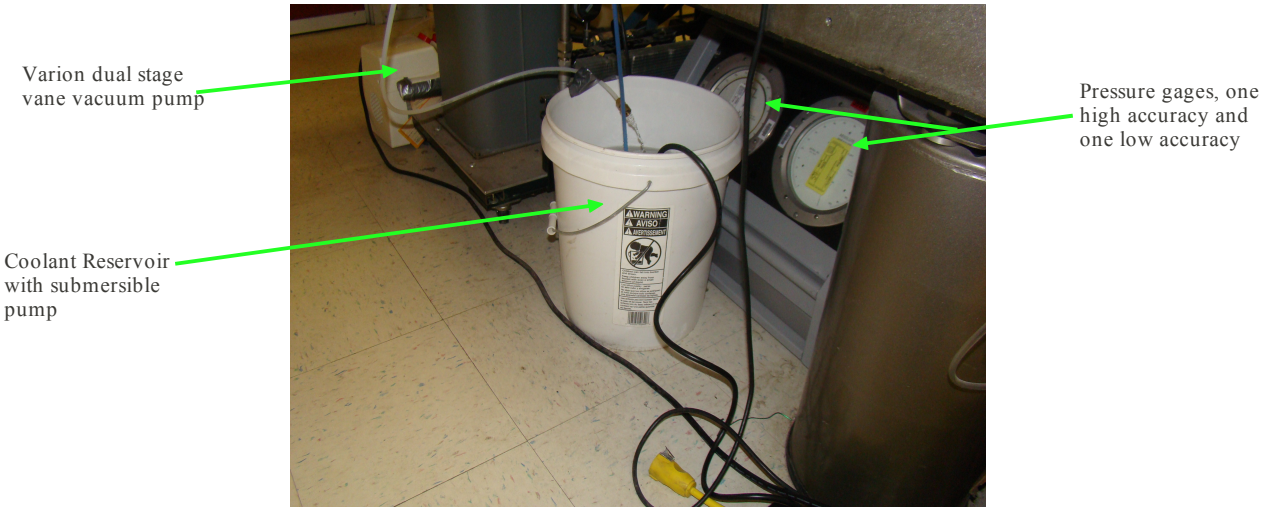


Figure 54: Chamber Setup, Below Table

· Coolant reservoir and submersible pump – the submersible pump and 5-gallon bucket served as a coolant reservoir, the pumps outflow is routed to coolant tubing that ports through the base slab into the chamber and the electromagnetic coil to cool the lower cavity.

· Multichannel thermocouple reader (Omega DP-41TC) – this was connected to the dummy specimen and allowed indirect monitoring of the specimens temperature. The dummy specimen is a piece of titanium of similar surface-to-volume ratio as the beam and suspended proximate to it on a piece of magnet wire where it will not interfere with

the suspension or irradiation of the free-free beam. Changing temperature in concert with the free-free beam it allows for closed loop temperature monitoring without contacting the beam.

· Computerized DAC system (NI-MIO-16E-4(6040F)) – This was a PC equipped with a National Instruments NI-MIO-16E-4(6040F) multipurpose data acquisition card (DAC) and the Labview v2007 software. This system was used to both excite the beam system via the electromagnet and record the stimulation signal and the beam response as well. A virtual instrument (VI) program was developed to handle the timing issue and data collection as well as perform some data analysis. It had the ability to estimate system damping against the classic linear model by fitting the classic linear decay model to the envelope function. The details of this programming will be covered in Chapter 6.

Through the next sections the chamber and its components are described, Appendix Error: Reference source not found does have some mechanical drawings for reference.

3.1. Main Chamber Pressure Housing (Vacuum)

The most obvious component of the chamber is the pressure housing, which allows for the maintenance of vacuum to minimize air damping as well as ensure a high Stark number heat transfer environment. The main pressure chamber is a two-piece affair, a removable bell jar lid and a base slab to which most of the components are mounted to. An axial O-ring gland seals them together.

Vacuum was reliably maintained to 7.5-9.0 Torr (or mmHg, which is around 0.01atm) across all chamber temperatures and was provided via a hose in the base slab

that hooks to a Varion DS-301 dual-stage rotary vane pump. Pressure is monitored via a two-stage aneroid pressure gage, one high- and one low-range gage, together precise to about ±0.25 Torr. The target working pressures can be achieved within two minutes of pump start-up.

3.1.1. Main Housing and Optical Ports

The top jar of the setup is a cylindrical pressure case with a 0.375in thick aluminum 6061-T6 top plate. A 0.50in wall thickness pipe is welded with a base flange ring on the lower end and the top-plate above. The cylindrical inner cavity is 12.0in high by 13.0in inner diameter (ID). All welds were metal-inert-gas (MIG) fillet welds, continuous in form in order to maintain the low vacuum. Detail drawings of this construction can be referred to in Allen (Allen, 2005).

Two optical ports consisting of the same aluminum alloy are welded to the side of the chamber housing, 180-degrees apart. Figure 150 in Appendix 4 details the window positioning. Machined by CNC as a three piece assembly, these are to provide laser access and thermal infrared (IR) imaging access. For both windows, the optical pane is placed within a aluminum spacer ring that is inside an outer aluminum retainer piece. An axial gland seal of the 2XX-series containing a silicone rubber o-ring is on the mount flange of each window; silicone was chosen over the usual nitrile ("Buna-N") rubber as it has a higher thermal working limit. The optical piece rests against this and the spacer and retainer are clamped in place over it using a set of 1/4-20 bolts, washers, and nuts. A gasket of "Fiberfrax" high temperature cloth is sandwiched between the retainer ring and

the spacer/optical pane. This, in concert with the o-ring, protects the optical element against fracture from stresses that could occur from over clamping and/or differential thermal expansion. They also provide an initial compliance loading to allow seal-up upon the application of vacuum.

The laser access port, which is about 8.5in long (high) and 3.0in wide allows for employment of a scanning Doppler velocity laser (DVL) and is equipped with a 0.5in thick pane of borosilicate glass; this material was chosen for thermal shock resistance and transparency to the wavelength of the helium neon (~632.8 nanometer) DVL lasers in use at the TEFF laboratory. The thermal access port is round, 3.0in in diameter, 3/8in thick, and is equipped with a zinc selenide window (ZnSe) manufactured by Phoenix Industries of Lowell, MA. This window material features a high transmissivity for low infrared (IR) wavelengths at which the chamber interior will feature peak thermal radiation emissions. By Wien's law which is:

$$\lambda T_{max} = 2898\,\mu m \cdot K \tag{64}$$

one can see that the chamber which will radiate from about 70 to 900degF (21 to 482degC or 294 to 755K) corresponds to peak emission wavelengths (assuming a blackbody) of 9.9μm down to 3.8μm, respectively. At the design temperatures this window material is necessary to allowing remote IR imaging of the beam hanging within in order to assess whether it is isothermal. It is noted that most common glass and plastic materials are opaque to wavelengths emitted in the designed temperature range of the chamber.

Sealing between the lower flange of the chamber and the main base, is provided

by a AS568A-384 o-ring in an axial gland machined into the baseplate. All o-ring glands were designed to be grease-less in view of the high temperatures that the metal could achieve thus raising concerns about fumes, flammability, and out-gassing. The three layers of foil shielding, located about 1.0in inward from the pressure jar inner wall, ensured the that maximum outer chamber temperatures only reach round 180degF, when used in concert with the removal of heat in the lower cavity by the electromagnetic coils active cooling coils.

A ballcock screwed onto a pipe that is welded to the side of the chamber wall, used in former studies to supply vacuum, was used to break vacuum. All the services were routed through the base to enable easier removal of the top lid and therefore access into the chamber's interior. Procedurally, breaking vacuum was avoided above about 400degF to avoid flash oxidation of the hot metallic surfaces from oxygen in the in-rushing air, especially the lamp reflectors and 3-layer shielding, and to avoid thermal shocking of the components caused by rapid cool-down. It was found that the two part Durabond adhesive would pop loose with too rapid cooling of the beam and other bonded surfaces.

3.1.2. Base Slab

The base slab, which is the structural backbone of the rig, consists of a 1.0in thick Al-6061 aluminum slab approximately 20in square in size (See Figure 55). Most of the major components are mounted to it including the lamp support rods, the beam suspension rods, wire and shielding support rods, the electromagnets, and the service

wiring/tubing/hosing. The top pressure case rests upon the base and seals against it with the application of vacuum. Figure 56 is a photograph taken from above.

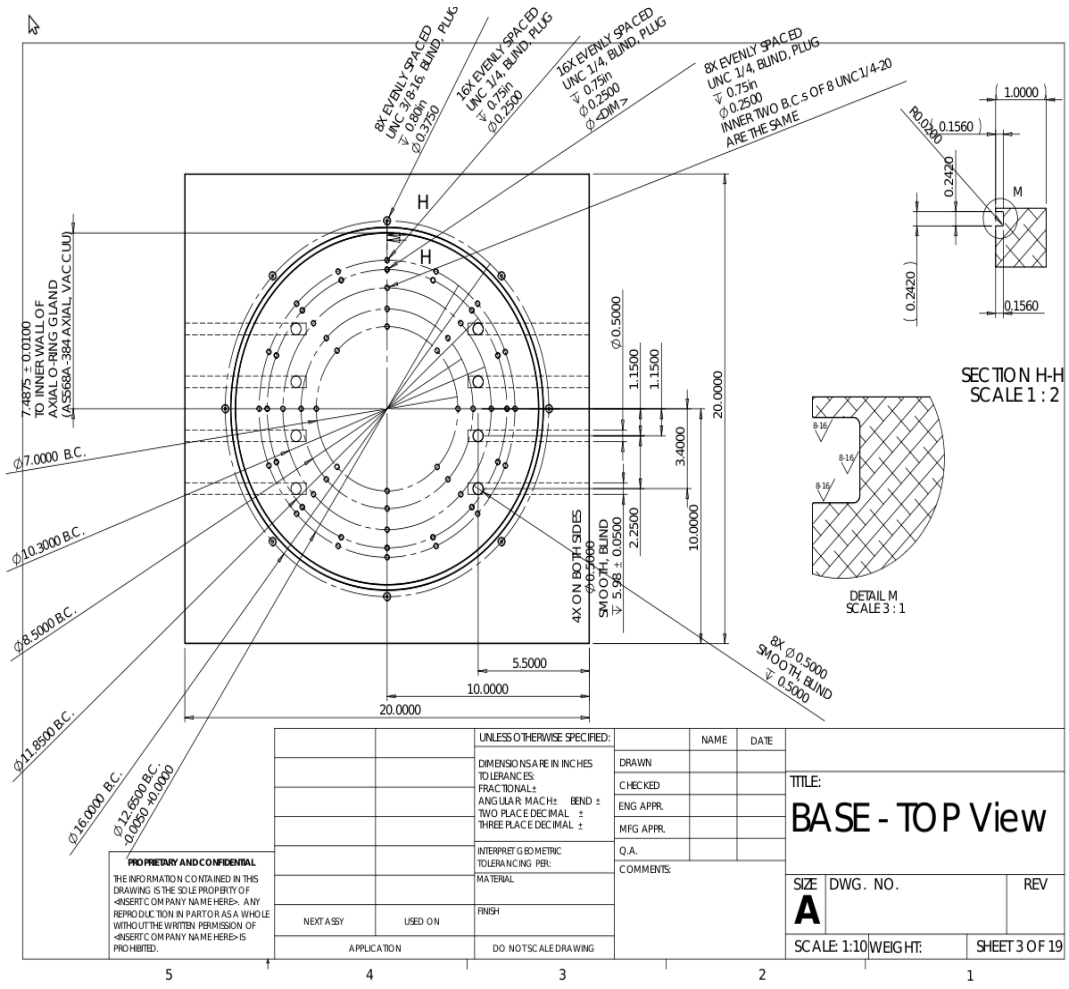


Figure 55: Base Slab Dimensions

Eight service pass through channels were drilled into the base, and these emerged inside. These allowed the passing of electromagnet power, lamp power, signals from the K-type thermocouple sense lines, vacuum porting, and cooling water in- and out-flow. Some of these ports are equipped with tapered pipe threads to allow use of fittings for fluids and vacuum connections, and others are smooth bored to help ensure good sealing

via potting of tubing and wires to maintain vacuum integrity. Silicone-based RTV compounds were used for potting the tubing and wires within the base pass-through channels. Some thermocouple sense lines were routed through tapered rubber stoppers as well, these were subsequently inserted into the smooth bore pass-through tubes. As seen from Figure 55, large array of standard of blind UNC 1/4-20 threaded screw holes were tapped into the base with several circles of varying diameter the interior of the chamber. These provided the means to secure down all off the interior items while allowing flexibility in positioning and aiming the various interior elements. The lamp support rods, beam support rods, wiring and radiation shielding supports, and bolts for tying down the wires and tubing used these holes.

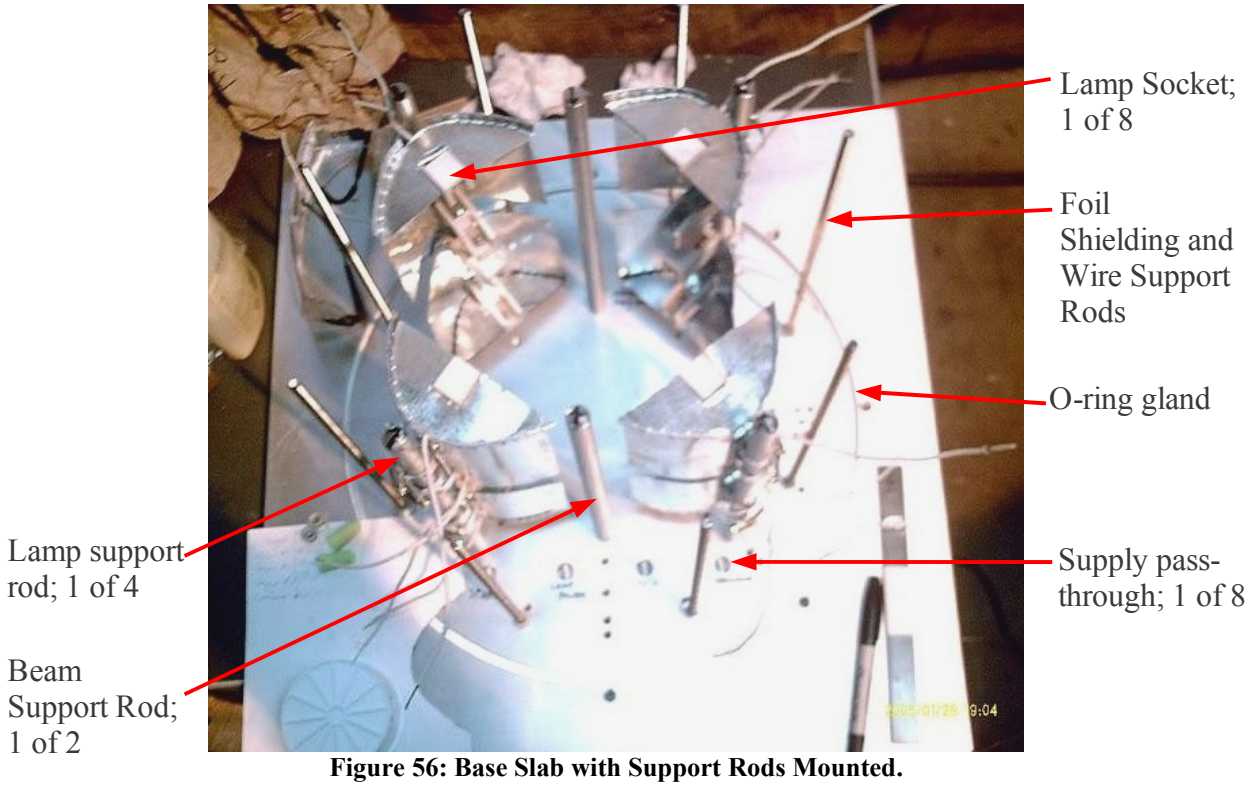


Figure 56: Base Slab with Support Rods Mounted.

Figure 56 shows the base slab from above, the two bare rods are for suspension of

the beam, the four rods with parabolic reflectors are the lamps located on a 10.3in diameter circle, and the eight (thinner) threaded rods are to secure the wires against and support the triple layer thermal shielding. These are located on a 12.65in diameter circle. The large circular channel located outside the threaded rods is the main axial O-ring gland that seals the top jar and the four smooth bore holes are the inner ends of the service ports; another four are on the other half of the slab obscured from view by the lamps. Many extra holes were provided in the base slab to allow some configuration changes and tuning of the setup placement. The electromagnet, not shown, sits at the center of all these concentric circles. The four relatively large holes in a straight row are the inner ports of four of the eight pass-throughs, the other four are mirrored across the center-line of the slab.

3.1.3. Lamps, Insulation, and Cooling (Method of Heating)

Within the high temperature cavity are eight lamp units reach consisting of a lamp holder assembly, a halogen bulb, and a parabolic trough reflector. These assemblies were fastened to ½-in diameter steel support rods in a end-to-end pair using stainless steel hose clamps. The intent was to approximate four constant linear sources in a polar array around the specimen located at the center where radial symmetry was approximated. The eight lamps were 100, originally, and later, 200 Watt halogen linear bulbs commonly used in “torchette” style halogen floor lamps. These were cylindrical quartz-envelope bulbs measuring 3.125in length by 0.375in diameter with end terminals (Cat #: Q100T3/S and Q200T3/S). These are mounted in high temperature fixtures equipped with glass-

braid insulated wires, crimped electrical connections, and ceramic insulators. Crimped connections had to be used in lieu of soldered connections, due to the anticipated service temperatures. Figure 57, shows the lamp array located around the free-free specimen hanging in the center of the array, the radiation shielding in this photograph has been installed in all locations save the top. The red dot on the beam is the DVL laser.

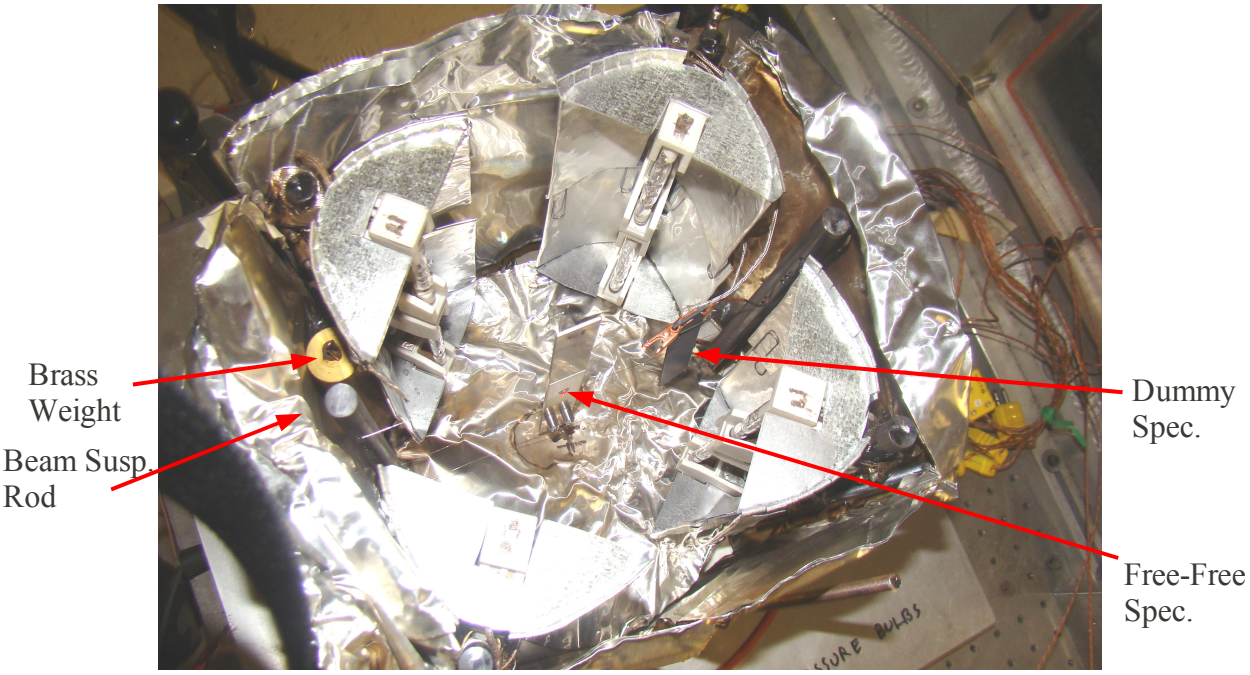


Figure 57: Chamber with Heating Lamps, Free-Free Beam, and Dummy Specimen, view from top

Before testing, it was thought the lamps might suffer premature failure in the chamber due two effects. The do produce, and need to dissipate, a lot of energy and it was thought the quartz bulbs would be prone to slow failure from softening of the glass bulbs in the extreme heat with no free convective cooling. The second was that the lamps often would be run at low to moderate power. This is problematic as the halogen refresh cycle that replenishes vaporized tungsten back onto the filament only begins to initiate at

higher power levels near the rated limit. As a result an extra set of the 100 and 200W bulbs were ordered and ready to use. This also motivated the sensitivity testing to assess the thermal effects of single bulb failures; opening the chamber in the middle of a test to replace and single failed bulb would be very procedurally cumbersome. The halogen lamps proved very effective in use when testing, quartz halogen bulbs survive operation in vacuum with no apparent problem, the original bulb set made it through all the testing intact as a set (about 70+ hours of duty evenly spread across 300/600/900degF).

Surrounding this core heated area is a triple layer of aluminum foil shielding. There is one more triple layer piece that is placed over the lamps and beam before lowering the pressure jar over the chamber. The foil is a 1000-series aluminum foil of about 0.0003in thickness chosen for the high reflectivity of its surfaces. Critical to multilayer thermal shielding maintaining a high thermal resistivity in the vacuum is the maintenance of a very slight gap between each layer, otherwise it forms a single conductive mass. Initially, bi-axial weave fiberglass tape of 3oz weight was sandwiched in strips between the foil layers to form a high conductive resistance spacer layer. In practice, this was not necessary as the foil layers were slightly wrinkled with use and this was sufficient to keep the conduction contact points between the layers to a very small fraction of the effective area, and the two inner gaps between the layers were easily maintained without the fiberglass tape layer. The three pieces of shielding in each location were cut to fit snug by a friction fit between the lamp support rods and the outer wire support rods, the three pieces were slid in from above as a unit. The pieces facing the laser access and IR camera ports had a thin slit aperture and a round hole cut into the

layers to allow DVL measurements and IR imaging of the beam, yet minimizing thermal radiation leakage out of the hot core. When not performing IR imaging, the thermal window set was simply solid pieces of foil to avoid excessive radiant loss from the beam out the ZnSe window.

It was initially thought the shielding would not be needed, but the radiation FEA analysis indicated that the chambers outer walls were unacceptably hot, and both the FEA results and classic thermal circuit analysis indicated that the power needed to reach 900degF (488degC) would be some 1.2-1.6X the rated output of the lamp power supplies. So the foil was added as a high resistivity element in the thermal circuit. Later testing would reveal that when the specimen is around 900degF, the inner layer of foil shielding could reach temperatures of almost 730-750degF while the outermost layer was around 220-240degF. A dramatic demonstration of this was from masking tape lengths that spanned across the three layers of foil (used for wire chaffing protection); these would be pure pyrolyzed carbon on the portion from within the inner cavity, intact on the portion outside the outermost layer and featuring a very rapid but smooth transition between the two extremes on the length that wrapped around the three layers.

The lamps are wired on two branches with four lamps in parallel on each branch. Each branch is supplied by one Superior Electric 0.8kVA variable AC transformer ("variacs"), allowing the setting of the voltage level supplied to the lamps on the branch from 0 to 120VAC. The lamp holders, wires, and connections in the inner cavity were free of soldier connections and all insulation was based on glass-fiber as the inner cavity

temperatures exceeded 700degF. Outside the radiation shielding, Teflon-jacketed hookup wires were used to route power to the lamps, these could survive in the reduced temperature outside the foil shielding. Special high temperature wire was ordered and planned for use, but it proved too stiff and bulky to be routed inside the chamber confines. Bare metallic spade crimp terminals were used to connect the lamp feed and power wires together. To insulate these connections so that they did not ground out on the metallic surroundings, paper fiber backed (masking) tape was used. Electrical and self-vulcanizing rubber tape were avoided due to the close proximity of these junctions to the very hot radiation shielding and concerns over melting and out-gassing. Due to the uncertain integrity of these joints from an electrical isolation standpoint and their inability to be inspected before being energized, three standard procedures when operating the chamber were always followed. One, the power to the lamp variacs was routed to a ground fault circuit interrupter (GFCI), two, the aluminum slab base of the chamber was connected to earth ground through a low gage bonding wire, and three, the resistance between the power lines and the ground was verified to be (near) infinite with a multimeter after any close-up of the chamber. The integrity of these joints could be compromised by heat breakdown of the tape as well as mechanical abrasion of the tape when placing the top chamber cover on. To help minimize the latter effect, a cage of outer threaded rods was formed and the wires and joints were routed on the inside of this protective layer.

Type K thermocouples (chromel-alumel) locally fabricated from 24 gage wire (Omega GG-K-24-SLE, calibrated deviation of 1.9degF at 752.0degF) were mounted to

the dummy specimen, the heavily-oxidized, almost black, piece of titanium located to the right of the beam in Figure 57. The gap between the nearest edges of the two pieces of titanium is around ¾ of an inch. The thermocouples were initially bonded to the dummy specimen using Durabond 952, a nickel-base high temperature two part adhesive. This worked, but the specimens had to be manipulated very carefully as the cured bond was quite brittle. This material also was prone to thermal shock therefore limiting the rate at which heating and cooling could be applied to the specimens. After both copper alligator clips and steel paper clips were found to introduce no significant thermal effects on the beam and/or dummy specimen during the temperature validation portion of the study using the IR camera, these were used instead to secure the thermocouple junctions to the specimen for the remaining portion of the studies.

There were 10 thermocouples (TC) that were available and were run in through one of the service ports and potted using silicone RTV sealant. These were connected to a Omega DP-41TC reader with a 10 channel rotary selector switch. This unit provided cold junction compensation and allowed for direct reading of the TC junction temperatures. Thermal data was recorded by hand against a stopwatch as the chamber's thermal time constant was slow enough to allow manual data collection. The thermocouple batch was checked for calibration on a two point test, the ice point and boiling points, and were found accurate by linear extrapolation over the measured scale from 70 to 900degF (21.1 to 482.2degC) to within ±9.5degF (about ±5.0degC). The full set of ten channels was used during the multi-point isothermality validation testing, the spares were simply coiled and secured with a piece of magnet wire in the lower chamber cavity when not in use.

During the thermal IR image validation two were left secured to the beam and two on the dummy specimen. During subsequent dynamic testing only the two on the dummy remained in use.

The beam support and lamp tower rods are ½-in diameter carbon steel rods. A bolt to stand the lamp holder off the rod was used inside the hose clamps. This helped to reduce the conduction heat path to a small contact point. The hose-clamps were also secured over multiple layers of spiral-wrapped fiberglass tape in order to further reduce heat conduction out though the base slab via the rods. The tape was added after initial heating tests showed a marked heating of the rods as revealed by the iridescent color banding down the length of the steel rods. The spiral wrapped glass fiber tape was secured by masking tape that held the fiberglass, after the chamber was heated once, the masking tape shrunk to a ring of carbon that continued to secure the glass tape in place. The rods were mounted by means of 1/4-20 UNC threaded rods into the base slab. The lamp holder and reflector assemblies were sized based on an aperture size, bulb power, and focal length that was estimated would irradiate the beam sufficiently to heat it to the target temperature. From the results of the analysis in Chapter 2 the parabolic size was scaled to a size desired and used to make end gage plates out of galvanized sheet steel. The lamps themselves were placed at the focal points, ensuring (theoretically) that the light reflected towards the beam was parallel; in this way a rectangular irradiative intensity profile was ensured for the reflected portion of the lamp emissions (See Section 2.5.2). These lamp reflectors were lined with a layer of aluminum foil to yield a higher reflectivity than the galvanized steel could provide, and these liners were secured in place

with steel paper clips. Made from the same foil as the radiation shielding, were intended to be easily replaceable in the event they became oxidized and had compromised reflectivity. It was anticipated that they would lose their luster quickly and that in the course of testing that the quartz envelopes of the lamps would plastically flow and fail from lack of any convection cooling. As a result, many spares of both were procured and/or fabricated. Not only would the envelopes melt but the running of halogen bulbs at lower power can reduce their lifespan in a marked fashion due to the inefficient activation of the halogen cycle that redeposits vaporized tungsten back onto the filament. These concerns were unfounded, in actual service the original set of lamps remained in use through the approximately 70 hours of testing along with all the original reflector liners.

The dummy specimen, comprised of Ti-6Al-4V alloy, the same as used in the beam specimens, is of the same dimensions as the specimen, save length where it is about 3.0in in length and with the same breath and depth (0.75in x 0.0625in). It is supported in the beam chamber on a piece of magnet wire affixed to one of the beam support rods, and is positioned from about 1.25 to 1.5in to the side, center-to-center, of the beam specimen under test. Care was used in making sure the dummy was co-planer to the statically hanging beam to minimize shadowing effects. The main purpose for the dummy beam is to allow closed loop temperature monitoring of the chamber in a fashion that does not interfere with the low damping condition of the main specimen. This was done as even fine gage thermocouple and/or strain gage wires routed in over the passive node (suspension wire) were thought to introduce significant damping to the beam system. Despite being located somewhat away from the focal center of the four lamp tower

arrays, the bias error between the dummy and the main specimen was small, typically under 1.5-2.0degF at 70degF to a maximum of about 6.0degF at 900degF.

Though the open loop temperature as a function of input power calibration curve proved to be highly repeatable (given the proviso below), having a closed loop temperature monitoring capacity proved to be valuable for two reasons. The first was that intentional overshoot could be used to much more rapidly reach and settle to the desired temperature level rather than waiting for a true thermal equilibrium to arrive in 4-5 pseudo time constants ("pseudo" as the system is not a linear system, e.g. exponential w.r.t. to temperature versus time), the second was that during test times in the middle of the summer days, the voltage had to be over-specified by about 5-7%; as confirmed by measurement using a voltage meter, high air conditioning loads would pull the wall voltages down thus the dummy specimen for closed loop control became quite useful. So two type K thermocouples remained clipped to it with copper alloy crocodile clips for the subsequent 8-YSZ characterization testing.

3.1.4. Electromagnet and Cooling System (Method of Loading)

The method of loading in the work of Reed and Pearson was via a non contact electromagnet-to-permanent magnet system. The permanent magnets were suspended over the electromagnet which is an air-core, finite-length solenoid. The beam's centerline axis is co-linear to that of the electromagnet's own thus ensuring that the field is constant between tests and that error resulting from beam misalignment in the magnetic field is

minimized, provided the beam to magnet separation distance is consistent. The volumetric centroid of the permanent magnet set mounted to the beam is kept at about 2.05in (0.05207m) above the top plane of the coil, to control for variability in the coupling force-with-height variation, and ensure the beam specimen's lower tip has a clearance high enough to allow the lower radiation shielding to be placed between it and the electromagnet. There is about a ¼in of clearance between the top of the coil and the lower tip of the beam. Avoiding contact between the beam and the shielding is critical; contact will severely damp the vibrations, and as discovered experimentally, will also markedly cool the beam.

3.1.5. Active Node of Specimen (Method of Loading)

Half of the non-contact excitation is the permanent magnets mounted to the beam. A set of eight ALNICO grade 8 magnets were used in the current study clamped to the beam using a UNC2-56 fine threaded rod with two nuts and four Belleville (“cup”) washers as in the left side of Figure 58. The threaded rod was routed through two fine bore holes that were water-jet cut through the specimen at the active node line as seen in the specimen in the upper portion of the right photo. Each is a cylinder with a hollow bore hole running through it, measuring 1/4in outer diameter (OD) by 1/8in high, with the smooth bore hole being 3/32in in diameter inner diameter (ID). As seen in Figure 58 on the right side, four different sets of magnets were examined.



Figure 58: Active Node of Beam (left), Magnets and Sets of Hardware (right)

Proceeding from right to left in Figure 58 are: the NdFeB magnets with no center bore holes used in the past studies, custom fabricated sintered Grade-8 ALNICO magnets, double thickness stock ALNICO magnets, and quadruple thickness ALNICO stock magnets. The latter two sets are standard disk shaped magnets (McMaster-Car: Ultra-High-Temp ALNICO 8 Disc Magnet 1/4" Diameter x 1/2” high, 1.06lb pull Cat# 57295K74 and ALNICO 8 Disc Magnet 1/4" Diameter x 1/4”high, 0.31lb pull, Cat. #57295K73) with a N-S pole orientation down the axis of radial symmetry, these sets required the bore holes to be machined in. The magnets chosen for the study of the coatings in Chapter 6, the custom fabricated set second from the left, are of dimensions 0.125in high by 0.25in diameter. These were custom fabricated with a bore hole in place and a N-S axis aligned with the radial symmetry axis by EA Magnetics.

All of the magnets have a N-S pole orientation down the axis of the cylinder and

were mounted to the beam in a sets of (proceeding on the photo now from left to right) 4, 4, 8, and 8, respectively. It is noted that all sets, save the first, conserve the volume of magnetic material and fastener material that are applied to the beam's active node from the past studies. The stock magnets were machined by the electrostatic discharge milling (EDM) process to make bore holes. The AFIT machinists/model shop tried the processes of ceramic drilling, water-jet piercing, and EDM plunge boring. The first process tended to fracture the magnets as ALNICO is very tough and brittle, the water-jet cutting tended to fan out and lose the cylindrical bore shape, but EDM managed to bore a clean hole, without adversely affecting the pole orientation and reducing the strength in proportion beyond the volume of material removed. Static pull testing and assessment of the pole directions with a gauss meter showed that the strength loss undergone was due to loss of volume in the magnet and not process-induced demagnetization, and that the pole orientation of the magnetic charge was preserved.

Tight attachment of the permanent magnets to the beam is critical as it allows for efficient transfer of any forcing moment into the beam and also because any slight movement of the magnets can contribute significant friction damping into such a low damped system. The NdFeB magnets were glued to the beam with super-glue during the aging tests that were conducted, as was done in the past studies. Since this method would not survive at the elevated temperatures when performing the damping tests, the following attachment methods were tried:

· High temperature glue, Durabond 952, a nickel-based high temperature two-part

adhesive was tried with some solid core magnets. The material held up, but had a long cure time and the specimen had to be heated and cooled very slowly as thermal shock was found to pop the bond loose.

· Riveting, use of blind rivets in a force fit was considered but based on previous exploratory work by the TEFF loosing of the magnets upon excitation and shattering upon initial installation were problematic. There was no element to maintain compliance in the rivet and magnet stack.

· Machine screw sets, the use of mild steel UNC2-56 threaded rod proved to be most effective. Critical to its employment was the use of two stacks of Belleville washers. These allowed for pre-loading of the magnet stacks into compression. As the stack, beam, and threaded rods system thermally cycled and underwent differential expansion and contraction, this prevented the magnets from coming loose and chattering. This proved to be procedurally simple and provided a firm attachment. As an additional benefit misalignment issues with the magnets as explored by Deleon were avoided due to the precise hole to thread the machine screws through.

The custom made ALNICO magnets were selected for all the tests, save performance of the age-in protocol due to the best compromise on volume requirements, temperature resistance, and magnetic coupling moment (See Section 3.7).

3.1.5.1. Electromagnet

The previous studies at the TEFF used a novel electro-magnet that featured integral water cooling. This magnet was not used in the chamber as it was deemed that

enhanced water cooling was needed due to a much more severe thermal environment. The electromagnet is located in the center of the lower (cooler) cavity of the chamber below the floor layer of triple layer foil shielding. To prevent migration of the coil from any vibration, it is secured to the base using spare runs of magnet wire twisted to some bolts that are screwed into the base slab. A natural rubber pad of about 1/8in thickness is between placed between the coil and the base slab to provide compliance and isolation.

Comprised of an estimated 595turns (100 feet) of 12AWG solid thin enamel coated copper wire, the current electromagnet is wired around an air core in the inner bore and two independent sets of cooling tubes located about halfway between the bore and outer diameter. The cooling coils are copper tubing of 1/8in tube size with a ¼ in outer diameter (OD), and 0.190in inner diameter (ID) bore with a wall thickness of 0.030in that were fashioned into separate but interlocking coils. A K-type thermocouple was wound into the magnet about halfway between the ID and OD of the coil, this allowed monitoring of the bulk temperature to ensure that cooling flow was adequate to avoid breakdown of the insulation in the magnet from overheating. Heating of the coil came from two sources; 1) Joule heating from resistance to the driving currents in the coil, and 2) heat from the lamps leaking from the beam cavity through the thermal radiation barrier above the coil. The coil was structurally held together by permeating it with cynoacrylic glue (super-glue) and allowing it to cure into a mass. Several applications were made until it no more glue would soak in, the cured solid helps to conduct heat in the vacuum conditions as well as provide more insulation to the windings. Dimensions of the coil is about 3-1/2in outer diameter, about 3-1/2in height,

and with a 1-1/2in inner bore. Direct measurement of the coil's DC resistance using a four wire prescribed current, voltage drop technique yielded 1.401 Ohms. Use of Eq. (55) estimates a cutoff frequency for this coil with and can be used to generate a Bode plot. The electro-magnet temperatures remained below 105degF with the triple layer lower foil shielding between it and the beam cavity when the coil was de-energized. Maximal temperatures occurred with the coil being driven at high levels of current; this was a stronger source of heat than the approximately 200degF foil shield atop the coil. At around 27.45Amps, the highest driving current imposed when the MB-Dynamics power amplifier was being driven with a 7,500m$V_{p\text{-}p}$ signal (Gain is 3.66Amps output per 1V signal input to the amplifier) the temperature hit the maximum at around 130degF with the coolant pump on.

There was intention to keep a detailed winding diary for the coil and it was kept to allow estimation of the magnetic field strength using first principles. In practice though, the ideal geometry of a finite length coil was not achieved as the irregularities introduced by winding around the large bore cooling tubing are substantial. Because of this uncertainty, the coil was characterized for the various permanent magnets sets used in the current and past studies using a force-balance lever technique (Hoover, 2004). The calibration curves are detailed in Section 3.7.

Power to the magnet was supplied with power from an MB-Dynamics SL600VCF waveform amplifier, which is a high current power amplifier typically used for low impedance loads (e.g. vibration shakers), the amplifier was set in current mode wherein

the output excitation sourced to the coil is a function of the prescribed waveform fed to the amplifier input. The prescribed signal either came from an Agilent 33120A function generator or a National Instruments PCI-MIO-16E-4(6040F) computer DAC card, depending on what measurements were sought at that particular time. Constant current mode was used to overcome the changing series resistance-inductance (impedance) of the coil (making it in effect a low-pass filter) that had a cut-off frequency within a frequency decade of the beam's bending mode-I frequency. Although the free-decay technique avoids the traversing of a large frequency range in this magnitude roll-off region, by placing the amplifier in this mode the change in the coils AC-impedance is corrected for.

The coolant was ordinary tap water pumped in through nylon tubing; brass compression sleeve fittings were used to provide for connect-disconnect of the coil. The coolant reservoir was a 5 gallon bucket with a submersible centrifugal pump located outside the chamber, water was pumped up to the chamber, into it through the base slab, routed through the embedded copper cooling coils and then returned to the reservoir through another nylon tube potted into the base slab. Some extra T-junctions and tubing were designed into the system to allow for branches to be installed into the coolant system, should other components have required spot cooling (the IR window seal for instance). It turns out the foil thermal shielding was so effective that auxiliary cooling of other chamber components was not needed and the electromagnet's own bulk temperature rarely exceeded 105degF (40.5degC). The bucket water could get quite hot, up to 110-120degF, so a small 8in x 8” heat exchanger core radiator, like found in most automobiles, in conjunction with a electric fan was installed in the pump supply line to

reject heat to the room and keep the reservoir cool.

3.1.6. Passive Node of Specimen (Method of Suspension)

The passive node of the specimen is where the suspending wire was passed through, it was a real feat of precision EDM machine work featuring a 0.0080in diameter hole that was bored through the beam; a diameter to depth ratio of over 93:1. This hole was kept to a tight tolerance on the mid-plane of the beam, to within ±0.0020in of the hole-center to mid-plane distance. Maintenance of this tight tolerance was critical to avoid eccentric loading from the suspending wire and the undue loss of bending stiffness is the beam at the passive node. This is due to the fact that the contribution of any given

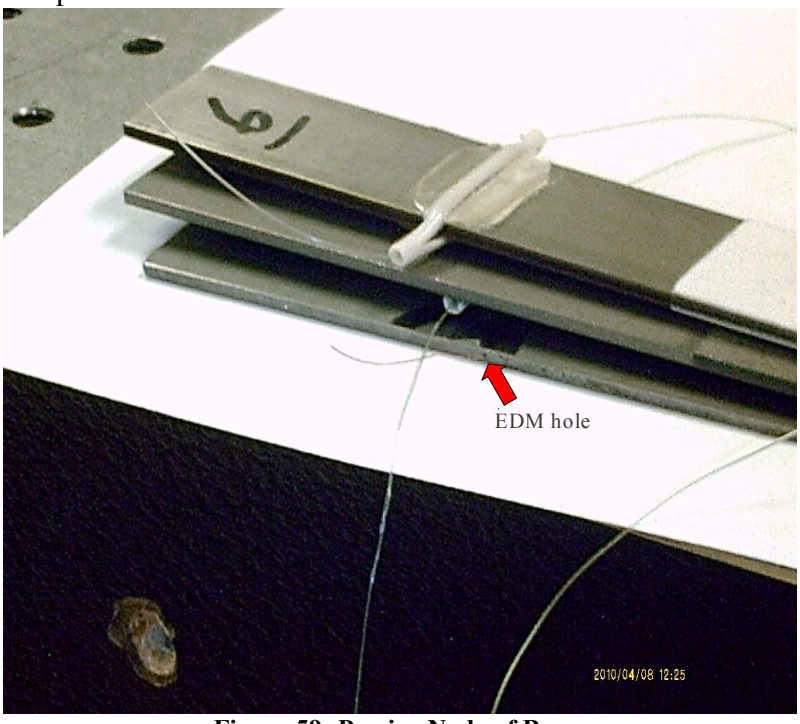


Figure 59: Passive Node of Beam

differential area in the cross-section to flexural stiffness is proportional to the cube of its distance from it to the neutral axis, so it is critical to keep the hole centered close the mid-plane of the beam to avoid removal of material away from it.

Figure 59 shows the evolution of the beam suspension at the passive node, the top specimen in the Reed study used a straw with the beam inserted into a split within it, and with the nylon line routed around the beam in an attempt to center the beam, the middle specimen (one of Pearson's) uses a surface-mounted, split, half-straw bonded to the beam with epoxy to route the line through, both of these studies used 6lb test nylon mono-filament. The current study, of which the bottom beam is a specimen, routes a fine wire through a 0.008in diameter EDM hole. The tolerance of the hole diameter is held to ±0.004in, but the centering of the hole to the mid-plane of the beam (containing the neutral axis) was deemed more critical. It was suspected before commencement of testing that the slight eccentricity caused by running the line through a surface mounted tube as well as the material of the suspension wire would not reduce system damping markedly, in fact sensitivity testing found that these changes reduced the damping of the system in a very significant fashion, thus rendering worthwhile the trouble required to bore these fine holes (See Section 5.3.1).

The beam was suspended using a 0.0050in diameter nickel chromium ("nichrome") wire, which is a stiff, high-temperature alloy commonly used in resistance heating elements. Selected for resistance to creep at elevated temperatures, the wire is suspended between the two ½in diameter low-carbon steel rods, and this forms the main span. These rods have a series of cross-drilled holes that have been countersunk and highly polished to reduce friction on the wire as it is routed through the rods. There is a tapped hole in the lower end to allow them to be screwed into the main baseplate. A set of holes were bored a various location to allow suspension of the beam at periodic

intervals above the top plane of the electromagnet. The wire on one side was led to a nut and washer clamp assembly to tie it off. On the other end, it was routed over one of the wiring/shield support tie rods and then tied off again using a nut and washer on another rod. Deflection of the last tie-off rod allowed for pre-tensioning of the wire. Additionally, the short span of nichrome wire was created by routing the wire back which allowed for the hanging of a 500gram brass weight (this can be seen in Figure 57, to the left side, behind the lamp reflector) behind one set of lamp reflectors, inside of the thermal shielding but out of the view angle from all areas of the beam, thus avoiding being a radiant heat capacitance. Initial testing of the chamber without any weight and relying solely on pretensioning of the wire proved unsatisfactory as the degree of sag in the wires required a gross vertical translation of the DVL laser up and down roughly 1.5-2.0mm for every 300degF of temperature change. As the sagging wire loosened, greater rigid body motion appeared, and a change in beam-to-magnet top plane distance occurred. After use of the weight was implemented, no gross vertical adjustment of the DVL was needed when testing across the full temperature range.

Concerns were raised that the beam would wander back and forth on the wire, with no means to fix it from sliding along the axis of the EDM hole, especially when harmonically vibrating at mode-I. When testing the beam sought and was stable at the midspan of the wire which was the low point in the catenary of the loaded wire, slight as the deflection was. That being stated, any slight kinks placed in the wire did create enough friction to prevent the beam from freely sliding along the wire; one was placed in the center of the span to take advantage of this.

In previous studies a pair of lower 6lb test nylon mono-filaments were run in parallel across the beam's active node either resting against the magnets (Pearson, 2008) or magnetically clamped between the inner and outer magnets in each stack (Reed, 2007). In either case, the line was routed across the mid-diameter of the stacks. This pair of lines was to prevent rigid body motion of the beam, chiefly, rotation around the passive node or what is called the “swinging mode”. A pair of nichrome wires that were rested with light tension across the mid-diameter of the outer ALNICO magnets were implemented in the current setup, but it was found during an accidental omission in procedure while performing age-in testing, that when the lines were left too low to contact the magnets there was a significant drop in the system's damping. As a result they were left in that position for the TBC characterization testing. It is hypothesized that rotary motion of the magnets imparts some vertical transverse excitation to the two lines with them 180^{o} out of phase to each other, this results in a large amount of damping added to the system. Also, to a much smaller extent, a very slight migration of the node lines that occurs with the added coating as a result slight vertical excitation of the lines may also be bleeding energy out as well (see Figure 99, Section 4.3.3).

The alignment of the beam within the chamber was important in two respects, ensuring no contact of the beam with the radiation shielding and a constant magnet to electromagnetic coupling strength. Positioning with respect to the magnet was critical in two dimensions. The first was that the beam centerline axis remain co-linear to the centerline of the electromagnet. This was achieved by ensuring the beam support rods were strung with the wire across the diameter of the electromagnet. The rods were on a

bolt-circle that was centered common to the centerline of the electromagnet. This ensured that the wire spans to each side of the beam were equal in length. When the beam was excited and seeking the lowest energy position it is aligned over the middle of the coil. The other critical positioning was the separation distance between the centroid of the eight permanent magnets and the top plane of the electromagnet coil, this was controlled by drilling a series of through holes in the beam support rods at regular intervals.

The DVL unit was clamped down and was not moved between tests and specimen change out, as a result the reflected beam dot was a useful locational reference to calibrate position of the beam with. All of the beam specimens had a diffusive reflector dot mounted in the center (x,y = L/2, w/2, and on the surface of the TBC), the beam could be moved back and forth on the wire and the beam suspension wire tensioned higher/lower until the laser spot was aimed on the reflector dot, thus ensuring alignment in the directions lateral to the beam and the proper vertical separation distance from the magnet. Very little adjustment had to be performed when exchanging specimens.

3.1.7. On Filtering

Due to the inability to eliminate all of the rigid body motion, and upon the discovery that the lower lines added significant damping, the use of filtering was required in either hardware or software form. Details of the implementation are deferred until Chapter 5

3.1.7.1. Characterization of Rigid Body Modes and Noise Floor

The rigid body modes and the systems random error needed to be characterized this information is in Chapter 5.

3.1.7.2. Reflectors Dots – 3M and Mica Tape

The reflector dots used in past studies were cut from 3M diffusive retro-reflective tape. It was suspected that these would not survive the design temperature range of the chamber so mica tape was bonded to the beam using Durabond 952 high temperature. Unfortunately, the Durabond adhesive added significant damping to the bare beam, and the mica tape was not a clean diffusive reflector, unlike the 3M tape, which lead to spikes and dropouts in the DVL signal. Ironically, later sensitivity testing on the chamber demonstrated that the 3M tape continued to provided an enhanced return up to 1050degF in vacuum. These issues are discussed in Chapter 5.

With the closure of this Section the detailed description of the chamber as finally implemented to characterize the beams is complete.

3.2. Multi-point Temperature Results

Though the analytical and numerical simulations of the beam covered in Chapter 2 gave confidence that the high Stark number heat transfer condition exists, and that it can reach the design test temperatures, experimental confirmation is the most direct evidence. This was attempted by two methods, by direct contact measurement by using type-K thermocouples bonded in various locations around the beam and by remote means

by capturing the infrared emission power via an infrared (IR) thermal camera. The thermocouples have the advantage of being a procedurally simple method, being able to be located around the entire beam (due to the view angle through the ZnSe window the camera was able to image about 50-60% of the window facing side of the beam), and not being affected by the changes in surface emissive properties between the metallic tails of the beam and the TBC patch. The advantages of the IR thermal camera are it can yield a whole temperature field with one image and it does not disturb the thermal balance of the beam with any wires or junctions conducting heat away from the body.

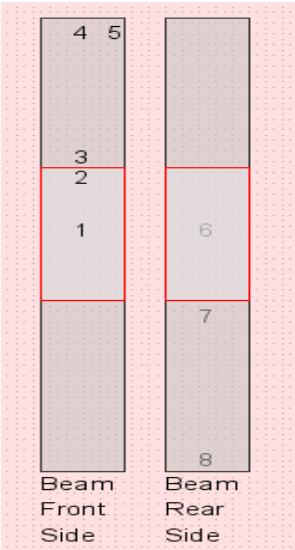


Figure 60: Thermocouple Channel Assignments

Eight type-K thermocouples (chromel-alumel) locally fabricated from 24 gage wire (Omega GG-K-24-SLE, calibrated deviation of 1.9degF at 752.0degF) were attached to the beam using

Durabond 952 high temperature nickel-based adhesive to various locations on the beam as shown in Figure 60, these included locations on both sides of the beam, close to either

side of the TBC-bare beam interface, the center of the tips and a beam corners. These locations where thought to be more prone to have steep thermal gradients, if such were to occur. Thermocouples were bonded to both sides of the beam to assess whether any asymmetries where occurring through the beam's thickness.

The thermocouples where hooked up to a 10-channel rotary selector switch and an Omega DP-41TC thermocouple reader unit that provides automatic cold junction compensation and an ice-point reference. Rated to about a ±0.3degF (±0.17degC) accuracy from temperatures ranging from -454 to 2500degF, this was more than sufficient for the validation effort. These were also the first heating tests of the chamber so the lamps were equipped with eight 100W bulbs. The 8-YSZ coated free-free beam with the eight thermocouples was suspended in the chamber, channels 9 and 10 were the embedded magnet coil and room ambient channel, respectively. The vacuum pump was switched on and allowed to settle at 7.5torr (0.01atm). The timer was started and the lamps switched to 100% power. As the chamber heated rapidly, only the middle of the beam thermocouple was recorded do to rapid changes on all the channels, but as the rate of temperature change slowed, all of the 10 channels were recorded. Figure 61 displays the temperatures of the chamber plotted against time up to one hour after which the lamp power was switched off.

Several things were noteworthy: first, the ability of the eight 100W lamps to reliably heat to 900degF was immediately in question, this and the next test's results, motivated the increase of the wattage to 200W per lamp. Second, the chamber takes some

time to heat to the steady state value, about 3600sec, to reach equilibrium at around 810-820degF. Third, the beam shows an alarmingly high spread in temperatures, even when in the vicinity of the equilibrium state, where the range in temperature is from about 760 to 820degF, about 60degF. This third point was alarming and a closer inspection of the beam within the chamber revealed that the upper corner of it was touching the innermost layer of foil shielding, with about a 0.5-1.0mm^2 contact patch. The two channels that are noticeably depressed below the rest in Figure 61 are #4 and 5. These were the two that were in the upper tip center and corner. Accounting for the localized depression of temperatures in the upper tip of the beam and neglecting these two channels the spread drops to 30degF. This was a clear demonstration of how critical that the non-contact thermal boundary condition was to an isothermal beam-coating system, in other words to maintain the high Stark number condition.

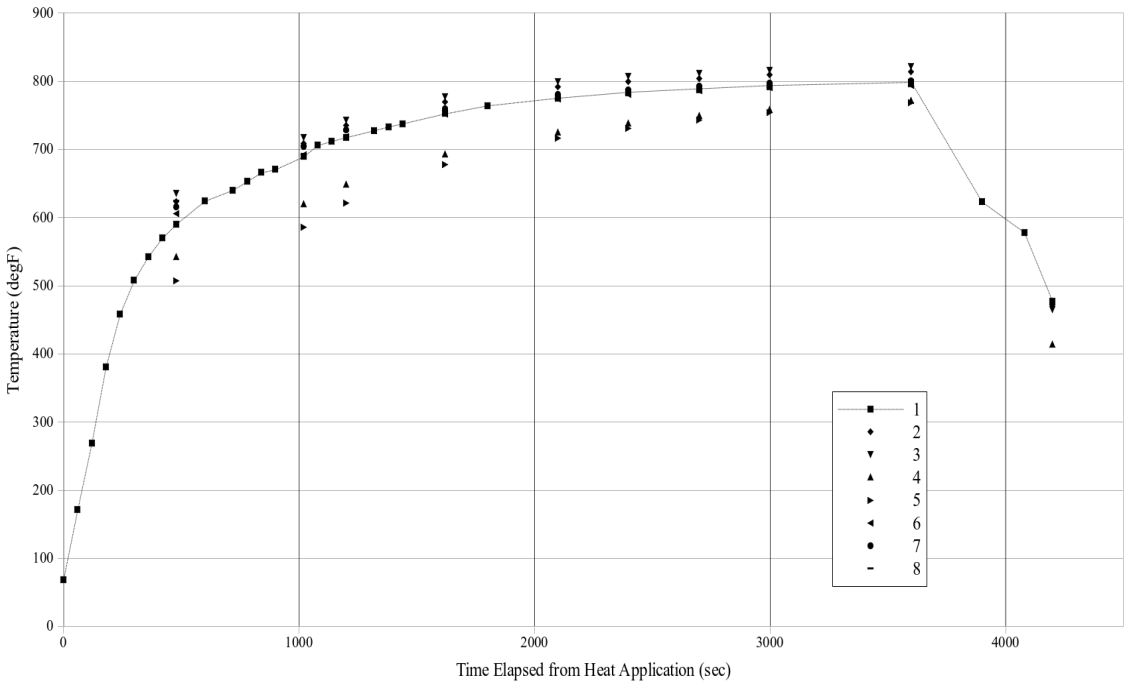


Figure 61: First Heated Run-up of Chamber, TC Temperatures vs Time

Due to the error of not checking for a non-contact condition, a second thermal run up test was readied using the same channel assignments, beam specimen, and power settings. Figure 62 shows the results of this test. In the absence of thermal contact, the beam's average temperature is up about 15-20degF and the variation is within about 30-35degF, except for channel #8. This is the bottom tip thermocouple. Peering into the chamber had revealed the bond cementing it to the beam had failed and it had fallen onto the the radiation shielding floor and was measuring its respective temperature, about 725degF at the 3600sec mark. Again, the beam bulk temperature failed to reach 900degF, the target design maximum temperature, so based on these tests a set of eight 200W lamps and spares were ordered for the chamber.

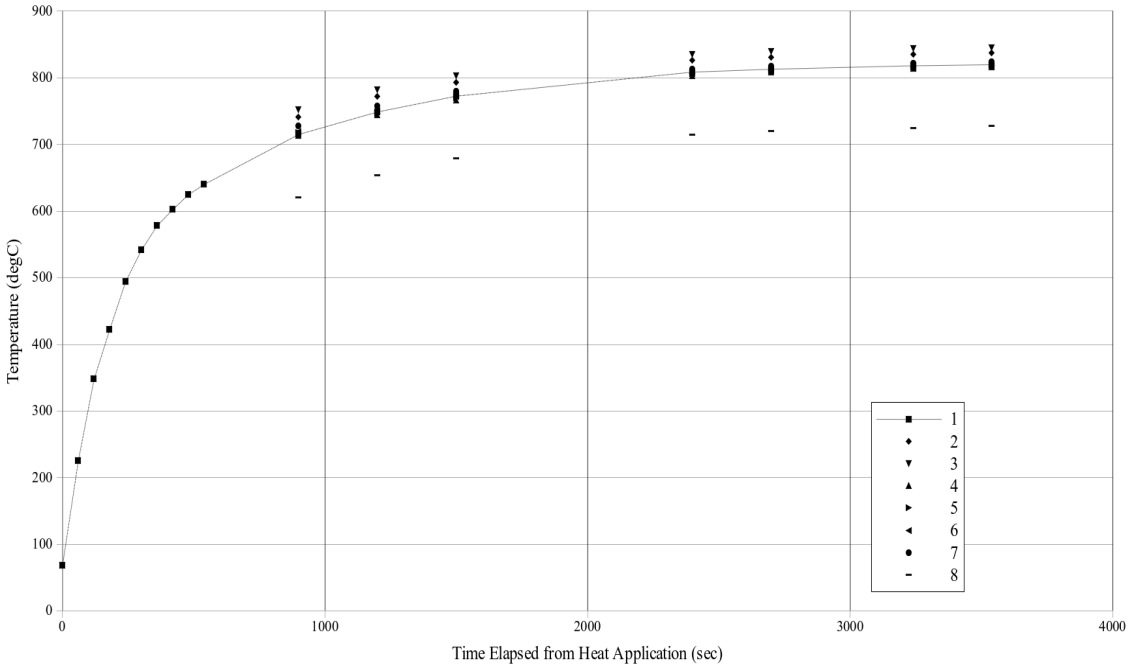


Figure 62: Second Heated Run-up of Chamber, TC Temperatures vs Time

Based on the second run up test the degrees of spread among the thermocouples on the beam was smaller (excepting channel #8) and the first experimental confirmation of a high Stark number environment was promising with less than about 30-40degF variation in the beam.

3.3. Thermal IR Imaging

Multi-point thermocouple measurements established the near isothermal state of the beam, and unwittingly, yielded some insight into the radiation shielding effectiveness and temperature. This information was used to refine the FEA radiation model in Chapter 2 by driving the inclusion of a shielding layer in the 1/4-domain model. But it is useful to use a whole-field technique to capture the thermal gradients. To accomplish this a FLIR-SC660 infrared camera system in conjunction with a 3.0” diameter zinc-selenide window

was used to image the beam, or rather the portion that was able to be imaged at near-perpendicular angles through the window. It is noted that two factors limited the amount of the beam that could be imaged at one time; the first was the limitation of the field of view of the FLIR camera when set outside the tunnel-like port of the chamber. The second factor that further limited the effective image-able area was the optical aberrations from the edges of the window that attenuated IR emissions at the more extreme angles as well the as the reflections off of the aluminum lining the optical port. Moving the camera around while remaining focused on the beam established that these cooler temperature bands were artifacts not fixed to the beam in the chamber, but to the window.

3.3.1. Thermal IR Imaging Technique

The multi-point thermocouple measurement validation of the chamber yielded promising results, but to gain a deeper understanding of the system thermal imaging of the beam chamber was attempted using a FLIR SC660 infrared camera system. This system, featuring a 640x480 pixel resolution and a 0.04°C sensitivity and ±1°C (1.8°F) accuracy, directly measures the radiosity coming from an object, which is the visible and infrared light that enters the camera's aperture from the imaged object. From application of the Stephan-Boltzmann law to the emitted radiation, the temperature of the object can be determined within the camera's on-line software or in post processing software. Figure 63 gives an idea of the potential complexity of the system under measurement and what needs to be characterized before measurement of the free-free beam solid can proceed with accuracy. To review, radiosity as the total energy arriving at the camera and

is a sum of transmitted, reflected, and emitted radiation. Received radiosity is measured pixel-by-pixel and converted into a thermal temperature map given some characteristics of the system under measurement.

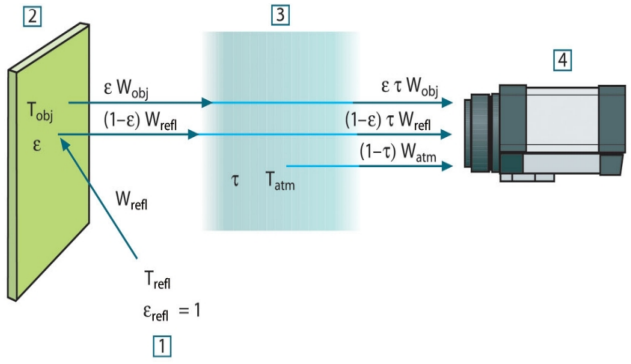


Figure 63: Thermal Camera Characterization (FLIR SC600 User Manual, 2010)

The most important of these are: the emissivity of the solid (ε_{TI}, ε_{TBC} object "2" in Figure 63), the temperature of the lamps and chamber environment (T_{refl} object "1"), the transmissivity of the window port and atmosphere (τ, object "3"). Of lesser influence over short distances and dry conditions, are the emissions from and absorption to the passing thermal radiation from the air (T_{atm}, object "3") (FLIR SC600 Series Users Manual, 2010).

To begin characterization, the camera was aimed at a piece of black electrical tape fastened to a beaker of vigorously boiling water. The camera's object emissivity was adjusted until the tape was at measured at 212degF, that of the boiling water. The ε_{TAPE} was about 0.95 (FLIR SC600 Series Users Manual, 2010). Care was maintained to minimize the distance to the camera lens through the air, to minimize the emissivity and absorptivity effects of the air. The ZnSe window was then placed in the small gap between the tape and the IR camera lens and the built in transmissivity compensation

setting of the camera was adjusted until the temperature came back to 212degF, at around $\tau = 0.75\text{-}0.76$. Keeping the ZnSe window at room temperature by blowing room air on it with a fan while working so close to the hot plate source ensured the window would not start radiating energy in of itself in a significant manner. This agreed well with the included data chart of transmissivity versus wavelength (see Phoenix Optics website).

The transmitted energy is negligible for an opaque solid in a vacuum. An assumption was made that thermal radiation absorption by the air along the image path from the chamber ZnSe port out to the FLIR camera lens was minimal. Since the TEFF lab had low humidity and the lens to thermal (ZnSe) window separation distance was only about 6 to 8in this was deemed acceptable. This distance was chosen as it could capture the largest amount of the beam at the 45° field of view setting of the camera.

Determination of the emissivities of the bare titanium and the TBC beam was more problematic. The beams were immersed in the boiling water and then removed to be imaged within a dark box (to avoid specular reflections on the titanium region from the lamps and people). The problem was the beams cooled very rapidly on removal from the boiling water precluding the capture of good thermal images. Neither could they could be imaged within the beaker as the glass and water are both IR opaque. Placing the beam, equipped with two mounted thermocouples within the chamber, supplying a 0.01atm vacuum, and taking it to 300degF was attempted to determine the emissivities. The $\varepsilon_{TBC} = 0.92$, 0.88, and 0.87 at 300, 600, and 900degF, respectively was determined, while the titanium had regions of distressingly high temperature. With the surface

emissivity of camera set to around the book value given for ε_{TI} = 0.23-0.30, these patches were in well in excess of 700-720degF, which is very non isothermal and far from the thermocouple readings at around 300degF. Even heavily oxidized titanium, while appearing a diffuse reflector in the visible wavelengths, is a specular reflector in infrared wavelengths. A dramatic demonstration is that the FLIR camera can resolve individual fingers by their reflection from the beam when they are held splayed above the beam, even when waved around. Realizing that the lamp bulb envelopes' own reflections were the source of the dramatic hot spots upon the beam bare TI tail regions, the bare titanium regions were sprayed with Spotcheck SKP-02, a fluorescent dye penetrant inspection developer compromised of fine talcum power. It was thought that it may be a lot like snow optically speaking, that is a fractal-like surface with near-blackbody properties in the IR radiation bands. Upon reheating to 300, 600, and 900degF, this proved to be the case, the emissivity of the developer was around 0.94 to 0.91 as the temperature proceeds from room temperature to 900degF. The specular reflections were not existent with the sprayed on developer coating, this was verified by moving the camera around and hanging a bare beam side-by-side for comparison.

At this point, only the top of the three transmitted radiation modes from object 2 to the camera in Figure 63 was deemed to be significant and the system was deemed ready for validation measurements. It is noted that these surface emissivities are temperature dependent, and that if an FEA model of extreme accuracy is deemed important than these values would need to loaded as lookup tables into the code.

The chamber was now equipped with a free-free 8-YSZ partially coated beam, sprayed with developer on the bare titanium regions, along with the dummy specimen to the side. Each was equipped with two thermocouples. Using eight 200W lamps, the chamber was imaged at 70, 300, 600, and 900degF (148.8, 315.5, and 482.2degC), the planned test-points to evaluate the coatings for their complex modulus. Also, the beam was taken to 825degF in bulk averaged temperature and IR imaged as well, this was to be used to compare spatial temperature variation back against the second 8 channel beam run performed in Section 3.2, and the results are presented in Section 3.4. This was also for comparison of the FEA, finite difference, and analytical models against each other. Figure 64 shows the camera, thermal IR window port, chamber, and the heated beam glowing within the chamber.

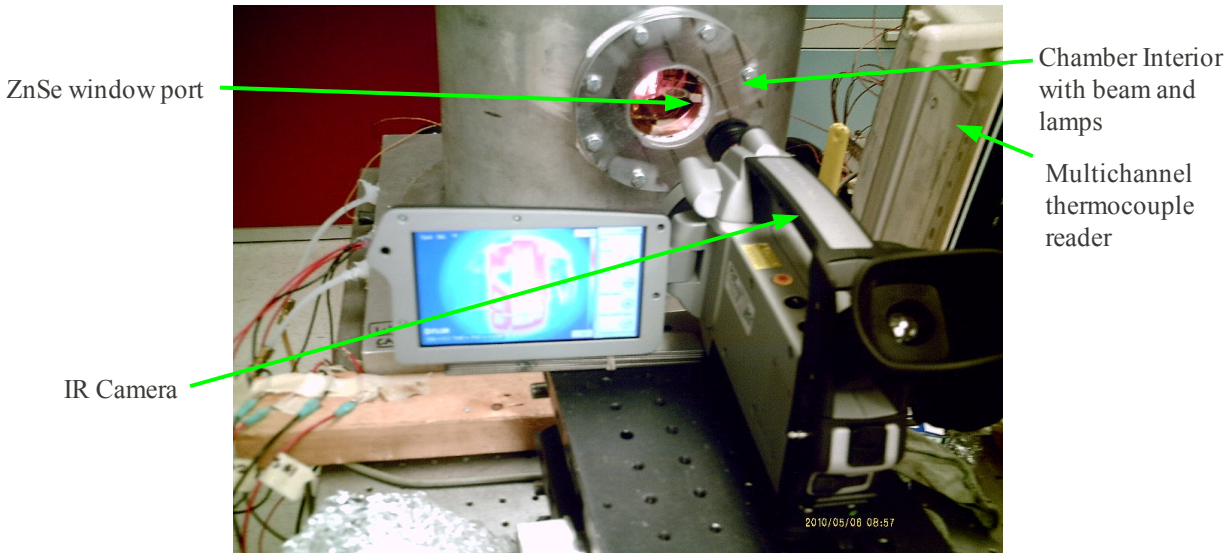


Figure 64: FLIR-SC660C Thermal Validation Setup

At each temperature condition, an image of the beam was captured in a still JPEG

image format using the FLIR camera. These pictures were later loaded into the FLIR "QuickReport" post processing software to allow adjustment of the emissivity for the two regions of the beam, setting the isotherm colors, and performing pixel block-averaging to determine sub-region average temperatures.

3.3.2. Thermal IR Imaging Results

Once all of the preliminaries of characterizing the window and beam were complete, two thermocouples were left bonded to the beam, channels #1 and #6 (See Figure 60) at the midpoints on the front and backsides of the beam. The 300degF beam image is shown in Figure 65, from it once can see that large swaths of the beam are nearly isothermal and close to the set point of 300degF. Furthermore the two boxes, one in blue on the upper, developer spayed region of the titanium with an average of 290.5degF and the lower pink one, over the 8-YSZ coating region, with an average temperature of 302.5degF. These boxes are an area of which the area-averaged temperature is reported by the FLIR either within the camera or the QuickReport software.

The main driver of the difference between the two is the difference in the emissivities

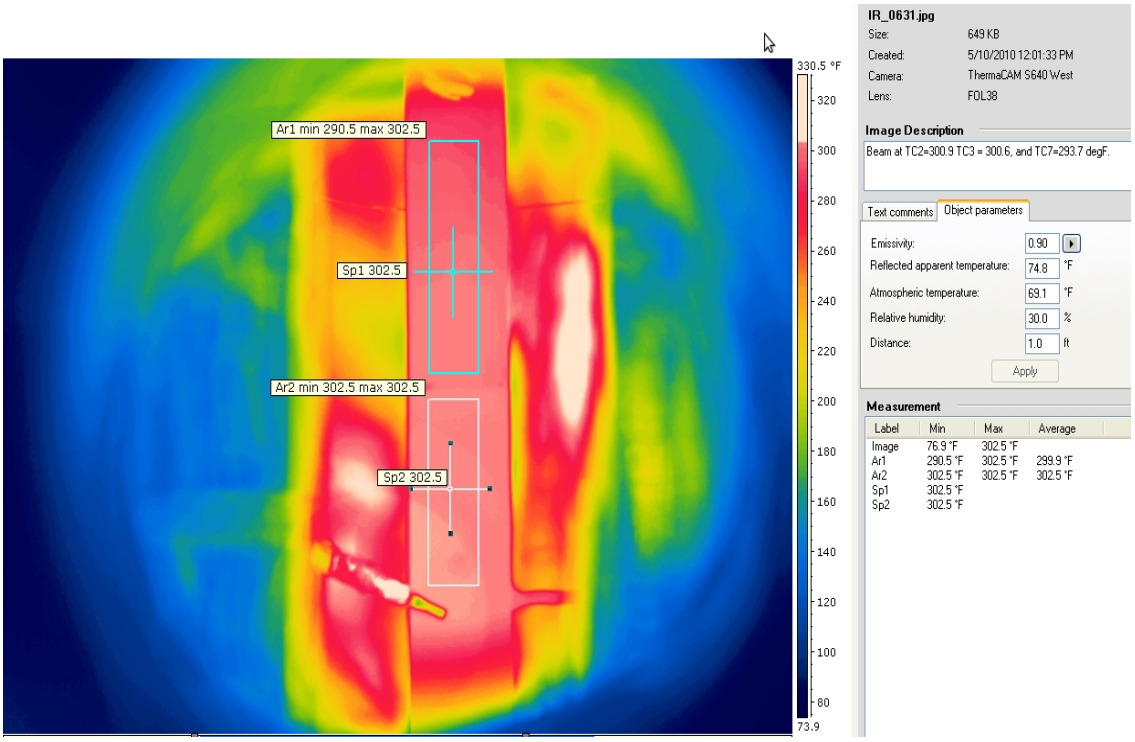


Figure 65: Thermal IR Image at 300degF Set-point (Temperatures are degF)

between the two regions which are $\varepsilon_{TBC} = 0.94$ and $\varepsilon_{TI} = 0.90$. As the emissivity is set to the lower value of the powder coated titanium, the more efficient radiative region of the TBC appears hotter as the emissivity is artificially low for this region, as a result it appears hotter than it would be if the camera's surface emissivity value is tuned into it. Notable from the thermo-graphic image is the lack of any large isotherms upon the specimen except at the top and bottom edges of the window where diffraction of the infrared light occurs.

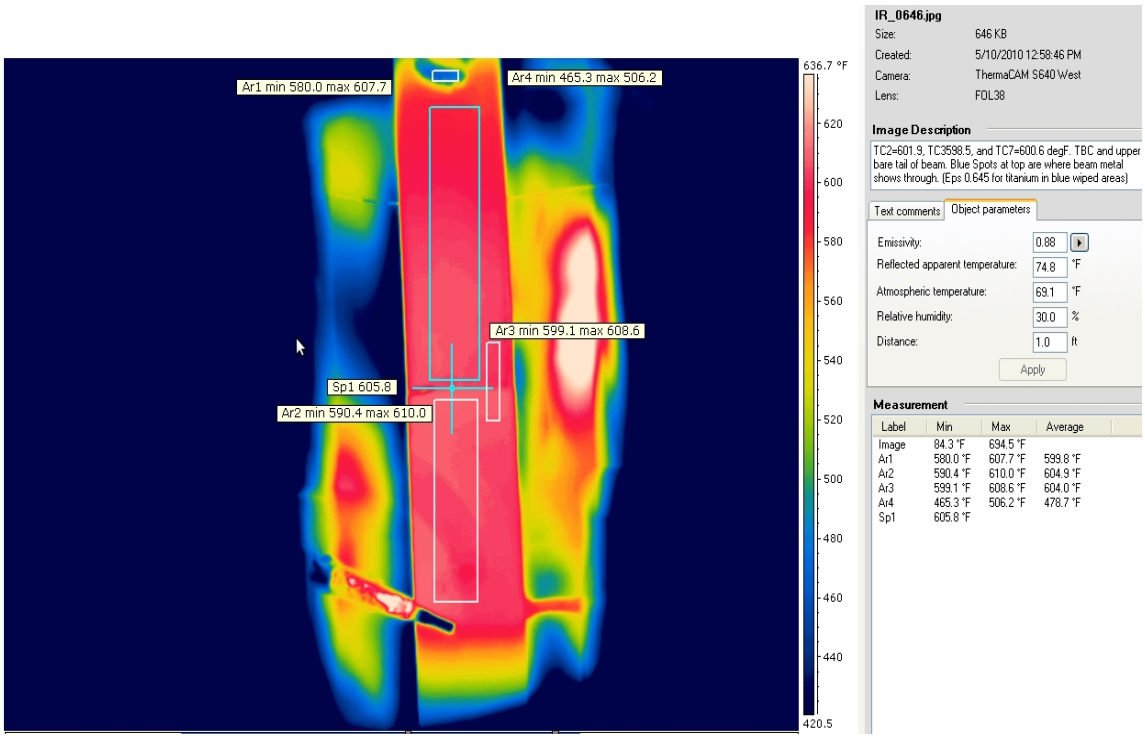


Figure 66: Thermal IR Image at 600degF Set-point (Temperatures are degF)

These apparent isotherms were confirmed to be an artifact of the window and not real isotherms on the beam. When moving the camera around, they stay fixed with respect to the edges of the window and move over the beam itself, hence fixing the source of their existence to the window. They could be reduced in apparent size by lining the short tunnel to the ZnSe port with black felt or other non-IR reflective material and by moving the camera further out from the window thus reducing the angle of refraction for IR light emitted through the window. This second correction was not done though as the pixel resolution on the beam would drop. Another notable takeaway is the closeness in emissivity between the coated beam and the TBC coating, there is little thermal gradient across the beam-TBC interface. Another notable finding is the crocodile clip, seen clipped below the pink and clipped to the beam, introduces no visible localized cooling in

the beam, the clip itself appears colder as it is bare, burnished copper and therefore has a much lower emissivity, about 0.07, than the coating region it is clipped to (FLIR SC600 Series Users Manual, 2010). As a result of this finding, clipping of the thermocouple junctions to the beam and dummy specimen was performed in the remaining work, these being much easier to work with than potting them with the Durabond adhesive. This whole-field image gives confidence that the chamber is a high Stark number, lumped capacitance situation.

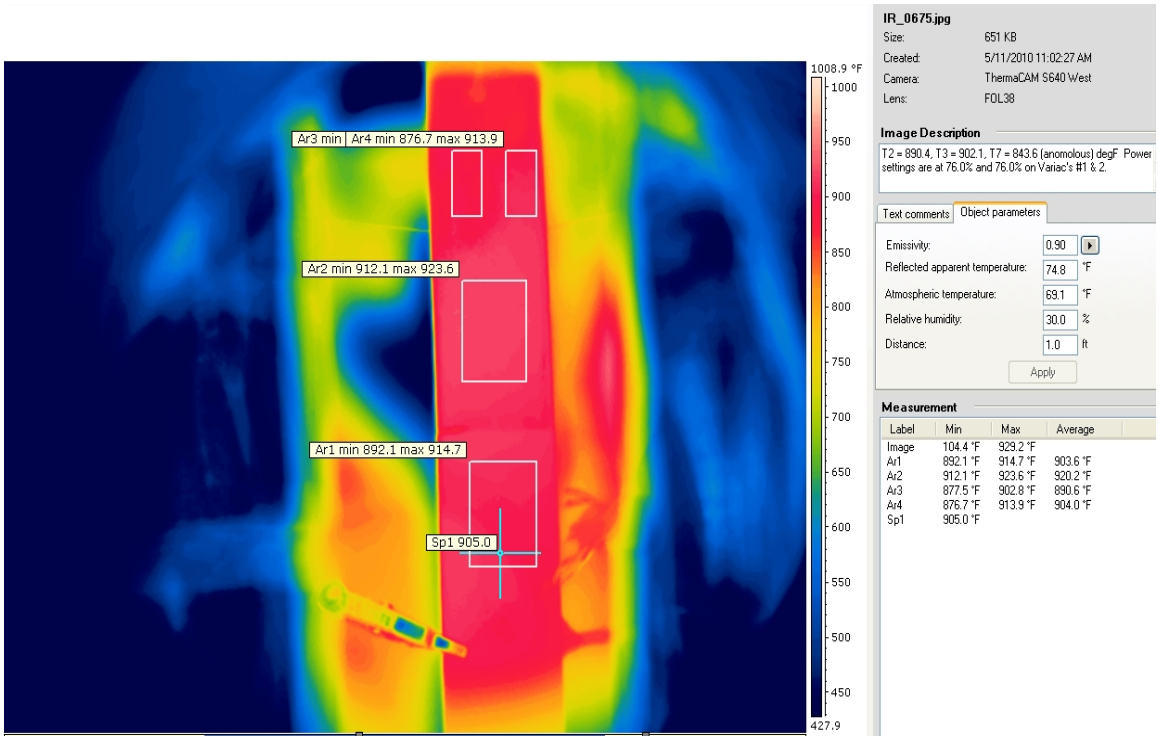


Figure 67: Thermal IR Image at 900degF Set-point (Temperatures are degF)

Figures 66 and 67 show the thermo-graphic images that were taken at 600degF and 900degF as indicated by the thermocouple channels. Again, the same general features were noted at the 600 and 900degF set-points that were seen at 300degF. The beam

remained quite close to a uniform isothermal state, the clip introduced no discernible local thermal disturbance into the beam system, and the TBC coated regions emissivity is slightly higher than that of the developer coated TI. One interesting takeaway from the image can be seen in the small white rectangular box ("Ar4") in the blue isotherm. This was a small region where the developer was wiped away accidentally while suspending the beam in the chamber. By adjusting the emissivity for these location at all three temperature conditions and matching the reported temperature of them to those of the surrounding powder-coated regions, the beam's underlying titanium was determined to have an emissivity at around 0.60, 0.645 and 0.67 at 300, 600, and 900degF, respectively. This is somewhat higher, about 0.15 higher, than the values reported over a similar range of temperatures, but perhaps the removal of the talc was not complete when the smearing occurred (FLIR SC600 Series Users Manual, 2010).

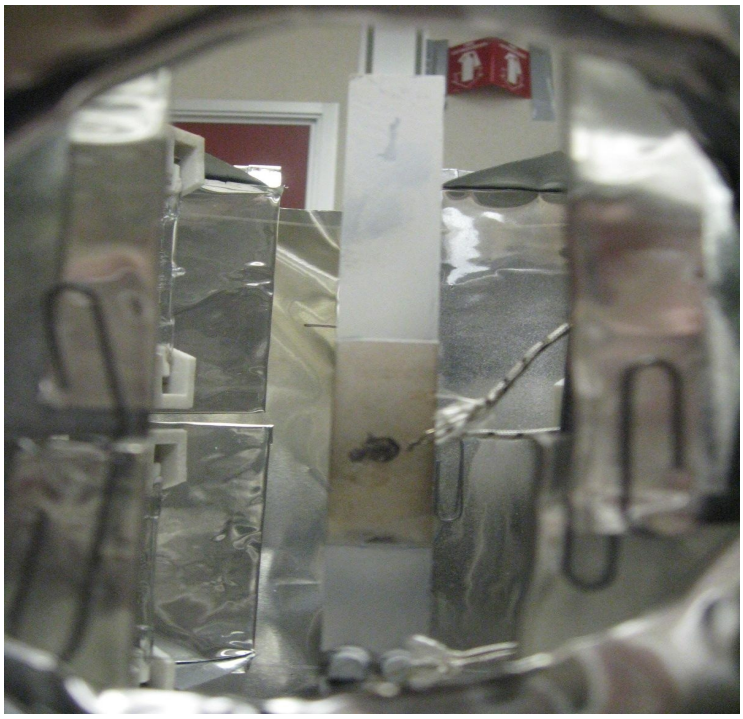


Figure 68: Optical Image of Beam in Chamber from IR Camera View

The beam setup as seen from the vantage point of the camera in visible light is instructive for comparison and to help identify image artifacts as per Figure 68. Note that the smeared region was re-coated and the crocodile clip had been removed before this image was taken. The remaining features remained the same. As can been seen from the thermocouple wires coming in from the side and their signatures on the FLIR thermographs on the right side of the beam, the aperture angle of the visible light camera is somewhat wider than that of the IR camera. The optical camera sits at a little higher height relative to the beam than the IR camera did, it being a smaller unit, yet with a higher lens.

A natural question to raise is did coating of the bare regions of the beam with laser developer to eliminate specular reflections from the lamps radically shift the beam's bulk thermal equilibrium temperature away from that of the uncoated state? Also, did artificially closely matching the surface emissivities between the bare and coated regions enforce an isothermal state that was aberrant in nature? To address these, the FEA ¼ domain model detailed in Section 2.4.5 was used to run two cases. All the boundary

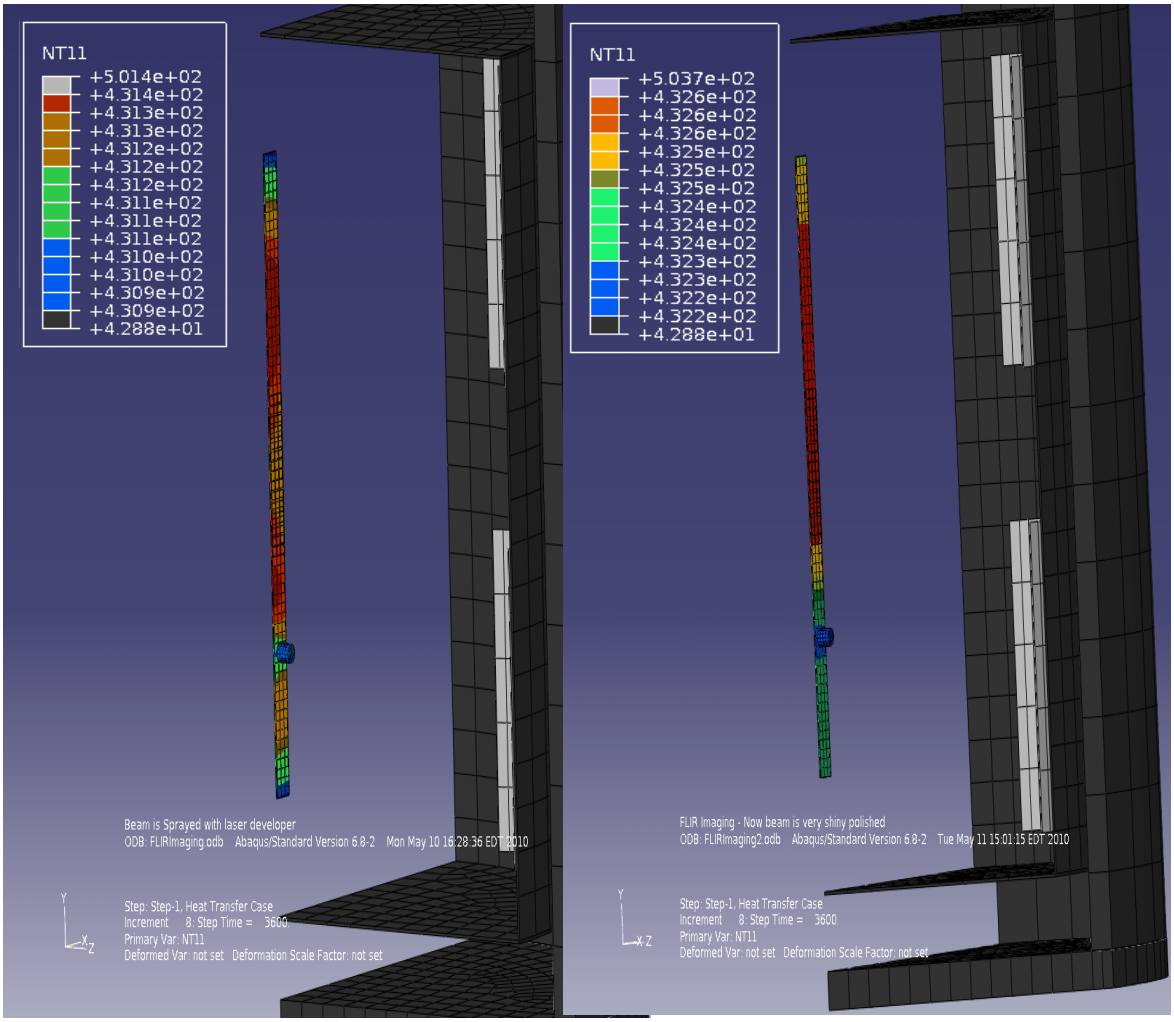


Figure 69: FEA; (left), Highly Polished ($\varepsilon_{TI} = 0.10$), (right), Near Blackbody ($\varepsilon_{TI} = 0.95$)

conditions and material properties were the same for the two cases, except for the emissivity of the bare titanium which in one case was set to 0.95, representing the

developer coated titanium. For the other is was set to 0.10, representing a highly polished beam. The second case is quite conservative an assumption as highly oxidized titanium is more in the range from 0.23 to 0.40 emissivity. Figure 69 shows the isotherm plots of these two cases, in the second case the beam average temperature is around 431.1degC (ε_{TI} = 0.10) ranging across about 0.5degC, and for the other case the beam average temperature is around 432.5degC (ε_{TI} = 0.95) and ranging across about 0.4degC. Between these bounding solutions, global temperature shift is small (about 1.4degC) and the isothermal state is still preserved despite drastic change in the emissivity of the metallic titanium surfaces.

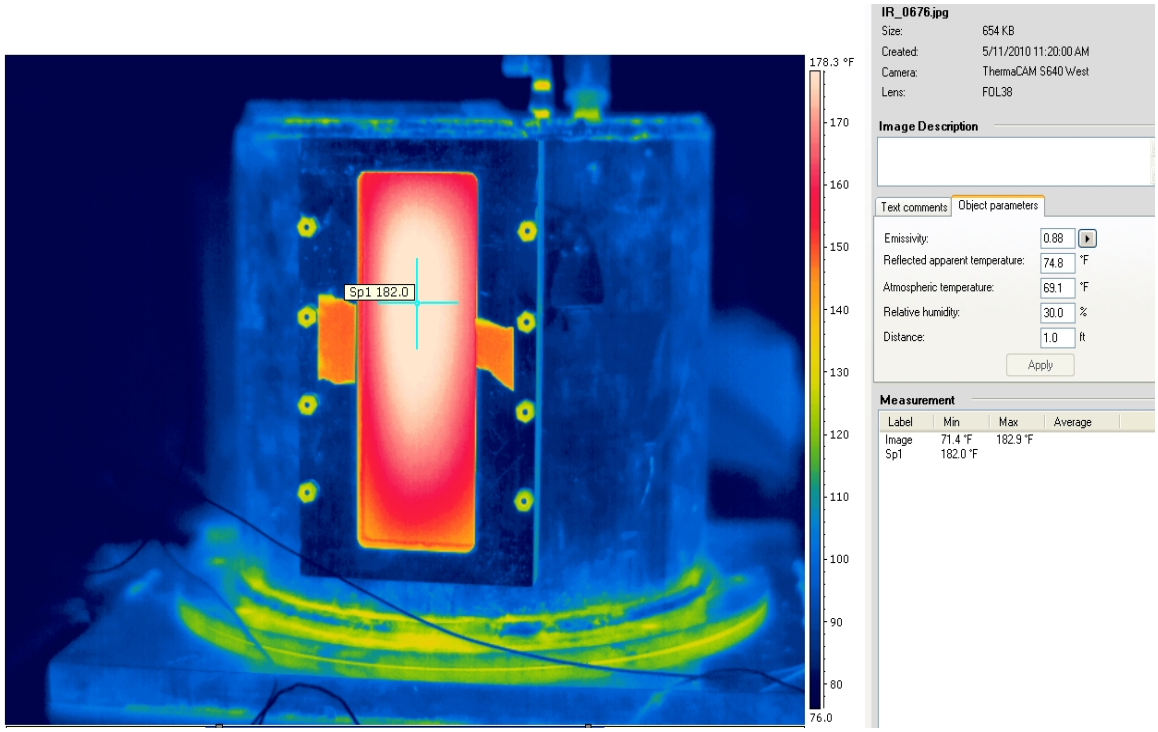


Figure 70: IR Imaging of outer chamber.

Concerns of safety were raised about the chamber's outer walls being too hot when at at highest design heat setting, based on the initial FEA work, the outer walls

were about 140degC, well above boiling temperature. This was due to the omission of radiant heat shielding in the initial design; it was assumed that vacuum and well-aimed lamps would be sufficient (See Section 2.5.2). As a result triple layer aluminum foil shielding surrounding the lamps and beam was added to the design and based on modeling, this dropped the outer chamber walls temperature to around 40degC in the hottest spot in the aluminum. The FLIR camera was aimed at the chamber, with a piece of black electrical tape of known emissivity affixed to the surface. The tape is of known emissivity and matching the temperature of the aluminum in its immediate vicinity by adjusting the camera emissivity allowed for determination of the emissivity of the outer aluminum pressure vessel walls. The chamber was then imaged from several angles, Figure 70 is an example of this. The hottest spot was revealed to be the laser glass window as shown in Figure 70, this region reached about 180degF when the beam was at 900degF, the two orange warm regions to either side of the glass are two pieces of masking tape with alignment marks (for vertical alignment of the beam in the chamber using the laser beam). As can be seen, the glass port was the hottest portion of the chamber being IR opaque (and therefore absorbing and re-radiating much of the heat) as well as exposed to the interior irradiation through the slit slot in the 3-layer shielding, it was a hot-spot that the experimenter had to remain mindful of.

3.4. Isothermality Findings

With the results to the analytical and numerical modeling presented in Chapter 2, and of the two experimental measurement methods presented in the previous sections, it

is worthwhile to compare the findings. Figure 71 details the comparison between the various methods in an absolute (right) and compressed temperature scale (left). The first thing to note is that all the methods are predicting a temperature field within a 50degC of variation; if the unoptimized nature of the severe irradiation assumptions in the FD code is acknowledged and the results of it discounted, the variation drops to about 20degC. The FEA and FD simulations, along with the analytical solution, predict a near isothermal beam with about ±1.0degC variation. These are all compared against the eight 100W lamps running at 100% power, for a bulk temperature around 435-437degC (815-820degF).

The analytical solution predicts essentially no variation down the length of the beam, despite the variation in surface emissivity of the finite length of the sources. To drive any significant variation in temperature, the illumination striking the beam would have to strongly vary, and even then, the temperature variation induced in the beam would be modest at best (See Section 2.4.1). The finite-difference solution over-predicts the beam's global temperature field, but this was due to using a severe assumption in the code, that is the beam radiating to a cold blackbody surroundings and having a higher impressed irradiation intensity to overcome it. This was in assumption of a constant field of 10X the solar constant striking the beam on all x-facing surfaces, despite the fact that the system is actually axisymmetric and that the real sources are finite linear sources. While the irradiation value (G) was adjusted for the analytical solution and its virtual source pair, this was not done for the finite-difference model as it would necessitate rerunning the model to convergence. The finite element model captured the full 3-D

effects of the chamber system and was fairly accurate after being tuned into the physically realistic flux values of the 100W lamps and having the layer of shielding added to the model (See Section 2.4.5). The model demonstrated that even large changes in the emissivity of the various regions of the beam, like a blackbody set of magnets imposed only minor variations in the temperature field. The thermocouples initially provided alarming results across the two trials of testing until anomalies in the experiment were observed. One was triggered by a beam observed to be in contact with the upper foil shield in one test, in the second it was triggered by a thermocouple that dis-bonded from the beam's lower tip and fell onto the lower foil shielding.

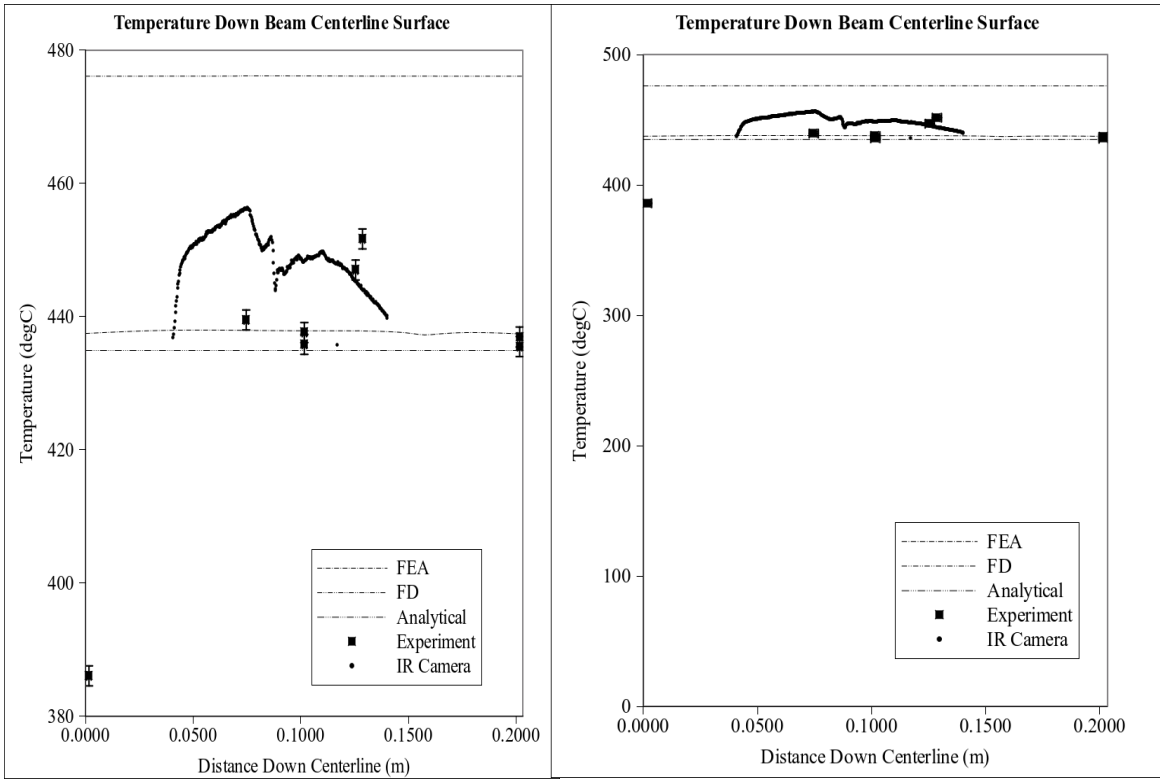


Figure 71: Comparison of Temperature Findings Down the Length of the Beam

All anomalies accounted for, the data as realized from the multi-point thermocouple measurements, only exhibit a 15degC total variation. This is with the

recognition that the very low temperature of the left-most thermocouple, represents the lower tip channel that had subsequently detached from the beam and fell onto the lower shielding. The thermal camera IR temperature range measured, which is over about half of the beam length (due to the limited imaging angle through the ZnSe port), exhibits the same measured variation. This is with the inclusion of the refractive effects that depress the temperature readings at the edges of the window. This can been seen with the roll-off in temperature at the ends of the measured range. Excluding these window edge variations reduced the temperature variation from the IR measurements to about 10degC. Random variations in the measurement precision, as can been seen from the 0.95CI error bars does not explain all the variation. For the thermocouple measurements, a likely cause of variation in temperature might be the integrity of the Durabond bonding to the beam, variations in the quality of the spot welding, and local manufacture of the junctions. (Recall the 2-point thermocouple calibration check placed the TC variations across the population of 10 channels at about ±9.5degF (about ±5.0degC)). These variances aside, the high Stark number (high Stark number is a strong radiation-conduction serial thermal circuit that is lumped capacitance in nature) of the experimental beam and chamber results in near isothermal conditions with only slight departure from it. Variations in coating emissivity, the lamps having bright spots, the reflectors having focal irregularities, are departures from the ideal model that the modeled system do not have. Evidence of the emissivity variations can be seen in the IR camera temperature plot at the beam coordinates of 0.075m and 0.125m, which are the boundaries between the developer coated bare titanium and the TBC patch the where camera exhibits a jump in

the measurement. Even for the worst case, where it is assumed where the measurement variations are mainly due to real isotherm variations within the beam, the variation of about 15degC would provoke only a small variation in modulus and therefore stiffness down the length of the beam. 15degC, which is about 27degF, corresponds to only about ±0.4 Gpa of variation in the modulus, about ±0.44% from the value that was determined to be around 91.4Gpa at 900degF (See Section 5.3). Given this fairly small temperature induced variation in modulus the of the tuned resonant method on the beading mode-I free-free beam seems a valid assumption.

3.5. Dummy Titanium Specimen Calibration/Bias

Closed loop monitoring of the temperature of the beam is a very useful task. Although initially deemed not necessary due to the repeatability of achieving points on the power curve determined in Section 3.6, it proved procedurally useful. Although the dummy specimen was suspended from a rigid wire about 1.5 inches to the side of the free-free specimen (See Figure 57, Section 3.1.3), the difference in temperature between it and the statically hanging free-free beam was small, under 2.5degC (4.5degF) across the design temperature range of the chamber. Despite not being located at the center (focal) point of the polar lamp array, it is within a highly-reflective, enclosing cavity and is closer to four of the eight sources than the beam itself, placing it into a very similar heat transfer environment. This is evidence that the positioning of the free-free beam in the chamber, while critical for consistency in the strength of the magnetic coupling moment, may not be so from a heat transfer standpoint. The advantages of the dummy

beam is that is allows for direct measurement of the thermal environment in the chamber, and allows for intentional overshoot in the heating methods with a closed-loop control thus reducing time to reach a desired thermal equilibrium state.

3.6. Chamber Power Curve Calibration

After confirmation of isothermal conditions over the beam-coating system, one of the important tasks to allow the imposition of the desired thermal environment in the chamber was to determine the equilibrium temperature of the beam and dummy specimens as a function of the power input to the lamps. Secondary to this task, was determining the time to come to an equilibrium (thermal pseudo time-constant, see Section 2.3) state, and the repeatability of reaching the same thermal state. For this a calibration effort was run.

The chamber was setup with 10 channels of thermocouples (as per Figure 60), two on the dummy specimen, five on the beam, one embedded within the electromagnet, one in the ambient lab, and one spare tucked away in the chamber. The lamps variable ac transformers were both set to levels of 20, 40, 60, 80, and 100% of full scale power in the course of the testing. The initial room temperature values were taken, the time noted and the first power level imposed. The power band was set to 0, 20, 40, 60, 80, and 100% of full power for the 100W set of eight lamps and 0,15,35,55, and 75% for the 200W set. Readings on just four channels on the beam and dummy were taken while temperatures changed rapidly. Once the rate of change slowed down all ten were recorded at regular intervals. Figure 72 displays the average of the two dummy beam and two channels in the

center of the free-free beam as a function of time. After the values were settled to to a slow rate of change

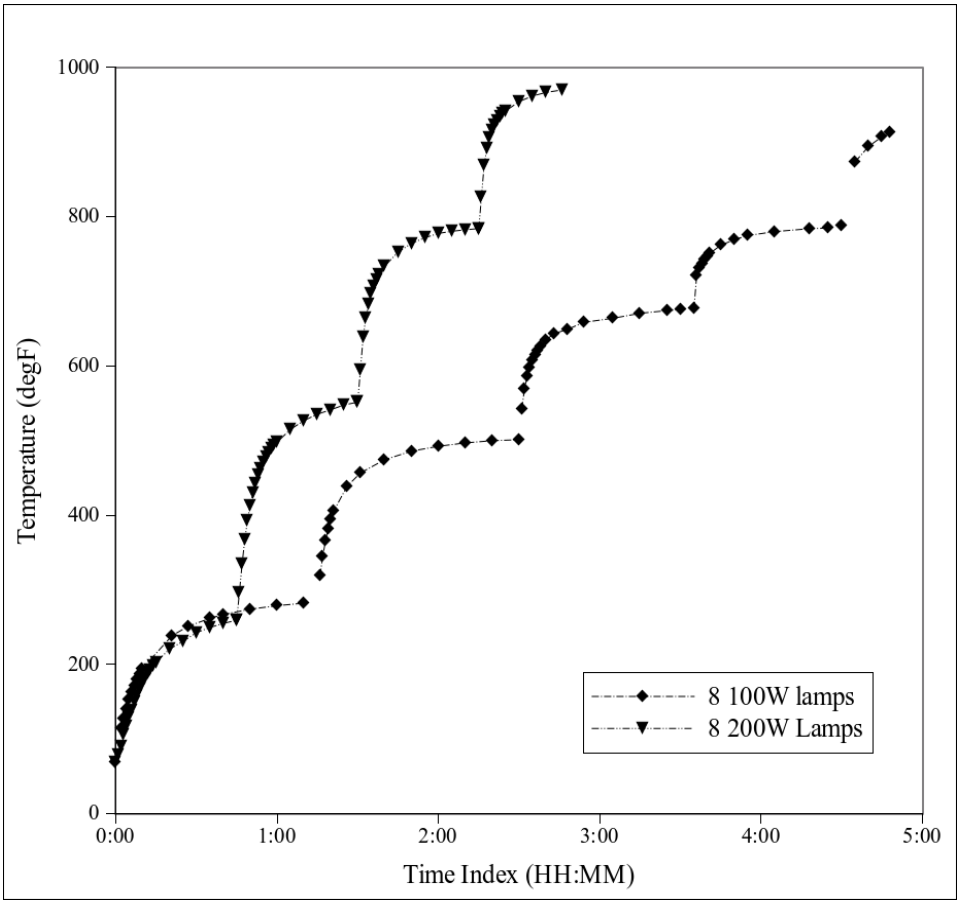


Figure 72: Temperature on Channel #3 versus Time Elapsed

(after about one hour and 15 minutes), the next power setting was imposed and the process repeated. The curve of the temperature versus time has a scalloped appearance, at each setting the system is settling towards some steady-state value. A hyperbolic functional regression fit at each power level was sought with special interest in the horizontal asymptote. This represented the steady state (equilibrium) value that particular power setting. These six points at 0, 20, 40, 60, 80, 100% and the attendant asymptotic values extrapolated from each hyperbolic fit from Figure 72 (for 0% the initial ambient

temperature readings were used) were then used to fit a second order polynomial fit as shown in Figure 73.

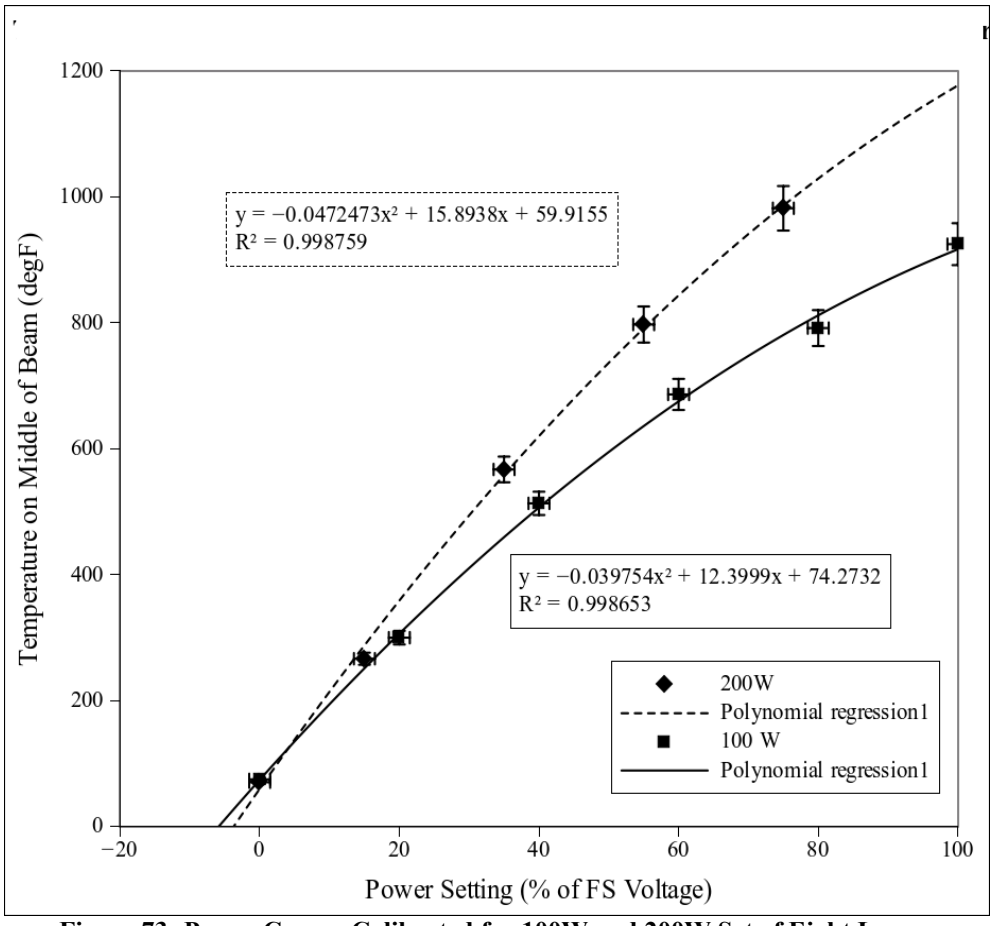


Figure 73: Power Curves Calibrated for 100W and 200W Set of Eight Lamps

The power curves from this were determined to be for a set of eight 100W lamps:

$$T = -0.0397x^2 + 12.399x + 74.273 \quad ; \quad (100\text{W}) \tag{65}$$

and for eight 200W lamps:

$$T = -0.0472x^2 + 15.893x + 59.915 \quad ; \quad (200\text{W}) \tag{66}$$

where "T" is the temperature of the beam and dummy in degF, and "x" is the percentage of full scale power (0-100%) of the two variable AC transformers; both are set to the

same level. The eight 100W lamps were used for initial testing and for the target test temperatures of 70, 300, 600, 900degF the power settings were 0.0, 19.4, 50.61, 96.3%, respectively. It was noted that in initial isothermal trials with 100W lamps that achieving 900degF was possible on some runs but not on others. There was minimal reserve capacity available and exploiting thermal overshoot to reach desired temperatures rapidly was limited at the higher settings. The occasional failure to reach 900degF on some heating trials probably had to due with depression of the mains voltages during the peak cooling months of summer, which were down 6-9VAC below the normal value during the hot hours of the day. Since the variable AC transformers had sufficient reserve capacity, a set of 200W bulbs were procured and the chamber was calibrated using the 200W set. As seen in Figure 72 besides the room temperature ambient, four settings were imposed on the system, this time at 15, 35, 55, and 75% of full power; these values were estimated to bracket the temperature set points desired. Taking the asymptotic temperature values from hyperbolic function fits at each individual power setting condition in Figure 72, similar to as was done for the 100W lamps, another 2^{nd} order polynomial was produced.

For the target temperatures of 70, 300, 600, 900degF the settings were 0.0, 15.8, 38.3, 65.6%, respectively. Since the power draw of the 200W lamps was very close to the max power factor of the transformers, care had to be taken to smoothly and (relatively) gradually vary the power settings to avoid destructive arcing of the transformer brushes as well as avoid surges that would blow the circuit protection fuses that were sized very closely to the variacs maximum power factor. But with the extra radiant power available

now, the rig could reliably reach the design maximum of 900degF, as well as allow overshoot to achieve any set point within 10-15 minutes. Maximum temperatures in excess of 1050degF were later obtained with an excited free-free beam using the eight 200W lamps.

The next thing determined was the thermal settling time of the system to reach equilibrium, in other words, how long does the chamber need to sit in order to reach the intended temperature setting? Typically linear systems are reported in terms of the time constant. This system, although it is non-linear, will be characterized using (See Section 2.3 for an analytical description) a "pseudo time constant", so dubbed recognizing that the system is non-linear. Figure 74 is a plot of the temperature of the beam under a 100W load-up calibration test towards the 300degF condition. No intentional overshoot was used, the system was set to the power setting based on the calibration curve for a desired target temperature and allowed to come up towards the equilibrium value monotonically. Superimposed on the temperature-versus-time plot are the values of 64%, 86%, and 95% of the change from the initial to the final value, known as the 1^{st}, 2^{nd}, and 3^{rd} time constants (or 1τ, 2τ, 3τ).

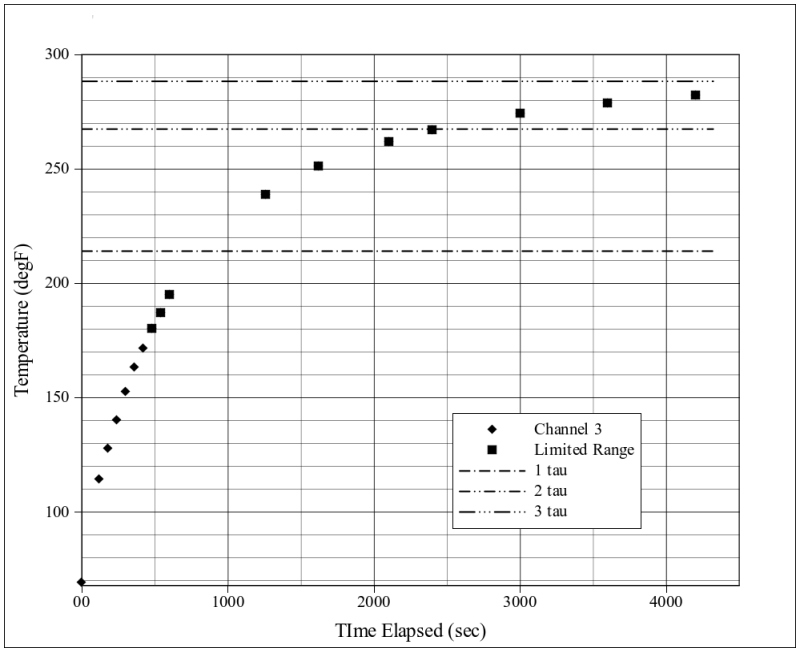


Figure 74: Beam Pseudo-Time Constants, Temp on Chan. #3

From Figure 74 is can be seen that 1τ, 2τ, and 3τ are found at 750, 2400, and ~5000sec after the lamps were switched on. The intervals between the time-constants are not the same as they would be for a linear system, and it can be seen that a good two hours would be needed to get the temperature within about ±2.0degF (more likely a -2.0degF bias error if heating from below up to the set point). As a result of this time length measured as well as estimated from Campos solution, it was decided to keep using the dummy specimen in order to enable intentional overshoot and shorten the time to arrive at a set-point temperature. A workable setting with minimal temperature drift to within ±2.0degF could be achieved within about 10-15 minutes. As can be seen from Figure 72 the various pseudo time constants are pretty much invariant of the equilibrium temperature as evidenced by the similar shape of the curves.

3.7. Magnet Coil Calibration

It is worthy to report the beam velocity and/or displacement in terms of the actual forcing moment acting on the beam, as opposed to the coil current, or the amplifier stimulation voltage, as it is a more directly applicable quantity to the energy storage and dissipation going on in the free-free beam system. Though this could be attempted by employing a analytical solution or by FEA analysis of the electro-magnetics, it was determined the best way to quantify this for the current study was by direct calibration of the method of loading. A method described by Hoover was adopted to the current apparatus (Hoover, 2004).



Figure 75: Static Magnet Moment Couple Calibration Setup

For this adaptation, the magnet and beam setup was tilted 90^{o} onto the side, as per Figure 75, the bottom edge of the beam is located 0.25in from the top plane of the coil and the centerline of the beam is lined up with the centerline axis of the coil. The beam is

setup as a lever where the moment load centroid and the fulcrum are coincident, the fulcrum is a piece of thin nichrome wire that is clamped to the beam using the magnets. The moment load into the beam is from the electromagnet-to-permanent magnet field coupling. The load point is on a piece of circular doweling that is a prescribed distance from the fulcrum wire. The doweling sits upon the pan of a precision balance, an AccuLab L-series, accurate to ±0.005g. The circular dowel minimizes friction and allows maintaining a precise and controlled contract point from the fulcrum wire which is 4.75in. The foam, which is a black slab under the electro-magnet and a white one under the dowel in Figure 75, provides shims to keep the beam level as verified by a bubble level and provide enough surface friction to keep the dowel from rolling away from its location.

The coil had prescribed currents placed into it by using a DC power supply in a current source mode, accurate to about ±0.05Amps (at 0.99CI). At each current value, after allowing the balance reading to settle, the weight is recorded. The current values were increased every 0.2A from 0.0 to 2.0A and then every 0.4A from 2.0 to 4.0A. Converting the measured mass to a force and using the method of static equilibrium, the moment impressed on the magnet stack is determined as the results for the four magnet systems tested is presented in Figure 76.

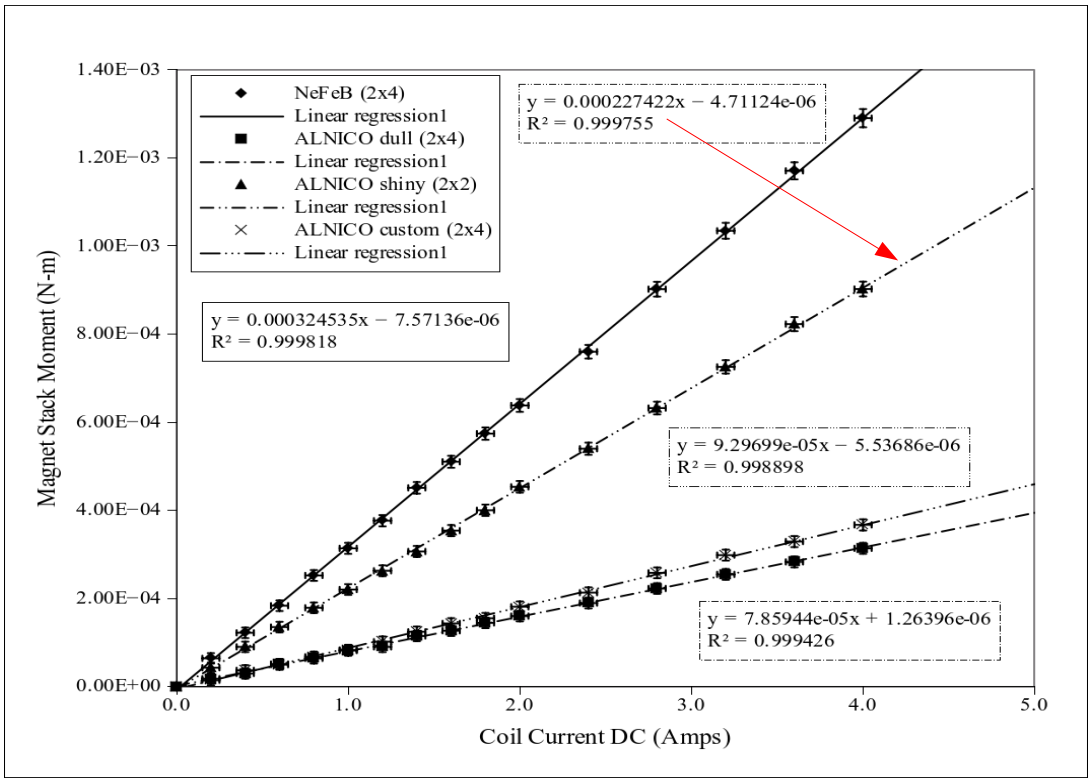


Figure 76: DC Coil Magnet Calibration Curves, Moment of a Function of DC Current

All of the curves are linear across the entire range of current imposed. The curves obtained by a linear least squares regression, and were: eight NdFeB magnets, y = $0.0003245x - 7.57x10^{-6}$, four tall (1/2"long) ALNICO magnets y = $0.0002274x - 4.71x10^{-6}$, eight custom-made ALNICO magnets, y = $0.0000929x - 5.53x10^{-6}$, and four medium-long (1/4" long) stock ALNICO magnets, y = $0.0000785x + 1.26x10^{-6}$. The value "x" is the DC current in the coil in Amps, and value "y" is the output of the couple moment in N·m.

A picture showing these magnets are in Section 3.1.5, Figure 58. The NdFeB magnets are the same set as was used in the previous studies and is included as a reference, they are limited to a working temperature range under 150degC (302degF). These magnets, unlike all the others that were secured with screws and nuts, were glued

to the beam with superglue. With about 70.1% of the strength in couple moment per Amp of the NdFeB magnets, were the four long ALNICO magnets that are ¼inch in diameter by ½inch long, these were stock ALNICO magnets that were custom machined with an EDM bore hole. This set had about twice the volume of magnet material as the other three sets. It was not used for the high temperature studies as it was felt that a fine mesh 3-D model might be needed to accurately model this set and its impacts on the systems dynamics. The next set, with 28.6% of the strength of the NdFeB, are the set of eight custom ALNICO magnets fabricated for this study. These are identical in size to the NdFeB set and were selected for the study of the coatings. Last, at 24.2% of the strength of the NdFeB magnets, are a set of four stock ALNICO magnets that are ¼inch in diameter by ¼ inch long.

These plots allow reporting of the beam stimulation as a function of the moment. It is noted that the static calibration has to be used with care using the driving current as the source variable. This is because the electromagnetic coil is a low-pass filter with a complex impedance (See Section 2.8.1), as the frequency it is driven with goes up, it will attenuate the current flowing through it, and therefore the amplitude of the B-field (and couple moment) unless the coil is driven with a constant current amplifier and/or power supply.

3.7.1. Dynamic Calibration

The static calibration curve above might not accurately capture attenuation that occurs with varying frequencies. Such things as variation in losses in eddy currents in the

shielding, core losses in the coil, and hysteresis of the permanent magnets in the AC generated B-field may result in inaccuracies when reporting the couple moment strength using the statically derived calibration curves in the previous section. One possibility that was raised was to use a dynamic calibration where the beam is assumed to be at a steady harmonic oscillation in bending mode-I. One can use the FEA modal models (introduced in Section 4.3) to derive the strain energy out of the beam at either extreme of the displacement, where all points at the beam are at zero velocity, momentarily. The non-dimensional strain energy can be scaled to the actual beam by using Eq. (67) for any given point in the beam for stress and strain in the x-direction (bending for example):

$$dU_{beam} = \int_0^{\epsilon_x} \sigma_x \delta \epsilon_x \quad \rightarrow \quad U_0 = \int_0^{\epsilon_x} \sigma_x \delta \epsilon_x = \frac{1}{2} E \epsilon_x^{\,2} = \frac{1}{2} E \tilde{\epsilon}_x^{\,2} \lambda^2 \tag{67}$$

where σ is the stress, ε is the strain at the point (the wave over-line indicates non-dimensional), δε is the strain increment, U_0 is the strain energy density, E is the elastic modulus, λ is the scaling factor between the experiment and the modal model (See Section 4.3.3). In equation (84), λ^2 maintains the conversion from non-dimensional strain, $\tilde{\varepsilon}$, to a dimensional strain, ε. To obtain the strain energy throughout the entire beam Eq. (67) must be integrated over the volume of the beam (or elastic solid) as per:

$$U_{beam} = \int_V \int_0^{\epsilon_x} \sigma_x \delta \epsilon_x dV \quad \rightarrow \quad U_{beam} = \sum_1^N \frac{1}{2} E_i \tilde{\epsilon}_{xi}^{\,2} \lambda^2 \tag{68}$$

Equation (68) leads to a technique to extract strain energy from a beam comprised of N elements that can vary in modulus and local strain. Recognizing that the beam is in a steady harmonic condition at a set amplitude, and with a loss coefficient determined by a

ring down trial, one can relate the energy change in the system per cycle as:

$$dU_{cycle}=0 \;\rightarrow\; U_{magnet}+U_{beamloss}+U_{air}+U_{Boundary\ Loss}=0 \tag{69}$$

If in a vacuum and the magnetic field is in phase (so the magnets are not driven into a field in which the electromagnetic coil has a reversed polarity still collapsing that is in repulsion), and the loss into the strings are neglected, then the 3rd and 4th terms in Eq. (69) are zero. Combining this with the definition of loss coefficient as per

$$\eta=\frac{1}{2\pi}\frac{D_s}{U_s} \tag{70}$$

(Lazan, 1968), and rearranging one obtains:

$$D_s=\eta 2\pi U_s=\eta 2\pi\sum_{1}^{N}\frac{1}{2}E_i\tilde{\epsilon_{xi}}^2\lambda^2 \tag{71}$$

where the loss factor, η, can be determined from a ring down test of the same level of amplitude as the steady harmonic excitation. The strain energy, U_s, can be determined using the modal beam modal (See section 4.3) and scaling it to the experimental output using the square of the scaling factor. During the course of one cycle of bending mode-I displacement, the beam enters two states of extreme deformation where all points in the beam are at zero velocity and all of the beam's energy is stored as elastic potential energy. The scaling function of the beam, λ, at either of these states can determined and the non-dimensional volumetric elastic strain energy ("ELSE") from the modal ABAQUS model can be scaled to the dimensional beam by multiplying by λ^2. With this quantity, U_s, and the loss factor determined based on a system ring-down trial, η_{sys}, D_s can now be calculated. This is the energy the magnets have to replenish in each cycle in order to

maintain the steady harmonic state. Where subscript “m” designates quantities of the magnet, the damping is in a steady harmonic condition is:

$$D_s = U_m = \int_0^{1/f_r} M(t)_m \theta(t)\, dt = \int_0^{1/f_r} M_m \cdot \sin(2\pi f_r t)\, \theta_{max} \cdot \sin(2\pi f_r t)\, dt \qquad (72)$$

where U_m is the energy lost per cycle , $M(t)_m$ is the moment from the electro- and permanent magnets interaction, $\theta(t)$ is the kinematic angle from the permanent magnet's pole axis from that of the electromagnetic coil, and f_r is the resonance frequency. Eq. (72) is the integration of energy over the cycle in the beam. The radial displacement, $\theta(t)$, of the active node of the beam, can be obtained from the FEA (or analytical) model and scaled by λ. Of course, the phase angle between M(t) and $\theta(t)$, which are both sinusoidal functions, may well skew the results but when the phase angle between them is zero, the maximum work will enter the system on each cycle as the magnet displacement and the polarity of the fields will be synchronized. Practically, this must be done from a de-tuned resonance state, that is, the beam must be excited some small frequency increment removed from the true resonance peak, as small errors in tuning the excitation frequency near the peak were found to drastically alter the output amplitude, whereas when some distance away in frequency, errors in magnitude with slight mis-tuning become much smaller.

It is noted that this can only give an upper bound estimate of what the force-couple (or moment) acting on the beam really is. That is because of the phase lag between the beam eigenvector and that of the coil field must be accurately measured, unless the phase lag is zero at the resonance. During the course of conducting both tuning

in the resonance points prior to a free-decay trial, as well a while performing FRF sweeps, the phase separation between these two states was not exhibiting a consistent pattern during this study. The coil excitation current sometimes led, sometimes was locked at 0-degrees, and sometimes lagged the beam's center-point DVL displacement signal (which is the as measured velocity signal shifted +90^{o} to integrate it into the displacement signal). If the beam's displacement signal leads or lags the coil current, the displacement of the beam motion of the beam may bleed a small but significant amount of energy by driving the magnet in the coil field when the polarity of the field is still decaying in the opposite polarity and is thus slightly in repulsion.

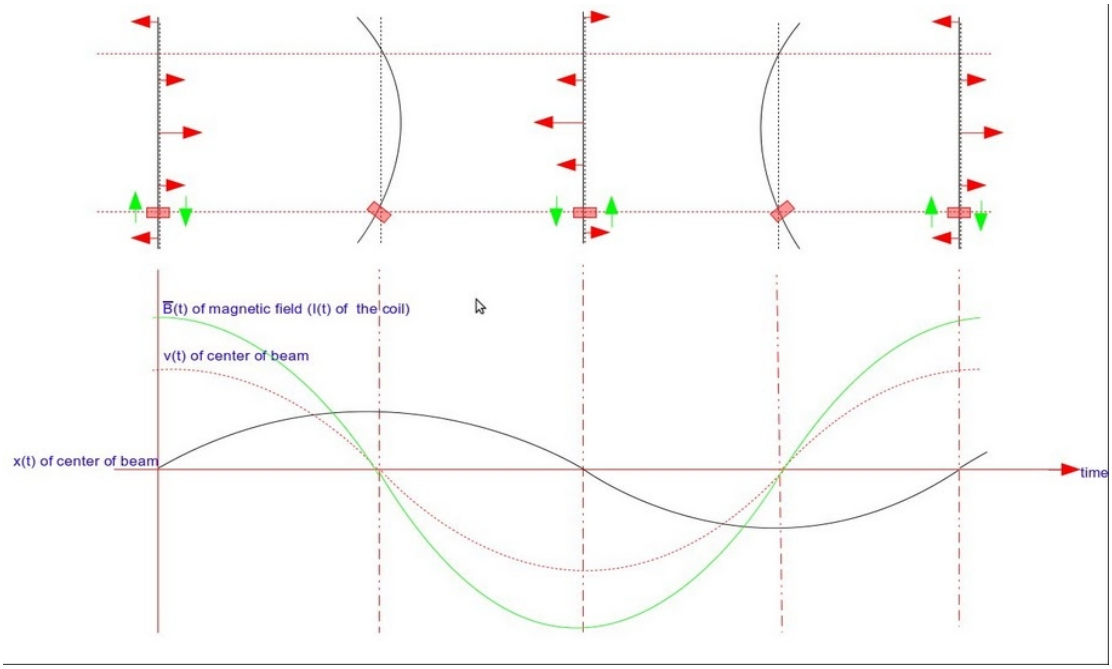


Figure 77: Phasing Between Beam and Magnetic Field.

Figure 77 illustrates the importance of the phase separation, depicted here is the maximal couple moment linkage at 0-degrees (or 360) between the magnetic field and the beam displacement. Otherwise, linkage of the product in Eq. (72) is unknown. To make

use of this technique in future work, the phase data between the beam displacement and coil excitation is going to have to be accurately recorded in the initial stimulation prior to initiating a free-decay. This would be a relatively straightforward addition to the LabView code programmed for this study.

3.8. Components Adaptability to High Temperature

Much of the effort of getting the chamber to be workable as a viable method was the adapting and hardening of miscellaneous components to the high temperature environment. A lot of the items presented here were most efficiently addressed by empirical methods ("trial and error") as opposed to analysis. Various observation of components in the chamber will be covered with relevant findings presented.

Coolant - The cooling of the magnet alone rejected enough heat to keep the chamber's lower cavity and its components cool enough to not break down from the heat. Water was pumped into the chamber at 70degF at 0.35-0.50gpm using nylon tubing, this flow was routed to the two intertwined copper tubing coils wound into the magnet. During the conceptual design of the chamber, it was planned that taps to route coolant to other locations in the chamber would be provided if needed. It turned out that the electromagnet coil served well enough to remove the heat from the chamber alone. The water reservoir was equipped with a centrifugal sump pump and cross flow radiator with fan on the coolant supply line. The latter proved to be very useful for keeping the water temperature cool. Even with about 3 gallons in a bucket the water temperature climbed to about 110-120degF when the radiator was bypassed for extended periods.

Foil – This was used for the 3-layer radiation shields and the lamp reflector liners. Based on sensitivity studies conducted by hand, retaining high reflectivity (and therefore low emissivity) was deemed critical to maintaining the high thermal resistance and the effectiveness of the reflectors. Knowing that aluminum is prone to strong oxidation, especially at higher temperatures, all the foil was made easily replaceable. The chamber was never relived of vacuum until the interior temperatures were below about 350degF. This was to prevent oxygen from reacting with the foil in the in-rushing air. Perhaps because the alloy of the foil was of the relatively inert 1000X series aluminum, the foil never acquired a significant oxide layer and the reflectivity remained high throughout testing. Little foil required replacement in the course of testing, that which acquired discoloration was from components that broke down under high heat, mainly masking tape.

Halogen lamps – The linear halogen bulbs adapted well to operation in vacuum as well as lower power operation. The former problem was anticipated to potentially be a problem with the quartz bulbs overheating and viscously flowing with no free convection cooling in the vacuum. The latter one was anticipated due to the lower power settings of the lamps which could have failed to activate the halogen cycle and replenish the tungsten in the coil. Two extra sets of spares were procured for both wattages in anticipation of these problems. In service neither of these turned out to be a problem, the original set of lamps was still in use after about 70-80 hours of operation.

Wiring – the power for the lamps and coil within the chamber was routed using

PTFE jacketed hookup wire of 12AWG for both the lamps and magnet. Originally, 1000degF rated, stainless steel braided wire was planned for use but the bend radius and thickness of the wire made it very impractical to route within the chamber. The PTFE jacket will not degrade until about 260degC (500degF) in temperature. Behind the inner layer of foil shielding this was not a problem, temperatures in the outer annular cavity rarely exceeded 250degF, and it was less in the lower cavity with the electromagnet, but within the inner cavity temperatures reached 700degF and up. Fortunately, the lamp holders were equipped with wire terminals with glass fiber braided jacket, and this insulation was resistant up to the design limit temperature. These leads were routed out beyond the inner annulus chamber past the shielding layers, all junctions and PTFE wire was located outside the inner chamber.

All the junctions in the wires were made using male-female spade connectors that mechanically crimped to the wires; no solder was used due to concern that it may melt and flow from the extreme heat. For the same reason, plastic and rubber electrical tape was not used, instead paper fiber masking tape was used. Outside the shielding layers it maintained its integrity. What little tape was inside the shielding layers would pyrolyze upon its exposure to the heat, decomposing into carbon in the vacuum, but continued to provide mechanical adhesion and electrical insulation. Where needed thin tubes of rolled up bi-axial wave fiberglass tape under the masking tape could be used to repair chafed wires.

Soft Seals – The chamber had three main axial gland seals between the hard shell

components, and about eight more plug seals for pass through ports in the baseplate. All of the axial seals were O-rings within machined glands. Using the gaskets and sealant grease as was used in the previous vacuum chambers would have resulted in much out-gassing at high temperature and low vacuum conditions. The dry silicone seals worked fine to maintain a low vacuum at around 0.01atm for the chamber. The hottest any of the seals achieved in temperature was the optical glass window for the laser. This seal heated up to about 175degF, the borosilicate glass absorbing much IR radiation when the chamber was active. The ZnSe window seal ran some 15-20degF cooler as the window was either shielded by foil layers when in normal operation without IR imaging, or when it was exposed to the inner chamber, the window would pass much of the thermal energy out to the lab, resulting in a less severe localized heating. None of the glands had to be cooled with routed coolant as was thought might be needed during design.

For the base slab the connectors were either potted in using silicone RTV compounds (after a good cleaning with isopropyl alcohol), plugged with a nitrile rubber stopper, or sealed using a brass tapered pipe plug or barb fitting with Teflon sealing tape applied to the threads. All these methods maintained a good low vacuum seal despite the base slab reaching temperatures of up to 105-110degF.

Laser Return Reflector - The measurement point of interest for the velocity was the midpoint on the side face of the beam ($x = L/2$, $y = w/2$, $z = (t_b + t_c)/2$) although all the presented results are for the interface location (e.g. $x = L/2$, $y = w/2$, $z = t_b/2$) between the titanium and TBC layer. Aimed at this point on the beam was a Polytec

PDV-100 Doppler laser velocity laser (DVL) system that can measure velocity from 0 to 500 mm/sec. Customarily, the Polytec is aimed at a small (diameter <0.5mm) dot of 3M retro-reflective tape. This helps to ensure proper aim of the laser, and enhances the signal return for the DVL so reducing noise and improving the measurement accuracy. As the laser is not moved during a specimen swap out, it also helps ensure that repeatability in the suspension and positioning of each sample is maintained. The laser dot provides a confirmatory check that the sample is being hung with the intended spacing distance over the top plane of the magnet and is centered over it as well. Anticipating problems with the polymeric 3M tape breaking down at high temperature, the samples were prepared with a small square (approx. 1mm x 1mm) of mica tape bonded to the beam with Durabond 952 nickel powder adhesive behind and around the tape flake's edges.

Later ancillary testing with the 3M retro-reflective tape on a specimen found that it did continue to provide an enhanced signal return to at least 1050degF, despite the polymeric binder breaking down above about 600degF. The enhanced return was checked by traversing the laser across the location of the tape location and assessing whether the return signal meter on the sensor head peaked as it crossed the dot location, which it continued to do. It seems to provide this at elevated temperatures only if a vacuum is maintained, if heated in a conventional oven the tape flashes/burns away and there is little to no enhanced return of the signal after that.

Slack Tension Weight - The chamber system, beam support rods, and nichrome wires suffered significant thermal distortion issues to such a degree where the hanging

beam specimen would incrementally migrate about 4-5mm down when the temperature changed from 70degF up to 900degF. Various solutions tried to pretension the wire included using coil-springs, pre-loading wire by tying off to a deflected wire support rod, and using a hanging weight on a sub-span of the wire. The last solution proved to be the most effective. Springs were prone to softening if placed within the thermal shielding, and the wire would bind from the friction of being routed around the shielding (and given the high temperatures, grease was out of the question); the deflected rod solution suffered the same binding issues. The workable solution, using a weight that was hung on a sub-span of the wire, required rigidly tying off the nichrome wire at one end, routing it through a hole drilled in the first support rod, across the main chamber through the beam (a total span of about 8.5in), through the second support rod across to a smaller span of about 4in to a rod where it as snugged down by a pair of nuts. The holes in the beam support rods were drilled in pairs at various heights and were highly flared and polished to allow the wire to pass through with minimal friction. The little energy lost from the beam into the wire helped to ensure that the whole span sought minimum energy, e.g. the weight would settle the sub-span and tension the main one. The nichrome wire tension weight is a cylindrical slug of brass, 0.50kg (1.10lbm) in mass, that is 4.5in long by 1.0in in diameter (11.43 cm x 2.54 cm). In the course of heating and testing a specimen, the DVL required no vertical adjustment due to the target dot moving up or down once the weight was used.

Alignment of the beam along the wire, initially thought to be a potential problem due to migration along the wire, proved to be a non-issue, despite the lack of anything to

prevent the beam from sliding along the wire, it remained in place during the ring-down testing. Being centered on the wire and as a concentrated mass it may deflected the and created a stable low spot that it did not migrate from.

Laser Window – Another potential problem reported by others working with DVLs was false returns from clear windows designed to allow the laser in. It was determined that to gain a good signal return for the DVL, as indicated by the signal return indicator on the DVL unit, as well as minimize the degree of distortion on the harmonic signal, that the angle of incidence of the laser had to be about 1-2 degrees off of perpendicular. The internal reflection in the glass otherwise results in a sizable fraction of the beam returning back along with the intended return from the beam. Indeed, this internally reflected spot can be seen on the DVL lens cowling that migrates back to the center aperture when the DVL beam is brought into a perpendicular alignment to the window. It was determined that, using both a static and harmonically excited beam, that the glass introduced no velocity shifts onto the reflected beam. This was confirmed by tapping on the glass while the DVL was aimed at the static beam specimen target. The beam also did not respond to the taps on the chamber walls, these being dynamically isolated from the beam when it was suspended on the nichrome wire.

A radiant shutter was built for the window to place over it when the chamber was heated but the beam was not being measured with the DVL. It was thought a lot of the radiant energy was lost from the chamber through this window, and conversely the beam would “see” a large cold surface, thus depressing its temperature. Imaging of the

borosilicate glass window with the FLIR SC660 IR camera revealed that the glass is IR opaque. Any heat escaping to the lab surroundings has to be absorbed by the window and then re-radiated to the room. This being the case, as opposed to direct radiation leaving from the hot chamber interior (and the free-free beam) to the (relatively) cold room directly through a IR transparent window, the shutter was not as critical as thought to preserving a uniform thermal surroundings.

Differential expansion and the formation of thermal stresses upon heating or cooling that could crack the window was avoided by use of a compliant layer made from corrugated cardboard sandwiched between the outer retaining ring and the glass window, while the axial o-ring sat between the inner gland seal and the glass window. Should excessive thermal stresses build up, the cardboard would collapse before the window would crack, in theory.

What was helpful to minimizing heat loss and depression of the beam temperature was placing only a narrow width slit (about 3/4in in width by 8.0in long) in the 3-layer shielding between the beam and the optical window. This slit ran the length of the beam to allow using a scanning DVL down the length of the beam, but was kept quite narrow to keep the view-factor from the beam to the (relatively) cold glass at 180degF down to a small value. It also prevented too much heat from escaping into the outer annular and lower cavities, thus decreasing the heat loss into these regions of the chamber.

ZnSe Window – The ZnSe window side of the hot core shielding was normally fitted with a solid piece, except when actively imaging the beam when the 3 layers had an

aperture hole in them. The port had an aluminum blank replaced in place of the ZnSe window as well to save the window from exposure to potential scratching and handling damage, except when performing IR imaging. The IR camera was able to image about 50-60% of the beam, of that about the interior 80% of the image was free of edge effects from the window.

Similar to the DVL window, compliance here was provided by using the axial o-ring on the interior side of the ZnSe window and a layer of Fiberfrax high temperature cloth between the window and outer retaining ring to prevent scratching the window and provide a compliant layer to relieve thermal stresses. Nothing here proved to be a problem with elevated temperatures.

Laser Beam in High Radiation Environment – The helium neon laser of the Polytec PDV100 emits at a wavelength of 632nm with spot area of about 200μm maximum diameter at 0.6mW power. Thus the area of the spot has a flux intensity of about 305,000 W/m^2, well above the radiant flux from the lamps at around 10,000-15,000 W/m^2, with peak energy emitted at wavelengths centered at around 3.2μm (3200nm). Based on the separation between the frequencies of the two and the intensity differences, it was suspected that the lamps would not introduce noise into the DVL signal. Experimental confirmation of this was demonstrated by shooting the DVL onto the specimen in the rest state and at low amplitudes of Mode-I excitation. Based on the equipment used the noise floor of the signal included a random noise level of about 2.5-3.0mV on the both the oscilloscope and the Labview system used on about a 45.0mV

harmonic signal. This noise was constant across all amplitudes, it did not scale with the signal amplitude nor the temperature. The results were not changed with the lamps being on or off either.

Field Shunting – The beam system in the current system did have a weaker dipole moment coupling output than the past setup. Two things contributed to this: a greater magnet-to-coil separation distance, and the use of ALNICO permanent magnets as opposed to the stronger rare earth magnets. The foil used in the three layers of the radiation shielding is para-magnetic and when not secured down in the chamber vibrates upon the AC excitation being provided to the coil. This is due to eddy currents forming in the foil and causing fluctuating attractive and repulsive forces in the foil layers that subsequently interact with the field of the electromagnet. To see whether the foil also shunted the magnetic field flux lines in any significant fashion and therefore partially suppressed the beam output response magnitude, a set of forced response FRF sweeps were performed with the coated beam specimen #9 suspended within the chamber. Excited with a 2000mV/p-p coil excitation signal, and swept across the bending mode-I, the maximum amplitude and resonance frequencies were essentially identical. It was suspected when designing the chamber that aluminum would not shunt magnetic fields in a significant fashion as the magnetic permeability is 1.2566650×10^{-6} H/m (relative permeability to that of free space is $\mu_{AL}/\mu_0 = 1.000022$); the magnetic permeability being a measure of how easy it is to concentrate magnetic flux lines within a material. Experimental investigation of the strength of the shunting effect is covered in Chapter 5.

Pearson suspended identically sized beam specimens with the active node of the beam located 2.54cm (1.00in) above the top plane of the magnet. This distance was enforced as otherwise the stronger rare earth magnets could drive the beam into (unwanted) rigid body motions along with bending mode-I. In the current study, the much larger separation distance was to allow the beam to entirely hang within the hot, reflective cavity and not suffer localized cooling from having the lower tip down in the colder electromagnet.

Heat Loss – Unanticipated until after the first heated runs of the chamber was the degree of thermal conductance that occurred down the lamp support rods, this was discovered by the heat zone discoloration bands on the carbon steel lamp support rods. It was clear that conductive losses from the lamp holders and reflectors into and down the lamp rods were high. To restrict this flow, glass fiber tape was spiral wrapped around the rods and taped off with masking tape. Subsequent heating pyrolyzes the tape into a ring of charred carbon that still held the tape tight to the rod. The hose clamps mounts of the lamp holder/reflector assemblies were then clamped over this layer. And so, a high contact resistance was maintained. Though it was not done, placing a high temperature, low conductivity washer between the lamp rods and the base may help to additionally reduce heat loss by this route.

3.9. Low Damping Chamber

The chamber, when employed in the testing for complex modulus for the bare specimens yielded very low loss coefficients, some 6-8X times less than reported in the

work of Reed and later confirmed in experiments with Deleon. This was enough of a discrepancy that it seems unlikely that variations between batches of AMS-4911 Ti-6Al-4V sheet could account for such a level of variance, so a parametric study was performed on the whole system and its free-free boundary condition. The default configuration assumed was the one used for all of the mechanical characterization studies discussed in Chapter 6. Examination of Table 8 shows that this was at low vacuum, with the lower wire pair not touching the beam, with a glued mica reflector on the beam, and with nichrome wire pre-tensioned with the brass weight and routed through the EDM hole.

One by one, a parameter from this default configuration was varied to allow the system to resemble the previous configuration in one aspect. At each condition of an altered parameter, the system was processed through five trials of ring down datasets to obtain the system loss coefficient and resonance frequency; it is the average of these trials that is reported in the Table. The grayed boxes indicate the individual parameters that are varied from the default testing configuration which is the first line and was used for the testing of all the bare, bond coated, and coated specimens in Chapter 5. An Analysis of Variances (ANOVA) had been planned to see which of the parameters were significant contributors to the much lesser damping in the current free-free setup, but it turned out that it was obvious that all of the factors were significant. Mere inspection as the “ratios” column in Table 8 makes clear. Obstinately made to harden it to higher temperatures, all of the changes made to the apparatus also seemed to have markedly reduced the inherent damping of the free-free system.

As the second line suggests, and consistent with Reed's findings, ambient air is a large damping source, damping increases some 250% with it present over the default configuration. But also significant were eccentricity introduced by the half tube at the passive node (over 200% increase), use of 6lb test nylon fishing line in lieu of nichrome wire (150% increase). Failing to use the tension, slack take-up weight would increase the damping by almost 170%. But overshadowing these all, with a 310% increase, was restoring the lower two lines to rest against the active node magnets used to prevent or limit rigid body beam motion, especially swinging rotation. This was

Table 8: Parametric Study of the Free-Free System Boundary Conditions for ANOVA

Beam #	Pres. (atm.)	Brass Tension Weight (0.5kg)	Active Node	Suspension Line	Passive Node	Reflector	Damping Ratio $\zeta\zeta$	Loss Coefficient η	Quality Factor Q	Ratio of Loss Factor	Resonance. Freq. (Hz) f_r
18	0.01	Yes	Free	Nichrome wire	EDM thru	Mica	0.0000375	0.0000750	13,500	1.00X	203.18
18	1.00	Yes	Free	Nichrome wire	EDM thru	Mica	0.0000943	0.0001887	5,333	2.52X	202.74
18	0.01	No	Free	Nichrome wire	EDM thru	Mica	0.0000623	0.0001247	8,033	1.66X	203.08
18	0.01	Yes	Between	Nichrome wire	EDM thru	Mica	0.0001450	0.0002900	3,433	3.87X	203.03
18	0.01	Yes	Free	Nylon fishing	EDM thru	Mica	0.0000567	0.0001133	8,800	1.51X	203.04
18	0.01	Yes	Free	Nichrome wire	½ tube	Mica	0.0000803	0.0001607	6,267	2.14X	
18	0.01	Yes	Free	Nichrome wire	EDM thru	Polymer	0.0000216	0.0000432	23,180	0.58X	203.44
23	0.01	Yes	Free	Nichrome wire	EDM thru	Mica	0.0000737	0.0001473	6,800	1.96X	204.57
21	0.01	Yes	Free	Nichrome wire	EDM thru	Mica	0.0000660	0.0001320	7,750	1.74X	203.580
19	0.01	Yes	Free	Nichrome wire	EDM thru	Mica	0.0000790	0.0001580	6,367	2.12X	201.930
	Reed's Reported Bare Specimen						0.00020	0.00040	2,500	5.33X	-

discovered by accident, but prior to the TBC characterization effort. It is suspected that the magnets, as they rotate as a mass about the active node on the neutral axis of the beam, are transversely exciting and pumping energy into this pair of wires. Close

examination of the setup was attempted using a stroboscope to freeze the displacement of this pair of wires was attempted but determining if significant displacement was occurring was difficult due to poor observational access in the current rig. Because of the heavy influence on the system from this, it was decided to keep the lower pair of wires non-contacting, there only to prevent extreme rigid body motion and rigid body rotation superimposed on the desirable bending mode velocity on the specimen signal was tolerated and dealt with by means of filtering. Details of this are in Section 4.5.3.

Specimen 18 was the original bare beam specimen to be carried through the chamber and tested as a bare beam. Ironically, is has much lower damping than specimens #23, 21, or 19 which were all tested as well in identical configurations and all exhibited roughly twice the damping of Specimen #18. This was an anomalously low loss factor when compared to the rest of the specimens and potential hypothesis as to its significantly different damping is addressed in Section 5.1.2.1.

The bare beam results indicated very low damping in the system, loss factors as low as 0.000085 were reported in some of the ring-down runs. Compared to the lowest values obtained by Reed using free-decay technique with η_{bare}= 0.0004, and confirmed by Deleon to within ±20% using forced response (Reed, 2007; Deleon, 2009), this was close to a order of magnitude lower. Even accounting for different runs of Ti-6Al-4V sheet this seems like an enormous inter-specimen variation, the chamber itself may account for a lot of the reduction. Also, a specimen from the current batch was tested for decay in a replica of Pearson's setup and was found to recover a value close to that of Reed. Of course the

logical question to be answered is how much lower can the damping ultimately be lowered to, and what is the true damping range for the beams?

3.10. Closure on the Chamber

This section closes and the free-free apparatus of Reed and Pearson has been adapted for high temperature testing. With the validation now established based on analysis and experimental results it has been shown that the apparatus preserves, indeed enhances, the low damping free-free condition, and provides an effective high Stark number environment with a near isothermal beam and with modest power requirements for heating, it was deemed ready for the 8-YSZ characterization studies. Some calibration work has also been performed; power for the lamps and couple moment transfer, and the chamber has been hardened to high temperature the study proceeds to extent the previous works by characterizing of the 8-YSZ coating across a range of temperatures.

The next two chapters concern the application of the chamber and procedures using it to characterize a common TBC thin coating in use, 8-YSZ. The first Chapter overviews the theory and conceptual ideas and the second delves into the experimental effort and presents the results.

4. Determining Coating Complex Modulus – Theory and Concepts

This Chapter will detail the theory that underlies the attempts to characterize the complex moduli of the 8-YSZ TBC material across various temperatures on the free-free beam system. The models presented will be both analytical and numerical with an emphasis placed on finite element models. These models are critical in determining values that, if they were to be measured directly in such a high quality factor system, would introduce large errors. For example, a strain gage mounted on the beam to determine the strain at the point of measurement would introduce significant stiffness and could influence mode-shape. Additionally, its connecting wires would introduce a lot of damping into the free-free system and bias the results to a large degree. The topic covered will be the problem under study and how to handle it in an analytical fashion, then how to approach it by modeling it in a finite element analysis (FEA) approach. The process and results of building the predictive polynomial functions will be covered. Then information on the extraction of the beam system values from the experimental data will be covered. The last step will be to join the FEA derived data together with the experimental system level data to derive the bulk modulus of the coating itself. The later portion of the chapter will detail some of the principles affecting the experimental characterization to be covered in Chapter 5.

4.1. Damping Models

A review of the damping models was deemed worthwhile as many TBC materials were known to exhibit non-linear material behaviors, both mag spinel and 8-YSZ are strain softening, and an overview of models to chose from may be worthwhile. This would also give the reader a sense of some of the artifacts to be alert for that may show up in a non-linear system.

4.1.1. On Damping and Complex Modulus

The damping model chosen for the beam system could come from one of several models that are proposed, these are covered in Section 4.1.2. The most commonly known one is the viscous damping model, probably in part due to its linear nature and the relative ease by which it is worked by classical analytical techniques. It also seems to describe classical engineering materials quite accurately as well.

The beams in the current study are quite under-damped in their bending mode-I response, even the thickly coated ones ring down over many cycles in the course of a decay. Typically a system is considered very under-damped if the damping ratio is much below 0.1. In this study most of the system-level damping ratios were determined to be under 0.012. The expression relating damped, ω_r, and natural frequencies, ω_n is:

$$\omega_d = \sqrt{1-\zeta^2}\,\omega_n \tag{73}$$

One can see that the damped frequencies and natural frequencies for all practical purposes coincide for our testing ($\omega_d = 0.999928\omega_n$). The resonance peak frequencies is given by:

$$\omega_r = \sqrt{1-2\zeta^2}\,\omega_n \tag{74}$$

The separation between the resonance peak and natural frequencies are again very small ($\omega_r = 0.999856\omega_n$). Hence, the resonance peak frequencies in this study are reported as the damped response frequencies, even though they are distinct and different values.

Complex modulus is a notational form that splits a given material's properties into two components, consisting of the elastic response, where energy is conserved through loading and unloading, and the non-conservative response, which is the deficit between energy placed into the structure on loading and the energy recovered from the structure upon unloading. These two components are combined in the complex modulus as per:

$$E^* = (\underbrace{E'}_{\text{storage modulus}} + \underbrace{jE''}_{\text{loss modulus}}) \quad \rightarrow \quad E^* = E'(\underbrace{1}_{\text{storage coeff.}} + \underbrace{j\eta}_{\text{loss factor}}) \tag{75}$$

where E^* is is the complex modulus, E' is the storage modulus, E" is the loss modulus, j is $\sqrt{-1}$, and η is is the loss coefficient. It is noted that the loss coefficient is related to the log decrement of the system, and is the ratio of the loss modulus over the storage modulus (e.g. $\eta = \tan\delta = E'/E''$). This is a compact notation to express the two components and is used in a lot of modeling, but use of complex moduli is limited to modeling structures with harmonic forcing inputs.

4.1.2. Constitutive Models and Damping Review

Important to the accurate mechanical characterization of the coating is an understanding of its constitutive properties, specifically how they respond in deformation (or internally speaking, strain) to applied loads (or internally speaking, stress). To date, the characterization of the coatings has been from a phenomenological approach, as

opposed to a constitutive one. This is because the various TBC materials are not fully understood in regards to their micro-mechanical interactions, though recent papers present a micro-mechanical FEA based modeling (Abu Al-Rub and Palazotto, 2010). A key to finding a good working constitutive model is determining the mechanism of energy loss (damping) that operates within the bulk material. Much of the constitutive modeling will be focused on this. However, determining the loss-less component of strain response to stress is important as well.

Some various loss models available include linear elastic (Hookian), classic viscoelastic (VE), Coulombic (dry) friction, and these can be both in simple form or complex. Some current thinking (Abu Al-Rub, Palazotto, 2008) suspects that a damage-based model for the ceramic coating may be most appropriate for two reasons: first, the material non-linearity seems to exhibit strong variation with strain magnitude, suggesting a displacement driven frictional loss element between and within the cracks of the TBC material. Second, is that the evolution of further cracking between and within the splats and voids may help explain the strain history evolution in damping that these materials typically exhibit. It is worth noting that Ungar (within Braun's compendium work) (Braun, 2002) notes that most damping treatments are polymeric plastics or elastomers, which are generally recognized as viscoelastic in their constitutive behavior. Later in the chapter, charts are shown for notional damping materials exhibiting strong temperature dependence as well as weak frequency dependence for both loss factor and effective shear modulus (Braun, 2002).

A quick overview of these damping models for a single degree of freedom (SDOF) system, schematic, equations, and various solution features along with some comments is worthy of coverage. The selection among damping types for the model, be it FEA, analytical dynamic, or mathematic, will result in certain features being captured in the experimental study and others not. Of course, the baseline for all studies is the undamped system, depicted in Figure 78. Without elaboration, the equation of motion for free- and forced-systems is:

$$m\ddot{x}+kx=0 \quad ; \quad m\ddot{x}+kx=Fsin(\omega t) \tag{76}$$

Meanwhile from Eq. (76), in this case the resonance frequency, magnification factor, and phase lag from a harmonic sine input-to-out, or FRF viewpoint are:

$$\omega_n=\omega_r=\sqrt{(k/m)} \; ; \; \frac{|X_{out}|}{|X_{in}|}=unity \; ; \; \phi=0^o \tag{77}$$

For lightly damped systems, of which even the coated beam is, the undamped system provides a very good first approximation of the resonance values and associated mode shapes. When modeling structures, simple or complex in geometry, it is almost standard practice to perform a eigenvalue-system decomposition to capture the lower roots and associated modes. For the vast majority of structures which are lightly damped this yields good insight into the vibrational shapes and frequencies. Typically LU, Cholesky, SVD, Lanczos, or other matrix decomposition methods are used to reduce a large, linearly independent system down for an large, multiple degrees of freedom (MDOF) or continuous system. For the details of decomposition techniques most texts on

linear system numerical methods should be a good recourse and/or a source code library like LAPACK or EISPACK.

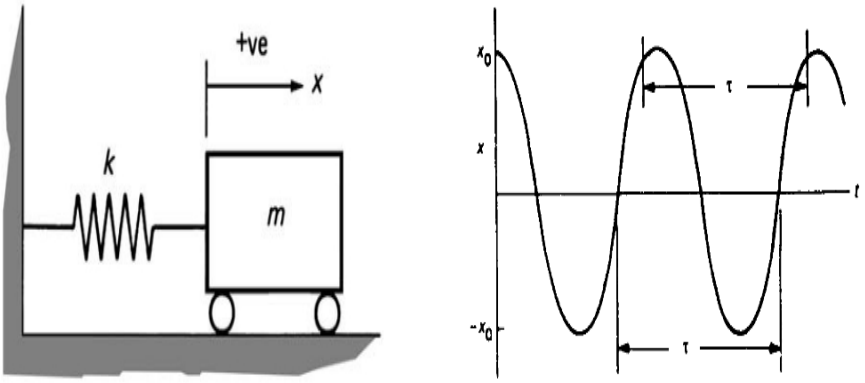


Figure 78: Undamped System and Response, SDOF (Beards, 1996)

Analytically speaking, the simplest method of modeling the coatings is to assume they are linearly elastic and lossless in nature. The beam can be modeled as a classic one of varying cross-section by using the adjusted modulus ratio area-moment correction method as per any classic strengths of materials texts. Beer and Johnson or Higdon, et al. are recommended (Beer, 2002; Higon,1985). A dynamic solution using a classic E-B beam model would account for three regions of stiffness, the end regions being bare titanium and the middle of the coated area with a corrected cross-section. This may yield a reasonable mode-shape and resonance frequency, as with the bare beam. Modal models just accounting for the mass and stiffness matrix effects are of this model.

The next level of complexity is the classic viscoelastic (VE) models. For the single degree of freedom (SDOF) system, as well as classic analytical dynamics (lumped MDOF systems) the damping is solely a function of the time-derivative of strain (or displacement). This is the classic linear 2^{nd} order ordinary differential equation (ODE), and uncoupled set of linear ODE's, for a SDOF and MDOF, respectively. Well-

established sets of techniques exist to model these structures. Whether by classic lumped analysis, or FEA techniques, most vibrations textbooks cover these techniques. In practice, these models work well for various polymeric materials like rubber, plastics, and other polymers. The fidelity of the VE models can be increased by combining the viscous and spring elements into higher order elements like the Maxwell solid, Kelvin-Voigt, or the commonly used standard linear solid (SLS). These models express their damping through the C-matrix in the dynamic system of $[M]\ddot{\vec{x}}+[C]\dot{\vec{x}}+[K]\vec{x}=\vec{F}(t)$.

For viscously damped system, depicted in Figure 79, is the well-known system with the following free- and forced-state equations, which are linear and 2nd order w.r.t. the displacement:

$$m\ddot{x}+c\dot{x}+kx=0 \quad ; \quad m\ddot{x}+c\dot{x}+kx=F\sin(\omega t) \tag{78}$$

These parameters apply upon the solution of Eq. (78) for resonance frequency and damping ratio in the time domain are:

$$\omega_r=\omega_n\sqrt{(1-\zeta^2)} \;\; ; \;\; \zeta=\frac{c}{\sqrt{2\text{km}}} \tag{79}$$

For the beam system in the current study, the under damped ($\zeta < 1.0$) solution is the one of interest,

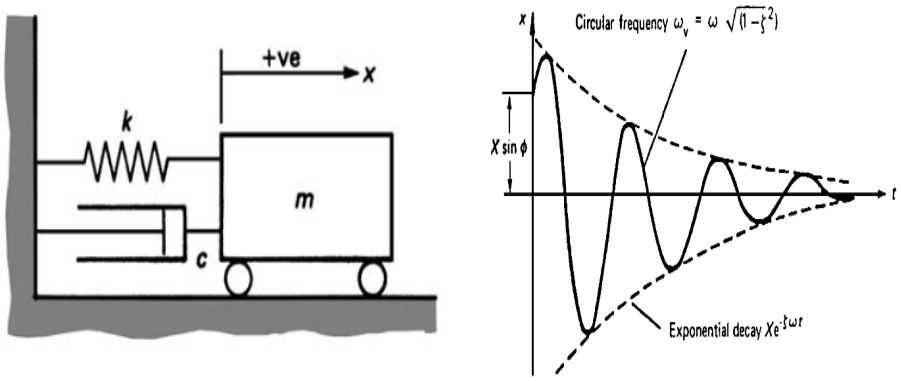


Figure 79: Viscously Damped System and Response, SDOF (Beards, 1996)

where displacement in time is of the combination of decay and harmonic functions for the free system response:

$$x(t) = Xe^{-\zeta\omega t}\sin(\sqrt{1-\zeta^2}\,\omega t + \phi) \tag{80}$$

Viewed from a frequency domain view point, the magnification factor and phase lag for the harmonically forced system, and plotting these over various forcing frequency values produces bode plots for magnitude and phase as per:

$$|X| = \frac{|X_{out}|}{|X_{in}|} = \frac{1}{\sqrt{\left\{\left[1-\left(\frac{\omega_{in}}{\omega_n}\right)^2\right]^2 + \left[2\zeta\frac{\omega_{in}}{\omega_n}\right]^2\right\}}} \quad ; \quad \phi = \tan^{-1}\left[\frac{2\zeta(\omega_{in}/\omega_n)}{1-(\omega_{in}/\omega_n)^2}\right] \tag{81}$$

A good treatment of the full viscous damping solution can be found in any introductory text of vibrations or dynamics, Meirovitch is a typical treatment (Meirovitch, 2002). Note that this is easily extended to MDOF systems and models while preserving linearity of the mathematics describing the model, hence the predominance of viscous damping techniques.

Proportional damping is a subset of viscous damping where the value of the dash-

pot element (or damping matrix for MDOF) is a linear combination of the spring and mass element matrices (e.g. $c=\alpha m+\beta k$; $[C]=\alpha[M]+\beta[K]$); this is the Rayleigh form proposed in 1877. This form tends to overly suppress higher modes due to its time-dependent element for both MDOF and continuous systems. A tailored version based in using the Caughey series $[C]=\sum \alpha_{k_i}[M]^{k_i}[K]^{l}$ can help correct for this. Sometimes known as “modal damping”, it can be tuned with a different series coefficient at each resonant frequency. It is noted this is the default damping system implemented in many commercial FEA packages capable of transient analysis. Again, this is due to the Rayleigh damping modes being orthogonal in nature across the damping matrix [C]. This allows the great variety of linear matrix mathematical tools to be applied and with the relief of computational burden for a MDOF system (Cook, 2001). A good overview of common damping models implemented in commercial FEA codes is given in an ANSYS memo (Imaoka, 2000).

TBC materials, which are in the ceramic class of materials, may not be well described by the viscoelastic models. Also, there are modeling issues such as the coatings based on materials well modeled using VE models have limited temperature range, durability issues, and structural fabrication issues. coulombic damping, sometimes known as "dry" damping or "friction" damping,

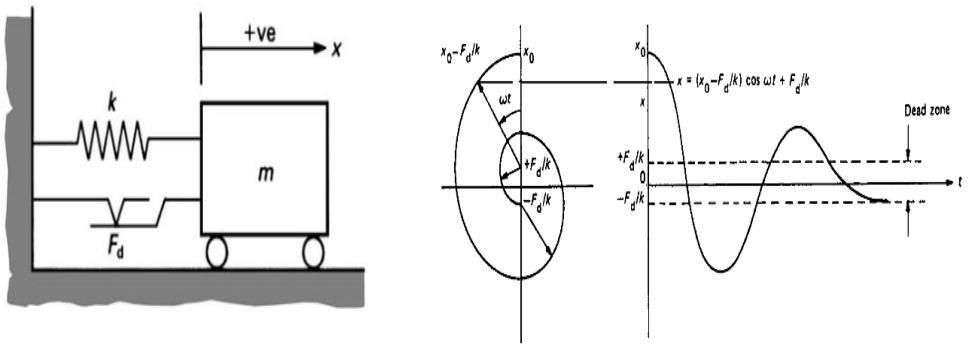


Figure 80: Coulomb (Dry) Damping System and Response, SDOF (Beards, 1996)

is predicated on the idea that energy loss is a function of friction forces acting on displacement of the system. Dry friction models admit damping based on frictional slider elements where the resisting (damping loss) forces act through the displacement of the element. coulombic damping exhibits many similarities to viscous damping in form and free response, as displayed in Figure 80.

Some salient features that are important to contrast with viscous damping are: 1) the decay envelope function is not exponential in nature but rather linear, and 2) the dry damping enters a region of dead-band, around which all motion ceases as the frictional force of damping F_d exceeds any inertial and/or elastic forces in the system.

The equations of state for the free and forced (harmonic) systems are for SDOF, respectively:

$$m\ddot{x} + F_d + kx = 0 \quad ; \quad m\ddot{x} + F_d + kx = F\sin(\omega t) \tag{82}$$

where the solution in time series is:

$$x(t)=\left(x_0-\frac{F_d}{k}\right)\cos(\omega t)-\frac{F_d}{k} \quad ; \quad n\pi<t<(n+1)\pi \qquad n=0,2,4,...$$
$$x(t)=\left(x_0+\frac{3F_d}{k}\right)\cos(\omega t)-\frac{F_d}{k} \quad ; \quad (n-1)\pi<t<n\pi \qquad n=2,4,6... \tag{83}$$

where x_0 is the initial displacement condition and F_d ($F_d=\mu mg$) is the frictional loss. The loss envelope function in this system (assuming the system is under-damped) is a linear one.

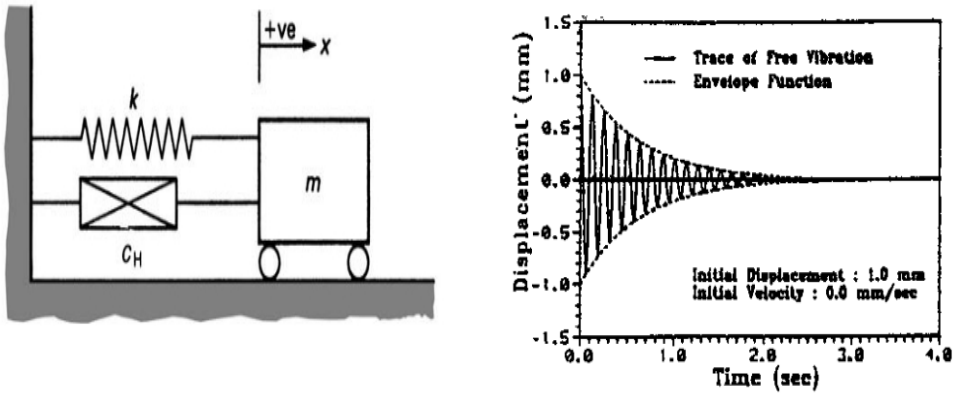


Figure 81: Hysteresis Damping System and Response (Beards, 1996)

Depicted in schematic form as per Figure 81, hysteresis damping is close to the concept of internalized, bulk material entropy (e.g. heat) forming type of damping.

Often described as due to "internal friction" (Meirovitch, 2002), hysteresis damping over the course of a cycle of displacement is a non-conservative loss in the system, whether a SDOF, MDOF, or continuous system, resulting in energy loss. For a SDOF system this form of the state equation in the free and forced forms is:

$$m\ddot{x}+k^*x=0 \quad ; \quad m\ddot{x}+k^*x=Fe^{(j\omega t)} \tag{84}$$

where the stiffness, k^*, is a complex number consisting of a real storage term for the elastic response and a imaginary loss term for the energy bled in each cycle. K^* is defined

as per:

$$k^* = k(\underbrace{1}_{storage} + \underbrace{j\eta}_{loss}) \tag{85}$$

where k is the effective stiffness of the spring (for a continuous system, the effective modulus), and η is the hysteresis damping ratio, that is, the fraction of energy lost in each cycle of the vibration; the imaginary number, j, allows the damping force to be brought into phase with the instantaneous velocity of the system. The continual system equivalent has the storage modulus, E', and loss modulus, E", as per:

$$E(\omega) = \frac{\sigma(\omega)}{\epsilon(\omega)} = \underbrace{E'}_{storage} + j\underbrace{E''}_{loss} = E'(1 + j\eta) \tag{86}$$

where these values tend to be dependent on frequency. The presence of the complex number for effective stiffness is to synchronize the damping force with the velocity of the system. Fractional derivatives allow for generality between the viscous and hysteresis damping models where A is a generalized damping coefficient as per:

$$m\ddot{x} + A\frac{d^r x}{dt^r} j + k x = 0 \tag{87}$$

where the order of the system, r, generally varies between 0 and 1. When r=0, the system is pure hysteresis and when r=1 the system is purely viscous in nature (Braun, 2002; Eldred, 1996). These fundamental models can be expanded and recombined to try to generalize their application to real world effects.

It is to be noted that these basic models can be extended. The classic viscous model in both SDOF and MDOF form can be extended into viscoelastic regimes with the

Kevin-Voight, Maxwell, and Standard Linear Solid (SLS) models. Additionally, multiple, tuned parallel-series combinations can be used to fine-tune the responses. Reed, for dry friction damping, used an Iwan model with multiple friction slider elements tuned to simulate SDOF hysteresis loop losses. The various friction elements in system were tuned to a distribution of slip levels (Reed, 2007). Patsias and Tassini have used similar loss modeling techniques to attempt to determine phenomenological models for TBC coatings. It is noted that for many of these models that Lazan's Law of unit volume damping losses using a power law form is widely utilized for many of the volumetric energy loss approaches, it relates the energy loss as a power law of the loading stress:

$$D(\sigma_a) = J_a \sigma_a^N \tag{88}$$

where, σ_a, is the stress amplitude, J_a, is the damping dissipated at unity stress, and N is a material constant (as is J). Typically, the leading coefficient and the power are figured from empirical curves when the system is loaded and unloaded at various amplitudes. (Lazan, 1968). It is used in the coated Oberst Beam theory to determine the strain energy, for more information Appendix 5 recaps the details.

It is noted that the loss modulus of a lot of the classic engineering materials (metals) is quite low, hence the classical, undamped (modal) structural techniques work well for determining the modal frequency peaks and shapes. Table 9 displays the values of some typical engineering materials.

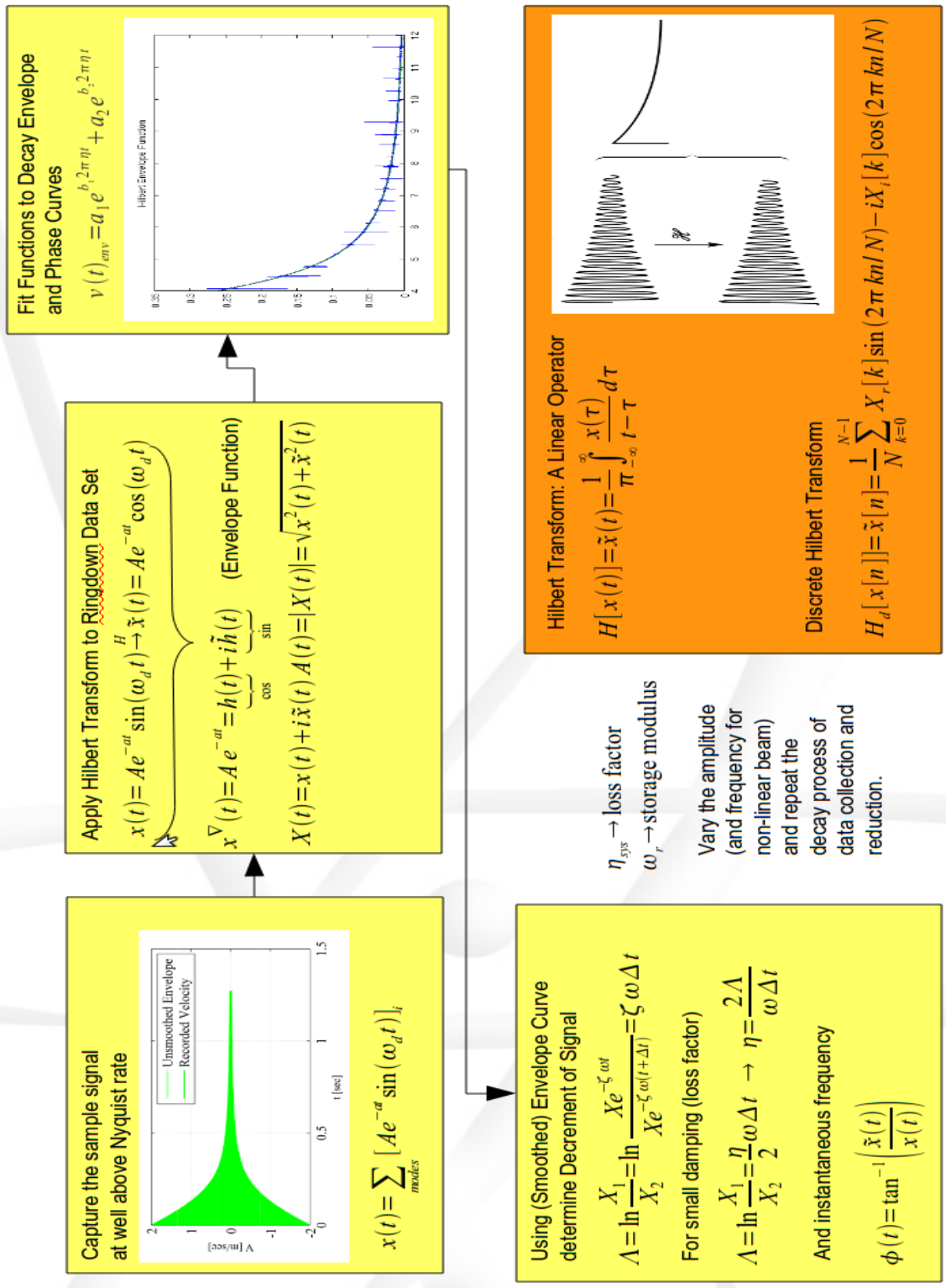


Figure 82: Process to Obtaining System Level Damping and Resonance frequency

Table 9: Loss Coefficients of some Bulk Materials (Beards, 2006)

Material	Loss Factor
Aluminum-pure	0.00002 - 0.002
Aluminum alloy-dural	0.0004 - 0.001
Steel	0.001 - 0.008
Lead	0.008 - 0.014
Cast Iron	0.003 - 0.03
Manganese Copper Alloy	0.05 - 0.1
Rubber-natural	0.1 - 0.3
Rubber-hard	1.0
Glass	0.0006 - 0.002
Concrete	0.01 - 0.06

It is interesting to note that the closest material in this table to the TBC, concrete, an aggregate ceramic-like material, has a relatively high loss factor, 2-3 orders of a magnitude over the value for titanium. For comparison the bare TI beam loss factor was determined the be around 0.0004 (damping ratio = 0.0002 << 1.0) by Reed and confirmed by Deleon (Reed, 2007; Deleon, 2009). While the loss coefficient for mag spinel and 8-YSZ reported by Pearson and Reed were up around 0.04-0.06 (or damping ratio 0.02-0.03 <<1.0), about 100X that of the bare beam, they are still a classic under-damped system. This can be seen in the datasets of both the coated- and bare-beam and both exhibit oscillatory decaying signals.

Table 10: Damping Model Comparison (Braun, 2002)

Name	Viscous	Dry	Phenomena
Linear Viscous Damping	$c\,\dot{x}$	c	slow fluid
Air Damping	$a\,sgn(\dot{x})\dot{x}^2$	$8a\,\omega\,X/3\,\pi$	fast fluid
Coulomb Damping	$\beta\,sgn\,\dot{x}$	$4\,\beta/\pi\,\omega\,X$	sliding friction, dry friction
Displacement Squared damping	$d\,sgn(\dot{x})\dot{x}^2$	$4d\,X/3\,\pi\,\omega$	material damping, elastic storage damping
Solid or Structural Damping (Hysteresis)	$b\,sgn(\dot{x})\lvert x\rvert$	$2b/\pi\,\omega$	internal damping,

The process of generating a linearized a model results in many damping models being transformed into a viscous equivalent model to allow linear decomposition techniques. Table 10 and Figure 83 summarize this well. Derivation of the equivalent values is performed by integrating the force versus displacement (or stress versus strain) load and unload curves' area enclosure which is the energy lost per cycle; a wholly conservative system will be a simple line or curve without area.

Damping Characteristics

Type	Equation of motion	Damping capacity	Q
Viscous	$\ddot{x} + 2\beta\dot{x} + \omega_0^2 x = 0$	$2\pi\beta\omega A^2 m$	$\frac{\omega}{2\beta}$
Hysteretic (lin. approx.)	$\ddot{x} + \frac{h}{m\omega}\dot{x} + \omega^2 x = 0$	$\pi h A^2$	$\frac{m\omega^2}{h}$
Hysteretic (mod. Coul.)	$\ddot{x} + c_h A\ sgn(\dot{x}) + w^2 x = 0$	$4c_h A^2 m$	$\frac{\pi w^2}{4c_h}$
Coulomb	$\ddot{x} + \frac{f}{m}\ sgn(\dot{x}) + \omega^2 x = 0$	$4fA$	$\frac{\pi m\omega^2 A}{4f}$
Ampl. Dep.	$\ddot{x} + c_f A^2\ sgn(\dot{x}) + \omega^2 x = 0$	$4c_f A^3 m$	$\frac{\pi\omega^2}{4c_f A}$

Figure 83: Damping Models for SDOF, Capacities and Quality Factors (Braun, 2002)

Equating this energy loss over each system gives the equivalent values. For a good overview of this process refer to Beards (Beards, 1996). So, why so much emphasis on damping and damping models? There are two main reasons: 1) in order to perform a transient FEA model analysis of the vibrating beam system, Deleon determined that he had to include proportional damping in his model to achieve successful convergence of this solution, and 2) the nature of the damping determined from the experimental data and matching numerical model, which includes the damping, that most accurately replicates the FRF and/or decay ring down for the beam could yield great insight into the constitutive model that applies to the beam system. The time-domain features in the ring-down may help with the selection of the most appropriate model for the TBC coated specimens in this study.

4.2. Analytical Modeling

The preliminaries of damping aside, the choice of a thin beam in bending mode-I made by Reed, Patsias, Tassini, et al. is fortuitous for several reasons. These include:

· The thin beam is easier to mount either in a cantilever or free hanging situation in a procedurally repeatable fashion to allow bending and minimize boundary condition induced variances to the system-level damping.

· For non-linear materials requiring large strain ranges to be imposed upon them, a beam geometry is much more easily driven to moderate to large strain amplitudes than plates, cylinders, shells, or axially loaded beams. This is especially true for non-contact excitation methods.

· The modes are more fundamental and easily distinguished in a beam geometry. This makes modeling and extrapolation of their strain, displacement, and elastic energy from modal FEA or analytical models more straightforward than for other geometries.

· The thin beam exhibits less sensitivity to non-isotropy in materials, for example, if Ti-6Al-4V sheet is orthotropic in modulus (as is found in Section 5.1.2 of this study) the predominance of only bending strain (and stress) along the long axis of the beam will minimize the error introduced by not accurately modeling the off-axis modulus.

Additionally, the free-free boundary condition geometry adopted by these previous works has a key advantage in the reduction of a major source of system damping and its associated uncertainty. This is a significant, if not major, fraction of overall damping in clamped systems. It is also was hard to obtain repeatable results across specimens and setup trials, and attempts to control the variances in clamp damping by means of guide shafts, torquing sequences, and precision machined roots has meet with mixed success. One of the most useful advantages of a thin beam is the ability to model the system using classical Euler-Bernoulli (E-B) thin beam theory and get reasonable approximations to the bare beam from it.

The system under study is either a bare or partially coated thin beam. Depicted in Figure 84, the beam is comprised of Ti-6Al-4V alloy. It is 8.00in in length (L = 0.2032m), 0.75in width (b = 19.05mm), and $1/16^{th}$ in thickness (t_b = 0.0625in = 1.587mm). A coated beam features a thin layer

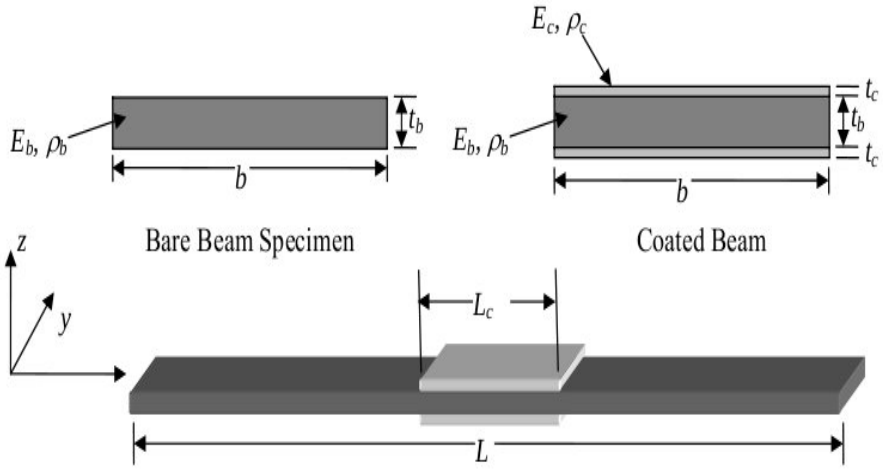


Figure 84: Diagram of the Beam (Reed, 2007)

of TBC compound applied centered on the mid-length of 25% the length of the specimen, L_c = 2.0in (0.0508m). The coating thickness that were desired for fabrication were 6-, 9- and 12-mils (milli-inches ("mils") or 0.152, 0.229, and 0.305mm, respectively), but based on precision micrometer and electronic balance measurements of the actual as-fabricated specimens these were 5.7, 8.3 and 12.5mils (or 0.145mm, 0.211mm, and 0.318mm, respectively). It is noted that despite the inaccuracy of the coating thicknesses, good precision tolerance of their thickness were maintained (See Section 5.1.1).

The metallic beam region is the Ti-6Al-4V alloy with the long axis oriented in the rolling direction of the plate stock (but was later determined is actually the transverse direction) and the TBC is applied. Both are modeled as homogeneous, elastic (Hookian), and isotropic solids in all of the modeling, whether by analytical or FEA modeling. The interface between them is treated as a strain compatible interface with no-slip.

4.2.1. Analytical Solution of Classic Free-Free Beam System

The familiar equation to model a transversely vibrating thin beam (sometimes referred to as a bar) is the Euler-Bernoulli (E-B) theory with an acceleration term to make the form dynamic. The differential equation takes the form:

$$EI\, w'''' + m\ddot{w} = 0 \tag{89}$$

where E is the elastic modulus of the beam material, I in the inertial moment, w is the displacement of any given portion of the beam's neutral axis off of the rest state, and m is the mass of the same differential portion of the beam. The primes (') designate a spatial derivative down the length and the dots (·) denote a derivative of time. Assumptions in this model include: only transverse acceleration of any beam location results in inertial forces, all the static E-B thin beam theory assumptions apply, the beam is uniform in cross-section, and material properties are constant down the length (e.g. EI in invariant).

Many texts cover this in detail; a good overview is in Braun, or Meirovitch for a good treatment on the cantilever system (Braun, 2002; Meirovitch, 2001). The derivation of Eq. (89) from first principles is demonstrated in Meirovitch, Section 8.3 (Meirovitch, 2001). This proceeds from a extension of E-B beam statics with a De' Alembert acceleration term added to the force balance of each differential element down the beam.

Assuming that the displacement function is separable in terms of space and time (e.g. $v(x,t)=X(x)\cdot W(t)$) and applying this to Eq. (89), gives the generalized spatial solution of:

$$X(x)=\alpha_1\sin(\kappa x)+\alpha_2\cos(\kappa x)+\alpha_2\sinh(\kappa x)+\alpha_2\cosh(\kappa x) \quad (90)$$

where X(x) is the displacement of the neutral axis off of the rest state of the beam (e.g. X = transverse displacement off the neutral axis, x = longitudinal coordinate down the beam). The boundary conditions, of which there are four, are now imposed on the two tips of the beam. These are shear- and moment-free loadings (e.g. V(0L)=V(1L)=0, and M(0L)=M(1L)=0). Integrating Eq. (90) up twice to obtain the moment function and three times to obtain the shear function w.r.t. to x allows a 4x4 system determinant to be formed using the free-free boundaries. From this the characteristic equation of (89) with the free-free boundary conditions applied is:

$$1=\cosh(\kappa L)\cos(\kappa L) \quad ; \quad \kappa=\sqrt[4]{\frac{\rho A\omega_n^2}{EI}} \quad (91)$$

where L is the length of the dimensional beam, the mass product, ρA, is the mass per unit length, E is the elastic modulus of the beam/bar material, ω_n is the natural frequency (in radians), and I is the area moment of inertia. The characteristic equation, when solved for the product κL, yields the non-dimensional roots. For the free-free configuration, the first 5 solutions (bending modes) are: 0, 4.730, 7.853, 10.996, 14.137,.... It is noted that, in the limit as κL gets large, that a periodic solution occurs at intervals of $(2n-1)\pi/2$ (Braun, 2002). Scaling these roots by the geometry of the beam of utilized in Reed and Pearson's studies and using (where $m=\kappa L$):

$$\omega_n=\frac{m^2}{L^2}\sqrt{\frac{EI}{\rho A}} \quad ; \quad m=4.73,7.85,11.0,... \quad (92)$$

After determining the natural frequencies, the general form of the homogeneous

solution is noted to be of the form in Eq. (90), Figure 85 shows the solutions to the characteristic equation and the associated solutions to Eq. (91) where the constants α_1 to α_4 determined. For bending mode-I, x/L = 0.224 and 0.776, forming the "active" and "passive" nodes for the suspension mono filaments and/or suspension mount tube.

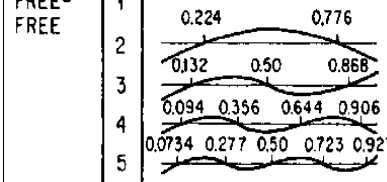
SUPPORTS	MODE n	(A) SHAPE AND NODES (NUMBERS GIVE LOCATION OF NODES IN FRACTION OF LENGTH FROM LEFT END)	(B) BOUNDARY CONDITIONS EQ (7.16)	(C) FREQUENCY EQUATION	(D) CONSTANTS EQ (7.16)	(E) kl EQ (7.14) $\omega_n = k^2\sqrt{\frac{EIg}{A\gamma}}$	(F) R RATIO OF NON-ZERO CONSTANTS COLUMN (D)
FREE-FREE	1		$x=0\begin{cases}X''=0\\X'''=0\end{cases}$ $x=l\begin{cases}X''=0\\X'''=0\end{cases}$	(COS kl) (COSH kl) = 1	B = 0 D = 0 $\frac{C}{A}=R$	0(REPRESENTS TRANSLATION)	
	2					4.730	-0.9825
	3					7.853	-1.0008
	4					10.996	-1.0000-
	5					14.137	-1.0000+
	n>5					$\approx\frac{(2n-1)\pi}{2}$	-1.0000-

Figure 85: Free-Free Beam Roots and Shapes (Braun, 2002)

Applying the free-free boundary conditions for bending Mode-I on the non-dimensional system results in:

$$X(x) = -B\sin(\kappa x) + A\cos(\kappa x) + -B\sinh(\kappa x) + A\cosh(\kappa x) \tag{93}$$

where:

$$B = -A\frac{\cosh(4.73) - \cos(4.73)}{\sinh(4.73) - \sin(4.73)} \quad ; \quad A \ \ (or \ \ \lambda) \ \ = \ \ scaling\,factor \tag{94}$$

A as a response is determined from the initial conditions or forcing function magnitude and has to be determined from empirical testing as it is set by systemic damping as well a the amplitude of forcing being supplied to a system. Working with this solution traces back to approximations by Rayleigh and exact solutions, that if not

derived, were covered by Timoshenko (Timoshenko, 1922).

In the studies employing the bare beam, the assumptions of the Euler-Bernoulli (E-B) static beam theory are all held to be in effect. Among these are: that curvature remains small, that no significant tension stress occurs (only bending), rotary inertia is negligible, and the materials remain in the linearly elastic ranges of loading in the dynamic beam situation. In the past these effects were assumed to be avoided by staying away from saturation regions in the beam operation, keeping displacements of the beam small, and keeping the beam's width and thickness small relative to the length.

The derivation of Euler-Bernoulli thin beam theory typically assumes that curvature is small so that the equation of the elastic curve reduces as per (Hidgen, 1985):

$$\frac{1}{\rho}=\frac{d^2y/dx^2}{[1+(dy/dx)^2]^{3/2}} \underset{\text{when curvature is small}}{\rightarrow} \approx \frac{d^2y}{dx^2} \tag{95}$$

This vastly reduces the complexity of integration in the beam equation for:

$$EI\frac{d^2y}{dx^2}=M_x \tag{96}$$

It is noted that the eigenvector shape yielded by Eqs. (93) and (94) are non dimensional (modal coordinates) in nature. As the response output is determined from the initial conditions and/or forcing function magnitude and frequency, it has to be determined from empirical testing, and at any point in time it is a function of the systemic damping as well as the amplitude of forcing function being supplied.

Avoidance of the large transverse displacement keeps the denominator in Eq. (95) close to unity. Nonetheless, the bare beam at larger amplitudes can display what appears

to be large displacement magnitudes when viewed under a stroboscope. Stated another way, past experimenters had avoided a large curvature condition by using small amplitudes. A quick simulation in Matlab was run to determine the degree to which the assumption of "small curvature" breaks down for the E-B solution for the beam in Eq. (95) and (96). The result, plotted in Figure 86, shows that this is within 10% and only at the outer regions when the tips were displaced out to 10.0 mm (a large displacement corresponding to around 6.3 m/sec, which was about 4X Reed's maximum observed velocity of a coated beam), where the moment loads within the beam are away from the ceramic and also much smaller in magnitude.

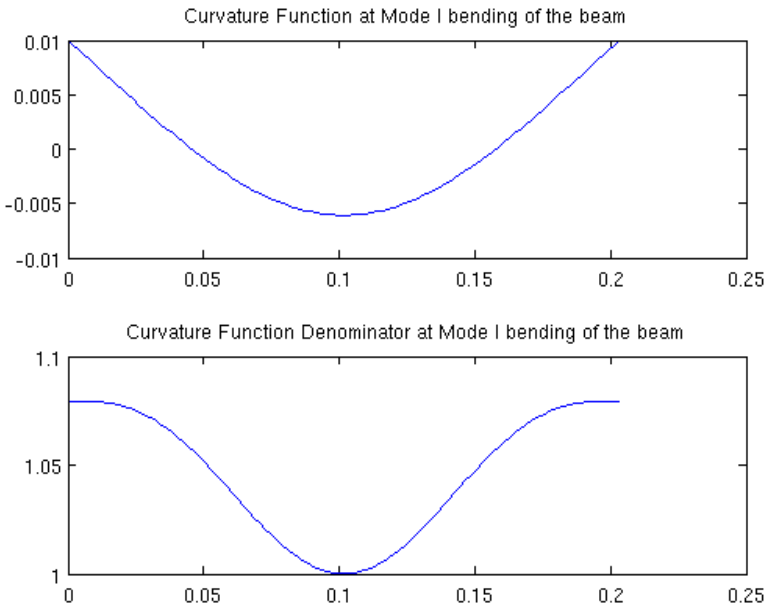


Figure 86: Whole and Denominator of Curvature Function

The current study stayed within the geometrically linear region as the current chamber's amplitude output is much smaller than the configuration Reed used; the ALNICO dipole

moment coupling is much weaker than that of NdFeB magnets. In summery, the current study features analytical simplicity as the actual high cycle fatigue amplitude is very small and non-linearities should be confined to the material properties of the coatings. Experimental confirmation as to the lack of rotary inertia and tension effects in the would be interesting but probably unnecessary given the well established results agreement between the experiment and classical solution for both frequency and shape.

4.2.2. Non-Uniform Dynamic Beam System

The coated beam system presents a problem in determination of the eigenvector in an analytical sense as the coating is discontinuous down the length of the beam, if the TBC layers were continuous for the whole length then the classical solution introduced in the section above would describe the system as it has constant stiffness down the length (e.g. EI is constant) as well as inertial mass (e.g. ρA is constant). The effective stiffness and density determined from the method of cross-sectional area correction as introduced in many standard strength of materials texts could be used to account for the stiffness contribution of the thin coating layers (Higdon, 1967). Unfortunately, the beam under study is only coated for the middle 25% of its length, breaking it into three effective regions, two bare titanium tails that are somewhat less stiff and massive, and a TBC-coated middle region.

Mathematical solutions determined by El-Din, Mahmoud and Nassar and Lee, Ke and Kuo (El-Din, et al., 2002; Lee, et al., 1990) provide an generalized expanded solutions to handle an n-sectioned beam with each section being an E-B beam piece

rigidly attached to the other sections. The papers also treated generalized global boundary conditions as well (cantilever, simple-supported, etc.). Using the work of the former and applying it to a 3-region beam, as shown in Figure 87 below, composed of uniform sections one obtains for the characteristic equation (El-Din, 2002) the following system which is a 12x12 system:

$$\begin{vmatrix} U_{2x4}^{(1)} & 0 & 0 \\ U_{4x4}^{(2-)} & U_{4x4}^{(2+)} & 0 \\ 0 & U_{4x4}^{(3-)} & U_{4x4}^{(3+)} \\ 0 & 0 & U_{2x4}^{(4)} \end{vmatrix} = 0 \tag{97}$$

where the subscripts denote the dimensions of the sub-matrix comprising the generalized solution for that region if the piece, where the superscripts denote the interface location that the solution region tends from, a "-" denotes from the left and "+" from the right.

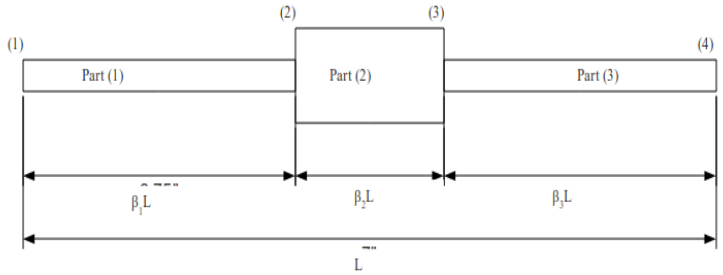


Figure 87: Three-Region Beam of Uniform Cross Section

With the modal frequency determined one now can determine the eigenvector in any given region of the beam the following applies for any uniform segment spanning from i to i +1 (El-Din, 2001), where at the beginning $(i),(\zeta_i=0)$:

$$y = a_1^{(i)} + a_3^{(i)} \tag{98}$$

and at the end $(i+1), (\zeta_i = \beta_i)$ yields;

$$y = a_1^{(i)} \cosh \gamma_i \, p \, \beta_i + a_2^{(i)} \sinh \gamma_i \, p \, \beta_i + a_3^{(i)} \cos \gamma_i \, p \, \beta_i + a_4^{(i)} \sin \gamma_i \, p \, \beta_i \tag{99}$$

where ζ_i is the local coordinate down the segment, and p is a global mass-stiffness aspect ratio to the base (first) segment defined by El-Din as:

$$p^4 = \rho \, L^4 \, \omega^2 \, A_1 / D_1 \quad ; \quad D_1 = E_1 \, I_1 \tag{100}$$

The means to solve this is to either guess a value for the the mode-I root of p close to the bare beam, work out the characteristic equation and hope it is close to zero, e,g, within a certain tolerance level, and if not, adjust the value of p- and repeat (e.g a contraction mapping approach). Or, assume the added layer thickness of the 8-YSZ to I (for stiffness) and A (for mass) is small layer dimensioned as δ. The expand the characteristic equation on O(1) and O(δ) and use the approximated characteristic equation to get the resonance frequency. This 12x12 determinant consists of many terms and no identities were found to readily collapse it with. So some approximated methods were considered based on energy approaches.

One particular method that may work well for this system is Rayleigh's Method, first mentioned in 1847. Cannon's text gives an overview of the method which basically consists of three steps: 1) assume an approximated shape for the mode of interest, 2) calculate the maximum potential energy and maximum kinetic energy for vibration in the assumed mode, and 3) equate the two energy expressions and solve for the frequency (Cannon, 2003). In this way the frequency of the system can be approximated (eigenvalue). With this information and the mode shape assumed function, if confirmed

to be a reasonably accurate one against the FEA model or the experimental coated beam, the SER, $\tilde{\tilde{\varepsilon}}_{11}(L/2,t_b)$, and $\tilde{\tilde{U}}(L/2,t_b)$ values can be backed out by assuming straightforward E-B deformation kinematics and strength of materials methods.

First, one can observe that there are two main drivers of strain energy ratio (SER) changes as the coating stiffness is systematically varied across the candidate values. The first is the difference in strain energy (SE) within the volume of the coating due to the direct modulus change (Ec), and second, very slight changes in the global curvature of the beam as the coating patch is stiffened (See Figure 99, Section 4.3.3) and the resulting localized coating and beam strain magnitude changes. It is suspected that the former is the much more dominant driver of SER changes. It is further noted that the derivation of the Torvik equation (Eq. 123, Section 5.3) invokes the assumption that the change in curvature for the titanium region between the bare beam and that of the coating clad region is negligibly small (See Appendix 6). This leads to the natural conclusion that one may obtain a reasonable SER approximation using the classical beam solution in conjunction with a single point velocity measurement and E-B kinematics to extract a good approximation to the SER.

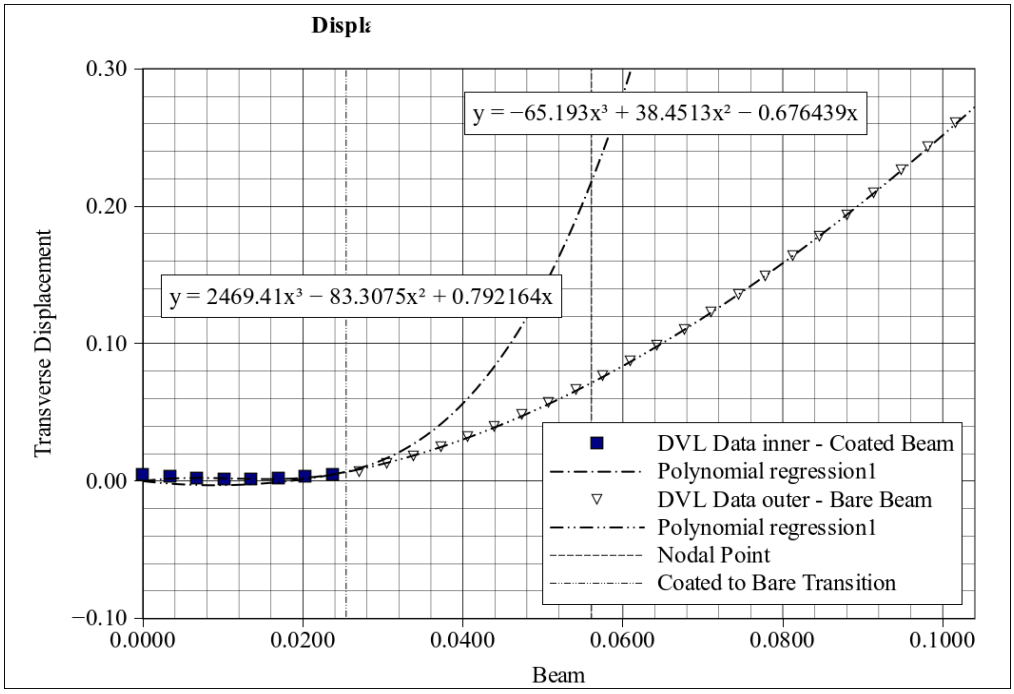


Figure 88: Fitted Cubic Functions on to Coated DVL Data

For a multi-point measurement one can characterize the beam deflection curve using a multi-point measurement with a single-axis DVL or scanning DVL to to get the resonance frequency where the Y(x) is the assumed (or experimentally determined by a scanning DVL laser) displacement function (a cubic function seems to work well in past attempts to characterize the partially coated beam. $Y_1(x)=a_0+a_1x^1+a_2x^2+a_3x^3$ and $Y_1(x)=b_0+b_1(x-L_1)^1+b_2(x-L_1)^2+b_3(x-L_1)^3$ would be determined for each of the intervals with the displacement compatibility between the two enforced (e.g. $Y_1(x)=\{a_1L_1+a_2L_2^2+a_3L_3^3\}+b_1(x-L_1)^1+b_2(x-L_1)^2+b_3(x-L_1)^3$). These cubic functions can fit from discrete experimental data taken down successive points by a single axis DVL or a from a 2-D scanning DVL capture. Figure 88 is a example of the functions that well describe the partially coated beam in transverse displacement in real

coordinates of length and non-dimensional transverse ones. These data-points were captured with scanning DVL on a coated specimen in vacuum and at room temperature (See Section 5.7). Two polynomial relations to describe the transverse displacements were fit to the data, one for the inner, coated region and one for the outer, bare region. This are cubic functions are higher as one will need to describe the third derivative of the displacement which is the moment function for employment in Eq. (107) to obtain the non-dimensional bending strain. An offset was added to both polynomials to translate them vertically until the nodal point is on the x-axis.

To obtain the natural frequency for the coated beam system Rayleigh's energy method where the kinetic energy of a long solid, like a beam is expressed as (Tomson, 1993):

$$T=\frac{1}{2}\int_0^1 \dot{y}^2\,dm=\frac{1}{2}\int_0^{L_1} \dot{y}^2\rho\,A(x)\,dx=\frac{1}{2}\left[\int_0^{L_1} \dot{y}_1{}^2(\rho_1 A_1)\,dx+\int_{L_1}^{L_2} \dot{y}_2{}^2(\rho_2 A_2)\,dx\right] \tag{101}$$

where ρ_1 and ρ_2 are the density of titanium, A_1 and A_2 are the cross sectional areas of the "mass equivalent beam" (see Figure 89) for the coated and bare sections, respectively, y is the non-dimensional displacement, and $\dot{y}$ is the non-dimensional velocity. x is the longitudinal coordinate down the beam. The maximum of the kinetic energy is expressed as Eq. (102), in reducing to this the assumption is made that the velocity is harmonic in form and allows for it to be recast as the product of displacement and frequency (e.g. $\dot{y}=\omega_r \cdot y$):

$$T_{max} = \frac{\omega^2}{2}\left[\int_0^{L_1} \rho_1 A_1 [y_1(x)]^2 dx + \int_{L_1}^{L_2} \rho_2 A_2 [y_2(x)]^2 dx\right] \quad (102)$$

Bending strain energy in the system is expressed as (Tomson, 1993):

$$U = \frac{1}{2}\int_0^L M\, d\theta = \frac{1}{2}\int_0^L \left(EI\frac{\partial^2 y}{\partial x^2}\right)\frac{d^2 y}{dx^2} dx \quad (103)$$

and this can be expanded to express the bending strain energy maximum for a 2-region beam with a TBC coated inner region as:

$$U_{max} = \frac{1}{2}\int_0^{L_1} E_1 I_1 \left(\frac{d^2 y_1(x)}{dx^2}\right)^2 dx + \frac{1}{2}\int_{L_1}^{L_2} E_2 I_2 \left(\frac{d^2 y_2(x)}{dx^2}\right)^2 dx \quad (104)$$

where E_1 and E_2 are the modulus of titanium, I_1 and I_2 are the composite moduli of the "stiffness equivalent beam" (see Figure 89) in the coated and bare sections, respectively.

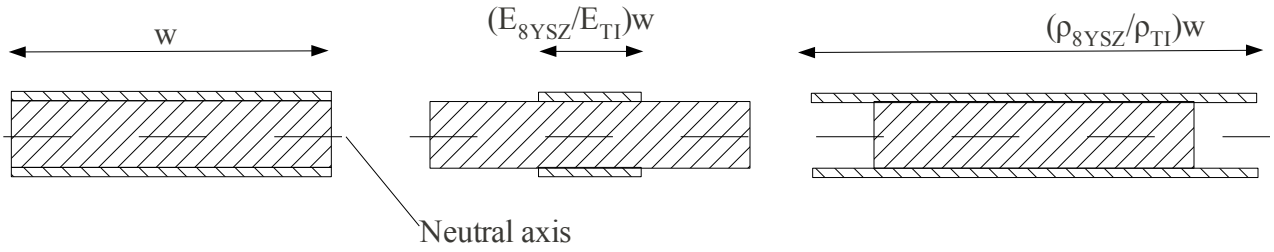


Figure 89: Real, Stiffness- and Mass-Equivalent Beams

Now one can obtain the equivalent resonance frequency between the bending and kinetic energy exchange in the oscillating, conservative system by equating $U_{max} = T_{max}$, which for an arbitrary 3-region beam looks like:

$$\omega_r^2 = \frac{\int_0^{L_1} E_1 I_1 \left(\frac{d^2 Y_1(x)}{d x^2} \right)^2 dx + \int_{L_1}^{L_2} E_2 I_2 \left(\frac{d^2 Y_2(x)}{d x^2} \right)^2 dx + \int_{L_2}^{L_3} E_3 I_3 \left(\frac{d^2 Y_3(x)}{d x^2} \right)^2 dx}{\int_0^{L_1} \rho_1 A_1 [Y_1(x)]^2 dx + \int_{L_1}^{L_2} \rho_2 A_2 [Y_2(x)]^2 dx + \int_{L_2}^{L_3} \rho_3 A_3 [Y_3(x)]^2 dx} \tag{105}$$

Recognizing that bending mode-I is symmetric across x=L/2, one can redefine x(L/2)=0 and Eq. (105) reduces to (where L_1 is the coated beam to bare beam transition, and L_2 is half of the beam length e.g., L_2=L/2):

$$\omega_r^2 = \frac{\int_0^{L_1} E_1 I_1 \left(\frac{d^2 Y_1(x)}{d x^2} \right)^2 dx + \int_{L_1}^{L_2} E_2 I_2 \left(\frac{d^2 Y_2(x)}{d x^2} \right)^2 dx}{\int_0^{L_1} \rho_1 A_1 [Y_1(x)]^2 dx + \int_{L_1}^{L_2} \rho_2 A_2 [Y_2(x)]^2 dx} \tag{106}$$

Now with the eigen-frequnecy determined in Eq. (106), it can be compared back to what was measured in the experiment, and hopefully they are close in value. One can extract the non-dimensional bending strain from the assumption of plane sections remain plane and enforcing strain compatibility across the beam-coating interface which leads to:

$$\sigma = \frac{M c}{I} \quad \rightarrow \quad \epsilon = \frac{[Y'''(x)]c}{EI} \quad \rightarrow \quad \tilde{\epsilon_{11}} = \frac{[Y'''(0)](t_b/2 + t_c/2)}{E_1 I_1} \tag{107}$$

The $\tilde{\tilde{U}}(L/2,t_b)$ is the value of Y(0) when $Y_1(x)$ is translated vertically to make sure the nodal points (Y(0.224L) and Y(0.776L)) are equal to zero. Now with this result the field variables can be arrived at using an experimental-analytical technique. Figure 88 and 90 show the fitting of scanning DVL measured data from down the center-line of the beam as measured from a coated and bare beam, respectively. Table 11 summarizes these findings as compared to the experimental-numerical values, here the middle line of the 2-

D FEA analysis. It is noted that the experimental values are fed into the Rayleigh solution, hence the first line, and the second being experimental-analytic in nature. It is noted that the classical solution, which assumes that the coated beam, essentially follows the same global displacement as the bar beam, and there only accounts for SER due to the modulus ratio between the coating and the titanium, over-predicts SER, strain in the coating, and displacement of the beam. This makes intuitive sense as the global displacement curve impacts of the coating are not accounted for, with their suppression of the displacement in the center region.

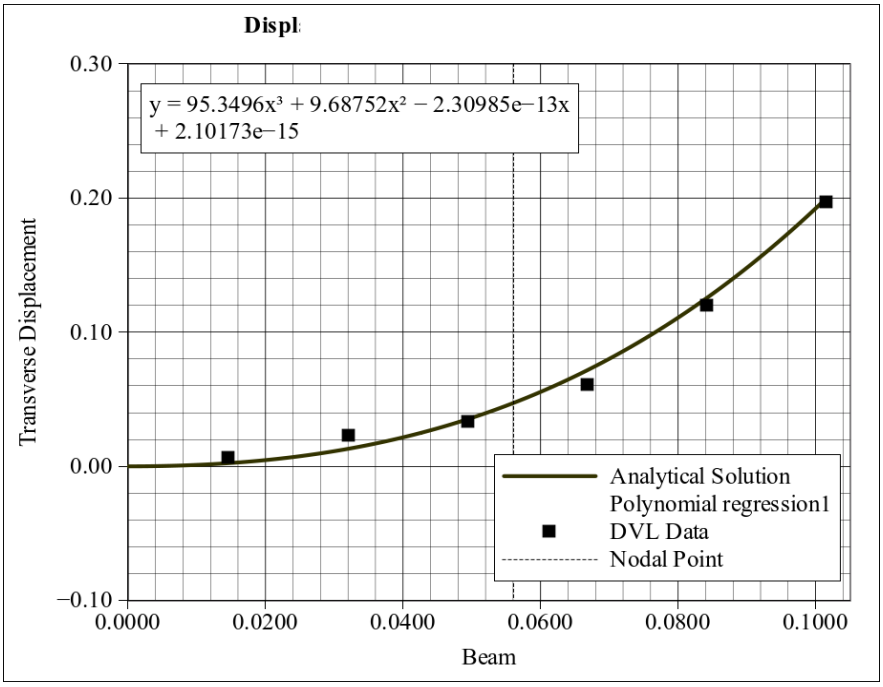


Figure 90: Cubic Fitted to Classical Solution with Bare Beam DVL Data

Meanwhile the Rayleigh's Method estimates are closer to the (assumed accurate) 2-D FEA model results, about 10%, 18%, and 20% for SER, displacement of the center-point, and the bending strain field, respectively. It is noted that getting clean 1-D array

datasets to build the displacement curves was not straightforward. This may well be due to the lack of familiarity with the Poytec 2-D scanning laser and not due to poor theory. One can see that the SER changes due to global curvature is significant and must be accounted for in a analytical model, along with SER changes due to material properties in the metallic versus TBC regions. This suggests, given the assumptions in the derivation of the Torvik equation, that the method be applied to thinly TBC coated beams.

Table 11: Classical and Rayleigh Beam Results

Comparison of Results	Bare Beam System			Coated Beam System				Notes
	f_r (Hz)	$\widetilde{U}(L/2,t_b)$	$\widetilde{\varepsilon}_{11}(L/2,t_b)$	f_r (Hz)	SER	$\widetilde{U}(L/2,t_b)$	$\widetilde{\varepsilon}_{11}(L/2,t_b)$	
Exp. Measurement	203.3			212.2				2-D scanning DVL used to fit two cubics for Rayleigh
Rayleigh's Method	213.46	-0.6091	0.4578	217.63	15.4	-0.4207	0.3684	2-regions of fit to the experimental data of bare and coated beam (Spec.07)
FEA (2-D)	203.66	-0.6074	0.3431	207.85	14.0	-0.5123	0.3007	2-D FEA modal model
Classical Solution	202.02	-0.6099	0.4588	215.14	18.9	-0.6099	0.4588	Global shape is the classical solution.
T = 70.0degF, E_c = 34.0Gps, t_b = 8.3mil								

4.3. Numerical Simulation Using Finite Element Analysis

Most past work for modeling of either the cantilever plate, freex4 plate, cantilever beam, or the free-free beam experimental configurations has been based on modal, eigenvector/value FEA decomposition of the stiffness matrix of the system. The solving of the associated stiffness matrix (or reduced form thereof) and determining the primary vector-shapes is applicable to lightly damped, linear structures. The system form for a

structural dynamics formulation for multiple degrees of freedom is typically expressed as:

$$[M]\ddot{\vec{x}}+[C]\dot{\vec{x}}+[K]\vec{x}=\vec{F}(t) \tag{108}$$

The eigenvalue-problem associated with this leads to:

$$|M-\lambda K|\vec{x}=\{0\} \tag{109}$$

and this yields the basic frequencies and mode shapes of the structure in normalized (often referred to as non-dimensional, or modal) coordinates. Note that information regarding real forcing inputs is not factored in the problem, merely the inherent response of the structure from its stiffness and inertial mass characteristics; the K- and M-matrices, respectively. Typically, in such an analysis, the damping of the beam structure is assumed to be negligible (e.g. [C] = 0), although decomposition for proportionally damped structures (where damping is a linear combination of the mass and stiffness of the structure, e.g. $[C] = \alpha[M] + \beta[K]$) can be worked by mass-orthonormal transformation into a self-adjoint problem and this decomposed.

Non-proportionately damped structures must undergo reduction of order into state-space form. This method is covered in texts by Slater, Cheng, and Hatch (Cheng, 2000; Hatch, 2001, Slater, 2002). This approach, while useful for gaining insight into a system's passive response, whether derived from a lumped structural dynamics model or reduced from an FEA model, does have limitations. These include a response output in normalized coordinates, assumption of a linearly (small) deformed structure, and a passive model response. For a specific response output to a particular input of interest;

Fourier analysis, convolution, or another linear signal has to be applied. Recent work has been performed to solve the full transient model with boundary conditions and loading of the beam structure (Deleon, 2009).

Section 1.4 covers the chronology of experimental measurement and development of the mechanical characterization of TBC coatings; most of the studies had associated FEA modeling of the specimen. All of the models were basic eigenvalue-solutions of the main modal displacements and characteristic frequencies, typically solved by Lanczos decomposition. Most of the work modeling plates by Ivancic, Lee, Allen and Blackwell confirmed the accuracy of the models with respect to the experimental systems of interest. It is noted based on the experimental findings presented in Section 5.1.2, that future plate-based work may want to consider controlling the grain orientation in the titanium and using an orthotropic modulus constitutive model for the titanium. Reed, Pearson, Patsias and Tassini used the FEA eigen-solutions, to adapt the partial Oberst beam theory using Torvik's relation to determine the TBC coating effective modulus and loss coefficients from their experimental systems. Whether by the forward, iterative process to iteratively find the coating modulus by matching to the experiment, or by using an inverse procedure by which the coating modulus was systematically varied and predictive relations built and placing in the values measured from the experiment the experimental-numerical technique is the same. All modeling efforts of the coated beam used Hookian constitutive models with homogeneous and isotropic material for the beam and coated regions without any internal damping.

It was concluded by Deleon that both Pearson and Reed employed the "Solid-45" ANSYS (C3D8 in ABAQUS) 8-noded brick element that is prone to a parasitic shear loss when employed in a bending load situation, thus requiring the authors to artificially deflate their Young's modulus and density below commonly cited book values for the Ti-6Al-4V in order to compensate for these losses in their models (Deleon, 2009). Procedural tuning of the FEA models to the bare beam experiment in both Reed and Pearson used the Young's modulus of the titanium, along the density to a lesser extent, to match the bending 1st mode frequency reported from the FEA to that measured. Deleon used a book value and matched the experiment very closely. (Pearson, 2008; Reed, 2007). Like Deleon, the current study used the ABAQUS standard v6.8-2 commercial FEA code to model the beam system with the lessons learned applied in terms of element selection.

4.3.1. Bare Beam FEA Models in 1-D, 2-D and 3-D

For the current study the FEA model was developed in 1-,2-, and 3-dimension. The models for building these polynomials were all modal based. The titanium beam beam part, two TBC layer parts, and magnet parts (in the 2-, and 3-D models) were modeled as homogeneous, isotropic, linearly elastic solids. The magnets were rigidly bonded to the beam using the “tie-constraint” in the ABAQUS modeling environment. Details on the FEA modeling beyond what is presented in this Section is covered in Appendix 7. Figure 153 in the Appendix shows the three models developed.

Care was taken to closely follow the dimensions of the beams as actually

measured in this study. A 3-part, 1-D, beam-element model ("B31" in ABAQUS element designation) with two coating layer parts and a beam part was generated. A 3-part model was made in 2-D using 4-noded plane stress, incompatible-mode elements ("CPS4I") that, again, were rigidly tied together at the interface to enforce strain compatibility. Two magnet masses that were representative of the cross sectional averaged mass and rotary inertia were added at the active node location. A third model, this one fully 3-D, was constructed again using three parts rigidly tie-constrained together at the coating-beam interface. In this last model, the default element selected was the 8-noded brick, incompatible modes (excluded) element ("C38I"). This selection of element for a thin structure in bending was a critical choice; Reed and Pearson had adjusted the modulus of their bare titanium beam to match the resonance frequency of their experimental bare beams, and the values used were artificially high and low, 118.5 and 110.4Gpa, respectively. Deleon determined a proper element type selection, namely the linear stress, incompatible-mode rejecting one, that allowed an FEA model using material book values to closely match the experiment. The incompatible mode elements prevent shear-locking despite being 1st order (e.g. linear function) elements used in a thin structure under bending (Deleon, 2009). Additional features of the current FEA models that were adopted based on Deleon's recommendations were: spatially accurate magnet masses at the active node in the 3-D model, and the use of free-free boundary conditions with high confidence based on extensive boundary condition sensitivity studies that the author had performed. The magnets were modeled as a point rotary and inertial mass in the 1-D model and as a spatially averaged cross-sectionally averaged, and distributed, mass in the 2-D model.

There are no explicitly defined geometric boundary conditions in any of the dynamic beam models as the system is a free-free one. Deleon did define explicit constraints to the beam model and performed extensive sensitivity analysis. The author reported that the explicitly defined boundary conditions were quite close to the defacto (implicitly defined) free-free condition. Deleon reported that the beam resonance shape, frequency, and field values were fairly hard to influence in any significant fashion with such imposed changes in slight mis-location of the passive node location, magnet stack misalignments, and suspending wire transverse spring stiffnesses (Deleon, 2009). Not defining explicit boundary conditions for the free-free beam does result in ABAQUS returning the lower six modes in its eigen-system decomposition as the three rigid body translations and three rotations, and the bending mode-I is the 7^{th} mode, but this is not a major complication in the application of the results.

4.3.2. Coated Beam FEA Models in 1-D, 2-D and 3-D

The finite-element models were developed in the ABAQUS v6.8-2. As a model was put together using each level of dimensionality, the first question posed was, which model dimensionality should be selected for use in building the polynomials? To help answer this, a set of polynomials was built for the room temperature beam with each dimension of model and these polynomial curve sets were compared. Additionally, mesh refinement was performed on the 2-D and 3-D models, along with some trials using some 2^{nd} order elements. All of the models used structured meshes, that is those that are of defined grids using elements that are regular solids in shape, in this case beams,

quadrilaterals, and bricks for 1-D, 2-D, and 3-D models, respectively.

It is noted that for all of these models, that the thickness of the bond coating layer was treated as if it were the 8-YSZ TBC material. This is the assumption Deleon and Pearson employed; it is noted that Reed's experimental specimens did not have a bond coat layer (Pearson, 2008; Reed, 2007; Deleon, 2009). This was felt valid on a couple of reasons. First, the bond coat layer as carefully examined under an optical microscope and measured, is highly discontinuous and localized in discrete blobs of material; it is quite incapable of sustaining a bending shear flow as an even continuous layer would. Second, the results of testing for frequency and damping of the bond coated only beam (Section 5.4) were very close to those of the bare beam set across all temperatures tested, suggesting that the bond coat has a very low influence on the coated beam system.

Both the beam and the TBC regions were modeled as linear elastic, isotropic, and homogeneous materials rigidly bonded at the interfaces between the regions. The strain compatibility was enforced across the boundary by usage of the rigid “tie constraint” construct in ABAQUS. The 1-D model consisted of three sets (denoted as “parts” in ABAQUS terminology) of 2-noded linear beam elements (in ABAQUS donated as “B31”) for the upper and lower TBC coatings and the TI beam, each of which is denoted a “part” in ABAQUS terminology. The two coating parts were rigidly tied to the main beam (ABAQUS denotes an “assembly”) node-by-node.

4.3.2.1. Results of Dimensionality, Mesh and Element Selection

The beam models were run with the candidate coating moduli for the 8-YSZ of 15, 30, 45, 60, and 90GPa and were run. Based on likely values for 8-YSZ and Mag Spinel reported in the literature, these values were chosen in an educated guess; it was felt they bracketed the likely range of variation of the coating modulus that would likely be found. An associated bare beam model was also run. All of these simulations were performed with a coating thickness of 6.0-mils and the titanium at a room temperature book value of 115.5GPa (Mil-Handbook-5H, 1995). For each of the fifteen runs for coated beams (3 model dimensions x 5 different coating candidate moduli) several values were extracted from the bending mode-I results. The first was the reported resonance frequency (or eigenvalue), f_r. Next were nodal values at the intersection of the center-point of the wide face on the coating and metallic beam interface plane. This is directly under where the DVL laser is aimed on the experimental specimens. From this nodal point, the non-dimensional displacement and bending strain are recovered; $\tilde{\tilde{U}}(L/2, w/2, t_b)$ and $\tilde{\tilde{\varepsilon}}_{11}(L/2, w/2, t_b)$. The last value to be extracted from the run is the elastic strain energy ratio (dubbed in ABAQUS as "ELSE" and extracted from the whole element), the elastic strain energy is non-dimensional in nature, but since a ratio of two different regions is being generated, the non-dimensionality is not an issue. The ELSE is tallied and totaled for the two coating part regions and then for the beam metallic part region. ABAQUS has the report generation feature to dump the element by element values and report the totals for each part. For the three bare beam runs the f_r, $\tilde{\tilde{U}}(L/2, w/2, t_b)$ and

$\tilde{\tilde{\varepsilon}}_{11}$(L/2, w/2, t_b) were extracted.

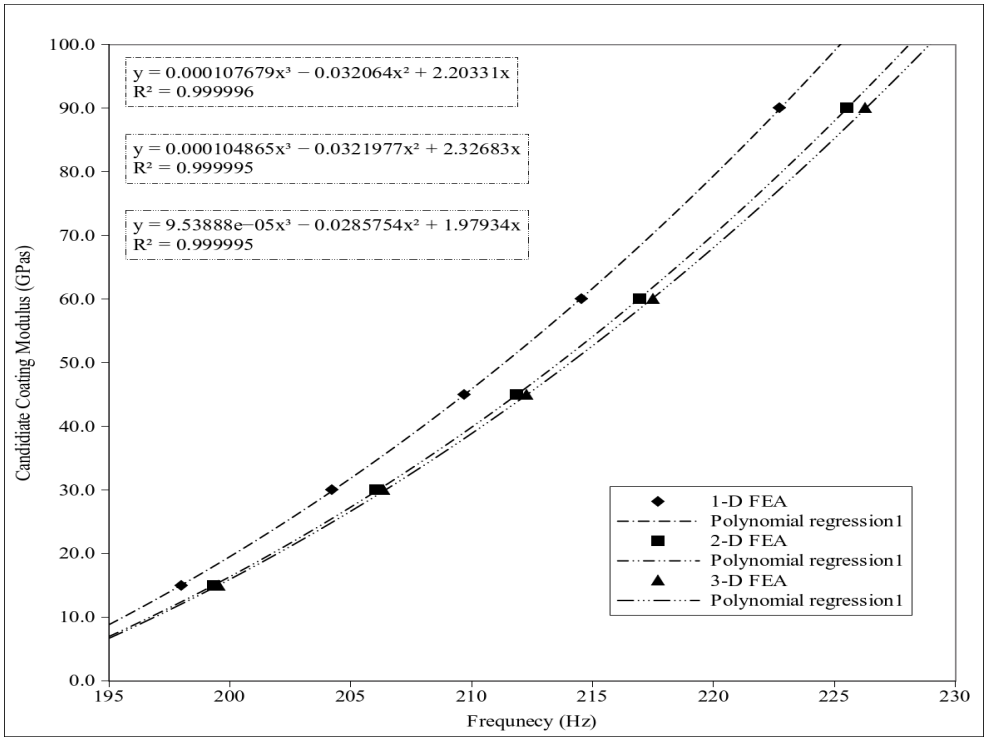


Figure 91: Coating Modulus as a Function of Frequency

The first predictive polynomial, that determining the coating modulus as a function of the experimental beam's measured resonance frequency, (e.g. $E_c = f(f_r)$), are plotted for the 1-, 2-, and 3-D models in Figure 91. As can be seen the agreement between the 2-D and 3-D models is very good. The 1-D is quite close as well, it is suspected that the main reason it predicts a higher stiffness in the coating for a given resonance frequency is due to the fact that the localized stiffening effect of the magnet stack is not modeled, only the point mass and rotary inertia is accounted for. Correction for the stiffness around the active beam node under the magnet clamp region would probably bring it into better agreement with the other two models. It could be determined by averaging across the width of the 3-D model in a fashion similar to what was done for

the 2-D magnet model.

The second polynomial, which determined the non-dimensional transverse displacement as a function of the candidate coating modulus ($\tilde{\tilde{U}}$(L/2, w/2, t_b) = f(E_c)) is shown in Figure 92. Here the agreement between all the three models is excellent.

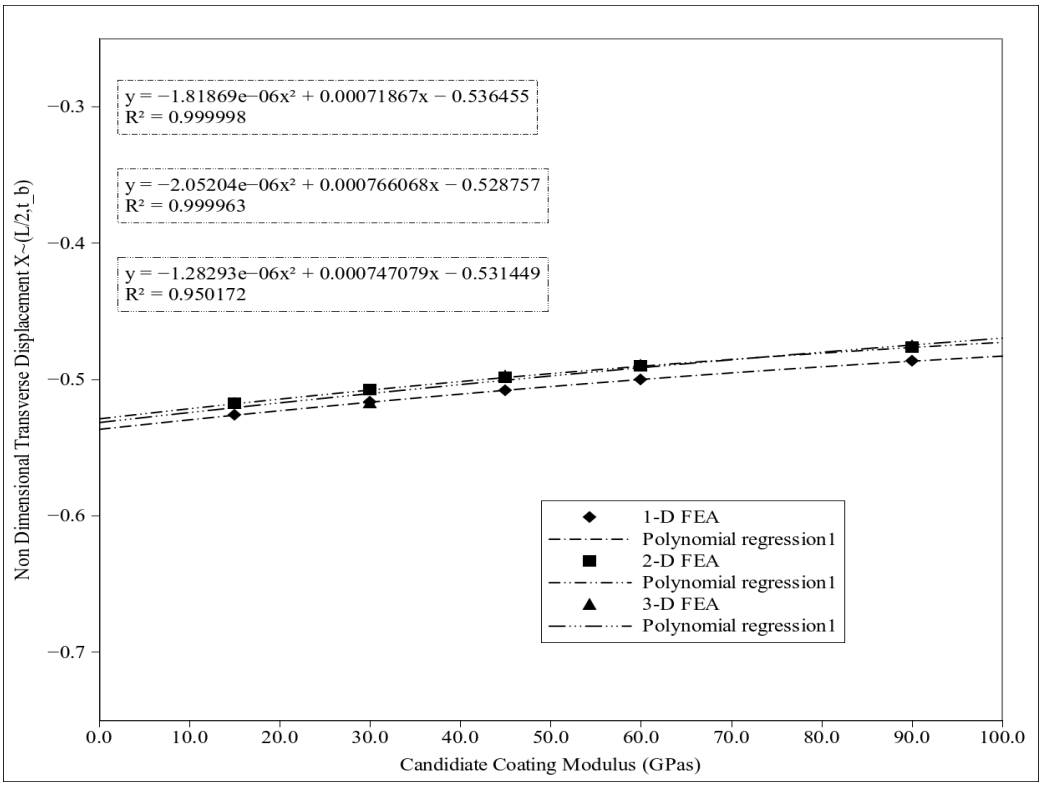


Figure 92: Transverse Displacement as a Function of Candidate Coating Modulus

This plot, along with the results for the third polynomial, indicate that the global shape (eigenvector) prediction between all the models is very good. The third polynomial results are plotted in Figure 93; these relate the non-dimensional bending strain at the point of interest as a function of the candidate coating modulus ($\tilde{\tilde{\varepsilon}}_{11}$(L/2, w/2, t_b) = f(E_c). Again, the dimensionality of the model does not influence the results in any significant fashion.

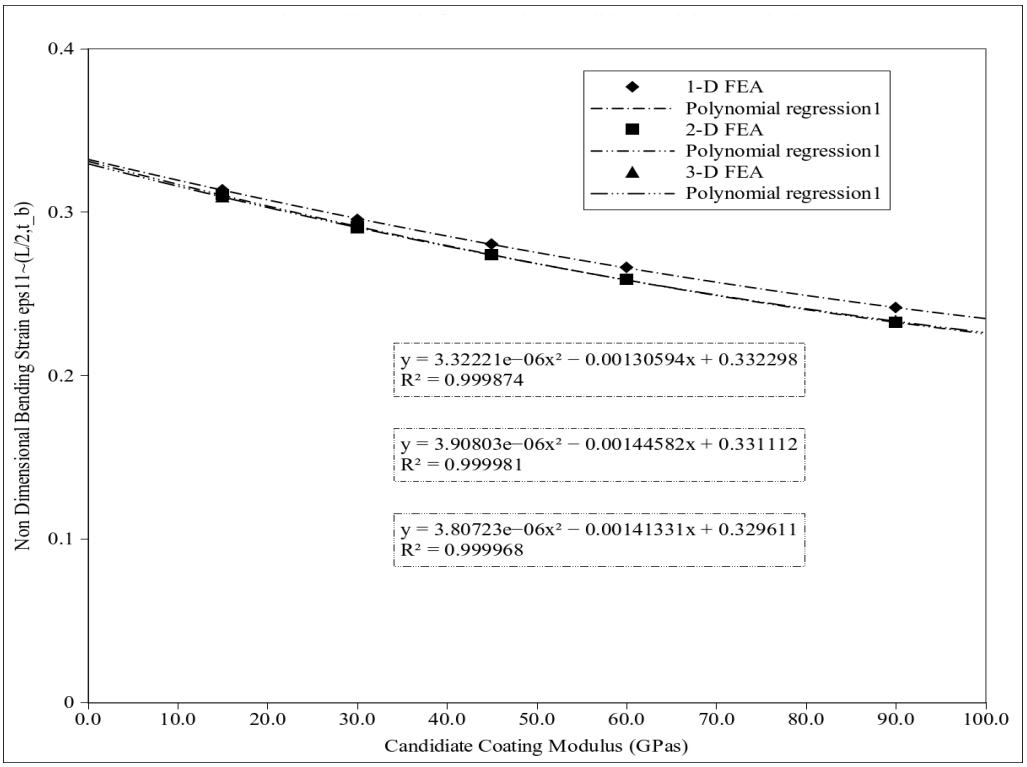


Figure 93: Bending Strain as a Function of Candidate Coating Modulus

The last polynomial, which relates the strain energy of the two coating layers over that of the metallic beam part region as a ratio (SER = $f(E_c)$) are plotted in Figure 94, there is only slight variation in the prediction of the three models. As the dimensionality goes up the off-axis stresses and strains contribute to the ratio, ε_{22} and σ_{22} in the 2-D and ε_{22}, σ_{22} and ε_{33}, σ_{33} in the 3-D model, this is likely the source of the slight variation in the 3-D and 2-D models from the 1-D model.

It appears that all of the models would be acceptable for building the predictive polynomials. Though the 3-D is the most accurate and precise in capturing the fine details of the coated beam geometry, it is the most computationally expensive and tedious to post-process for the extraction of the desired values. Also, the mesh density in certain regions suspected of high stress gradients may be below the fidelity required unless the

part is partitioned and assigned multiple meshes, and this requires some a-priori insight into the regions of large stress gradients. The 1-D model, while being computationally efficient, very simple to post-process, and workable for building polynomials that would have acceptable error was passed over in favor of the 2-D model. There are some explainable deviations, especially for the first polynomial, and to a lesser extent, the fourth. Given the (unexpectedly high) precision to which the experimental rig determines frequency makes the 1-D error a little too large to select. The 2-D model is a good compromise on all these issues as was selected as the model to use across all the temperatures to build the other polynomial sets. It also allowed for a finer mesh to be used in the coated region than the 3-D model did.

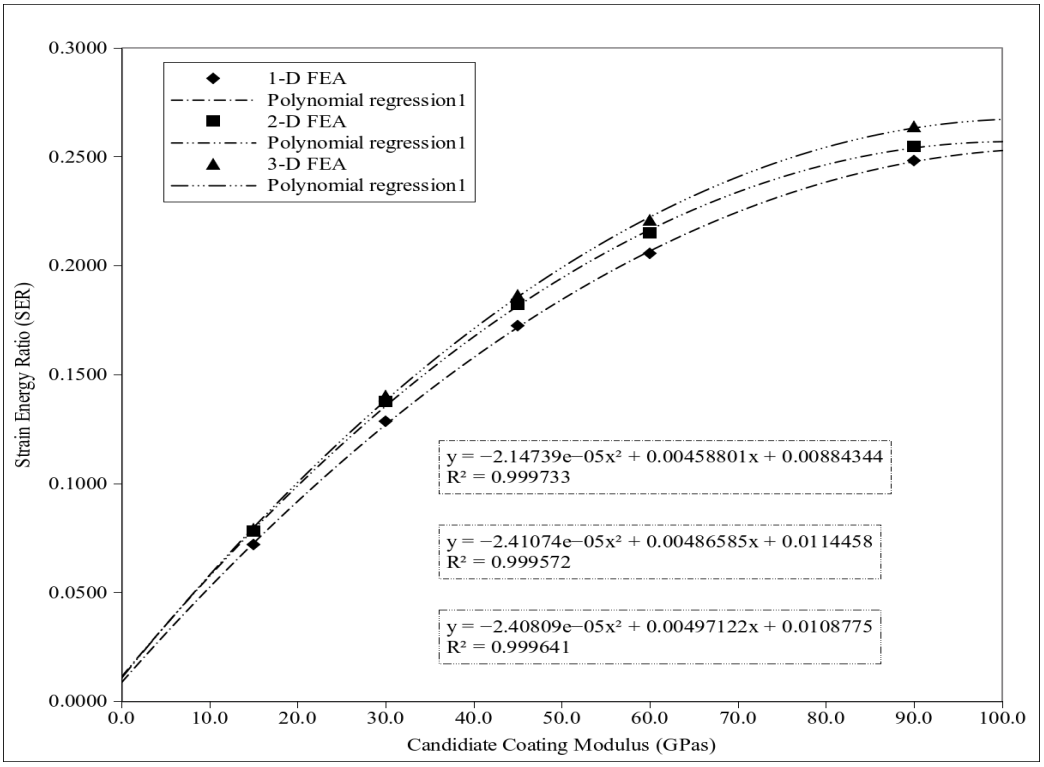


Figure 94: Strain Energy Ratio as a Function of Candidate Coating Modulus

To help determine an optimal model, some mesh refinement studies were

performed on the 2-D and 3-D models, Table 12 summarizes these runs. For most of the runs the 1st order (linear function), incompatible-mode rejecting elements were employed, an 8-noded brick for the 3-D and a 4-noded quadrilateral for the 2-D model, but for some of the runs the meshing was performed with 2nd order reduced integration (quadratic stress function) elements, a 20-noded brick and 8-noded quadrilateral for 3-D and 2-D model, respectively. The "seed" size mentioned in the Table, an ABACUS-specific term, is basically the inter-nodal spacing used to form elements.

As can be seen from the Table, for the 3-D model, the changes in the four values that were extracted to build the polynomials, f_r, $\tilde{\tilde{U}}(L/2, w/2, t_b)$, $\tilde{\varepsilon}_{11}(L/2, w/2, t_b)$ were minimal with mesh refinement, typically under 1-2%. This is consistent with grid independent findings. 2nd order reduced integration elements in bending also appear to give consistent results.

Table 12: Mesh Refinement and Element Selection Study on 2-D and 3-D Model

Mesh Refinement and Element Selection Study on 2-D and 3-D Model													
Dim	Mesh Grade	Element Type	No. Elem. Deep in Coat	No. Elem. Deep in Beam	Total # Elements	Seed-size (m)	First Bend Mode Freq. (Hz)	Strain Energy in top coating $U_{Coating}$	Strain Energy in lower coating $U_{Coating}$	Strain Energy in Beam U_{Beam}	Strain Energy Ratio SER	Non Dim. Displ. U(L/2, t_b)	Non Dim. Bend Strain $\varepsilon_{11}(L/2,t_b)$
3D	Ultrafine	C38I	2	6	NA	*	*	*	*	*	*	*	*
3D	Fine	C38I	1	6	24130	0.00025	217.67	542.90	542.90	4880.23	0.2225	0.2521	0.4890
3D	Medium	C38I	1	3	3876	0.0005	217.93	542.68	542.68	4878.72	0.2225	0.2577	0.4891
3D	Coarse	C38I	1	2	969	0.00100	217.69	539.56	539.56	4861.33	0.2220	0.2590	0.4896
3D	Coarse	C3D20R	1	2	969	0.00100	217.44	536.45	536.45	4870.4	0.2203	0.2587	0.4895
2D	Ultrafine	CPS4I	4	26	1561	$6.1x10^{-5}$	216.85	529.19	529.21	4944.42	0.2141	0.2584	0.4903
2D	Fine	CPS4I	2	13	766	0.00012	216.89	529.76	529.78	4943.43	0.2143	0.2585	0.4903
2D	Medium	CPS4I	1	6	180	0.00026	216.96	530.89	530.82	4941.56	0.2149	0.2586	0.4902
2D	Coarse	CPS4I	1	3	99	0.00053	217.03	532.24	532.25	4939.55	0.2155	0.2587	0.4902
2D	Coarse	CPS8R	1	3	99	0.00053	216.94	530.41	530.43	4941.88	0.2147	0.2585	0.4903
2D	Very Coarse	CPS8R	1	2	19	0.00079	216.98	531.17	531.19	4940.14	0.2150	0.2586	0.4902
2D	Ultra Coarse	CPS8R	1	1	18	0.0015	217.09	533.22	533.24	4935.98	0.2161	0.2588	0.4902
2D	Medium	CPE4I	1	6	180	0.00026	228.18	This model was 2-D, using plane strain elements, markedly higher frequency precluded further processing.					
* - Model exceed computational resources available.													

For the 2-D model all the cases, save one, yielded close results, even with reduced integration 2nd order elements. An especially fine grid could be achieved in the coating with a 4 element depth possible; this helps to capture large strain gradients in the thin coating. The one out-lier case was when the model was meshed with the plane strain element, this system, as expected was noticeably stiffer. It had a higher eigenvalue than the (default) plane stress element models. This is consistent with a constraint on out of plane strains in the beam leading to higher bending stresses in the beam through Poisson ratio effect coupling. The plane stress values are all much closer to the experimental

system, demonstrating the validity of the plane stress assumption in the model whether analytical or numerical.

4.3.3. Building the Predictive Polynomials

After the mesh refinement studies were completed and the 2-D model was found to be acceptable to use for this study, preparation for building the polynomial sets began with a selection of candidate coating moduli. The values of candidate E_c; 15, 30, 45, 60, and 90GPa were used to build this set.

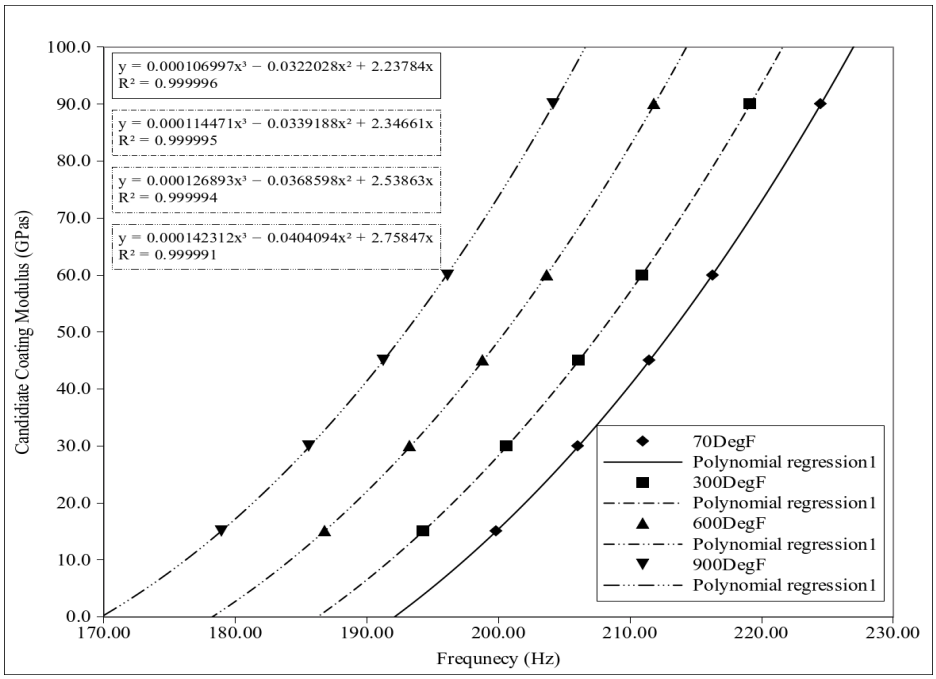


Figure 95: Coating Modulus as a Function of Frequency

The thickness of the coating layers in the models were now adjusted to accurately reflect the as measured beam specimens which were determined to be 5.7, 8.3, and 12.5mils (See Section 5.1.1). Additionally, the book values of the Ti-6Al-4V modulus,

the constitutive value that was changed as the beam model went from 70 to 900degF, were found to be inaccurate based on direct characterization of the bare beams across the temperatures (Section 5.3). With these updates to the 2-D model it was run at the four temperature conditions (70, 300, 600, and 900degF) and the three different coating thicknesses, yielding 36 polynomials in all. The temperature states were enforced by changing the modulus of the titanium beam as per Eq. (135) developed in Section 5.6.1. Figures 82-85 summarize the results.

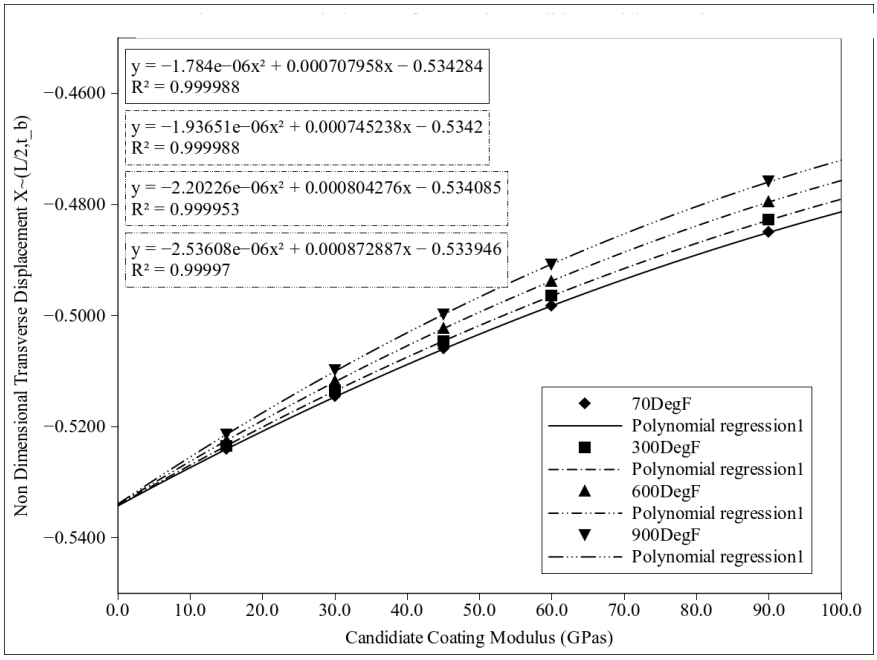


Figure 96: Transverse Displacement as a Function of Candidate Coating Modulus

The first polynomial which relates the candidate coating modulus of the coated beam back to the measured resonance frequency of the experiment (e.g. $E_c = f(f_r)$) determines the storage modulus (or "stiffness") of the TBC coating. Unlike the three other polynomial fits, it is a 3rd order polynomial fit. Figure 95 shows the fits for the 8.3mil thick coating at 70, 300, 600, and 900degF.

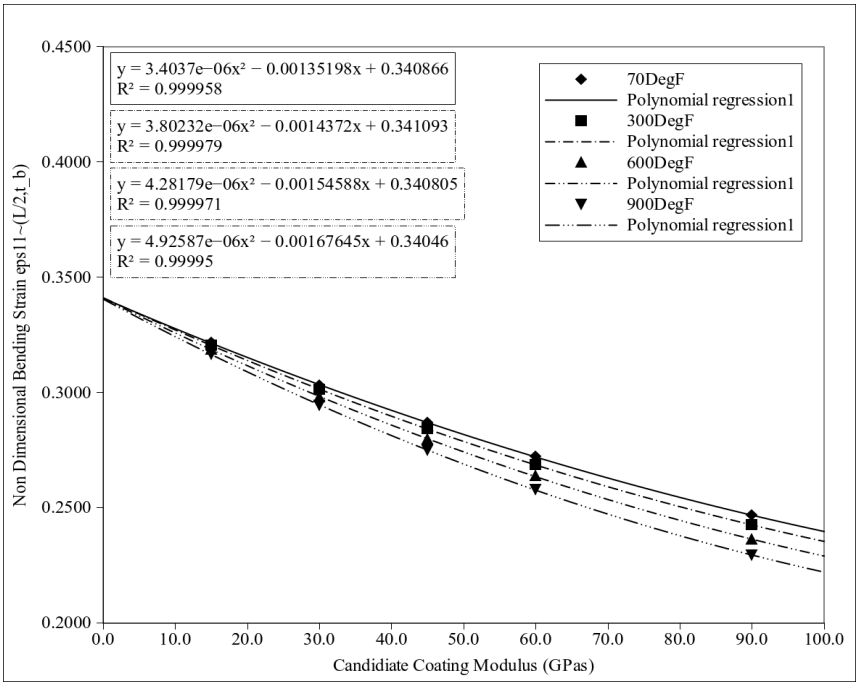


Figure 97: Bending Strain as a Function of Candidate Coating Modulus

The second polynomial is the prediction of the non-dimensional displacement of the coating-TBC interface located under the measurement point of the DVL as a function of the coating storage modulus (e.g. $\tilde{\tilde{U}}(L/2, t_b) = f(E_c)$). This polynomial is primarily used to scale the modal FEA results to the beam experiment, in other words, to determine the scaling factor ($\lambda = x(t)/\tilde{\tilde{U}}(L/2, t_b)$). Figure 97 shows the 2nd order polynomial fits for $\tilde{\tilde{U}}(L/2,t_b)$. These curves are fit to negative values of U, following the convention of the previous studies, but it is noted that the $+\tilde{\tilde{U}}$ values at the other extreme of the displacement curve, 180° away in phase, could also be used.

The third polynomial relates the non-dimensional bending strain at the beam-TBC coating interface under the DVL measurement point back to the candidate coating modulus ($\tilde{\tilde{\varepsilon}}_{11}(L/2,t_b) = f(E_c)$). This allows inference of the bending strain field within the coating region (in the general vicinity, provided the coating is thin, and relatively short in

comparison to the beam itself) without disturbing the experimental system. Figure 96 shows the 2nd order polynomial fits for the 8.3mil coating across 70, 300, 600, and 900degF. This third polynomial is what enables the reporting of loss factor and storage modulus across the strain variation. It does need to be scaled to the experimental strain through the scale factor, which is obtained from the second polynomial and the experiment.

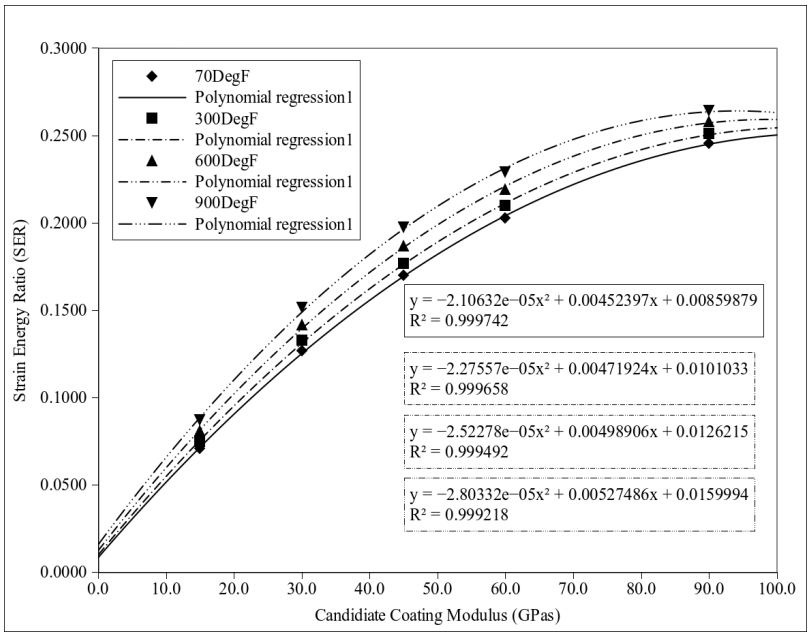


Figure 98: Strain Energy Ratio as a Function of Candidate Coating Modulus

The fourth polynomial is the strain energy ratio (SER), that is the ratio of elastic strain stored in the coating over that stored in the beam, as a function of the candidate coating modulus (SER = f(Ec)). It is non-dimensional, but being a ratio, it need not be scaled to the experimental system. The SER allows for the determination of the coating's damping influence on the system using the Torvik equation. Figure 98 shows the set of 2nd order curves that predict SER for an 8.3mil thick coating. Three tables (17, 18, and

19; all in Appendix 7) break down all of the polynomial coefficients for each of the three coating thicknesses. The bare beam findings are summarized in Table 17.

The Torvik equation is restated here for reference, and it is the relation in which the coating bulk loss coefficient is extracted from the experimental system in conjunction with the numerically extrapolated results;

$$\eta_c = \frac{\eta_{sys}(SER+1) - \eta_{bare}}{SER} \tag{110}$$

where η_c is the coating loss modulus in a bulk material sense, η_{sys} is the loss modulus of the beam system, η_{bare} is the loss modulus for the bare beam system (which can be regarded as synonymous with the loss modulus of the titanium as a bulk material, η_{TI}, given a sufficiently undamped apparatus), and SER is the strain energy ratio as predicted from the FEA model. Derivation of this equation is detailed in Appendix 6 and detailed in here are the assumptions inherent in its use. Some key ones are: the geometric deformation between the bare beam and the metallic titanium region in the coated beam is the same, the air damping can be neglected in the system, the clamp or suspending boundary damping can be neglected, the materials are linearly elastic ("Hookian"), isotropic, and homogeneous. It is noted that the first assumption is predicated on the relative invariance in global curvature despite coating stiffness variations. Figure 99 illustrates the relatively small variations in curvature that result as the coating is varied in elastic modulus. The curves are extracted from the long-axis centerline of the beam and are of U(x,0) versus x down the centerline. The bare beam is plotted in a solid bold line for comparison. It can be seen that global curvature changes are relatively small from

case to case, even compared back to the bare beam case. This helps buttress the validity of the assumption made in the derivation of the Torvik equation and suggests that the classical solution may yield a decent SER estimate for the coated beam. From

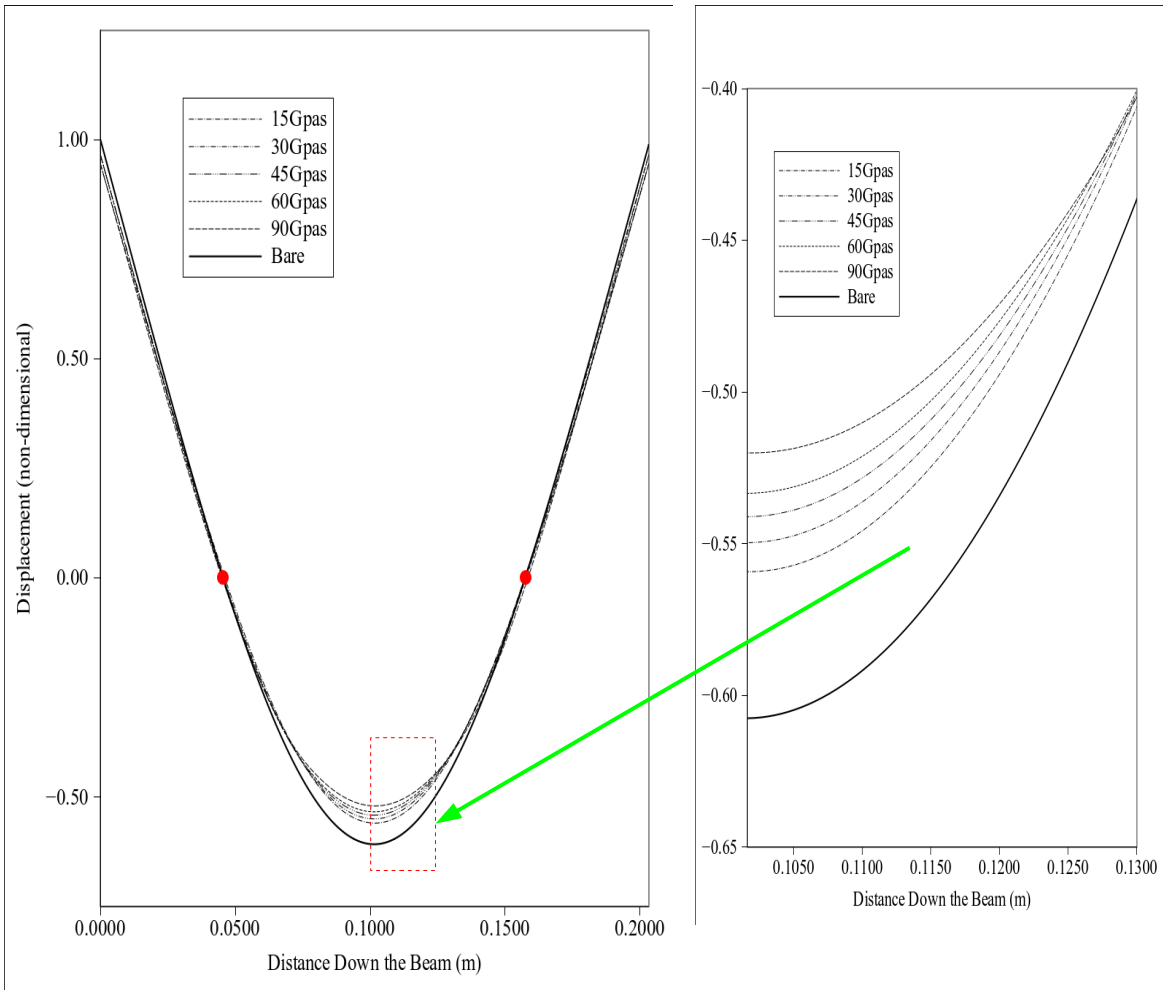


Figure 99: Beam Curvature Changes with Coating Moduli; whole (left), close up (right); 70degF

examination of Figure 99 it can be seen that the strain energy magnitudes will be over-predicted due to more severe curvature in the bare beam, but uncertainty as to how the ratio will fall will be unclear.

4.4. Sensitivity Studies to Magnet Mass in 1-D and 3-D

This was accomplished using the 1-D and 3-D bare beam models. The results are presented and discussed in Section 2.8.3.

4.4.1. Use of Harmonic Integration to Determine Scaling Factor

The DVL laser measures the velocity of the beam at a discrete point in a non-contacting fashion though the optical access port. The displacement of this point in space is needed to scale the modeled beam to the actual experimental beam through the scaling function. As the beam is a steady oscillating system, v(t) is a sinusoidal function of the form v(t) = sin(2πfrt). To obtain the displacement function x(t), v(t) is integrated over time as per:

$$x(t)=\int_{t_1}^{t_2} v(t)dt=\int_{0}^{2\pi} \cos(2\pi f_r t)dt=\frac{1}{2\pi f_r}\int_{0}^{2\pi} \cos(2\pi f_r t)\,dt \qquad (111)$$

Equation 111 is predicated on the beam being in a steady-harmonic state, whereas in actuality during the course of a free-decay run, it is an exponential decay. However the damping of the system is so small that the decaying oscillation is essentially a harmonic function. Appendix 8 details the math establishing the validity of this conclusion.

It is noted that some models of DVL can measure the displacement of the aim point, however this is not performed for two reasons, first the precision of the velocity measurements is much higher based on the data-plate information, and second, momentary shocks and disturbances to the system show up as momentary glitches in the

data instead of permanent offsets in the data record as would be the case with displacement data.

4.4.2. On the Mechanics of the Suspension Wires

The theory of the vibrating string and determining the rigid body modes that the beam exhibits due to energy loss on the strings is covered in Section 2.7.3. The suspension wires to be used in the experiment had to be modified, past experiments had employed Stren™ 6-lb test nylon mono filament fishing line. Obviously this material will creep under the higher temperature ranges anticipated, if not outright melt and vaporize as the temperature approaches 900degF. Due to this 0.005in diameter nichrome resistance wire was employed. It was planned that this wire would be tuned by controlling the tension and length of the free span to keep its resonance modes well separated from those of the beam. Nichrome is resistant to creep at the elevated temperatures, and adds minimal mass and damping to the beam system. Nichrome wire, with a melting temperature of around 1400degC, will barely exceed 1/3rd of its melting temperature and should stay well below the creep region even under tension. The material did not creep, but as seen in Chapters 2 and 3, significant sag entered the system as the chamber heated, and all the components expanded, including the wire; as a result a brass slack take-up weight had to be used.

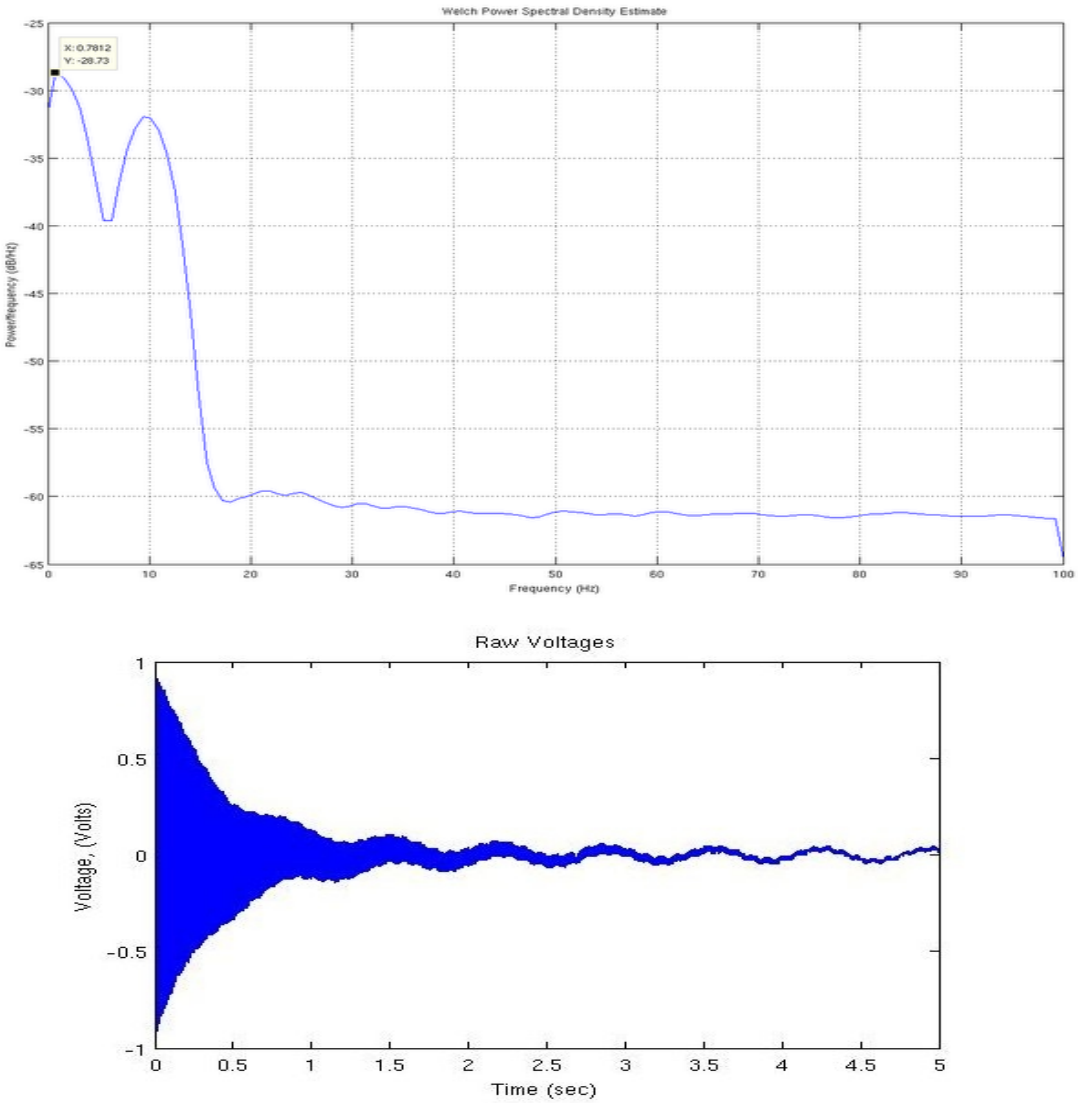


Figure 100: Fan Impingement FFT (top), Typical Free Decay Test with Rigid Modes (bottom)

After the current chamber was fabricated, a stroboscopic study of the free-free beam's rigid body motions was performed and three modes were identified as being significant. Least influential due to its orthogonal direction to the DVL beam was the "pogo" mode, the vertical up and down bouncing of the beam on the passive node line. More influential was the back and forth mode, dubbed "flutter", that was parallel to the

incoming DVL beam; it exhibited a frequency close to that of the pogo mode, around 10-11Hz. This is because the wire's transverse stiffness is roughly equivalent regardless of orientation, the same holds for the inertial mass of the beam. The most significant mode was the rigid body swinging around the passive node wire, called “nodding”, this was the largest rigid body mode that was around 1-3Htz in frequency. It is noted that all of these tests were conducted after the core 8-YSZ tests were done, and had similar environmental conditions except for the lack of a vacuum around the beam. To stimulate all of the modes in a somewhat random fashion the beam was stimulated with a fan aimed at it. The DVL was aimed at the usual measurement location and a 10 second v(t) signal was captured and processed through a Fourier decomposition. Figure 100 displays this, and the “nodding” peak can be seen at about 1Hz, to the right and down about 6dB (about %50 of the amplitude) is the “flutter” at about 10Hz. The right side of Figure 100, which is a typical ring-down trial, clearly shows the larger “nodding” signal imposed on the bending mode-I decay, with a much smaller amplitude and high frequency ripple from the “flutter” mode. Reed also measured these directly by means of Fourier decomposition of the velocity signal. Reed had filtered in software after data collection for the rigid body motion anticipated from the frequencies obtained via the wave equation using a localized cubic smoothing spline technique on the envelope function.

High temperatures required replacement of the nylon guide tube in the current study. Cross boring a fine hole through the beam to allow threading the nichrome wire through to be performed. Modeling of the passive node based on the locating of the suspension boundary condition on the neutral axis, as opposed to an eccentric location (as

would be with a surface mounted tube) was not performed as it was suspected that damping contributions from forcing the wire due to the slight eccentricity would be small. As later experimentally confirmed, this conjecture was wrong, the eccentrically located wire actually was forced in a significant fashion and significant energy loss through the passive node wire occurs if the hole is eccentric. It is suspected a similar pumping mechanism, stronger due to the larger radial axis of the magnets, was bleeding the vibrational energy out of the system when the lower two wires were resting against the magnets. The nylon mono filament line used in the previous studies will be replaced with the aforementioned nichrome wire of fine gage. American Wire Gage (AWG) size 36 is 0.005in in diameter and is an optimal size for the wire. This wire is selected based in the following properties; sufficient strength and stiffness, modest density, temperature resistance, creep resistance up to 950degF, ease of working into knots and through holes.

4.5. Combining the FEA Analysis with the Experimental Results to Extract Coating-Specific Properties

With the polynomials now determined for the coated beam system at various temperatures and a set of experimental beam system-level measured quantities, namely the instantaneous frequency and the instantaneous damping throughout the free decay response, the two can be brought together to extract the coating specific quantities. The process of experimentally obtaining the system-level loss coefficient and instantaneous frequency will be covered first, and then the extraction of the coating specific properties (complex modulus) after.

4.5.1. Extraction of System Damping and Resonance Frequency from Testing

For any given ring-down data run, the coated or bare free-free beam under test has been brought to a thermal equilibrium within the chamber under vacuum conditions and the resonance peak tuned in for the prescribed amplitude. The beam is allowed to come to a steady harmonic state under the sinusoidal excitation. Upon the settling of any transients, the excitation to the electromagnetic coil is cutoff at time t_0 and the system undergoes an under-damped exponential (-like) decay. Provision of the excitation signal on an output channel of the National Instruments data acquisition card/board (DAC) was done, while the excitation signal is feedback to one analogue input channel in the board to measure the input signal (from the reference of the beam being the plant), and the DVL was measured on another channel to recored the output signal from the free-free beam plant. Sampling for both of the measured signals as well as the generated one were at 2000Hz (a measurement/output every 0.5 millisecond). It was known a priori, from work on the specimen blanks with an oscilloscope, that the beam responses were smoothly varying sinusoidal signals of around 180-230Hz in frequency. The Nyquist criterion states that to accurately measure and characterize a harmonic signal, one must sample at least twice the highest frequency component of interest. At 2000Hz, which was used throughout all of the ring-down studies, the datasets were sampled at almost 10X the frequency of the desired components.

A LabView v2007 Virtual Instrument (VI) was written to automate the process of free-decay excitation, timing, and response measurement from the beam system. The

LabView code stored all of the raw measured signals to a data file to allow later off-line processing in Matlab or another similar software. The VI also did feature the ability to software filter to remove rigid body motion, apply the discrete Hilbert operator to the datasets, and determine the instantaneous frequency and damping from the envelope function of the free-decay. A last function the LabView code performed after a run was to attempt to fit the classic linear decay exponential function to the envelope function recovered from the Hilbert Transform. Recalling that the loss coefficient is twice the damping ratio $2\zeta = \eta$. the following is a reasonable approximation of the real signal:

$$v(t) = \sin(2\pi f_r t)\underbrace{v_0 \exp(\zeta\, 2\pi f_r)}_{decay\ kernel} \tag{112}$$

The LabView VI was able to fit the decay kernel above to the ring-down envelope function using the method of linear least squares. This worked well for all of the systems, even the thick TBC coated (12.5mil) one. Typically, the coefficient of determination (R^2) for these ranged from 0.98 to 0.99, for the bare and bond coated only specimens the R^2 values reported were typically 0.99 to 0.999. Due to the near constant nature of the mode-I frequency during the ring-down and the fact that the linear decay theory fit all the tested systems quite well, a lot of beam system-level trends will be reported in Chapter 6 from the on-line LabView data reduction results.

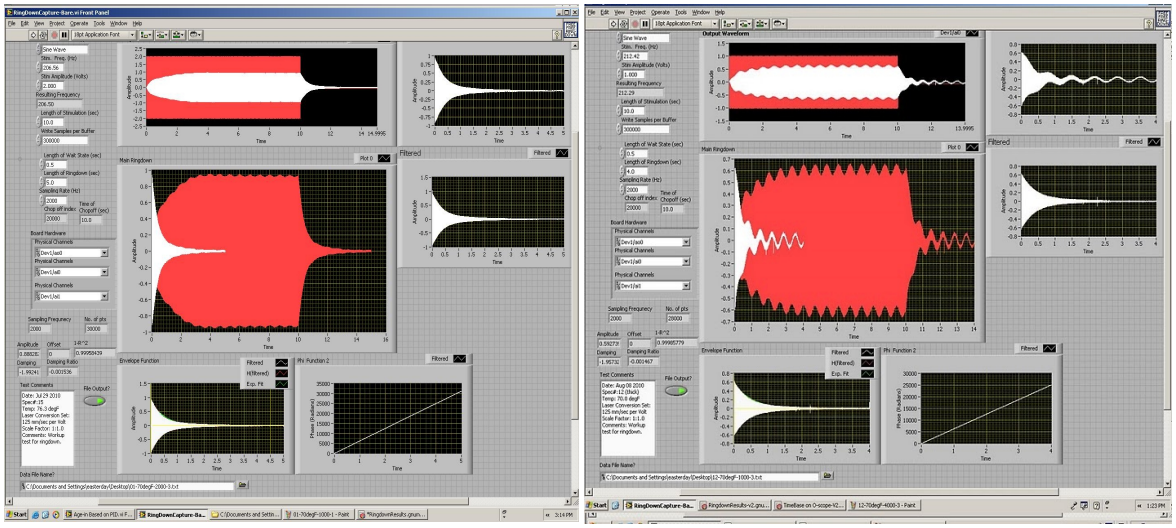


Figure 101: Typical Coated Beam Datasets, Clean (left) and with Rigid Body Motion (right)

Figure 101 displays the front panel of the VI. The interim processing steps are plotted to allow quick examination of the data set and allow for easy adjustment of parameters, among these

are: recording window (decay) time, record sampling frequency, excitation frequency and amplitude, excitation stimulation time, data file name, among others. It is noted that the left data set in the Figure is a "clean" dataset with little rigid body motion, while the right plot exhibits much rigid body motion superimposed on the dataset and the action of the 5^{th} order Butterworth software filter in action. These steps could also be accomplished off-line by Matlab code using the raw measured voltage data that was saved to a file.

The steps to obtain the data are outlined below with relevant comments to be addressed in the process. These were adapted from Reed (Reed, 2007) with some minor modifications. Figure 156 summarizes the process steps which are:

1) If needed, software filter the raw voltage data from the DVL, this is usually taken care of in the LabView VI. Stream the raw measured data to the disk for off-line processing.

2) Scale the voltage data into velocity data using the conversion for the Polytec PDV-100 (500mm/sec per 1.0V of electrical signal). This yields the instantaneous velocity, v(t).

3) Perform the Hilbert transformation on the v(t) dataset (function 'hilbert' in Matlab), and from this output use the real and imaginary components to determine the envelope function of v(t), $v(t)_{env}$, and the instantaneous frequency function, $\omega(t)$. More information on the details of this is in available in Appendix 9. Note that this transformation is the discrete Hilbert transform as the dataset is a set of points of v(t) versus t.

4) Remove out-lier spikes in the $v(t)_{env}$ envelope function using the Matlab 'smooth' function with the 'rloess' option. This is a local linear least squares regression fit using a 2^{nd} order polynomial (Matlab Documentation, 2010). This is a robust version of 'loess' that assigns lower weight to outliers in the regression fit and drops those more than six mean absolute deviations outside the curve. The fits were performed on 151 point wide sets, which is a $5/100^{th}$ second window width on the 2000Hz sampled data.

These spikes in the data-set are pseudo-random in nature and are not harmonic so filters cannot suppress them. They are caused by inhomogeneities in the reflectivity of as well as directional reflectivity of the mica tape dots.

5) Calculate the total phase accumulation, $\Phi(t)$, in the ring-down signal by harmonically using the 'unwrap' and 'angle' function on the instantaneous frequency, $\omega(t)$. The latter returns the phase angle from the phase accumulation, and the former ensures that the total angle is reported, not as a relative angle between 0 and 2π.

6) Determine the decrement at any time in the dataset using the relationship for

logarithmic decrement. From this the instantaneous loss coefficient can be determined, $\eta(t)_{sys}$.

At this point the data-set of instantaneous frequency and instantaneous damping are indexed against time and these describe the beam system-level response from the experiment. In this study though, the velocity of the envelope function ($v(t)_{env}$) and the total phase function ($\Phi(t)$) were passed on for post-processing due to the desire to perform another step in the post-processing Matlab code.

7) Reed employed smoothing splines at this point to remove unwanted rippling in the data sets, in the current study, a functional fit to the envelope function and the phase function was determined and used instead. This was done on two grounds, first, it was felt that a well chosen function could concisely and accurately convey the decay envelope physics, and, second, the functional fit would suppress global anomalous trends in the dataset beyond the mere width of a smoothing window. One function that was considered to be physically realistic in describing the envelope data set of v(t), whether a linear or non-linear system, was a linear combination of two exponentials as per (usually i=2):

$$y = \sum_{i=1}^{n} a_i e^{(b_i x)} \tag{113}$$

Where "a" and "b" are the coefficients to be determined from the regression fit to the data. This was the most physically realistic model for the decaying system and usually described the system well with a R^2 of 0.98-0.99. If the data-set had a region of lesser curvature in the very beginning of the decay envelope due to initial transients, a combination of Gaussian distributions of the form:

$$y = \sum_{i=1}^{n} a_i e^{-\left(\frac{x-b_i}{c_i}\right)^2} \tag{114}$$

worked well to describe the $v(t)_{env}$, here "a", "b", and "c" were the coefficients to be found. In Equation (114) a_i is the amplitude, b_i is the centroid, c_i is the width of the peak and n is the # of peaks and, typically, i = 2. Failing either Eq. (113) or (114), but not as physically realistic in describing a decay envelope model due to a lack of asymptotic far-time behavior, is a polynomial of 2nd or 3rd order. For Φ(t), a cubic or quadratic polynomial usually produced a good fit, though occasionally a linear fit had to be selected with some ill-conditioned data sets due to upward or downward wandering of the phase time relationship in far time (e.g. $t > \sim 3$ to 4τ). Often this upward or downward shift in phase versus time was due to random noise in the signal beginning to make an adverse impact on the intended signal biasing the phase versus time relationship. This was avoided as much as possible as the linear fit would suppress any stiffness modulus changes with temperature. A discussion of the strengths and weaknesses of the functional fits is discussed in Section 4.5.5

The functional fits of v(t) and Φ(t) are now known in a continuous fashion over the course of the ring-down and can be combined with the predictive polynomials to extract the complex modulus of the coating.

4.5.2. Combining the FEA Analysis with the Experimental Results to Extract Coating-Specific Properties

After processing of the data from the experiment to characterize the system and obtain v(t) and Φ(t) for the system in a continuous function fit, these two relations could

now be combined with the predictive polynomials built in Section 4.3.3 and the Torvik relation to obtain the coating complex modulus in a bulk material fashion. These steps are covered below with specific details elaborated as needed. Note the "[t]" designator is used to indicate a discrete array of data that is time-indexed and needs to be carried through the relations; it does not imply a direct functional dependence per say but rather aligns the data in-dices using time.

1) Into the first polynomial ($E_c = f(\omega_r)$), map the data vector of instantaneous radial velocity, $\omega_r[t]$, from the experimental data to obtain $E_c[t]$. Note that $\omega_r[t]$ is the time derivative of $\Phi(t)$. At this point one has the complex bulk storage modulus indexed against time.

2) Take the $v(t)_{env}$ from the ring-down data-set and integrate it along time using the harmonic integration relation, to get x[t] (or $\delta[t]$). There was debate as to whether an exponentially decaying harmonic function can be integrated using this relationship without introducing unacceptably high error. Appendix 8 addresses this issue.

3) Place the time-indexed coating modulus, $E_c[t]$, into the second polynomial, ($\tilde{\tilde{U}}(L/2,t_b) = f(E_c)$), to obtain the non-dimensional displacement, $\tilde{\tilde{U}}(L/2,t_b)[t]$, as indexed against time (this needs to be done as the modulus is potentially varying during the course of the ring-down).

4) Now obtain the scaling function $\lambda[t]$ from:

$$\lambda[t]=\frac{\delta[t]}{\tilde{U}(L/2,t_b)[t]} \tag{115}$$

The scaling function basically allows the modal FEA (or analytical) model field data to be dimensionalized to the experimental beam system. As a result, $U(L/2,t_b) = \lambda \cdot \tilde{\tilde{U}}(L/2,t_b)$ and $\varepsilon_{11}(U/2,t_b) = \lambda \cdot \tilde{\tilde{\varepsilon}}_{11}(U/2,t_b)$.

5) Determine the non-dimensional bending strain in the beam from the third polynomial ($\tilde{\tilde{\varepsilon}}_{11}(U/2,t_b) = f(E_c)$); again this will need to be time-indexed to account for any changes in the coating modulus encountered during the ring-down, $\tilde{\tilde{\varepsilon}}_{11}(U/2,t_b)[t]$.

6) Now scale the non-dimensional bending strain using

$$\epsilon_{11}(L/2,t_b)[t] = \lambda[t] \cdot \tilde{\epsilon}_{11}(L/2,t_b)[t] \tag{116}$$

7) Use the fourth polynomial ($SER = f(E_c)$), determine, yet again in a time-indexed fashion, the SER[t].

8) Now apply the key step of determining the loss coefficient of the coating material using the Torvik relation which is in time-indexed form:

$$\eta_c[t] = \frac{\eta_{sys}[t](1+SER[t]) - \eta_{bare}}{SER[t]} \tag{117}$$

From this the $\eta_c[t]$ is obtained, and one now has the coating bulk loss coefficient in time-indexed form.

9) To obtain the complex modulus of the material as a function of strain, plot $\eta_c[t]$ as a function of $\varepsilon_{11}(U/2,t_b)[t]$, and $E_c[t]$ as a function of $\varepsilon_{11}(U/2,t_b)[t]$. This results in the plots that show $\eta_c(\varepsilon)$ and $E_c(\varepsilon)$, as a functions of the numerically-extrapolated, real strain. These plots exhibit the materially non-linear nature of the coatings. They are are usually

non-linear for the coated beam material, especially for the loss coefficient. Plotting these drops out the time index and the graphs are of the form η_c versus ε_{11} and E_c versus ε_{11}. These are the imaginary and real components of the complex modulus, respectively. For the linear beam they are constant, or nearly so.

Figure 102 details in a flow-chart form the process of obtaining the coating complex modulus from the polynomials and system level experimental data.

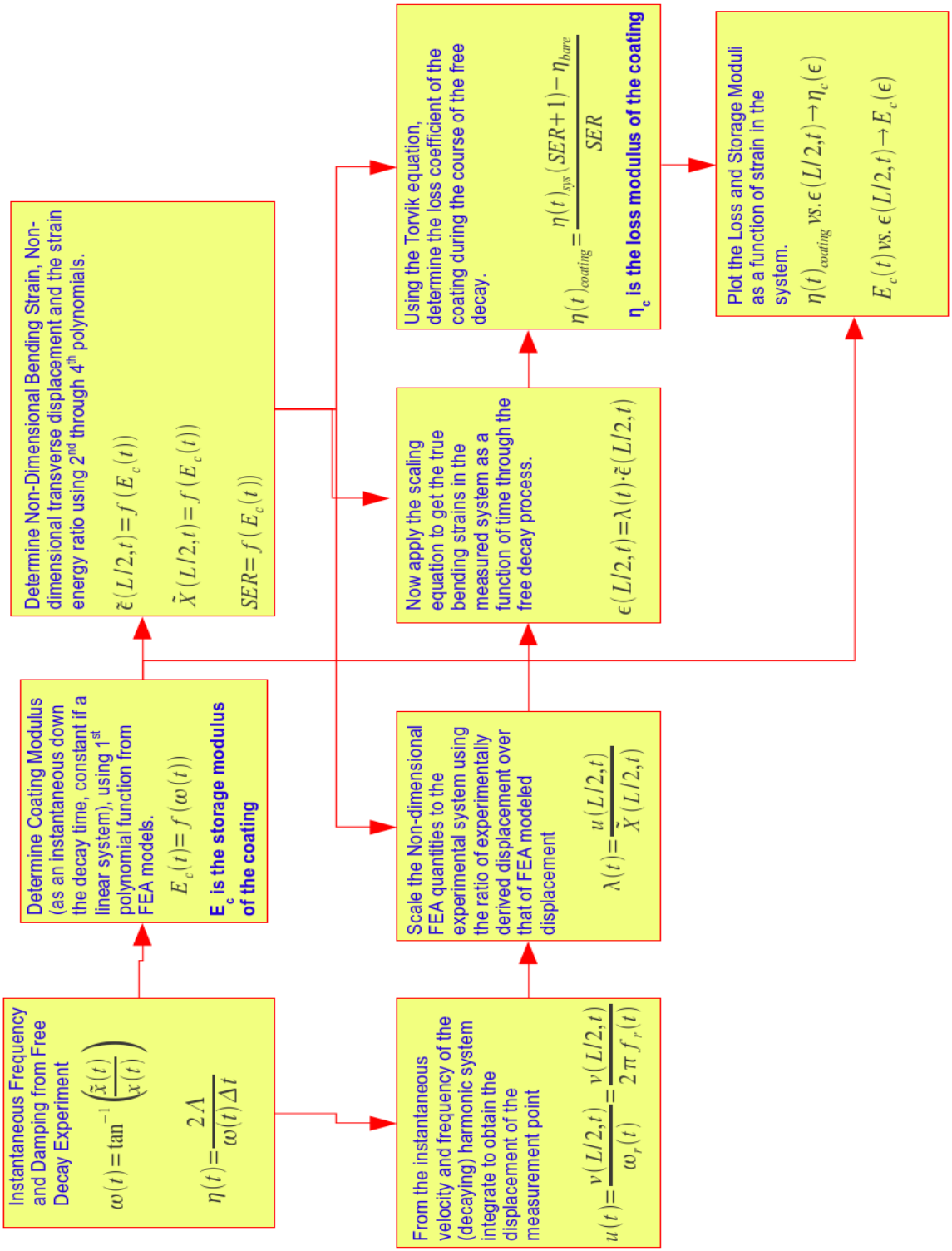


Figure 102: Off-Line Process Reduce System Properties to Bulk Coating Complex Moduli

4.5.3. On Use of Filtering

The use of taught and short suspension wires was to be employed to prevent issues with rigid body motion, however during the age-in cycling of the beams, it was discovered that the lower lines added significant damping into the chamber setup, some 3X more so at the system-level. So they were kept in their lower non-contacting position for all of the testing, but this made the system subject to exhibiting rigid body modes. Worse, they would not damp out reliably either. Reed dealt with minimizing rigid body modes by free-hanging and restraining the beam with clamped lower lines; what rigid body motion he was unable to eliminate, he used a cubic smoothing spline algorithm after passing the ring-down decay time signal through the Hilbert transform. Pearson was able to eliminate any noticeable rigid motion with a combination of short suspension lines and by using a lot of tension on the lines.

For the current study, the wire spans were necessarily long, to avoid any heat shadowing effects from support structure interposed between the lamps and the beam and/or dummy specimen. The wires were under more moderate tension, to avoid parting under fatigue. These factors, combined with a system that had inherently less damping in the suspension lines, required filtering of the signal for most datasets. A software filter using a 5^{th} order high-pass Butterworth with a cutoff frequency, f_c, of 30Hz was provided within the LabView VI code developed. Both the original as-measured voltage, as well as the filtered signal, were saved to the ring-down datafile(s). Figure 103 shows the phase and magnitude Bode plots for the filter. A Butterworth filter was chosen for the following

reasons: the passband magnitude is of unity gain and flat when well removed from the cutoff frequency, the phase does undergo a constant shift from the filter, and since the separation between the stop-band and passband components are large enough, the relative simplicity is justified. The phase shift imparted to the signal is not a problem for testing in this work as the instantaneous frequency is derived from the slope of the phase-time curve, not the magnitude of the phase itself, therefore a constant shift in the phase itself is not a problem.

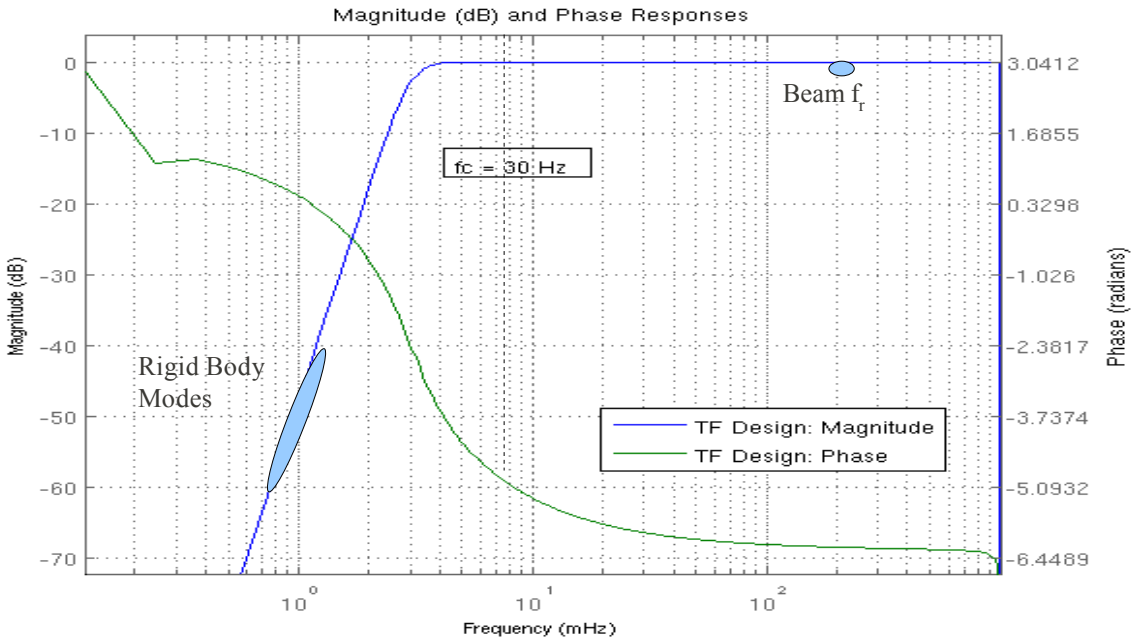


Figure 103: 5th-Order Butterworth High Pass Filter Bode Plot

To gain insight into the rigid body modes without the lower wires in place, a bare beam was suspended at a static hanging state upon which the wire was plucked and/or the beam tapped to provoke various rigid body modes. Using a variable frequency strobe light in the darked lab in conjunction with a contrasting background three rigid body modes were discovered as per Table 13. For each rigid mode of interest, it was excited

and the motion was "frozen" at the same spot in its harmonic motion against a marked background, after freezing it, the strobe frequency was read. As can be seen from the table, the modes are all 10Hz or less in frequency, well-separated from the Mode-I bending frequencies ranging from about 175-215Hz.

Table 13: Rigid Body Motions (Modes).

Rigid Body Motion (Mode)	Frequency	Influence on Error
Rigid body rotation around passive node "swing"	0.8 Hz	High
Horz.-plane motion (parallel to DVL Laser)	9 Hz	Moderate
Vert.-plane motion (parallel to DVL Laser) "pogo"	9 Hz	Low

To assess the impact of the filter on (not) corrupting the measured data, an artificially synthesized dataset was constructed using typical values determined by from Reed's work. The loss coefficient (η_{sys}) was set to 0.0004, the resonance frequency (f_r) was 202.5Hz, and the initial velocity (v_0) was 1.3 m/sec, resulting in:

$$v(t)=v_0 \sin(2\pi f_r t) e^{(-2\pi f_r \eta t)} \tag{118}$$

To the ring-down signal in Eq. (118), a noise mode of 4.0 Hz frequency and 1/20th of the magnitude of the original signal was added as per:

$$v(t)_{noisy}=v(t)+0.05 v_0 \sin(2\pi \cdot 4 t) e^{(-0.004 \cdot 2\pi 4 t)} \tag{119}$$

This is a representative and noisy signal much like what was encountered during the workup testing while readying the VI data collection codes. Figure 104 shows the Eqs. (118) and (119) and the results of Eq. (119) after passing through the filter.

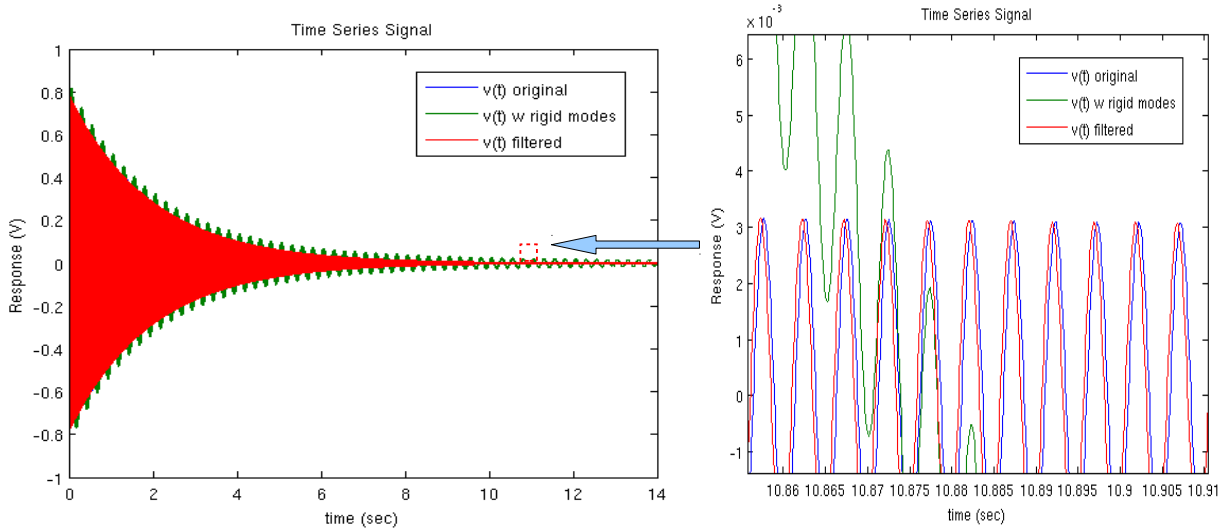


Figure 104: Original, Noisy, and Filtered Ring-down Signals

Figure 104 shows a close in at around 10 seconds out, it is noted that the phase-shift is constant and the magnitude of the original signal is preserved, so either a software or hardware Butterworth will not distort our data and suppress the desired data features needed to extract complex modulus.

4.5.4. FRF Forced Response Measurements for the System

Some confirmatory qualitative tests were run on the free-free system using the ½ power bandwidth technique. These forced response tests were run to qualitatively confirm some trends in stiffness and damping of the coated beam system with variation in temperature and some forcing conditions in the system related to the chamber configuration. These include variations in location of the beam beam, and the thermal shielding. Appendix 10 covers the basics of drawing quantitative data from the method. The use of the predictive polynomials to infer the data-fields, once the system level resonance frequency and loss factors are obtained, is the same as with the free-decay based datasets.

4.5.5. On Use of Functional Fits Instead of Smoothing Splines

It will be noted when the complex modulus results are presented that the lower limits of the strain range are prone to errors. This is due to the signal to noise ratio as the v(t) signal voltage heads out to 1-2% of its initial amplitude (5τ to 4τ in time constants). For this study is was procedure to select and fit physically descriptive functions to describe the functions of $v(t)_{env}$ and $\Phi(t)$; e.g. exponential and/or of ½ Gaussian functions that decay to a steady state value are more desirable than polynomial functions.

Figure 105 depicts a typical plot of the components of the complex modulus as a function of the strain field inferred from the modal FEA analysis, in this case for a 8-YSZ coated specimen. The curves clearly display strain softening characteristics with the E_c increasing in the smaller strains of far time (near the left side of the plot), while the energy dissipation in η_c is enhanced in the larger strains of time near the initiation of the free-decay (the right side of the plot). Each red "X" on the curves denotes a one second (1.0sec) interval with the t = 0 start of the decay at the right side of the curves and proceeding left. One can see behavior in the storage modulus plot that seems implausible in the far-time plot near the y-axis. Though not seen in the sample plot above, the loss factor plot often will sharply vary up or down near the y-axis/far-time/small strain regions as well. This is an artifact of the gamma function (Eq. (295)) as the instantaneous frequency wanders above or below the mode-I fundamental due to signal noise and rigid body motion.

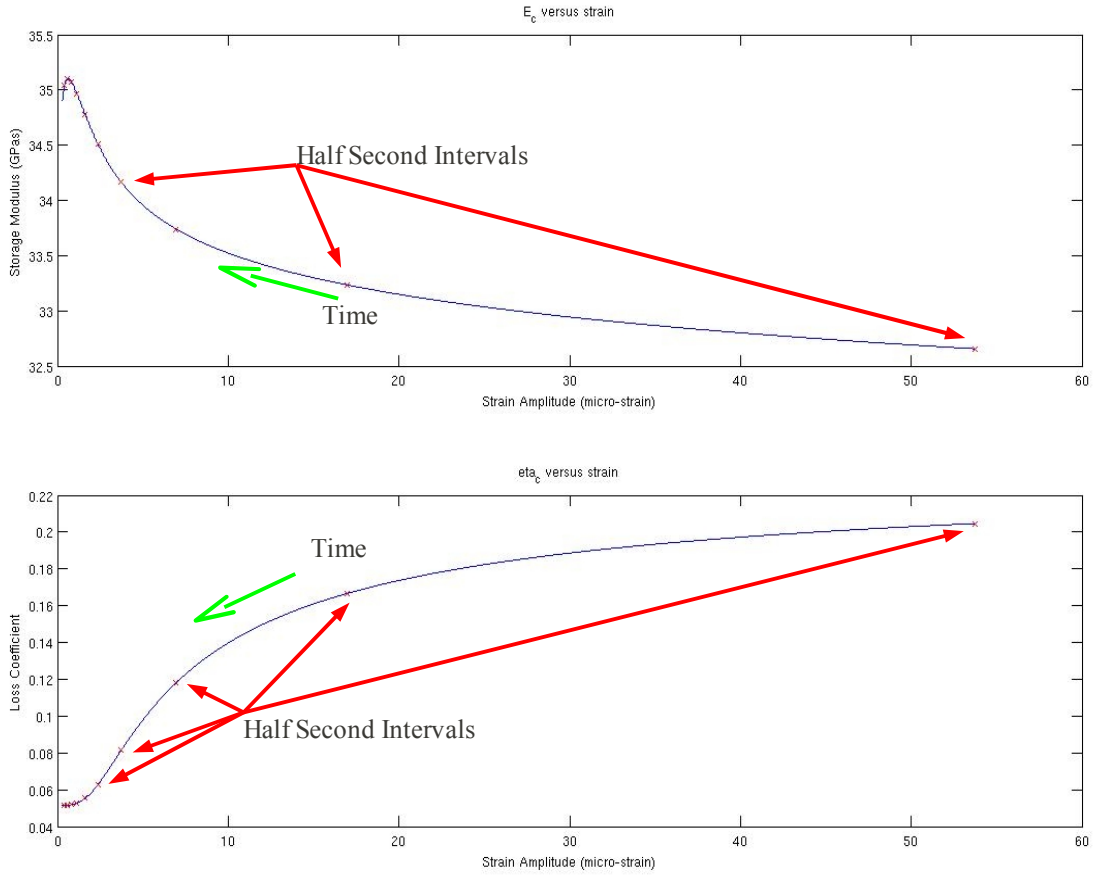


Figure 105: Time Indexing of Decay Signals

Examination of the time domain amplitude versus time plot displays a clear decay envelope as can be seen in the upper right of Figure 106. The Figure is a fairly typical dataset from a free-free specimen. The upper left plots the raw DVL voltage versus time from the DVL, the upper right is the 5th order Butterworth filtered (f_c=20Hz) of v(t) versus t. The scaling is performed using the laser gain setting. The lower left figure is the envelope data plot, it is obtained by applying the discrete Hilbert transformation to the v(t) versus t dataset and taking the square root of the sum of the squares of the real and analytical signals coming out of the transform. The spikes on all three of these plots are

caused by the mica tape used as the high temperature resistant diffusive reflectors. These are absent when later tests were run with 3M reflector tape. The last plot, on the lower right, is of the total phase accumulation (Φ(t)) over time in the course of a free-decay. With such under-damped systems it is very close to being linear in nature until the fundamental bending mode-I signal fades into the baseline noise, whereupon the phase accumulation curve tends to wander up or down off of the linear.

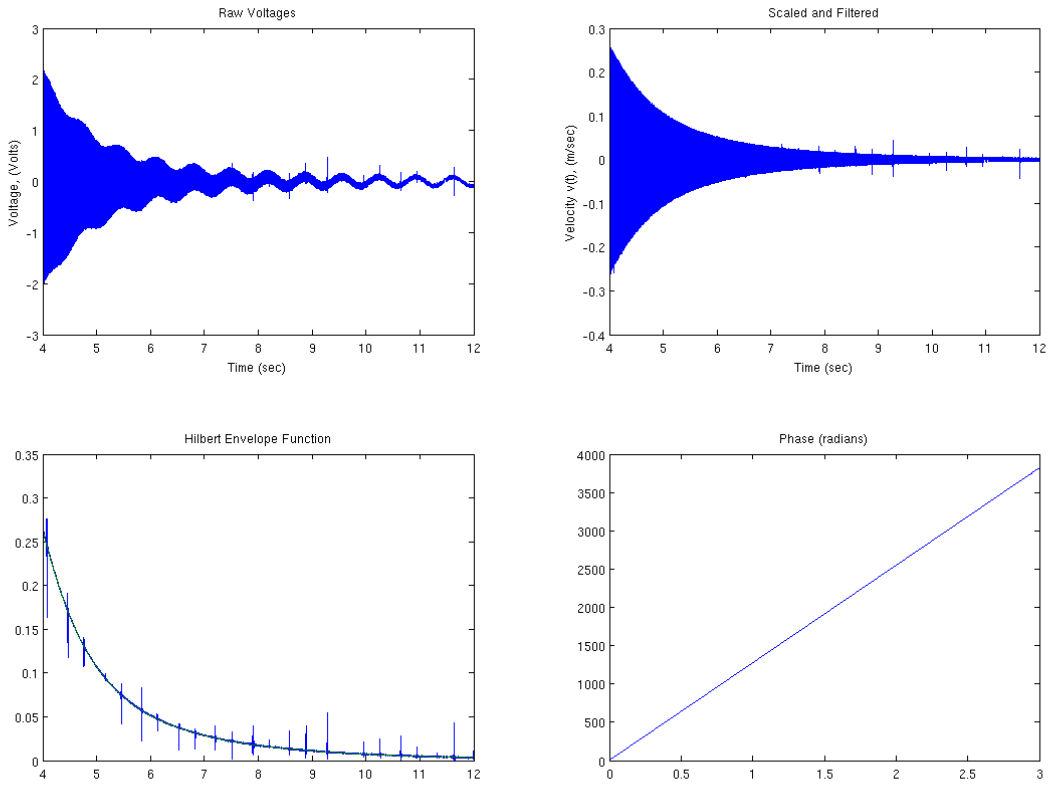


Figure 106: Interim Off-Line Processing Plots

The baseline noise floor of the system used to record the free-decay ring-downs was measured to be around v =±15.0to 20mV using an oscilloscope hooked up in parallel to the data acquisition circuit. The signal to noise ratio at the start of the runs was very

favorable but as the signal decayed out it would become less favorable. About 3 to 4 time constants out noise on the signal can bend the phase function up or down from the linear trend it followed up to that point. This hooking of the phase function up or down resulted in the storage modulus and loss factor curves sometimes swinging up or down radically at the very low strain levels of the plots of these values versus the beam strain. These regions in close to the 0 to 5-10 μstrain (μm/m) are the "far time". The strain at any velocity can be obtained by using the scaling function as per:

$$\epsilon_{11} = \lambda \tilde{\epsilon}_{11} = \frac{\delta \tilde{\epsilon}_{11}}{\tilde{U}(L/2, t_b)} = \frac{\frac{v(t)\tilde{\epsilon}_{11}}{2\pi f_r}}{\tilde{U}(L/2, t_b)} \tag{120}$$

With this noise floor the signal to noise ratio is about 100:1 a the start of the lowest amplitude ring-down decays (of 250 mm/sec and 109.81με), by roughly 2 seconds out 90% of the signal had decayed, to about 25mm/sec or 10.9με and signal to noise was around 10:1. As these far times if their was noise on the signal the phase function would sometimes pick some of it up.

It can be considered that the plots are generally reliable when within the range of decay from about 0.25τ out to about 3.5-4τ on the time domain curve. This excludes the initial region where transients show up from the harmonic sinusoidal step input removal and the far-time region where the system decays into than 2% of the initial signal. While the functional fits are prone to these trends in the data, a localized spline smoothing technique as also vulnerable similar roll of of the phase accumulation curve in far time. The functional fits also provide a concise description of $v(t)_{env}$ and $\Phi(t)$ data-sets and

allow the use of symbolic techniques in data reduction, along with localized and global smoothing of the data-sets. It is known that numerical taking derivatives from discrete data-sets can be very prone to amplifying noise.

4.5.6. Closing the Loop for Fully Transient Modeling

For this study attempts were made to fully characterize the couple moment acting on beam during the steady harmonic excitation, prior to a free decay event (or during an FRF forced response sweep) or during an FRF sweep. This would be useful for fully transient modeling of the system as the forcing function needs to be placed in a fully transient model (if not a ring-down simulation from an imposed initially deformed state at an extreme of the oscillation where all v(t)=0 across the solid). In order to do this the chain of gains from the function generator, the power amplifier, and the magnet to coil dipole moment coupling are needed. The function generator (or NI DAQ board) generates a specified voltage signal, while the MB-Dynamics SL600VCF amplifier has a output gain of 3.666 Amps for every 1.0Volt input signal, and the calibration curve of the magnet is y = 0.0000929x – 5.53x10-6, where y is the output in moment of couple in N·m while the x-input is the coil current, I(t), in Amps (Section 3.7). Putting these together the product of these relates the moment couple as a function of the imposed voltage signal as per:

$$M(t)(N\cdot m)=0.0000929\left[v\sin(2\pi f t)(Volts)\cdot 3.666(Amps/Volt)\right]-5.53\text{x}10^{-} \qquad (121)$$

where $v\cdot\sin(2\pi f_r t)$ is the voltage signal specified to excite the beam system. Unfortunately to know the true moment coupling of the magnets to the field and therefore the energy addition per cycle (or work) and therefore the work per cycle one must carefully record

the phasing between the magnetic field (magnet current I(t) would be a acceptable proxy) and the displacement of the beam during the FRF or the harmonic steady stimulation. If not separated by 0 (or 360) degrees a situation where the magnets are being driven into a repelling magnetic field could be occurring and some energy loss (and damping) occurring through this mechanism. Unfortunately in the study in Chapter 6 precise measurement of phase coupling was not implemented.

5. Determining Coating Complex Modulus – Experimental Study

This Chapter details the application of the theory and concepts covered in Chapter 4 that were utilized to test free-free beam specimens coated with 8-YSZ in order to determine the bulk properties of the coating layer. The beam geometry, the details of preparation, fabrication, and characterization of the specimens is detailed. The apparatus proved so sensitive when characterizing the bare beam specimens that it can easily discriminate specimens based on the rolling grain orientation, as a result, a micro-structural investigation was performed. A section will cover how the history effects of the TBC coatings were controlled for using an age-in protocol; this also includes the coverage of how aging was demonstrated to be largely independent of temperature (for the ranges tested), therefore allowing the same specimens to be declared fully mature and taken through all of the temperature conditions in a serial fashion. After full fabrication, the bare beam's, bond coated (only) beam, and TBC-coated beams, were all run through the experimental process across variations in amplitude and temperature. This yielded beam system level data in terms of damping and resonance frequency. From these experimental results coupled with the modal FEA analysis from Chapter 4, the details of how coating specific properties were extracted is covered and these results are presented.

5.1. The Specimens

The free-free specimens were fabricated out of cold-rolled 1/16in thick (0.0625in

or 1.5875mm) titanium Ti-6Al-4V alloy sheet stock. This is the most common alloy of titanium and is widely used in the “cold-sections” (compressor) of modern turbo-machinery. Each beam was 8.000in in length by 0.0750in in width (0.20320m x 0.01905m). The beams were cut from the sheet by the water jet process, the majority of the specimens aligned to be parallel to the rolling grain of the stock. This was indicated by the inked specifications that are rolled onto sheet stock; remaining scrap was cut into specimens that ran across the grain. (The situation was later proved to be the opposite, that is the ink marks actually ran **perpendicular** to the direction of the rolling, see Section 5.1.2.1.) Care was taken from this point forth to segregate the two populations of specimens by means of both labeling and separate bagging. Figure 107 depicts three typical specimens after being tested to 900degF, proceeding from top to bottom, they are: a bare, a bond coat only, and an 8-YSZ upon-bond coat specimen. The discoloration is from the high temperature oxide that forms on the surface after thermal cycling. Both the bare and 8-YSZ coated specimens have ALNICO magnets mounted to them at the active node while the bond coat specimen shows the twin holes through which the magnets are attached with a nut and threaded rod set. The reflective spots are dots of mica tape used to enhance the Doppler velocity laser (DVL) return. On some specimens they are arranged in a linear array to allow experimental characterization of the mode-shape by providing targets of known length down the beam.

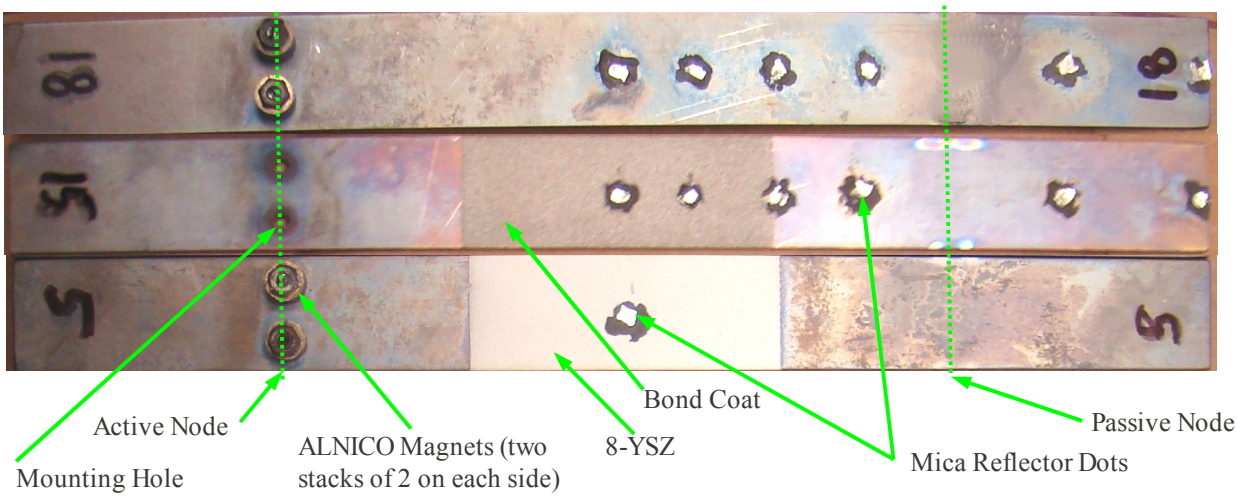


Figure 107: Bare (upper), Bond Coated (middle), and 8-YSZ Coated (lower) Beam Specimens

At the passive node of each beam, located at x/L = 0.224, an 0.0080in diameter hole was machined through the width of the beam coplanar to the plane of the neutral axis. Slight iridescent discoloration on the edges of the middle beam in the figure is a byproduct of this machining. This was performed by plunge electrostatic discharge milling (EDM) and the tolerance of the hole centers were maintained to within 0.0020in of the neutral axis plane. At the location at x/L = 0.776, the active node, a pair of small holes were cut through the thickness of the beam by the water-jet process, this allowed for mechanical fastening of the magnet stacks. The relative loss of beam stiffness at both locations was quite localized and the lack of impact on the eigenvector shape was verified in the 3-D FEA model with addition of these features.

The coated regions are applied to the center 25% of the length of the beam. APS Tech of Dayton performed the bond coat and 8-YSZ TBC application to the beams. The bond coat was a NiCrAlY blend applied to an average thickness of 0.0030in (0.0762mm). It is noted that the bond coat layer is quite irregular in thickness and was applied by the air plasma spray process (APS). The TBC coating of 8% yttrium stabilized zirconium (8-

YSZ) was applied to fill out the total coating layer thickness to 6-, 9-, and 12-mils of thickness (e.g. 0.006in/0.1524mm, 0.009in/0.2286mm, and 0.012in/0.3048mm). These layers were applied to both sides of the beam.

Though the total thickness of the bond coat and 8-YSZ TBC layer over it was specified to be a nominal value of either 6-, 9-, or 12-mils, upon precision measurement of length and mass the actual coating thicknesses were confirmed at 5.7, 8.3 and 12.5mils, respectively. Additionally, the nominal thickness for the BC only specimens was 2-mils but upon measurement by precision weighing, the BC only layers averaged 1.2mils in thickness (in terms of the equivalent homogeneous, regular slab layer). Thus, the polynomial relations based on the nominal dimensions had to be replaced with those modeled based on the as-measured TBC layers to address the difference.

5.1.1. Fabrication of Specimens

Attention was given to the fabrication of the beam specimens in order to reduce error and procedural uncertainties. One of the greatest sources of variances would be the APS process. For application of the 8-YSZ coating to the beams, technical specifications were sought (ASTM, ANSI, ASME, SAE, Mil-Spec, etc.) to help to standardize the application process to the specimens and therefore minimize both intra- and inter-specimen variation. The search was not successful, so an experienced fabricator familiar with air plasma spray processes was selected and given a set of locally determined procedures in an attempt to standardize the process. Analogous to the process of spray painting, such parameters as gun angle and distance, gas feed rate, droplet size and

velocity, substrate temperature, sweep rate, among others, could all have significant impact on the final structure of the TBC layer. Since they are typically applied with thermal protection properties in mind, the strict control of the micro-structure may not normally be of concern. During the process of fabrication much interim measurement was performed to try to make more precisely quantify the results. This allowed modeling of the specimens as they were actually fabricated in lieu of using the nominal dimensions and assuming that tight manufacturing tolerances were achieved. The basic steps in the procedure were:

1) Cut the bare TI specimens to the specified dimensions, label, and segregate by orientation. The $1/16^{th}$ inch thick AMS 4911 titanium sheet was ruled parallel and across the inking marks, which are parallel (correction were thought to be parallel) to the rolling grain axis. The beams were water-jet cut from the Ti-6Al-4V stock, this yielded 23 specimens 8.0in long by 0.75in wide that were parallel to the rolling axis, and 8 that were cut from the remaining scrap of the same size, these were the longitudinal and transverse populations of specimens respectively. These were immediately labeled and segregated to ensure the two orientations would not be mixed.

2) Machine/EDM/water-jet cut the passive and active node holes. The blank specimen had two small holes water-jet cut at the active node 0.0455m (1.79in) from one end, these holes were sized to snugly accept a UNC#2 screw-threaded rod and centered the eight-magnet stack center of mass over the middle of the beam width. Meanwhile, located 0.1576m (6.21in) from the same end, at the passive node, a 0.008in diameter hole was

bored by plunge EDM through the beam specimen. Careful guidance was given to ensure that the center of the hole remained within 0.002in of the mid-plane of the beam's thickness. This was because any significant wandering from the neutral plane would trigger eccentric loading and the bending stiffness contribution of any given material in the beam is the cube of this distance removed from the mid-plane. Due to the high precision and skill needed to EDM the holes, consideration was given to water-jet cutting a pair of holes at the passive node as well, and threading the beam with the wire passed through these with a offset dog-leg loop through the holes. Fortunately this was not done as the chamber system featured such minimal damping that the holes would have been a significant source of energy loss through the slight eccentricity in the wire suspension boundary condition (see Section 3.9).

3) Suspend the uncoated beams and find the resonance peaks to determine E_b (Section 5.1.2). After completion of the machining on each blank, the beams were suspended on a nylon mono filament, equipped with eight ALNICO magnets, and were vibrated using an older electromagnetic coil to seek the resonance frequency peak of that particular sample. Particular attention was given to determining if the orientation of the beams made for a significant difference.

4) Measure dimensions and weigh all the bare beams. This procedure is covered in Section 5.1.1. Set some aside some specimens and label these as bare beams.

5) At APS Tech., apply the NiCrAlY bond coat to the remaining beams to 0.003in specified average thickness (BC) using the APS process.

6) Again the linear dimensions are measured and precision weighing of the now bond coated beams is performed on all the specimens. Remove, label, and set aside some specimens as bond coat (BC) only specimens.

7) At APS Tech., topcoat using APS the remaining BC specimens to 6-, 9-, and 12-mils (0.006in, 0.008in, 0.012in) specified coating thickness (including the bond coat layer) with 8-YSZ applied by the APS process.

8) Again, measure the linear dimensions and weigh the 8-YSZ coated specimens. Label these.

The length and width of the beams in steps 4, 6, and 8 above was determined using a Starret 0-12 dial indicator caliper precise to ±0.0005in (half of one-thousandth of an inch). Three readings were taken along each primary dimension to help reduce measurement scatter error. Thicknesses were measured using a slip clutch equipped Mitoyo rotary digital micrometer precise to ±0.00005in (half of one ten-thousandth of an inch). These measurements were taken in three locations, all located along the long, mid-line axis of the beam, once at the first coating-bare beam interface, then in the dead center, and then at the second coating beam interface. The diameter of the micrometer anvil was much larger than the perceived roughness texture of the bond coat. As a result, these measurements yield the highest peak values of thickness as the anvil picks up the peaks of the surface asperities, not the average. As a result, precision mass weighings were performed as well. In contrast, the 8-YSZ coatings were much smoother in finish, as the measured thickness is much closer to the average value as determined by mass and

density methods.

Mass weights were taken at each step (bare, BC-only, and fully coated) using an Ohaus Model VP214CN enclosed pan electronic balance precise to ±0.0001g. Before weighing, the beams were cleaned with isopropyl alcohol, wiped with a clean paper towel, allowed to dry thoroughly, and then weighed. Using the delta between the initial weights and the bond-coat weights, along with the density of NiCrAlY at 7320 kg/m^3, the average thickness of the bond coating layers was determined to be 1.26 mils with a tight tolerance across the samples (±1σ S.D. = 0.04 mils across N=17 samples). Using the delta between the final 8-YSZ sprayed beams and the bond coat only in conjunction with the density of APS 8-YSZ of 5566kg/m^3 the coating thicknesses for the nominal 6-, 9-, and 12-mil beams were determined to be (including the bond-coating layer), 5.66mil (±1σ S.D. = 0.02mil, N=3), 8.34mil (±1σ S.D. = 0.04mil, N=11), and 12.48mil (±1σ S.D. = 0.06mil, N=3), respectively. These values are determined as the total coating thickness. If the bond layer is subtracted, then these values are 4.40mil (±1σ S.D. = 0.02mil, N=3), 7.08mil (±1σ S.D. = 0.04mil, N=11), and 11.21mil (±1σ S.D. = 0.06mil, N=3). It is noted that the direct thickness measurements of the coating layers were 8.14mil (±1σ S.D. = 0.07mil, N=3), 10.84mil (±1σ S.D. = 0.03mil, N=11) and 15.35mil (±1σ S.D. = 0.03mil, N=3). This systematic undershoot suggests that the BC has a rough texture where the micrometer anvil picks up the peaks of instead of the average thicknesses. Based on the smaller inter-sample variation, as well as intra-sample micrometer measurement variation, APS Tech. maintained a consistent process for their application for both the bond coat and the 8-YSZ TBC. This was true intra-sample as well; the three locations of

measurement varied little from one location to the next. What is notable is that, while APS Tech. was inaccurate to the specified tolerances, they did have a precise control of the process. This may be due to only being able to add thickness in discrete amounts per each APS gun traverse. Appendix 11 is a table with the dimensional details of the specimens. As a result of the dimensionality and coating mass findings the FEA modal dynamics polynomials were run with the revised dimensions.

5.1.1.1. Partially Coated Specimen

It is a worthy to inquire as to why the beams are only coated for a fraction of their length as opposed to the whole length, after all a partial coating makes analytical and numerical modeling much more complex. But there a two very good reasons: the first was that in order to capture the full range of non-linear behavior of the material, a large range of strains must be generated in the coating. Since the coating is such an effective damping material, a smaller volume of it is needed to prevent over damping of the excitation moment supplied. The second reason is due to the fact that the curvature down the thin beam in dynamic bending mode-I is not constant, and therefore the strain variation is not constant either. Figure 108, a plot obtained by Deleon using a 3-D modal model, displays the variation in bending strain down the length of the coating along the beam-TBC interface at the mid-width of the beam (Deleon, 2009). As can be seen from the figure, the relative variation in bending strain is about 10-11% along the length of the partial patch running from x/L=0.375 to x/L=0.625. The method in this study reports the non-conservative values of complex modulus against the strain at x/L =0.500. But,

realizing that a sufficient volume of TBC is needed to influence the system and that this volume needs to be close to the reported strain, the TBC patch was held to 25% of the length of the beam.



Figure 108: Bending Strain at Coating-Beam Interface Mid-plane along Length (Deleon, 2009)

It would be a logical extrapolation to make the coating patch very short, but as can been seen in Figure 108 (and 51), there are strong edge effects as well; make the patch length too short and the edge stress discontinuities will influence the global averaged solution in an adverse fashion. It is noted that these edge effects also were revealed in the thermal stress FEA results (See Section 2.10).

5.1.2. Testing the TI Blanks for Modulus-Orientation Findings

Both Reed and Pearson mentioned that control over the Ti-6Al-4V grain

orientation for the specimens was maintained. The current study continued that practice but sought to establish if this was necessary to do, and if so, quantify the significance of the grain orientation upon the beam modulus. Deleon also recommended obtaining the modulus by experiment to seed any FEA models. Given the discrepancy of the samples as measured compared to the book values from Mil-Handbook-5H, this was good foresight.

The 0.0625in Ti-6Al-4V sheet stock in the study yielded 8 beam blanks that featured a transverse grain orientation and 23 with a longitudinal grain orientation, e.g. the rolling axis was parallel to the long axis of the beams. Segregation of the specimens was maintained upon cutting from the sheet stock by means of labeling and separate bagging. After all the blanks were machined at the active and passive nodes they were tested for elastic modulus. This was performed at 68-72degF, in ambient air. An older electromagnetic coil was used to provide excitation along with the ALNICO magnet set, four in each of two stacks. Each stack had four magnets on each half-width of the beam, with two on either side of the thickness. All of the poles of the individual magnets in both stacks were aligned to all face in the same direction. Since the DVL lasers were unavailable for use at the time of testing, a A Brüel and Kjær 2238 Mediator hand-held sound-meter was employed to find the resonance peak(s).

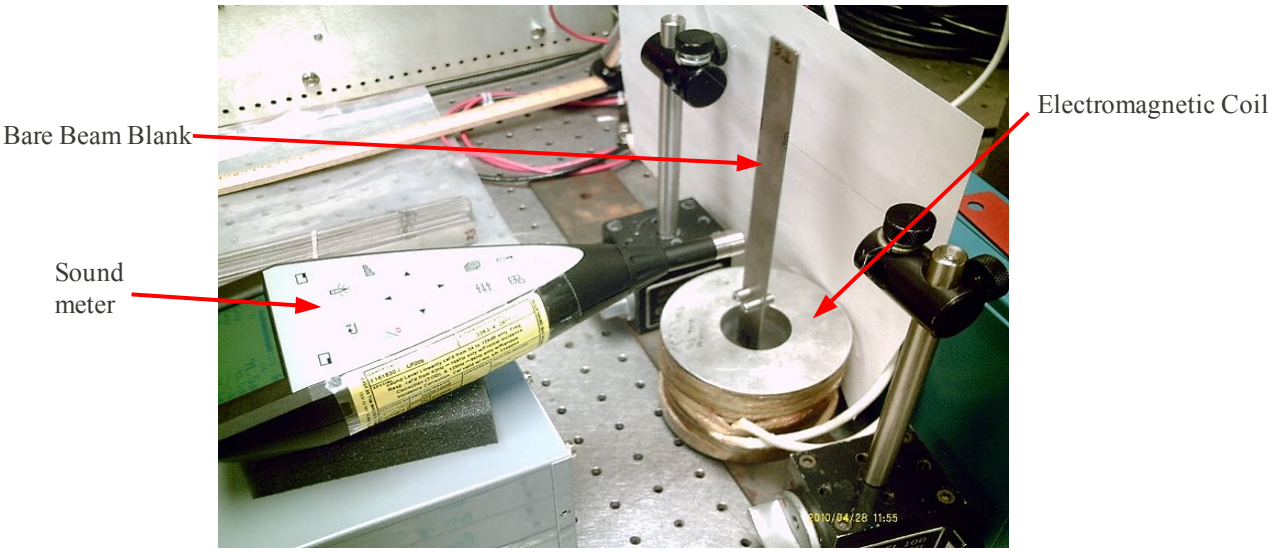


Figure 109: Characterizing the Bare Beams for Modulus

As shown in Figure 109, the beam blanks were suspended on an approximately 6.0in span of 6lb test "Stren" nylon mono-filament line hung with the centroid of the magnets located 1.00in above the top plane of the magnet and on the centerline axis. The mono-filament was threaded through the passive node EDM hole. The background sound level in the lab was measured to be about 52.1±0.2dB at different times. The sound-meter was placed on an isolating foam pad and the directional microphone located 0.50in (0.0127m) away from and centered upon the beam center-point. The electromagnet coil was driven using a function generator via the MB-Dynamics AC amplifier in current mode output. The level of sound emitted from the beam was monitored as the function generator was tuned up in frequency until the value of sound emitted from the beam blank peaked and rolled off. When that happened, the amplitude and the frequency were recorded, and the blank was assigned an index number. Confirmation of the value of the peaks was performed by overshooting and reversing the excitation frequency until the peak was obtained again. Using this measurement, one can utilize the first bending mode

of the characteristic equation as per:

$$\omega_r = \left(\frac{4.73}{L}\right)^2 \sqrt{\frac{EI}{\rho A}} \quad \rightarrow \quad E_{TI} = \omega_r^2 \left(\frac{L}{4.73}\right)^4 \frac{\rho A}{I} = \omega_r^2 \left(\frac{L}{4.73}\right)^4 \frac{12\rho}{t_b^2} \tag{122}$$

where E_{TI} is the elastic modulus of the titanium, ω_r is the radial resonance frequency, ρ is the density of the titanium, and t_b is the thickness of the beam. All of the beams were run through this test at least once, and some were tested a second or even third time to check on repeatability of the data (This included rehanging of the specimens between

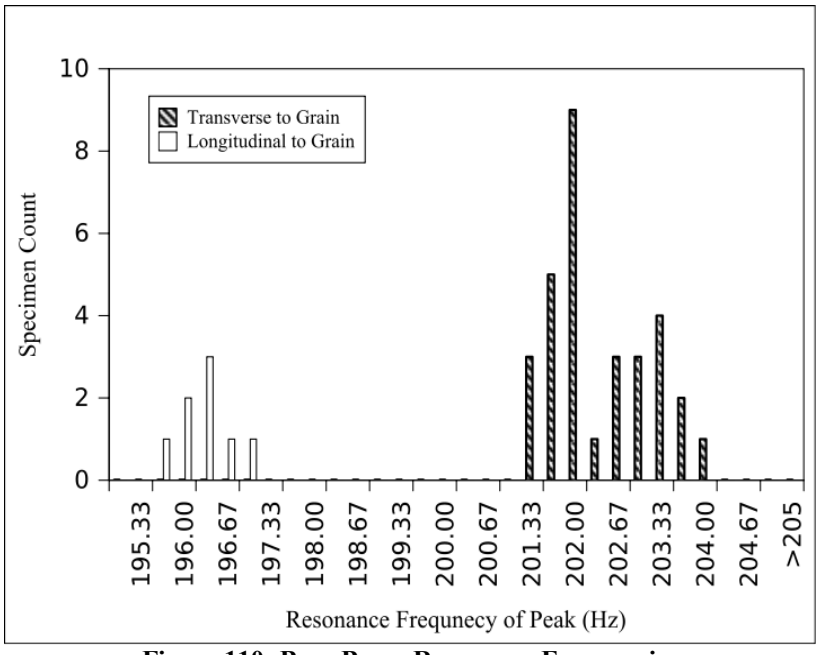


Figure 110: Bare Beam Resonance Frequencies

measurements). An independent two-sample t-test (of unequal samples and unequal variance) applied to the set of data from the two populations of longitudinal and transverse beams would establish a degree of confidence that there is a casual mechanism, in this case orientation, with respect to the rolling direction of the sheet stock. This would be in lieu of the null hypothesis (e.g. random measurement error) that would explain the difference in moduli, and was so. As can be seen from Figure 110,

which is a histogram plot of the peak frequencies from all the trials on the beams performed, there was no need to perform a t-test at all. By visual inspection, the null hypothesis definitely does not account for the variation between the two populations based on the inter-sample variation. The grain orientation of the sheet is either the causal reason, or a feature associated with the cause.

It turns out that the orientation of the rolling axis is significant in its effects on the titanium modulus, the transverse set of specimens had a mean modulus of 109.05Gpa (15.81Mpsi), with 0.95CI of 0.96Gpa across N=8 measurements, while for the longitudinal set the values are 116.02Gpa (16.82MPsi) with a 1.78Gpa 0.95CI across N=31 samplings. This is a variation of the mean 6.4% from the longitudinal mean value. It is small, but significant, and easy for the chamber to discriminate between given the sensitivity of the free-free apparatus. It is noted the confidence intervals are for the variation in the titanium sheet, using the 1st order replication analysis (Coleman and Steele, 1999) to control for the variations encountered due to measurement across the specimen set. This is strong evidence that the Ti-6Al-4V sheet elastic modulus is actually orthotropic, where E_{11} = 116.02Gpa and $E_{22} = E_{33}$ = 109.05Gpa.

These results suggest several things: first, an orthotropic modulus model for FEA analysis of plate specimens is warranted, in this study an isotropic model using the transverse modulus in the ABAQUS FEA models can be, and was, employed due to close approximation of the thin-beam situation. Second, the careful control of specimen orientation by Reed and Pearson was warranted and is now substantiated and quantified

by testing. Third, the variance in the sheet stiffness in the longitudinal axis is almost twice that of the transverse direction. Technique-wise the use of a sound-meter worked well for measuring the response for the beams, perhaps this is not surprising as sonic methods are often used to excite low damped structures.

Leaving the explanation with just a macroscopic observation but no causal mechanisms required an examination of the metallurgical properties of the AMS4911 sheet in a micro-structural fashion. It is noted that all of the specimens used in the BC and TBC coated specimens to extract the system level and coating specific properties were from the longitudinal (well though to be) oriented population of specimens.

5.1.2.1. Micro-scale Investigation

In order to seek the underlying mechanism of why the orientation of the specimens with respect to rolling direction affected the modulus, an orientation imaging microscopy (OIM) study was used to assess the electron backscatter diffraction (EBD) of the specimens. This process uses a scanning electron microscope to image highly polished samples cut from the TI sheet stock to assess the crystallographic composition and orientation of the TI sheet. An overview of this process in Appendix 11.

AMS4911 Ti-6Al-4V features a heavily lamellar micro-structureee formed in near-α and α + β titanium alloys that are cooled from above the β-transus under conditions near equilibrium (Pilchak, 2009). The β-transus is the condition of temperature and concentration of alloying material under which the β-phase begins to solidify and form. Figure 111 depicts an illustration of the formation of the micro structure upon

cooling. The lamellar micro-structure refers to the elongated α-phase crystal structures that form off of the initial (β) grain boundaries. It is noted that the α-phase is a hexagonal close packed (hcp.) crystal structure while the β-phase is a body centered cubic (bcc.) one. Most Ti-6Al-4V alloys become predominately α-phase with some minor β-phase remaining between the lamellar structures as cooling proceeds.

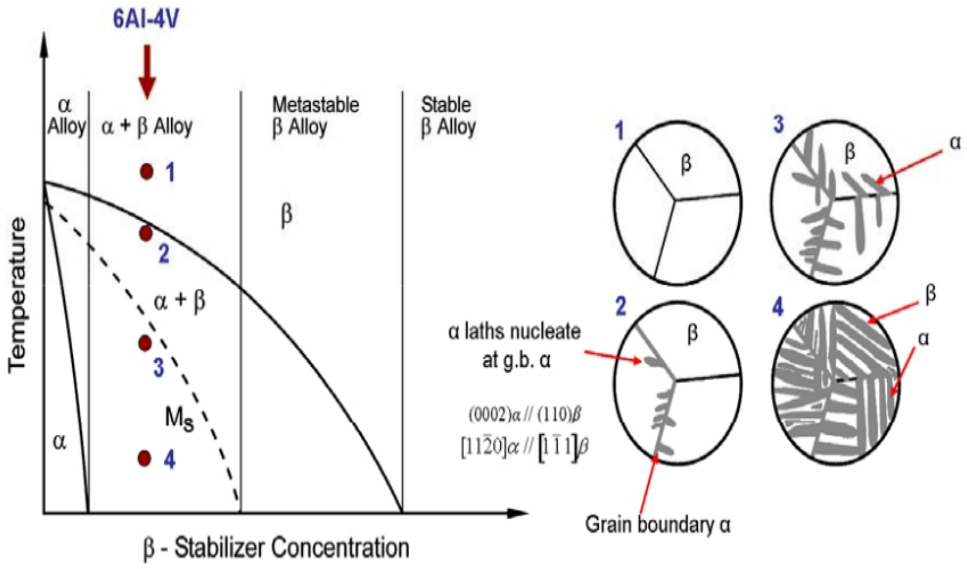


Figure 111: Titanium Cooling and Micro Structure Forms (Pilchack, 2009)

Subsequent rolling of the sheet is performed below the beta transus (phase transition line/curve) to align the long axes of the crystals, designated the “c-axis” (or “0001” in unit vector notation), transverse to the rolling direction of the sheet. This results in greater modulus parallel to the transverse direction, typically designated “TD”, and much greater toughness with somewhat reduced modulus parallel to the rolling direction (designated as “RD”). Figure 112 displays the orientation of the structure with rolling, the modulus parallel to the rolling axis if offset by a much greater ductility before

failure, due to a greater density of slip planes than across the long axis of the hcp. crystals. (Wang, 2003).

In order to determine the micro-structure of the sheet stock used for the coated

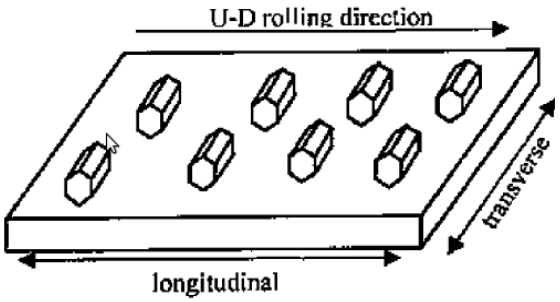


Figure 112: Titanium Cooling and Micro Structure Forms (Wang, 2003)

beams, two 1.0in diameter circular disks were cut from the remaining AMS4911 Ti-6Al-4V titanium sheet scrap. Care was taken to notch the disks on the diameter that ran parallel to the direction of the rolling axis of the sheet (so it was thought). The disks were initially ground with fine diamond grit polish to achieve a very flat surface free of oxidation. Electro-polishing followed to remove the colloidal layer. This prepared a true flat surface that was cleaned of any impurities.

The disk samples were loaded into a FEI XL30 ESEM (environmental scanning electron microscope) operating in high vacuum mode. The electron beam accelerating voltage of 20 kV and a probe current of ~10.5 nA was applied to the samples which were tilted to 70^{o}. This resulted in the electron beam being incident at 20^{o} relative to the polished surface. A working distance of 25mm was set and two scans were performed. These disks were subject to two orientation imaging microscopy (OIM) scans, the first was a scan of 0.35μm step size to determine the phase composition of the sample

between the bcc. structured beta phase and the hcp. structured alpha phase. The volume fraction of each phase, grain size distribution, grain mis-orientation distribution, etc. were also revealed by this scan. In the second scan, a 2 micron step size was used in order to sample a statistically significant region of the sample from which the macro-texture of the material could be deduced. In addition, this data was used to investigate the propensity for "micro-texture" in the material. Micro-textured regions are defined as regions of alpha grains which share nominally the same c-axis orientation, that is the radially symmetric long axis of the hcp. crystal, despite being equiaxed and appearing recrystallized.

Figure 113 displays the phase map, as can be seen the sampled area, it is about 94% α-phase, this indicates the anisotropy of the hcp. crystal structure is the predominating mass fraction in the beams. The range of grain sizes range from 2 to 12 microns with the median size around 7 microns.

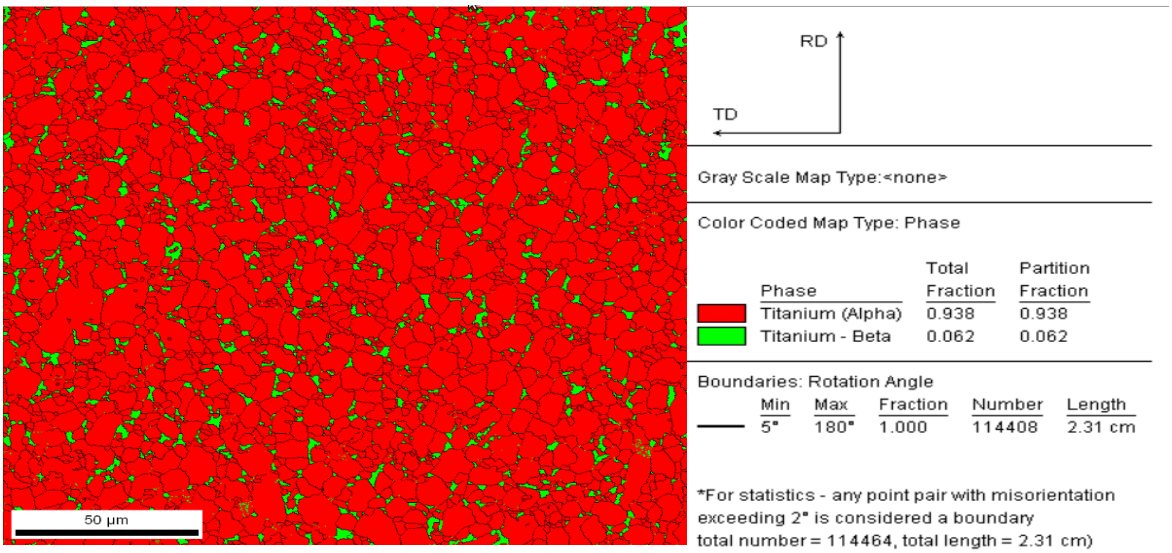


Figure 113: α- and β-phase Phase Fraction Map

Since the beam Ti-6Al-4V is heavily dominated by the hcp. alpha phase, this would tend to drive anisotropic properties in the continuum elastic media as this crystal structure is more directional than other crystal structures. To obtain a macro-scale sense of the orientation probability of the c-axes of the crystalline structure across many grains, the second scan was run with results shown in Figure 114. The upper plot is calibrated to show in red color the grains that have the long axis of the hcp. crystals preferentially oriented towards to the view oriented out of the page (or 180^{o} to that). The lower plot is calibrated with the c-axis in red when it is oriented w.r.t. to the RD axis. By inspection it is hard to distinguish a predominating orientation in this stochastic distribution. Figure 115 is a polar plot showing the predominance of the c-axis, indicated by the lighter colors which stand for higher incidence probabilities, from the course scanning lining up along the rolling axis of the specimens.

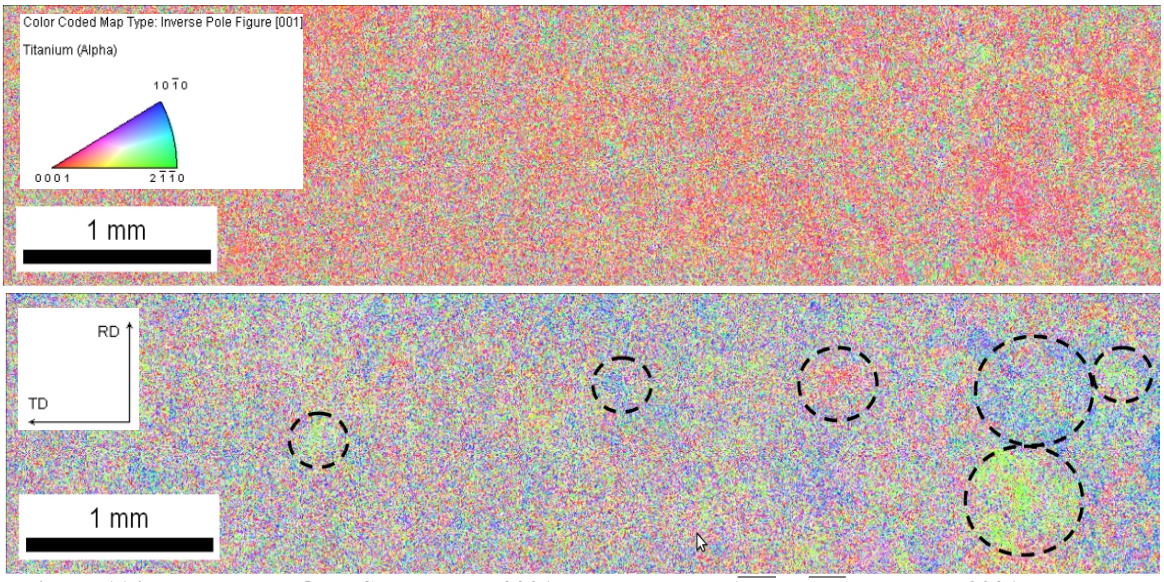


Figure 114: Large-scale OIM Scans; Top, 0001 parallel to ND (RD X TD), Bottom, 0001 Parallel to RD

It is suspected that the sheet stock that the beams were cut from was equipped

with its ink markings **across** the direction of rolling. When the beams were cut from the stock, the assumption that the markings were parallel to the rolling direction was an erroneous one. As a result for the OIM disk specimens (and the beams) the RD and TD should be exchanged. The "longitudinal" beams are actually transverse to the sheet, and there stiffer than the "transverse" beams. Despite this erroneous assumption about the ink mark orientation, the fact is that the Ti-6Al-4V is mildly orthotropic in nature regarding elastic modulus, and the care to fashion beams and plates with attention given to orientation is warranted.

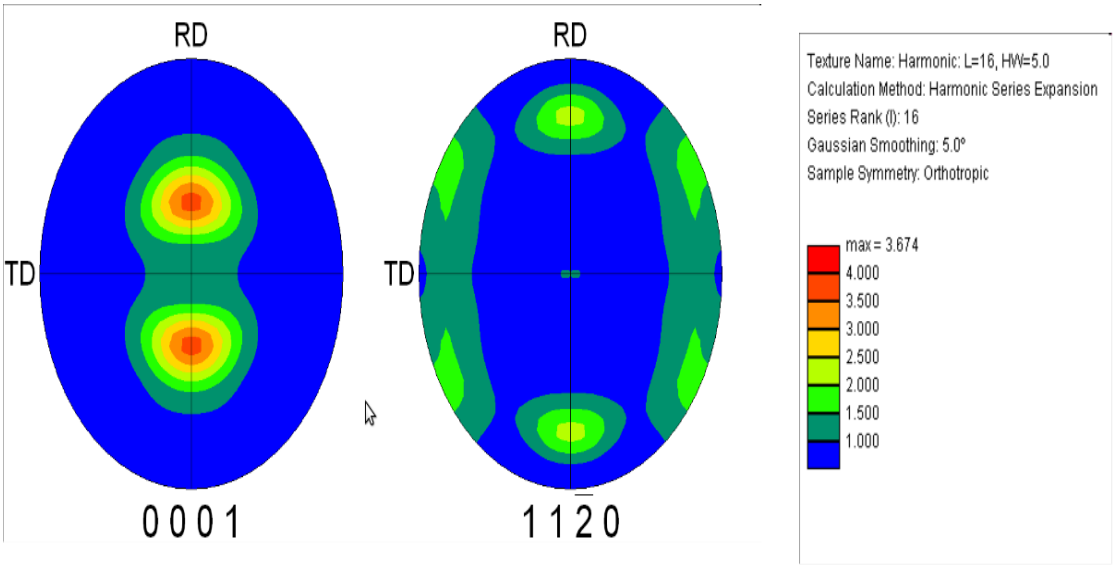


Figure 115: Macroscopic α-Phase Texture, Probabilistic Density

One other finding illustrated in the lower scan in Figure 114 is that localized regions occur as regions of inhomogeneity in the micro-structure of the sample. These are highlighted in black dashed ovals. These are only from a limited sample, and they appear too small in characteristic size to definitively explain the anomalously low damping the bare beam specimen #18.

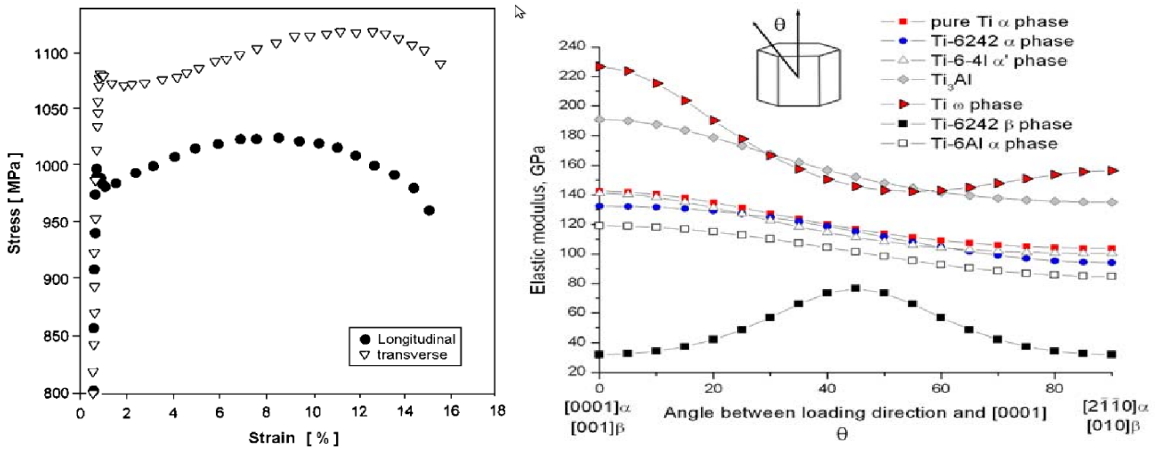


Figure 116: Ti-6Al-4V Modulus by Axial Pull (left), α-crystal Orientation Summary (right) (Wang, 2003)

The left side of Figure 116 is illustrative as to why a uniaxial tension test may not easily discriminate between E_{11}, and E_{22}, from E_{33}. The right plot shows the variation with orientation for various alloys of TI; this current study appears to be the "Ti-6AL-α phase entry" which varies from about 85 to 118Gpa depending on the orientation. Being that this is an idealized crystal structure, it bounds our median measured values of 109.05 and 116.02Gpa. The slopes are very close to one another, a bare specimen from each population would feature only a slightly different slope on the load-unload linear elastic line. The advantage of uniaxial testing is that data over a wide range of strains from one test can be obtained. This is true even up to plastic failure, while with the free-free rig one must run a whole different set of amplitudes to capture behavior across a range of strains.

5.1.3. Aging-In Protocol

Reed noted that strain history effects in his study of Mag Spinel could be driving large changes of properties observed in the course of conducting his tests, he had

postulated this could be do to history development of coating with subsequent loading. Pearson attempted to remove the history effects (or at least minimize them) by "breaking in" his 8-YSZ and Mag Spinel specimens on an aging protocol. Pearson successfully demonstrated the ability to reduce the changes in both damping and effective modulus of the coatings with sufficient harmonic loading at a specified input amplitude. This was a constant input dwell. Imposing an initial amplitude of 2.2m/sec on his samples and dwelling at this input magnitude, he determined that 8-YSZ was broken in after 2.5 million cycles. While Mag Spinel was settling down with decreasing cycle-to-cycle changes in resonance frequency, it had not yet achieved a steady condition by 4.0 million cycles (Pearson, 2008). Periodic FRF sweeps were performed by him to determine the change in the resonance frequency and loss coefficient of the coated system.

For the current study, this protocol was modified. For the current test, the beam was harmonically stimulated but the dwell was at a fixed output amplitude. This offered two advantages, first, despite being a non-linear material with a leaning backbone curve, direct comparison of frequency was easier as the amplitude curve remained the same, and second, this ensured the coatings experienced a consistent loading across all the cycles of accumulation. The formation of damage cracks in the coating is thought to be a function of the strain level and cycles experienced. It is important to note that the current study used eight NdFeB magnets bonded with cynoacrylic glue. Similar in configuration to the previous studies, this was done in order to achieve from 1,200 to 1,300mm/sec velocity output. The ALNICO magnets did not have a strong enough coupling dipole moment to impose this level of strain. The beams were suspended using the coil and setup of the

previous studies using 6-lb test nylon mono filament routed through the wire EDM hole. A set of three ring-down trials to track current resonant frequency (and therefore storage modulus of the coating) and damping of the system were performed at intervals of: 0, 5,000, 10,000, 20,000, 50,000, 100,000, 250,000, 500,000, 750,000, 1,000,000, 1,500,000, and every 500,000 cycles thereafter. When the values rate of change between two trials had settled to less than 3-5% change between test points the coating was considered aged in.

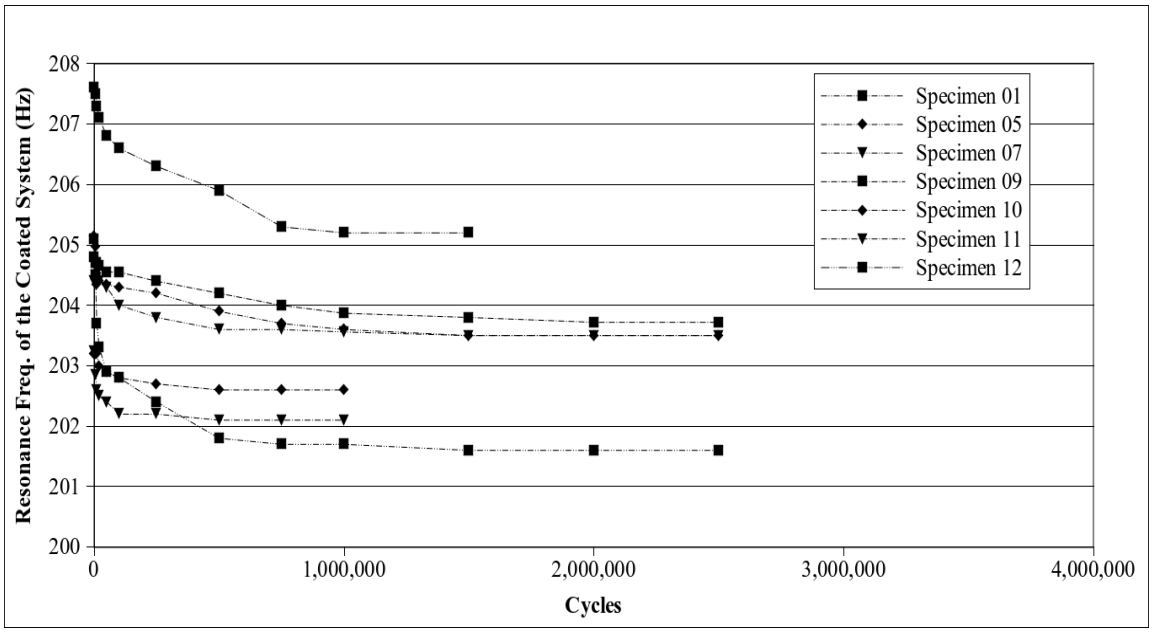


Figure 117: Coating Beam Aging, Resonance Frequency as a Function of Cycles

As can be seen from Figure 117 which shows Beams #1, 5, 7 (8.3 mil-inch of TBC, 9mil nominal), 9, 10, 11 (5.7 mil-inch of TBC, 6mil nominal), and #12 (12.5 mil-inch of TBC, 12 mil nominal); the beams all undergo a large degree of modulus softening, as manifested by a lowering of the resonance peak frequencies as more strain cycles are accumulated. The most radical softening of the coating occurs within the first

250K cycles. The damping ratio (which is twice the loss factor) also trends upward as the coating develops as seen in Figure 118. Again the majority of the development of the coating occurs in the first 250K cycles. For all the specimens, both the damping and elastic modulus can be considered fully developed after about 1.5M cycles.

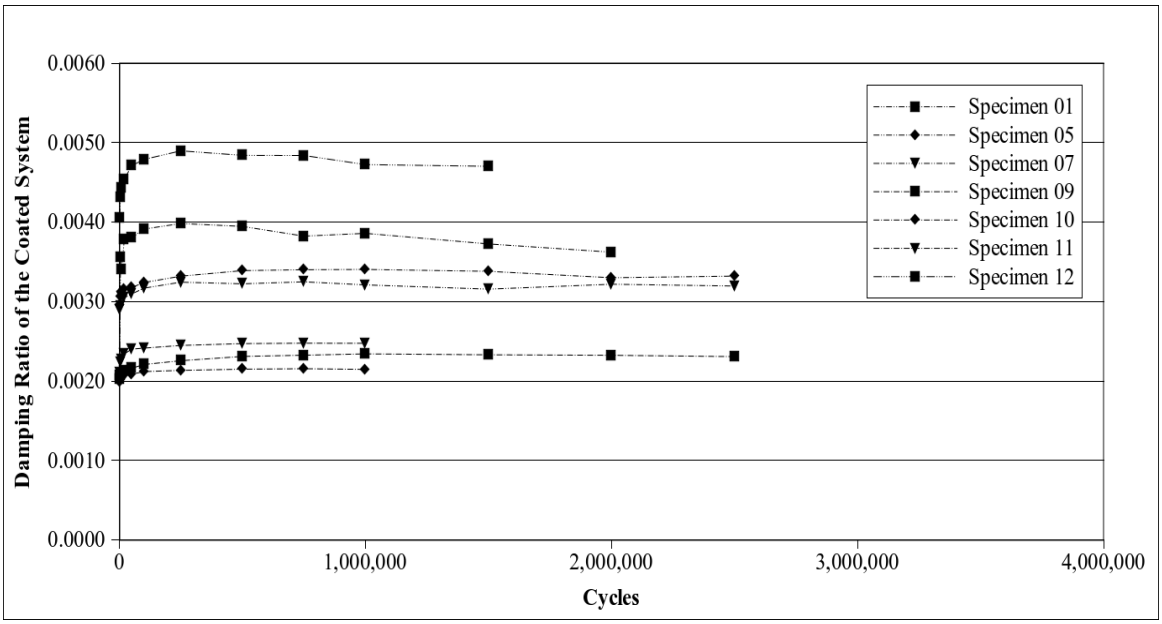


Figure 118: Coating Beam Aging, Damping Ratio as a Function of Cycles

Specimen #1 underwent more radical damping and resonance frequency (modulus) changes from its virgin state to the fully mature state than the other specimens. This was due to a miscalculation error that led to it being broken in at 1,500mm/sec. This does indicate that magnitude of dwell plays a role in the nature of micro-structural evolution of the coating. It features a different trajectory of $\omega_r(N)$ as a function of cycles with a more extreme decrease from $\omega_r(0)$ to $\omega_r(2.5M)$; one can see and a more rapid settling, essentially ceasing to show history effects by 1.0M cycles. This raises the question for future efforts to how cycles and magnitude of the strain both contribute to the breaking in of the coatings.

An important issue to be resolved prior to the commencement of the complex modulus characterization testing was to establish whether history effects could be minimized by aging the coated beams merely at room temperature. The other outcome would be where damage evolution in the coating depended not only on the cycling magnitude and count, but would also be dependent on temperature. This would have made testing logistics more complex as the beams would have to be aged in at each temperature condition before characterization testing began. To establish whether maturation of the coating is independent of temperature, specimen #01 was run through

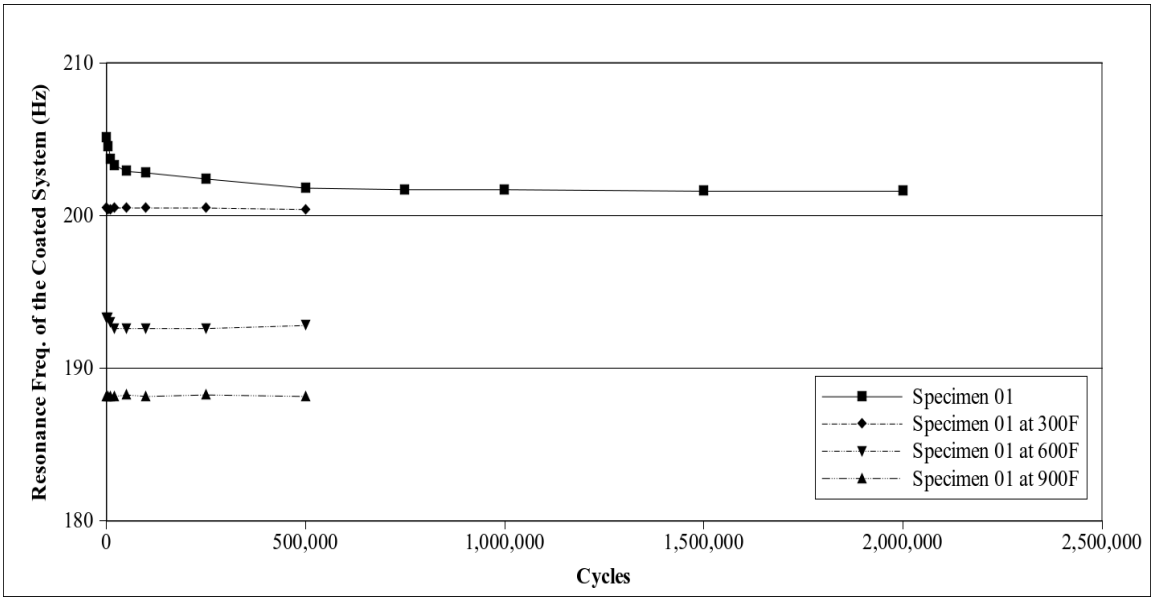


Figure 119: Aging; Resonance Frequency as a Function of Cycles at Various Temperatures

a similar age-in routine but with three changes in procedure: 1) a constant input dwell of 3,000mV$_{p\text{-}p}$ was applied to the coil ($I(t)_{coil\ p\text{-}p}$ = 10.99Amps), 2) it was equipped with ALNICO magnets and therefore driven at lower amplitude, and 3) it was suspended in the high Stark number chamber and the beam was brought to thermal equilibrium at each of the temperatures of: 300, 600, and 900degF. Figure 119 shows the evolution of the

resonance frequency versus cycle accumulation at each temperature condition, while Figure 120 displays the damping ratio evolution in the same fashion.

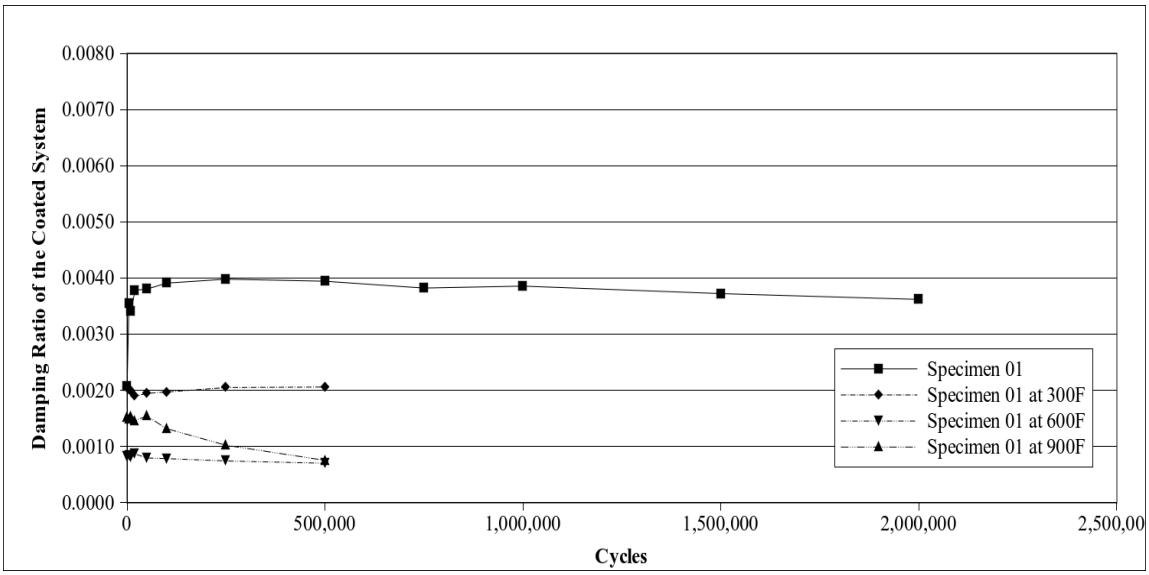


Figure 120: Aging; Damping Ratio as a Function of Cycles at Various Temperatures

Notable is that the resonance frequency settles by 500K cycles, and the changes are small, less than 1-2Hz. For damping the values at the 300 and 600degF conditions are pretty much constant through the process. Damping at 900degF was decreasing weakly and appeared to be continuing and not fully mature; the test was terminated though as the coating modulus seemed to have settled. Based on these results it seemed that the initial room temperature age in had matured the 8-YSZ coating and additional cycles added at higher temperatures did not induce significant history effects. This allowed the decoupling of coating development from temperature and consider all the beams as fully mature and ready for testing across all temperature conditions.

5.2. Testing Procedure

With the chamber validated, the specimens fabricated and matured to a fully

developed state, the main testing to characterize the beam system resonance frequencies and loss factors was ready to proceed. The general procedure was to setup a specimen in the chamber, close the chamber, and proceed to set the temperature condition. Upon reaching thermal equilibrium at that specified temperature, the lowest amplitude was imposed. The resonance peak was found via manual tuning using a function generator. The frequency was then loaded into the Labview DAQ VI and the program to stimulate the beam and record the outputs ran for three trials. After completion of the third trial, the next higher amplitude was set on the function generator and the resonance peak located. Loading of these parameters into the Labview VI and the next set of three ring-downs was run. After the last amplitude was captured, the temperature was increased to the next setting and the chamber allowed to come the thermal equilibrium. This was repeated until the last trial at 900degF was completed whereupon the chamber was cooled. Vacuum was maintained until the interior temperature was below 350degF whereupon the vacuum was relieved and the chamber opened. Testing proceeded to the next sample. The temperatures that were imposed were: 70, 300, 600, and 900degF (21.1, 148.8, 315.5, and 482.2degC), while the amplitudes tested were 250, 500, 1000, 2000, 3000, 4000, 5000, 6000, and 7500$mV_{p\text{-}p}$ (which is 0.91, 1.83, 3.66, 7.33, 10.99, 14.66, 18.33, 21.99, and 27.49$Amps_{p\text{-}p}$ coil current). Three bare beams (Specimens #18, 19, 21) were tested first, along with one bond-coat only beam (Spec. #15). The three bare beam were used to verify that linear behavior continued across the temperature range and characterize the η_{bare} for use in the Torvik relation. The bond coat only beam was to see how much influence the bond coat exerted on the coated beam system. The 8-YSZ coated beam

specimens run through were #01, 05, 07 (normal thickness), 09 (thinner coating), and 12 (thicker coating).

5.2.1. Specimen Prep and Loading Into Chamber

Each specimen is aged and established to be fully mature before commencement of testing upon it. The beam specimen under test was hung by threading the nichrome wire through the EDM hole, suspended over the centerline axis of the magnet, and its alignment was verified by sighting down from above and checking that the DVL landed on the mica dot at the center. Care was taken to make sure the beam and magnet centerlines are coincident. The slack was worked out of the wire and the wire was routed to the tie of rod where is was clamped between a pair of nuts and washers. On the span between the rod and the wire tie off point the 0.5kg brass weight was hung. The next step was to replace the radiation shielding pieces removed to access the beam and the wire suspension. Next the chambers top lid is lowered and sealed to the base, originally it was designed to be fastened down with large wing nuts, but its weight alone combined with the vacuum closure force was sufficient to set the seal. At this point electrical continuity checks using a handhold multimeter on each branch of the lamp power circuits were performed to make sure none of the connections were shorted out to the chamber. The check were performed as closure of the chamber sometimes abraded off the junction insulators made from masking tape, or grounded a wire out. Alignment of the beam with the DVL laser was also verified to make sure it had not shifted from the intended location.

5.2.2. Reaching Set-point Temperature

After chamber seal-up and continuity checks, the vacuum was supplied to the chamber from the Varion dual stage vane pump and the chamber would reliably hold at about 6.0 to 7.5mmHg (about 0.01atm). If testing above room temperature, the two variable AC transformers were set. Generally they were set to a level much higher than needed to maintain the thermal equilibrium as the system required over an hour to reach within 2% of the intended temperature. With intentional overshoot and ramping the overshoot back by hand, while monitoring the dummy specimen's thermocouple readings, one could get the chamber to the thermal condition within about 10 minutes. Once within ±10.0degF and with a change of temperature of less than 2.0degF/min, the system was deemed to be at equilibrium. In practice it was easy to halve these tolerance bands in reasonable time.

5.2.3. Core Testing

There were two main steps to obtaining the data to characterize the coating, the first was to obtain the system-level damping and resonance frequency for the whole coated beam. These values are strain amplitude dependent in nature and hence they are indexed and collected in time which serves as a proxy variable for instantaneous strain amplitude until the end of the processing.

There are several methods in use that can be used to extract the damping of a structure, two of the more prevalent and used in previous efforts are the Free-decay and forced response techniques. Free decay is a transient technique where the system is

allowed to decay from a steady, harmonically-excited initial state. Processing of the ring-down envelope and phase shifts allows for extraction of the damping and instantaneous frequency. The forced response technique entails harmonically exciting the structure while slowly, and systematically, varying the excitation frequency, in this fashion the response is built in the frequency domain. This response, often termed a frequnecy response function (FRF), is repeated at different amplitudes to capture the various strain amplitude levels. The free decay technique was chosen as the main approach in this study as it was felt it would capture the material non-linearity of the 8-YSZ coating in the course ring-down decay where the strain level experienced is varying as the system decays. In this fashion free-decay allows for a whole range of strains to be captured in one run while multiple FRF sweeps are needed at different resonance peaks to build a strain range. Another advantage of the free-decay approach is the short time span required to characterize high quality factor systems, which the free-free chamber with a bare beam was, in comparison to forced response.

For this step, an on-line LabView virtual instrument (VI) code was developed to stimulate and then record the free decay response of the beam. The code was capable of processing data to allow preliminary assessment of the system in addition to streaming raw measurements to storage. It also took care of software signal filtering to eliminate rigid body motion from the beam. The second step was to extract the bulk complex modulus for the coating from the system-level data by using the FEA modal analysis derived polynomials to determine the coating effective modulus, extrapolate the strain field within the beam, and determine the coating modulus by use of the Torvik equation.

For this portion of the study an off-line Matlab code was developed.

The basic steps to record a ring-down trial on a specimen involve:

1) Determine the excitation function: one sets the amplitude of forcing function moment, then proceeds to down-sweep to find the resonance peak by lowering the frequency of the function generator. It was good practice to proceed over it and then perform another down-sweep to confirm the measured resonance frequency. The sweep was accomplished by rotating the function generator knob smoothly and slowly, for the bare beam one must tune the function generator in at 0.001 to 0.0001Hz increments as the FRF peak is very sharp for the bare and bond-coat only beams. For the bare beams re-tuning was accomplished with each change in forcing function magnitude to verify if the peak frequencies were remaining fixed, and therefore, linear in nature. The coated beams, despite having to be re-tuned with each forcing amplitude and temperature change due to their strain softening FRF backbone curves, were much easier to tune in. This was due to their much higher damping levels and broader FRF resonance peaks, for these typically tuning in was performed on the 0.01 to 0.001Hz per second ranges.

2) After determining the resonance frequency for a given temperature and forcing amplitude conditions the parameter from step 1 was input into the Labview code to allow it to generate the forcing function. (This was done as the National Instruments board did not have a frequency resolution that was fine enough to tune to the resonance peak, it would change up and down in discrete steps.) This will allow the computer DAC channel to harmonically excite the beam, allow it to settle into a steady condition, then chop the

excitation, and allow the decay to occurr. During this time the raw voltage signals from the DVL laser (the beam plant output) as well as the output channel of the NI board driving the coil amplifier (the beam plant input) are recorded. On-line processing of the data within the code also occurs. This includes filtering the DVL data with a 5th order Butterworth high pass filter, passing the filtered signal to a discrete Hilbert transformation to recover the magnitude envelope function and instantaneous frequency, and then fitting a classic linear system decay curve (e.g. $v(t)_{env}=v_o e^{(-\zeta 2\pi f_r t)}$, where $v(t)_{env}$ is the current voltage, v_0 is the stimulation voltage amplitude, ζ is the damping ratio of the system, and f_r is the resonance frequency of the system to the envelope function).

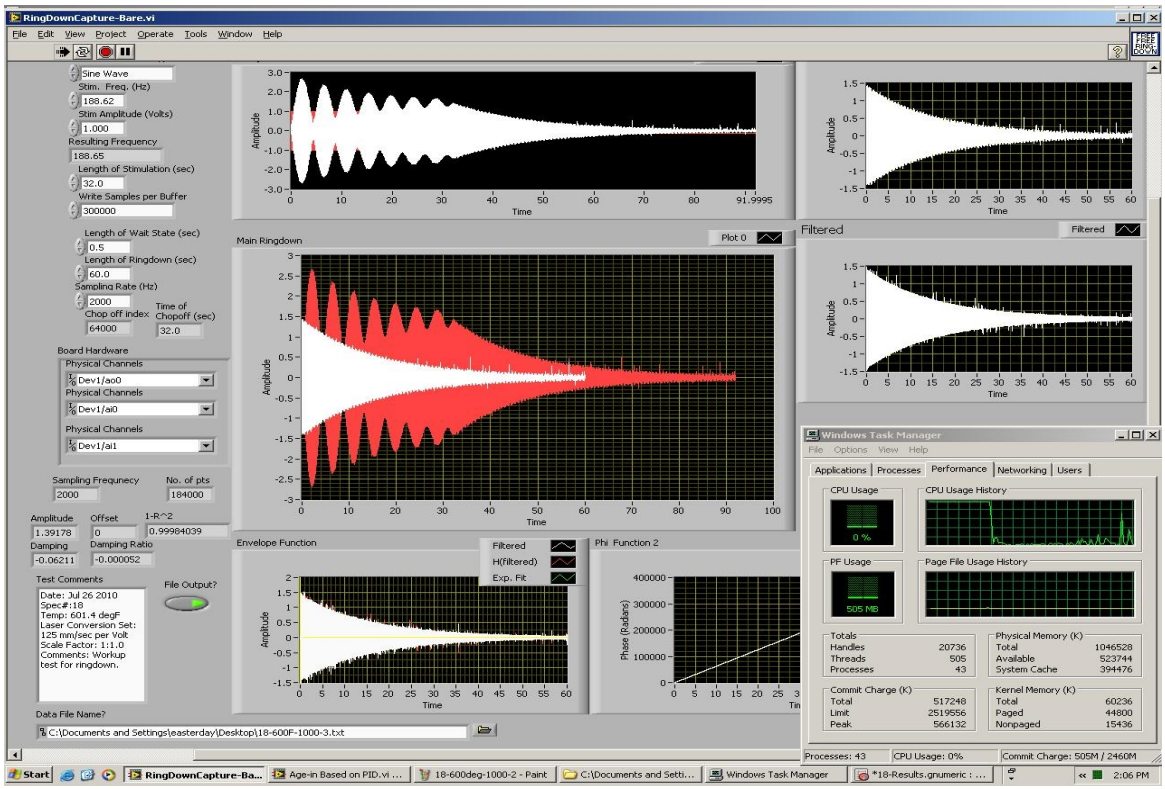


Figure 121: Typical Bare Beam Dataset

Figure 121 shows a screen-shot of the VI with a typical bare beam decay response

on the screen. The VI does display a lot of interim processing steps to allow monitoring of the process and help tune the VI settings to the test conditions. The upper center graph window is the raw data as collected on the stimulation (plant input in pink/darker shade) of the coil and the response (plant output in white/lighter shade) as measured from the DVL. This is the raw data, all the other displays are post-processed from this raw data set.

The plot below is the chopping of the DVL response dataset whereby the set is chopped of data in the time before cutting of the coil stimulation signal. The pink/darker shade is the whole data set and the white/lighter shade is the truncated one. The upper right plots display the truncated signal before and after being passed through the 5th order Butterworth filter (in this particular dataset there is very little rigid body motion to filter out). The bottom center pot is of the final set and shows the on-line fitting of the classic linear exponential decay function ($v(t)_{env}=v_o e^{(-\zeta 2\pi f_r t)}$) to the decay envelope function $v(t)_{env}$. In so doing the global damping ratio, ζ, was extracted. The R^2 residual measure is typically is very high, from about 0.999 to 0.9999 for a bare beam. What was unexpected was how high it was for the coated beams as well; from 0.098 to 0.99 or higher for 8-YSZ coated ones. Coated beams even featured a classic viscous type decay envelope. That, despite to coating increasing system damping by over 10X, typically. As a result the global damping ratio (or loss faster derived from it) were considered reportable for all the systems as it was a very good global single valued approximation of the behavior.

One situation was encountered where the linear decay envelope typical of dry damping occurred (See Figure 122) as had been anticipated. But it was discovered to be an erroneous condition triggered by loose magnets that were chattering due to failure to use the Belleville washers to take up thermal compliance when that specimen was setup for collection run. This condition went undetected as the system was in vacuum, but upon opening up the chamber the buzzing noise of the magnets was immediately apparent when the beam was excited. As can been seen from Figure 122, this was the one case where the linear form of the decay envelope was obtained. Despite all the review of the literature and anticipation of this type of time series signal, even the thickest coat beam (Spec. 12) exhibited a decay envelope very close to that a a classical viscous system.

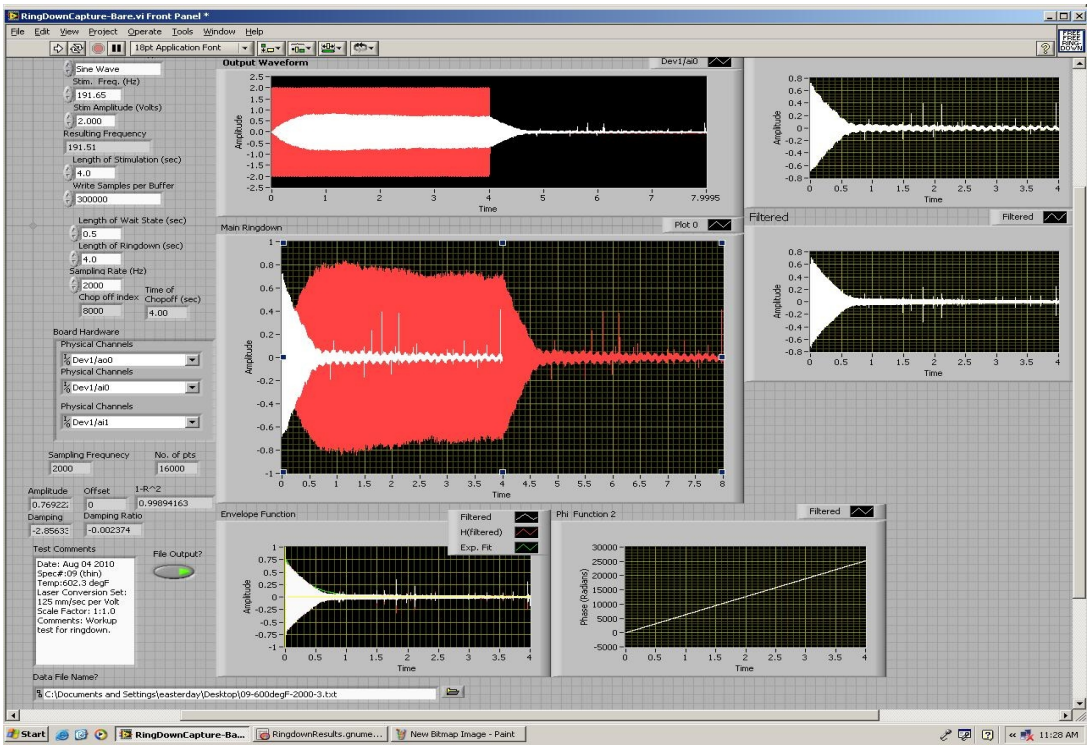


Figure 122: Chattering Magnets with Linear Decay Envelope

Some trials of system damping for the bare and bond coat only beams were done using a manual method. This involved using an oscilloscope to monitor the decay signal. The system was tuned for the temperature and amplitude at mode-I bending. On the oscilloscope, the voltage amplitude was measured. After that the vertical scaling was magnified and the horizontal cursor lines set to 2% (or 1%) of the amplitude just measured. A timer was started at the same time the harmonic stimulation was shut off and stopped when the signal went below the cursor which is the 4^{th} time constant (4τ, or 5τ if at 1%). A bare beam typically took from 30 to up to 90 seconds to decay out so far so slight errors introduced base on reaction times were not unacceptable. For comparison, a coated beam would decay out to the 4^{th} time constant in 2 to 6 seconds.

5.2.4. Extract Coating Bulk Modulus

Upon completion of the testing, the beam system datasets were run through a Matlab script to process the data, apply the polynomials and extract the complex modulus of the coating. A sample code is listed in Appendix 12, and an overview of the process is in Section 4.5.1.

5.3. Bare Beam Specimen Findings

The first specimens to be characterized for their complex moduli were the bare beams, as their loss modulus which is for Ti-6Al-4V is needed for the Torvik equation (as η_{bare} in Eq. (123)). The bare beams provided an unexpected challenge to determine a value to seed into the Torvik equation. This was because of the sensitivity of the chamber being so high due to drastic reduction of boundary condition damping over the previous setup. Free-free damping as low as $\eta_{sys} = 0.000084$ was obtained across the bare specimens, stimulation amplitudes, and temperature conditions imposed; this was almost 5X lower that Reed's reported value of 0.0004. Quality factors for the bare beams within the chamber at the room temperature ranged from 5,900 to 8,200. Figure 123 summarizes

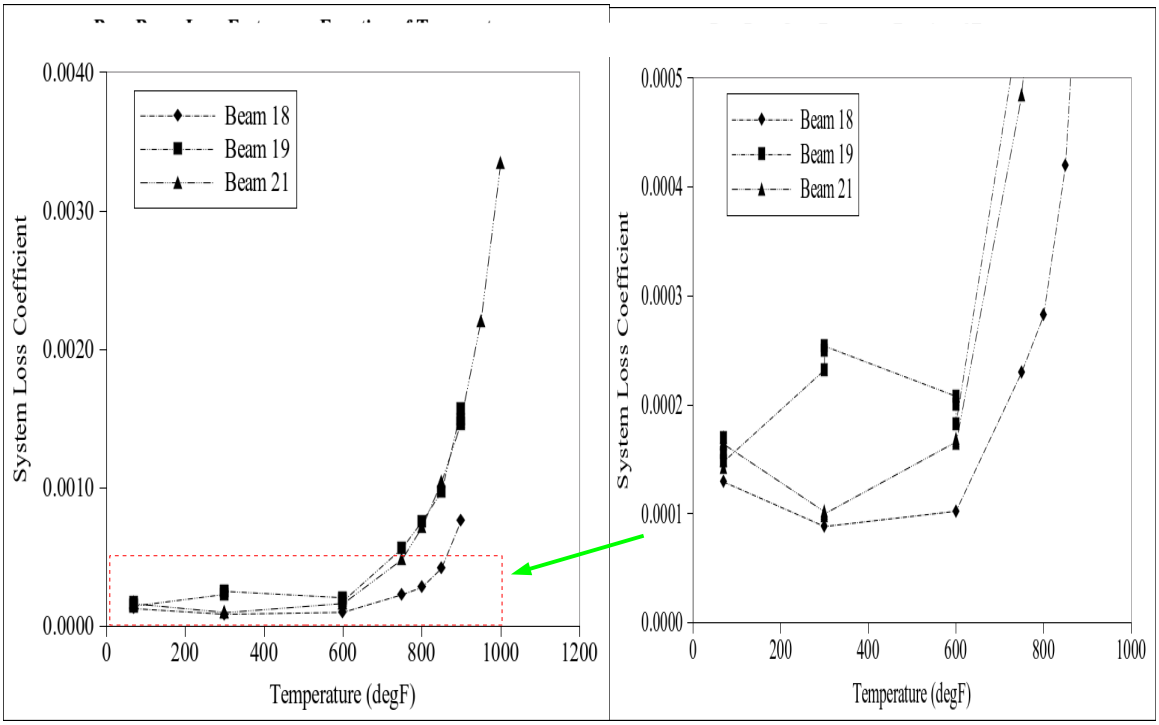


Figure 123: Ti-6Al-4V Loss Factors Versus Temperature; data set (right), close-in plot (left)

the bare beam results with a plot of the loss factor versus temperature for the three specimens.

Some results that can be deduced from the Figure: first, the damping recovered was very low at the lower end of the temperature range. Second, the damping minimums for the two of the bare beams (Spec. 18, 21) were somewhere between 300 and over 600degF; this is counter intuitive to would be expected for classical engineering materials, but it was a repeatable trend uncovered across these two specimens. It was also obtained through multiple trials with separate heating events so it was a reversible state. Third, the damping of the bare beams increases radically as the temperature climbs past 600degF towards 900degF. It remains a linear system due to several things: the envelope function remains very viscous in form, the resonance frequency does not change with stimulation amplitude changes, and the principle of superposition of signal (for reasonable amplitudes) holds. The bare beams displayed no significant variation in loss factor as the amplitudes were shifted from 250 to 500 to 1000m$A_{p\text{-}p}$.

Specimen #18 features damping almost 1/2X that of #19 and 21, across the prescribed temperature range. This was also the fact for comparison against #23 at room temperature (#23 was tested only at room temperature). No plausible cause was discovered but experts in metallurgical testing often advise to cut specimens only from the center of a rolled sheet to ensure controlled properties. For future studies conducted on such low damping material, indexing of the cut locations might be worthy to track. Despite this wide variation is the loss coefficient curves across the temperatures the influence of a large variation in η_{bare} is small on η_c. The Torvik equation:

$$\eta_c = \frac{\eta_{sys}(1+SER)-\eta_{bare}}{SER} \tag{123}$$

has error sources enter through the fidelity of the strain energy FEA modeling, UNC_{SER}, and the bias and random error in the system level measurement of damping for the coated and bare beam systems, $UNC\eta_{sys}$, and $UNC\eta_{bare}$, respectively. Applying propagation of error to Eq. (123) yields:

$$UNC\,\eta_c^{\,2} = \left(\frac{1+SER}{SER}\right)^2 (UNC\,\eta_{sys})^2 + ((\eta_{sys}-\eta_{bare})\ln(SER))^2 (UNC_{SER})^2 + \left(\frac{1}{SER}\right)^2 (UNC\,\eta_{bare})^2 \tag{124}$$

The typical measured values of the coated system's loss factor, the bare beam's loss factor, and the SER were around 0.0020, 0.00016, and 0.125, respectively. 0.95CI uncertainties for the same three values were around 0.0001, 0.00008, and 0.01, respectively. When all but the $UNC\eta_{bare}$ are assumed exact (e.g. UNC_i is zero), and this value is held to 50% of its nominal value, a rather large uncertainty typified bare beam #18 in the current study, η_c is influenced by a 1.6% relative uncertainty, a fairly weak influence on the coating loss factor determination.

Using Mil-Handbook-5H for elastic modulus values of Ti-6Al-4V to employ within the FEA modal analysis models proved to be less than accurate. The book modulus values had a discrepancy of up to about 11-12% below those found by testing the bare specimens. Figure 119 shows the data from Mil-Handbook-5H as well as the data from the testing of specimens #18, 19, and 21, which are all longitudinal hcp. oriented. The error bars are indicative of the inter-sample variation combined with the precision uncertainty from the chamber setup. The 0.95CI curves bound the functional

fits indicating that even in a most favorable case that it is best to model with the locally determined modulus values as opposed to values in the literature. It is also noted that the onset of accelerated softening of the modulus reported in the literature was not encountered in the testing of these specimens, which ranged up to 1050degF (565.5degC).

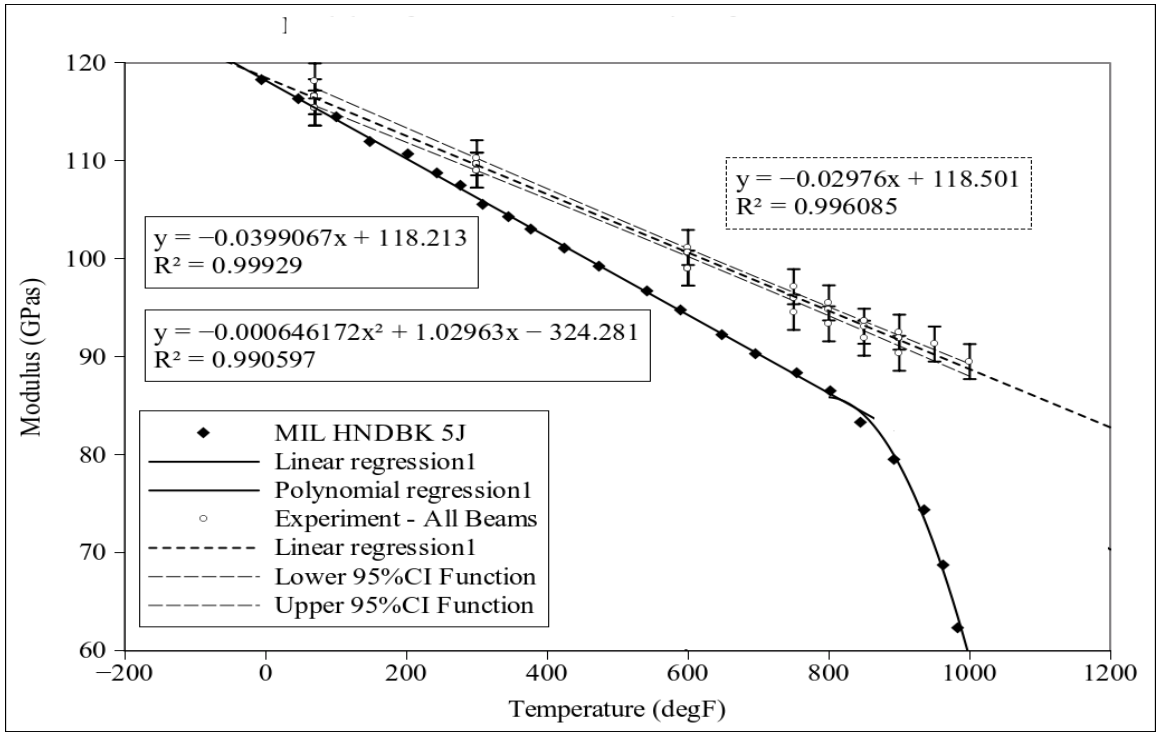


Figure 124: Titanium Ti-6Al-4V Modulus Versus Temperature

The determined functional fit for the longitudinal grained bare Ti-6Al-4V beams is:

$$E_{TI}(in\,GPas) = 118.501 - 0.02976 \cdot T \quad ; \quad (70\,degF \le T \le 1050\,degF) \tag{125}$$

where the modulus, E_{TI} ,is in Gpa, and the temperature, T, is in degF. Equation (125) is used to seed the FEA models for building the predictive polynomial functions (See Section 4.3.3) at the temperature points of interest. Another important thing to establish is

that the titanium remains linearly elastic throughout this range of temperatures, that no creep, viscoelastic effects, or plasticity became a problem. This is important to establish as the FEA models are predicated on the TBC and the metallic beam behaving in a linearly elastic fashion. Plasticity can be discounted right away as the highest deformations imposed on the bare beam are at the 2.0 m/sec velocity ($v(t)_{p\text{-}p}$), and this scales to about 104MPa of maximum stress in any region of the beam. This estimate was arrived by using the scale function from the FEA model as per:

$$\sigma_{11} = E\,\epsilon_{11} = E\,\tilde{\epsilon}_{11}\frac{\delta}{\widetilde{U}(L/2, t_b)} = E\,\tilde{\epsilon}_{11}\frac{2\pi f_r \cdot v(t)_{p-p}}{\widetilde{U}(L/2, t_b)} \tag{126}$$

Per Mil-Handbook-5H, for the Ti-6Al-4V alloy, the proportional limit at 1000degF (537.7degC) is around 32,000psi (220.6MPa) (Figure 5.4.1.2.4 in Mil-Handbook-5H)). This is where yielding begins to occur in the metal and is over double the maximum strain the magnet system could impose on the bare beam.

Regarding creep, the testing is on a short time-scale; a typical ring-down, even for a bare beam with very high Q-factor is complete within a minute and the imposed loading is alternating. This happens from around 300 to 600degF, whereupon the material damping goes up and the time required for accomplishing a ring-down goes down. Some creep testing has shown both metallurgical stability and surface stability under conditions of stressed exposure for up to 500 h at 450°C (840degF). While the current study exceeds those temperatures, the time duration of loading is for much smaller time-intervals, typically 20-30 seconds at most. Wegmann showed that α + β alloys, like Ti-6242 have

been shown to have adequate creep resistance up to ~550degC (~1022degF) (Wegmann, 1999).

As to visco-elastic effects, it is noted that even at the 900degF condition that the ring-down envelope function is well described by a classic exponential fit and the damping is very small, with Q-factors for the free-free beam system varying from about 1,500 to 22,500, the loss coefficients are very small hence viscous effects are minimal.

5.3.1. Chamber Characterization of Boundary Conditions

The Q-factors obtained over the previous setup were anomalously high so a study with the parametric variation between the old and new configurations were performed, the details and results are in Section 3.9. The question was posed in the section as to how low can the chamber damping be ultimately reduced.

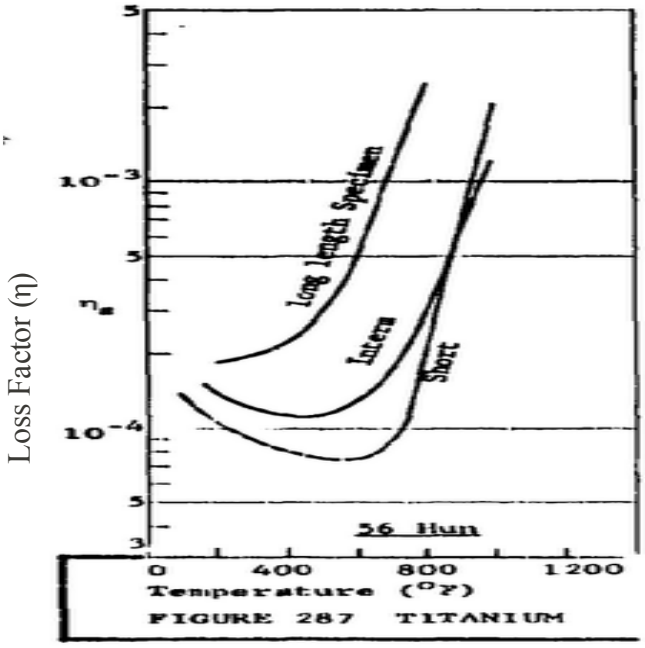


Figure 125: Ti-6Al-4V Loss Factor versus Temperature (Lee, 1966).

The best gauge of the validity of the current bare beam study as well as the chamber is against Figure 125, this is a plot of the loss factor of Ti-6Al-4V as a function of the temperature. It an be seen that two of the sample types depicted show a similar damping minimum (from about 450-650degF) above room temperature, much like the current study. The lowest value reported is around $7.5x10^{-4}$ (or 0.00075) which is almost 10X the damping minimum in the current study. Unfortunately this is a secondary, compendium source so the difference between a “long length specimen”, “Inter[mediate]”, and a “Short” specimen is indeterminate. Damping data is very sparse in the literature, Lee's secondary compendium source is among the couple resources found.

5.4. Bond Coat Only Specimen

A bond coat only specimen was tested after the bare specimens to assess its impact on the coated beam system. Figure 126 is a plot of the bond coat results for loss factor, shown by hollow circles superimposed over the earlier bare beam results at the various temperatures. The bond coated specimen behaves almost like a bare beam, with a slightly higher damping than a bare one.

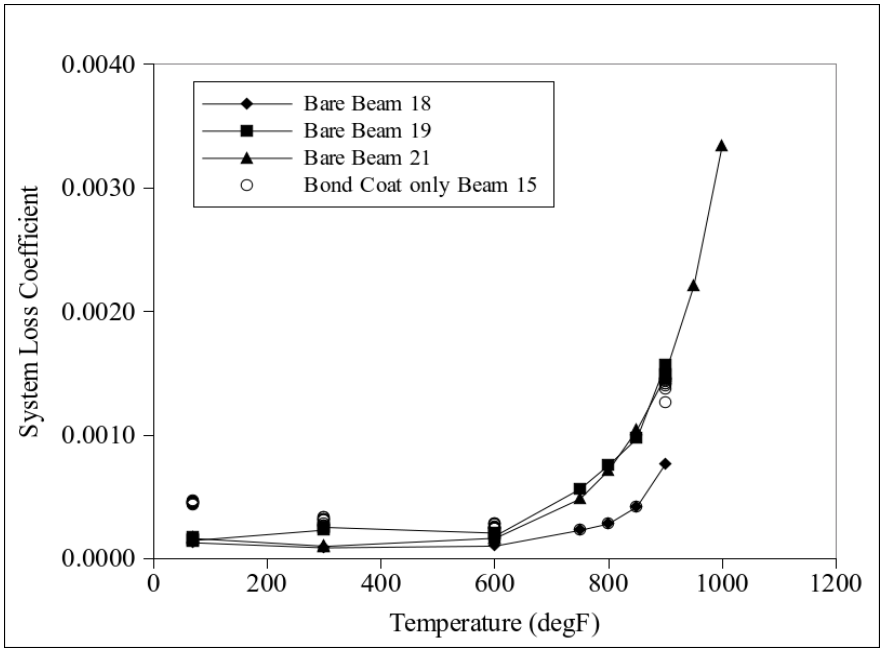


Figure 126: Bond Coat Specimen System Loss Coefficient

Since any of the coated beam systems tested at the same conditions have almost 10X the loss factor of either the bare or bond coated beams, the influence of the coating on the damping is minimal.

Figure 127 displays the fact that the bond coat layer adds little stiffness to the beam system either. This plot of resonance frequency as a function of temperature for the mean of the bare beams and the bond coated beams shows an almost collinear set. The coating appears to little effect the stiffness the beam system. There is a slight variation in the slope compared to the bare beam set but it is rather small.

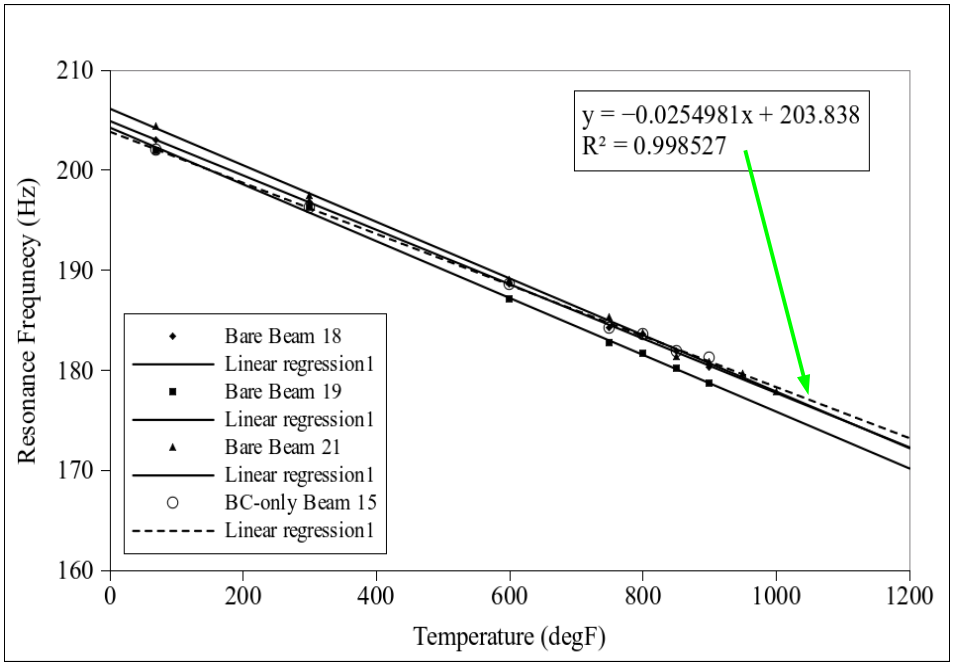


Figure 127: Bond Coat Specimen System Resonance Frequencies across Temperature

Originally it was planned to process the BC layer as if was a TBC layer with a set of polynomials, but given the irregularity of the BC layer (e.g. it not a nice homogeneous slab of material as a layer on top of the beam, Section 5.1.1), and the relative lack of impact of the BC on the specimen's system-level damping and resonance frequency, this was not performed. Additionally, it was concluded that the FEA modeling assumption both Deleon and Pearson made in regards to the bond coat was valid. This assumption was to model the BC layer as if were part of the slab of the TBC material. Based on the discontinuous and irregular nature of the BC layer it seems unable to sustain bending shear flow, nor features much continuous volume to dissipate energy.

5.5. Coated Beam Specimens

The fully TBC-coated specimens were tested and processed. The system-level

findings will be presented and then the coating bulk properties. To start, it was noted that the strain softening non-linear property of 8-YSZ was confirmed. Figure 128 shows the output amplitude and resonance frequency as three of the coated beams (the 8.3mil coated ones at 70degF) were tuned in at difference stimulation amplitudes. These trace the backbone curve and lie at the bending mode-I resonance peaks of the FRF functions.

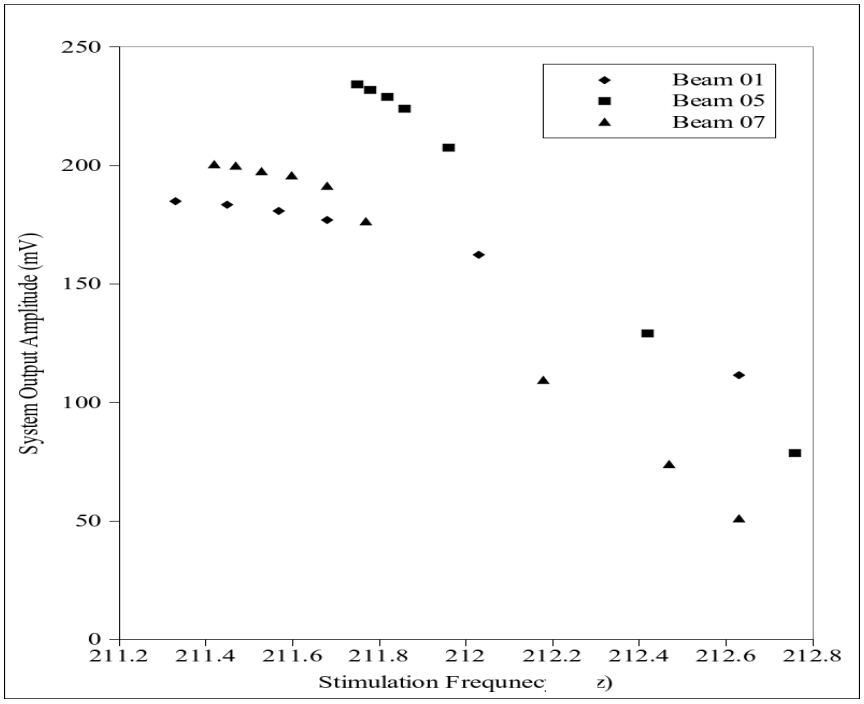


Figure 128: Resonance Frequency Peaks at Various Amplitudes

Several things are apparent, first the initial jumps in output response amplitude are large, but then the beam system begins to saturate and the dots pile up. Each dot represents a fixed stimulation amplitudes increment of 1000mV$_{p\text{-}p}$ (beyond the first three which are 250, 500, and 1000mV). The curves lean to the left and show that the 8-YSZ layers stain soften and so material non-linearity is confirmed.

5.6. System Level Damping and Resonance Frequencies

A product of the LabView code was an estimation of the global system loss coefficient, even for the coated beams, a linear system estimate accurately described the decay envelope function through the 4th to 5th time constants. As a result these values are presented in plots for 500, 1000, and 2000mV$_{p-p}$ stimulation amplitudes (coil I(t)$_{p-p}$=1.83, 3.66, and 7.33Amps) as a function of the temperatures at 70, 300, 600 and 900degF. The

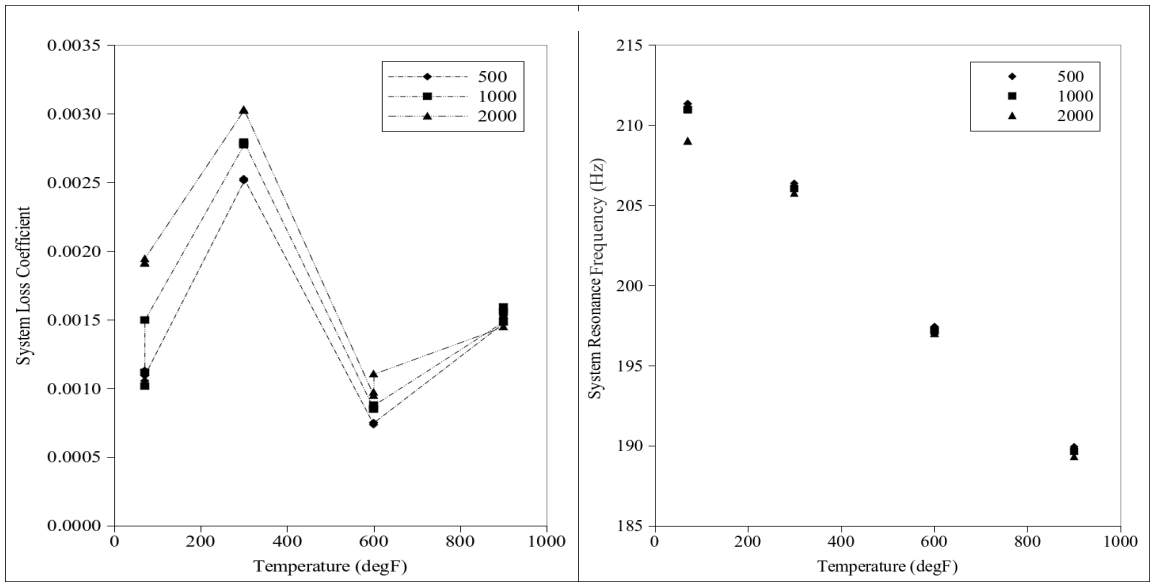


Figure 129: System Loss Factor (η_{sys}) and Resonance Frequency (f_r) – Specimen 05

frequencies change with temperature, but the shift is small relative to the change in frequency between each temperature condition.

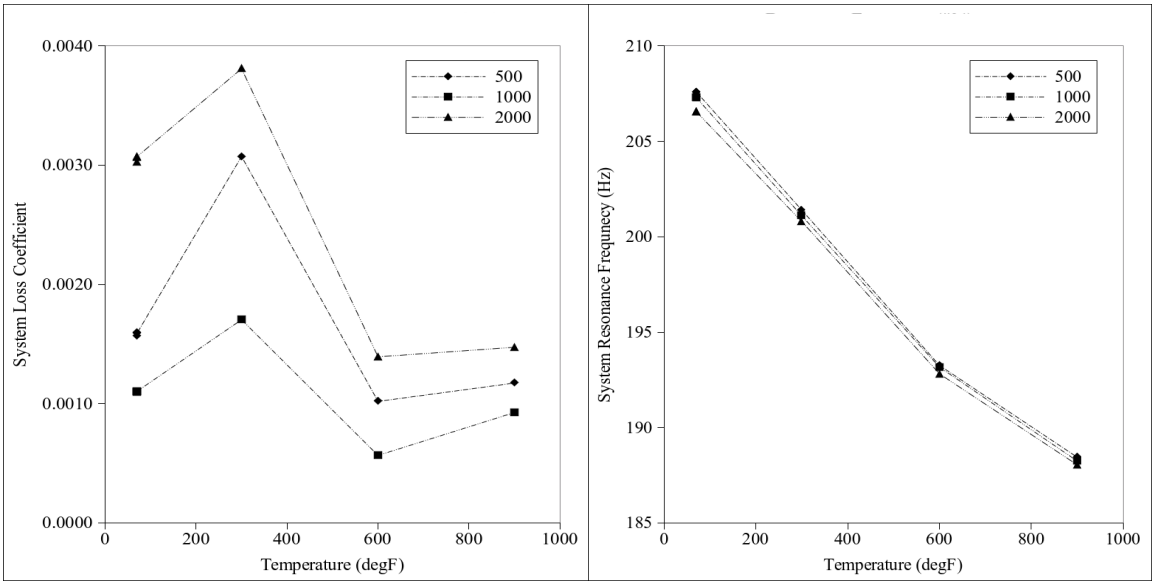


Figure 130: System Loss Factor (η_{sys}) and Resonance Frequency (f_r) – Specimen 01

The left of Figure 130 is the plot of the coated system loss coefficient, $\overline{\eta}_{sys}$, as the temperature is varied for specimen 01 at the three amplitudes that were imposed. The bar notation indicates that the reported loss factor is a regression estimate using a fit linear viscous model from the Labview VI to the (weakly) non-linear system. The right side of the Figure plots the resonance frequencies as a function of the temperatures and the amplitudes. This was determined when tuning in the resonance peaks.

In contrast to the bare beam, where the damping went down and had a minimum in that general region of temperature, the coated beam specimens' damping actually increased and had a maximum, bottoming out around 600degF and then slowly increasing as the temperature was further increased. Resonance frequencies of the coated specimens declined in an almost linear fashion as temperature increased. Examination of the other plots for specimens 05, 07, 09 and 12 showed this pattern held, even for the thicker and thinner coatings on #12 and 09, respectively.

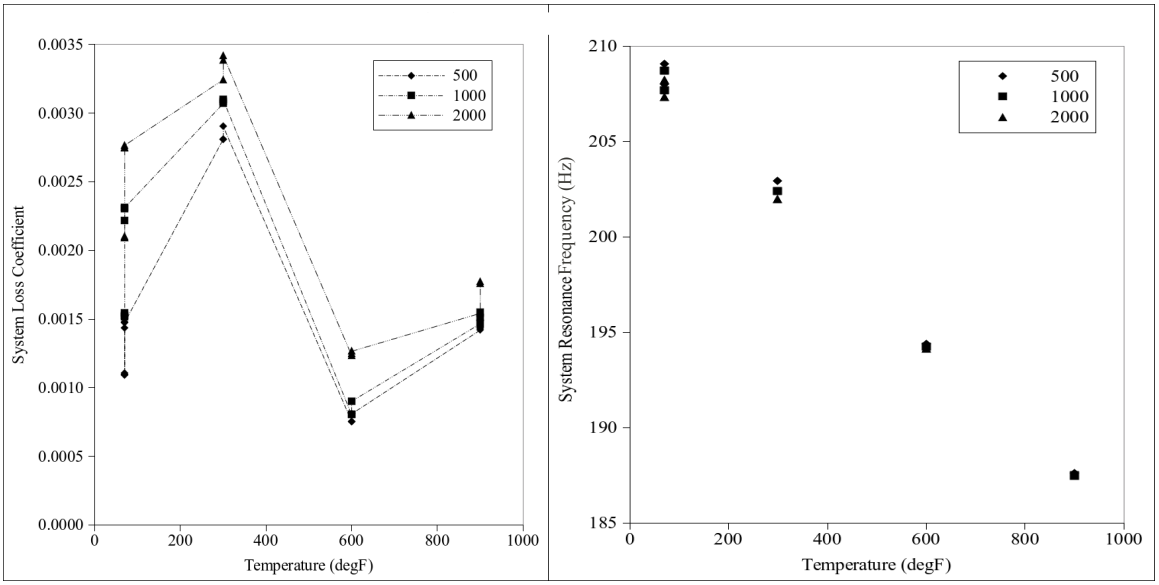


Figure 131: System Loss Factor (η_{sys}) and Resonance Frequency (f_r) – Specimen 07

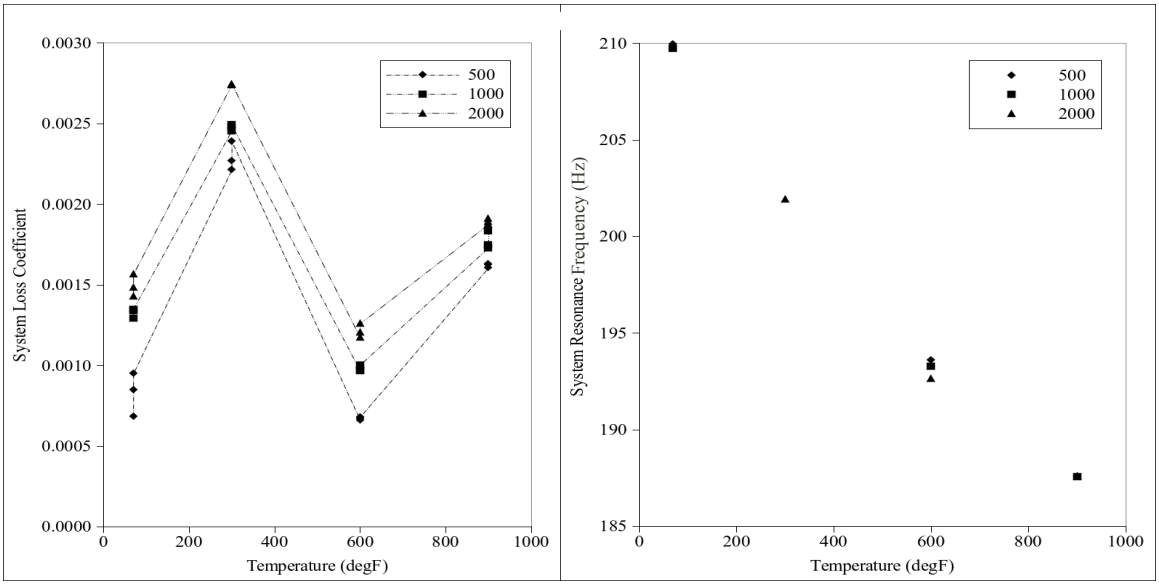


Figure 132: System Loss Factor (η_{sys}) and Resonance Frequency (f_r) – Specimen 09 (thin)

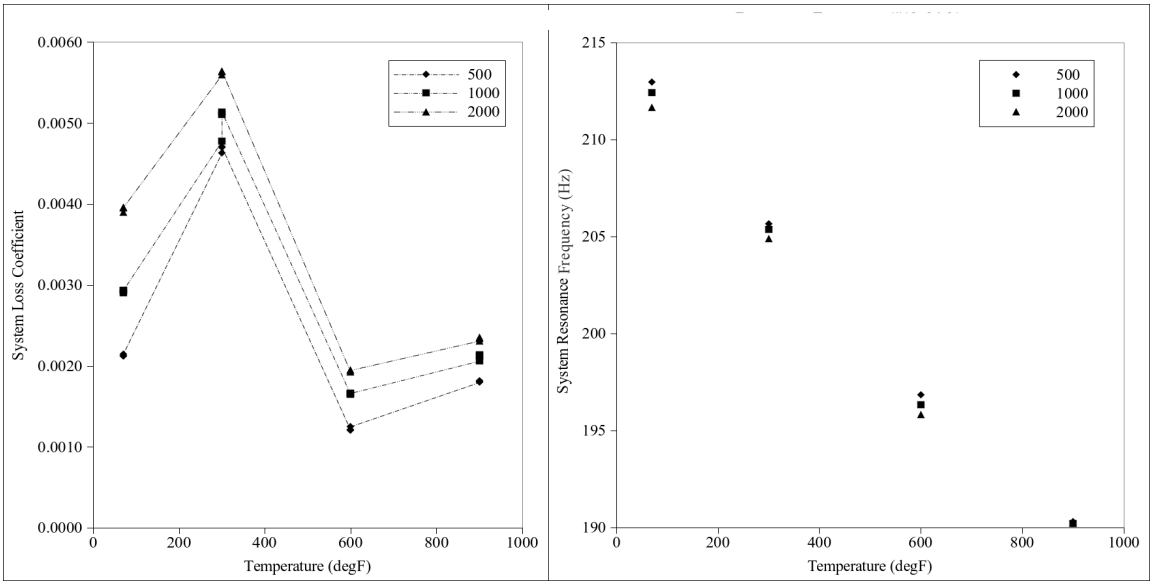


Figure 133: System Loss Factor (η_{sys}) and Resonance Frequency (f_r) – Specimen 12 (thick)

It is clear that for the system loss coefficient, a compound interaction of the coating with beam is occurring, and it is known that the Ti-6Al-4V metallic region of the coated beam changes with temperature as well, radically so, somewhere above 600degF. The system-level damping of the 8-YSZ coated beams are about 4X to 10X that of the bare beams when temperature ranges from 70-600degF (where $\eta_{bare} \sim 0.00025$), while at 900degF (where $\eta_{bare} \sim 0.0015$) this drops radically to around 1X that of the bare beam.

It is noted that these system-level plots trends are similar to those reported by Gregori for a dual layer 7-YSZ coated cantilever beams within an air-filled furnace. Figure 20 (Section 1.4) shows a damping peak for his beams at about 220degC (428degF) which is reasonably close to the peaks on the plots in this chapter. The curve damping curve in Figure 20 does not climb again to the right of the peak as these plots do, but the metallic substrate for this author's beams were nickel based super-alloys which are stable to very high temperatures for metallic solids.

It is already clear that the 8-YSZ TBC can provide enhanced damping for blades, especially in intermediate stages of the compressor where the Ti-6Al-4V blades encounter the temperatures that are associated with the peaks of these curves. The outermost stages also benefit from an enhanced loss factor from the thin coating as well, though not as pronounced. In the innermost, high-pressure stages of the compressor, the system level benefit is decreased and indeed almost of dubious value. This is probably not due to a failure of the 8-YSZ coating but rather to the fact that as the titanium reaches its service temperature limit (due to creep issues) it features radically enhanced damping and this itself serves to suppress HCF.

5.6.1. Coating Specific Loss-Factor and Storage Moduli

When obtaining the coated beam response during the ring-down free-decay runs, recording of the stimulation and response signals was performed at 2000Hz. These values were stored for later processing to characterize the coatings from moment to moment in the course of the free-decay where there is a continuous decline in the strain amplitude. The LabView VI streamed this data to disk for post processing in Matlab where combining it with the FEA model assumed field variables using the method covered in Section 4.5.2 allowed coating modulus determination.

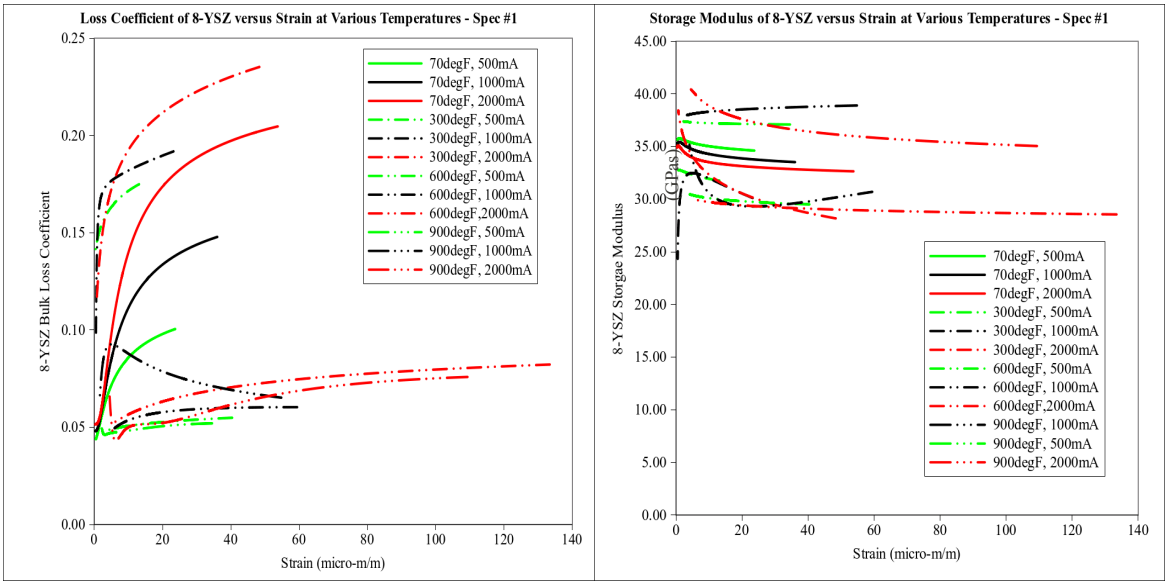


Figure 134: Complex Modulus; Loss Coefficient η_c and Storage Modulus E_c – Specimen 01

Figure 134 shows the results for specimen 01, the loss factor as a function of the bending strain field in the coating is plotted on the left while the storage modulus as a function of the bending strain is on the right. It is immediately apparent that the coating is nonlinear in regards to damping with the strain, but only weakly so for storage modulus. The solid lines, which denote the room temperature tests, indicate that the damping is enhanced as the magnitude of the forcing function is increased. The topology of the loss coefficient curves is very similar to those obtained by Reed for free-decay of Mag Spinel (Figure 15, Section 1.4). The values for the room temperature are close to those obtained by Pearson (Figure 16, Section 1.4) for 8-YSZ by means of forced response for the low bound estimates, although the current studies values are higher at higher strain levels. The low level strains at 70degF approach a value of η_c of about 0.04. The storage modulus curves however are much less pronounced in non-linearity compared to Reed's mag spinel findings, however the 70degF (solid lines) E_c curves on the right of Figure are

close in shape magnitude in the low range of strain to the 8-YSZ results obtained by means of forced response by Pearson (Figure 16, Section 1.4).

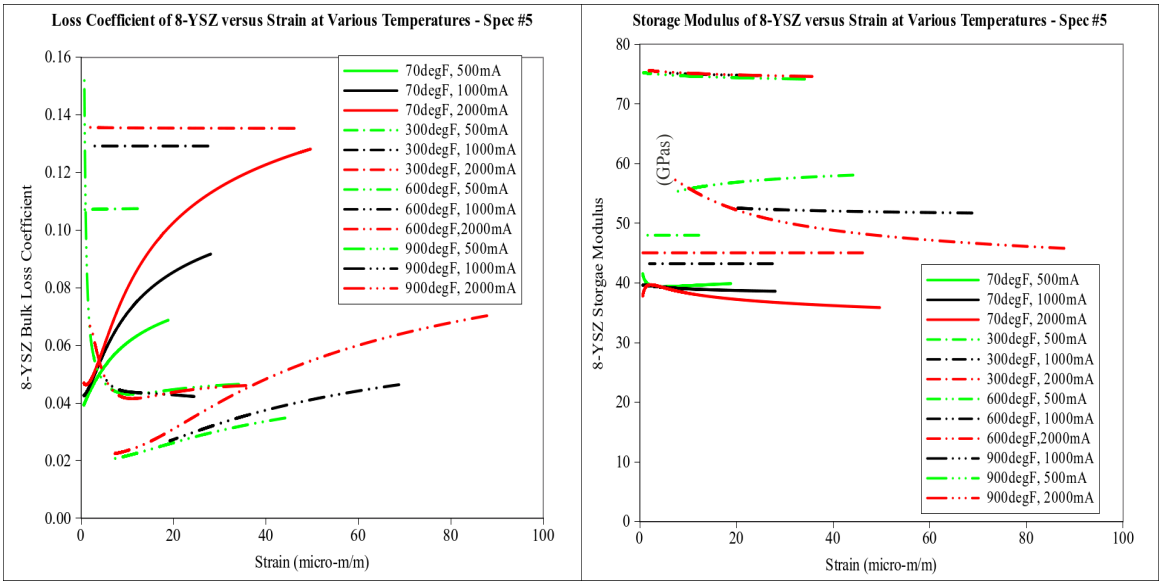


Figure 135: Complex Modulus; Loss Coefficient η_c and Storage Modulus E_c– Specimen 05

Pearson's storage modulus curves for 8-YSZ have a weak rise in value at very low strains but are near constant throughout the range of ε_{11} tested. As the temperature climbs to 300degF most of the specimens see a mild enhancement in the coating's loss factor, which then proceeds to drop as the temperature continues towards 600 and 900degF. There is a wide variation in behavior among the specimens, it is suspected that much tighter control over the APS application process is needed to control the underlying micro-structure in the coating. Nonetheless, the qualitative trends hold among the specimens.

The storage modulus seemed to have a very weak non-linearity with the strain-magnitude, but did vary quite strongly with temperature. For the room temperature tests, the E_c ranged from about 25 to 40Gpa, most of the variation was between specimens, but

intra-sample variation across excitation amplitude and strain were small. As the temperatures changes there were significant changes in magnitude, but the curves still remained close to constant in the course of a ring-down decay.

The three 8.3mil thick coated specimens exhibited a marked increase in the coatings' apparent stiffness as the temperature increased. Care should be taken in interpreting these results as the coating is part of a composite structure, where there is

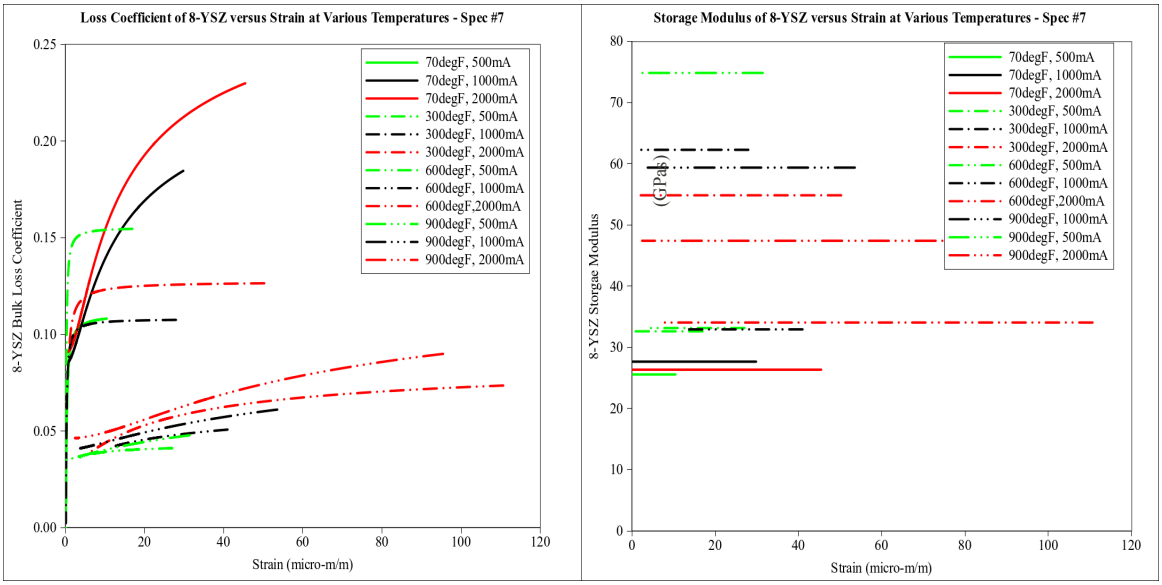


Figure 136: Complex Modulus; Loss Coefficient η_c and Storage Modulus E_c– Specimen 07

differential expansion occurring. Based

on the thermal stress modeling performed in Chapter 2 and the fact the coating is expanding faster than the titanium substrate, it could be hypothesized that a compressional stress field in the coating occurs as the system is heated, and therefore might be forcing closed voids and cracks in the TBC coating layer as it is further heated and driving up the apparent stiffness of the coating layer. The material itself may not necessarily be changing, in terms of its inherent properties in a homogeneous state

sampled on a level smaller than the inhomogeneities of the cracks, splats, and voids.

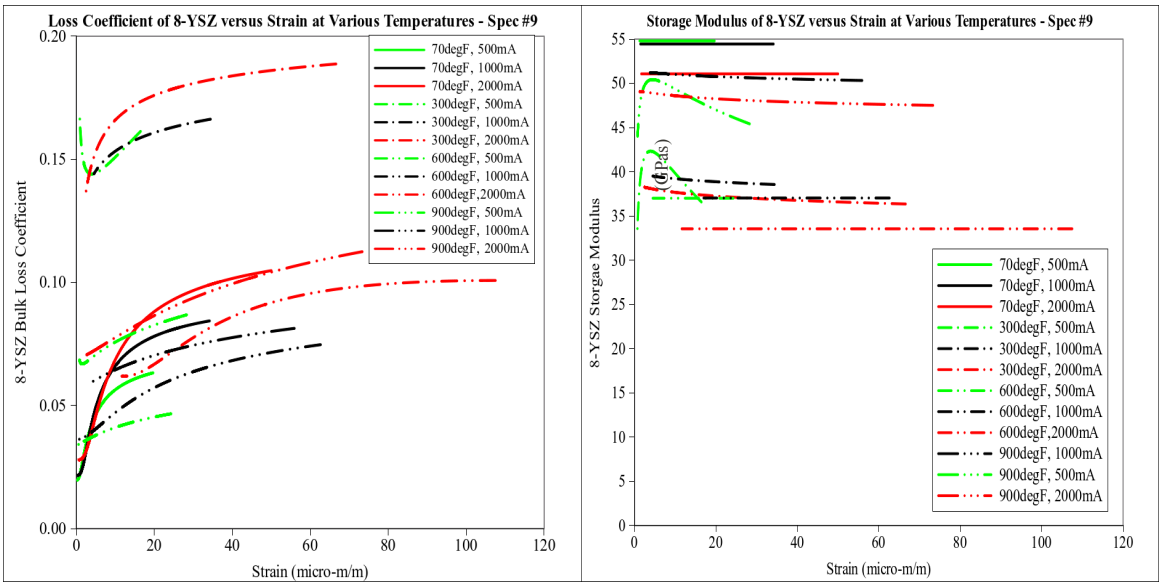


Figure 137: Complex Modulus; Loss Coefficient η_c and Storage Modulus E_c– Specimen 09 (thin)

Another thing to bear in mind is that these values of E_c and η_c may well be orientation-specific values for the -11, and -22 directions that are perpendicular to the incoming APS spray jets. Bending mode-I on the thin beam results in strains that are parallel to the long axis of the beam.

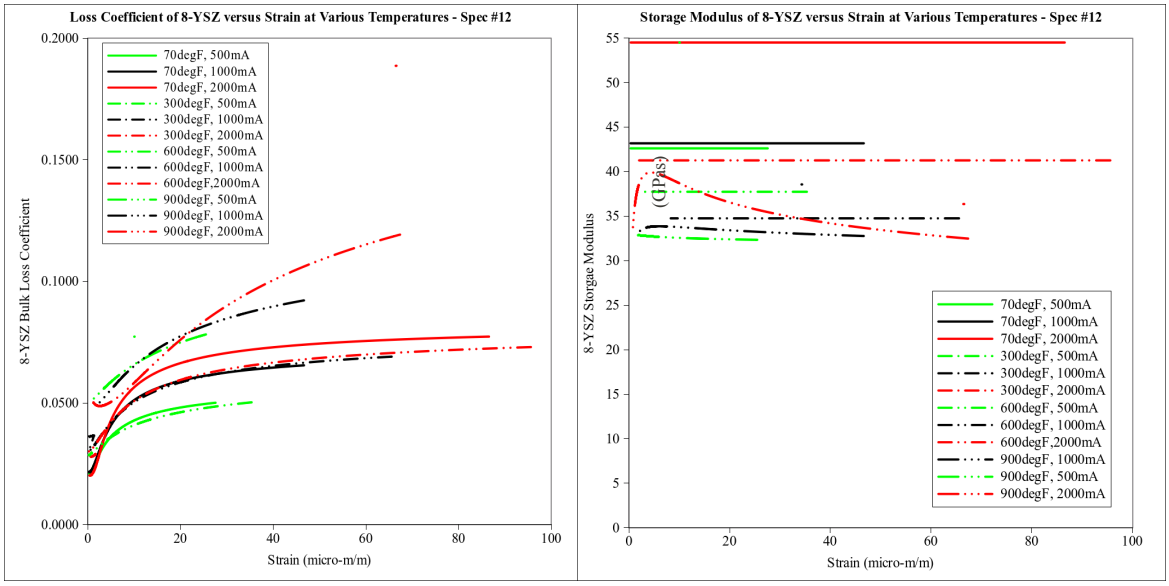


Figure 138: Complex Modulus; Loss Coefficient η_c and Storage Modulus E_c– Specimen 12 (thick)

The loss coefficient is moderately non-linear with the strain field variations whereas the coating modulus is weakly non-linear to constant with the strain field variations. The phase function, Φ(t), is a straight line with near constant slope throughout free-decay

From a designer's perspective it would be worthy to extract some low order values to use in esign. The first would be that there appears to be a floor value for the loss factor of about 0.02 that is applicate across all strain levels, temperatures and amplitudes; this low bound value is quite high for a non-rubber material. One level up in refinement is to address the strain dependence in a step-function form:

$$\eta_c = \begin{cases} 0.02 & ; \quad 0 \le \epsilon_{11} < 20\,\mu\epsilon \\ 0.04 & ; \quad 20 \le \epsilon_{11} < 100\,\mu\epsilon \\ 0.05 & ; \quad 100 \le \epsilon_{11}\,\mu\epsilon \end{cases} \tag{127}$$

or a logarithm lower boundary form:

$$\eta_c = 0.00621 \ln(\epsilon_{11}) + 0.021 \quad ; \quad \epsilon_{11} in\,\mu\epsilon \tag{128}$$

All of these would be be very conservative lower bound estimates, but still offer a great

improvement in damping over the bare system. Refinement of these could be approached by either testing a statistical population of samples and working with the lower population bounds to set the design damping versus strain curves, and/or, tightly control the APS application process onto the beams to try to get a consistent micro-structural from within and across speciemens.

5.7. Scanning DVL Study

The marriage of the modal FEA model to the experiment assumes faith that the experiment is achieving a clean bending mode-I shape. To verify if this is the case a 2-D scanning laser, the Polytec PSV-400, was setup and aimed at the beam through the borosilicate glass window from about 2m away. A bare and a coated beam were suspended in the chamber and were driven at their resonance frequencies at 1000mV$_{p-p}$ stimulation and maintained in a steady harmonic state.

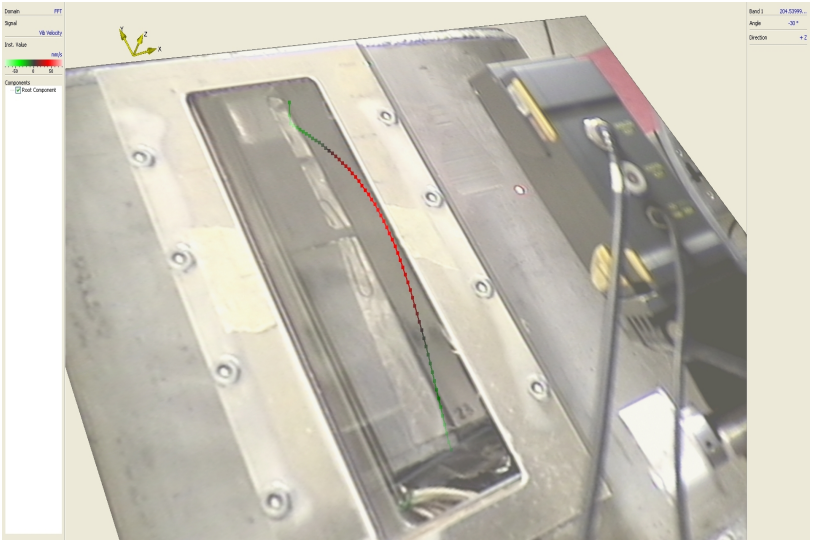


Figure 139: DVL Scan of Bare Beam, Specimen #23, 70degF

One finding was that beam #18, a bare beam equipped with multiple localized

mica tape dots affixed down the centerline of the beam with the Durabond 952 epoxy, had significant localized impact on the mode-shape with a scalloping shape in the eigenvector coinciding with each reflector dot. This also drove an additional test of the beam without the mica dots in the ANOVA sensitivity study (Section 3.9); the dots and the high temperature epoxy added significant damping to the bare beam. This 1-D array of dots was done to allow multiple point capture of the v(t) data using the single-axis DVL. The clean mode shape in Figure 139 was obtained only after cleanup of the mica dots and their replacement with 3M tape. The dogleg at the top of the beam is due to problems with internal reflection of the DVL beam within the borosilicate glass at the more extreme angles of incidence art the upper tip of the beam. Using a stroboscope set to the harmonic frequency of the beam the lack of this artifact on the specimen was confirmed.

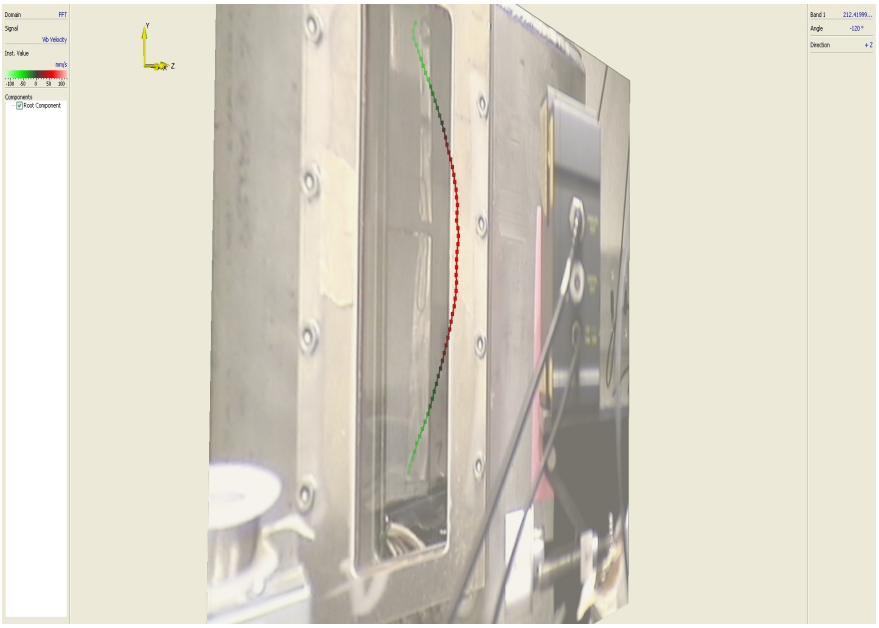


Figure 140: DVL Scan of Coated Beam, Specimen #7, 70degF

Figure 140 is the measurement of a coated beam.

These points were taken for a few sets, two illustrative sets of DVL measured points are shown plotted for one-half of the beam in Figure 141. These two beams were a sparsely measured bare beam on the left-side of the Figure and a more densely measured coated beam on the right. The solid lines are assumed modal functions that were normalized and extracted out of the FEA analysis of the bare and coated beams, respectively. Scaling and vertical offset was applied to the normalized curvature functions to minimize the sum of least squares fit to the DVL data. As can be seen the fits can be discerned. The bare beam FEA curve is very close to the classical analytical solution. For the coated beam one can see that there is a flattened region up to the coating-to-bare beam junction (indicated by the dot), it is hard to see in the dimensional coordinates as the difference is small, but when scaled up in normalized coordinates it becomes very clear. Both of these specimens were measured at 70degF in a the low vacuum (~0.01atm).

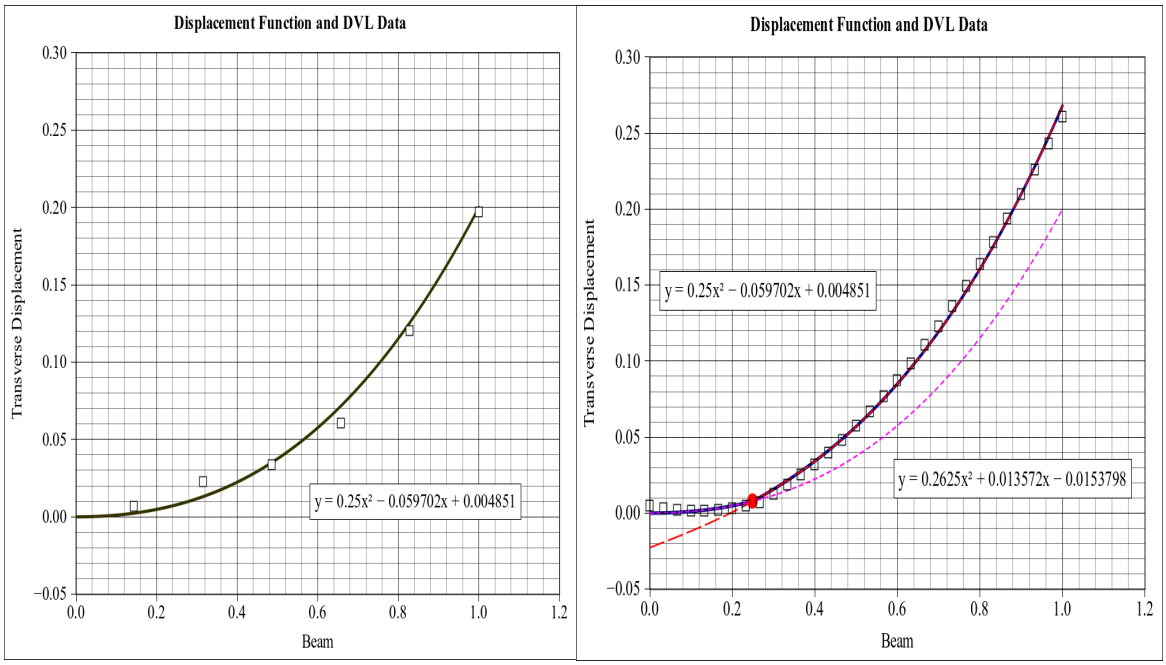


Figure 141: DVL Data Plotted Over Assumed Mode Curves for ½ Beam; (left) Bare, (right), Coated

Although these two figures are very good, it should be mentioned that obtaining sets of data that are well described by the FEA/analytical mode shape is not easy, perhaps 1 in 3 sets of data comes out like these. Internal reflection in the window, proper use of the filtering settings, removal of rigid body motion as the scanning laser traverses, may introduced errors into the scanning data. Nonetheless, the sets that do fit well to the data, plus careful observation of the beams when frozen under a matched frequency strobe light lend credence to the use of the FEA (or analytical models) to assume the field data. The scanning DVL also triggered the discovery that the mica dots and adhesive could influence the bare beam mode shape (and damp it as well) in a significant fashion as seen with a scalloping shape where the cusps matched the location of the mica dots on bare Specimen #18.

This scanning DVL work was important to establish that the eigenvector shape simulated in the numerical codes was obtained in the experiment. Strain gages adhered onto the beam are not very tenable without inducing significant damping from the wires, as well as the gauge and adhesive itself. A micro-sized gage may help along with careful routing of the wires but still significant damping is to be expected, especially on a bare beam.

5.8. FRF Studies

Some characterization studies of the three coated beams and chamber were run using the forced response technique to build frequency response functions (FRF's). Details of the technique are in Appendix 10. The physical apparatus was little changed except for the substitution of the Vibration View computer DAQ hardware and software system for the National Instruments/Labview computer.

The FRFs were used to assess the effect of shielding layers on the free-free beam system, specifically the interaction between the coil and the ALNICO magnets, the height of the beam on the system amplitude response, and the effect of temperature on one beam.

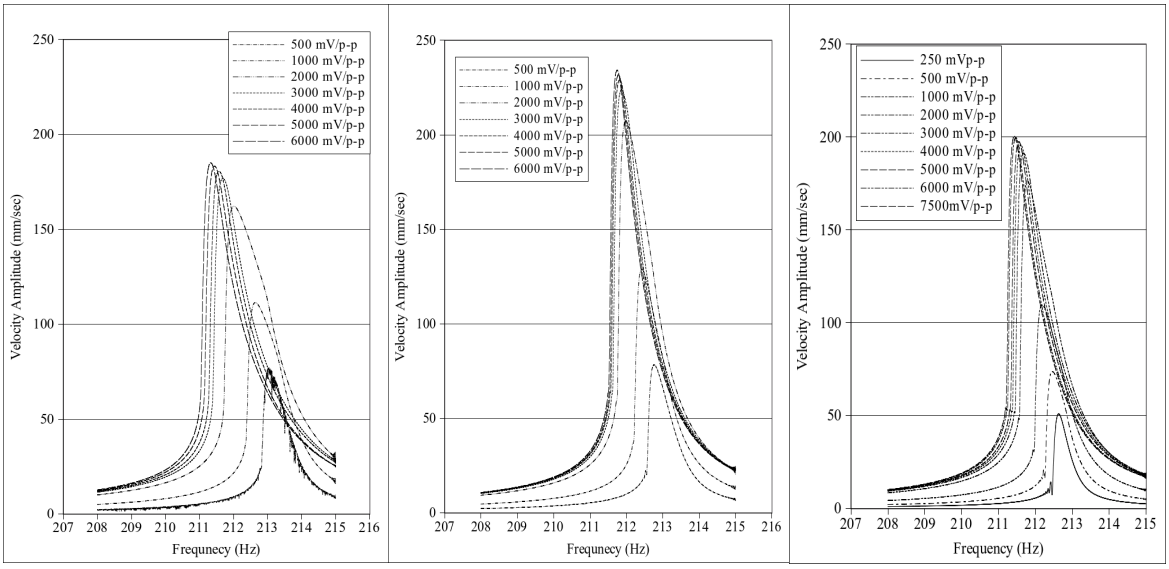


Figure 142: Beam Specimen #1 (left), 5 (ctr), and 7 (right) FRF Sweeps

The three 8.3 mil coated specimens (Spec. #01,05,07) where swept at the same set of amplitudes as the free-decay set at room temperature. The recovered FRF curves all were down-swept, in order to capture the resonance peak. Figure 142 is a plot of the FRF's for the three specimens. Despite the non-linear nature of the plots, the amplitudes of the curves generated by the ALNICO magnets were low enough that the peaks were more symmetric than the previous studies and the ½ power bandwidth method recovered loss factors that were in fairly good agreement with those obtained by free-decay (Figure 147, Section 5.8.1). Judging from the succession of peak heights at the higher amplitudes, the system damping rises in the order from 05 → 07 → 01. This trend is corroborated by the values obtained in Figures 130 to 131. The jump phenomenon can be seen by the sudden vertical drop on the low frequency side of the FRF peak.

5.8.1. FRF Sensitivity Studies

The FRF technique was used to assess some changes to the chamber's configuration. The first was to assess what influence the triple layer foil shielding had on the magnetic field coupling between the electromagnet below the foil layers and the eight ALNICO magnets of the beam above. The system was run with a coated specimen mounted in the chamber, with the top pressure jar off. The excitation amplitude for the chirp signal was 2000mV$_{p\text{-}p}$ (7.32A$_{p\text{-}p}$) with a down swept sweep rate of 2.0 Hz/min. After each sweep was completed one layer of foil was pulled and the test was repeated, including a final FRF with no foil.

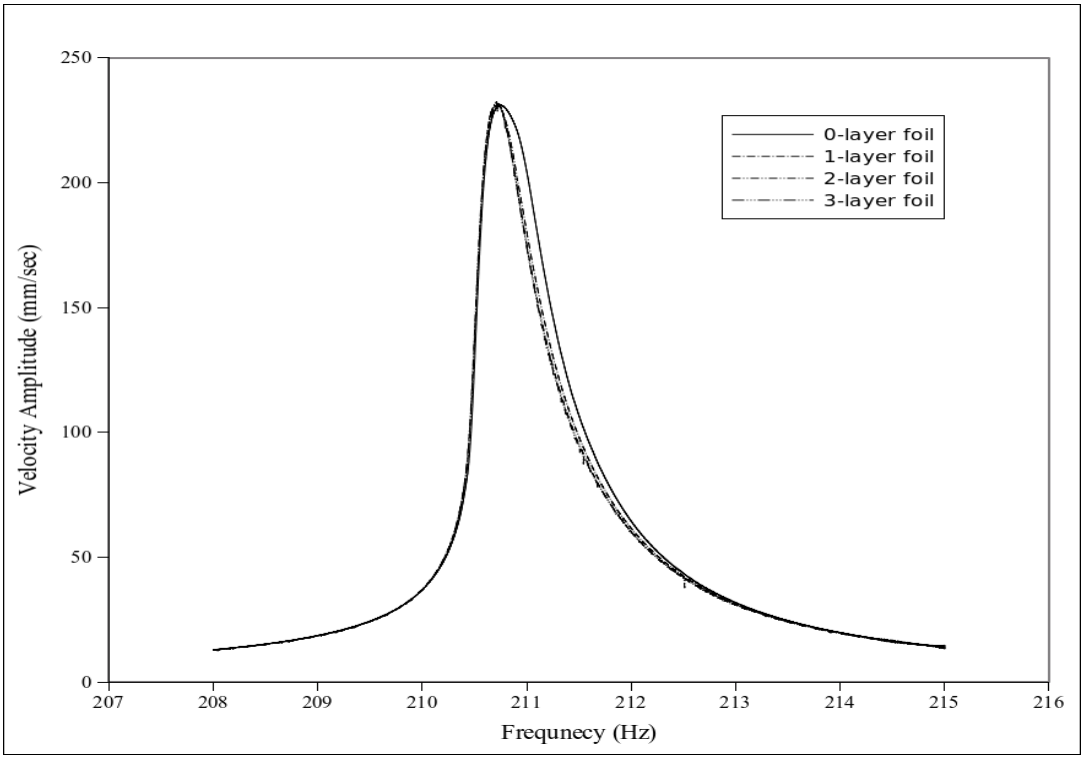


Figure 143: FRF Sweeps 2000mA with Varying Shielding Thicknesses.

As can be seen from Figure 143, the only thing that really was significant was whether any foil was present. The presence of the foil had not effect on the strength of the

coupling moment as the resonance peak height remained the same across all the trials, but the presence of foil did cause a reduction in the system damping. One hypothesis is the metallic layers perhaps had induced weak eddy currents within them from the coil field and shunted some of the field when the beam displacement and coil current were somewhat out of phase, this reducing the magnetic braking effect.

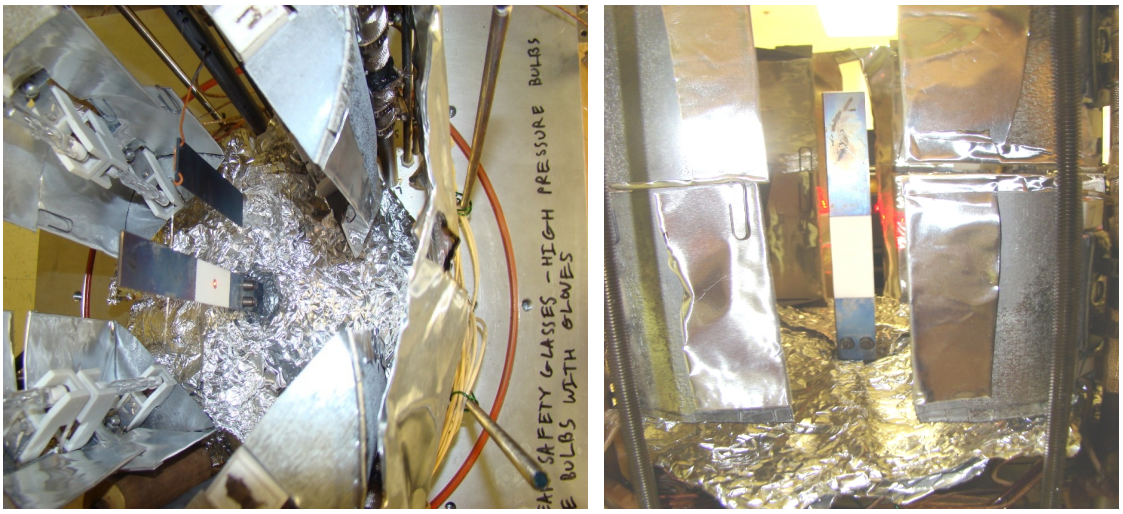


Figure 144: Low-Hanging Beam in Foil Cup

The second FRF based study was to ascertain how beam position w.r.t. the coil could be reduced to improve the magnetic coupling moment. Figure 144 shows the chamber modified to attempt this. The triple layer foil shielding was formed into a cup that lined the inner bore of the electromagnet, keeping the high reflectance shielding surrounding the beam as it was successively lowered into the magnet bore. A set of 2000m$V_{p\text{-}p}$ down-swept forced response curves were captured with the beam at 2.05, 1.125, and 0.175inches above the end plane of the magnet, as measured for the centroid of the ALNICO magnet set. Figure 145 displays the results of this series of FRFs.

Though no quantitative comparison was performed, the curves maintain a similar aspect ratio to each other which indicates that the system damping values are close in value. The frequency peaks do shift, but this is to be expected as the real excitation magnitude is increased as the beam is successively lowered while the coil current is kept constant. It seems that this will yield a much higher strain range than the magnets in their current position but there are concerns to be addressed. One, the clearances are very tight as can be seen by the noise in the data of the highest FRF caused by rigid body motion in the beam after the jump causing the beam to brush the shielding. Two, the validation to make sure the beam stays isothermal has to be repeated.

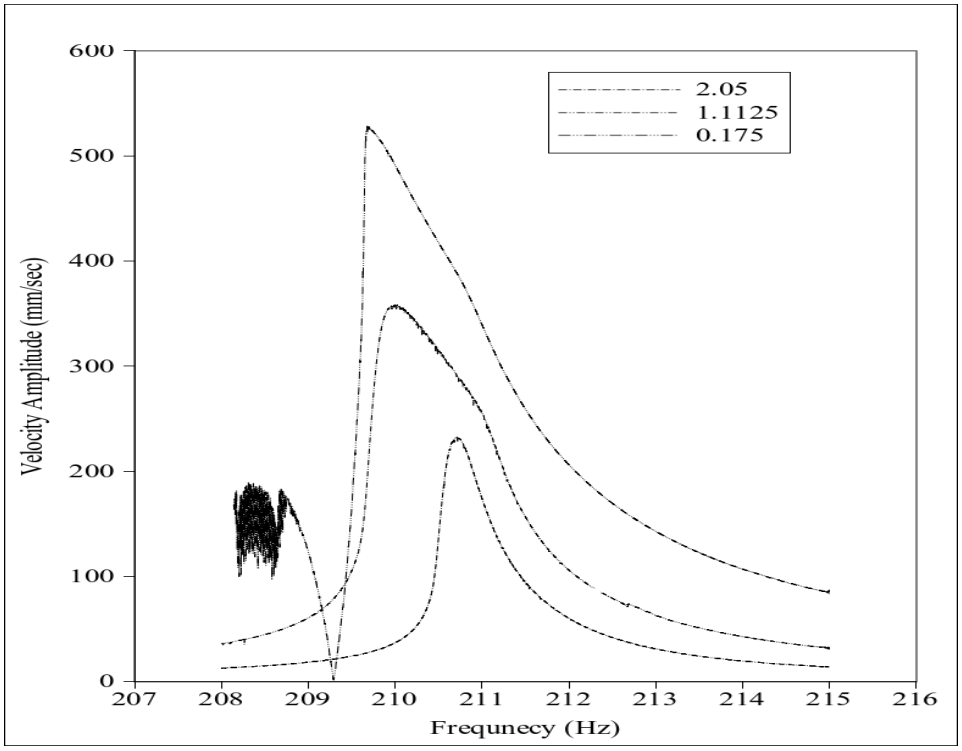


Figure 145: FRF Sweeps at Various Beam to Electromagnet Distances

The next quick study was to assess the variation of the FRF peaks on one coated specimen with temperature changes. This specimen was down-swept at 2000mVp-p at

2.0Hz/min. The sweeps were conducted at 70, 200, 300, 400, 500, 600, 700, 800, and 900degF. Figure 146 shows the FRF results. The FRF peaks are separated by frequency distances (abscissa) that are fairly regular, like the temperature intervals. What is interesting is the loss factor goes down slightly from 70 up to 200degF and the goes up to a maximum at 300degF as shown by the suppression of the peak amplitude. It then drops again as the peaks get taller towards 600degF and then climbs again, probably as the Ti-6Al-4V beam begins to increase its damping above 600degF. This plot indicates in a clear way that a phenomenological model the coatings behavior will be a function of temperature and strain field, but it will not necessarily be monotonic in temperature.

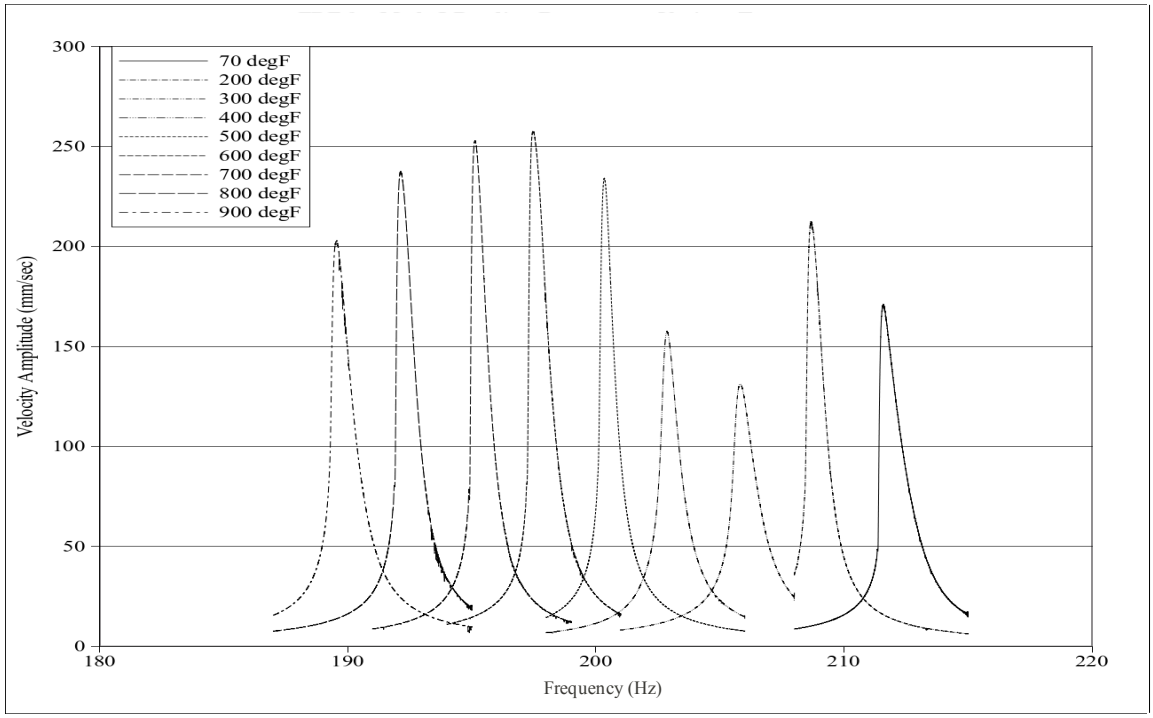


Figure 146: FRF Sweeps at Various Temperatures, 2000mV Stimulation.

The FRF's of the three beams at room temperature did have their loss factors extracted by the ½ power bandwidth method to allow comparison to the loss factors

obtained by free-decay. These η_{sys} values for these three specimens at 2000mVp-p are plotted in Figure 147 to allow a comparison. It seems that, save for an out-lier value at 300degF for the free-decay at 300degF that the two methods are reasonably close, bearing Lazan's observation quoted in Chapter 1 in mind.

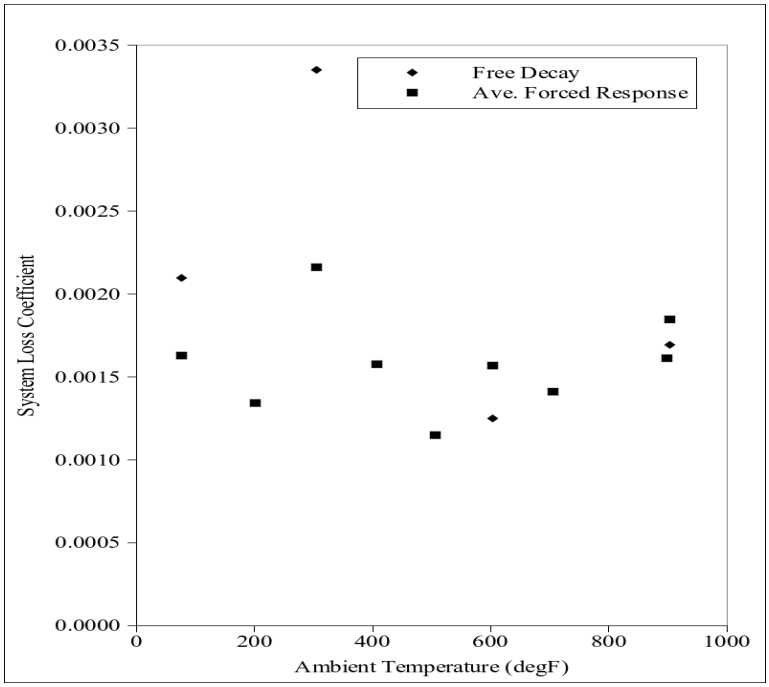


Figure 147: Free-decay versus FRF based System Loss Factors

This section is closed with one more plot that illustrate the relationship of the temperature dependence of the coatings bulk loss factors. Figure 148 is a plot of the damping for the specimens taken at the 20 and 40 micro-strain levels from the free-decay derived plots of damping as a function of strain; this plot emphasizes the temperature dependence of the damping. It appears that the coatings have a bulk damping maximum somewhere in the vicinity of 300degF. It is interesting to note that this may be near the processing temperature of the titanium beam when the APS coating is applied and further it is near where the minimum damping of the titanium was observed. It is noted though

the titanium damping minimum was observed on bare beam specimens and so it not related to coating-beam interaction. It also appears from this figure that the bulk damping is only weakly dependent on the coating thickness, being that this is the material bulk data, this would be an outcome that would be expected.

The spread in the data sets between specimens, while having decent range with strain and intra-trial repeatability, indicates that processing control of the APS process is necessarily to avoid testing whole populations of beams and taking the lowest bound of the set as the damping design line/curve.

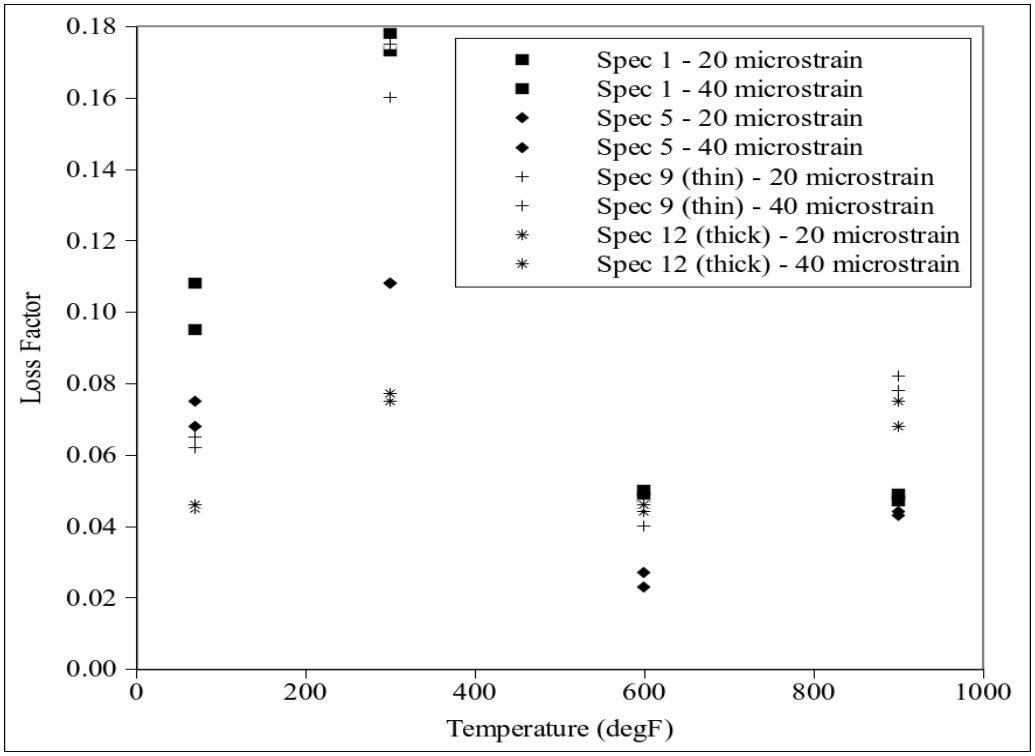


Figure 148: Coating Bulk Loss Factors for Various Temperatures (500mVp-p excitation)

6. Conclusions and Recommendations

The testing accomplished the major objectives. The first was adaptation of the free-free apparatus to higher temperature testing of coated and bare specimens that were isothermal but elevated above room temperature up to what is typical in modern high bypass compressors, 900degF. The second main objective was utilizing the rig to mechanically characterize 8-YSZ, a typical TBC that has potentially useful mechanical characteristics at these temperatures. This was done at a beam-TBC system level, as well as at a coating bulk material-specific property level, namely complex modulus. The general values achieved for the coated beam system agree trend well when previous studies at the system and coating specific level are taken into account. However, there remains a lot of variance in the data between the individual specimens and refinement of both the testing process and the fabrication specifications is something to consider investigating further.

6.1. Chamber Findings

The chamber did meet its basic functional objective. It heated a free-free beam in ma isothermal fashion within a high Stark number environment. It allowed for non-contact excitation and measurement of the response. The chamber was more successful at mechanical characterization of low damping materials, like the bare beam, than was expected, but it did fail to characterize the non-linear coating across as much of a range of strain as was done in the past. This is somewhat mitigated by the fact the high cycle

fatigue in the cold section of turbo-machinery tends to also be low amplitude in nature. There may be some remedies to this that will be covered under recommendations.

Some aspects of the chamber worked well, these include:

· The EDM hole reduced the damping of the free-free system significantly. It was thought that the effect would be very small as the eccentricity of the line from the center axis is so small, but it was a major source of energy loss. The beam also reliably self-aligned on wire, when excited, it sought the center of the wire and remained there.

· Heating by halogen lamps was effective, quartz halogen bulbs survive operation in vacuum with no apparent problem, the original bulbs made it through all the testing. Near uniform irradiation seemed to occur in conjunction with the reflective enclosure and parabolic reflectors. Based on sensitivity testing with the FEA radiation model and the experimental rig, exact focusing was not critical.

· 3-layer foil radiant shielding is highly effective. Objects inside the inner layer, but out of the direct radiation in the cavity, heated to over 750degF on their surfaces, while those 0.5in away outside the outermost layer exhibited from 150-200degF in temperature.

· The temperature settings in open-loop mode were repeatable (excepting the depressed AC line voltage condition suspected from heavy AC power usage in middle of hot days), so the dummy specimen for closed loop monitoring is accurate to within ±5degF, otherwise without it, the accuracy is about ±10degF assuming a good mains supply voltage to the lamps.

· The chamber was not entirely successful in capturing the full range of strains anticipated to characterize the non-linear TBC material, but characterizing the lower values does give a conservative low-bound estimate for employment in designs incorporating HCF suppression. The combination of weaker magnets and a larger beam-to-coil separation distance causes this.

· The chamber was verified to work with a bare beam up to 1050degF which was the volt-amp capacity limit of the lamp power supplies, or rather the protection fusing sized for them. The ALNICO magnets it was found can be used for excitation up to at least 1050degF, though this may be beyond the working temperature limit for some grades of ALNICO.

· The chamber can determine the complex modulus of classical engineering materials in a repeatable fashion and is very good at discriminating small changes in modulus in the material. Unlike trying to determine a minor difference in a stress-strain slope from a uniaxial tension test, very small shifts in modulus were readily apparent. This holds true across the temperature range tested. The drawback is that the strain ranges are limited, many different excitation amplitudes need to be imposed in to obtain the behavior across varying levels of strain. This repeatability held up through re-mounting of specimens and thermal cycling, which was surprising given how sensitive the chamber was.

6.2. Coating Study

The study of the coatings was accomplished and the results are consistent with the previous studies in this area. Nonetheless the procedure needs refinement. The main

conclusions are broken down by the type of free-free specimen tested, which were the bare, bond coat only, and fully coated beams.

6.2.1. Bare Beam

The bare beam acted as a linear system. All three had vertical and symmetrical FRF response (or "backbone") curves, featured f_r and η_{sys} that were invariant of the excitation amplitude, and demonstrated scalability and additivity of the output repose to the input forcing function. The bare beams appear to have no significant viscoelastic effects or plasticity up to 900degF. The ring-down envelope magnitude is very well fitted by a classic exponential decay function.

· There is a large variation in the internal bare beam damping across the specimen set tested. One specimen's damping was much lower then the median of the other three tested (about 0.5X); a definitive cause for this was not determined. It is a possible conjecture that it may come from the edge region of the rolled sheet that the specimens were cut from. The thermal cycling of the specimens to 900degF and back do not appear to induce any permanent changes in the beams mechanical modulus or damping, despite the heavily oxidized appearance of the beam after the first cycle of heat exposure. The values obtained for resonance frequency and damping were very repeatable across multiple trials and setups for each specimen.

· The chamber's damping is so low as a result of the design changes made to harden it to high temperature that it is very effective at characterizing low damping materials for storage modulus and loss factor. This may be potentially its most useful application. The

chamber achieved Q-factors in excess of 22,500 at certain combinations of temperature, specimen, and excitation amplitude. Among the configuration changes critical to driving the damping of the boundary conditions so low were: removal of the lower constraint wire pair, elimination of the eccentricity in the passive node by routing the suspension line through a hole bored through the neutral axis, use of a stiffer metallic wire for the suspension, using a weight to pre-tension the wire, minimizing the amount of reflector dot adhesive, and tight clamping of the magnets to the beam.

· The free-free system is so sensitive it can easily discriminate between bare Ti-6Al-4V specimens based on rolling orientation. The tuned resonator can very easily detect small changes in elastic modulus. That being said, the free-free rig does not test into the failure regions and much be tuned at various amplitudes to capture behavior over a wide range of strain.

· Care paid to the orientation of the specimens with regard to the parent sheet stock in previous studies was warranted, it is clear from orientation imaging microscopy studies that the crystalline structure of α-phase dominated Ti-6Al-4V is orthotropic in nature for elastic modulus. Future modeling efforts for plates and blades comprised of Ti-6Al-4V probably should use such a material model for Young's Modulus.

6.2.2. Bond Coat Only Test

The bond coat only specimen behaves as a linear system. When tested this beam had a vertical backbone curve, featured an f_r and η_{sys} that were invariant of the excitation amplitude, and the system demonstrated scalability and additivity, just like the bare

specimens.

· Damping contribution of the bond coat layer is quite small, close to the population average of the bare beams. A very slight shift in the slope of the resonance frequency versus temperature line occurred, probably due to slight added mass of bond coat material. As a result Deleon and Pearson's assumption regarding the bond coat layer in their FEA modeling is an appropriate simplification. It is suspected that the discontinuous nature of the bond coating prevents it from adding much effective bending stiffness into the system due to lack of a homogeneous layer to allow shear flow and its relative mass contribution is very small, compared to the beam, hence the results are very close the those of the bare beams.

6.2.3. TBC Coated Beam Study

The coated beams were non-linear in their behavior. The specimens all featured a strain softening backbone curve, leaning towards the lower frequency range as stimulation amplitude increased. Ironically, the times series decay signals did not exhibit dramatic dry friction type decay curves. Despite a dramatic increase of the damping of the coated system over that of the bare beam, the coated beam system was very well described by a linear, viscously-damped decay model for the ring-down envelope function. Some key findings include:

· Aging is important to reduce and control for damage accumulation (or history) effects. The protocol developed by Pearson in a modified form (the modification being to dwell at a controlled output amplitude) worked well with 8-YSZ. Only about 1-1.5M cycles

was needed to effectively remove the change in properties. The bulk of changes where the stiffness (storage modulus) softened and the damping enhanced was within the first 100K cycles of dwell loading.

· Aging in at each temperature does not appear to be necessary when characterizing 8YSZ,n except for a short break in period that might have to do more with ridding the passive node suspension wire of slack and compliance. Thermal cycling probably adds damage, but the accumulation of it is so much slower as thermal cycles are very few in number relative to dynamic loading cycles.

· Even with the weak magnet-to-coil coupling due to adoption of ALNICO magnets, the coated beams exhibited classic strain softening behavior as found per: the tuned in resonance peaks decreased in frequency as the excitation amplitude was increased, when sweeping up- or down for the FRF the amplitude "jump" phenomenon was encountered, and the scalability of the response output was not evident.

· The ring down envelope functions of the coated beams, despite being from a non-linear system, are nonetheless well described by a classic exponential decay function (regression R^2 values of 0.98 to 0.99 were obtained on coated beams). Despite all the focus given to various forms of damping systems, including the dry friction (Columbic) one, during the testing of all the samples, even the 12.5mil thick coated specimen exhibited a classic viscous damping envelope. Ironically, the only way a classic friction damping form (with a clear linear decay envelope) was manifested in the coated specimens when the magnets chattered due to loose mounting screws, clearly an

anomalous state.

· Bending mode-I works well for mechanical characterization as it has large amplitude for moderate couple-moment input, it has a nearly constant strain magnitude in the center region of the beam, and had clearly identifiable anti-nodes that do not shift in any significant fashion with the addition of the coating or its changes in properties as the temperature changes.

· The storage modulus, E_c, seems to be fairly constant as the strain field and excitation amplitudes are varied. This is consistent with Pearson's findings for 8-YSZ. The storage modulus is affected by temperature and it stiffens as the temperature increases. Whether this is due to a change in the micro-structure as a result of thermal stresses setup in the inhomogeneous, composite system or inherent to the 8-YSZ material is not clear. Like Pearson found, the non-linearity of the coatings loss factor is stronger than for the storage modulus across the strain ranges tested. Both the damping and well as the resonance frequency, at the system level, as well as the complex modulus for both components change strongly with temperature. This is rather unexpected for a ceramic class material. It suggests that further study of the thermal stress and micro-structural interaction between the TBC and substrate is needed.

6.3. Recommendations

For future work some lessons learned from the work are detailed, broken down between the chamber and the coating characterization studies.

6.3.1. Chamber

The chamber is effective for vibrational studies and achieved very high Q-factors up to 22,500 with the bare beams. It exposed the materially non-linear nature of the 8-YSZ coating. Nonetheless, many refinements and improvements to the rig and procedures can be made.

· Use samarium cobalt magnets and/or a localized radiation shield for neodymium iron boron magnets to drive the beam system to higher strains, or alternatively, lower the beam into the coil throat and/or use the longer ALNICO magnets to drive the system to higher strain ranges. This could be done by fashioning a reflective foil cup to line the magnet bore and lower the beam to free hang with the magnets within in the bore of the magnet. The lower wire pair has been deemed a high damping source as well. The high Stark number of the chamber will likely preserve isothermality, though thermal validation using the analytical or numerical models should probably be performed. Up to 30-40% of Reed's nonlinear strain range (as opposed to 10-20% in this study) could be recovered with ANICO magnets of mass similar to the NdFeB set used by Reed and Pearson. More wire turns could be added to the coil to increase its field strength as well.

· To successfully scan the whole beam with a 2-D DVL, consider reducing the specimen size by 30%, or scale the chamber up slightly to allow imaging through the window without internal reflection in the glass or off of the shielding around the beam. An ancillary benefit of a slightly smaller specimen and/or enlarged chamber slightly would be the easier avoidance of the specimen contacting the shielding which results in

localized cooling and damping of specimen.

· Use mechanical clips, preferably non-ferrous, to attach thermocouples to the dummy specimen. Copper alligator clips worked well, steel paper-clips work as well but they can shunt the magnetic field if too close to the coil.

· Consider replacing the mica tape with the dye penetrant developer or the 3M retro-reflective polymeric tape; if used in vacuum the latter pyrolyzes around 700degF but the inorganic reflective matter seemed to remain and continued to enhance the DVL return up to higher temps of 900-1050degF. Interestingly, it has been observed to not survive in air for very long at these temperatures. Mica tape causes spikes in the return signal of the DVL and the high temperature epoxy used to adhere it can add a marked amount of damping to the bare beam and other low damped specimens.

· Add high thermal contact resistance washers (fiberfrax) between the lamp and beam support rods and the base slab to reduce a major conductive heat loss path in the chamber, that down the lamp and beam suspension rods.

· Procedurally speaking, adding a channel(s) for the thermocouple monitoring to the LabView data acquisition system would be useful to keep a temperature record. Manually recording the temperatures in a book against the clock worked fine for steady state testing, but if any transient thermal states are desired for testing conditions automatic logging of temperatures would be highly desirable.

· Find a safer alternative to masking tape for insulating the lamp power splices. Some type of compact high temperature electrical connectors would make the chamber

procedurally simpler and safer to use.

6.3.2. Coated Beam Study

In the course of this study a decent set of basic results was obtained, nonetheless much improvement in the technique is possible. Most of the difficulties that were encountered in the course of running the experiments were unforeseen. The extreme sensitivity of the chamber, due to a large reduction in damping from the baseline setup that it was derived from, was unexpected and caused many difficulties with the bare beam, which in of itself was to anticipated to be a quantity that would be readily obtained to use in the Torvik equation, before testing the TBC coated ones. Instead, the extreme low damping of the chamber prompted a sensitivity study of it to determine what factors actually drove the damping of the beam system so low. And a further exploration of the bare Ti-6Al-4V beams was performed as inter-sample variations now could easily be picked up, including rolling orientation dependence of the Young's modulus. Specific improvements include:

· Use a precision external frequency source with future efforts, the tuning resolution demanded by the system with Q > 20,000 is very high, avoiding overshoot of the resonance frequency peak required tuning in a significant figure of 0.00X to 0.000X Hz. The FRF curves are very narrow with very steep slopes around the resonance points. Since the NI-DAQ board lacked the fine frequency generation resolution needed for such Q-factors, it is best to modify the Labview code to allow excitation by and trigger off of an external source, e.g. a function generator. Alternatively, the VI could drive most

medium to higher end generators over a RS-232C, USB, or Centronics interface, offloading the task from the plug-in DAQ board.

· The thermal stress analysis was thought to be unimportant due to the low stresses generated, but may well be a critical operating mechanism that needs to be studied to gain further insight into the beam and TBC acting as a composite system as temperature changes are imposed. Although the blending of the bond coat layer into the TBC has found to be an acceptable simplification for the overall dynamic and thermal stress simulations, future work may want characterize the layer using profilometry measurements to extract the spatial frequency and roughness characteristics to allow the layer to be modeled more precisely. This very important if a mezo-scale numerical model is constructed.

· Consider refining the forced response testing, it probably allows more realistic simulation of loading conditions on a blade in service and is not so sensitive to external disturbances to the system. Refinements need to focus on how deal with the jumps around the resonance peaks in the FRF's. Deleon's work hints at some ideas to reconcile the use of the linear techniques with non-symmetric FRF peaks that result from the strain softening coatings. Repeatability of FRF tracings with this rig was very high.

From a time to test viewpoint, free-decay works well for high Q systems, like the bare beam, and forced response seems to work well with low Q systems, like the coated beam. The tests both seemed to achieve similar coating modulus and loss factor values when run on the specimen set.

· Smoothing splines in future free-decay studies, as Reed had used, may be a better technique than the functional fits used in the current study. Fits using realistic function based models, while they do yield some insight into the behavior of the system, may end up removing important localized artifacts in the dataset. The realistic functions that worked best in this study were the linear combination of exponentials and linear combination of ½ Gaussian functions. Polynomials are best avoided due to the manner in which they tend to increase or decrease without bound outside the fit region, resulting in extremely anomalies in the complex modulus in the low strain, far-time regions.

· For characterizing very low strain levels of the 8-YSZ ceramic coating, consider making a couple of monolithic 8-YSZ specimens. They could be laid up on a thin metal base that could subsequently be etched away after fabrication. For insight into the coating modulus in a homogeneous system, consider modulus testing by micro-indentation methods, if the same upward trend in the value of E_c with temperature is seen, as was measured in the free-free beams with 8-YSZ, then the modulus rise would be inherent to the TBC material and not the coating-TBC interaction from thermal loading.

· Index where in the metal sheet specimens are cut from. AFRL Materials Lab personnel made mention to use the center span of rolled sheet in forming test coupons, with the outer regions of the sheet typically being discarded. This should be done in future testing, or at the very least track where each specimen in the sheet came from. Also, when testing for the storage modulus by measuring the resonance frequency it is probably worthy to also explore how rolling orientation affects the bulk damping of the bare beams.

Certainly, this apparatus has proven to be sensitive enough to perform this on low damped materials. In the current study these tests were carried out in air with a sound meter to determine the bare TI modulus, they probably should be carried out in the vacuum with the DVL.

· In the future studies, avoid building the polynomials from the FEA until after the specimens are fabricated, though the fabricator had very good precision and intra- and inter-sample variation were kept very small (tight tolerances were maintained), the final mean coating thicknesses in each case were significantly off the nominal specified dimensions. Our normal thickness set was 8.3mil (±0.1mil at 95% CI) was off the specified mean of 9.0mil, almost 10% off. This probably had to do with setting the spray parameters (droplet size, feed rates, sweep rate, # passes) and only a finite amount can be applied on each pass of the APS gun. The APS process needs to be standardized and though the fabricator strove to tightly control the processing dimensions, there was enough variation between the specified values and the nominal ones to warrant re-running the modal analysis.

· The free-decay technique magnifies errors out in the far-time of the ring-down data set (e.g. at small strain levels) and the changes in the storage modulus and damping are very sensitive to polynomial fits; this manifests itself in the loss factor curves sometimes bending away either above or below the apparent convergence (static) loss factor value below about 5-10 microstrain. This is driven by the unwrapped phase function deviating slightly above (or below) the linear function due to superimposed noise on the signal. For

such low amplitudes from about 5 to 20 microstrain, the forced response on the quasi-linear (at low amplitudes) coated beams may yield more consistent results. It is noted that the FRF resonance peaks for the coated system at lower amplitudes are more symmetric and linear in form, thus allowing reasonable estimation of damping using the ½ power bandwidth technique. Another means to increase the amount of time (and therefore reduce the strain levels) that are reportable with confidence in the data trends is to program the NI board to make better use of the voltage and resolution ranges of the NI-DAQ board. The current study used the largest range to split the 12-bits of A/D resolution among (±10Volts), while in practice during the testing the signal rarely exceeded ±2volts. Dropping to a more appropriate voltage range may have help cut the noise floor from about 10-15millivolts down by a factor of at least two.

· Momentary spikes and dropouts in the laser signal were caused by large variations in the reflectivity and the angle of surfaces in the mica tape definitely caused large and seemingly random outliers on the DVL velocity signal; these necessitated outliers removal from the datasets using the Matlab 'loess' function. Unlike rigid body motion, this is not a harmonic component that can be readily filtered out, whether by hardware or software. Fortunately, these spikes were very short in duration (well under 0.5% of the entire data set across the ring-down trials on a “dirty” dataset) and the source was identified to allow their dismissal from the datasets that had them using appropriate processing techniques.

Follow up testing on the titanium beam and chamber sensitivity study resulted in

the observation that the 3M diffusive reflector (polymeric) tape survives to 1050degF in vacuum, or at least the diffusive reflector component does, while the polymeric binder gasifies. Another group at the TEFF found that the 3M tape did not continue to reflect diffusively on cantilever beams heated to over 400degF in ambient air so the tape was discounted at the beginning of this study which was a mistake. An additional advantage for the 3M tape is that it does not require use of the Durabond 952 adhesive which provided significant additional damping to the bare and bond coat only beams.

· Filtering was originally added to make processing easier while programming the Labview data acquisition code and was to be bypassed once the testing commenced, but based on the (accidental) finding that the lower restraints lines were adding significant damping to the system, the filtering in software form was retained. The Butterworth filter worked well for this purpose as the separation between the bending mode-I frequency and that of the undesirable rigid body (back-and-forth, pogo, and swinging on the wire) modes was large. As a result, the modest sharpness of the filter was fine. The unity gain of the Butterworth in the pass-band was desirable and the constant phase shift imparted to the pass-band signal was also acceptable as the instantaneous phase was extracted from the slope of the phase signal, not the magnitude. As a precaution the raw unfiltered signal was captured and saved as well during ringdown dataset collection.

· The global decay curve of the non-linear TBC beam system was well-approximated by a linear fit (e.g. $v(t) = v_0 \exp(-\eta 2\pi f_r t)$); this may allow for a reasonable estimation of the coating's bulk damping from using the fit values and the Torvik equation in a once-off

manual calculation as opposed to processing of the whole temporally-indexed dataset through a Matlab script.

· Careful control of the manufacturing process for the coatings is critical, a diligent search in the literature for ANSI, ASME, SAE and/or other standards for APS prior to fabrication of the beams failed to uncover anything for either bond coating or top-coating with 8-YSZ. As can be seen with Spec # 01, 05, and 07, variations were encountered in both the loss coefficient and the storage modulus. Pearson also experienced such a wide variation in his samples as well. It can be suspected that such things as spray angle, atomization from gas flow rate, nozzle size, plasma gun speed, and other such factors can alter the fusion temperature of the droplets and the splat and void density and size.

Even the aging-in protocol, as Beam #01 (mistakenly aged in at a larger dwell outout amplitude) seems to hint, can affect this and may need inclusion into such standards. It is probably best to quantify these variables using a micro-structural SEM study, similar to those of Patsias, Tassini, and Pearson. The fabricator did try to control macroscopic parameters and achieved tight tolerances on these, (coating thickness, evenness, etc.) both inter- and intra-sample. Nonetheless, standardization of technique and development of specifications and standards that achieve a standard micro-structure in the coating is a necessary antecedent to employing any values determined from testing in any aggressive design models used for life estimation of components. As stated, this may also extend to a “break-in” protocol as well.

· Given the variation in bare beam modulus and damping, each coupon should be tested

for not only modulus, but damping as well, before proceeding into processing for BC and/or TBC coatings. Either that, or a larger population of bare specimens needs to be tested. It is noted however, in the context of the current study, that based on propagation of error analysis, that a large amount of error in loss factor for the bare beam has a relatively weak influence on bulk loss factor determined for the coating.

· Consider shortening the length of the coating to reduce strain variation down its length, but do not make it too short as the edge stress effects will overwhelm the bulk average value. Strain through the thickness of the coating varies, but it is small if the coating is kept thin, relative to the beam, but it may be better to report strain at the mid-layer of the coating (e.g. $X(L/2, t_b/2+t_c/2)$) in the future.

· The values of E_c and η_c reported here should be considered as orthotropic in nature for two reasons: 1) the bending of the beam only significantly strains the bending mode-I direction (ε_{11}), and 2) the APS and EB-PVD processes both produce a micro-structure that is known to be orthotropic in regards to heat transfer, this is probably true of energy dissipation mechanisms within the micro-structure as well. (An additional question is, does the APS gun traverse pattern influence the ε_{11} and ε_{22} values or can the be assumed to be the same?)

· Initially it was thought that a 3-D FEA model was over-extravagant, but given the precision of the free-free apparatus in its current form that picks up very slight changes in frequency and very low decay rates (high Q), a likewise high-fidelity FEA model is needed to compliment the system. That being said, the 1-D and 2-D models generated

polynomials that were very close to those of the 3-D system, with the exception of the 1-D for the $E_c = f(\omega_r)$ which was due to lack of capturing localized stiffening effects from the magnet stacks. Adjustment of the stiffness of the neighboring elements could close the gap. Returning to the original recommendation, the 3-D model is more direct approach to assuming the field variables in the experiment requiring less modeling assumptions to correct for multidimensional effects.

· To truly report the required forcing energy in the beam system, the Labview program needs to be modified to not only save the DVL laser data but also the magnet excitation signal, this is vital to know the phase lag between the beam's excitation and displacement output. If the displacement and magnet stimulation are not 0^o apart then the magnets may be driven into a field that is still repelling them, thus bleeding off some energy in the forced response scenario and also suppressing the maximum amplitude in the build-up phase prior to chopping the stimulation in the free-decay method.

· The work of Deleon to model the partially coated beam using a fully implicit transient time-dependent model should be attempted again with a 1-D model using the results of this and Pearson's studies. One, the coated beam system is a nearly viscous system in the form of its decay envelope function, despite the strong material non-linearity of the coating and its strong increase in the system damping level. This lends confidence that a Rayleigh damping model may well capture and allow accurate modeling of the system using the values determined for 8-YSZ in this study. Two, the modal 1-D FEA model with the coating seems to match predictions of the 2-D and 3-D coated FEA models quite

well. Three, when tuning in the bare bare during Labview data acquisition code the same lobed envelope containing the overshoot and settling of the harmonic beam signal was found experimentally (See Figure 121, Section 5.2.3) and this was the same result Deleon generated while modeling the bare beam while attempting to achieve a settled harmonic solution for his fully transient time-dependent model that was complete with boundary conditions and forcing function. The relative time scale of the lobe lengths, height overshoot and settling time could be used to help tune Deleon's model using the experimental results found here.

6.4. Impact

The main impact of the study is that a vacuum chamber faculty for using the free-free beam with a high Stark number has been shown to be a workable concept. Only modest power is needed, it features a near-isothermal beam, and preserves non-contacting in excitation, measurement, and suspension (boundary condition). Due to this, the modified free-free rig and chamber has very low inherent damping as opposed to the original configuration; Q-factors at some test conditions are up to 22,500. It has achieved free decay on beams up to 1050degF with 200W lamps; and about 850degF with 100W lamps. Forced response techniques have been shown to yield equivalent damping values to those obtained by free decay.

Thermal stresses from the inhomogeneous beam system do not appear to drive to total stress into a state where non-linear material effects occur, and peel stress induced failures in beams seem unlikely under thermal strain levels from the heat range imposed.

However, thermal stress may play an important role in the property changes of the coating with temperature observed and temperature does have a marked effect on both the coating effective storage modulus and loss factor determined for 8-YSZ. Meanwhile, coating thickness affects system level damping and resonance frequency, but appears to have some influence on bulk properties of the 8-YSZ as well.

The bare beam yielded some unexpected findings; titanium is anisotropic in modulus and the chamber easily discriminates this using a continuum-level testing approach. The damping minimum of TI-6AL-4V is somewhere from 300-600degF, unexpected above room temperature. The bond coat only beam behaves as a linear system. The bond coat adds very little damping to the system, nor changes the system's effective stiffness either. For the coated beam, the global decay curve, though technically non-linear, is well described by a linear decay function fit to the envelope curve; this allows for a reporting of system-level damping with a scalar. Despite the, the coating's influence is large and it adds significant damping to the bare system (at room temp about 0.02 minimal as opposed to 0.00008-0.00012.

With the current study complete, the next logical step is to determine conservative design values for the storage modulus and loss factor from these measured values. Refinement of numerical models to allow for design with inclusion of an 8-YSZ, or other TBC thin coat, can be attempted to determine the damping enhancement on the system. Micro-structural interactions may be occurring, numerical and experimental investigations of this interaction are needed for accurate characterization of the

interaction between the coating and substrate to include the enhancement of damping from the coatings.

APPENDICIES

1. Analytical Model - Heat Transfer in a Thin Beam

This section covers the derivation of the radiation-conduction problem based on notes by Baker (Baker, 2008). Two approaches are worked by this author, the second was based on a boundary layer approximation approach, with the realization that conduction along the length (y-coordinate) of the beam will be a much larger flux and driving gradient that across the other two dimensions of the beam. Thus the partial differential equation of 3-dimensions reduced to an ordinary differential equation along the long axis of the beam. Simple perturbation and a stretched coordinate system were used to capture thermal gradients at the tip regions. The first approach was to integrate up to obtain a Green's function for the temperature variation and seek a stable solution function by iterative contraction updating using the boundary conditions, this was deemed rather cumbersome. So a second approach inspired by boundary layer theory was attempted.

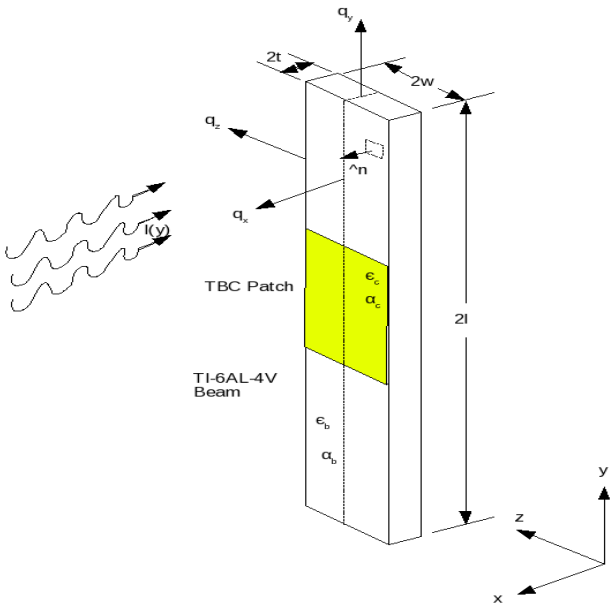


Figure 149: Beam coordinate system, dimensions.

This was predicated on the fact that heat gradient along the long axis of the beam would predominate over those through its thickness or across its width. This was felt reasonable as the largest resistance to conductive flux is through the smallest cross-sectional area, that normal to the long axis of the beam. Both approaches utilized normalized coordinates and non-dimensional variables.

The formulation starts by assigning a coordinate system to the solid domain of the coated beam as per Figure 149. The yellow region is the patch length, denoted as LC, and it is noted that, like the real beam/coating system that 2t << 2w << 2L, and that the thickness of the TBC coating patches, which are on both sides of the beam, are much less than that of the titanium beam, e.g., t_c << 2t. The problem is assumed to be fully developed in time, that is, steady-state, with no storage of thermal energy within the beam. Fourier's law states that within the solid domain, D, of the beam:

$$\vec{\nabla}(K\vec{\nabla}T)=\rho C_P\frac{\partial T}{\partial t} \tag{129}$$

holds, and with steady state conditions Eq. (129) reduces to:

$$\vec{\nabla}\cdot K\vec{\nabla}T=0 \tag{130}$$

If the conductivity of the beam is not strongly dependent on temperature (e.g. k is not a function of T) the previous further reduces to:

$$K\nabla^2 T=0\,;\, x\in D\rightarrow\begin{cases}|x|<t\\|y|<l\\|z|<w\end{cases} \tag{131}$$

where x is the depth coordinate into the beam of thickness 2t, y is the distance coordinate

down the length, which is 2l, and z is the location along the width which is of 2w as shown in Figure (136). Now enforcing the boundary conditions on the surface of the domain, where the surface heat flux is defined, where $-\hat{n}$ is the the surface in-ward normal, K_S is the conductivity of the solid at the surface (which can vary based on the y-coordinate to account for the TBC patch) in W/m·degK, and q is scaler function of the surface heat flux magnitude at a given point on the surface in W/m^2:

$$-\hat{n}\cdot K_s(y)\vec{\nabla}T = q\,;\, x\in\partial D \rightarrow \begin{cases} |x| = t \\ |y| = l \\ |z| = w \end{cases} \tag{132}$$

Taking Eq. (132), and integrating across all the surfaces of the solid should equate to zero, if the solid is at thermal equilibrium. The application of the Divergence Theorem to the surface and interior allows rewriting the surface integral of heat fluxes into the beam surfaces a volumetric form as per:

$$0 = \int_D \vec{\nabla}\cdot(K\vec{\nabla}T)\,dV = \int_{\partial D} \hat{n}\cdot(K\vec{\nabla}T)\,dS \tag{133}$$

The left term is zero due to steady state conditions exiting in a global fashion over the entire surface, despite any localized hot or cold spots, the middle term is the volumetric flux of heat by conduction within the interior, and the right term is the surface heat fluxes into the beam solid.

Now the following assumptions are invoked, that the surface and interior thermal conductivities of the titanium are the same (e.g. $K/K_s = 1$), that the conductivity of titanium is isotropic and also invariant w.r.t temperature, and that the only significant driver to conductive resistance within the solid therefore is cross-sectional area. Since w

<< l and t << l, the lateral and transverse cross sectional areas are much smaller than the longitudinal one, therefore the areas for heat flow. From this the thermal resistance to significant heal flow across the width or through the thickness is much lower, leading to less thermal gradients being formed. Restated, the heat flow within the beam exhibits a functional dependence on the y-coordinate alone, and that q"(x,y,z) collapses to q"(y). With this the areal averaging of q can be performed both within the solid and on the surface:

$$\begin{aligned} q_y^{\pm} &= constants \\ q_z &= q_z(y) \\ q_x &= q_x(y) \end{aligned} \tag{134}$$

The variation in q that is due explicitly to variation in shadow, illumination non-uniformities, and/or the presence of coating with a differing surface emissivity, absorptivity, and reflectivity than that of the bare titanium. This is asserted where $K_s(y)$ indicates the relative change in surface conductivity into the beam as manifested from surface emissivity changes, and q is the flux into the beam surface.

$$0 = \int_D \vec{\nabla} \cdot (K \vec{\nabla} T)\, dV = \int_{\partial D} \hat{n} \cdot (K \vec{\nabla} T)\, dS = \int_{\partial D} \frac{K}{K_s(y)} q\, dS \tag{135}$$

The Stephan-Boltzmann Law is utilized for the surface emission boundary condition for radiation leaving the beam as

$$E = \sigma \epsilon T^4 \tag{136}$$

where E is the emission power flux from the surface (W/m^2), σ is the Stephan-Boltzmann constant ($\sigma = 5.67 \times 10^{-8}\ W/m^2 \cdot K^4$), ε is the emissivity efficiency of the surface relative to the perfect blackbody (where ε =1.0), and T is the absolute surface temperature (in K).

The more familiar form given as $q=\sigma\epsilon A(T^4-T_{surr}{}^4)$ is applied as the surface boundary condition, where q is the surface thermal heat flow in Watts, and T_{surr} is the temperature of the surroundings enclosing the hot body. On the surface at steady-state, the local thermal energy into or out of the surface is the difference of the incident absorbed energy minus the re-radiated energy as per:

$$q_s=\alpha G-\epsilon\sigma T^4 \tag{137}$$

where G is the surface radiance received from the lamps (in W/m^2), q_s is the net thermal flux into or out of the surface, and α is the surface reflectivity (a dimensionless efficiency compared to a perfect reflector where α =1). The surface is opaque and the Kirchhoff assumption is employed which states that absorptivity is equivalent to the emissivity across all of the thermal spectra, for both the bare titanium and ceramic regions (e.g. $\alpha=\epsilon$). As a result Eq. (137) now can be written as:

$$q_s=\alpha G-\epsilon\sigma T^4 \tag{138}$$

It is noted that the heat flow flux into the surface, q_s, is still a function of spatial location, e.g. $q_s(x,y,z)$. Application of the Kirchhoff Law and assuming the spatial variation of illumination in only along the long axis of the beam (along y) to (138) yields:

$$q_s=\epsilon(y)G(x,y)-\epsilon(y)\sigma T(x,y)^4=\epsilon(y)[G(y)-\sigma T(y)^4] \tag{139}$$

It is noted that there is no participating medium around the solid, that coating variation can be expressed in the term ε(y), and shadowing effects can be expressed through functional variation of G(y). Since flux variation is only a function of y, one can now define a transverse (xz-plane) cross-sectional averaged value, W(y), as per:

$$W(y)=\frac{1}{A}\int\int_{A} T(x,y,z)da=K\frac{\partial^2 W}{\partial y^2} \quad ; \quad da=dxdz \quad ; \quad A=4\text{wt} \tag{140}$$

This represents a spatial averaging from a weighted average across the cross-sectional area of the temperature field at any given point down the length of the beam. Applying this spatial averaging to Eq. (135) yields:

$$\frac{1}{4\text{tw}}\int_{-w}^{w}\int_{-t}^{t}\vec{\nabla}\cdot(K\vec{\nabla}T)\,dx\,dz \;=\; 0 \tag{141}$$

and expanding Eq. (141) in each of the three Cartesian coordinates, yields:

$$0=\frac{1}{A}\int\int_{A}\frac{\partial}{\partial y}K\frac{\partial T}{\partial y}da+\frac{1}{A}\int\int_{A}\frac{\partial}{\partial x}K\frac{\partial T}{\partial x}da+\frac{1}{A}\int\int_{A}\frac{\partial}{\partial z}K\frac{\partial T}{\partial z}da \tag{142}$$

The expansion within the solid boundary limits is now performed on Eq. (142):

$$0=\frac{1}{A_{xz}}\int_{-w}^{w}\int_{-t}^{t}\frac{\partial}{\partial y}K\frac{\partial T}{\partial y}dx\,dz+\frac{1}{A_{yz}}\int_{-w}^{w}\int_{-l}^{l}\frac{\partial}{\partial x}K\frac{\partial T}{\partial x}dy\,dz+\frac{1}{A_{xy}}\int_{-l}^{l}\int_{-t}^{t}\frac{\partial}{\partial z}K\frac{\partial T}{\partial z}dx\,c \tag{143}$$

The operations of differentiation and integration are now interchanged, using Leibniz's rule, and the constant conductivities are removed outside the integrands to yield:

$$0=K\frac{\partial^2}{\partial y^2}\frac{1}{A_{xz}}\int_{-w}^{w}\int_{-t}^{t}T\,dx\,dz+K\frac{\partial^2}{\partial x^2}\frac{1}{A_{yz}}\int_{-w}^{w}\int_{-l}^{l}T\,dy\,dz+K\frac{\partial^2}{\partial z^2}\frac{1}{A_{xy}}\int_{-l}^{l}\int_{-t}^{t}T\,dx\,dy \tag{144}$$

In a general sense, across area, and proceeding with integration on x, this is restated as:

$$0=\frac{1}{A}\int\int_{A}\frac{\partial}{\partial y}K\frac{\partial T}{\partial y}dx\,dz=K\frac{\partial^2}{\partial y^2}\frac{1}{A}\int\int_{A}T\,dx\,dz=\frac{1}{A}\int_{-w}^{w}K\frac{\partial T}{\partial x}\Bigg|_{t}^{-t}dz \tag{145}$$

The boundary conditions at the main surface are recognized to be. The sign convention is that positive heat flow is out of the beam slab, a + q_x value as per:

$$K_s \left.\frac{\partial T}{\partial x}\right|_{x=t} = -q_x \tag{146}$$

Dividing (146) by the quantity of the surface conductivity, K_s, and rearranging one obtains:

$$\left.\frac{\partial T}{\partial x}\right|_{x=t} = \frac{-q_x}{K_s} \tag{147}$$

Placing the right hand side of (145) into (147), yields for y-direction facing surfaces (the tips),

$$\frac{1}{A}\int_{-w}^{w} \frac{-K}{K_s} q_x \, dz = \frac{-1}{t}\frac{K}{K_s} q_x(y) \tag{148}$$

and for the z-direction facing surfaces (the thin edges) one gets:

$$\frac{1}{A}\int_{-t}^{t} \frac{-K}{K_s} q_z \, dx = \frac{-1}{w}\frac{K}{K_s} q_z(y) \tag{149}$$

Placing (140), (148), and (149) into (142), and rearranging yields:

$$K\frac{\partial^2 W}{\partial y^2} - \frac{K}{K_s}\frac{1}{t} q_x(y) - \frac{K}{K_s}\frac{1}{w} q_z(y) = 0 \tag{150}$$

And:

$$W''(y) - \frac{1}{K_s(y)}\left(\frac{1}{t} q_x + \frac{1}{w} q_z\right) = 0 \tag{151}$$

Equation (150) is a one-dimensional 2nd order ordinary differential equation that relates

the average (spatial) distribution of the spatially averaged temperature, W. For closure, a compatibility condition is now imposed, and this is based on global conservation of energy across the surface of the beam solid, expressed as:

$$\oint_S q(x, y)\, dS = 0 \tag{152}$$

Dividing (150) through by K and reducing leads to:

$$W'' - Q(y) = 0 \quad ; \quad Q(y) = \frac{1}{K_S(y)}\left\{\frac{1}{t} q_x(y) + \frac{1}{w} q_z(y)\right\} \tag{153}$$

The term of Q(y) is the influence of any incident fluxes conducting into the element from the faces of the differential length. The boundary conditions at the beam tips where y = ±L are defined as:

$$K_s \frac{\partial T}{\partial y}\bigg|_{\substack{(x,l,z) \\ y=l}} = q_y^+(x,z) \quad (top); \quad K_s \frac{\partial T}{\partial y}\bigg|_{\substack{(x,-l,z) \\ y=-l}} = q_y^-(x,z) \quad (bottom) \tag{154}$$

At this point the assumption is made that the variations of heat flux and temperature gradient at any given section (along the y-coordinate) across the x- and z-directions are small. This is the boundary layer inspired assumption. Averaging these values across the cross-sectional surface area results in:

$$\frac{1}{A}\int\int_A -K_s \frac{\partial T}{\partial y}\, da = \frac{1}{A}\int\int_A q_y{}^+(x,z)\, da \tag{155}$$

Meanwhile, for the tips of the beam the area based averages of the boundary conditions take the form:

$$\begin{matrix} \frac{-K_s(l)}{A}\int\int_A \frac{\partial W}{\partial y}da\Big|_{y=l}=\bar{q}_y^{+} \\ \frac{-K_s(-l)}{A}\int\int_A \frac{\partial W}{\partial y}da\Big|_{y=-l}=\bar{q}_y^{-} \end{matrix} \quad \rightarrow \quad \begin{cases} K_s(l)\,W'(l)\equiv\bar{q}_y^{+} & ave.\,top\,surfac \\ K_s(-l)\,W'(-l)\equiv\bar{q}_y^{-} & ave.\,bottom\,surf \end{cases} \tag{156}$$

The tip temperatures and heat fluxes (q+y and q-y) are linked by the Fourier heat law and are specified as a controlled constant in the analysis. Experimentally, this is manifested by having lamps of controllable power focused on and used to irradiate the beam tips. The ordinary differential equation of the system is now:

$$W''(y)-\frac{1}{k_s(y)}\{\frac{1}{t}q_x(y)+\frac{1}{w}q_z(y)\}=0 \tag{157}$$

with end boundary conditions for the upper and lower tips of:

$$W'(l)=\frac{-\bar{q}_y^{+}}{k_s(l)} \quad ; \quad W'(-l)=\frac{\bar{q}_y^{-}}{k_s(-l)} \tag{158}$$

The redefinition of the flux tips is noted in Eq. (159) where the lower and upper tip fluxes are recast as $-R^{+}$ and R^{-} at the upper and lower tips with $K_s(\pm L) = K$.

$$\begin{aligned} R^{+}&=\frac{\bar{q}_y^{+}}{K} \\ R^{-}&=\frac{\bar{q}_y^{-}}{K} \end{aligned} \tag{159}$$

Now

$$W''-Q(y)=0 \quad ; \quad W'(l)=-R^{+} \;, \quad W'(-l)=R^{-} \tag{160}$$

Variation of the temperature down the length of the beam can be be expressed as a variation from the lower tip temperature (at -1) along the coordinate of η and the flux

incoming along that length (as Q(η)). To solve Eq.(160) can be integrated:

$$\int_{-l}^{y} W''(\eta)\,d\eta = W'(y) - W'(-l) = \int_{l}^{y} Q(\eta)\,d\eta \tag{161}$$

Where η is a dummy coordinate of length down the beam. Rearranging Eq. (161) lead to:

$$W'(y) = R^{-} + \int_{-l}^{y} Q(\eta)\,d\eta \tag{162}$$

A compatibility condition of globally conserved energy, as per Eq. (152), at the top tip should be enforced. This implies that:

$$W'(l) = \underbrace{-R^{+}}_{top\ tip\ flux} = \underbrace{R^{-}}_{bottom\ tip\ flux} + \underbrace{\int_{-l}^{l} Q(\eta)\,d\eta}_{internal\ energy\ distribution} \tag{163}$$

One can integrate up from the bottom tip and solve for the distribution function, knowing the applied surface heat flux (Q(η)), this yields the Green's function of the solution. Integrating again for

$$W'(y) = W(-l) + R^{-}(y+l) + \int_{-l}^{\eta}\int_{-l}^{\xi} Q(\eta)\,d\eta\,d\xi \tag{164}$$

yields

$$W'(y) = W(-l) + R^{-}(y+l) + \underbrace{\int_{-l}^{y} (y-\eta)\,Q(\eta)\,d\eta}_{Greens\ function} \tag{165}$$

This gives the thermal distribution down the beam knowing the magnitude of the temperature at the lower tip and the associated flux along the length. The former is to

bound the tip condition and the latter is controlled as an independent parameter of the illumination down the beam. In the physical system this would manifest itself as a illumination source of known intensity distributional.

Rearranging Eq. (165) results in:

$$W'(y) = \underbrace{W(-l)}_{\text{unknown constant } C_1} + \underbrace{R^-(y=-l)}_{\text{flux across bottom tip}} + \underbrace{\int_{-l}^{y} (y-\eta) Q(\eta)\, d\eta}_{\text{flux sources / sinks}} \tag{166}$$

Proceeding to apply the limits between the two tips from -l to +l on y leads to:

$$W(l) - W(-l) = R^-(2l) + \int_{-l}^{l} (l-\eta) Q(\eta)\, d\eta \tag{167}$$

And now dividing through by the length of the beam (2l) and separating the integrand, leads to:

$$\frac{W(l) - W(-l)}{2l} = R^- + \frac{1}{2l}\int_{-l}^{l} Q(\eta)\, d\eta - \frac{1}{2l}\int_{-l}^{l} \eta Q(\eta)\, d\eta \tag{168}$$

The middle term on the r.h.s. is evaluated and leads to:

$$\frac{W(l) - W(-l)}{2l} = -\frac{R^+ - R^-}{2} - \frac{1}{2l}\int_{-l}^{l} \eta Q(\eta)\, d\eta \tag{169}$$

Equation (167) describes the thermal profile of temperature down the length, of the (relatively) long and thin beam. The l.h.s. is the prescribed tip temperatures and the first term of the r.h.s. is the tip flux conditions, again controlled by known illumination flux levels. The second term of the r.h.s. is the first moment of any sources and sinks of heat within the beam, if the function Q is constant, this term, which specifies the heat flux into the beam, equates to zero.

Further definition of the boundary conditions is now needed, so one can proceed to break down the incident radiation into source and background radiation from the specular, but uniform flux lamp illumination field, and the enclosing black-body enclosure around the beam:

$$G = G_{source} + G_{background} = G_S + G_B \tag{170}$$

G_s is governed by Lambert's Law of view factor as per:

$$F_{ij} = \frac{1}{A_i} \int^{dA_i} \int^{dA_j} \cos\theta \cos\phi \, dA_i \, dA_j \tag{171}$$

where G is the radiosity, with both the sources and background emitting energy. The beam sees the influx of energy as per:

$$q_{in} = \epsilon \, G_{total} = \epsilon \, G_{sources} + \epsilon \, G_{background} = \epsilon \, G_s + \epsilon \, G_a \tag{172}$$

with the total exchange being, as the beam re-radiates according to the Stephan-Boltzmann law:

$$q_{total} = q_{out} - q_{in} = \epsilon (\sigma T^4 - G_s - G_a) \tag{173}$$

On any given surface region of the beam and applying the conservation of energy (the compatibility condition) with any heat arriving/leaving by conduction from within the beam solid one obtains:

$$\int_{\partial D} \frac{K}{K_S} q \, dS = 0 \;\rightarrow\; \int_{\partial D} \frac{K}{K_S} \epsilon(x, y, z) \left[\sigma T^4 - G_s - G_a \right] dS = 0 \tag{174}$$

The quantity ε is the emissivity of the surface of the beam, G_s is the imposed radiation from the lamps, and G_a is that from the background surroundings which is assumed to be uniform and constant. It is noted that if the lamps are off (e.g. $G_s = 0$), then

the only source is the background radiation, σT^4, and temperature field of the beam approaches the ambient temperature. If the surroundings temperature and therefore the background irradiation is constants, then Eq. (174) reduces to:

$$(\sigma T_a^4 - G_a) \underbrace{\int_{\partial D} \frac{K\epsilon}{K_s} dS}_{non-zero} = 0 \tag{175}$$

and this leads to the surroundings temperature effect that (where T_a is the ambient temperature around the beam)

$$G_a = \sigma T_a^4 \quad . \tag{176}$$

As a result the heat flux for the beam can be expressed as:

$$q = \epsilon\sigma(T^4 - T_a^4) - \epsilon G_s \tag{177}$$

The general problem is now stated as:

$$\begin{aligned} \nabla^2 T &= 0 \quad in \quad D \\ -\hat{n}\cdot k_s \nabla T = q &= \epsilon\sigma(T^4 - T_a{}^4) - \epsilon G_s \quad on \quad \partial D \end{aligned} \tag{178}$$

Knowing that a unique solution exists to this functional relation is important, details of the proof are covered in Appendix 2. Physically interpreted, the system should come to a unique temperature distribution for the same boundary conditions (source intensities, beam emissivity, etc.) no matter the initial field. Knowing that there is a unique distribution of temperature that the problem yields gives confidence in a (the) numerical finite difference model should be stable in its solution, that the analytical problem is well formed and stable in nature when at steady state.

Recalling the definition of Q(y) (in Eq. (153)) and using an approximated surface temperature arrived at by the cross-sectional average temperature as per:

$$T\big|_{\partial D} \approx W(y) \tag{179}$$

one can arrive at:

$$\begin{aligned} q_x(y) &= \epsilon(y)\sigma(W^4(y) - T_a^4) - \epsilon(y)G_x(y) \\ q_z(y) &= \epsilon(y)\sigma(W^4(y) - T_a^4) - \epsilon(y)G_z(y) \end{aligned} \quad . \tag{180}$$

Now

$$Q(y) = \frac{\epsilon(y)}{k_s(y)}\left(\frac{1}{t} + \frac{1}{w}\right)\sigma\left[(W^4(y) - T_a^4)\right] - \underbrace{\epsilon\frac{(y)}{K_s}(y)\{\frac{1}{t}G_x(y) + \frac{1}{w}G_z(y)\}}_{source\ influx,\ \ G_s} \tag{181}$$

where at the tips (where y=± l) the variation is $w'(l) = -R^+ + w'(-l) = R^-$. This, at the tips, leads to:

$$R^{\pm} = \frac{q_y^{\pm}}{K_s(\pm l)} = \frac{\epsilon(\pm l)}{k_s(\pm l)}\left[\sigma(w^4(\pm l) - T_a^4) - G_y^{\pm}\right] \tag{182}$$

Non-dimensionalization of the problem is now sought, this involves the introducing of a length scale, where the length, l, is 1/2 the length of the beam as per

$y = l\,\hat{y}$. Similarly, a temperature scale as per $\delta = \left(\frac{T_a}{T_r}\right)^4$ is introduced. Conductivity

and emissivity spatial effect terms are $\beta(\hat{y}) = \left(\frac{\epsilon k}{k_s}\right) = \left(\frac{\epsilon(l\,\hat{y})}{k_s(l\,\hat{y})}\right)k$, a dimensional aspect

ratio $\alpha=\left(\frac{1}{t}+\frac{1}{w}\right)l$, a radiation-power-to-conductivity amplification factor

$\lambda=\frac{l\sigma T_r^3}{k}$, and an irradiation flux $\hat{G}(\hat{y})=\frac{G_s(y)}{\sigma T_r^4}$ are now defined. The temperature difference is defined in terms of a reference temperature (Tr) as per:

$$W(y)=T_r V(\hat{y}) \quad . \tag{183}$$

From this the first and second derivatives of W are

$$W'(y)=\frac{T_r}{l}V'(\hat{y}) \quad ; \quad W''(y)=\frac{T_r}{l^2}V''(\hat{y}) \tag{184}$$

Placing these into Eq. (181) and reducing leads to:

$$\hat{Q}(\hat{y})=\beta(\hat{y})\alpha\lambda[v^4(\hat{y})-\delta^4-\hat{G}_s(\hat{y})] \tag{185}$$

It is noted that all of these quantities are non-dimensional in nature. For the aspect ratio of the beam, where t<<w<<l, recognizing $v''-\hat{Q}=0$, $v'=\epsilon\lambda$, and imposing the boundary conditions on the tips in the normalized length coordinates as per:

$$v'(\pm 1)=\epsilon\lambda[v^4(\pm 1)-\delta^4-\hat{G}_y^{\pm}] \quad ; \quad -1<\hat{y}<1 \tag{186}$$

One obtains upon integrating up once on the non-dimensional length (y-hat):

$$v'(\hat{y})=v(-1)+\alpha\lambda\int_{-1}^{y}\beta(\eta)[v^4(\eta)-\delta^4-\hat{G}_s(\eta)]d\eta \tag{187}$$

Applying the boundary condition at ŷ=1, the upper tip:

$$v'(1)=\epsilon\lambda[v^4(1)-\delta^4-\hat{G}_y^+]=\epsilon\lambda[v^4(-1)-\delta^4-\hat{G}_y^-]+\alpha\lambda\int_{-1}^{1}\beta(\eta)[v^4(\eta)-\delta^4-\acute{C} \quad (188)$$

Now accounting for the lower tip and

$$\begin{aligned} v'(1)-v'(-1)=v^4(1)-v^4(-1)-(\hat{G}_y^+-\hat{G}_y^-)... \\ -\alpha\int_{-1}^{1}\frac{\beta(\eta)}{\epsilon}[v^4(\eta)-\delta^4-\hat{G}_s(\eta)]d\eta \end{aligned} \quad (189)$$

Integrating v-hat (of y-hat) up one more time yields:

$$\begin{aligned} v'(\hat{y})=v'(-1)+\epsilon\lambda(v^4(-1)-\delta^4-\hat{G}_y^-)(y+1)+... \\ \alpha\lambda\int_{-1}^{\hat{y}}(y-\eta)\beta(\eta)[v^4(\eta)-\delta^4-\hat{G}_s(\eta)]d\eta \end{aligned} \quad (190)$$

Equation (165) is a non-linear Volterra equation of the second kind, with the impressed radiation driving the non-linear effects. Integrated up, it yields:

$$\begin{aligned} v(\hat{y})=v(-1)+\epsilon\lambda(v^4(-1)-\delta^4-\hat{G}^{-_y})(y+1)+... \\ \alpha\lambda\int_{-1}^{\hat{y}}(y-\eta)\beta(\eta)[v^4(\eta)-\delta^4-\hat{G}_s(\eta)]d\eta \end{aligned} \quad (191)$$

Now at the upper tip of the beam one can obtain:

$$\begin{aligned} v(1)=v(-1)+\epsilon\lambda(v^4(\eta)-\delta^4-\hat{G}_y^+)2... \\ \alpha\lambda\int_{-1}^{1}(1-\eta)\beta(\eta)[v^4(\eta)-\delta^4-\hat{G}_s(\eta)]d\eta \end{aligned} \quad (192)$$

The process of finding a distribution of temperature, v(ŷ) is as follows. First, start with assuming the lower tip temperature is at the surroundings, v(-1) = v_0 =1. Second use Eq. (163) to determine the temperature distribution down the beam v(ŷ) based on that assumed tip temperature (and the boundary conditions). Third, the upper tip temperature,

v(1), is determined using Eq. (162). Fourth, use the following equation to recompute v_0, which is derived from the difference:

$$-v^4(1)-v^4(-1)+(\hat{G}_y^+ + \hat{G}_y^-)-\alpha\int_{-1}^{1}\frac{\beta}{\epsilon}(\eta)[v^4(\eta)-\delta^4-G_s(\eta)]d\,\eta+2\,\delta^4=0 \qquad (193)$$

The process will be repeated successively, from this a sequence of lower tip temperatures (v_0) will be generated and a sequence results ($\left\{v_0^{(n)}\right\}_{n=0}^{\infty}$). If a solution is admissible, than this sequence is Cauchy and will convergence. The sequence of lower tip temperatures should converge to a steady value when the infinity norm is used ($v\in[-1,1]$). When, within an acceptable tolerance on the lower tip, the distribution of temperature ($v(\hat{y})$) also converges. This in a fashion can be used to iterate into the final, unique temperature distribution.

Baker noted that the beam specimens used by Reed and Pearson were much longer than they were wide, and furthermore, that the width was much larger than the thickness as well, e.g. t << w << l. As a result, an approach inspired by boundary layer theory was proposed. To start, the following non-dimensional terms are defined. First, is effective emissivity, where k_s denotes the conductivity just under the surface, it is noted that $\varepsilon(l_y)$ and $k_s(l_y)$, which denote the surface emissivity and the just-under-the-surface conductivity vary down the length coordinate of the beam. In other words accounting for the change in these properties in the central fourth of the beam where the TBC coating is located:

$$\beta(y)=\frac{\epsilon(l_y)}{k_s(l_y)} \tag{194}$$

Then the non-dimensional temperature, where T_a is the ambient (background) temperature of the surroundings and T_r is a scale (or reference) temperature, are defined:

$$\delta=\frac{T_a}{T_r} \quad ; \quad (\delta \ll 1) \tag{195}$$

The amplification factor, which is equivalent to Biot number, is a scaling the radiative loss to the surroundings against the conductivity of the beam solid:

$$\lambda=\frac{l\sigma}{k}T_r^3 \quad ; \quad (\lambda \approx 1) \tag{196}$$

The aerial aspect ratio, which is based on the ratio of surface area to cross-sectional area of the beam, is defined as:

$$\alpha=\frac{(t+w)l}{t\cdot w} \quad ; \quad (\alpha \approx 14 \gg 1) \tag{197}$$

Again, the governing equation, Eq. (153), is non-dimensionalized by placing Eqs. (161)-(159) into Eq. (153), and applying the non-dimensional variables defined on page 441, yields:

$$v''-\alpha\lambda\beta(y)v^4=\alpha\lambda\beta(y)[\delta^4+\hat{G}_s(y)] \tag{198}$$

Applying the tip boundary conditions to Eq. (154), non-dimensionalazing results in:

$$\mp v'(\pm 1)-\epsilon\lambda(v^4(\pm 1))=-\epsilon\lambda[\underbrace{\delta^4}_{background}+\underbrace{\hat{G}_y^{\pm}}_{source\ top/bottom}] \tag{199}$$

Now Eq. (198) is divided through by the aerial aspect ratio (α) and this leads to:

$$\frac{1}{\alpha}v''-\frac{\alpha}{\alpha}\lambda\beta(y)v^4=\frac{\alpha}{\alpha}\lambda\beta(y)[\delta^4+\hat{G}_s(y)] \tag{200}$$

A singular perturbation expansion is applied on the aspect ratio of the beam (α); it is noted that the expansion is valid only well removed from the tip boundaries, which are the regions of the outer solution. So assuming α >>1 and that one is well-away from the tips at y=±l

$$v(y,\alpha)=v_0(y)+\frac{1}{\alpha^{\mu}}v_1(y)+.... \tag{201}$$

Expanding on the order of unity the following is obtained:

$$O(1)\rightarrow-\beta(y)v_0^4=\beta(y)(\underbrace{\delta^4+\hat{G}_s(y)}_{u}) \quad ; \quad v_0(y)=u^{1/4}(y) \tag{202}$$

Choosing the order of mu at unity (μ=1) and expanding w.r.t. to 1/α yields for the outer expansion:

$$v_1=\frac{1}{4\lambda\beta}\frac{v_0''}{v_0^3} \tag{203}$$

From Eq.(202) the derivatives of expansion are obtained

$$v_0'=\frac{1}{4}u^{-3/4}\cdot u^1 \quad ; \quad v_0''=\frac{-3}{16}u^{-7/4}\cdot(u')^2+\frac{1}{4}u^{-3/4}u'' \tag{204}$$

Placing Eq.(204) into Eq.(203) yields:

$$v_1=\frac{1}{16\lambda\beta}\{u''-\frac{3}{4}\frac{(u')^2}{u}\}/u^{3/2} \tag{205}$$

Now with $V(y,\alpha) = V_0 +(1/\alpha)V_1+ O(1/\alpha^2)$.... this leads to

$$u(y)=\delta^4+\hat{G}_s(y) \tag{206}$$

Proceeding with the inner expansion now, where y is very close to the beam tips (e.g. y=-

1) and the influence of the boundary layer effects are significant the coordinate y is defined as per:

$$y \equiv -1 + \eta/\sqrt{\alpha} \tag{207}$$

so that the non-dimensional temperature is now

$$V(\eta) = v(-1 + \eta/\sqrt{\alpha}) \quad . \tag{208}$$

Using the chain rule yields for V' and V" ($\frac{dv}{dy} = \frac{dV}{d\eta} \cdot \frac{d\eta}{dy}$) the following:

$$V' = v'\sqrt{\alpha} \qquad ; \qquad V'' = \alpha v'' \quad . \tag{209}$$

Now

$$\alpha V'' - \alpha \lambda \beta(-1 + \eta/\sqrt{\alpha}) V^4 = \alpha \lambda \beta(y(\eta)) u(y(\eta)) \tag{210}$$

and

$$\sqrt{\alpha} V'(0) - \epsilon \lambda V^4(0) = -\epsilon \lambda \{\delta^4 + G_y^-\} \quad . \tag{211}$$

Perturbing on alpha as per:

$$V(\alpha;\eta) \approx V_0(\eta) + \frac{1}{\sqrt{\alpha}} V_1(\eta) + \ldots \tag{212}$$

The first two terms of expansion yield for O(1):

$$V_0'' - \lambda \beta(-1) V_0^4 = -\lambda \beta(-1) u(-1) \tag{213}$$

Recognizing that the flux at the tip is zero (V'(0) = 0) the unity expansion is a constant as per:

$$V_0(\eta) = u(-1)^{1/4} \tag{214}$$

For the order of 1 over the square root of alpha (O(1/√α);

$$V_1'' - \lambda \beta(-1) 4 V_0^{\,3} V_1 = -\lambda \beta(-1) u'(-1) \eta \tag{215}$$

To simplify this let $Q^2 = 4 \lambda \beta(-1)(u(-1))^{3/4}$ so that

$$V_1(\eta)=Ae^{Q\eta}+B^{-Q\eta}+\frac{u'(-1)}{4(u(-1))^{3/4}}\eta \quad . \tag{216}$$

Now at the tip the flux condition is imposed at (η=0) so that

$$V'(0)-\epsilon\lambda V_0^4(0)=-\epsilon\lambda\{\delta^4+G_y^-\} \quad . \tag{217}$$

This combined with the first order expansion (where $V_0(\eta) = \{\delta+G_s(\eta)\}$, leads to:

$$v_1(0)=-\epsilon\lambda\{G_y^-+G_y-V_0^4(0)\}=-\epsilon\lambda\{G_y^--G_s(-1)\} \quad . \tag{218}$$

Now

$$V'_1(0)=Q(A-B)=\frac{-\epsilon\lambda}{Q}\{G_y^1-G_s(-1)\}-\frac{u'(-1)}{4Q[u(-1)]^{3/4}} \tag{219}$$

Note that because the effective emissivity,β, is piecewise constant (β(-1)=ε, β'(-1)=0) one can reduce using:

$$Q^2=4\lambda\beta(-1)[u(-1)]^{3/4} \quad \rightarrow \quad Q=2\sqrt{\epsilon\lambda}[u(-1)]^{3/8}\geqslant 0 \tag{220}$$

so that

$$B=A+\frac{\sqrt{\epsilon\lambda}}{2}[u(-1)]^{-3/8}\{G_y^--G_s(-1)\}+\frac{u'(-1)}{8\sqrt{\epsilon\lambda}[u(-1)]^{9/8}} \quad . \tag{221}$$

So the lower inner solution is now:

$$V(\eta;\alpha)\approx[u(-1)]^{1/4}+\frac{1}{\sqrt{\alpha}}\left(Ae^{Q\eta}+Be^{-Q\eta}+\frac{u'(-1)}{4[u(-1)]^{3/4}}\eta\right)+O\left(\frac{1}{\alpha}\right)+... \tag{222}$$

The inner solution process is applied similarly for the upper tip where y=+1, and where y is defined in terms of stretched coordinate ξ as per $y=1-\xi/\sqrt{\alpha}$. Similarly, $W(\xi) = v(y) = v(1-\xi/\sqrt{\alpha})$. Without elaboration and similar to the expansion from the lower tip, doing so from the upper tip yields for O(1) on $W(\xi;\alpha)\approx W_0(\xi)+\frac{1}{\sqrt{\alpha}}W_1(\xi)+O\left(\frac{1}{\alpha}\right)+...$:

$$W_0(\xi)=[U(1)]^{1/4} \tag{223}$$

and $O(1/\sqrt{\alpha})$:

$$W(\xi)=Ce^{R\xi}+De^{-R\xi}-\frac{1}{4}[u(1)]^{-3/4}u'(1)\xi \tag{224}$$

where

$$R^2=4\lambda\beta(1)[u(1)]^{3/4}\geqslant 0 \quad \rightarrow \quad R=2\sqrt{\epsilon\lambda}[u(1)]^{3/8} \quad . \tag{225}$$

Again exploiting piecewise linearity on β, the solution for W is

$$V(\eta;\alpha)\approx[u(-1)]^{1/4}+\frac{1}{\sqrt{\alpha}}\left(Ae^{Q\eta}+Be^{-Q\eta}+\frac{u'(-1)}{4[u(-1)]^{3/4}}\eta\right)+O\left(\frac{1}{\alpha}\right)+... \tag{226}$$

where

$$D=C+\frac{1}{2}\sqrt{\epsilon\lambda}[u(1)]^{-3/8}\{G_y^+ +G_s(1)\}-\frac{1}{8\sqrt{\epsilon\lambda}}[u(1)]^{-9/8}u'(1) \quad . \tag{227}$$

Now the inner and outer solutions need to be matched so the outer expansion in terms of the inner variable at y=-1 yields:

$$\begin{aligned} V(-1+\eta/\sqrt{\alpha};\alpha)&=[u(-1+\eta/\sqrt{\alpha})]^{1/4}+\frac{1}{\alpha}\frac{1}{16\lambda\beta(-1+\eta/\sqrt{\alpha})}\{u''(-1+\eta/\sqrt{\alpha})-\frac{3}{4}\frac{(u')^2}{u}\}/u^{3/2} \\ &\sim \quad [u(-1)]^{1/4}+\frac{1}{4}[u(-1)]^{3/4}u'(-1)\eta/\sqrt{\alpha}+O\left(\frac{1}{\alpha}\right) \end{aligned} \tag{228}$$

Now taking the limit of Eq.(228) as $\eta \rightarrow 0$ results in:

$$\begin{aligned} lim_{\eta\rightarrow 0}[V(-1+\eta/\sqrt{\alpha};\alpha)-V(\eta;\alpha)]&=lim_{\eta\rightarrow 0}\{[u(-1)]^{1/4}+\frac{1}{4}[u(-1)]^{-3/4}u'(-1)\eta/\sqrt{\alpha}-[u(-1 \\ &-lim_{\eta\rightarrow 0}\{\frac{1}{\sqrt{\alpha}}\left[Ae^{-Q\eta}+Be^{-!\eta}+\frac{1}{4}[u(-1)]^{-3/4}u'(-1)\eta\right]+O\left(\frac{1}{\alpha}\right)\} \end{aligned} \tag{229}$$

If Q≥0, then choose A=0 and,

$$B=\frac{\sqrt{\epsilon\lambda}}{2}[u(-1)]^{-3/8}\{G_y^- - G_s(-1)\}+\frac{u'(-1)}{8\sqrt{\epsilon\lambda}[u(-1)]^{9/8}} \tag{230}$$

Now matching the outer expansion in terms of the inner variable at y=1 is performed

$$\begin{aligned} V(1-\xi/\sqrt{\alpha};\alpha) &= [u(1-\xi/\sqrt{\alpha})]^{1/4}+\frac{1}{\alpha}\frac{1}{16\lambda\beta(1-\xi/\sqrt{\alpha})}\{u''(1-\xi/\sqrt{\alpha})-\frac{3}{4}\frac{(u')^2}{u}\}/u^{3/2} \\ &\sim \quad [u(1)]^{1/4}+\frac{1}{4}[u(1)]^{3/4}u'(1)\xi/\sqrt{\alpha}+O\left(\frac{1}{\alpha}\right) \end{aligned} \tag{231}$$

And taking the limit

$$\begin{aligned} lim_{\xi\to 0}[W(1-\xi/\sqrt{\alpha};\alpha)-W(\xi;\alpha)] &= lim_{\xi\to 0}\{[u(1)]^{1/4}-\frac{1}{4}[u(1)]^{-3/4}u'(1)\xi/\sqrt{\alpha}-[u(1)]^{1/4}\} \\ &-lim_{\xi\to 0}\{\frac{1}{\sqrt{\alpha}}\left[Ce^{-R\xi}+De^{-R\eta}-\frac{1}{4}[u(1)]^{-3/4}u'(1)\eta\right]+O\left(\frac{1}{\alpha}\right)\} \end{aligned} \tag{232}$$

Now choosing C = 0 the following is obtained for D,

$$D=\frac{\sqrt{\epsilon\lambda}}{2}[u(1)]^{-3/8}\{G_y^+ - G_s(1)\}-\frac{u'(1)}{8\sqrt{\epsilon\lambda}[u(1)]^{9/8}} \quad . \tag{233}$$

Now for a uniform expansion, where $v_u = v_{outer} + v_{inner} - v_{match}$, the solutions are put together

$$v_u(y)=u^{1/4}(y)+[u(-1)]^{1/4}+\frac{1}{\sqrt{\alpha}}\left(Be^{-Q\eta}+\frac{u'(-1)}{4u(-1)^{3/4}}\eta\right)+[u(1)]^{1/4}+\frac{1}{\sqrt{\alpha}}\left(Be^{-R\xi}+\frac{u'(1)}{4u(1)^{3/4}}\xi\right) \tag{234}$$

And with terms canceling removed

$$v_u(y)=u^{1/4}(y)+\frac{1}{\sqrt{\alpha}}\{B\exp[-Q\sqrt{\alpha}(y+1)]+Dexp[-R\sqrt{\alpha}(1-y)]\}+O\left(\frac{1}{\alpha}\right) \tag{235}$$

.

So in summary the following is the solution for the non-dimensional temperature:

$$v_{uniform}(y)=u^{1/4}(y)+\frac{1}{\sqrt{\alpha}}\{B\ \exp[-Q\sqrt{\alpha}(y+1)]+D\ \exp[-R\sqrt{\alpha}(1-y)]\}+\frac{1}{\alpha}V_1(y)+O\left(\frac{1}{\alpha}\right) \tag{236}$$

where

$$v_1(y)=\frac{1}{16\lambda\beta(y)}\{u''-\frac{3}{4}\frac{(u')^2}{u}\}u^{-3/2} \tag{237}$$

$$u(y)\equiv\delta^4+\hat{G}_s(y) \tag{238}$$

The terms in Eq. (236) are as follows:

$$B=\frac{\sqrt{\epsilon\lambda}}{2}[u(-1)]^{-3/8}\{G_y^- -\hat{G}_s(-1)\}+\frac{u'(-1)}{8\sqrt{\epsilon\lambda}[u(-1)]^{9/8}} \tag{239}$$

$$Q=2\sqrt{\epsilon\lambda}[u(-1)^{3/8}] \tag{240}$$

$$D=\frac{\sqrt{\epsilon\lambda}}{2}[u(1)]^{-3/8}\{G_y^+ -\hat{G}_s(1)\}-\frac{u'(1)}{8\sqrt{\epsilon\lambda}[u(1)]^{9/8}} \tag{241}$$

$$R=2\sqrt{\epsilon\lambda}[u(1)^{3/8}] \tag{242}$$

and

$$\beta(y)=\epsilon(y)\frac{K_{TI}}{K_s(y)} \quad ; \quad \lambda=l\frac{\sigma}{K}T_r^3 \quad ; \quad \alpha=\frac{(t+w)l}{t\cdot w} \quad . \tag{243}$$

Expressing the non-dimensional variation in a canonical form that is grouped by the order of expansion yields the following:

$$v(y)=\{\underbrace{\delta^4+\hat{G}_s(y)}_{\text{source radiation = u(y)}}\}^{1/4}+\frac{1}{\sqrt{\alpha}}(\textit{boundary})+\frac{1}{\alpha}(\textit{surface prop. variations}) \tag{244}$$

From this it is clear the most dominating influence on the non-dimensional temperature distribution is the imposed radiation incident on the beam as the leading term shows. Of next most in influence are the boundary variations from the tips. Least in influence is the surface property variations in the beam, most notably the difference in the intensity of emissivity from the beam versus the coating.

$$Q = R = 2\sqrt{\epsilon\lambda}\left[u(\pm 1)\right]^{3/8} \quad ; \quad v = u^{1/4} \tag{245}$$

This is the inner solution and yields insight that the temperature distribution ($v_0(y)$) is dominated by the incident irradiation distribution ($\hat{G}_s(y)$) as opposed to surface emissivity variations or beam conductivity variations. Indeed, the temperature variation down the beam's length (v) is 1/4 the power of the background temperature and surface irradiation variance ($u = \{\delta^4 + \hat{G}_s(y)\}$).

Equation (236) was very useful for the early conceptual design of the chamber. It was used to evaluate the departure from idea that using end-to-end finite lamp sources would have on the temperature profile. It also allowed for a quick sizing of the likely power settings when going from 100W to 200W lamps prior to building the calibration curve for them.

2. Uniqueness Proof of Thermal Distribution in Solution

Baker (Baker, 2008) established uniqueness and existence to the solution of the temperature distribution in the beam. Not only is this important for establishing the uniqueness of the solution, it also provides confidence in the numerical model, in that it will converge towards the same steady state condition, irregardless of the initial state of the beam-coating system. Following the geometry and the assumptions established in Section 2.4.1 and the previous Appendix, he attempts proof by contradiction.

Assumptions: suppose there exists a solution T_1 and T_2 that are both valid solutions such that $T_1 \neq T_2$. It is noted that T_1, T_2, and the enclosing surroundings, T_a, are all absolute temperatures. Fourier's Law applies for heat flow and therefore the Laplace equation for heat distribution within a body. Define $V \equiv T_1 - T_2$, then taking the Laplacian of V, one obtains:

$$\nabla^2 V = \nabla^2 T_1 - \nabla^2 T_2 = 0 \tag{246}$$

In a similar way, dotting the gradient of V by the surface normals scaled to the surface conductivities results in:

$$-\hat{n} \cdot K_s \vec{\nabla} V = -\hat{n} \cdot K_s \vec{\nabla} T_1 + \hat{n} \cdot K_s \vec{\nabla} T_2 \tag{247}$$

Replacing the vectorial conduction surface thermal flux terms with their surface radiation equivalents (the body enclosed in a surrounding, ambient isothermal surrounding at T_a) and using the Conservation of Energy and Stephan-Boltzmann laws:

$$-\hat{n} \cdot K_s \vec{\nabla} V = \{\epsilon \sigma (T_1^4 - T_a^4) - \epsilon G_s\} - \{\epsilon \sigma (T_2^4 - T_a^4) - \epsilon G_s\} = \epsilon \sigma (T_1^4 - T_2^4) \quad . \tag{248}$$

Eq. (246) multiplied by through by V, taking the temperature difference on both sides and applying the identity, $\vec{\nabla}\cdot f\,\vec{\nabla} g=\vec{\nabla} f\cdot\vec{\nabla} g+f\,\nabla^2 g$, the Laplace expansion leads to:

$$0=V(\nabla^2 V) \quad \rightarrow \quad 0=V(\nabla^2 V)=\vec{\nabla}\cdot V\,\vec{\nabla} V-\left|\vec{\nabla} V\right|^2 \tag{249}$$

Recognizing the identity in Eq. (253) and placing it into Eq. (249) yields:

Now, integrating across the solid body volumetrically leads to:

$$0=\int_D V\,\nabla^2 V\,dV=\int_D \vec{\nabla}\cdot V\,\vec{\nabla} V\,dV-\int_D \left|\vec{\nabla} V\right|^2 dV \tag{250}$$

Employing the Divergence Theorem, the left term of the l.h.s. of Eq.(250) is converted from a volume to a surface integral. The r.h.s. is zero due to the condition of steady state and conservation of energy, this leads to:

$$0=\underbrace{\int_{\partial D} \vec{n}\cdot V\,\vec{\nabla} V\,dS}_{surface\ fluxes\ \ of\ heat}-\underbrace{\int_D \left|\vec{\nabla} V\right|^2 dV}_{internal\ storage\ \ of\ heat} \tag{251}$$

Rearranging Eq.(251), and enforcing that condition that the energy content in the domain must be positive-definite, one obtains:

$$0\leqslant\int_D \left|\vec{\nabla} V\right|^2 dV=\int_{\partial D} \vec{n}\cdot V\,\vec{\nabla} V\,dS=\int_{\partial D} V\,\frac{-\epsilon\sigma}{K_s}(T_1{}^4-T_2{}^4)\,dS \tag{252}$$

or

$$\int_{\partial D} \vec{n}\cdot V\,\vec{\nabla} V\,dS=\int_D \left|\vec{\nabla} V\right|^2 dV\geqslant 0 \quad . \tag{253}$$

Expanding the r.h.s. of Eq.(253) with the Stephan-Boltzmann Law integrated across the surface, substituting in for V, and algebraically expanding the term (T_1^4-T_2^4) (e.g. = (T_1-T_2)(T_1+T_2)(T_1^2+T_2^2)) leads to:

$$\int_{\partial D} \frac{-\epsilon\sigma}{K_S} V\,(T_1^4 - T_2^4)\,dS = -\int_{\partial D} \frac{\epsilon\sigma}{K_S} \underbrace{(T_1 - T_2)^2}_{\geq 0} \underbrace{(T_1 + T_2)}_{\geq 0} \underbrace{(T_1^2 + T_2^2)}_{\geq 0} dS \tag{254}$$

Recognizing that T_1 and T_2 are both absolute temperatures (e.g. Rankine or Kelvin) and so therefore are positive-definite, as a result $(T_1\text{-}T_2)^2$, (T_1+T_2), and $(T_1^2+T_2^2)$ are all positive definite as well. Thus the l.h.s. of Eq. (252) is negative semi-definite while the r.h.s. is positive semi-definite. For equality to hold, it is required that both integrals to vary. Thus $T_1 = T_2$ on the surface from Eq. (254) and:

$$\left|\vec{\nabla} V\right|^2 \quad \rightarrow \quad \vec{\nabla} V = 0 \qquad , \qquad \forall\, x \in D \quad . \tag{255}$$

As a result, $T_1 = T_2$ everywhere in the interior of the solid. At this point a contradiction exists with the assumption that $T_1 \neq T_2$ and one has arrived at a contradiction with the assumptions. So $T_1=T_2$ in D and the solution to the PDE satisfying the non-linear boundary conditions is unique. Q.E.D.

3. Source Code for Finite Difference Heat Transfer Model

This Matlab source code listing is for the 2-D steady-state finite difference model used to model the TBC coated titanium beam. Relevant parameters are called out at the top of the code. Convergence is by manual monitoring of the convergence, operating through definite iteration. This code was developed off of notes by Branam and Bohnert when modeling a Hall Effect thruster with a radiation exchange with interior conduction (Branam, 2008; Bohnert, 2008). It is recognized that determination of the location of the thermal stencil based on a state table would be far more efficient than the nested if-then constructs but the code is still illustrate of the handling or radiation conduction boundaries.

```
%%%%%%%%%%%%%%%%%%%%%%%%%%%%%%%%%%%%%%%%%%%%%%%%%%%%%%%%
%%% Script to solve the heat equation for Titanium Beam with TBC coating
%%% Irradiation BC's on surfaces from line sources
%%%%%%%%%%%%%%%%%%%%%%%%%%%%%%%%%%%%%%%%%%%%%%%%%%%%%%%%
%  AERO 899
%  October 2008
%%% Initialize variables
% This code is attempting to solve the conduction problem in a 2-D domain
% of a mid-center plan slice of a coated beam in
% Two symmetries are exploited to reduce to this a 2-D 1/2-domain problem
%  1) The mid plane symmetry of the beam across the width (3/4" dimension)
%  2) The adiabatic surface down the middle of the longitudinal plane of the beam at
%  the mid-thickness (0.0063" length)
%
% Procedural note iterations across x (i-index) and y (j-index) dimensions
% always outer loop on i, from left to right, and inner on j, from down to
% up. (1,1) node is at lower left of grid domain.
%
% Bookkeeping of Temperature will be in a 1-D vector of Temperatures to
% submit the form A_ij*t_i + B_ij*(t_i)^4 = C_i for solution
%
clc; clear all;
max = 500; % maximum iterations to convergence
q_in = 0.01;  % set flux in BC, temporary (W/m^2 K)
% Geometry of System
coating = 1; % (Is YSZ coating present (0 = no coating, 1 = YSZ coating)
L_b = 8.000*(2.54/1)*(1/100);  % (8.0) length of TI beam (y-direction)
L_c = 0.25*L_b;  % length of YSZ coating patch (y-direction)
y_c = 0.50*L_b;  % location of center of YSZ coating patch (y-direction)
yc_up = (1/L_b)*( (1/2)*L_c + y_c) % fractional location of coating upper
yc_lw = (1/L_b)*(-(1/2)*L_c + y_c) % fractional location of coating lower
t_b = 0.063*(2.54/1)*(1/100);  % (0.063) thickness of TI beam (x-direction)
t_c = 0.008*(2.54/1)*(1/100);  % thickness of YSZ coating (x-direction)
W = 0.750*(2.54/1)*(1/100);   % width of TI beam and coating (z-direction)
% Physical properties of interest
k_ti = 29.0; % conductivity of titanium in W/(m deg K)
k_c = 2.0; % 2.0 conductivity of titanium in W/(m deg K)
sig = 5.67e-08; % Stephan-Boltzmann constant in W/(m^2 K^4)
I = 1370.0*10.0 % Irradiance of Lamps in W/m^2
I_bot = I*1; % Bottom Tip Irradiance of Lamps in W/m^2
I_top = I*1; % Top Tip Irradiance of Lamps in W/m^2
eps_c = .3;
```

```
%eps_c = 0.3; % emissivity of YSZ
alp_c = eps_c; % absorptivity of YSZ (invoke Kirchhoff's law)
eps_ti = .3;
%eps_ti = 0.3; % emissivity of TI
alp_ti = eps_ti; % absorptivity of TI (invoke Kirchhoff's law)
% Nodal array setup
scale = 1;
Nx_b = 5*scale; % (5) number of nodes through the TI beam thickness (x-dir)
Nx_c = 5*scale; % (5) number of nodes through the coating thickness (x-dir)
Nx = Nx_b + Nx_c - 1  % number of nodes through the system thickness (x-dir)
dx_b = t_b/(Nx_b - 1); % cell size delx in beam
%dx_c = t_c/(Nx_c - 1); % cell size delx in coating
dx_c = dx_b;
alpha = 10.
dy = alpha*dx_b;
Ny = int16(L_b/dy);  %650*scale  % (61500) number of nodes along the TI beam length (y-dir)
Ny_c_u = ceil(yc_up*Ny);
Ny_c_l = floor(yc_lw*Ny);
%dy = L_b/(Ny-1); %
% Set up parameters to problem
% Temperature non-dimensionalization limits
T_max = 450.0+273.0             % Normally (450+273)
T_min = 273.0                   % Normally (273)
T_surr = T_min;
Nodes = Nx*Ny
for j = 1:1:Ny ; for i=1:1:Nx ; Ti(i,j)=T_min ; end ; end % Initial guess is that Ti is 0.0 everywhere.
% Ti = ones(Nx+1,Ny+1);
% Everything is initialized proceed into outer loop
% for t = 1:1:max
T = zeros(Nx,Ny);
T = T + 273 + 0.0*(I/sig + T_surr^4)^(1/4); Tn = T;
err = 100.0;t = 0.0;
%%
T_his = zeros(2000,1);
% First, Set up interior properties of conductivity and initial temp field
radgo = 1;
for o = 1:1:2000000;  % Iterate to 2 million iterations

for j = 1:1:Ny;
for i = 1:1:Nx;

    for k = 1:1:radgo; % when radiation is active set to 1000-10000

    if j == 1 & i < Nx_b;  %% FREE SPACE
        T(i,j) = T_surr;
    elseif j == 1 & i == Nx_b; %% LL CORNER of TI
        q_in1 = eps_ti*sig*(T_surr^4-T(i,j)^4)+eps_ti*I_bot;
        q_in2 = eps_ti*sig*(T_surr^4-T(i,j)^4)+eps_ti*I;
        T(i,j) = (1/(dx_b/dy+ dy/dx_b))*((dx_b/dy)*T(i,j+1) + (dy/dx_b)*T(i+1,j)+ 2*q_in1*dx_b/k_ti + 2*q_in2*dy/k_ti);
    elseif j == 1 & (i > Nx_b &  i < Nx); %% LOWER EDGE of TI
        q_in=eps_ti*sig*(T_surr^4-T(i,j)^4)+eps_ti*I_bot;
    T(i,j)=(k_ti*dy/dx_b/2*(T(i+1,j)+T(i-1,j))+k_ti/dy*dx_b*T(i,j+1)+q_in*dx_b)/(k_ti*(dx_b/dy+dy/dx_b));

    elseif j == 1 & i == Nx; %% LR CORNER of TI
        T(i,j) = T(i,j+1);
        q_in1 = eps_ti*sig*(T_surr^4-T(i,j)^4)+eps_ti*I_bot;
T(i,j) = (1/(dx_b/dy+ dy/dx_b))*((dx_b/dy)*T(i,j+1) + (dy/dx_b)*T(i-1,j)+ 2*q_in1*dx_b/k_ti);

    elseif (j>1 & j< Ny_c_l) & (i < Nx_b); %% FREE SPACE
        T(i,j) = T_surr;
    elseif (j>1 & j< Ny_c_l) & (i == Nx_b); %% LEFT EDGE of TI w/RADIATION
        for p = 1:1:100;
q_in=eps_ti*sig*(T_surr^4-T(i,j)^4)+eps_ti*I;
T(i,j)=(k_ti*dx_b/dy/2*(T(i,j+1)+T(i,j-1))+k_ti/dx_b*dy*T(i+1,j)+q_in*dy)/(k_ti*(dx_b/dy+dy/dx_b));
        end;
     elseif (j>1 & j< Ny_c_l) & ((i > Nx_b) & (i < Nx)); %% INTERIOR TI
T(i,j) = 1/(2*((dx_b/dy)+(dy/dx_b)))*((dy/dx_b)*(T(i,j+1)+T(i,j-1))+(dx_b/dy)*(T(i+1,j)+T(i-1,j)));
    elseif (j>1 & j< Ny_c_l) & ((i > Nx_b) & (i == Nx)); %% ADIABATIC WALL
            T(i,j) = 1/(2*((dx_b/dy)+(dy/dx_b)))*((dy/dx_b)*(T(i,j+1)+T(i,j-1))+(dx_b/dy)*(2.0*T(i-1,j)));
    elseif ((j == Ny_c_l) & (i == 1)); %% LL CORNER of YSZ w/RADIATION
        T(i,j) = (1/2)*T(i+1,j)+(1/2)*T(i,j+1);
    elseif (j == Ny_c_l) & ((i > 1)& (i < Nx_b)); %% LOWER EDGE YSZ w/RADIATION
        q_in=eps_ti*sig*(T_surr^4-T(i,j)^4)+eps_ti*I_bot;
        T(i,j)=(k_c*dy/dx_c/2*(T(i+1,j)+T(i-1,j))+k_c/dy*dx_c*T(i,j+1)+q_in*dx_c)/(k_c*(dx_c/dy+dy/dx_c));

    elseif (j == Ny_c_l) & (i == Nx_b); %% LR CORNER OF YSZ TO TI w/RADIATION
        T(i,j) = T(i,j+1);
    elseif (j == Ny_c_l) & ((i > Nx_b) & (i < Nx)); %% INTERIOR TI
T(i,j) = 1/(2*((dx_b/dy)+(dy/dx_b)))*((dy/dx_b)*(T(i,j+1)+T(i,j-1))+(dx_b/dy)*(T(i+1,j)+T(i-1,j)));
    elseif (j == Ny_c_l) & ((i > Nx_b) & (i == Nx)); %% ADIABATIC WALL
T(i,j) = 1/(2*((dx_b/dy)+(dy/dx_b)))*((dy/dx_b)*(T(i,j+1)+T(i,j-1))+(dx_b/dy)*(2.0*T(i-1,j)));
    elseif (j > Ny_c_l & j < Ny_c_u) & ((i == 1)); %% L EDGE of YSZ w/RADIATION

        for p = 1:1:1;
        q_in=eps_ti*sig*(T_surr^4-T(i,j)^4)+eps_c*I;
```

```
        T(i,j)=(k_c*dx_c/dy/2*(T(i,j+1)+T(i,j-1))+k_c/dx_c*dy*T(i+1,j)+q_in*dy)/(k_c*(dx_c/dy+dy/dx_c));
        end;

     elseif (j > Ny_c_l & j < Ny_c_u) & ((i > 1)&(i < Nx_b)); %% INTERIOR YSZ
T(i,j) = 1/(2*((dx_c/dy)+(dy/dx_c)))*((dy/dx_c)*(T(i,j+1)+T(i,j-1))+(dx_c/dy)*(T(i+1,j)+T(i-1,j)));

    elseif (j > Ny_c_l & j < Ny_c_u) & (i == Nx_b); %% INTERIOR INTERFACE OF YSZ TO TI
T(i,j) = 1/(2*((dx_c/dy)+(dy/dx_c)))*((dy/dx_c)*(T(i,j+1)+T(i,j-1))+(dx_c/dy)*(T(i+1,j)+T(i-1,j)));

    elseif (j > Ny_c_l & j < Ny_c_u) & ((i > Nx_b) & (i < Nx)); %% INTERIOR TI
T(i,j) = 1/(2*((dx_b/dy)+(dy/dx_b)))*((dy/dx_b)*(T(i,j+1)+T(i,j-1))+(dx_b/dy)*(T(i+1,j)+T(i-1,j)));
    elseif (j > Ny_c_l & j < Ny_c_u) & ((i > Nx_b) & (i == Nx)); %% ADIABATIC WALL
           T(i,j) = 1/(2*((dx_b/dy)+(dy/dx_b)))*((dy/dx_b)*(T(i,j+1)+T(i,j-1))+(dx_b/dy)*(2.0*T(i-1,j)));
    elseif ((j == Ny_c_u) & (i == 1)); %% UL CORNER of YSZ w/RADIATION
        T(i,j) = (1/2)*T(i,j-1)+(1/2)*T(i+1,j);

    elseif (j == Ny_c_u) & ((i > 1)& (i < Nx_b)); %% UPPER EDGE YSZ w/RADIATION
        q_in=eps_ti*sig*(T_surr^4-T(i,j)^4)+eps_ti*I_top;
        T(i,j)=(k_c*dy/dx_c/2*(T(i+1,j)+T(i-1,j))+k_c/dy*dx_c*T(i,j-1)+q_in*dx_c)/(k_c*(dx_c/dy+dy/dx_c));
    elseif (j == Ny_c_u) & (i == Nx_b); %% UR CORNER OF YSZ TO TI w/RADIATION
        T(i,j) = (1/2)*T(i+1,j)+(1/2)*T(i,j-1);
    elseif (j == Ny_c_u) & ((i > Nx_b) & (i < Nx)); %% INTERIOR TI
T(i,j) = 1/(2*((dx_b/dy)+(dy/dx_b)))*((dy/dx_b)*(T(i,j+1)+T(i,j-1))+(dx_b/dy)*(T(i+1,j)+T(i-1,j)));
    elseif (j == Ny_c_u) & ((i > Nx_b) & (i == Nx)); %% ADIABATIC WALL
T(i,j) = 1/(2*((dx_b/dy)+(dy/dx_b)))*((dy/dx_b)*(T(i,j+1)+T(i,j-1))+(dx_b/dy)*(2.0*T(i-1,j)));
    elseif (j>Ny_c_u & j< Ny) & (i < Nx_b); %% FREE SPACE
        T(i,j) = T_surr;
    elseif (j>Ny_c_u & j< Ny) & (i == Nx_b); %% L EDGE of TI w/RADIATION
        for p = 1:1:1;
q_in=eps_ti*sig*(T_surr^4-T(i,j)^4)+eps_ti*I;
T(i,j)=(k_ti*dx_b/dy/2*(T(i,j+1)+T(i,j-1))+k_ti/dx_b*dy*T(i+1,j)+q_in*dy)/(k_ti*(dx_b/dy+dy/dx_b));
        end;
     elseif (j>Ny_c_u & j< Ny) & ((i > Nx_b) & (i < Nx)); %% INTERIOR TI
T(i,j) = 1/(2*((dx_b/dy)+(dy/dx_b)))*((dy/dx_b)*(T(i,j+1)+T(i,j-1))+(dx_b/dy)*(T(i+1,j)+T(i-1,j)));
    elseif (j>Ny_c_u & j< Ny) & ((i > Nx_b) & (i == Nx)); %% ADIABATIC WALL
T(i,j) = 1/(2*((dx_b/dy)+(dy/dx_b)))*((dy/dx_b)*(T(i,j+1)+T(i,j-1))+(dx_b/dy)*(2.0*T(i-1,j)));
    elseif j == Ny & i < Nx_b;  %% FREE SPACE
        T(i,j) = T_surr;
    elseif j == Ny & i == Nx_b; %% UL CORNER of TI
        q_in1 = eps_ti*sig*(T_surr^4-T(i,j)^4)+eps_ti*I_top;
        q_in2 = eps_ti*sig*(T_surr^4-T(i,j)^4)+eps_ti*I;
T(i,j) = (1/(dx_b/dy+ dy/dx_b))*((dx_b/dy)*T(i,j-1) + (dy/dx_b)*T(i+1,j)+ 2*q_in1*dx_b/k_ti + 2*q_in2*dy/k_ti);
    elseif j == Ny & (i > Nx_b &  i < Nx); %% UPPER EDGE of TI
        q_in=eps_ti*sig*(T_surr^4-T(i,j)^4)+eps_ti*I_top;
    T(i,j)=(k_ti*dy/dx_b/2*(T(i+1,j)+T(i-1,j))+k_ti/dy*dx_b*T(i,j-1)+q_in*dx_b)/(k_ti*(dx_b/dy+dy/dx_b));
    elseif j == Ny & i == Nx; %% UR CORNER of TI
        q_in1 = eps_ti*sig*(T_surr^4-T(i,j)^4)+eps_ti*I_top;
T(i,j) = (1/(dx_b/dy+ dy/dx_b))*((dx_b/dy)*T(i,j-1) + (dy/dx_b)*T(i-1,j)+ 2*q_in1*dx_b/k_ti);
    else;
    end;
    To = T;
    end;
end; % of 1
end; % of j

if mod(o,10) == 0.000;
figure(1);
surf(T);
title(sprintf('%s %f ', 'Iteration',o));
end;

if mod(o,1000) == 0.000;       % Store results for T every 1000 iterations
fo = strcat('Tfield',num2str(o));
save(fo, 'T');
%save(fprintf('Tfield%d.csv',o),'T');
end;

end;
%%
%
% Solve for Temperatures ("T") Vector (by Gauss-Sidel Iteration)
%
T_Celsuis = T - 273.0;
```

Matlab 1-D Test Code Fragment for testing forward and backward pseudo-time convergence. This code fragment is explicit formulation.

```
for o = 1:1:1000;
j = 1;
for j = 1:1:Ny;
for i = 1:1:Nx;
    for k = 1:1:100;
    if i == 1;       % Left hand node with radiation
        T(i,j) = (k_ti*T(i,j) + sig*eps_ti*dy*T_surr^4+I*eps_ti*dy)/(k_ti + sig*eps_ti*dy*T(i,j)^3);
    elseif i == Nx;  % right hand adiabatic node
        T(i,j) = T(i-1,j);
    else;            % interior node
        T(i,j) = (1/2)*T(i-1,j) + (1/2)*T(i+1,j);
    end;
    T_his(i,1) = T(i,j);
    end;
end; % of 1
end; % of j
end;
```

4. Chamber Detail Drawings

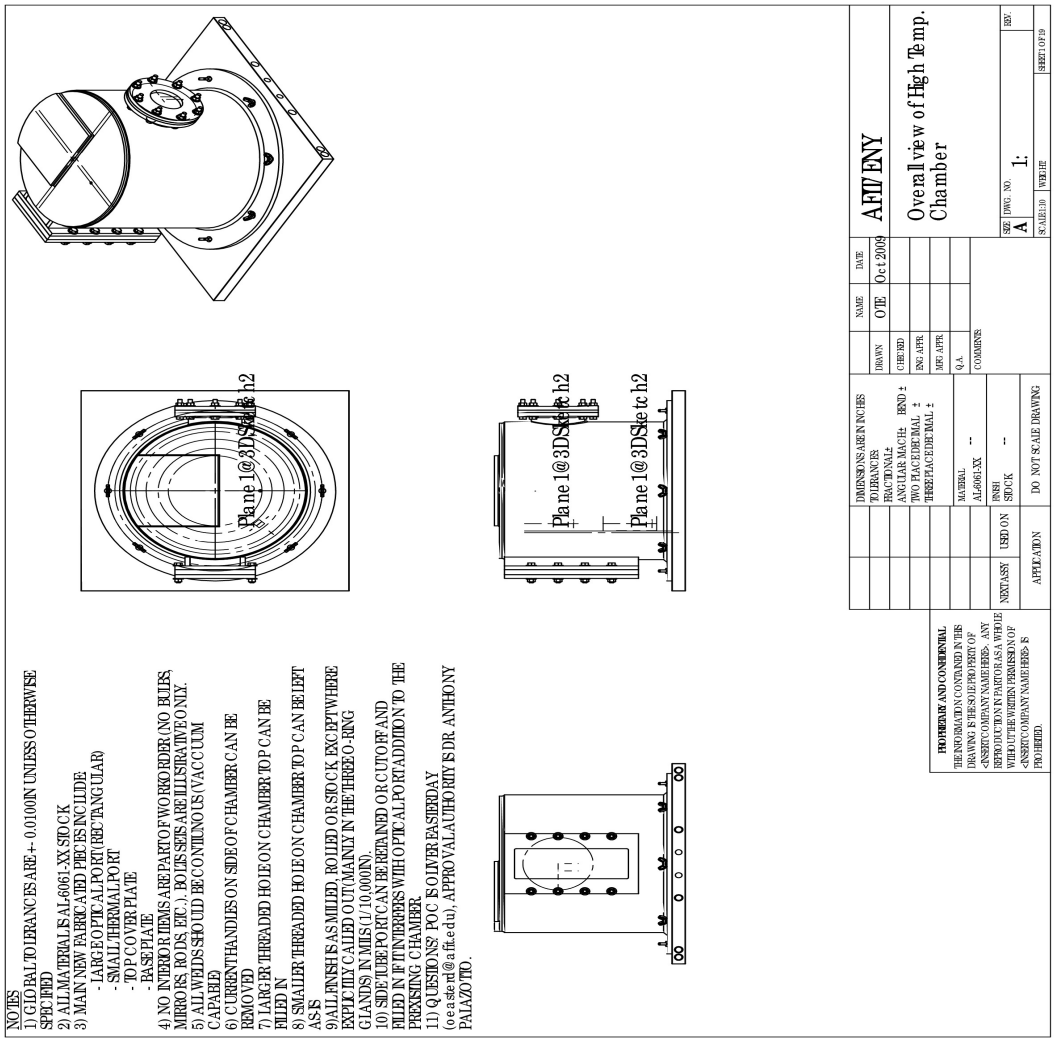


Figure 150: Chamber Assembly – View 1

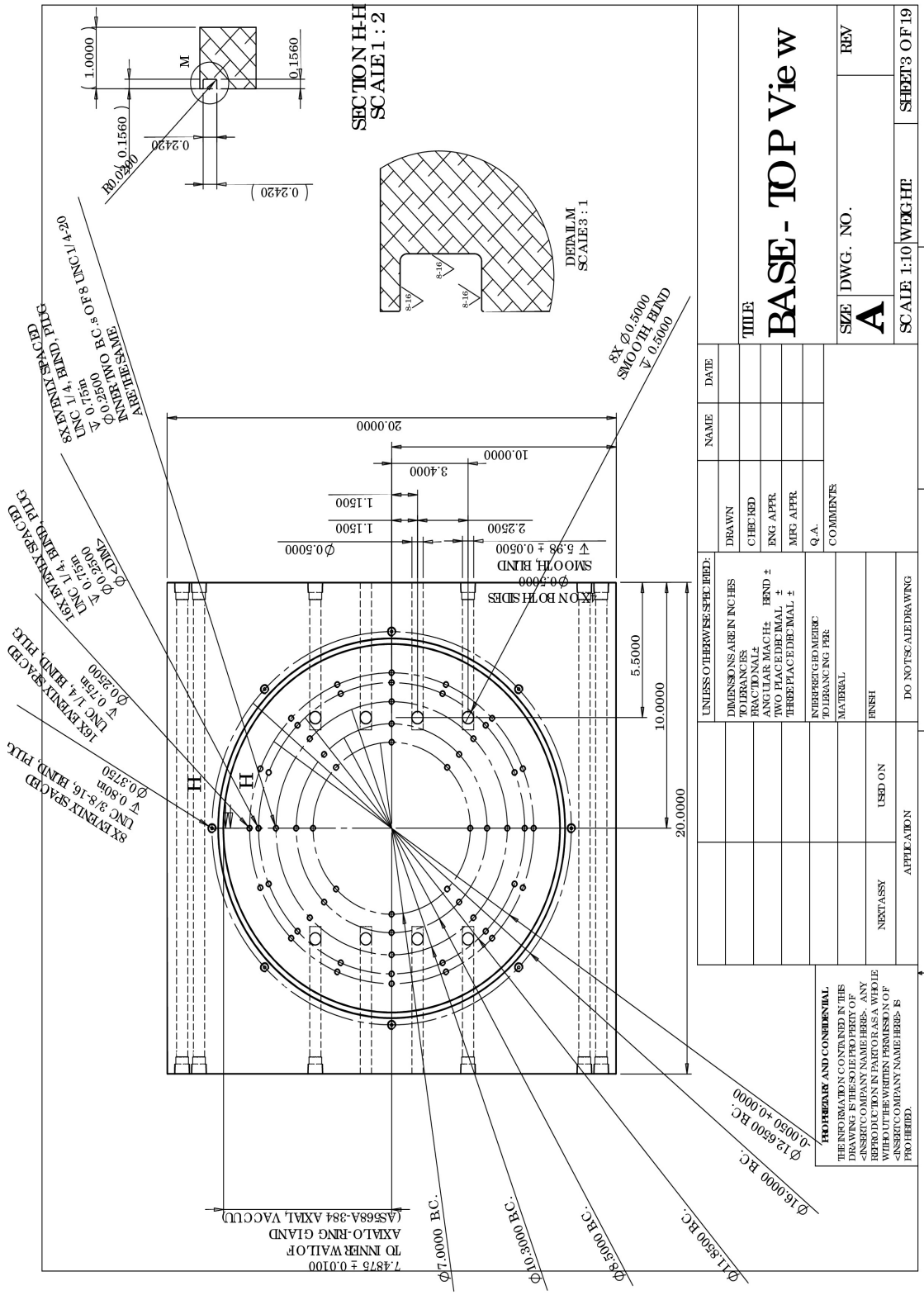


Figure 151: Chamber Assembly – View 2

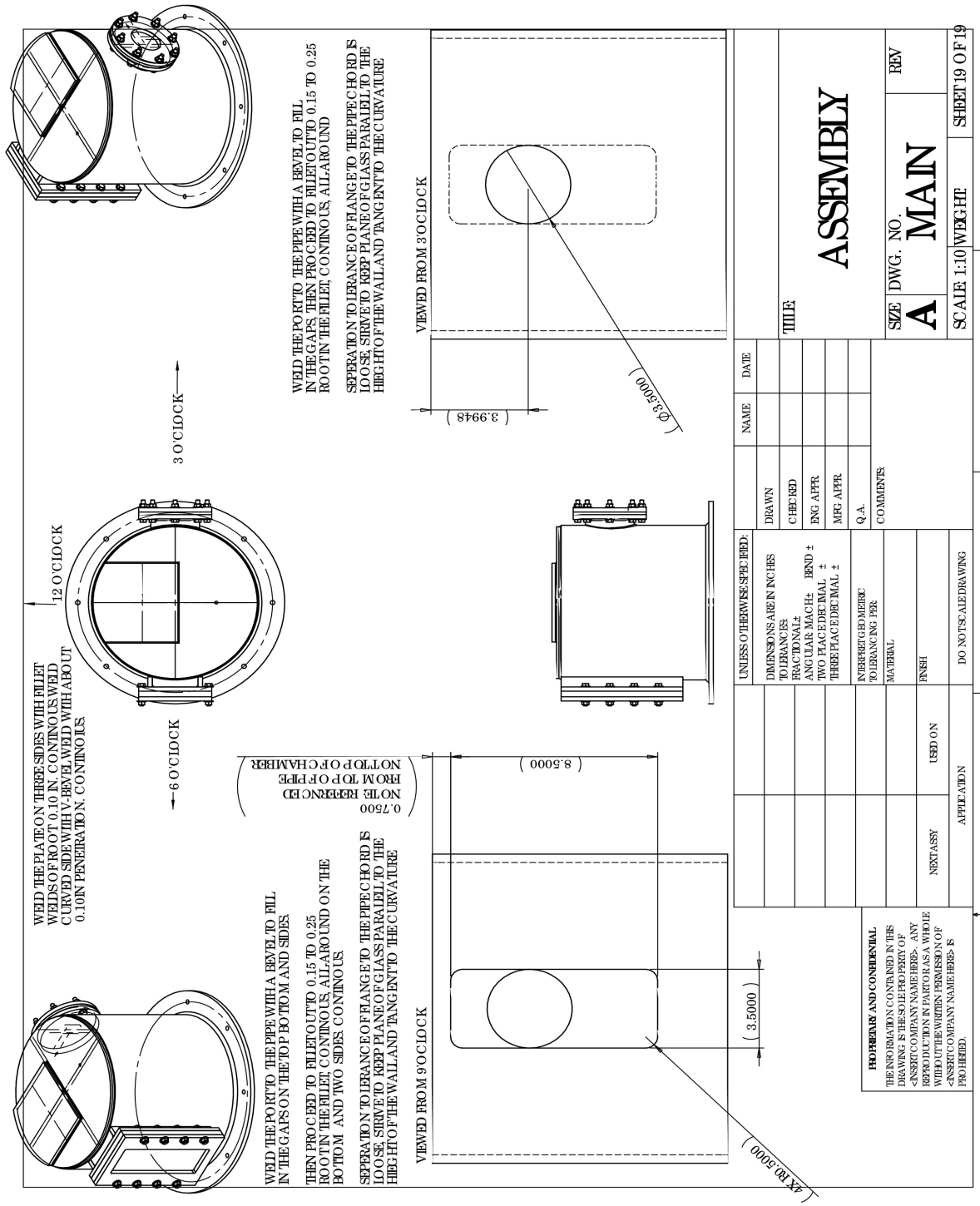


Figure 152: Chamber Assembly – View 3

5. Coated Oberst Beam Theory

Basically the adapted from the method derived by Torvik (Torvik, 2003) and summarized by Reed (Reed, 2007) are:

1) Establish a controlled temperature set point, T, and coil voltage amplitude, $v_c(t)$ for the characterization.

2) Collect: η_{BARE}, ω_{BARE} for the bare Ti-6Al-4V alloy beam using free-free setup.

3) Collect the macroscopic data of η_{SYS}, ω_{SYS} for the YSZ/mag spinel coated beam using the free-free setup. (These steps can be either by 1/2 power bandwidth or log-decrement techniques).

4) Using the data for the coated and associated bare beam, determine stiffness factor using:

$$\frac{\omega_{SYS}^{\ 2}}{\omega_{BARE}^{\ 2}} = \frac{\left[1 + \frac{6tE_C}{hE_{EFF}} T(2, t/h)\right]}{1 + \frac{2t\,\rho_C}{\rho\, h}} \tag{256}$$

5) Determine effective coating modulus, E_C for all strains up to the maximum using:

$$\frac{E_C}{E_{EFF}} = \frac{\left[\frac{\omega_{SYS}^{\ 2}}{\omega_{BARE}^{\ 2}} - 1\right]\frac{h}{6t} + \left[\frac{\omega_{SYS}^{\ 2}}{\omega_{BARE}^{\ 2}}\frac{\rho_c}{3\rho}\right]}{T(2, t/h)} \tag{257}$$

where T(N,t/h) is defined by:

$$T(N,t/h)=\frac{1}{t}\int_{h/2}^{h/2+t}\left[\frac{2z}{h}\right]^N dz=\left(\frac{h}{2t}\right)\frac{\left(1+\frac{2t}{h}\right)^{(N+1)}-1}{N+1} \tag{258}$$

6) Evaluate the energy ratio of the coating to the bare and full system using the stiffness of the coating obtained in 5:

$$\frac{U_C}{U_B+U_F}=6\frac{t\,E_C}{h\,E_{EFF}}T(2,t/h) \tag{259}$$

7) Over a significant range of strain; determine loss factor of bare beam.

8) Repeat 7 for the coated beam with a substrate beam with geometry identical to the bare beam in step 7.

9) Using the method of least squares, determine the log-log fit of the loss factor as a function of the strain for the curves in steps 7 and 8. The bare beam curve will form the "master curve" of the linear behavior of the beam system.

10) Using these fits and the results of step 6 determine the contribution of the coating material to the total system's loss factor at each strain level used in step 8 by means of η_{SYS}, η_{BARE}, the energy ratio of the coating, and:

$$\eta_{SC}=\eta_{SYS}-\frac{\eta_{BARE}}{1+\frac{U_C}{U_B+U_F}} \tag{260}$$

11) Again using least squares, determine the fit to η_{SYS} as a function of strain on a log-log curve plot.

12) Substitute the observed slope, m, into the following equation to find the damping parameter N.

$$N = m + 2 \tag{261}$$

13) Substitute the intercept (η_{OSC}) found in step 11 into:

$$J_\epsilon = \pi \frac{h E_{EFF}}{6t} \frac{\left[1 + 6 \frac{E_C}{E_{EFF}} \frac{twL}{whL}\right] I(2,n)}{T(N, t/h)\, I(N,n)} \eta_{OSC} \tag{262}$$

to find the damping parameter, J.

14) Apply the following equation to find the coefficients for the material loss factor.

$$\eta(\epsilon_a) = \left(\frac{J_\epsilon}{\pi E}\right) \epsilon_a^{N-2} = \eta_0 \epsilon_a^{m} \tag{263}$$

At this point the characterization of the material in accordance with the power law of Lazan. Torvik's method is predicated on the following assumptions:

· Lazan's observation of power law unit damping for structural materials, D, where J_σ and N are empirically determined, where as per (Lazan, 1968):

$$D(\sigma_a) = J_\sigma \sigma_a^{N} \tag{264}$$

· A fully-reversed state of stress in the beam system exists

· Loss factors in the material can be represented by a complex modulus

For partially coated cantilever beams, Torvik modified the procedure. For this the strain energy ration in equation (259) is

$$\frac{U_C}{U_B+U_F}=6\frac{tE_C}{hE_{EFF}}T(2,t/h)\left(\frac{4\frac{L_C}{L}\lambda^2\alpha^2}{1-4\frac{L_C}{L}\lambda^2(1-\alpha^2)}\right) \tag{265}$$

These following assumptions are invoked in this extension to partially coated beams:

· The addition of the coating does not significantly change the distribution of curvature down the beam.

· The interface strain in the coated region is nearly constant and some fraction, λ, of the maximum strain at the root.

· The moment must be continuous across the ends of the coated region

· The interface strain at the edge of the coating is some fraction, α, of the adjacent strain in the uncoated portion of the beam. or the coated and associated bare beam, determine stiffness factor.

6. Derivation of Experimental Free-Free E_C and η_c.

The techniques to capture the effective modulus of the coating, E_C, and the bulk damping loss factor of the TBC material, $\eta_{mat,}$ are developed by Torvik for use on a modified Oberst beam. The Oberst beam is a laminated beam structure, and modified implies the coating is partial down the length, but is the same length above and below the substrate. The bulk of this derivation is from page 125- in Reed (Reed, 2007), and is included here due to its importance in the current study.

Reed determines the displacement at the centerline of the beam (w(L/2,t)) as a time integral of the harmonic velocity (e.g. a cosine function), which upon integration yields the velocity (V(L/2,t)) over the radial frequency ω(t) as per:

$$w\left(\frac{L}{2},t\right)=\frac{V\left(\frac{L}{2},t\right)}{\omega(t)} \tag{266}$$

Defining the scaling function (λ(t)) between the model (X(x, ε(t)), FEA or analytical) and empirical displacement w(x,t) as a function of the location down the length (x) and distance off of the neutral axis (t) of the system:

$$\lambda(t)=\frac{w(x,t)}{X(x,\epsilon(t))} \tag{267}$$

Torvik asserts that the true strain ($\varepsilon(x,t_b,t)$) in the modified Oberst beam is a function of the scaling function and the non-dimensional strain (~ε(x)) from the model which is a function of the location down the length (x), thickness to the surface from the neutral axis through beam (t_b) and coating (t))

$$\epsilon(x,t_b,t)=\lambda(t)\tilde{\epsilon}(x)=t_b\frac{\partial^2 w(x,t)}{\partial x^2}=t_b\lambda(t)\frac{\partial^2 X(x,t)}{\partial x^2} \tag{268}$$

The definition of the loss coefficient (η_{sys}) over one cycle of motion is the ratio of the energy dissipated to (D_{sys}) the work energy needed to accomplish the deformation (U_{sys}) over the course of one cycle, corrected for the radial cycle is per:

$$\eta_{sys}=\frac{1}{2\pi}\frac{D_{sys}}{U_{sys}} \tag{269}$$

Bare beam system energy is dissipated in the fixture (D_f), air friction (D_a), and beam itself (D_b):

$$D_{sys}=D_f+D_a+D_b \tag{270}$$

Elastic energy is likewise stored in fixture (U_f), and the beam's material (U_b):

$$U_{sys}=U_f+U_b \tag{271}$$

This leads to the bare beam system loss coefficient as expressed in:

$$\eta_{bare}=\frac{1}{2\pi}\frac{D_f+D_a+D_b}{U_f+U_b} \tag{272}$$

with the equivalent relation for the coated system is, denoted with the prime ('), and realizing the coated system regions store (U_c') and dissipate energy (D_c), in the coating:

$$\eta_{sys}=\frac{1}{2\pi}\frac{D'_f+D'_a+D'_b+D_c}{U'_f+U'_b+U'_c} \tag{273}$$

Rearranging this by separating out the coating energy loss term, D_c, into its own term results in:

$$\eta_{sys}=\frac{1}{2\pi}\frac{D_c}{U'_f+U'_b+U'_c}+\frac{1}{2\pi}\frac{D'_f+D'_a+D'_b}{U'_f+U'_b+U'_c} \tag{274}$$

and then multiplying through by unity (U_c/U_c) and expanding leads to:

$$\eta_{sys}=\frac{1}{2\pi}\frac{\frac{D_c}{U_c}}{\frac{U'_f+U'_b}{U_c}+1}+\frac{1}{2\pi}\frac{\frac{D'_f+D'_a+D'_b}{U'_f+U'_b}}{\frac{U_c}{U'_f+U'_b}+1} \tag{275}$$

At this point it is asserted that the energy storage ratios of the bare beam is linear (As per Eq. (272)) and is negligibly different as the storage ratio from the same components in the coating clad beam (upper-left numerator in Eq. (275)), which is the loss factor of the bare beam. In other words the curvature of the coating clad beam titanium region is assumed to be very close to that of the bare beam absent of any coating.

This assumption assumes the beams geometric deformation is pretty much equivalent between the bare beam system and the beam material region within the coated system, and invoking the assumption that the strain energy in the beam that is coating clad (U_c') is the same as the bare beam (U_c) which leads to:

$$\frac{1}{2\pi}\frac{D_f+D_a+D_b}{U_f+U_b}\approx\frac{1}{2\pi}\frac{D'_f+D'_a+D'_b}{U'_f+U'_b} \tag{276}$$

Evidence of the reasonableness of this assumption is alluded to in the similarity of the curves generated from some 2-D FEA modal simulations as plotted in Figure 99, Section 4.3.3. Placing Eq. (276) into Eq. (275) and rearranging yields:

$$\eta_{sys}=\frac{1}{2\pi}\frac{\frac{D_c}{U_c}}{\frac{U'_f+U'_b}{U_c}+1}+\frac{1}{2\pi}\frac{\frac{D_f+D_a+D_b}{U_f+U_b}}{\frac{U_c}{U'_f+U'_b}+1} \tag{277}$$

Now the definition of loss coefficients are applied for the bare beam and coating regions:

$$\eta_{sys} = \frac{\eta_c}{\frac{U'_f + U'_b}{U_c} + 1} + \frac{\eta_{bare}}{\frac{U_c}{U'_f + U'_b} + 1} \tag{278}$$

Now for the free-free beam replacing the clamp fixture with thin mono filament wires reduces the energy storage to a very small value (e.g. $U_f \approx 0$). Defining the strain energy ratio (SER) as the elastic energy stored in the coating region to that stored in the beam region of the coated system as per :

$$SER = \frac{U_c}{U'_b} \tag{279}$$

Eq. 279 reduces to:

$$\eta_{sys} = \frac{\eta_{mat}}{\frac{1}{SER} + 1} + \frac{\eta_{bare}}{SER + 1} \tag{280}$$

And finally rearranging results in the "Torvik" equation:

$$\eta_{coat} = \frac{\eta_{sys}(SER + 1) - \eta_{bare}}{SER} \tag{281}$$

Equation (281) is a key relationship to relate the system-level measured quality of damping, η_{sys} , the measured bare beam damping, η_{bare}, and the simulated modal strain energy ratio, SER, from the FEA codes, down to coating-bulk loss coefficient portion of the complex modulus, η_{coat}. For non-linear systems, like the mag spinel and 8-YSZ coated beams, the quantities of η_{sys} and η_{coat} will be time varying in the course of a free decay due

to differing levels of bending strain occurring. In the current studies it was noted that η_{bare}, which is typically constant during a ring-down decay (as the bare beam is linear), is much less than the coated system loss factor η_{sys}. η_{sys} ranged from approximately 0.0005 up to 0.006 in value depending on the initial excitation amplitude, the temperature, and coating thickness. Meanwhile, the loss coefficient of bare titanium, η_{bare}, ranged from 0.00008 to 0.00070; this varying mainly due to temperature. When compared across the range of temperatures, $\eta_{sys} >> \eta_{bare}$, usually by at least an order of magnitude so a good first approximation to the Torvik equation is:

$$\eta_{coat} \approx \underbrace{\eta_{sys}}_{experimental} \underbrace{\left(\frac{SER+1}{SER} \right)}_{numerical} \tag{282}$$

It is also noted elsewhere that large uncertainties in the determination of the bare beam damping will not unduly influence the coating modulus derived (See Section 5.3).

7. Dynamic FEA Details, Information, and Results

The dimensions of the beam models are the same as those measured for the physical specimens as in Figure 84, Section 4.2. The nominal coating thicknesses modeled were 5.7, 8.3 and 12.5mils thick. The bond coating layer was blended into the TBC ceramic layer, this was the assumptions invoked by previous modeling efforts (Pearson, 2008; Deleon, 2009). This was deemed a reasonable assumption based on the relative lack of influence that the bond coat only layer had relative to the bare beam response (See Section 5.4); the bond coat layer is not an even homogeneous sheet on the beam that is capable of sustaining a bending shear flow through it and therefore adding to the bending stiffness of the coated beam system.

As seen in Figure 153 a 1-D, 2-D and 3-D model were all developed in the ABAQUS v6.8-2 FEA commercial code. All of these models, termed in ABAQUS as an "assembly", were approached as a 3-region model (ABAQUS terminology is a "part") consisting of one beam and two coating layers. For the 3-D model four dimensionally accurate ALNICO magnets were added as well, each of these cylinders represents two of the actual ALNICO magnets stacked end-to-end. For the 2-D beam two parts used at the active node that were tuned to have mass and inertial equivalence to the average cross-section through the 3-D model of the magnets. The 1-D beam had a point mass and rotary inertia equivalent to the magnets added at the node coincident to the active node. The two neighboring elements to either side of the node had their cross-sectional areas modified to reflect the additional cross section contributed by the magnet stacks. The beam and

coating parts were all rigidly adhered to each other with a strain compatibility condition across the interface, in ABAQUS this is accomplished as a rigid “tie constraint”. Regardless of the dimensionality of the model, the opposing surfaces were defined as “sets” in ABAQUS and the opposing nodal sets were “tie constrained” together.

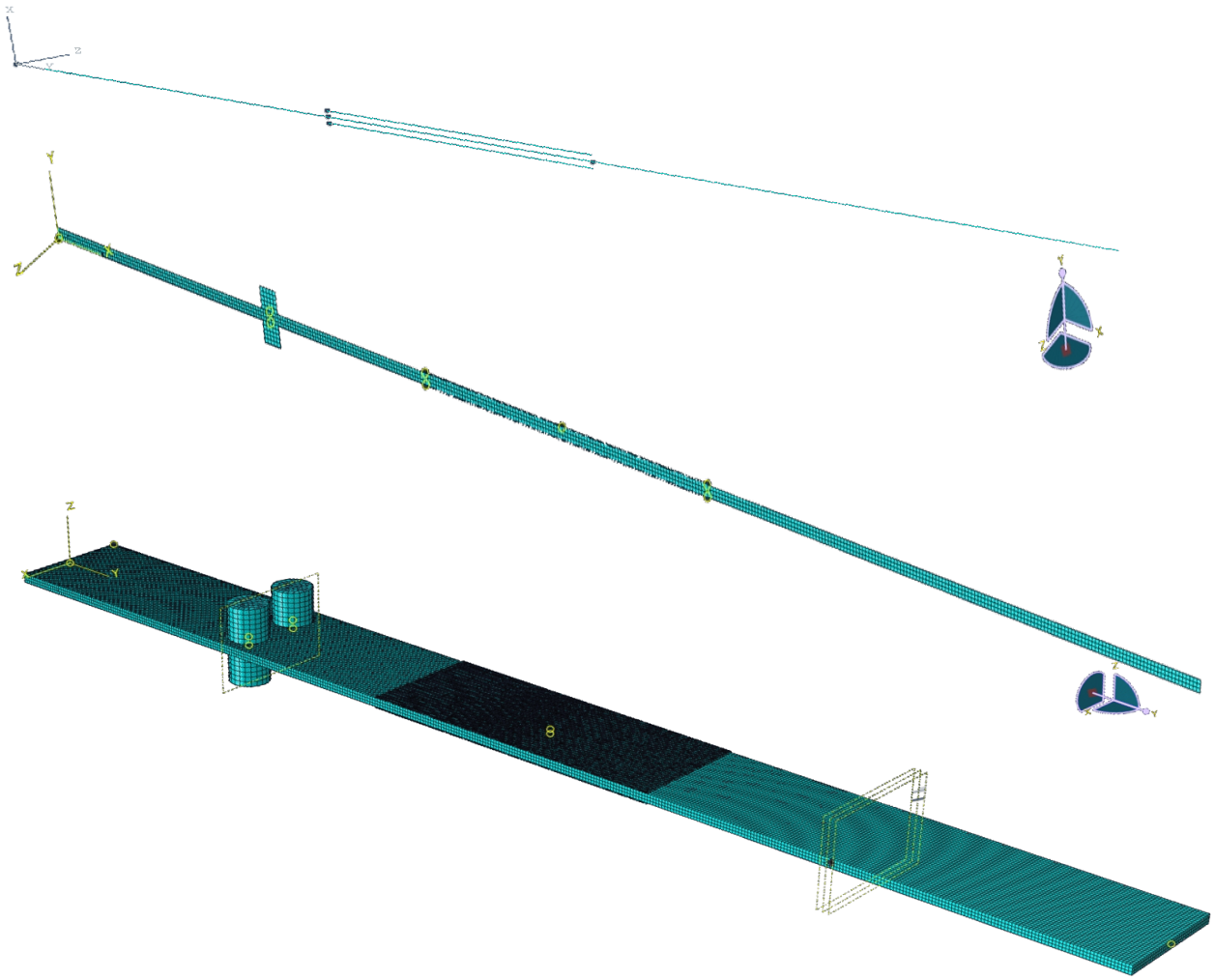


Figure 153: 1-D, 2-D and 3-D FEA modal models for the Polynomial extraction.

The default constitutive properties of materials in the FEA models are listed in Table 14, these include the properties for both the modal dynamic analysis as well as heat transfer related property values used in the FEA heat transfer modeling in Chapter 2.

Table 14: The Material Properties Used in the Simulations

	Units	Sym.	Ti-6Al-4V	8%-YSZ	ALNIC O	Al-6061
Density	kg/m^3	ρ	4420.0	6600.0	7300.0	2700.0
Elastic Modulus	$N/m^2 x10^9$ or Gpa	E	115.5 book (116.4, 109.5, 100.64, and 91.7 at 70/300/600/900degF)	Candidate values = 15.0,30.0,45.0,60.0,90.0 from experimental = 34.0	160.0	68.9
Poisson Ratio	-	ν	0.31	0.31	0.24	0.33
Surface Emissivities	-	ε	0.23 (default)	0.40 (default)	0.8	0.20 (oxidized) 0.02-0.04 (foil)
Conductivity	W/m·deg C	k	6.6	2.2, 2.2, 0.9 (orthotropic)	12.0	167.0
COTE	m/m per degC	α	$9.0x10^{-6}$	$10.5x10^{-6}$	$12.0x10^{-6}$	$10.5x10^{-6}$
Heat Capacity	J/kg·degC	C_p	586.0	400.0	1200.0	896.0

Without elaboration Table 15 summarizes the default mesh density utilized for the 3-D, 2-D, and 1-D models. Table 16 presents the resonance frequency, non-dimensional transverse displacement, and non-dimensional bending strain for the 2-D bare beam model across the four temperatures at which the tests were conducted. It is noted that the later two values are invariant and indicate a mode shape that does not change with the temperature changes, and subsequent modulus softening, of the bare titanium beam.

Table 15: FEA Model Mesh Summary

Coated FEA Beam Default Mesh Details								
Dimension	Part	Elements in long length (approx.)	Elements in long width (approx.)	Elements in thickness	Total Elements	Total Nodes	Type	Notes on Elements
3-D	Beam	420	38	3	47956	65325	C3D8I	3-D, 8-noded brick element, incompatible nodes rejected (e.g. shear locking) and 20-noded reduced integration
	Coating (X2)	168	63	1	10816	22100	C3D8I	
	Magnets (X4)	cylindrical volume			385	1973	C3D20R	
	TOTAL				71128	117417		
2-D	Beam	406		3	1218	1628	CPS4I	2-D, 4-noded, plane stress element, incompatible modes rejected (e.g. shear locking)
	Coating (X2)	508		2	1016	1527	CPS4I	
	Magnets (X2)	cylindrical volume			25	36	CPS4I	
	TOTAL				3300	4754		
1-D	Beam	203			203	204	B31	1-D, 2-noded beam element (linear shape functions), in 3-space (can bend on xx- and yy-)
	Coating (X2)	51			51	52	B31	
	Magnets (X2)	magnets not modeled as a part; point mass and inertia					B31	
	TOTAL				305	308		

Tables 17 ,18, and 19 present the main polynomial runs as determined in the refined analysis using the experimentally determined values of Young's Modulus for the titanium beams and using the as-measured data for each of three as-manufactured coating thicknesses. The frequencies are expressed (in Hertz), the elastic modulus (Gpa); the non dimensional bending, $\tilde{\tilde{U}}(L/2, t_b)$, the non-dimensional ending strain, $\tilde{\varepsilon}(L/2, t_b)$, and the strain energy ratio, SER.

Table 16: 2-D FEA Polynomials, Bare Beam

Bare Beam FEA			
Temp (degF)	f_r (Hz)	$\tilde{\tilde{U}}(L/2, t_b)$	$\tilde{\tilde{\varepsilon}}(L/2, t_b)$
70	203.66	-0.6074	0.3431
300	197.60	-0.6074	0.3431
600	189.38	-0.6074	0.3431
900	180.79	-0.6074	0.3431

Table 17: 2-D FEA Polynomials, 8.3 mil TBC coating (normal)

$E_c = a_3 \omega^3 + a_2 \omega^2 + a_1 \omega^1 + a_0 \omega^0$					
Temp (degF)	a_3	a_2	a_1	a_0	R^2
70	10.6997 x10^{-5}	-0.0322028	2.23784	0	0.999996
300	11.4471 x10^{-5}	-0.0339188	2.34661	0	0.999995
600	12.6893 x10^{-5}	-0.0368598	2.53863	0	0.999994
900	14.2312 x10^{-5}	-0.0404094	2.75847	0	0.999991
$\tilde{\tilde{U}}(L/2, t_b) = a_3 E_c^3 + a_2 E_c^2 + a_1 E_c^1 + a_0 E_c^0$					
Temp (degF)	a_3	a_2	a_1	a_0	R^2
70		-1.784 x 10^{-6}	0.00070795	-0.534284	0.999988
300		-1.936 x 10^{-6}	0.00074523	-0.5342	0.999988
600		-2.202 x 10^{-6}	0.00080427	-0.534085	0.999953
900		-2.536 x 10^{-6}	0.00087288	-0.533946	0.99997
$\tilde{\tilde{\varepsilon}}(L/2, t_b) = a_3 E_c^3 + a_2 E_c^2 + a_1 E_c^1 + a_0 E_c^0$					
Temp (degF)	a_3	a_2	a_1	a_0	R^2
70		3.4037 x 10^{-6}	-0.0013519	0.340866	0.999958
300		3.8023 x 10^{-6}	-0.0014372	0.341093	0.999979
600		4.2817 x 10^{-6}	-0.0015458	0.340805	0.999971
900		4.9258 x 10^{-6}	-0.0016764	0.34046	0.99995
$SER = a_3 E_c^3 + a_2 E_c^2 + a_1 E_c^1 + a_0 E_c^0$					
Temp (degF)	a_3	a_2	a_1	a_0	R^2
70		-2.10632 x 10^{-5}	0.00452397	0.00859879	0.999742
300		-2.27557 x 10^{-5}	0.00471924	0.0101033	0.999658
600		-2.52278 x 10^{-5}	0.00498906	0.0126215	0.999492
900		-2.80332 x 10^{-5}	0.00527486	0.0159994	0.999218

Table 18: 2-D FEA Polynomials, 12.5 mil TBC coating (thick)

$E_c = a_3 \omega^3 + a_2 \omega^2 + a_1 \omega^1 + a_0 \omega^0$					
Temp (degF)	a_3	a_2	a_1	a_0	R^2
70	9.58056 x10^{-5}	-0.0318289	2.61127	0	0.999978
300	10.4005 x10^{-5}	-0.0340174	2.76076	0	0.999975
600	11.7096 x10^{-5}	-0.0374577	2.99012	0	0.999966
900	13.3642 x10^{-5}	-0.0416969	3.26263	0	0.999957
$\widetilde{U}(L/2, t_b) = a_3 E_c^3 + a_2 E_c^2 + a_1 E_c^1 + a_0 E_c^0$					
Temp (degF)	a_3	a_2	a_1	a_0	R^2
70		-3.4001 x 10^{-6}	0.00010210	-0.503112	0.999913
300		-3.6632 x 10^{-6}	0.00010697	-0.502867	0.999900
600		-4.1138 x 10^{-6}	0.00114435	-0.502451	0.999856
900		-4.5249 x 10^{-6}	0.00121882	-0.501882	0.999803
$\widetilde{\varepsilon}(L/2, t_b) = a_3 E_c^3 + a_2 E_c^2 + a_1 E_c^1 + a_0 E_c^0$					
Temp (degF)	a_3	a_2	a_1	a_0	R^2
70		7.02373 x 10^{-6}	-0.00207063	0.33469	0.999903
300		6.82834 x 10^{-6}	-0.00207357	0.331471	0.999979
600		8.34921 x 10^{-6}	-0.00230619	0.3332	0.999935
900		9.28653 x 10^{-6}	-0.00246467	0.332103	0.999793
$SER = a_3 E_c^3 + a_2 E_c^2 + a_1 E_c^1 + a_0 E_c^0$					
Temp (degF)	a_3	a_2	a_1	a_0	R^2
70		-3.70139 x 10^{-5}	0.00609328	0.0313202	0.997272
300		-3.87705 x 10^{-5}	0.00620998	0.0359047	0.99641
600		-4.10631 x 10^{-5}	0.00633612	0.0432302	0.994733
900		-4.32536 x 10^{-5}	0.00641516	0.0525123	0.992012

Table 19: 2-D FEA Polynomials, 5.7 mil TBC coating (thin)

$E_c = a_3 \omega^3 + a_2 \omega^2 + a_1 \omega^1 + a_0 \omega^0$					
Temp (degF)	a_3	a_2	a_1	a_0	R^2
70	1.310848 x10^{-4}	-0.0363038	2.09443	0	0.999999
300	1.36433 x10^{-4}	-0.0369344	2.09547	0	0.999999
600	1.50564 x10^{-4}	-0.0401259	2.31814	0	0.999999
900	1.6511 x 10^{-4}	-0.0428923	2.47158	0	0.999999
$\widetilde{U}(L/2, t_b) = a_3 E_c^3 + a_2 E_c^2 + a_1 E_c^1 + a_0 E_c^0$					
Temp (degF)	a_3	a_2	a_1	a_0	R^2
70		-9.31108 x 10^{-7}	0.00049052	-0.55572	0.999986
300		-9.67108 x 10^{-7}	0.000513083	-0.55556	0.999992
600		-11.8933 x 10^{-7}	0.000563083	-0.555656	0.999993
900		-13.3824 x 10^{-7}	0.00060944	-0.555519	0.999996
$\widetilde{\varepsilon}(L/2, t_b) = a_3 E_c^3 + a_2 E_c^2 + a_1 E_c^1 + a_0 E_c^0$					
Temp (degF)	a_3	a_2	a_1	a_0	R^2
70		7.02373 x 10^{-6}	-0.00207063	0.33469	0.999903
300		6.82834 x 10^{-6}	-0.00207357	0.331471	0.999979
600		8.34921x 10^{-6}	-0.00230619	0.3332	0.999835
900		9.28653 x 10^{-6}	-0.00246467	0.332103	0.999793
$SER = a_3 E_c^3 + a_2 E_c^2 + a_1 E_c^1 + a_0 E_c^0$					
Temp (degF)	a_3	a_2	a_1	a_0	R^2
70		-1.08385 x 10^{-5}	0.00311488	0.00241779	0.999969
300		-1.19143 x 10^{-5}	0.0032821	0.00287987	0.999958
600		-1.35628 x 10^{-5}	0.00352609	0.00367232	0.999938
900		-1.55518 x 10^{-5}	0.00380364	0.004773	0.999904

8. Exponential Decay Harmonic Function Integration

Concern was raised as to the validity of using a simple relation to integrate the velocity signal, v(t), from the DVL, that assumes a steady harmonic system. This relationship was fundamental to obtaining displacement of the beam, x(t), from velocity data in Reed, Pearson and Deleon's work. Velocity data was collected as opposed to displacement data, which can be obtained from most DVL systems for two reasons, first any gross displacement to the system imposes a shift to all the data as opposed to a momentary aberration in velocity data, and two, the measurement precision of the DVL systems in velocity mode is much greater. For the forced response system the velocity as a function of time function is of the form:

$$v(t)=A\cos(\omega t)\rightarrow x(t)=\int A\cos(\omega t)=\frac{A}{\omega}\sin(\omega t)=\frac{A}{2\pi f}\sin(\omega t) \tag{283}$$

which integrates to:

$$x(t)=\frac{v}{2\pi f} \tag{284}$$

For the free response system the velocity form is of the under damped decay form

$$v(t)=A\cos(\omega t)e^{-\eta t}\rightarrow x(t)=\int A\cos(\omega t)e^{-\eta t}=\frac{e^{-\eta t}}{\eta^2+\omega^2}\left(\eta\underbrace{A\cos(\omega t)}_{v(t)}+\omega\underbrace{A\sin(\omega t)}_{v(t)}\right) \tag{285}$$

which integrates to:

$$x(t)=\frac{e^{-\eta t}}{(\eta^2+\omega^2)}(\eta+\omega)v(t) \tag{286}$$

This is of a different form from the harmonic forced response one. It is noted that

Reed, who used free decay methodology applied the form in Eqs. (283) and (284). It is noted that the taking the limit as damping becomes small that Eq. (286) simplifies to (284). Restated:

$$\lim x(t)(as\,\eta \to 0) \approx \frac{v(t)}{\omega} = \frac{v(t)}{2\pi f} \tag{287}$$

The question is as to what level of damping of error is the use of the simpler form justifiable? Basically one way is to evaluate the difference between the two forms as a a function of the damping ratio. For the non-dimensional, 2nd order harmonic equation the percentage of difference is displayed here in Table Error: Reference source not found.

Table 20: Error Between Free-Decay and Forced Response Forms

Damping Ratio (η)	x(t) % difference (*)
0.15	-25.7%
0.10	-17.9%
0.05	-9.3%
0.04	-7.4%
0.03	-5.5%
0.02	-3.7%
0.01	-1.8%
0.004	-0.73%
0.002	-0.36%
0.001	-0.18%
0.0004	-0.07%
0.0002	-0.03%
$\Delta x(t) = 100.0\% \times \frac{x(t)_{\text{harmonic form}} - x(t)_{\text{decay form}}}{x(t)_{\text{decay form}}}$	

It is noted that in worst case studies of the Reed using the simpled form of the free decay over-predicted by about 5%, when damping ratio was around 0.03. For the bare

beam the error was to over-predict displacement by about 0.03%. Generally most consider a system as minimally damped when damping ratio is around 0.1 or less.

The numerical integration of velocity data to obtain displacement data may require more a more precise specification of the integration. It is noted by Palazotto that the harmonic function can be readily integrated to recover displacement of the beam from the velocity data. For a forced response testing this may be acceptable as the output is s steady harmonic signal (Actually, not strictly true as the very slow chirp sweep frequency is applied but it is around 0.30Htz, as opposed to the mode-I frequency around 230 Hz). For a free decay test one actually has a damped oscillatory response where the integration is different (Palazotto, 2009).

9. Time Domain Data Reduction

The reduction of free-decay data by the Hilbert Transform allows for some advantages. These include a relaxation in the density of data capture needed, as the exact peak heights aren't as critical to be captured, ability to capture time-varying loss factors from the envelope curve, and phase function. Luo and Thrane covered the applied employment of Hilbert Transform for practical dataset processing (Luo, 2009; Thrane, unknown).This section is a quick overview of the process as employed by Reed. Basically the ring down signal consists of a directly measured or numerically integrated displacement signal with a dominant mode of interest (mode-I bending) and some contaminants (rigid body motion, higher harmonics, etc.). It is a classic sinusoidal decaying signal:

$$x(t)=\sum_{modes}\left[Ae^{-at}\sin(\omega_d t)\right]_i \tag{288}$$

The Hilbert Transform, a linear operator, convolves out a signal that for a harmonic signal is the orthogonal function.

$$x(t)=Ae^{-at}\sin(\omega_d t)\overset{H}{\rightarrow}\tilde{x}(t)=Ae^{-at}\cos(\omega_d t) \tag{289}$$

Taken together the original signal and its transform are analytic and can be written in complex form.

$$x^{\nabla}(t)=Ae^{-at}=\underbrace{h(t)}_{\cos}+i\underbrace{\tilde{h}(t)}_{\sin} \tag{290}$$

The magnitude of the complex form positive and is called the envelope function.

$$X(t)=x(t)+i\tilde{x}(t)\,A(t)=|X(t)|=\sqrt{x^2(t)+\tilde{x}^2(t)} \tag{291}$$

Reed did have rigid body motion (Pearson did not) and so he took the additional step of smoothing the envelope function with a cubic spline to remove beats phenomenon driven ripples in the envelope function. As a result he removed rigid body motions and influences from the displacement signal transforming from content like this:

$$x(t)=\sum_{modes}\left[Ae^{-at}\sin(\omega_d t)\right]_i \tag{292}$$

to this:

$$x(t)=\left[Ae^{-at}\sin(\omega_d t)\right]_{Bending\ I} \tag{293}$$

To the smoothed envelope function the log decrement was now applied, in a form adapted to a continuous function.

$$\Lambda=\ln\frac{X_1}{X_2}=\ln\frac{Xe^{-\zeta\omega t}}{Xe^{-\zeta\omega(t+\Delta t)}}=\zeta\omega\Delta t \tag{294}$$

When the system is well under damped (or restated, the loss-factor is small), Eq. (294) reduces to (295).

$$\Lambda=\ln\frac{X_1}{X_2}=\frac{\eta}{2}\omega\Delta t\ \rightarrow\ \eta=\frac{2\Lambda}{\omega\Delta t} \tag{295}$$

Instantaneous (relative) frequency can also be extracted from the phase lag between the signal and its transformed image as well:

$$\phi(t)=\tan^{-1}\left(\frac{\tilde{x}(t)}{x(t)}\right) \tag{296}$$

From this the instantaneous frequency, ω(t), can be found from the slope of Φ(t) or d[Φ(t)]/dt if the phase accumulation is in a functional form. It is to be noted that the datasets are sets of collected data points to the analytic form of the Hilbert Transform, given in Eq. (297), is not used to process the data set,

$$H[x(t)]=\tilde{x}(t)=\frac{1}{\pi}\int_{-\infty}^{\infty}\frac{x(\tau)}{t-\tau}d\tau \tag{297}$$

but rather the discrete form of it as per here (Eq. (298)):

$$H_d[x[n]]=\tilde{x}[n]=\frac{1}{N}\sum_{k=0}^{N-1}X_r[k]\sin(2\pi kn/N)-iX_i[k]\cos(2\pi kn/N) \tag{298}$$

The end result of this work is the curves of the system loss factor and resonance frequency as a function of time for a system undergoing free decay.

10. FRF to Measure Damping and Natural Frequencies

The method of sine sweeping, also known as either: "chirp excitation", forced response, frequency domain measurement, and/or half-power bandwidth, is a well-established technique to capture a systems frequency response function (FRF); that is the output it generates as a ratio over the known input of controlled amplitude and frequency. For under-damped structures it is the most common method used to characterize its vibrational response. Pearson and Reed both used it with success to characterize free-free beams at room temperature in as far as system damping and effective modulus, which are the two macroscopic qualities sought. A good overview of the technique is in many texts,

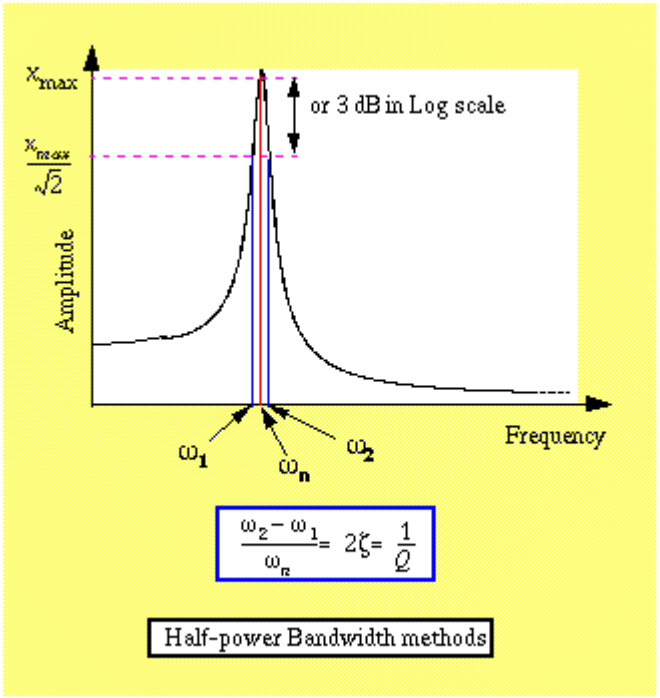


Figure 154: Forced Response FRF Frequency Domain Signal

among them Slater's and Meirovitch's texts. (Slater, 2002; Meirovitch, 2001). In the

current study it is used an a supplementary method to double check the results of the free-decay. It was also good for identifying and confirming qualitative trends in the observed data in the current study.

The half-power bandwidth technique assumes the system damping is viscous in nature, linear, and relates that around a resonance peak in the system frequency response function that

$$\frac{\omega_2^{\,2}-\omega_1^{\,2}}{\omega^2}=4\zeta\sqrt{1-\zeta^2} \tag{299}$$

which if ζ is small can be approximated by

$$\zeta=\frac{\omega_2-\omega_1}{2\omega} \tag{300}$$

For the non-linear (material-wise), TBC coated beams the half-power bandwidth techniques has proven somewhat difficult to implement; complications are the shifting resonance frequency (ω_r) as a function of driven couple amplitude (M(t)), asymmetric resonance peaks, leaning of the resonance peaks, and the jump phenomena (See Section 10) as well as ω_f comments on sine sweep rate and adaptive sine sweep.

With the bare beam half power bandwidth works well to identify both resonance frequency as well loss factor as long as the sine excitation frequency sweep rate is carefully controlled to eliminate transient second order effects; Deleon, when re-accomplishing measurement of the loss coefficient for the bare beam using Pearson's specimens, down adjusted the sweep rate from 2.0 Hz/min to 0.35Hz/min to eliminate impulse-type ringing artifacts that Pearson reported as non-linearities in his bare-beam

FRF sweep plots (Deleon, 2009; Pearson, 2008). The determined loss factor for the Ti-6Al-4V bare beam, $\eta_{bare} = 0.0004$ agreed with Reed's free-decay measurements (Reed, 2007). It is also important to note that Deleon and Palazotto obtained a fairly good agreement with Reed's results when two things were applied to Pearson's data: 1) use the up-swept FRF curve, and 2) use care in integrating the SER over the volumetric area of the beam only in the coated beam system (Deleon, 2009). One sweep rate guidance put forward is the relation by Torvik for determining an upper bound to the appropriate sweep rate as per:

$$S = \frac{\pi \omega_n^2}{M Q^2} \tag{301}$$

where S is the sweep rate, Q is the quality factor of the system, ω_n, is the natural frequency, in Hertz, of interest, and M is the number of time constants of the system (Reed, 2007). For the free-free setup of Reed and Pearson to the 4th time-constant, Eq. (301) predicts a 0.30Hz/min sweep rate.

A key difficulty to using this techniques with non-linear materials, in this case the strain softening 8-YSZ is that the resonance peaks are not symmetric at all. The left side of Figure 118 shows the FRF curves. To stimulate the true peak in the 8-YSZ the chirp excitation must down sweep towards the peak resonance. If up-sweeping is performed the jump phenomenon would cause a premature change of non-linear states and miss the true resonance peak. Furthermore, whether an up-swept, down-swept, or combination of the two FRF's is used the curves usually exhibit marked asymmetries. Deleon attempted numerous techniques to handle the asymmetry including techniques to combine up- and

down-sweeps, using a polynomial across FRF resonance peaks on a family of curves at different amplitudes, using a lower power bandwidth (¼-power), using a Torvik derived correction factor, among others (Deleon, 2009).

The 8-YSZ and mag spinel coated beams both exhibit strain softening behavior as per the left side diagram of Figure 154. This figure suggests a powerful fashion in which to approach half power bandwidth sweeping of the beam. Harris mentions that the undershot portion of the curve appears to exhibit three particular amplitudes for some frequencies but in fact the point on the "face of the wave" is a unstable equilibrium point. Any slight disturbance or perturbation of the system will result in a quick and decisive shift to one of the other two solution points. This is referred to as the region of instability by the authors. (Harris, 2002).

Meirovitch in Chapter 11.8 has a good overview of using 2nd order perturbation expansion modeling of Duffing's equation for a SDOF system with a strain-hardening spring to model the jump phenomenon. The FRF curve obtained is similar in form to the experimental FRF obtained for the coated beams. (Meirovitch, 2001). It is thought that this may be applicable as an analogy system to reduce the continuous beam free-free mode-I bending system to a SDOF (non-linear) analogue system that can be determined for the coated beam, if, just like Palazotto and Deleon proposed for the the bare beam to linear SDOF system analogue, see Appendix 13 for details on this potential method. This may be a powerful way to characterize coatings without need for numerical analysis.

Various attempts have been made to reconstruct the FRF curve from the

experimental sweep data and deal with the instabilities in the jump region. This uncertainty in how to handle reconstructing the backbone curve for the non-linear coated system is the main reason that the current study will collect data set by free-decay at the commencement and conclusion of each beam FRF sweep. Pearson (Pearson, 2008) merely utilized the up sweeps, concluding that based on the bare beam results and coated beam results the data was more closely resembling each other, little quantitative justification was elaborated on.

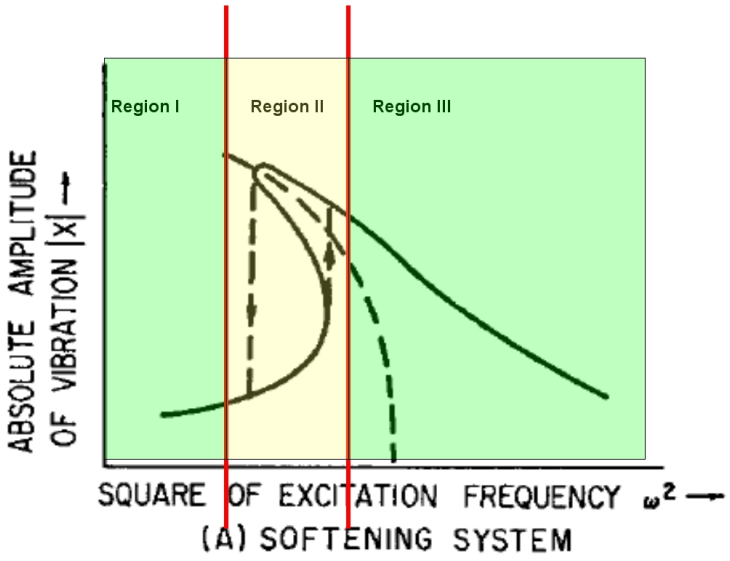


Figure 155: Section of non-linear FRF (Braun, 2002)

Meanwhile Deleon (Deleon, 2009), using Pearson's datasets, tried several techniques to determined the resonance frequency for the softening curves. Besides applying the linear theory outright, one method from Palazotto was to sweep across several amplitudes and determine a polynomial function curve to describe the path of the resonance frequency across amplitude and forcing frequency. This polynomial curve,

rather than the midpoint between was used as the resonance peak determination point. Another technique Deleon studied was developed by Torvik, this was to evaluate the resonance using power ratios removed from 1/2, as lower values are used say 1/4 or 1/8 less of the non-linear effects near the peak come in to the data. Torvik cautions however that influence of other modes may affect such low power ratios. The method is laid out in "A Note on the Estimation of non-linear System Damping " (Torvik, 2003)

The revised algorithm this author determined, is to perform both the up and down sweep but favor and discard neither. The up-sweep, where the sinusoidal excitation function is increased in frequency, approaches the lower magnitude stability points in region II (see Figure 77) while the down-sweep captures the upper amplitude ones in Region II. The up-sweep has a characteristic "shark-fin" shape that is exhibited in the datasets of the previous researchers. It is proposed that the two curves be analytically combined by least squares regression of the FRF data. However it is proposed to first section partition the three regions by identifying the boundaries frequencies, from the up-sweep data the boundary between Region II and III would be identified, somewhere above the frequency of the tip of the "shark-fin. Meanwhile, the boundary between Region I and II would be similarly identified by partitioning somewhat below the peak and roll off frequency. The data in Regions I and III along can then be used for a regression fit between the curves with the datasets in Region II translated in common. Synthesis of the Region II features can than occur from the combined curves.

Half power assumes a linear (e.g. viscous) damping mechanism is in effect in the

derivation of the relationship to extract damping ratio (or loss coefficient) based on resonance peak width. So does the log decrement method, but the time domain curves may be easier to separate the various mechanisms out by capturing non-linear decay features in a more intuitive format. Some methodologies to handling the frequency domain non-linearities have included:

· Taking 1/4 or 1/8 power bandwidth around the peak to capture more effects away from the non-linear region as proposed by Torvik (Torvik, 2007). This essentially isolates the problematic jump region, but presumes there are no other closely spaced modes around the resonance of interest.

· Using a polynomial extrapolation technique trended across multiple amplitudes of FRF curves to attempt to better locate the peak frequency as proposed by Palazotto (Deleon, 2009).

· Using the unmodified linear technique of 1/2 power bandwidth.

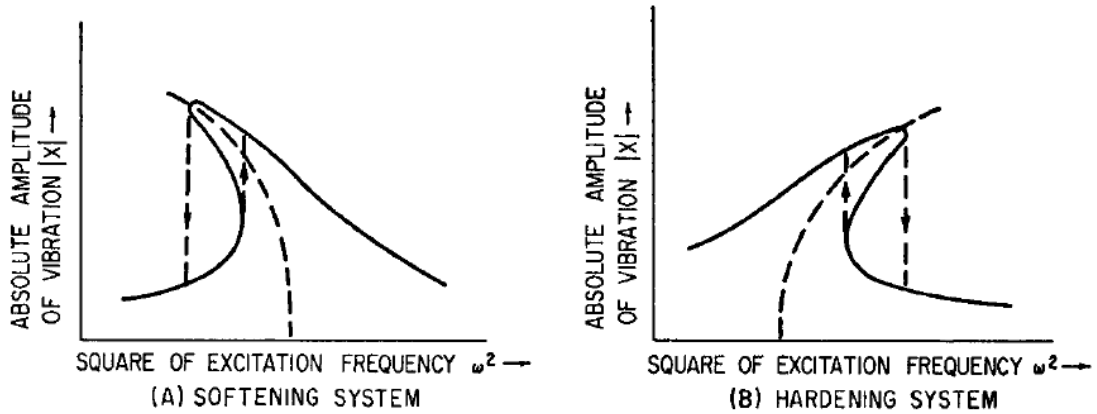


Figure 156: The "Jump" Phenomenon (Braun, 2002)

In closing, Palazotto makes a key observation that whether temperature sensitivity is determined to be a strong driver of changes in the beam system's effective modulus and loss coefficient, or not, it will be a key discriminator to determine to what degree viscoelastic damping plays (strong temperature dependence) or dry friction damping (weak or no temperature dependence). This observation can also be applied to the time domain datasets as well.

11. Orientation Imaging Microscopy Background and Details

The orientation imaging microscopy (OIM) process is useful to characterize the micro-structure of conductive materials. With metallic solids it is a useful technique to map the grain size, structure, form and the phases within sample. At a smaller scale it can be used build a probabilistic profile as to the orientation of the crystals within the

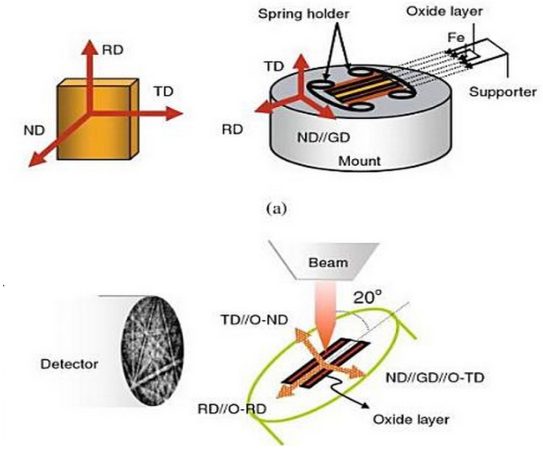


Figure 157: Orientation Imaging Microscopy (OIM) Schematic (Schwartz, 2000)

grains themselves. A beam of electrons is directed at the sample surface at about 20° angle of incidence. The electrons disperse beneath the surface and diffract among the crystallographic planes, analogous to visible light in a grating as shown in the schematic (Figure 158). The diffracted electron beam produces a pattern of intersecting bands, termed Kikuschi bands, these form an electron backscatter pattern that are oriented preferentially to the layers of the planes (much like the grating orientation sets the color and intensity of a visible ligh diffraction). Imaging of these by placing a suitable film or phosphor screen in close proximity to the SEM allows them to be captured. From the width and intensify of the band the spacing of the atoms in the crystal planes can be

deduced, while the angle between the bands are related to the angles between planes in the crystal lattice.

Since most metallics are polycrystalline, with multiple phases (and therefore crystal structures like body centered cubic, hexagonal close packed, simple cubic, and face-centered cubic among others) this is a stochastic process that involves reporting a preferential probability of the orientations. This is typically done via a polar plot by color maps. An example of a color map used for Ti-6Al-4V with its h.c.p structure is in Figure 157. This shows how the h.c.p. crystal orientations would be reported in a color key. The hexagonal shape in the figure would be bright red if the 0001 direction is set in the normal direction out of the page as it is end on aligned. If it was precessed by 10-20^{o} it would be more orange colored, if lying on its side it would be blue or green whether a rectangular crystal face or long edge was facing the page, respectively.

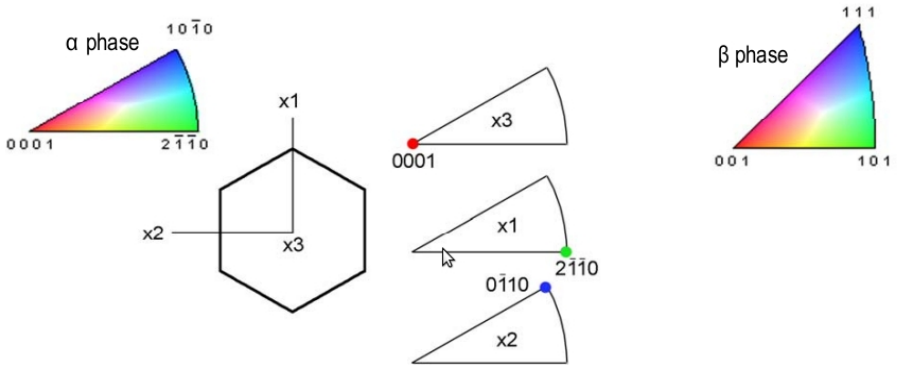


Figure 158: OIM Colormap Interpretation (Pilchak, 2009)

The OIM settings used in the characterization of the Ti-6Al-4V disks in the current study are summarized here.

Disc1-FineScan

Operator: Supervisor
Calibration: 0.513931 0.610448 0.606634
Working Distance: 25.000000

Number of points: 331475
Number of good points: 331475

Dimensions:
X Min: 0.00 microns
X Max: 187.25 microns
Y Min: 0.00 microns
Y Max: 187.32 microns
Step: 0.35 microns

Average Confidence Index: 0.32
Average Image Quality: 1618.08
Average Fit [degrees]: 1.47

Minimum boundary mis-orientation: 2.0 degrees (see Settings>Preferences)
Number of boundary segments: 284008
Length of boundary segments: 5.73902 cm

Phases:
Titanium (Alpha)
Titanium - Beta

Operator: Adam Pilchak
Sample ID: Oliver-2umStep
Calibration: 240.000000 240.000000 240.000000
Working Distance: 20.000000

Number of points: 2068693
Number of good points: 2068693

Dimensions:
X Min: 0.00 microns
X Max: 6164.00 microns
Y Min: 0.00 microns
Y Max: 1340.00 microns
Step: 2.00 microns

Average Confidence Index: 0.27
Average Image Quality: 1085.85
Average Fit [degrees]: 1.55

Minimum boundary mis-orientation: 2.0 degrees (see Settings>Preferences)
Number of boundary segments: 3800100
Length of boundary segments: 7.6002 m

Phases:
Titanium (Alpha)
Name:All data (Alpha phase only!)
Formula:
Number of points in partition: 2068693
Fraction of points in partition: 1.000
Number of indexed points: 2068693

Average Confidence Index: 0.27
Average Image Quality: 1085.85
Average Fit [degrees]: 1.55

Phases:
Titanium (Alpha)

Grain Size (Excluding Edge Grains):
Averages are number averages
Number of Grains: 252065
Number of Edge Grains: 1492
Average Diameter: 4.28 (4.27) microns
Equivalent Area: 14.35 (14.35) square microns
Equivalent ASTM No.: 13.1 (13.1)

note that these grain sizes are not trustworthy because of the coarser step size.

12. Matlab Data Reduction Routine

This code is used to reduce the beam system effective properties of damping and resonance frequency into coating specific bulk effective storage modulus and loss coefficient given several inputs. These include the four polynomials from the FEA modal models, the experimentally determined modulus of the bare titanium beam, and the experimentally determined v(t) and PHI(t) values for the beam in the ring-down dataset. The Torvik equation ties it all together effectively.

Matlab Code

```
% Data Processing Script for Ring-down Sets
% Must load datasets into the workspace
fid = fopen('09-70degF-2000-1.txt','rt');
dat = textscan(fid,'%f %f %f %f %f','Delimiter','\t','headerlines',9);
fclose(fid);
data = [dat{1,1} dat{1,2} dat{1,3} dat{1,4} dat{1,5}]';
data = transpose(data);
%trunc = 10.0;
%trunc_index = int32(trunc*2000);
%data = data(1:trunc_index,:);
%% Define data for Curve Fits
% For 5.7-mil coated beam
%%%%%%%% 70 degF %%%%%%%%%%%%%%%%%%%%%%%%%%%%%%%%%%%%
FEA1 = [0.0     2.09  -0.0363    0.000131]; % cubic
FEA2 = [-0.555      0.000490    -9.31e-07]; % quadratic
FEA3 = [0.334      -0.00207     7.023e-06]; % quadratic
FEA4 = [0.00241     0.00311    -1.083e-05]; % quadratic
eta_bare = 0.00006; % Loss Coefficient of the Bare Beam
%%%%%%%% 300 degF %%%%%%%%%%%%%%%%%%%%%%%%%%%%%%%%%%%%
%FEA1 = [0.0    2.09    -0.0369   0.000136]; % cubic
%FEA2 = [-0.555      0.000513    -9.67e-07]; % quadratic
%FEA3 = [0.331      -0.00207      6.82E-06]; % quadratic
%FEA4 = [0.00287     0.00328    -1.191E-05]; % quadratic
%eta_bare = 0.000045; % Loss Coefficient of the Bare Beam
%%%%%%%% 600 degF %%%%%%%%%%%%%%%%%%%%%%%%%%%%%%%%%%%%
%FEA1 = [0      2.31     -0.0401  0.0001505]; % cubic
%FEA2 = [-0.555   0.000563      -1.189E-06]; % quadratic
%FEA3 = [0.333      -0.00230    8.349E-06 ]; % quadratic
%FEA4 = [0.00367    0.00352     -1.356E-05]; % quadratic
%eta_bare = 0.00007; % Loss Coefficient of the Bare Beam
%%%%%%%% 900 degF %%%%%%%%%%%%%%%%%%%%%%%%%%%%%%%%%%%%
%FEA1 = [0  2.47     -0.0428      0.0001651]; % cubic
%FEA2 = [-0.555    0.000609     -1.338E-06]; % quadratic
%FEA3 = [0.332    -0.00246       9.28E-06 ]; % quadratic
%FEA4 = [0.00477    0.00380     -1.555E-05]; % quadratic
%eta_bare = 0.00012; % Loss Coefficient of the Bare Beam
%
% For 6-mil coated beam
% For 12-mil coated beam
clc ;
freq = 202.5 ; %
```

```
laser_scale = 0.125 ; % Laser scale in m/sec per volt
%% If dataset is "wrapped" by LV capture buffer, unwrap it
num_data = size(data);
chop_pt = 0;
for i = 2:1:num_data;
    if(data(i,1).*data(i-1,1) < 0); % Find the index of the points where time goes negative
    chop_pt = i
    end;
end;
if(chop_pt > 0);
    stub = data(1:chop_pt-1,1);
    tail = data(chop_pt:end,1);
    tail = max(stub) + (tail - min(tail));
    data(:,1) = [stub ; tail];
    data(:,2:5) = [data(1:chop_pt-1,2:5); data(chop_pt:end,2:5)];
end;
%% Rename the data matrix to familiar 1-D vector variables
t_data_capture = max(abs(data(:,1))) % Find the timescale of ringdown
t = data(:,1); raw_volt = data(:,2); filtered_volt = data(:,3);
v_t = data(:,3).*laser_scale; f_env = data(:,4);
if(min(t)<0); t = t+(-1.*min(t)) ;end;
%% Obtain the Phase Info from the filtered signal data(:,3)
% First Filter with a high-pass, 5th order Butterworth Filter, f_c = 20Htz
% High pass 5th order filter with normalized frequnecy
% fc = 30/((1/2)*2000Htz) = 0. 03 normalized cutoff freq.
%
% [b,a]=butter(5,0.002,'high');
% v_t=filter(b,a,v_t);
%
% Now Apply the Hibert Transform
hil = hilbert(data(:,3));
realsig = real(hil);
analsig = imag(hil);
% plot(t,realsig,t,analsig);
mag = sqrt(real(hil).^2 + imag(hil).^2);
phase = unwrap(angle(hil));
plot(t,phase); % plot(t,mag);
%% Now on to scale the laser, remove beond time data, and smooth outliers out
%x_env = data(:,6).*(t_data_capture./num_data(1,1)); ...
%y_env = data(:,7).*laser_scale; % from LabView Processed Dataset
x_env = t; y_env = mag.*laser_scale; % From Matlab Hilbert Function
x_env_chop = find(x_env, 1, 'last'); % Find index of last non-zero element in time
x_env = x_env(1:x_env_chop,:); y_env = y_env(1:x_env_chop,:);
y_env_smooth = smooth(y_env, 151, 'rloess'); % Smooth the Hilbert Evelope function
phase_smooth = smooth(phase, 151, 'rloess'); % Smooth the Phase function
%% Plot the Various Raw Data Findings Here
figure(1);
subplot(2,2,1); plot(t,raw_volt);
title('Raw Voltages'); xlabel('Time (sec)'); ylabel('Voltage, (Volts)');
subplot(2,2,2); plot(t,v_t);
title('Scaled and Filtered'); xlabel('Time (sec)'); ylabel('Velocity v(t), (m/sec)');
subplot(2,2,3); plot(x_env,y_env,x_env,y_env_smooth);
%plot(x_env,y_env,x_env,y_env_smooth);
title('Hilbert Envelope Function');
subplot(2,2,4); %plot(data(:,8),data(:,9));
title('Phase (radians)');
%% Generate Functional Fit to the Envelope and Phase Functions
% For the envelope function  --- Create fit "fit 1"
%
%ft_1 = fittype('gauss2');
ft_1 = fittype('a*exp(b*x) + c*exp(d*x)','dependent',{'y'},'independent',{'x'},...
     'coefficients',{'a', 'b','c','d'});
%
% Try the cubic function
%ft_1 = fittype('a + b*x + c*x^2 + d*x^3 + e*x^4','dependent',{'y'},'independent',{'x'},...
%     'coefficients',{'a', 'b','c','d','e'});
%
%opts = fitoptions('Method','NonLinearLeastSquares','Robust','On'); %,'Algorithm',...
%    'Levenberg-Marquardt','TolFun',1.0e-7);
%[cf_1,gof_1] = fit(x_env,y_env_smooth,ft_1,opts)
%
%st_1 = [3.9-09 -0.73 0.00625 0.2211];
st_1 = [max(y_env_smooth) 0.35210694524343056 0.1*max(y_env_smooth) 0.01];
```

```
[cf_1,gof_1] = fit(x_env,y_env_smooth,ft_1,'Startpoint',st_1)
%[cf_1,gof_1] = fit(x_env,y_env_smooth,ft_1)
%[c1,ypred1] = predint(cf_1,x_env,0.95,'fun','on');
ft_2 = fittype('e*exp(f*x)','dependent',{'y'},'independent',{'x'},...
    'coefficients',{'e', 'f'});
%st_2 = [max(y_env_smooth) 0.35210694524343056];
%[cf_2,gof_2] = fit(x_env,y_env_smooth,ft_2,'Startpoint',st_2)
ft_2 = fittype('poly1');
[cf_2,gof_2] = fit(x_env,y_env_smooth,ft_2)
%
% Now the phase function
% Linear Function
%ft_3 = fittype('m*x + b','dependent',{'y'},'independent',{'x'},...
%     'coefficients',{'m', 'b'});
%st_3 = [100.0 0.1];
%[cf_3,gof_3] = fit(t,phase,ft_3,'Startpoint',st_3)
% Cubic Function
%ft_3 = fittype('a + b*x + c*x^2 + d*x^3','dependent',{'y'},'independent',{'x'},...
%     'coefficients',{'a', 'b','c','d'});
%st_3 = [1.0 100.0 0.1 0.1];
%[cf_3,gof_3] = fit(t,phase,ft_3,'Startpoint',st_3)
ft_3 = fittype('poly1');
[cf_3,gof_3] = fit(t,phase,ft_3);
figure(2)
subplot(1,2,1); plot(cf_1,'r-',x_env,y_env_smooth,'k.'); % hold on; plot(x_env,c1,'k-.');hold off;
title('Decay Envelope Function'); xlabel('Time (sec)'); ylabel('v(t) (m/sec)');
subplot(1,2,2); plot(cf_3,'b-',t,phase_smooth,'k.')
title('Phase Function (unwrapped)'); xlabel('Time (sec)'); ylabel('Total Phase Angle, (Radians)');
% Col Reed used the numerical data in numerical operations, since here we've reduced
% fits to functional form we need to work with the functions.
% Compute the Log Decrament
for i = 2:1:size(mag); dt = t(i)-t(i-1);
     gamma(i) = log(feval(cf_1,t(i-1))/feval(cf_1,t(i))); %1/(t(i)-t(i-1))*
end; gamma(1) = gamma(2); a = size(gamma); if(a(1,1) == 1); gamma = transpose(gamma); end;
%% Compute Instantenous Frequnecy using the products of the Hibert
% Transform
omg_t = differentiate(cf_3,t).*(1/(2*pi)); % Convert to Hz for FEA1
eta_t = (2.*gamma)./(omg_t.*dt);
figure(3); %plot(t,gamma); %plot(t,omg_t); %plot(t,eta_t);
% map the time, t, to the beam velocity, v(t),
Ec_t    = FEA1(1) + FEA1(2).*omg_t + FEA1(3).*omg_t.^2 + FEA1(4).*omg_t.^3;
U_ND    = FEA2(1) + FEA2(2).*Ec_t  + FEA2(3).*Ec_t.^2;
eps_ND  = FEA3(1) + FEA3(2).*Ec_t  + FEA3(3).*Ec_t.^2;
SER     = FEA4(1) + FEA4(2).*Ec_t  + FEA4(3).*Ec_t.^2;
y_env_func = feval(cf_1,t);
subplot(2,1,1);
plot(y_env_func.*1000, eta_t); title('Beam System Loss Factor'); xlabel('Velocity
(mm/sec)');ylabel('Loss Factor');
subplot(2,1,2);
plot(y_env_func.*1000, Ec_t); title('Beam Coating Storage Modulus'); xlabel('Velocity
(mm/sec)');ylabel('Storage Modulus (Gpa)');
% Now integrate v_t to get u_t
u_env_func = y_env_func./(2*pi*mean(omg_t));
lambda = u_env_func./U_ND;                      % Determine the scaling function here
eps = lambda.*eps_ND;                           % Applying scaling to get true strain
eta_c = (eta_t.*(SER+1) - eta_bare)./SER;          % Apply the Torvik Equation
figure(4);
subplot(2,1,1); plot(-eps.*1.0e6,Ec_t);
title('E_c versus strain'); xlabel('Strain Amplitude (micro-strain)'); ylabel('Storage Modulus
(Gpa)');
subplot(2,1,2); plot(-eps.*1.0e6,eta_c);
title('eta_c versus strain'); xlabel('Strain Amplitude (micro-strain)'); ylabel('Loss Coefficient');
```

13. SDOF Analogy Method

This method was proposed by Palazotto and Deleon in an attempt to determined the coil voltage amplitude for an given experimental beam from the observed center velocity maximum and frequency using the construct of an "effective force" and a 1-D SDOF dynamic analogue (Deleon, 2009). Basically, if the beam is being excited at some velocity maximum and resonance frequency that are measured, we can find the displacement by:

$$\delta = \frac{v(t)_{p-p}}{f_n \cdot 2 \cdot \pi} \tag{302}$$

Continuing (302) is re derived from

$$s = C sin(\omega t) \quad . \tag{303}$$

Taking the derivative w.r.t. to time, as per,

$$\frac{\partial s}{\partial t} = V = \omega C cos(\omega t) \tag{304}$$

and then again for acceleration leads to

$$\frac{\partial^2 s}{\partial t^2} = a = -\omega^2 C sin(\omega t) \quad . \tag{305}$$

Now the displacement amplitude can be determined using:

$$\delta = \frac{V}{\omega} = \frac{a}{\omega^2} \tag{306}$$

Point acceleration is then obtained from the following manipulations:

$$a = \delta * \omega^2 = V * \omega \tag{307}$$

$$F = ma = A\sin(\omega t) \tag{308}$$

$$F = V * \omega * m = A\sin(\omega t) \tag{309}$$

$$A = \frac{V * \omega * m}{\sin(\omega t)} \tag{310}$$

where A is the force effective amplitude imposed on the beam. This is very concise approach and worth investigating and refining. It is proposed in the current study to adapt the system to the equivalent SDOF resonator of the forced kind; by using this "effective force", neglect the damping (c) for the bare beam, and determine the "effective" k. Effective mass can be the actual mass of the beam system as per Palazotto and Deleon.

$$m_{beam}\ddot{x} + c\,\dot{x} + k_{eff}\,x = F(t)_{eff} \tag{311}$$

In essence a 1-D analogue that is the frequency equivalent for the free-free beam system has been tuned in and all of the tools for working (110) are now available to the analyst. Running a free decay will yield an effective damping value if desired.

Can this technique also be used to tune in the Duffing equation model of Meirovitch to capture non-linearities of the coated material in a effective k that is non linear?

$$\ddot{x} + \omega^2 x = \epsilon[\underbrace{-\omega^2(\alpha x + \beta x^3)}_{nonlinear\ tuning\ for\ k_{effective}} + F\cos\Omega t\,]\ ;\quad \epsilon \ll 1 \tag{312}$$

Recalling that $\omega = \sqrt{k/m}$ it is tantalizing to see if such a simplified model will work. From experimental data calculation of the system, it is important to note that while damping is not captured in these analogue model, they are appropriate for forced response and FRF and for a lightly damped system and may yield some insight into the

system in the jump region without the need for numerical simulation using FEA or matrix methods.

14. A Note on Damping Ratio, Quality Factor, and Loss Coefficient

These terms are used interchangeably and frequently when discussion of vibrational and resonant systems. It is good to recall the definition of each and their relation to one another:

Quality factor or Q factor is a dimensionless parameter that compares the time constant for decay of an oscillating physical system's amplitude to its oscillation period. Equivalently, it compares the frequency at which a system oscillates to the rate at which it dissipates its energy

$$Q_{sys}=\omega\frac{U_{sys}}{D_{sys}}=2\pi f\frac{U_{sys}}{D_{sys}} \tag{313}$$

Damping ratio is the measure of the critical stability of a system where it transitions from under-damped oscillatory decay to over-damped monotonic decay. Stated in terms of the system's stiffness, k, damping coefficient, c, and mass, m it is defined as:

$$\zeta=\frac{c}{\sqrt{2\mathrm{km}}} \tag{314}$$

It is related to the quality factor by:

$$\zeta=\frac{1}{2Q} \tag{315}$$

Loss factor derives from the fact that η is equal to the ratio of energy dissipated for one cycle $E_d=\int_0^T\sigma\epsilon dt$ by 2π the maximum potential energy $E_p=1/2E$. If all the dissipative

materials used have a loss factor property. The loss factor is related to the damping ratio and the quality factor as per:

$$\eta = 2\zeta = \frac{1}{Q} \tag{316}$$

Conventional axial cycling of the TBC, whether as a sputtered or plasma sprayed coated material on laminated "dog-bone" tensile specimens can be performed. The single axis tensile load and unload testing has the advantage of well established procedures and techniques. MTS and Instron are two well known makers of load cell equipped loading machines that, loaded with a specimen outfitted with an extensometer, can produce stress versus strain plots in load and unload curves. Figure 159 is typical load-unload plot for a "dog-bone" specimen that is axially cycled.

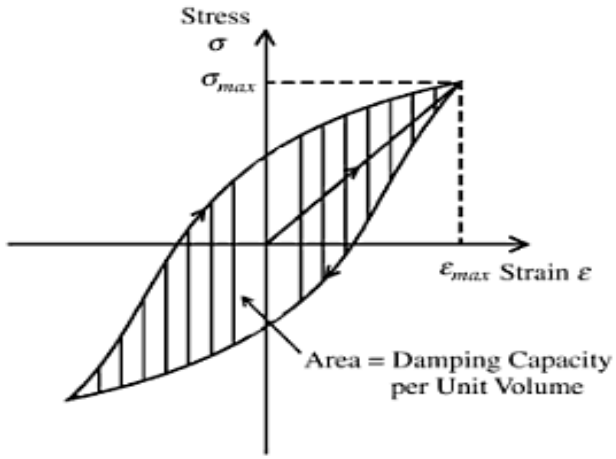


Figure 159: Typically Axial Load and Unload Curve

Axial testing geometry offers considerable advantages: 1-D stress field and simpled theory using 1-D material models, zonal heating apparatus, no need for vacuum to control damping losses, precise control over stress or strain over time.

There are some major disadvantages though as well; for a material that is non-linear with respect to strain magnitude this configuration may not produce the large strains that a bending specimen can achieve and thereby test the specimen across a large range of the backbone curve, the loading history to the same degree of cycle accumulation may be up to an order of magnitude slower as Instron/MTS tension testing machines will have a much reduced ability to accumulate strain and cycles, typically only 10-30 Hz (as opposed to over 200 Hz) may be possible at any reasonable amount of strain, and finally, for a non-monolithic specimen, the effects of coating imposed variations may be overshadowed within the measurement precision of the hardware as the much more stiff titanium element in a coated sample may drive the effective response and coating effects will be hidden in the noise.

On the other hand, the free-free beam system is a tuned resonant system, wherein small changes made around the resonant point(s) can drive large and relatively easily measured changes in the beam system. A good electrical analogy would be a harmonically excited LRC circuit, small changes in the "storage modulus" (e.g. the capacitance C or inductance L) or "loss modulus" (the resistance R) will drive large and easily measurable changes in the frequency of resonance or the magnitude of the output waveform if input frequency is locked. Direct measurement of such component changes in the circuit in situ would be rather difficult to accomplish without the change being buried in the precision of the measurement.

Nonetheless, the performance of a static cycling load and unload curve on a

coated beam specimen of a bare, 8-YSZ, and mag spinel coated specimen may yield a good insight into the quasi-static realm of how the non-linear coated beams behave.

The basis of the method is essentially to obtain the load and unload curves over various portions of the history. A fully mature specimen would have coincident sets of load and unload curves. The area between the curves as depicted in Figure 159, denoted as D, is the energy lost per each cycle of loading as per:

$$D = \oint \sigma \, d\epsilon = \int_0^{2\pi/\omega} \sigma \dot{\epsilon} \, dt \tag{317}$$

It is noted for a perfectly elastic material Hook's Law ($\sigma = E\epsilon$) is obeyed and the loop collapses to a straight line (Reed, 1967). The loss factor is then the the ratio of this lost energy to the response of the material based on its initial, purely, elastic storage over the same load cycle as per:

$$\eta = \frac{D}{\pi \sigma_0 \epsilon_0} \tag{318}$$

Loss factor can be determined from this testing, but it is again noted that for non-linear materials that have loss coefficient(s) as a non-linear function of either strain, strain-rate, or a combination there-off, that quasi static testing while valuable for the low end range will not sufficient to characterize the TBC material across its full spectrum of behavior.

The reduction of the stress strain load unload plots to obtain damping is rather straightforward. Since the loading is almost quasi static in the rate of load/unload the

effective elastic response of the material is obtained at the very low initial load-up curves this linear behavior can be estimated in a number of ways. Some include: drawing a line between the maximum loading points, using the average of the tangents on the two curves at the zero strain crossing, using an areal centroid fit line slope. This would yield the storage modulus (E), processing of the data by equations 317 and 318 will yield the loss factor.

It is noted that after the current study this method may be worth applying to the a couple of the fully mature specimens, including a bare one, upon conclusion of the other testing for comparative purposes. There are some issues besides those raised above. The "dog-bone" configuration will not be excited in bending as in the straight beams, careful sizing and placement of the extensometer gage with respect to the length of the ceramic patch, clamping of the specimen within the jaws of the tensile testing machine will be problems to be explored. Finally it is noted that the age in history will have involved a bending stress field as opposed to a 1-D axial one, so the specimens will have varying loading history through the layers of ceramic coat, so of the inner ones may not be in the fully mature state.

References

Abu Al-Rub, R. K., and Palazotto, A. N. "Micro-mechanical theoretical and computational modeling of energy dissipation due to nonlinear vibration of hard ceramic coatings with micro-structural recursive faults," *International Journal of Solids and Structures, 47*(16), 2131-2142, 2010.

Adhikari, S. *Damping models for structural vibration*. PhD Thesis, Cambridge University, Trinity College, 2000.

Allen, K. *Evaluation Techniques for Determining Damping Mechanisms on Titanium Plates.* MS Thesis, AFIT/GAE/ENY/05-M01. Graduate School of Engineering and Management, Air Force Institute of Technology (AU), Wright Patterson AFB OH, 2005.

APS Materials, Inc., Magnesium Aluminate (Spinel) Datasheet, Dayton, OH. Website, www.apsmaterials.com . 2001.

Baker, W. *Nonlinear Oscillations (and Differential Equations): Course notes.* Unpublished manuscript, 2008

Bartlett, D. *Determination of the Complex Elastic Moduli of Materials Using A Free-Free Bar Technique fields and groups,* MS Thesis, Naval Postgraduate School (NPS), Monterey, CA 93943-5000 *,* 1994.

Beer, F. P., Johnston, E. R., & DeWolf, J. T. *Mechanics of materials* (3rd ed.). Boston: McGraw-Hill. 2002.

Blackwell, C. *The Evaluation of the Damping Characteristics of a Hard Coating on Titanium.* MS Thesis AFIT/GAE/ENY/04-M03. Graduate School of Engineering and Management, Air Force Institute of Technology (AU), Wright Patterson AFB OH, 2004.

Bohnert, A., *Heat transfer project*. AFIT: AFIT Course Report. 2008.

Bohnert, A. M. *Thermal Characterization of a Hall Effect Thruster.* MS Thesis, AFIT/GA/ENY/08-M01 . Graduate School of Engineering and Management, Air Force Institute of Technology (AU), Wright Patterson AFB OH, 2008.

Boley, B. A., & Weiner, J. H. *Theory of Thermal Stresses*. New York: Wiley. 1960.

Bose, S. *High Temperature Coatings*. Amsterdam; Boston: Elsevier Butterworth-

Heinemann. 2007.

Branam, R. *Notes on Numerical Heat Transfer - Highly Nonlinear Boundaries.* Unpublished manuscript. 2008

Braun, S., Ewins, D. J., & Rao, S. S. *Encyclopedia of vibration*. San Diego: Academic Press. 2002.

Brun, K. *Southwest Research Institute: Gas Turbine Technology Center.* http://www.swri.org/4org/d18/mechflu/planteng/gasturb/gtexp.htm. 2009.

Burgreen, D. (1971). *Elements of Thermal Stress Analysis.* C.P. Press, 1971.

Campo, A., and Villaseñor, R. (1996). "Subregion of Validity of the Lumped-Based Model for Transient, Radiative Cooling of Spherical Bodies to a Zero Temperature Sink," *International Communications in Heat and Mass Transfer, 23*(6), 855-864. 1996.

Cannon, R. H. *Dynamics of physical systems* Dover Publications. 2003.

Cervenka, M. *The Rolls Royce Trent Engine.* Unpublished manuscript. 2000.

Cheng, F. Y., and Ebrary, I. *Matrix Analysis of Structural Dynamics*. New York: M. Dekker. 2001.

Coleman, H. W. *Experimentation and Uncertainty Analysis for Engineers* . New York: Wiley. 1999.

Cook, R. D. *Concepts and Applications of Finite Element Analysis, 4th ed*. New York, NY: Wiley. 2001.

Cowles, B. "High Cycle Fatigue in Aircraft Gas Turbines—An Industry Perspective," *International Journal of Fracture, 80*(2-3), 147-163. 1989.

Cumpsty, N. A. *Jet propulsion: A Simple Guide to the Aerodynamics and Thermodynamic Design and Performance of Jet Engines* (2nd ed.). Cambridge, U.K.; New York: Cambridge University Press. 2003.

DeLeon, A. A *Finite Element Evaluation of an Experiment Related to Coating Damping Properties.* MS Thesis, AFIT/GA/ENY/09-M03 , Graduate School of Engineering and Management, Air Force Institute of Technology (AU), Wright Patterson AFB OH. 2009.

De Silva, C. *Vibration Damping, Control, and Design*. CRC Press, Boca Raton, FL. 2007.

Dennison, E. *Magnet Formulas: A Small Web Site Devoted to the Vanishing Art of Practical Magnet Design Without FEA (Finite Element Analysis).* Retrieved 04 20, 2009, from http://www.netdenizen.com/emagnet/. 2005.

El Din, S., Mahmoud, A., and Nassar, M. "Exact Solution of Free Vibrations of a Continuous Stepped Beam with M Uniform and/or Tapered Parts," *Indian Journal of Pure and Applied Mathematics, 33*(9), 1337. 2002.

Eldred, L. B., Baker, W. P., and Palazotto, A. N. "Numerical application of fractional derivative model constitutive relations for viscoelastic materials," *Computers & Structures, 60*(6), 875-882. 1996.

Farchaly, S. H., and Shebl, M. G. "Exact Frequency and Mode Shape Formulae for Studying Vibration and Stability of Timoshenko Beam System," *Journal of Sound and Vibration, 180*(2), 205-227. 1995.

Fertis, D. G. *Mechanical and Structural Vibrations,* Wiley-Interscience. New York, NY. 1995.

Fung,Y., and Tong, P. *Classical and Computational Solid Mechanics*. World Scientific, River Edge N.J. 2001.

FLIR Systems Inc., *FLIR SC660C IR Camera Users Manual*. FLIR Systems, Boston, MA. 2010.

Garrison, B. et al. *High Cycle Fatigue (HCF) Science and Technology Program 2000 Annual Report*. AFRL-PR-WP-TR-2001-2010, Wright Patterson Air Force Base, OH, 2001.

Gregori, G., Lì, L., Nychka, J., and Clarke, D. "Vibration Damping of Superalloys and Thermal Barrier Coatings at High-Temperatures," *Materials Science and Engineering: A, 466*(1-2), 256-264. 2007.

Guidoni, G., Dudek, A., Patsias, S., and Anglada, M. "Fracture Behaviour of Thermal Barrier Coatings after High Temperature Exposure in Air," *Materials Science and Engineering A, 397*(1-2), 209-214. 2005.

Hamming, R. W. *Digital Filters.* Dover Publications. 1998.

Han, S. M., Benaroya, H., and Wei, T. "Dynamics of transversely vibrating beams using four engineering theories," *Journal of Sound and Vibration, 225*(5), 935-988. 1999.

Harris, C. M., and Piersol, A. G. *Harris' shock and vibration handbook* (5th ed.). New York: McGraw-Hill. 2002.

Hass, D. Directed Vapor Deposition of Thermal Barrier Coatings. PhD Dissertation, University of Virginia. 2000.

Hatch, M. R. *Vibration Simulation Using MATLAB and ANSYS*. Boca Raton: Chapman & Hall/CRC. 2001.

Hibbitt, K., and Sorensen, I. *ABAQUS Theory Manual. User Manual and Example Manual, Version,* ANSYS Corp. 6(3). 2002.

Higdon, A. *Mechanics of Materials* (2d ed.). New York: Wiley. 1967.

Hoover, T. *An Electromagnetic Tool for Damping and Fatigue Analysis,* MS Thesis, AFIT/GSS/ENY/04-M04 , , Graduate School of Engineering and Management, Air Force Institute of Technology (AU), Wright Patterson AFB OH. 2004.

Imaoka, S. *ANSYS Memo: STI:001021A Tips and Tricks: Structural Damping*. Memo Number STI:001021A. 2001.

Incropera, F. P., & DeWitt, D. P. *Fundamentals of Heat and Mass Transfer* (4th ed.). New York: Wiley. 1996.

Ivancic, F. *The Effect of a Hard Coating on the Damping and Fatigue Life of Titanium.* MS Thesis, AFIT/GAE/ENY/03-12 , Graduate School of Engineering and Management, Air Force Institute of Technology (AU), Wright Patterson AFB OH. 2003.

Ivancic, F., and Palazotto, A. "Experimental Considerations for Determining the Damping Coefficients of Hard Coatings," *Journal of Aerospace Engineering, 18*(1), 8-17. 2005.

Lambrinou, K., Lauwagie, T., Chalvet, F., de Portu, G., Tassini, N., Patsias, S., et al. "Elastic Properties and Damping Behaviour of Alumina–Alumina/Zirconia Laminates," *Journal of the European Ceramic Society, 27*(2-3), 1307-1311. 2007.

Lazan, B. J. *Damping Materials and Members in Structural Mechanics* (1st ed.). Oxford; New York: Pergamon Press. 1968.

Lee, D. *Evaluation of Factors Contributing to Damping of Coated and Uncoated Titanium Plates.* MS Thesis, AFIT/GA/ENY/06-M06 , Graduate School of Engineering and Management, Air Force Institute of Technology (AU), Wright Patterson AFB OH. 2006.

Lee, L. T. *A Graphical Compilation of Damping Properties of Both Metallic and Non-Metallic Materials*, University of Minnesota, Minneapolis Dept. of Aeronautics and Engineering Mechanics. 1966.

Lee, S. Y., Ke, H. Y., and Kuo, Y. H. "Analysis of Non-Uniform Beam Vibration," *Journal of Sound and Vibration, 142*(1), 15-29. 1990.

Liessa, A. *Vibration of Plates.* Report No. NASA SP-160. Washington, DC: US Government Printing Office, NASA. 1969.

Lim, G., and Kar, A. "Modeling of Thermal Barrier Coating Temperature due to Transmissive Radiative Heating," *Journal of Materials Science, 44*(13), 3589-3599. 2009.

Limarga, A., Duong, T., Gregori, G., and Clarke, D. "High-Temperature Vibration Damping of Thermal Barrier Coating Materials," *Surface and Coatings Technology, 202*(4-7), 693-697. 2007.

Luo, H., Fang, X., and Ertas, B. "Hilbert transform and its Engineering Applications," *AIAA Journal, 47*(4), 923-923-932. 2009.

Meeker, D. *Finite Element Method Magnetics Version 4.2 User's Manual.* 2007

Meirovitch, L., and Parker, R. *Fundamentals of Vibrations.* McGraw-Hill. 2001.

Mensah, P., and Uppu, N. "Comparison of Thermo-Physical Properties and Thermal Performance of Macro-Cracked Thermal Barrier Coating Processed by APS with EB-PVD Thermal Barrier Coaitngs," *Thirteenth International Heat Transfer Conference,* Sydney, Australia. 2006.

MIL-HDBK-5H , *Metallic Materials And Elements for Aerospace Vehicle Structures*, AFRL/MLSC, 2179 Twelfth St., Room 122, Wright-Patterson AFB, OH 45433-7718 . 1998.

Movchan, B., and Ustinov, A. *Highly Damping Hard Coatings for Protection of Titanium Blades* Ukrainian Academy of Sciences Kiev E O Paton Institute of Electrical Welding. 2005.

Nagaoka, H. "The Inductance Coefficients of Solenoids," *Journal of the College of Science, Vol XXVII*, 1-33. 1909.

Nashif, A. D., Jones, D. I. G., and Henderson, J. P. *Vibration Damping*. New York: Wiley. 1985.

Nayfeh, A. H., and Pai, P. F. *Linear and Nonlinear Structural Mechanics*. New York: Wiley. 2004.

Nilsson, J. W., and Riedel, S. A. *Electric Circuits.* Prentice Hall. 2007.

Noda, N. *Thermal Stresses.* Taylor & Francis. 2002.

Oldfield, M., Ouyang, H., and Mottershead, J. E. "Simplified Models of Bolted Joints Under Harmonic Loading," *Computers & Structures, 84*(1-2), 25-33. 2005.

Scott-Emuakpor, S., Shen, M., George, T., and Cross, C. "An Energy-Based Uniaxial Fatigue Life Prediction Method for Commonly Used Gas Turbine Engine Materials," *Journal of Engineering for Gas Turbines & Power, 130*(6), 4:1-4:15. 2008.

Padture, N., Gell, M., and Jordan, E. *Thermal Barrier Coatings for Gas-Turbine Engine Applications* . Science Magazine, Vol 296, 280-4. 2002.

Patel, R. S., and Palazotto, A. N. "Finite-Element Method-Based Model to Study High-Cycle Fatigue in Turbine Blades," *Journal of Aerospace Engineering, 17*(2), 45-55. 2004.

Patsias, S. "Composite Damping Ceramic Coatings by Polymer Impregnation," *Key Engineering Materials, 319*, 181. 2006.

Patsias, S., Saxton, C., and Shipton, M. "Hard Damping Coatings: An Experimental Procedure for Extraction of Damping Characteristics and Modulus of Elasticity", *Materials Science and Engineering*, A 370: 412-416. 2004.

Patsias, S., Tassini, N., and Lambrinou, K. "Ceramic Coatings: Effect of Deposition Method on Damping and Modulus of Elasticity for Yttria-Stabilized Zirconia," *Materials Science and Engineering: A, 442*(1-2), 504-508. 2006.

Pearson, L. *Vibration Analysis of Commercial Thermal Barrier Coatings*. MS Thesis AFIT/GAE/ENY/08-J05 , Graduate School of Engineering and Management, Air Force Institute of Technology (AU), Wright Patterson AFB OH. 2008.

Peters, R. *Damping - Part I Background and Theory Damping - Part II Experimental Techniques.* Retrieved November 2010, 2009, from http://physics.mercer.edu/hpage/peters.html.2002.

Pilchak, A. *The Effect of Friction Stir Processing on the Microstructure, Mechanical Properties and Fracture Behavior of Investment Cast Ti-6Al-4V*. PhD Dissertation, Ohio State University, Materials Science and Engineering. 2009.

Poudou, O. *Modeling and Analysis of the Dynamics of Dry-Friction-Damped Structural Systems*. PhD Dissertation, The University of Michigan , Dept. of Mechanical Engineering. 2007.

Racher, R. P. *Magnesium Aluminate Spinel Raw Materials for High Performance Refractories for Steel Ladles*. Almatis Inc. Leetsdale, PA. unknown.

Reed, Shad. A. *Development of Experimental, Analytical, and Numerical Approximations Appropriate for Nonlinear Damping Coatings*. PhD Dissertation, AFIT/GA/ENY/DSY-07S. Graduate School of Engineering and Management, Air Force Institute of Technology (AU), Wright-Patterson AFB OH, March 2007.

Reed, S., Palazotto, A., and Baker, W. "An Experimental Technique for the Evaluation of Strain Dependent Material Properties of Hard Coatings," *Shock and Vibration, 15*(6), 697-712. 2008.

Rejda, E. F., Socie, D. F., and Itoh, T. "Deformation Behavior of Plasma-Sprayed Thick Thermal Barrier Coatings," *Surface and Coatings Technology, 113*(3), 218-226. 1999.

Robert H., J. B. *Dynamics of Physical Systems.* Dover Publications. 2003.

Runyon, B. "Automated Identification of Damping Material Properties," *Collection of Technical Papers - AIAA/ASME/ASCE/AHS/ASC Structures, Structural Dynamics and Materials Conference*, p 412-419. 2004.

Schwartz, A. J., Kumar, M., Adams, B. L., and Field, D. *Electron Backscatter Diffraction in Materials Science* Springer. 2000.

Sevostianov, I., and Kachanov, M. "Plasma-Sprayed Ceramic Coatings: Anisotropic Elastic and Conductive Properties in Relation to the Microstructure; Cross-Property Correlations," *Materials Science and Engineering A, 297*(1-2), 235-243. 2001.

Shen, M., Scott-Emuakpor, S., George, T., Cross, C., and Calcaterra, J. "Development of an Improved High Cycle Fatigue Criterion," *Journal of Engineering for Gas Turbines & Power, 129*(1), 162-169. 2007.

Shipton, M. and Patsias, S. "Hard Damping Coatings: Internal Friction as the Damping Mechanism", *Proceedings, 8th National Turbine Engine High Cycle Fatigue Conference*, Monterey, CA, April 2003.

Siegel, R., & Howell, J. R. *Thermal Radiation Heat Transfer.* Taylor & Francis. 2002

Simulia. *ABAQUS/CAE User's Manual, v6-7*. Rising Sun Mills 166 Valley Street Providence, RI 02909, USA: SIMULIA. 2007.

Slater, J. C. *Vibration Testing, with Modal Analysis and Health Monitoring*. Unpublished Book, Wright State University. 2002.

Smith, S. *The Scientist and Engineer's Guide to Digital Signal Processing*. San Diego, Calif.: California Technical Pub. 1997.

Sridharan, P. *Damping in Porcelain Enamel Coatings [Final Report, Aug. 1971 - Sept. 1974]*. Corporate Author: Minnesota Univ., Minneapolis Dept. of Aeronautics and Engineering Mechanics. 1974.

Stickler, D. C. *Heat Transfer to a Metal Slab with Radiation Boundary Conditions*. Report under AF 30(602)-2305 . The Ohio State University Research Foundation, Rome Air Force Base Air Force Systems Command . 1961.

Tamarin, Y., and ASM International. *Protective Coatings for Turbine Blades*. Materials Park, Ohio: ASM International. 2002.

Tan, Z., Su, G., and Su, J. "Improved Lumped Models for Combined Convective and Radiative Cooling of a Wall," *Applied Thermal Engineering, 29*(11-12), 2439-2443. 2009.

Tassini, N. "Comparison of the Damping and Stiffness Properties of 8wt% Yttria Stabilized Zirconia Ceramic Coating Deposited by the APS and EB-PVD Techniques," *Proceedings of SPIE, the International Society for Optical Engineering, 5760*(1), 109. 2005.

Tassini, N., Patsias, S., and Lambrinou, K. "Ceramic Coatings: A Phenomenological Modeling for Damping Behavior Related to Microstructural Features," *Materials Science and Engineering: A, 442*(1-2), 509-513. 2006.

Telford, W. M., Geldart, L., and Sheriff, R. E. *Applied Geophysics.* Cambridge Univ Press. 1990.

Thrane, N., Wismer, J., Konstantin-Hansen, H., and Gade, S. *Application Note - Practical Use of the "Hilbert transform"*. Naerum, Denmark: Brüel & Kjær, Denmark. (unknown)

Timoshenko, S. "On the Transverse Vibrations of Bars of Uniform Cross-Section," *Philosophical Magazine, 43*(6), 125-131. 1922.

Thomson, W., *Theory of Vibration with Applications*. Taylor & Francis, 1993.

Torvik, P. "Structural Dynamics," *Aerospace America, 30*(12), 70. 1992.

Torvik, P. "A Note on the Estimation of Nonlinear System Damping," *Journal of Applied Mechanics, 70*(3), 449. 2003.

Torvik, P. "Analysis of Free-Layer Damping Coatings," *Key Engineering Materials, 333*,

195-214. 2007.

Torvik, P., and Runyon, B. "Modifications to the Method of Modal Strain Energy for Improved Estimates of Loss Factors for Damped Structures," *Shock & Vibration, 14*(5), 339-353. 2007.

Torvik, P. J., Patsias, S., and Tomlinson G.R. "Characterizing the Behavior of Hard Coatings: Comparisons from Two Methodologies", *Proceedings, 7th National Turbine Engine High Cycle Fatigue Conference*, West Palm Beach, FL, May 2002.

Tzimas, E., Müllejans, H., Peteves, S., Bressers, J., and Stamm, W. "Failure of Thermal Barrier Coating Systems Under Cyclic Thermomechanical Loading," *Acta Materialia, 48*(18-19), 4699-4707. 2000.

Vaidya, R. "Effect of Plasma-Sprayed Alumina on the Strength, Elastic Modulus, and Damping of TI-25Al-10Nb-3V-1Mo Intermetallic," *Journal of Materials Engineering and Performance, 4*(3), 252-258. 1995.

Wachtman, J., and Haber, R. *Ceramic Films and Coatings*. Park Ridge, N.J., U.S.A.: Noyes Publications. 1993.

Wang, Y. N., and Huang, J. C. "Texture Analysis in Hexagonal Materials," *Materials Chemistry and Physics, 81*(1), 11-26. 2003.

Wegmann, G., Yamamoto, R., Maruyama, K., Inui, H., and Yamaguchi, M. *Gamma Titanium Aluminides*, ed. Y.-W. Kim et al., 717-724. 1999.

Wheeler, H. "Simple Inductance Formulas for Radio Coils," *Proceedings of the IRE,* 16(10), 1398-1400. 1928.

Younossi, O. *Military Jet Engine Acquisition: Technology Basics and Cost-Estimating Methodology*. Santa Monica, CA: Rand. 2002.

Youssef, F., and Lagache, M. "Simple Lumped Model Damping of Flexural and Torsional Vibration", Last retrieved December 2009, from http://www.polytech.univ-savoie.fr/fileadmin/polytech_autres_sites/sites/locie/Fiches_theses/Youssef_Fakher.pdf

Zhou, H., Li, F., He, B., Wang, J., and Sun, B. "Air Plasma Sprayed Thermal Barrier Coatings on Titanium Alloy Substrates", *Surface & Coatings Technology,* vol 201 pgs7360 – 7367. 2007.

REPORT DOCUMENTATION PAGE

Form Approved
OMB No. 074-0188

The public reporting burden for this collection of information is estimated to average 1 hour per response, including the time for reviewing instructions, searching existing data sources, gathering and maintaining the data needed, and completing and reviewing the collection of information. Send comments regarding this burden estimate or any other aspect of the collection of information, including suggestions for reducing this burden to Department of Defense, Washington Headquarters Services, Directorate for Information Operations and Reports (0704-0188), 1215 Jefferson Davis Highway, Suite 1204, Arlington, VA 22202-4302. Respondents should be aware that notwithstanding any other provision of law, no person shall be subject to an penalty for failing to comply with a collection of information if it does not display a currently valid OMB control number.

PLEASE DO NOT RETURN YOUR FORM TO THE ABOVE ADDRESS.

1. REPORT DATE *(DD-MM-YYYY)*	**2. REPORT TYPE**	**3. DATES COVERED** *(From – To)*
24-03-2011	Dissertation	Sep 2007-Dec 2010

4. TITLE AND SUBTITLE

An Experimental Characterization of Damping Properties of Thermal Barrier Coatings at Elevated Temperatures

5a. CONTRACT NUMBER

5b. GRANT NUMBER

5c. PROGRAM ELEMENT NUMBER

6. AUTHOR(S)

Oliver Easterday, Capt, USAF

5d. PROJECT NUMBER

5e. TASK NUMBER

5f. WORK UNIT NUMBER

7. PERFORMING ORGANIZATION NAMES(S) AND ADDRESS(S)

Air Force Institute of Technology
Graduate School of Engineering and Management (AFIT/EN)
2950 Hobson Way WPAFB OH 45433-7765

8. PERFORMING ORGANIZATION REPORT NUMBER

AFIT/DS/ENY/11-17

9. SPONSORING/MONITORING AGENCY NAME(S) AND ADDRESS(ES)

Air Force Research Laboratory - Turbine Engine Fatigue Facility
Attn: Dr. Tommy George, DSN 986-5531, tommy.george@wpafb.af.mil
1950 Fifth Street, Building 252
Wright-Patterson Air Force Base, OH

10. SPONSOR/MONITOR'S ACRONYM(S)

AFRL/RZTS

11. SPONSOR/MONITOR'S REPORT NUMBER(S)

12. DISTRIBUTION/AVAILABILITY STATEMENT

APPROVED FOR PUBLIC RELEASE; DISTRIBUTION UNLIMITED

13. SUPPLEMENTARY NOTES

14. ABSTRACT

This research program developed the apparatus and associated techniques to mechanically characterize the complex modulus of hard coatings across a temperature range from about 70degF to 900degF. Major effort in designing, analyzing, and experimentally validating the chamber were performed to establish that it isothermally heated a beam specimen, accomplished modal detuning, and achieved a near "free-free" boundary condition, and that the chamber was characterized for its forcing excitation. Novel aspects of the chamber include non-contact for the excitation, nearly non-contacted boundary conditions, and measurement of the field variables within the specimen using a hybrid experimental-numerical approach. This allowed for very low damping values to be measured. A common thermal barrier coating material, 8YSZ, was characterized in the chamber to determine its loss-factor (damping) and storage modulus (stiffness), at both a system-level, and well as, extracted bulk material properties-sense at temperatures from 70 to 900degF. The use of the free-decay technique using logarithmic decrement was the primary means used to characterize the coating, although some forced response was also performed and showed agreement. Some specimens that were bare titanium and bond-coat-only were studied as well. The former resulted in the discovery that the chamber is a very sensitive to slight modulus changes in classical engineering materials and the latter was shown to have fairly minimal influence on the coated beam system dynamics.

15. SUBJECT TERMS

vacuum chamber, non-linear vibration, yttrium stabilized zirconium, non-linear damping, numerical-experimental

16. SECURITY CLASSIFICATION OF:			**17. LIMITATION OF ABSTRACT**	**18. NUMBER OF PAGES**	**19a. NAME OF RESPONSIBLE PERSON**
REPORT	**ABSTRACT**	**c. THIS PAGE**			Dr. Anthony N. Palazotto
U	U	U	UU	534	**19b. TELEPHONE NUMBER** *(Include area code)* (937)-255-3636 ext. 4599 email: anthony.palazotto@afit.edu

Standard Form 298 (Rev: 8-98)
Prescribed by ANSI Std. Z39-18